Contrasting Normal and Extreme Environments: A Multiwavelength Census of Star Clusters and Star Forming Regions in Nearby Galaxies

Draft: May 11, 2020

Sean Thomas Linden

Western Springs, Illinois

B.S. Astronomy, Case Western Reserve University 2014
M.S. Astronomy, University of Virginia, 2017

A Dissertation Presented to the
Graduate Faculty of the

University of Virginia

in Candidacy for the Degree of

Doctor of Philosophy

Department of Astronomy

University of Virginia
May 2020

Committee Members:
Aaron S. Evans
Eric J. Murphy
Nitya Kallivayalil
Robert E. Davis

Abstract

This thesis is a study of star formation in a sample of luminous infrared galaxies (LIRGs) and normal star-forming galaxies in the local ($z < 0.1$) Universe. The study makes use of Hubble Space Telescope (HST), Spitzer Space Telescope and Jansky Very Large Array (VLA) data. The analysis of these data sets has allowed us to make fundamental conclusions about the nature and (in the case of star clusters) fate of star formation in a broad range of star-forming environments. The results are presented in four Chapters. In Chapter 2 I will discuss my work in identifying and characterizing the UV-bright population of super star clusters (SSCs) in a large sample of 22 LIRGs in the Great Observatories All-Sky LIRG Survey (GOALS) with HST. A major result of this work is the discovery that, relative to the normal star-forming galaxies studied with the Legacy Extragalactic UV Survey (LEGUS), the survival rate and maximum mass of SSCs is affected by the active merging-environments of U/LIRGs. In particular, the large number of $10^6 M_\odot$ young clusters identified in the sample demonstrates that LIRGs are capable of producing more high-mass clusters than what is observed to date in any lower luminosity star-forming galaxy in the local Universe. In Chapters 3 and 4 I will present results from two large VLA 33 GHz, 15 GHz, and 3 GHz imaging campaigns of star-forming regions in 50 normal star-forming galaxies, taken from the SINGS/KINGFISH legacy survey as part of the Star Formation in Radio Survey (SFRS), and 68 LIRGs taken as part of GOALS. We have measured

flux densities, spectral indices, star-formation rates (SFRs), and ages for nearly 400 individual star-forming regions across a combined galaxy sample which spans nearly 4 decades in stellar and molecular gas mass. Overall, we find that extranuclear regions identified in our LIRG survey have radio spectral indices and thermal fractions consistent with circumnuclear star-forming regions found in the SFRS, and that on 10-100 pc scales radio emission from individual star-forming regions in both normal and extreme galaxies is dominated ($> 90\%$) by free-free emission, making it one of the most direct and universal probes of the ionizing photon production rate from massive star-forming regions, free from the complications of spatially varying dust extinction. When we place all regions on the star-forming main sequence of galaxies (SFMS), defined here by the SFRS galaxy sample, we find that the star formation rates of extranuclear star-forming regions in LIRGs are not consistent with their host galaxies' globally averaged values, and have a considerably shallower SFR-M_* slope. Finally, in Chapter 5 I will present results of a HST WFC3 NUV and ACS/WFC optical study into the cluster populations of a sample of 5 LIRGs in GOALS. The filter selection and the depth of the WFC3 NUV images provide an improved age estimate and wider field of view, respectively, over our prior (Chapter 2) study. This study has yielded strong evidence that SSCs are being rapidly destroyed in luminous galaxy mergers at a rate that exceeds the cluster destruction process occurring in nearby normal galaxies at all galactocentric radii. Further, we show that the overall magnitude of this disruption is location-dependent: clusters found in the inner-regions of LIRGs show greater disruption rates relative to SSCs identified in their outer-disks. Thus, not only does rapid cluster disruption appear to be ubiquitous in LIRGs at all galactocentric radii, the magnitude of the differences between inner- and outer-disk cluster disruption are amplified relative to observations of nearby normal star-forming galaxies.

Acknowledgements

I will admit, before I start, that this will likely be the hardest section of my thesis to write, because it implies that I am really at the end, and that I have to say goodbye to so many wonderful people at the University of Virginia and in Charlottesville as a whole.

From the beginning, my love of Astronomy started at Case Western Reserve University, where I had the opportunity to work with Dr. Earle Luck and Dr. Chris Mihos. Fresh off declaring Astronomy as my undergraduate major, I was thrilled that Dr. Luck gave me a summer research project to work on in my second year. This was the first time I had ever seen what real research looked like, the first time I had ever had to use programming as part of my job, and it was the first real litmus test for if this Astronomy thing was really going to be right for me. Needless to say the project he had me working on (stacking years worth of high-resolution spectra of classical cepheid variable stars) was probably the most simple and repetitive research I have ever done in my entire life. Crazy enough, I actually loved it! I loved being able to solve problems, and in the end I am sure he re-did and re-made all the spectra I ever gave him, but it was fun to feel apart of research and apart of the greater Astronomical community as a whole.

Going into my Senior year at Case Western, Dr. Mihos took me on to complete a senior research thesis. This is where my love of galaxies, and galaxy mergers started.

Chris is one of the nicest and most down-to-earth people I have ever met in Astronomy, and I will always be grateful to him, because he started me down the path that led me here today. However, I also have Chris to thank for indoctrinating me into Supermongo, which in retrospect may have been the worst thing he could have done for me since I will likely die on that hill for the rest of my career. At that time, Chris and I were wrestling with how to properly match simulations of the M101-NGC5474 galaxy interaction with new Neutral Hydrogen observations from the Green Bank Telescope. This is when Chris suggested we reach out to a colleague of his, Josh Barnes, who had a student working with him specializing in a galaxy merger visualizations. That is where I met George Privon, who I would later find out was completing his PhD thesis at the University of Virginia with Dr. Aaron Evans.

When it came time to apply to Graduate School, I had my heart set on following in George's footsteps and attending the University of Virginia. Funny enough, I found out I had been accepted to UVA on Valentines day later that year. From the moment I got on grounds, and got a chance to meet all the students and faculty, I knew it was the right place for me. Dr. Evans took me in as his new student, and the rest you could say is history.

For my time at UVA, I want to start by thanking my research supervisors Aaron Evans, Eric Murphy and Nitya Kallivayalil who have always believed in me as a scientist and encouraged me, even in the most difficult moments. It is impossible to fully thank them enough for the endless inputs, corrections, ideas, and insights into the many random avenues and rabbit holes my research has led me down. I cannot imagine having a more supportive group of people guiding me through this journey, and one of the many things I will miss about Charlottesville is getting to interact with you all on a daily basis. I truly consider you to be my colleagues and friends, and although I will be leaving Charlottesville, this is by no means the end of our work

together.

I would also like to thank all of the wonderful collaborators I have met along the way. Specifically those in the Great Observatories All-Sky LIRG Survey (Lee Armus, Tanio Diaz-Santos, Kirsten Larson, Justin Howell, Vivian U, Anne Medling, Yiqing Song, Loreto Barcos-Munoz, Jeff Rich, Vassillis Charmandaris, Joe Mazzarella, Dave Sanders, Jason Surace, and Jason Chu), whose faces I have been staring at over telecons for many years. From the beginning you all made me feel welcome, and even though I was the youngest and least experienced member of the group, you always encouraged me to share my thoughts and valued my contributions. I would be a fraction of the scientist I am without the support from all of you, and I feel truly blessed to continue to be apart of such an amazing research group. Their is also a countless number of people I have been able to meet through conferences, workshops, and research meetings that have turned into new and exciting collaborations. To Angela Adamo, Brad Whitmore, Daniela Calzetti, Susanne Aalto, Rob Kennicutt, Adam Leroy, and many others, thank you for offering support, advice, and encouragement.

I want to also thank Dr. Wes Peters, who is the reason I decided to declare Astronomy as my major in the first place, and without him I can confidently say their is no way I am sitting here today. Wes and I entered astronomy graduate school at the same time, and although he beat me to the finish line by one year, the end of this journey feels very much like the end of an era. We started this crazy adventure together 10 years ago and now we will both finally be finished.

For all my friends in Charlottesville, both those who have moved away and those who are here, you have given me so much happiness in my life outside of science, and although it is terribly cliche, their is really nothing I can say to let you all know how important your friendships have been to me. To Trey Wenger, Lauren Bittle, Thankful Cromartie, Riley Hurst, Matt Pryal, Paul Zivick, Katrina Beitz, Molly Finn, Robby Wilson, Allison Matthews, David Bordenave, Kim Sokal, Patrick King, and Sandy Liss thank you for making graduate school all that much more bearable. The best part about staying here in for my sixth year was the extra time I got to spend with all of you.

Finally I want to thank my family, for whom I owe more to than to anyone else. To Thomas Linden, Lindy Linden, Tyler Linden, Joan Linden, and John Linden, you have made me the person I am today, and have shown me what it means to be kind and thoughtful person. Although I will not be able to celebrate my defense with you in person, your support means the world to me.

As I wrap this up, it dawns on me just how many people I have met along the way, how much love and encouragement I have received, and how lucky I am to be here. In many ways my PhD is a culmination of all of your support and guidance, and I cannot wait to continue to build upon the friendships and professional relationships I have gained in my time at UVA. People say Charlottesville is a special place, and I wholeheartedly agree. The last six years have been the best years of my life, and I will always remember my time here with the fondest of memories.

Table of Contents

List of Figures

List of Tables

Chapter 1

Introduction

1.1 Star Clusters Across Cosmic Time

Throughout the lifecycle of galaxies, molecular gas in their interstellar media is converted into stars. This process of star formation proceeds in different ways: either quiescently such that a small amount of stars are formed constantly over a period which can be as long as the age of the Universe (i.e. the Hubble Time); or at a high rate such that the fuel supply (gas) can sustain the burst for only a short period of time. A closer look at star-forming regions in our Milky Way Galaxy (MW) reveals amazingly complex modes of star formation driven by the interaction between gravitational and magnetic forces acting on the gas.

In the nearby Universe, observations of star-forming regions show us that star formation happens in a clustered fashion, i.e. stars form in ensembles, and the ones which are gravitationally bound may survive as individual objects for billions of years. These systems are commonly called star clusters and appear to be a typical outcome of the star formation process. Observations in the MW reveal that star cluster formation has proceeded more or less constantly in our Galaxy throughout its lifetime. The most

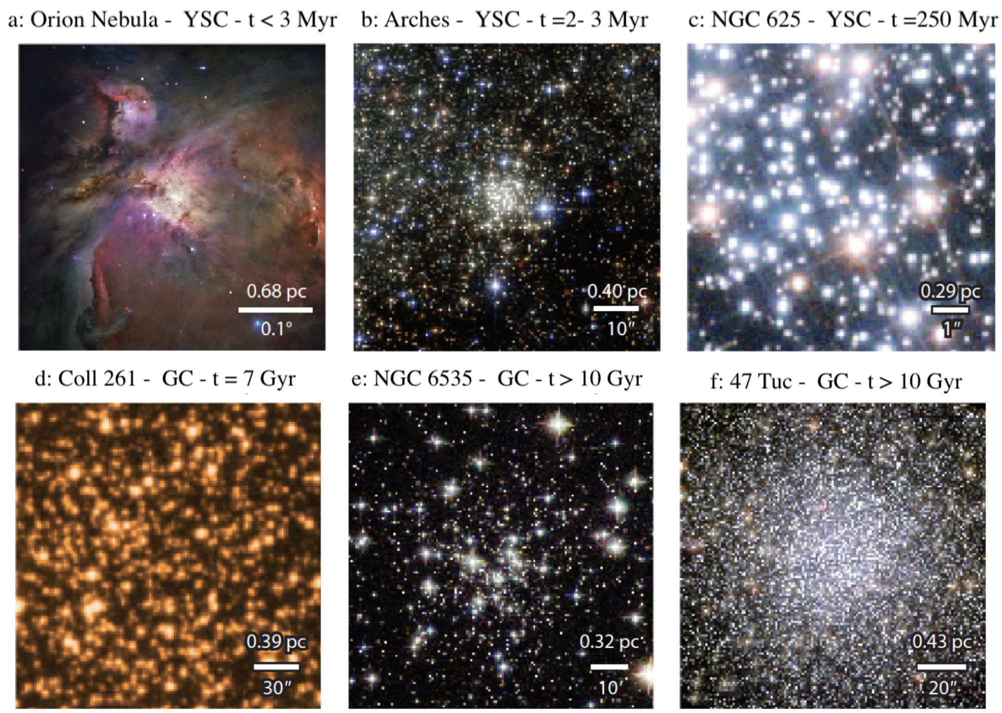

Figure 1.1: This Figure is adapted from a 2019 Annual Review of Astronomy and Astrophysics by Mark Krumholz, Christopher Mckee, and Joss Bland-Hawthorn. Shown are images of a range of YSCs, and GCs and various stages of their evolution in both the MW and nearby galaxies. The field of view in all frames is 3 pc x 3 pc, and angular sizes are indicated by scale bars. Panel a adapted from Robberto et al. (2013); Panel b from NASA press-release photography; Panel c is from Davide De Martin (ESA/Hubble) and Edward W. Olszewski (University of Arizona, USA); Panel d is from ESO/Digitized Sky Survey; Panel e from Gilles Chapdelaine; Panel f from J. Mack (STScI) and G. Piotto (University of Padova, Italy.)

massive known stellar clusters are globular clusters (GCs) with ages of a few Gyr and masses of $\sim 10^4 M_\odot$. Younger stellar clusters (YSCs) have a wide age range (usually 10-100 Myr or older) and are often formed at much smaller masses (see Figure 1.1). In the spiral arms and the galactic centre, where star formation is actively ongoing, we also observe very young stellar clusters with ages less than 10 Myr, which are still embedded or partially embedded in the cloud of gas and dust where they have formed, and have masses consistent with their ancient GC counterparts.

This early stage of YSC formation represents the most crucial moment in the lifetime of a cluster. The strong UV radiation produced by massive stars ionizes the interstellar medium (ISM) and creates emitting HII regions. Moreover, stellar winds and supernova explosions (SNe) produce feedback which act to expel any remaining gas into the surrounding ISM on timescales of a few Myr (Lada & Lada, 2003). The UV radiation can even escape the host galaxy and ionize the intergalactic medium (IGM; Bik et al., 2015, 2018; Herenz et al., 2017). For this reason, understanding the physics of cluster feedback and the escape of radiation from galaxies is fundamental to understanding galaxy formation and evolution, and even the reionization of the Universe as a whole (Bouwens et al., 2015). In the case of lower-mass dwarf galaxies, cluster feedback from very massive clusters (up to $10^7 M_\odot$) can be so strong that the radiation may alter the entire morphology of the galaxy. Despite having such a big effect on its surroundings, detailed simulations have found that the escape of UV radiation is possible only after clearing the dense gas which surrounds these very massive star clusters (Dale et al., 2015; Howard et al., 2018). If we assume that SNe dominate the gas clearing, this is achieved only after ~ 10 Myr, and thus a significant UV photon escape cannot be achieved (Kim et al., 2013b; Ma et al., 2015; Oey et al., 2017). A better understanding of how the star formation and feedback processes occur during the very first few years after massive stars are born is needed to solve this puzzle.

Although I have discussed the study of star clusters in nearby galaxies, at larger scales (for what concerns both sizes and masses) the study of clumps, still retain much of the fundamental physics described above. Star-forming clumps are generally defined as stellar ensembles with masses ranging 10^7-$10^9 M_\odot$ and sizes of approximately $100-1000$pc (Elmegreen et al., 2005). Clumps can be observed in much more distant galaxies than clusters, and the structure of high redshift galaxies are often defined by the presence of large clumps. The interest in studying such systems, and in general the clumpiness of star formation, has grown due to evidence that high redshift galaxies have on average more irregular, asymmetric, and clumpy morphologies (Glazebrook et al., 1995; Driver et al., 1995, 1998; van den Bergh et al., 1996; Im et al., 1999) relative to star-forming galaxies at lower redshifts (Lotz et al., 2004; Cassata et al., 2005; Overzier et al., 2010; Cameron et al., 2010). All these observations suggest that star formation has on average happened in a more clumpy fashion in the past. Their characterization is therefore crucial for understanding how the star formation process evolves with redshift.

The ISM conditions of local starburst and merging galaxies (where on average the cluster population is more numerous and massive, see e.g., Bastian & Silva-Villa, 2013; Whitmore et al., 2010) are in many ways similar to the intense star-forming galaxies of the early Universe. Their cluster populations can therefore help our understanding of what happens at high redshift, where our ability to study YSC formation is limited by resolution and sensitivity. Further, finding young massive clusters within local starbursts (see e.g. Larsen & Richtler, 2006) has pushed the idea that these objects are connected to the globular cluster systems observed in the MW today. Even if simple and appealing, the direct link from young massive clusters to globular clusters presents a number of still unsolved issues, from the shape of the mass function to the presence of multiple populations (and multiple metallicities) inside globular clusters (see Gratton et al., 2012; Bastian & Lardo, 2018) and not in their YSC counterparts, makes this an area of active debate.

1.2 Radio Emission as a Probe of Star Formation Activity

The link between radio continuum emission and massive star formation ($\geq 8M_{\odot}$) has been established since Bolton et al. (1949) first identified the Crab Nebula supernova remnant (SNR) as a bright, compact radio continuum source. Soon after this initial discovery, numerous other compact radio sources observed in the MW were found to be associated with known SNR (Hanbury Brown & Hazard, 1952; Baade & Minkowski, 1954), with Shklovskii (1953) identifying synchrotron radiation as the process producing the observed radio continuum. Synchrotron emission is produced by cosmic ray electrons (CRe) which are accelerated by magnetic fields found within the SNRs themselves, and is characterized by a steep power-law spectrum at radio frequencies. The discovery of the diffusive shock acceleration mechanism (DSA: Krymskii, 1977; Axford et al., 1977; Bell, 1978a,b; Blandford & Ostriker, 1978) provided a convenient process to accelerate the charged particles in SNR shock fronts, and successfully explained the radio properties of Galactic SNR (Harris, 1962; Lerche, 1980).

However not all compact radio sources identified in the MW were associated with known SNR. A study of the Rosette Nebula HII region (Ko & Kraus, 1955), demonstrated that the observed radio continuum emission was attributed to Bremsstrahlung radiation, which originates from the free-free interactions between charged particles in an ionized plasma (i.e., typically within an HII region), and is characterized by a flat power-law spectrum at radio frequencies. Even from these early observations, it was clear that free-free emission could explain many of the flat-spectrum radio sources observed in the star-forming disk of the Milky Way.

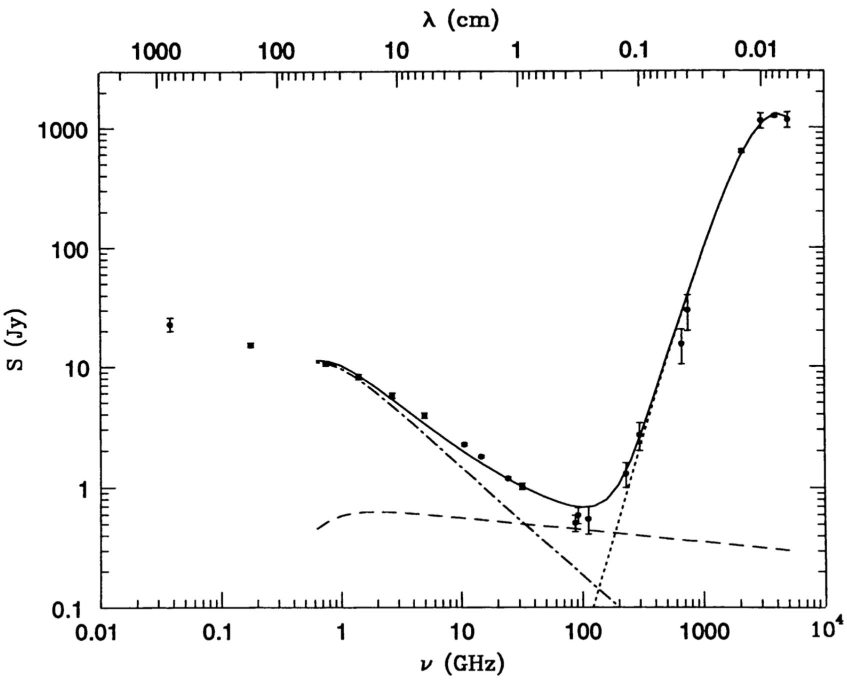

Figure 1.2: Adapted from Figure 1 in Condon (1992), a fit to the observed radio/FIR spectrum of M82 is shown. The solid line is the sum of synchrotron (dot-dashed line), free-free (dashed line), and dust (dotted line), and illustrates the contributions of these various emission processes as a function of frequency. It is clear from this fit that the HII regions in this nearby starburst galaxy start to dominate the observed spectrum at frequencies above ~ 30 GHz.

Thus a simple paradigm emerged where the radio continuum emission from a normal star-forming galaxy encompasses two main components: a thermal component originating from the ionized gas surrounding massive stars and a non-thermal component originating from cosmic ray electrons, which have been accelerated when these massive stars end their lives in supernova explosions. As both of these components are closely related to the products of massive star formation and evolution, and the typical lifetimes of massive stars are very short (a few million years; e.g., Kennicutt & Evans, 2012), radio continuum emission offers a unique tracer of star-formation activity.

Generally, the radio continuum spectral energy distributions (SED) of normal star-forming galaxies follow the same approximate shape (see Figure 1.2 Condon, 1992). Starting at low-frequencies (< 1GHz), we find that the observed radio SED is dominated by the non-thermal synchrotron component with a spectral index that closely resembles the injection index ($\alpha \sim -0.5$). At mid-radio continuum frequencies (1-10GHz; Tabatabaei et al., 2017), this non-thermal component tends to steepen due to CRe energy loss processes (with a power-law index ~ -0.8), and the thermal component starts to play a larger role in the observed SED. Finally, at even higher frequencies (≥ 10GHz) the observed SED tends to be dominated by the thermal component. At frequencies above ~ 30GHz their may be a requirement for an additional component describing Anomalous Microwave Emission (AME; however the total contribution of AME to an integrated galaxy SED is not yet known due to generally poor frequency coverage at radio continuum frequencies above 10 GHz; Dickinson et al., 2018), and at ~ 100GHz, we encounter the Rayleigh-Jeans tail of the thermal emission from cold dust in the ISM.

Thus radio continuum observations from 1-100 GHz can provide maps of the ionizing luminosity from individual massive star-forming regions, and can be used to accurately measure the current $\Sigma_{\rm SFR}$ in galaxies similar to what has been done using optical spectral line diagnostics (Calzetti et al., 1997). Further, since radio emission is optically thin, and therefore insensitive to the effects of dust extinction, we can directly probe very young ($\sim 1-2$ Myr) star clusters and HII regions still too near (or immersed in) their natal gas to be visible in the near-UV and optical with instruments like the *Hubble Space Telescope* (e.g. Kobulnicky & Johnson, 1999; Turner et al., 2000a; Johnson et al., 2001, 2003; Johnson & Kobulnicky, 2003; Johnson, 2004). Ultimately, the timescale for a cluster to escape its birth cloud is likely dependent on the density and size of the star cluster's giant molecular cloud (GMC), as well as the dynamical state and specific star formation rate (sSFR) of the galaxy.

1.3 Luminous Infrared Galaxies

Over the last three decades there has been mounting evidence to suggest that a significant mode of galaxy evolution occurs via galaxy mergers (Schweizer, 2000). This process links gas-rich disk galaxies like the Milky Way, star-bursting galaxies, active galactic nuclei (AGN), post-starburst galaxies, and gas-poor elliptical galaxies, as objects representing different stages of major galaxy mergers. Luminous and ultra-luminous infrared galaxies (LIRGs: defined as having IR luminosity, L_{IR} [$8-1000\mu m$] $\geq 10^{11} L_{\odot}$; ULIRGs $\geq 10^{12} L_{\odot}$) are the most extreme, massive, star-forming galaxies in the local Universe. The Infrared Astronomical Satellite (*IRAS*) detected a large population of these galaxies in the 1980s, and optical follow-up showed them to be primarily interacting or merging disk galaxies. As these galaxies interact the large reservoirs of gas in their discs are compressed, which triggers an enhancement of the star formation activity, particularly in their central regions (Sanders & Mirabel, 1996). Additionally, some fraction of the gas feeds giant black holes (i.e., with masses a million to a billion times the mass of our Sun) in the centers of the merging pair, which at times makes their active galactic nuclei (AGN) outshine all of the stellar light in the system.

U/LIRGs have since been established as an important extragalactic population. The primary reasons are: (i) With star formation rates (SFR) up to 2 orders of magnitude larger than what is seen in our Milky Way galaxy, these luminous infrared galaxies are essentially giant stellar nurseries for high-mass star formation (Downes & Solomon, 1998). (ii) A strong evolution in their space density with increasing redshift, z, is observed, with LIRGs becoming the dominant contributor to the IR luminosity density at $z \geq 0.5$ (Magnelli et al., 2011). (iii) Many U/LIRGs are known to host AGN, making them ideal for studying the connection between AGN and starburst

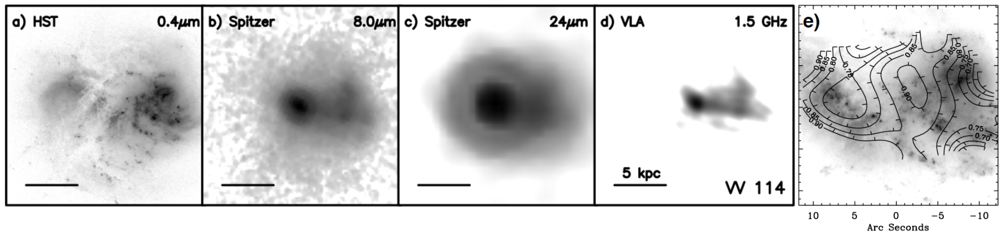

Figure 1.3: HST, Spitzer Space Telescope and VLA images of the LIRG VV 114. The source of the bulk of the energy is obscured by dust in the optical, and is thus not visible in the B-band image (Evans 2008). For e) (Murphy et al. 2013a), 8.4/1.5 GHz flux density ratio contours are shown.

activity.

However the detailed nature of U/LIRGs has proven difficult to unravel. The problem is well illustrated for VV 114 in Figure 1.3, where the optical dust lanes in the eastern part of the galaxy (Figure 1.3a) hide the sources of the bulk ($\geq$ 90%: Howell et al., 2010) of the bolometric luminosity, which emanates at mid-to-far IR wavelengths (e.g., Figure 1.3b, 1.3c). This general conclusion is representative of the U/LIRG galaxy class as a whole (e.g., Armus et al., 2009; Howell et al., 2010).

Therefore, understandably, the ultraviolet (UV) properties of these very IR-luminous galaxies have received far less scrutiny. However, the small fraction of the UV radiation from super star clusters, AGN, and diffuse stellar emission that escapes can nonetheless make LIRGs powerful sources of UV radiation (e.g., Armus et al., 2009; Evans et al., 2008; Howell et al., 2010; Inami et al., 2010). Of interest for our study of LIRGs are the luminous star clusters, which track basic information regarding the formation and fate of star formation in a variety of different environments. The *Hubble Space Telescope* (HST) has revealed evidence of star formation not only in the extended discs and tails, but also in the central regions of LIRGs where one would expect the optical light to be completely enshrouded by dust (Figure 1.3a). An analysis of these bright star clusters in the central regions form part of the star formation picture of the nuclear regions, and are clearly complemented by tracers of the more embedded star formation that accounts for the bulk of the energy generated in these galaxies.

1.4 The Great Observatories All-Sky LIRG Survey and My Contributions to Open Questions

The Great Observatories All-sky LIRG Survey (GOALS: Armus et al., 2009), is a complete, multiwavelength, census of the SF and AGN activity in all 202 U/LIRGs in the IRAS Revised Bright Galaxy Sample ($f_{60\mu m} \geq 5.24$ Jy: Sanders et al., 2003). One of the primary purposes of GOALS is to quantify the degree to which the merging environment affects the nature of star formation and AGN activity in LIRGs. Since these merging systems take a few hundred million years to coalesce, large samples of objects must be studied in order to evaluate each phase in the life cycle of LIRGs and correlate interaction stages with the evolution of star formation activity. Further, the complex structure of these dynamically evolving systems and the presence of both dust-obscured and un-obscured activity necessitates the need for high-resolution observations that sample as much of the electromagnetic spectrum as possible to best identify and reconstruct the distribution and luminosity of star-formation and AGN-related phenomena. Therefore, to understand the power sources in these galaxies, it is essential to characterize the energy budget by measuring both the emerging UV/optical and the more embedded, longer wavelength, radio emission.

As a member of GOALS my PhD thesis is focused on understanding the details of star cluster and HII region formation, their evolution (including both stellar feedback), and the impact of this process on the ISM of galaxies. In particular, the three key questions we will address are: (1) How do the properties of extra-nuclear star-forming regions in LIRGs compare to those of nearby normal star-forming galaxies, and what is their contribution to star formation in LIRGs as a whole? (2) How do the derived physical properties of HII regions and YSCs (age, mass, size, and ionizing luminosity) fit within the context of star cluster formation and evolution in extreme environments? (3) Can high-frequency radio emission be used as a measure of star formation rates in both normal and starburst galaxies (and by extension, high-z galaxies)? Local LIRGs are the only nearby massive galaxies with the appropriate physical conditions within their ISMs to directly address the open questions surrounding cluster formation and evolution discussed above.

We emphasize that in order to properly place these results in the greater context of galaxy evolution we must compare the star formation properties of LIRGs to nearby, generally isolated, normal star-forming galaxies. Additionally, since the progenitors of these IR-luminous starbursts are gas-rich spiral galaxies, it is most appropriate to compare our LIRG sample to a sample of spiral galaxies similar in nature to the Milky Way. By studying both types of galaxies at high spatial resolution we can make detailed morphological and physical comparisons of individual regions of both obscured and un-obscured star-formation activity. Ultimately we hope that by establishing what the key physical differences between LIRGs and normal star-forming galaxies are we can understand how galaxies have evolved over time and how they will continue to evolve in the future.

The research contained within this dissertation was led by the author with contribution from several collaborators. Chapters 2-3 are published in the Astrophysical Journal with co-authors which include A. Evans, E. Murphy, L. Armus, T. Diaz-Santos, K. Larson, J. Howell, V. U, G. Privon, Y Song, L. Barcos-Munoz, J. Rich, and V. Charmandaris, each of whom provided useful feedback on both the methods and the manuscripts. Chapter 4 has been accepted for publication in the Astrophysical Journal with co-authors E. Murphy, D. Dong, E. Momjian, R. Kennicutt, E. Schinnerer, J. Turner, and D. Meier, each of whom provided useful feedback on both the methods and the manuscripts. Finally, feedback on Chapter 5 was provided primarily by A. Evans with input from L. Armus and E. Murphy. The author was supported by several funding sources for his dissertation work, including the Grote Reber Doctoral Fellowship from the National Radio Astronomy Observatory and the Graduate Research Fellowship from the Virginia Space Grant Consortium.

Chapter 2

Massive Star Cluster Formation and Destruction in Luminous Infrared Galaxies in GOALS

2.1 Introduction

Galaxies with high infrared (IR) luminosities, e.g., luminous infrared galaxies (LIRGs: $L_{\rm IR}[8-1000\mu{\rm m}] > 10^{11.0}$ L$_\odot$), are rare in the local Universe, yet they are a cosmologically important class of objects because they dominate the infrared luminosity density at redshifts $z = 1-2$ (Magnelli et al., 2013). Their high bolometric luminosities emanate from energetic star-formation (SF) regions, and sometimes active galactic nuclei (AGN), which are primarily triggered by interactions and mergers of gas-rich galaxies (e.g., Sanders & Mirabel, 1996). Further, the complex structure of these dynamically evolving systems and the presence of both dust-obscured and unobscured activity necessitates the need for high-resolution observations that sample as much of the electromagnetic spectrum as possible to best identify and reconstruct the distribution and luminosity of star-formation and AGN-related phenomena, and to probe the connection between merger stage and the observed activity. Understandably, the ultraviolet (UV) properties of these very IR-luminous galaxies have received far less scrutiny. However, the small fraction of the UV radiation from super star clusters, AGN, and diffuse stellar emission that escapes can nonetheless make LIRGs powerful sources of UV radiation (e.g., Evans et al., 2008; Armus et al., 2009; Howell et al., 2010; Inami et al., 2010).

Of interest for the present study of LIRGs are the luminous star clusters (SCs), which track basic information regarding the formation and fate of star formation in a variety of different environments. The *Hubble Space Telescope* (HST) has been instrumental in the detection of numerous star clusters ($\gtrsim 1000$) in gas-rich mergers (e.g. Zepf et al., 1999; Whitmore & Schweizer, 1995; Whitmore et al., 1999) and recent merger remnants (e.g. Schweizer et al., 1996; Miller et al., 1997; Schweizer & Seitzer, 1998; Whitmore et al., 1997). The presence of young ($\lesssim 10$ Myr) and intermediate age (100 - 500 Myr) star cluster populations in late stage mergers such as the Antennae galaxies (NGC 4038/4039; Whitmore et al., 1999), Arp 220 (Wilson et al., 2006), the Mice galaxies (NGC 4676 A/B; Chien et al., 2007) is consistent with the description of these galaxies as experiencing powerful starbursts triggered by the interaction and merger of pairs of gas-rich galaxies. However, optical studies of other late stage mergers such as NGC 6240 (Pasquali et al., 2003) and NGC 7673 (Homeier et al., 2002) reveal only young star clusters, indicating that older star clusters, which would have formed earlier on in the merger, are either undetected or rare. In contrast, the lack of young star clusters in the tidal tails of NGC 520 and NGC 2623 (Mulia et al., 2015) relative to what is observed for NGC 3256 suggests that the remaining reservoirs of predominately neutral hydrogen (HI) gas in the tails cannot always form new clusters.

Many studies have been devoted to understanding the long-term stability of the youngest clusters in mergers (e.g. Fall et al., 2009; Whitmore et al., 2007). It appears that only those which survive the disruption processes and are still dense and gravitationally bound are likely to become the globular clusters (GCs) we observe today (Zhang & Fall, 1999). The relative contributions from various cluster disruption mechanisms such as infant mortality (Fall et al., 2005; Chandar et al., 2010), two-body relaxation (Fall et al., 2009), and tidal shocks (Gnedin & Ostriker, 1997) as a function of galactic environment continues to be the subject of much work. Infant mortality or rapid disruption, is caused by mass-loss during the early gas expulsion phase of cluster evolution and is expected to work on timescales of ≤ 10 Myr. In contrast, disruption from large scale shocks is expected to be important over roughly 10^8 yr timescales, and two body relaxation will cause disruption on even longer timescales (on the order of a Hubble time). Ultimately, the manner in which these young massive clusters (YMCs) evolve is crucial to connecting them to present day globular clusters. If YMCs are indeed local analogues to present-day GCs, then by understanding their formation and evolution, it is possible to gain insight into the formation of the earliest most massive clusters in the Universe (Kruijssen, 2014).

In addition to understanding the fate of clusters, it is important to understand to what degree their environment affects where and how they form, as well as what their collective properties are – e.g., the distribution of massive clusters (Initial Cluster Mass Function: ICMF) and the efficiency with which bound star clusters form (Larsen & Richtler, 2000; Bastian, 2008a). Although the low mass end of the ICMF appears to be universal (de Grijs et al., 2003; Fall & Chandar, 2012), the formation conditions of the highest-mass clusters are still subject to debate.

One idea is that the formation mechanism of the most massive clusters is independent of environment (Whitmore et al., 2007; Chandar et al., 2015), and thus the total number and maximum cluster mass scale linearly with the star formation rate of the galaxy (Hunter et al., 2003; Whitmore et al., 2010; Vavilkin, 2011). Alternatively, the formation of the most massive clusters may require special physical conditions, such as high ambient pressure or enhanced gas densities. Kruijssen (2012) predicts that the formation of bound stellar clusters takes place in the highest-density peaks of the ISM. Therefore, YMCs should form more efficiently at high gas pressures (and hence gas surface densities), because these conditions lead to higher density peaks. This leads to a non-linear scaling of the maximum cluster observed and the star formation rate surface density (Σ_{SFR}) of the galaxy.

To really quantify the role of galactic environment in shaping massive cluster formation and destruction, we need to study the properties of star clusters in a statistically larger sample of Luminous Infrared Galaxies which represent the most extreme star-forming systems observed in the local Universe. The Great Observatories All-Sky LIRG Survey (GOALS Armus et al., 2009), is a multi-wavelength imaging and spectroscopic study of a complete flux density-limited ($S_{60\mu\mathrm{m}} > 5.24$ Jy) sample of the 202 LIRGs in the *IRAS* Revised Bright Galaxy Sample (RBGS; Sanders et al., 2003). The proximity, size, and completeness of the sample, combined with broad wavelength coverage, makes GOALS the definitive sample for studying star clusters in local, luminous star forming galaxies. The present study makes use of HST UV and optical images from GOALS to estimate the cluster age distribution, the cluster mass function, and the cluster formation efficiency in a sample of 22 LIRGs.

The paper is organized as follows: In §2, the sample selection is summarized. In §3, the observations and data reduction are described, as well as our method for identifying clusters. In §4, the manner in which the cluster ages are estimated is described. In §5, the age distribution, the mass function and the cluster efficiency are discussed within the context of lower luminosity star-forming galaxies. Section 6 is a summary of the results.

Throughout this paper, we adopt a WMAP Cosmology of $H_0 = 70$ km s^{-1} Mpc^{-1}, $\Omega_{\mathrm{matter}} = 0.28$, and $\Omega_\Lambda = 0.72$ (e.g., see Armus et al., 2009).

2.2 Sample Selection

Within GOALS, there are HST B- and I-band observations of all 88 LIRGs with $L_{\mathrm{IR}} \geq 10^{11.4}$ L$_\odot$. Of those, we select the 22 LIRGs observed to have greater than 100 B-band luminous clusters ($m_{\mathrm{B}} \sim 21-23$ mag) within the central $30x30$" of the galaxy (i.e, a limit imposed by our far-UV imaging field of view – see below). In total we observed 9131 B-band luminous star clusters from galaxies in the sample (see Table 2.1).

Table 2.1: Properties of the 27 GOALS Galaxies in the sample

Name	RA	Dec	Log(LIR)	D(Mpc)	SFR[a]	IR/UV[a]	$f_\nu(FUV)$[a]	MS[b]	A_V[c]
NGC 0017	00:11:06.5000	-12:06:26.00	11.49	83	55.25	31.2	1.53e-14	5	3.0
Arp 256S	00:18:50.9000	-10:22:37.00	11.45	110	48.63	7.6	1.42e-14	3	1.7
Arp 256N	00:18:50.0430	-10:21:43.62	10.36	110	3.95	7.6	1.24e-14	3	1.7
NGC 0695	01:51:14.2000	+22:34:57.00	11.68	130	84.64	37.1	2.50e-16	0	2.8
UGC 02369	02:54:01.8000	+14:58:25.00	11.60	132	50.11	39.81	-	2	2.3
NGC 1614	04:33:59.8000	-08:34:44.00	11.60	67	51.28	15.13	-	5	4.0
2MASX J06094582-2140234	06:09:45.8000	-21:40:24.00	11.60	165	-	-	-	3	1.0
2MASX J08370182-4954302	08:37:01.8000	-49:54:30.00	11.60	115	-	-	-	3	3.7
NGC 2623	08:38:24.1000	+25:45:17.00	11.60	84	69.19	95.6	5.44e-15	5	1.5
UGC 04881	09:15:55.1000	+44:19:55.00	11.74	178	97.13	52.3	2.52e-15	2	1.9
IC 2545	10:06:04.5810	-33:53:05.55	11.70	150	-	-	-	4	4.0
NGC 3256	10:27:51.3000	-43:54:14.00	11.64	38	76.46	71.6	3.10e-14	5	3.7
Arp 148	11:03:53.2000	+40:50:57.00	11.60	160	-	-	-	2	2.1
NGC 3690E	11:28:33.4470	+58:33:46.08	11.41	45.2	45.19	29.4	3.59e-14	3	3.4
NGC 3690W	11:28:30.3390	+58:33:39.48	11.77	45.2	101.44	29.4	8.32e-14	3	3.9
NGC 5257E	13:39:57.6830	+00:49:49.80	11.32	99	36.06	9.1	2.84e-14	2	2.6
NGC 5257W	13:39:52.9530	+00:50:23.10	11.31	99	35.66	9.1	1.10e-14	2	1.8
NGC 5331S	13:52:16.2140	+02:06:03.28	11.54	139	60.78	32.7	1.32e-15	3	3.6
NGC 5331N	13:52:16.3810	+02:06:29.88	11.02	139	18.10	32.7	3.89e-15	3	1.8
UGC 09618NED02	14:57:00.8000	+24:37:04.00	11.70	150	65.56	10.47	-	1	2.4
IC 4687N	18:13:39.7490	-57:43:29.20	11.32	77	38.51	35.3	4.11e-15	2	2.8
IC 4687S	18:13:40.4750	-57:44:53.95	11.02	77	15.49	35.3	1.92e-15	2	3.7
NGC 6786	19:10:53.9000	+73:24:37.00	11.40	101	-	-	-	2	1.0
IRAS 20351+2521	20:37:17.8000	+25:31:38.00	11.50	15	-	-	-	1	9.4
II ZW 096	20:57:23.3000	+17:07:34.00	11.94	150	156.77	23.9	1.64e-14	2	3.0
ESO 148-IG002	23:15:46.8000	-59:03:16.00	12.06	190	204.60	48.8	5.88e-15	4	2.5
NGC 7674	23:27:56.7000	+08:46:45.00	11.56	120	61.26	16.4	1.42e-14	2	2.0

[a] SFRs calculated using IR+UV data taken from Howell et al. (2010) and U et al. (2012).
[b] Merger Stages taken from Haan et al. (2013) and and Stierwalt et al. (2013).
[c] The maximum A_V adopted for each galaxy taken from the literature.

2.3 Observations, Data Reduction, and Cluster Selection

The HST B- (F435W) and I- (F814W) band images were obtained with the Wide Field Camera (WFC) on the Advanced Camera for Surveys (ACS) during the period 2005 August to 2007 January (PI: A. Evans; PID 10592). In all but a few cases, the wide field-of-view of the WFC (202"x202") enabled the full extent of each LIRG to be observed. Each galaxy was observed in both filters per orbit, with two and three dithered exposures in ACCUM mode in the F814W filter and F435W filters, respectively. The approximate integration times for each filter were 21 minutes in F435W and 12 minutes in F814W. The ACS data were reduced with the Multidrizzle software included in *IRAF/STSDAS* provided by STScI, to identify and reject cosmic rays and bad pixels, remove geometric distortion, and to combine the images into mosaics. Because of the limited number of dithers, additional cosmic rays rejection routines were run on each image prior to drizzling (see Kim et al., 2013a, for a detailed description).

The HST far-UV (F140LP) and optical images in the sample were obtained with the Solar Blind Channel (SBC) on the Advanced Camera for Surveys (ACS) during the period 2008 April – 2009 August (PID 11196; PI: A. Evans). The field of view of the SBC is $\sim$ 30" x 30" – this placed a limit on the area within each LIRG over which the clusters could be analyzed. The data were taken in the ACCUM mode using the PARALLELOGRAM four-position dither pattern for a total integration time per galaxy of 40–45 minutes. We further reduced the SBC data with the Multidrizzle software included in *IRAF/STSDAS* provided by STScI, to identify and reject cosmic rays and bad pixels, remove geometric distortion, and to combine the images into mosaics.

Before an automated routine for cluster identification could be applied to the images, contamination from foreground stars and distant background galaxies outside of the area of each image subtended by the LIRG (i.e., the "sky" area) had to be minimized. Masks of each image were made by first creating a median-smoothed version of the F435W and F814W images. The effect of this filtering is to minimize structures in the sky region with spatial extents significantly smaller than the filter size (i.e., faint stars and distant background galaxies). The backgrounds, containing low pixel values, were then set to zero, while the high pixels corresponding to the LIRG were set to one. Finally, pixels associated with any bright stars in the image were set to zero. The original reduced image was then multiplied by the final mask of the galaxy to set the regions outside of the galaxy equal to zero.

Star clusters in all three bands were selected using the program SExtractor (Bertin & Arnouts, 1996). The identification of clusters and the extraction of photometry is complicated by the non-uniform surface brightness of the underlying galaxy. To estimate and subtract the underlying galaxy, Source Extractor iteratively computes the median and standard deviation of the pixels within a mesh of nxn pixels. During each iteration, outlier pixels are discarded until all of the pixels within each mesh are within 3σ of the median value. Several mesh sizes were tested, and for each mesh the photometry of several of the clusters was separately computed via the IPAC image display and analysis program Skyview and compared to values estimated from the original image (Skyview allows users to manually size and place apertures on clusters, and it allows for local background around the aperture to be subtracted). The mesh sizes varied between 9 and 14 pixels, and overall did an efficient job of removing the underlying galaxy and minimizing the creation of negative value holes surrounding clusters created through over-subtraction of the local background. Cluster photometry across all background-subtracted images was then calculated using the IDL package APER (originally modified from DAOPHOT). We used an aperture of radius 6.0 pixels for the HRC images and 3.0 pixels for the WFC images (= 0.15" in both cases). An annulus with radius 4 pixels and a thickness of 5 pixels was used to measure the local background in the WFC images; the radii and thickness of the annulus was adjusted accordingly for the SBC images. Aperture corrections were calculated based on the flux calibrations of unresolved sources by Sirianni et al. (2005). We corrected the photometry for foreground Galactic extinction, using the Schlafly & Finkbeiner (2011) dust model combined with the empirical reddening law of Fitzpatrick (1999) available through the NASA Extragalactic Database (NED).

In the process of doing the photometry, we filtered out all sources which had a signal-to-noise ratio, $S/N < 5$ and which were not visible in all three filters. This left us with a total of 1186 cluster candidates identified in the sample. We then used ISHAPE (Larsen, 1999) to measure the FWHM values for all remaining sources in all three wavelengths; this was done in order to separate stars and background galaxies from clusters. ISHAPE measures FWHMs by de-convolving the HST instrumental point spread function with a King profile, then performing a χ^2 calculation to test the goodness of fit to each individual cluster (King, 1966). ISHAPE iterates through different values for the effective radius until a minimum χ^2 is found. Similar to the approach in Mulia et al. (2015), we find that a conservative cut of 2 pixels FWHM effectively removes extended sources in both the nearest and furthest galaxies in the sample. Additionally, we made a cut of $M_B \leq -9.5$ mag, corresponding to the Humphreys & Davidson (1979) limit, where we might expect contamination of the cluster sample from single bright yellow supergiants in the Milky Way. This was shown in Whitmore et al. (2010) to be an effective way to remove foreground stars by their luminosity alone. A total of 665 clusters across all 22 LIRGs (27 nuclei) meet the above criteria.

One remaining concern with this approach was that at the average distance of the galaxies in our sample (115 Mpc), our size estimates would not correspond to physically relevant values for individual clusters. Indeed a 2 pixel FWHM at the resolution of WFC gives an average cluster size of $R_{eff} \sim 24$ pc. For the most nearby galaxies in the sample, we derive consistent results with the established cluster size in the Antennae of $R_{eff} \sim 5-10$ pc (Anders et al., 2007). However, for the most distant galaxies in the sample our size estimates are nearly three times larger (~ 37 pc), which is an effect we must take into consideration when interpreting our results (see §5). Importantly, the measured cluster sizes are all still well below the average size of an entire cluster complex or OB association ($R_{eff} \sim 100-200$ pc: Bastian et al., 2006), where the application of simple stellar population (SSP) models would be questionable.

2.4 Age-Dating Clusters

2.4.1 Model Fitting

For each cluster in each galaxy, the measured colors were compared with the evolutionary tracks from GALAXEV (version 2003), a library of evolutionary stellar population synthesis models that were computed using the isochrone synthesis code of Bruzual & Charlot (2003), hereafter referred to as BC03. This code computes the spectral evolution of a stellar population based on a stellar evolution prescription (Bertelli et al., 1994) and a library of observed stellar spectra. The output of the model SED was multiplied by the ACS F435W, F814W, and SBC 140LP filter response functions in order to obtain magnitudes and colors in these filters. We first estimate the age and the extinction A_V by performing a χ^2 fit assuming an instantaneous burst simple stellar population (SSP), a Salpeter IMF (Salpeter, 1955), and both solar and sub-solar metallicities as suggested for LIRGs by Kewley et al. (2010). We also apply a Calzetti extinction law of the form $k(\lambda) = A(\lambda)/E(B-V)_* = a + b/\lambda + c/\lambda^2 + d/\lambda^3$, where a, b, c, and d are constants in a given wavelength range, and $A(\lambda)$ is the attenuation in magnitudes. The total attenuation of the stellar continuum, $R_V = A(V)/E(B-V)_* = 4.05 \pm 0.8$, is calibrated specifically for starburst galaxies and differs from the typical Milky Way value of $R_V \sim 3.1$ (Calzetti et al., 2000). It has been shown empirically that clusters and HII regions are more heavily attenuated than the underlying stellar continuum, due to the fact that these objects are often found near dusty regions of ongoing star formation (Calzetti 1994). From galaxy to galaxy, there can be considerable variations in the detailed dust distributions, but Calzetti et al. (2000) points out that in all the cases they studied, the empirical law recovers the total dust optical depth of UV-bright starburst galaxies within a factor of two.

It is worth noting here that a major concern in estimating cluster ages is the effect of stochasticity which affects clusters with low masses. Such clusters have too low a mass to adequately produce a sufficient of number of stars in all mass ranges, and thus any age-dating prescription making use of a standard IMF fails to predict the correct cluster age. Given the distance of the LIRGs in the sample and thus the brightness of clusters detected by our HST observations, the detected clusters are unlikely to have low masses. Indeed, stochastic fluctuations are relatively minor for clusters with masses greater than $10^4 M_\odot$ (Fouesneau et al., 2012), which in our case is the lower limit of clusters we can observe.

Another factor affecting the age estimates is the metallicity. LIRGs are known to have gas-phase metallicities within 0.2 dex of solar in $12 + \log[\mathrm{O/H}]$ (Relaño et al., 2007; Rupke et al., 2008). Thus we consider both a solar ($z = 0.02$) and sub-solar

($z = 0.008$) BC03 model for each galaxy. Rich et al. (2012) also finds that the metallicity gradients in LIRGs are flattened by the merging process, allowing us to parameterize the metallicity of clusters with a single value for each galaxy.

The mass of each cluster is estimated from the observed B-band extinction-corrected luminosity and the mass-to-light ratios ($M(M_{\odot}) = L_B x(M/L)$) predicted by the unextincted model at the fitted age. The models assume that the stellar IMF for each cluster is fully sampled. The largest contribution to the uncertainty in the mass estimates are the uncertainties in the estimated ages, which are typically on the order of 0.3 dex in $\log(\tau)$. These translate to similar uncertainties of 0.3 and 2 in $\log(M)$ and M, respectively. The derived masses of the clusters depend on the IMF assumed in the stellar population models. For example, if a Chabrier IMF is adopted, the estimated mass of each cluster would decrease by a near constant 40 percent (although the shape of the mass function would not change). The average fractional uncertainty in the distances of each galaxy taken from NED are $\sim 7\%$. This would introduce uncertainties in the cluster mass estimates of roughly 13%, which is less than the error contribution from our cluster age fitting procedure.

The age and mass estimations using color-color diagrams together with evolutionary tracks suffer from age–reddening degeneracy. As pointed out in Maoz et al. (2001), the use of a UV filter when examining the colors of star clusters does help to avoid the issue of "backtracking," whereby the reddening shifts the models in a direction nearly parallel to the aging direction. However, a cluster that appears red in the FUV-B, B-I color space can still be either very old, or young and heavily obscured by dust. In particular, young star clusters are assumed to be embedded in dust that is present in the star-forming region. Despite the fact that a fraction of the dust can be cleared away from young star-forming regions in as little as a few Myr (Larsen, 2010), $0.5 \leq A_V \leq 2.5$ mag extinction has been reported for 4 Myr old clusters in nearby, lower luminosity galaxies (Whitmore & Zhang, 2002; Reines et al., 2008). Since our analysis involves the use of three filters, we cannot break this degeneracy with our photometry alone. Thus, the ages of clusters in our LIRG sample are solved for by creating a suite of SSPs within the FUV-B, B-I color space, incrementing by 0.1 in A_V as input to the extinction law, then solving for the age–reddening of each cluster based on the best χ^2 fit to an individual model within the suite. Further, it is important to note that because FUV light can accurately trace the ages of star clusters over two orders of magnitude (Meurer et al., 1995) our analysis of cluster ages is not biased by the requirement to detect a cluster in the F140LP SBC filter.

In order to better refine the age–reddening estimates for each cluster, two additional constraints were applied: First, we required that the extinction of any given cluster could not exceed estimates for the A_V of its host galaxy taken from the literature. Considering the fact that our F140LP cluster detections often span the entire SBC field-of-view, the average galaxy A_V is a good proxy for the amount of reddening one would expect each cluster could have before we are unable to detect it. It is important to note that only 5% of clusters in the final sample have extinctions which are equal to the maximum allowed for their host galaxy based on our fits, meaning that our choice of A_V is not systematically biasing our final derived values. This constraint additionally prevents our model from obtaining cluster properties with arbitrarily high extinctions and therefore cluster masses, which exceed what is possible for bound stellar clusters so far observed in extragalactic systems (Maraston et al., 2004). Second, we constructed B-I color images in order get a visual clue of where the projected dust lanes are in each galaxy. The reasoning is that by making a manual assessment of each image we can distinguish globular clusters, which have much redder colors and are often found in uncrowded regions away from sites of recent star formation (e.g., see Whitmore et al., 2014). One complicating factor is that a YMC that forms behind a projected dust lane can appear to have a color similar to these old GCs. By overlaying the cluster centroids, we identified which clusters had no obvious dust lanes in a surrounding annulus of $4-9$ pixels. These clusters are therefore more likely to be young and extincted as opposed to relatively old and dust-free clusters. The results can be seen in the false-color images shown in the appendix. In total, only 10% of the clusters modeled had ages which differ by 0.6 dex (roughly twice the expected uncertainty) when including or excluding the additional dust-lane constraints. Whitmore et al. (2014) used this additional constraint when looking at the cluster populations of 20 star-forming galaxies in the Local Universe, and found it to be effective regardless of the detailed galaxy morphologies seen in the color images.

We consider here how these constraints can be understood based on the $F435W-F814W$ value of each cluster: Clusters designated with $(F435W-F814W)<0.51$ mag can be reliably age-dated as being younger than 7 Myr, because the old-age track of the model never reach that part of the parameter space. Clusters with $(F435W-F814W)=0.51-1.0$ mag have a wide range of possible ages ($7-500$ Myr), but if the cluster resides in a dustier region of the galaxy, then it is either an unreddened to moderately reddened old cluster or a young, heavily reddened cluster. This color bin covers the widest range of cluster ages and therefore contains the largest number of SCs. Finally, any SCs with $(F435W-F814W)=1.0-1.5$ mag that do not reside in a more heavily extincted region of the galaxy are old, with ages between 500 Myr and 1 Gyr. The ages of clusters in these last two regions that lie in and around dust lanes are the ones most affected by our above criteria for solving the age–reddening degeneracy. Clusters with $(F435W-F814W)>1.5$ have ages older than 1 Gyr assuming reasonable values for the internal extinction within the galaxy.

By examining the distributions of internal visual extinction and age for each cluster derived from the model, we see that nearly 1/3 of all young clusters in the sample have a relatively small dust correction ($A_V \leq 1$), and nearly 80% of all young clusters have an $A_V \leq 2$ correction. Thus the majority of all clusters in the sample need only a relatively modest dust correction, compared to a galaxies global average, to properly derive young ages.

2.4.2 Consistency Checks: Comparison with Direct SED-Fitting

In order to account for the effect our chosen filter set has on the derived cluster properties as described above, we compare the results of anchoring each color to the F435W measurement, with the results from fitting the three broadband photometric measurements (F140LP, F435W, and F814W) simultaneously, as was similarly done in Maoz et al. (2001), and shown to be an effective way to further improve our ability to separate the effects of age and extinction. To perform this full "SED-based" fitting we use the same galaxy evolution code, extinction model (minus the additional dust-lane constraints in both cases), IMF, and metallicity. From our sample of 665 clusters, we further remove from the final analysis any clusters for which the method described in Section 4.1 and this SED fitting method do not produce ages which agree within 0.6 dex of each other. These clusters are almost always ones for which their is nearly equal probability of the cluster being young and highly-extincted or old and less heavily extincted. These highly degenerate cases are therefore removed due to their uncertain contribution to the overall shape of the age and mass distributions to be derived. This leaves us with a final sample of 484 ($\sim$ 83% of verified clusters) clusters that have age and mass estimates independent of the fitting method chosen for deriving cluster properties. We also note that of the original 67 clusters which provide inconsistent age results in our own dust-lane vs. no-dust-lane analysis, 48 ($\sim$ 83%) are kept when comparing to the results of the full SED-fit. This again shows that our additional dust-lane constraints did not systematically bias the estimation of cluster ages.

2.4.3 Consistency Checks: Comparisons with Spectroscopic-Derived Ages

Chien (2010) measure Balmer line-derived cluster ages for a sample of GOALS LIRGs. Three of the systems in their sample overlap with our present study (NGC 2623, Arp 256, and Arp 299). Figure 2.1 is a comparison of our photometrically derived ages and the Balmer line-derived ages. Approximately 77% (17 of 22) of the clusters have ages that agree to within ± 0.3 dex, and 91% (20 of 22) have ages that agree to within ± 0.6 dex. This means that the majority of our 3-band cluster ages agree with the spectroscopic ages within the uncertainty of the BC03 models. Further, it is important to note that we derive young ages for all seven of the star clusters in our sample with identified Wolf-Rayet spectral features from Chien (2010). Wolf-Rayet features are very sensitive probes of young cluster ages since they only exist for clusters with ages of $3-7$ Myr (Leitherer et al., 1999; Chien, 2010).

It is potentially not surprising that the older clusters in the sample have more uncertain spectroscopic age measurements. In particular, as a cluster ages, the strength of the Balmer lines is significantly decreased (González Delgado et al., 2005). Finally, the most discrepant age estimates come from NGC 2623. This could be due to the fact that the galaxy has a complicated morphology (Evans et al., 2008). All the young clusters identified come from a single "pie-wedge" structure to the right of the nucleus (see Additional Figures and Tables), while all the older clusters come from the nuclear regions. This makes using a simple prescription for an A_V correction over the entire FOV more uncertain.

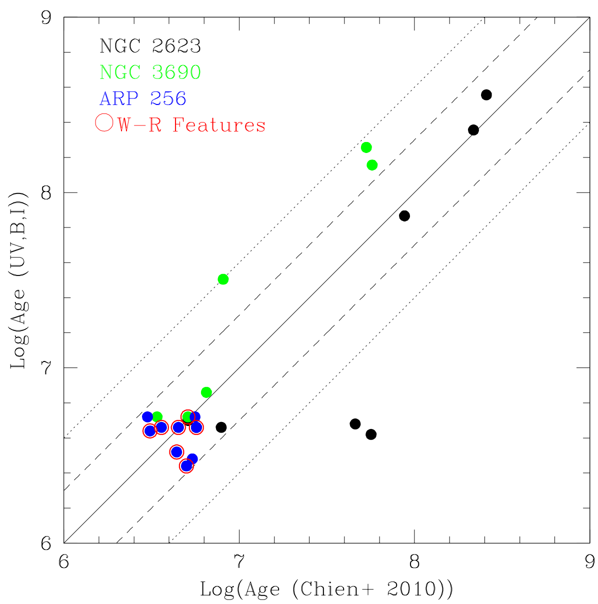

Figure 2.1: A comparison between the spectroscopically derived ages from Chien (2010) to to our UV, B, I broadband age estimates for NGC 2623, NGC 3690E/W, and ARP 256N/S. The red circles denote star clusters which have Wolf-Rayet spectral features as identified in (Chien, 2010). The solid line represents the 1 : 1 correlation, whereas the dashed and dotted lines are within 0.3 and 0.6 dex of the 1 : 1 correlation.

2.4.4 Consistency Checks: Comparisons with Paschen-β Equivalent Widths Derived from WFC3 Imaging

Larson et al. (2020) obtained Paschen-α and Paschen-β imaging for a subset of the GOALS sample, with 6 LIRGs (9 galaxies) overlapping our present HST sample. For any B-band cluster centroid that is spatially coincident with a high density clump in the Paβ images we can directly compare our cluster ages to ages derived via the equivalent width (in Angstroms) of the Paβ emission line. For an instantaneous burst SSP and a Salpeter IMF, the presence of Paβ emission constrains the burst age to less than 20 Myr because stars with masses greater than 10 $M_\odot$ are required for significant production of ionizing photons. We utilize Starburst99 models of Paβ equivalent width as a function of clump age to independently derive ages for 27 clusters in the sample (Leitherer et al., 1999).

From Figure 2.2 we find that approximately 78% (21 of 27) of the clusters have ages that agree to within ± 0.3 dex, and 96% (26 of 27) have ages that agree to within ± 0.6 dex. This shows us that the majority of all clusters we identify as having bright Paβ counterparts are indeed young. Additionally, 89% of the clusters (= 24 out of 27) which are photometrically identified as having ages less than 20 Myrs have a mean Paβ equivalent width of $\log(W(Pa\beta)[])\sim 1.7$ or $\log(Age_{SB99}(yr))\sim 6.8$. It is important to note that of the 142 young ($t \leq 10^7$ yr) star clusters photometrically identified in these 6 LIRGs, we only associated a strong Paβ clump in the continuum-subtracted image with 19% (27 of 142) of them. This fraction is likely low for two reasons: (1) Our clusters are located primarily in the central regions of the galaxies, where the continuum subtraction is much more uncertain due to the larger contribution of diffuse large-scale NIR emission. As a result, the minimum equivalent width of a marginal 3σ Paβ detection can vary by a factor of a few within a galaxy and by

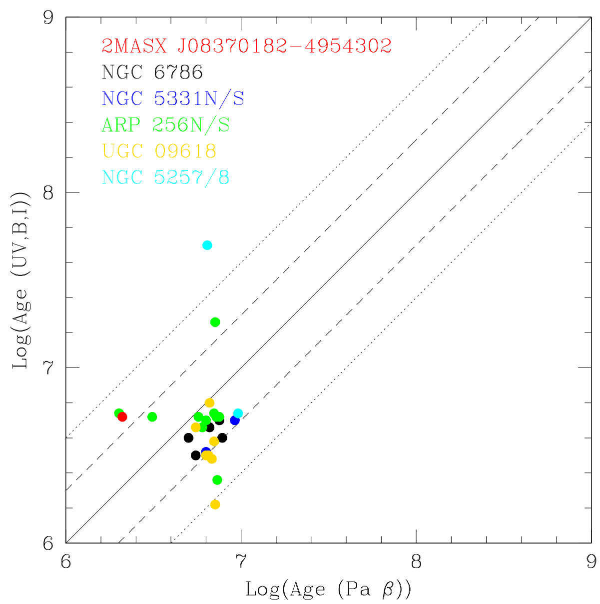

Figure 2.2: The 1 : 1 comparison of cluster ages derived using our UV, B, and I photometry and the equivalent width of the Paβ emission line associated with the cluster centroid from Larson et al. (2020). The solid line represents the 1 : 1 correlation, whereas the dashed and dotted lines are within 0.3 and 0.6 dex of the 1 : 1 correlation.

almost an order of magnitude on a galaxy-by-galaxy basis. This variation corresponds to ~ 0.3 dex change in the maximum derivable age using the SB99 model, which if we assume a $1:1$ correlation, changes the age of the oldest cluster for which we would expect a counterpart in FUV emission by the same amount. (2) The resolution of the NIR Paβ images is $0.12''$/pixel, which is a factor of two lower than what we achieve in the FUV and optical imaging. This makes detecting bright compact sources of Paβ line emission embedded in a larger diffuse GMC cloud difficult at the distance of the galaxies in our sample.

Ultimately, both the local background subtraction and resolution contribute to the lack of overlap we observe in the Paβ and FUV emission. Regardless, this is an independent verification of our ability to derive accurate young ages for clusters in the sample, and shows us that our A_V corrections can do a reasonable job at photometrically separating young and old clusters.

2.4.5 Mass-Age Diagram and Completeness

Figure 2.3 shows the derived age and corresponding mass of each cluster identified in the sample. An immediate observation one can make is the lack of low-mass, old clusters. This is due to the fact that clusters dim as they age and eventually become fainter than our UV detection limits. We also note the large number of clusters seen with ages below 10 Myr over the full range of masses.

Although the cluster fitting method can create some observed structure in the mass-age diagram, it is unlikely to do so over all masses at young ages. In particular the lack of clusters with ages of $\sim 10^7$ Myr is a common feature of model-derived mass-age diagrams of star clusters in galaxies (Gieles et al., 2005; Goddard et al., 2010). This is due to the limited age resolution and overall degeneracy of the UV-B, B-I color track at these ages (See color-color diagrams in the Additional Figures and Tables). From the histograms in Figure 2.3, we conclude that there is a genuine over-density of clusters with ages below 10 Myr compared to above 10 Myr.

In order to determine the completeness limit of the cluster sample, we used a similar prescription to Whitmore et al. (1999), and set the limit for each galaxy as the magnitude at which 50% of the clusters are detected at B and I, but are missed at FUV. The magnitude distributions for each band are corrected for foreground galactic extinction, and spatially matched to the FOV of the SBC. Of the 22 LIRGs in the sample, 19 have magnitude distributions which span the full range of observed cluster values ($M_B = -10 \sim -15$ mag), and have a mean completeness of $M_B \sim -11.2$ mag. The three remaining sources have completeness limits which are shifted to higher magnitudes $M_B \sim -13$ mag, likely due to the fact that they are all further away than the mean distance of the galaxies in the sample (115 Mpc). It is important to note however, that there are several other galaxies for which a larger distance did not result in a shifted magnitude distribution, meaning that the actual 50% limit for the sample is not a strong function of the mean distance to any galaxy. Additionally, these outliers represent only 7% of the total cluster population. Therefore, to minimize their contributions to the final adopted limit for the entire sample, we calculated a cluster-weighted mean completeness limit, and found that the mean shifted only slightly to $M_B = -11.26$.

By applying this completeness limit to the BC03 model, we can define regions of this parameter space (both as a function of cluster ages over a mass range and masses over an age range) where we are observationally complete and thus working with a mass-limited sample of clusters. Mass-limited cluster samples have the advantage over luminosity-limited samples because they recover the underlying shape of the age distribution, and are thus not affected by the distance to each galaxy. However, the total number of clusters can be highly uncertain simply because the lower mass clusters are not included. We will discuss the implications for this fact in §5.

The four cuts were selected to sample distinct regions of the mass and age distribution for which we could maintain completeness. We define Region 1 to be:

$$6 < log(M/M_{\odot}) < 8 \tag{2.1}$$

$$6.5 < log(\tau) < 8.7 \tag{2.2}$$

Region 2 to be:

$$5.3 < log(M/M_{\odot}) < 6 \tag{2.3}$$

$$6.6 < log(\tau) < 8 \tag{2.4}$$

Region 3 to be:

$$log(\tau) < 7 \tag{2.5}$$

$$5.3 < log(M/M_{\odot}) < 8 \tag{2.6}$$

and Region 4 to be:

$$7.5 < log(\tau) < 8.7 \tag{2.7}$$

$$6 < log(M/M_{\odot}) < 8 \tag{2.8}$$

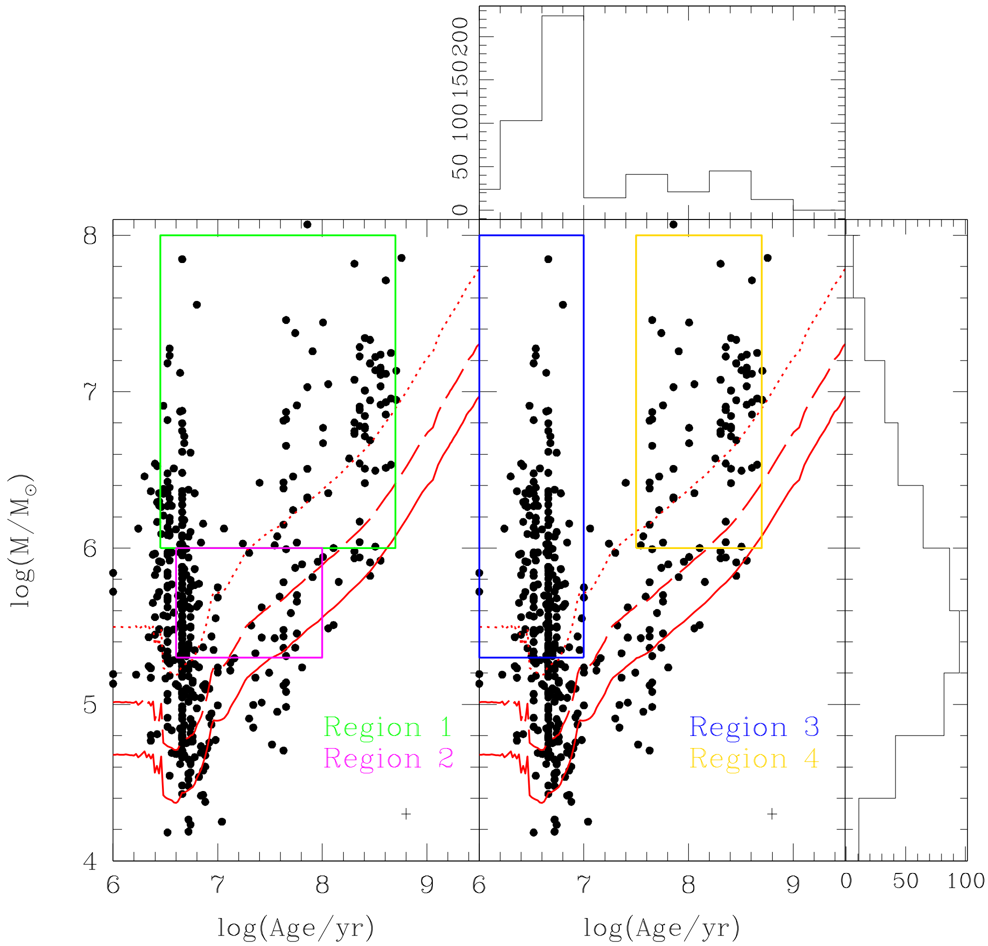

Figure 2.3: The mass, age distribution of all 484 clusters found in the 27 galaxies. The solid, dashed, and dotted red curves represent mass-age tracks produced from the BC03 model with an input of $M_B = -11.26$, $M_B = -12.07$, $M_B = -13.31$ for the 50%, 75%, and 100% completeness limits respectively. The green and purple boxes in the left panel represent Regions 1 and 2 respectively, and are used for the two mass-age cuts applied when analyzing the cluster age distribution. The blue and gold boxes in the middle panel represent Regions 3 and 4 respectively, and are used for the two mass-age cuts applied when analyzing the cluster mass distribution. The histograms show the distribution of cluster ages and masses for the full sample. The cross on the bottom right of each panel represents the median errors in cluster age and mass bootstrapped from our model.

The two mass cuts are marked as Regions 1 and 2 in the left panel of Figure 2.3. Since older clusters are intrinsically fainter, a higher mass limit will result in a cluster population that is mass-limited to a wider range of ages. Note that the chosen mass-regimes do not contain the youngest least massive clusters that are only observed in a subset of our galaxies, and thus would bias any estimate for the global mass and age distributions of all the galaxies combined. Region 2 is chosen to match the age and mass limits from Fall et al. (2005), allowing us to make accurate comparisons to the cluster population of the most well-studied nearby major merger, the Antennae Galaxy. Regions 3 and 4 are chosen to sample the young (≤ 10 Myr) and old ($\tau \geq 10^{7.5}$) clusters respectively within the completeness limit. When analyzing Regions 1, 3, and 4 we will exclude the largest mass bin of $log(M/M_{\odot}) = 8.0$. These very high masses are most likely the result of either an imperfect extinction correction or multiple star clusters in close proximity appearing as a single star cluster at the resolution of these images, resulting in a large derived total mass (See §5.2). While clusters of these masses have rarely been observed in abundance, we note that Bastian & Silva-Villa (2013) studied several young star clusters in NGC 7252 with masses greater than $10^7 M_{\odot}$, including one cluster with a total mass of $\sim 10^8 M_{\odot}$.

2.5 Discussion

After determining ages, masses, and extinctions for the entire cluster sample we directly compare these distributions with those of nearby normal and interacting galaxies. We focus on the interpretation of the derived cluster age distribution and mass function, and briefly discuss the implications for cluster formation efficiency. Ultimately, we discuss to what degree the differences observed in our cluster population can be attributed to the extreme star-forming environment unique to LIRGs in the local Universe. Individual cluster age and mass functions for the most 'cluster-rich' (i.e. greater than 25 detected clusters) galaxies are computed in Table 2.2.

2.5.1 Age Distribution

We consider the age distribution of clusters in our complete LIRG sample over the two mass ranges (i.e., Regions 1 and 2) described in §4.3. Specifically, we are interested in measuring the power law index γ, where $dN/d\tau = \tau^{\gamma}$. Figure 2.4 is a plot of the logarithm of the number of clusters per time interval, $\log(dN/d\tau)$, versus the logarithm of the cluster age, $\log(\tau)$. The plotted data are binned by 0.4 in $\log(\tau)$ so as to fully encapsulate the model errors of 0.3 in $\log(\tau)$ discussed in §4.1. We see that that a large fraction ($\sim$ 30%) of the clusters have ages less than 7.5 Myr. For the youngest most massive clusters in the sample (contained in Region 1), a weighted linear least-squares fit to the cluster age distribution gives a power law index of $\gamma = -0.9 \pm 0.3$, consistent with the derived power law index for the Antennae Galaxies within 1σ (Fall et al., 2005, ; Figure 2).

The distribution of the lower mass clusters (Region 2) can be fit with a power law index of $\gamma = -0.87 \pm 0.1$, also consistent with the derived power law index for the Antennae Galaxies within 1σ. The change in γ ($\sim$ 0.04) for the solar and sub-solar models was less than the uncertainty in the fit to the data in Figure 2.4. The similarity in the slope of the power-law index between the two mass-cuts is also further confirmation that we are working in a mass-limited regime, where the slope of the age distribution does not get systematically flatter with increasing cluster mass or distance to the host galaxy (Bastian, 2016).

Also plotted in Figure 2.4 are the age distributions for M83 and the LMC, normalized to the fitted-number of clusters in the youngest age bin. As can be seen, γ for the LIRG sample is steeper than what is measured for these lower mass, normal star-forming systems. In addition, Adamo & Bastian (2015) provide a Table summary

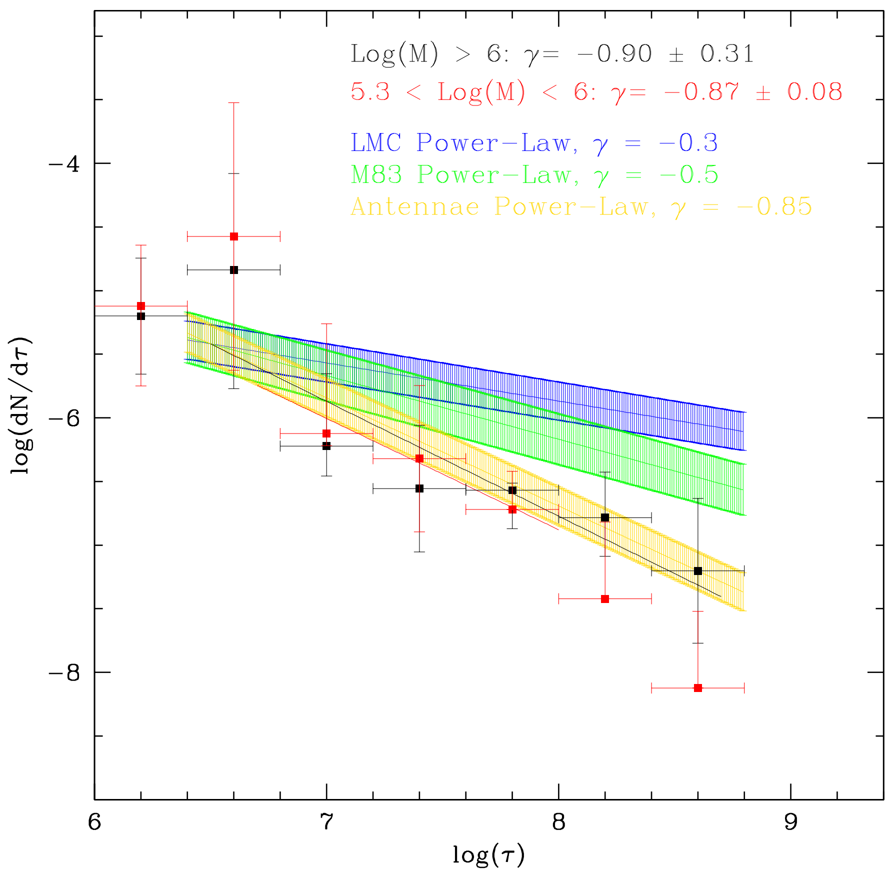

Figure 2.4: The stacked age distribution functions for all 27 galaxies. We have broken our age distribution up into the two age-mass ranges described in Equations 1 and 2, and shown as Regions 1 and 2 in the left panel of Figure 2.3. The red and black lines represent weighted linear least squares fits to the data. The blue, green, and yellow age functions of the LMC, M83, and the Antennae respectively, are taken from Adamo & Bastian (2015), and are normalized to the total number of clusters in our sample to best compare the slope for each galaxy.

of γ for several local galaxies; in all cases, γ is flatter than -1.

There are two possible interpretations of this plot:

(1) If a continuous (or near continuous) cluster formation rate is assumed during the merging process for each LIRG, then the index of $\gamma = -1$ is an indication that 90% of the clusters formed are disappearing every age dex. In the case of the Antennae Galaxies, Fall et al. (2005) concluded that the majority of the clusters are rapidly disrupted within the merger via 'infant mortality'. This scenario not only seems to fit into the nature of the violent environments of galaxy mergers, but may also explain the negative value of γ (albeit, not as negative as measured for mergers) observed in lower-mass, less star-forming, quiescent nearby spirals.

We note that when discussing 'infant mortality', it is important to mention that the rapid decrease in the number of clusters as a function of age could be due to the inclusion of young, low-density, unbound OB associations in cluster catalogues (e.g., Bastian et al., 2012; Silva-Villa et al., 2014). When these associations are removed, the age distributions for local star-forming galaxies appear to flatten. Kruijssen (2015) point out that these effects can be minimized by selecting slightly older clusters ($10-50$ Myr), so that associations will have already been dispersed into the field. If this were a dominant effect in our sample, we would expect the age distribution of Region 2 to be much flatter and inconsistent with the Antennae value. Further, while we cannot verify the amount of contamination from OB associations for the youngest clusters ($t < 10$ Myr) in our sample, the high mass cut-off for Region 1, ensures that the this effect is minimized.

(2) The star formation rate has increased such that the bulk of the star formation, and cluster formation, has happened fairly recently as a result of the interaction of the two galaxies. This seems unlikely due to the fact that many of the galaxies within the sample have been interacting for a few hundred million years, whereas

the median age of clusters for the whole sample is only $\sim 10^7$ years. Hopkins et al. (2013) finds that when simulations use realistic prescriptions for galaxy feedback, the star formation in a galaxy merger can in fact be time-variable and drops between each passage. Therefore, the average SF enhancement is only ever a factor of a few during the course of a merger, which is not enough to explain a 90% decrease in the number of clusters at each age dex (Karl et al., 2011). We could assume that all of the galaxies across the various merger stages are being viewed at these bursty peaks in the star formation rate, but we also consider this an unlikely scenario.

Under this framework, we would also be forced to accept that the star formation rates in nearby normal galaxies (which have negative γ values - though, note the above discussion of possible OB association contamination) are also increasing. In well-studied star-forming galaxies like the Milky Way and the Magellanic Clouds, the SFR is observed to have been nearly constant over the last Gyr, which argues strongly for the fact that the decline in $dN/d\tau$ is primarily a consequence of disruption in the MW and Magellanic Clouds (Harris & Zaritsky, 2009; Chandar et al., 2010).

Given the above, the most plausible explanation is that clusters are being rapidly destroyed in luminous galaxy mergers at a rate that exceeds the cluster destruction process occurring in nearby normal galaxies.

2.5.2 Mass Function

The cluster mass function (CMF) has the form $dN/dM \sim M^{\beta}$. For star clusters in our sample, this was derived by stacking the mass distributions of each galaxy, keeping the binning constant (0.4 in $\log(M)$), and then performing a cluster-weighted linear least-square fit as a function of derived mass. For clusters with ages $t \leq 10^7$ years and $t \sim 10^8$ years, we derive a mass function with a $\beta = -1.95 \pm 0.11$ and -1.67 ± 0.33, respectively (see Figure 2.5). By comparison, β is commonly measured to be -2

for the majority of lower luminosity star-forming galaxies, as well as the Antennae Galaxies (Larsen, 2010). The change in β for the solar and sub-solar models was less than the uncertainty in the fit (i.e., < 0.1) to the data in Figure 2.5.

An alternative approach to modeling the ICMF is with a two component Schechter function of the form $dN/dM = (M/M_c)^{\alpha} e^{(M/M_c)}$. For reference, the M_c, or characteristic mass, measured for the Milky Way is $\sim 10^5 M_\odot$ (Bastian, 2008b). If we assumed that a star formation rate of $\sim 100 M_\odot$/yr went into forming only clusters, the number clusters with $M \geq 10^7 M_\odot$ would still be negligible for $M_c = 10^5 M_\odot$; even if these high SFRs could be sustained for $\sim$ 100 Myrs. Thus, the mere presence of $10^7 M_\odot$ clusters in our sample indicates that the cluster formation environment in more extreme systems is different than that observed in lower-luminosity spiral galaxies.

Larsen (2010) shows that a Schechter function with a canonical -2 power-law slope and $M_c = 10^{6.3} M_\odot$ can reproduce the observed distribution in the Antennae galaxies equally well. In Figure 2.5 it is clear that we cannot simply adopt these parameters to fit our observations. Instead, we require both a slightly shallower power-law slope and a slightly larger cut-off mass due primarily to the fact that we are observing clusters with masses greater than $10^{6.5} M_\odot$, which simply are not observed in the Antennae. It is important to note that our data (Region 3 + 4) is consistent to within 1σ of a -2 power law in dN/dM over the same mass range as the Antennae, but can also be fit at the high-mass end using a modified Schechter function with a cut-off mass of $10^7 M_\odot$. This is clearly larger than what has been recently observed in M31, where the observed cut-off mass for the cluster sample is $M_c \sim 8x10^3 M_\odot$ (Johnson et al., 2017). Interestingly, in that work, the authors define a relationship for the expected M_c as a function of Σ_{SFR} as: log $M_c = (1.07 \pm 0.10) x log \Sigma_{SFR} + (6.82 \pm 0.20)$. If a typical value of Σ_{SFR} for LIRGs in the GOALS sample is used (U et al., 2012), we expect an $M_c \sim 10^7 M_\odot$, which is consistent with our derived fit, and indicates that high-mass clusters can indeed form more efficiently in higher star-forming environments.

When interpreting these results, it is important to consider several possible factors which could affect our derived mass functions:

(1) If lower-mass star clusters are preferentially disrupted, the mass distribution of the surviving star clusters in a merger remnant will be shallower than what is observed in a quiescent spiral galaxy (Kruijssen et al., 2012; Li et al., 2017). We might also expect this to correspond to a steeper age distribution for the lower-mass cluster sample (Figure 2.4; Region 2), but given that our 'low-mass' clusters are still rather massive, the lack of a clear difference in $dN/d\tau$ is not surprising. Therefore, the cluster disruption in these galaxies appears to be mostly mass-independent (i.e., we find that $\gamma \sim -1$ over the mass range of $M_{\odot} = 10^5 - 10^6$), a finding that Whitmore et al. (2010) confirmed for the Antennae over the same range of cluster masses (Figure 2.5; yellow track).

When we increase the lower limit cluster mass for Region 1 to $10^{6.5} M_{\odot}$ in Figure 2.4, we observe a disruption rate of $dN/d\tau \sim \tau^{-0.75\pm0.4}$. This leads us to conclude that cluster disruption in LIRGs appears largely consistent with what is seen in the Antennae up to $10^{6.5} M_{\odot}$. We note that the uncertainty on the measured slope is much larger than for Region 2, so in principle, gamma could be shallower than the Antennae Galaxies in this mass regime. However, if this were a strong effect in our data we would expect our observed CMF in Region 3 to be shallower than the -2 power-law used to represent the underlying ICMF.

(2) The choice of bin size for our data could systematically flatten the measured β (Maíz Apellániz et al., 2005). We use bin sizes in mass and age of 0.4 dex in $Log(M)$ and $Log(t)$, chosen to fully encapsulate the typical uncertainty associated with our age and subsequent mass estimations. To test the effect this choice has on the measured slope, we explored two other bin sizes, 0.2 and 0.6 dex respectively. We found that

the slopes derived for $dN/d\tau$ and dN/dM change on average by $0.1-0.2$ dex. As this is comparable with the 1σ uncertainties on each slope measurement, we conclude our choice of bin size is not significantly affecting our determination of the shape of the cluster mass distribution.

(3) At the resolution of our observations, multiple lower mass clusters may appear as one, massive cluster, and thus systematically flatten the CMF. To test this possibility, we ran Source Extractor on B-band and I-band WFC images of NGC4038/9 from the Hubble Legacy Archive (HLA) to identify star clusters. The distance used for NGC4038/9 is $\sim$ 24Mpc, but the median distance of our sample is four times farther away. Since the pixel scale of the Drizzlepac output images is the same, we simply smoothed the HLA images with a boxcar function of 4 pixels. Source Extractor was then run on this smoothed image with the Source Extractor results from the original, pre-smoothed images as a reference. For this step, Source Extractor only outputs sources which are both identified in the smooth image and also match a source in the original list (within a search radius of 4 pixels, i.e., the same size as the smoothing). The ratio: $(N_{orig} - N_{smoothed})/N_{orig}$ should give a upper limit for the fraction of dual sources identified as 1 in the smoothed image.

For the B-band and I-band image comparisons, this ratio is 0.3 and 0.26, respectively. Thus, roughly 30% of 'blended clusters' identified in our LIRGs with $D \geq 100$Mpc would actually be identified as a complex of single clusters at the resolution of the Antennae. By redistributing to the lower mass end this percentage of clusters, with masses greater than $5x10^6 M_{\odot}$, we observe a steepening of the mass function $\sim$ 0.1 dex. Despite this fact, it is clear that the existence of young high-mass ($\geq 10^7 M_{\odot}$) clusters in our sample cannot be solely attributed to a resolution limit. Finally, it is worth noting that cluster blending can effect the estimated cluster ages. The effect most likely pushes clusters toward the median cluster age, and thus if de-blending randomly populates the young and old cluster parts of the age distribution, there will not be a dramatic effect on γ.

Given the above, it appears that the differences in the slope observed in the LIRG sample relative to the Antennae mass function is not caused by mass-dependent cluster disruption from $10^5 - 10^{6.5} M_\odot$. When we consider the effect of a resolution limit on the high-mass end of the distribution, we can reconcile the small discrepancies in the observed slopes. Therefore, cluster formation in these galaxies can be explained with a universal -2 power law fit to the mass distribution up to at least $10^{6.5} M_\odot$. However, we emphasize that the prevalence of the most-massive clusters observed in the sample is compelling evidence that these clusters exist more predominately in the more extreme star-forming environments of LIRGs.

This idea is further supported by the fact that a Schechter function, with an $M_c \sim 10^7 M_\odot$, can also fit our data over the full range of observed cluster masses relative to a simple power-law formalism. This implies that GMCs in LIRGs can have higher ISM pressures and densities than what has been seen in other galactic environments. Recently, Maji et al. (2017) used hydrodynamic simulations of two equal-mass MW-like merging galaxies to show that such ISM conditions are actually capable of producing clusters in the range of $10^{5.5-7.5} M_\odot$ (Figure 2.4), consistent with the mass-scales we observe in our LIRG sample.

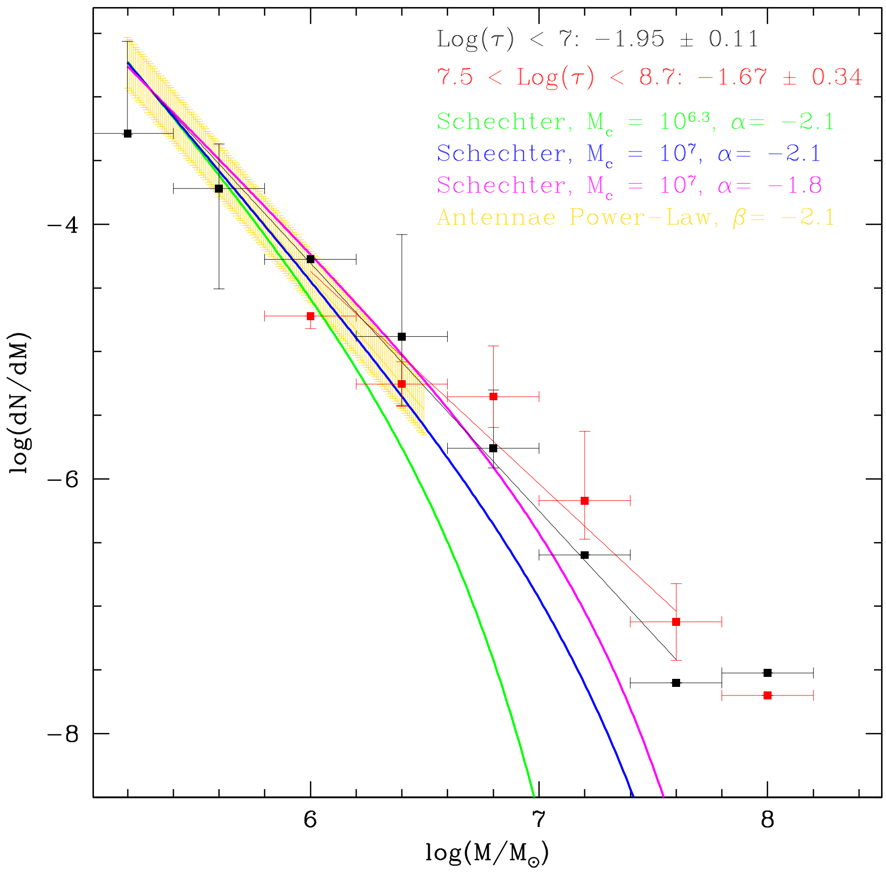

Figure 2.5: The stacked mass distribution functions for all 27 galaxies. We have separated our mass distribution up into two mass-age ranges described in Equations 3 and 4, and shown as Regions 3 and 4 in the right panel of Figure 2.3. These cuts allow us to test the effects of our completeness limits and the mass dependence of cluster disruption in the sample. The red and black lines represent weighted linear least squares fits to the data. The yellow error bars represent the mass function of the Antennae taken Whitmore et al. (2010), and is normalized to the total number of clusters in our sample. The green, magenta, and blue lines represent three different analytic Schechter function fits to the empirical distribution.

Table 2.2: Derived Age and Mass Function Slopes

Name	$\gamma_{0.02}$	σ_{γ}	$\gamma_{0.008}$	σ_{γ}	$\beta_{0.02}$	σ_{β}	$\beta_{0.008}$	σ_{β}
NGC 1614	-0.96	0.18	-1.16	0.17	-1.35	0.23	-1.60	0.10
NGC 7674	-1.67	0.46	-0.78	0.28	-1.15	0.12	-1.32	0.29
NGC 3690E	-0.62	0.54	-1.01	0.44	-1.44	0.14	-1.31	0.23
NGC 3690W	-1.26	0.12	-1.24	0.14	-1.92	0.24	-1.45	0.26
Arp 148	-0.87	0.38	-1.38	0.69	-1.44	0.17	-1.8	0.18
IRAS 20351+2521	-1.19	0.11	-1.27	0.10	-1.60	0.52	-1.12	0.25
NGC 6786	-1.29	0.18	-1.17	0.26	-1.40	0.12	-1.58	0.21
UGC 09618NED02	-1.18	0.23	-1.42	0.12	-2.13	0.47	-1.52	0.31

2.5.3 Merger Stage Dependence

Since our LIRG sample spans the full range of merger stages, we can test if our explanation of cluster formation and destruction depends on the dynamical state of the galaxy. Haan et al. (2013), Kim et al. (2013a), Stierwalt et al. (2013) have classified the merger stage of each U/LIRG in the GOALS sample based on their morphological appearance at multiple wavelengths. These merger classification schemes run from pre-first passage to single coalesced nuclei. We separated the sample into early (classes 0-2), middle (classes 3-4), and late-stage (classes 5-6) mergers. In order to quantify any differences in each age distribution we ran a KS-test comparing the normalized distributions of the early, middle, and late-stage mergers to the total sample. We find that within our sub-sample of GOALS LIRGs these individual merger stage distributions are drawn from the same parent distribution of ages with a 92% probability or higher.

For galaxies classified across all merger stage bins we find that the most massive clusters in the sample (Region 1) are always consistent with a -1 power law in $dN/d\tau$, which is further justification for combining the cluster populations for each galaxy into a single sample, and indicates that disruption does not vary much, within uncertainty, throughout the merger. It also provides credence to the idea that the SFR of a merging galaxy is bursty, which given the large size of our age bins, is an effect on the age distribution we can safely ignore. This allows us to characterize each galaxy as having an elevated but roughly continuous SFR.

When breaking the sample down to early and mid-stage mergers in Figure 2.6 we find that star clusters in both early and mid-stage mergers show a power-law distribution of $dN/dM \sim M^{-1.8}$ across both age-regimes. Additionally, each mass function is normalized by the total duration within their respective age bin in order to remove

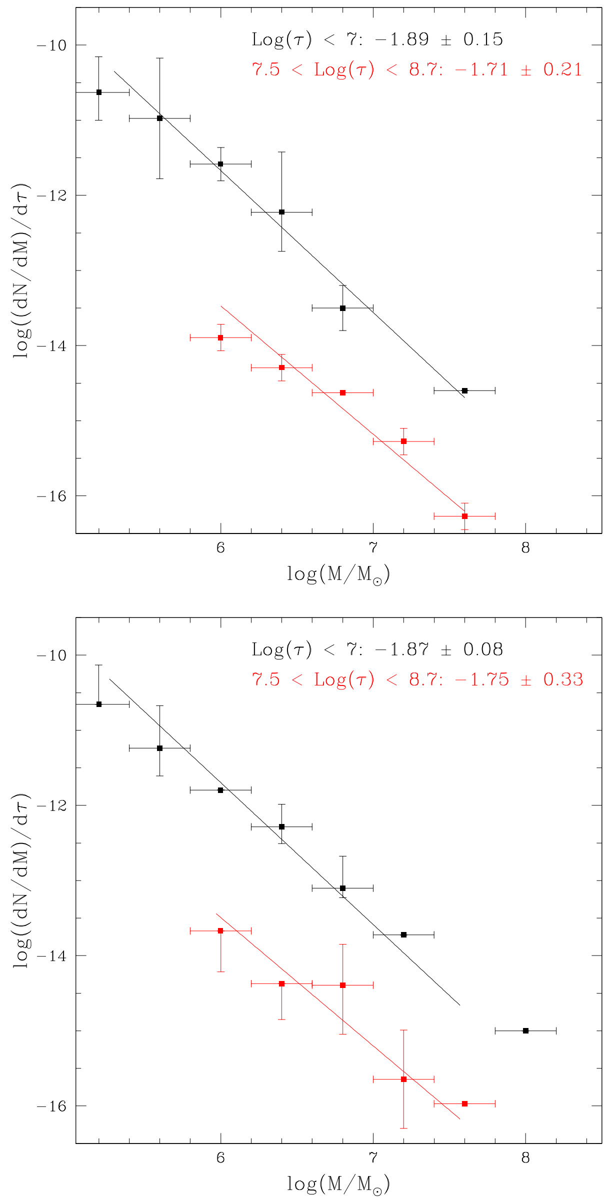

Figure 2.6: The stacked age-normalized mass distribution functions for the 11 galaxies with a merger class of 0-2 (Top Plot) and the 8 galaxies with a merger class 3-4 (Bottom Plot) identifying them as early-stage and mid-stage mergers respectively. The total number of clusters in each class is 260 and 154 for pre- and mid-stage mergers respectively. We have broken our mass distribution up into the same age ranges as in Figure 2.5

any artifacts of the bins having different time ranges. This helps to emphasize that the number of clusters that survive decreases in absolute number and independent of mass from the pre- to ongoing-merger systems.

Under the assumption of a constant SFR, the youngest clusters in each galaxy merger class will show the same slope in dN/dM. Our results are consistent with the idea that the star formation history is not changing significantly between merger stages, and thus cannot be a dominant effect in driving the observed age distributions we see for our sample, when combing all galaxies together.

Additionally, when analyzing the cluster mass distribution we assumed that the formation conditions (i.e characteristic mass M_c and slope α) do not change significantly throughout the merging process. The similarity of the slopes between each merger class is consistent with simulations of merging disk galaxies, which find that the characteristic mass M_c evolves at a rate of only $\sim 0.3 - 0.4$ dex/Gyr (Kruijssen, 2012).

2.5.4 Cluster Formation Efficiency

Finally, we consider the efficiency of cluster formation (CFE) within the high star formation rate environments of LIRGs. CFE, or Γ, is defined the ratio of the rate of stellar mass formation in bound clusters, $\dot{M}_{\mathrm{SC}}$, to the global star formation rate, $\dot{M}_{\mathrm{SF}}$, over the same time interval, i.e.,

$$\Gamma = \frac{\dot{M}_{\mathrm{SC}}}{\dot{M}_{\mathrm{SF}}} x100\%. \tag{2.9}$$

For our sample, the fact that we do not detect clusters well below $10^5 M_{\odot}$, and that we have significant cluster disruption over all masses, makes the estimation of the cluster formation efficiency (CFE) highly uncertain.

This is compounded by the fact that our UV-Bright cluster population is not sampling the full SFR as traced by the total UV+IR based SFR measurements from Howell et al. (2010). Additionally, we cannot match our UV-based CFR to the total GALEX UV SFR estimation because the field of view of the SBC is $\sim 1/140$ that of GALEX, and thus a correction for the clusters we miss is uncertain. The large amount of obscuring dust also makes a completeness correction to derive a total mass and CFR based on our mass distributions difficult for our LIRG sample. Johnson et al. (2016) notes that CFE calculations are best done in dust-free environments that show little sign of significant cluster disruption, a scenario we are simply not presented with in our sample. Therefore we leave a discussion about CFE in LIRGs to future studies involving deep IR-based observations that have both a larger FOV, and the ability to detect more dust-enshrouded low-mass clusters.

2.6 Summary

Hubble Space Telescope ACS/HRC FUV (F140LP) and ACS/WFC optical (F435W and F814W) observations of a sample of 22 star cluster-rich LIRGs in the GOALS sample were obtained. These observations have been utilized to derive the ages and masses of the star clusters contained within these systems in order to examine the cluster properties in extreme starburst environments relative to those in nearby, lower luminosity star-forming galaxies. The following conclusions are reached:

(1) We have detected 665 clusters within the inner 30"x30" of these 22 LIRGs (27 nuclei). These clusters have $S/N \geq 5$ in all three filters and de-convolved FWHMs as measured by ISHAPE of ≤ 2 pixels.

(2) Cluster ages have been derived by assuming an instantaneous SSP, Salpeter IMF, and either a solar or sub-solar metallicity. By requiring the derived cluster ages to be consistent when using both a color-color and SED-based fitting technique, we obtain a final sample of 484 clusters whose properties are reliably constrained within the

1σ uncertainties of the SSP models. The derived cluster ages imply a disruption rate of $dN/d\tau = \tau^{-0.9+/-0.3}$ for cluster masses $\geq 10^6 M_\odot$, and $dN/d\tau = \tau^{-0.87+/-0.08}$ for cluster masses $10^{5.3} < M < 10^6 M_\odot$. This is consistent with what is seen in the Antennae, and indicates the general influence mergers have on the creation and destruction of star clusters. The measured γ is steeper than that measured for lower mass, less star-forming systems in the local Universe, implying that the merging process produces a fundamentally different cluster disruption law.

(3) We have identified a large number of $M \geq 10^6 M_\odot$ clusters in the sample, which indicates that the more extreme star-forming environments of LIRGs are capable of producing more high-mass clusters than what is observed in galaxies like the Milky Way or even the Antennae (Larsen, 2009; Bastian et al., 2012; Whitmore et al., 2010). The derived cluster masses also imply a CMF for the sample of $dN/dM = M^{-1.95+/-0.11}$, which is consistent with a -2 power law in dN/dM. Together with the fact that we do not see a significant change in the age distribution slope as a function of mass, we interpret our mass function slope as evidence against mass-dependent cluster disruption at $M \geq 10^{5.3} M_\odot$ which would flatten the observed CMF relative to a canonical -2 power law in this regime.

2.7 Additional Figures and Tables

In the following sections we give a brief description of the basic morphology and star cluster spatial distributions within each galaxy, as well as the adopted values for the maximum amount of visual extinction we use in our model. See Evans et al. in prep for a detailed description of all 88 LIRGs in the GOALS sample that have been observed with HST.

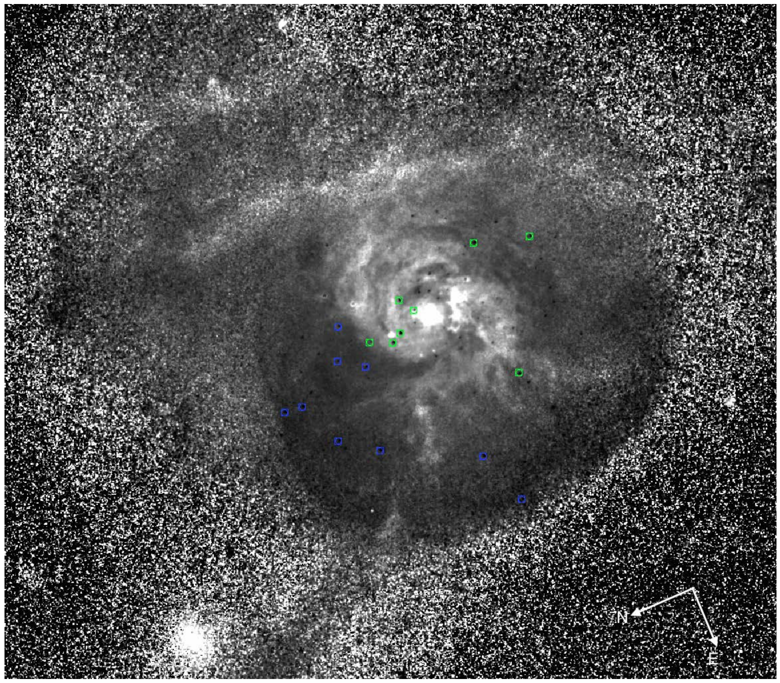

Figure 2.7: Inverted black and white B-I image of NGC 0017 taken with HST ACS/WFC F814W and F435W. The bright emission corresponds to redder (i.e. dustier) regions of the galaxy. The blue centroids correspond to clusters found in relatively "dust-free" regions of these galaxies, whereas the green centroids correspond to clusters found in relatively dustier regions of the galaxy.

2.7.1 NGC 0017

NGC 0017 is a late stage merger that contains a single resolved nucleus surrounded by dust lanes associated with spiral arms in the inner few kpc. Several bright star clusters are visible within this nuclear spiral region. The maximum A_V adopted for this galaxy is 3.0 mags of visual extinction (Dametto et al., 2014).

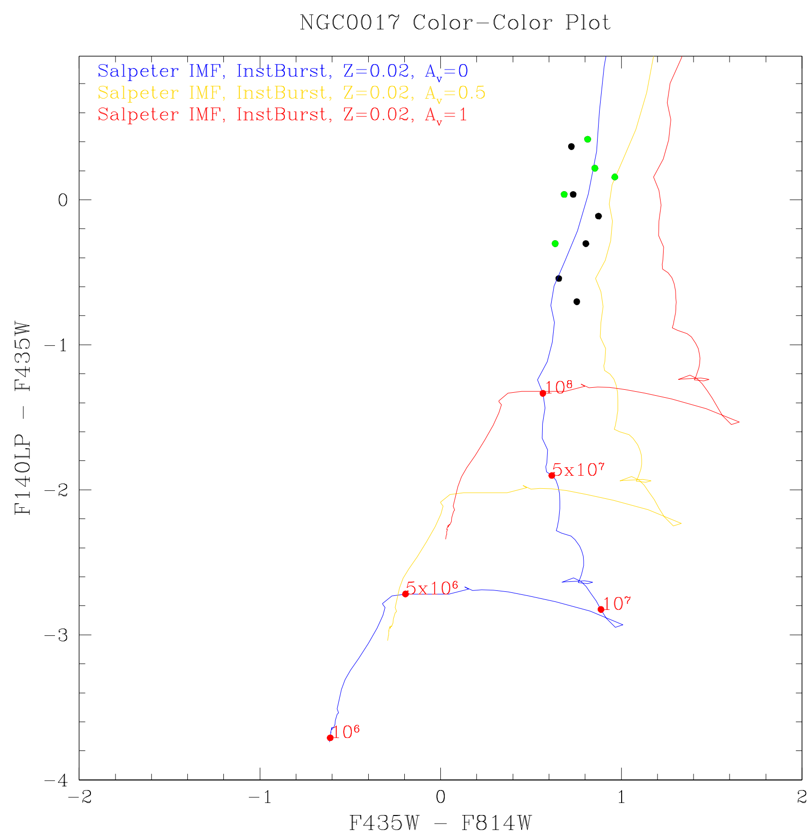

Figure 2.8: Color-Color plot of all star clusters identified in NGC 0017 in F814W, F435W, and F140LP plotted against SSP models with various amount of visual extinction. The green points correspond to the clusters found in dustier regions of the galaxy in Figure 2.7.

Table 2.3: Observed Properties of Star Clusters in NGC 0017

ID	RA	Dec	M_B	σ_B	M_I	σ_I	M_{FUV}	σ_{FUV}
1	2.776819641	-12.10616498	-13.81	0.01	-14.87	0.01	-12.67	0.03
2	2.777320196	-12.10713204	-13.89	0.01	-14.53	0.01	-14.20	0.01
3	2.777273773	-12.10658526	-11.05	0.06	-11.91	0.05	-10.84	0.18
4	2.777432692	-12.10695518	-13.56	0.01	-14.43	0.01	-12.32	0.05
5	2.777660645	-12.10636335	-12.56	0.01	-13.44	0.01	-12.68	0.03
6	2.778745035	-12.10880075	-14.29	0.01	-15.27	0.01	-12.96	0.02
7	2.777920896	-12.10509066	-12.03	0.01	-12.76	0.01	-11.67	0.08
8	2.778717571	-12.10546794	-10.72	0.02	-11.38	0.02	-11.27	0.12
9	2.779140091	-12.10608216	-15.05	0.01	-15.86	0.01	-15.36	0.01
10	2.779887259	-12.10772035	-11.65	0.01	-12.39	0.01	-11.62	0.16
11	2.780845501	-12.10807908	-10.35	0.03	-11.11	0.03	-11.06	0.02
12	2.777023706	-12.10749699	-13.10	0.04	-14.80	0.16	-11.10	0.14
13	2.776766427	-12.10731248	-13.23	0.02	-14.20	0.02	-13.08	0.02
14	2.776532232	-12.10983287	-11.54	0.01	-12.36	0.01	-11.13	0.08
15	2.776287946	-12.10888848	-13.35	0.01	-14.04	0.01	-13.32	0.02

Table 2.4: Derived Properties of Star Clusters in NGC 0017

ID	Log(Age)	σ_{Age}	Log($M/M_{\odot}$)	σ_M	A_V	σ_{A_V}
1	8.61	0.02	7.34	0.16	0.20	0.05
2	8.36	0.02	7.11	0.17	0.10	0.06
3	8.46	0.58	6.04	0.61	0.10	0.63
4	8.66	0.02	7.18	0.16	0.01	0.04
5	6.66	0.81	6.18	0.70	1.90	0.77
6	8.66	0.69	7.47	0.16	0.01	5.27
7	6.66	0.03	6.08	0.16	2.10	0.04
8	6.66	0.79	5.29	0.69	1.60	0.74
9	6.64	0.10	7.10	0.16	1.80	5.62
10	6.66	2.37	5.87	0.16	2.00	4.73
11	6.34	0.86	5.65	0.67	2.10	0.71
12	8.46	0.18	7.55	0.52	1.40	0.51
13	8.36	0.29	7.00	0.37	0.40	0.33
14	8.51	1.93	6.23	0.16	0.01	0.03
15	8.46	5.32	6.91	0.16	0.01	0.78

2.7.2 Arp 256S

Arp 256 is a mid-stage merger containing a southern (MCG-02-01-051) and northern (MCG-02-01-052) galaxy. Arp 256S has an elongated $\sim 1''$ (400 pc) nucleus, and the north and southwest tails contain the majority of the star clusters in the galaxy. The maximum A_V adopted for this galaxy is 1.7 mags of visual extinction (Smith et al., 2014).

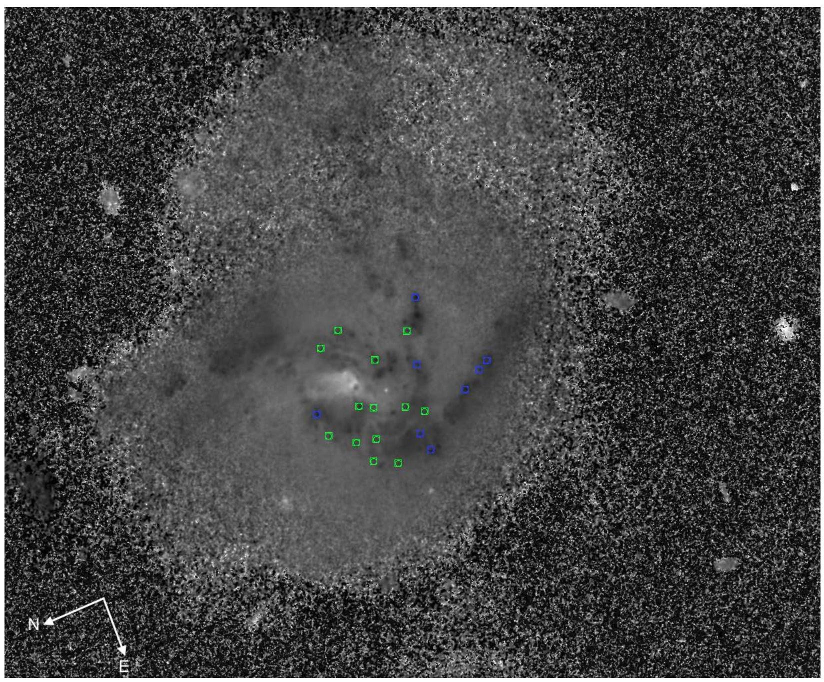

Figure 2.9: Inverted black and white B-I image of Arp 256S taken with HST ACS/WFC F814W and F435W. The bright emission corresponds to redder (i.e. dustier) regions of the galaxy. The blue centroids correspond to clusters found in relatively “dust-free” regions of these galaxies, whereas the green centroids correspond to clusters found in relatively dustier regions of the galaxy.

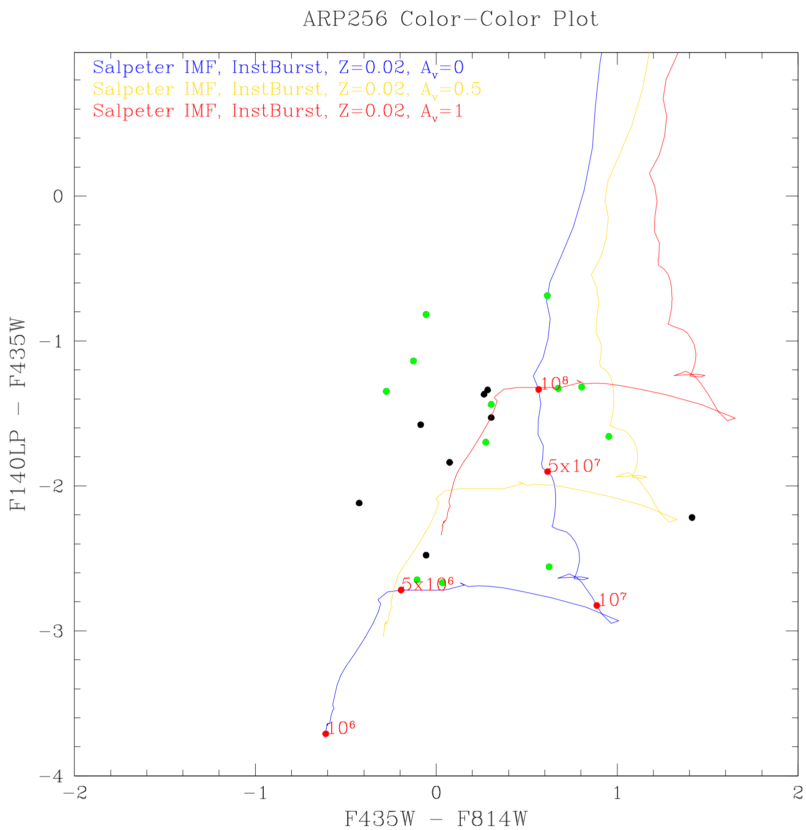

Figure 2.10: Color-Color plot of all star clusters identified in Arp 256S in F814W, F435W, and F140LP plotted against SSP models with various amount of visual extinction. The green points correspond to the clusters found in dustier regions of the galaxy in Figure 2.9.

Table 2.5: Observed Properties of Star Clusters in Arp 256S

ID	RA	Dec	M_B	σ_B	M_I	σ_I	M_{FUV}	σ_{FUV}
1	4.713679548	-10.37685826	-10.41	0.05	-11.03	0.07	-12.97	0.05
2	4.710809481	-10.37888736	-12.54	0.01	-12.61	0.02	-14.38	0.01
3	4.710599656	-10.377146	-10.45	0.13	-10.34	0.22	-13.10	0.04
4	4.711341331	-10.37839176	-11.99	0.02	-12.79	0.02	-13.31	0.03
5	4.71074686	-10.37664793	-12.51	0.03	-13.46	0.04	-14.17	0.03
6	4.711535325	-10.37750998	-13.53	0.02	-13.80	0.02	-15.23	0.02
7	4.712724227	-10.37952183	-10.43	0.15	-11.84	0.08	-12.65	0.13
8	4.712065091	-10.37821862	-12.93	0.03	-13.21	0.04	-14.27	0.03
9	4.712819126	-10.37928414	-11.79	0.05	-12.05	0.09	-13.16	0.08
10	4.713033719	-10.37882884	-12.69	0.02	-12.63	0.05	-15.17	0.02
11	4.712218761	-10.37674074	-14.31	0.02	-14.61	0.02	-15.75	0.01
12	4.712398738	-10.3769871	-12.19	0.03	-12.13	0.21	-13.01	0.05
13	4.712719547	-10.37756498	-11.80	0.06	-11.67	0.12	-12.94	0.10
14	4.71300344	-10.37787256	-12.42	0.03	-13.03	0.03	-13.11	0.04
15	4.71191981	-10.37588942	-12.99	0.03	-12.56	0.06	-15.11	0.01
16	4.713366435	-10.37755202	-13.26	0.05	-13.56	0.07	-14.79	0.03
17	4.713006219	-10.37670878	-11.65	0.10	-11.37	0.15	-13.00	0.05
18	4.712859587	-10.37631389	-11.93	0.03	-12.60	0.05	-13.26	0.04
19	4.713776161	-10.37757731	-12.27	0.04	-12.18	0.04	-13.85	0.06
20	4.713381893	-10.37643331	-10.68	0.07	-10.71	0.14	-13.35	0.03

Table 2.6: Derived Properties of Star Clusters in Arp 256S

ID	Log(Age)	σ_{Age}	Log($M/M_{\odot}$)	σ_M	A_V	σ_{A_V}
1	6.88	0.17	4.60	0.20	0.10	0.07
2	6.64	0.02	5.51	0.18	0.70	0.05
3	5.10	0.43	5.10	0.33	0.80	0.23
4	7.81	0.42	6.12	0.34	0.30	0.28
5	7.54	0.28	6.24	0.26	0.40	0.18
6	6.46	0.27	6.49	0.33	1.30	0.27
7	5.10	0.09	5.57	0.29	1.70	0.16
8	6.66	0.04	5.85	0.20	1.00	0.09
9	6.66	0.41	5.40	0.29	1.00	0.22
10	6.40	0.64	5.78	0.35	0.80	0.30
11	6.60	0.06	6.34	0.23	1.00	0.15
12	6.66	0.25	5.66	0.28	1.20	0.21
13	6.66	0.72	5.40	0.21	1.00	0.10
14	6.66	0.81	5.92	0.68	1.50	0.73
15	6.66	0.76	5.56	0.18	0.40	0.04
16	6.56	0.17	5.99	0.35	1.10	0.30
17	6.66	0.76	5.29	0.24	0.90	0.11
18	6.74	0.53	5.48	0.43	1.00	0.39
19	6.66	0.27	5.48	0.19	0.80	0.06
20	6.74	0.38	4.45	0.31	0.01	0.24

2.7.3 Arp 256N

Arp 256N has a central, point-like nucleus. The majority of the star clusters are seen along the tidal tails in this galaxy. The maximum A_V adopted for this galaxy is 1.7 mags of visual extinction (Smith et al., 2014).

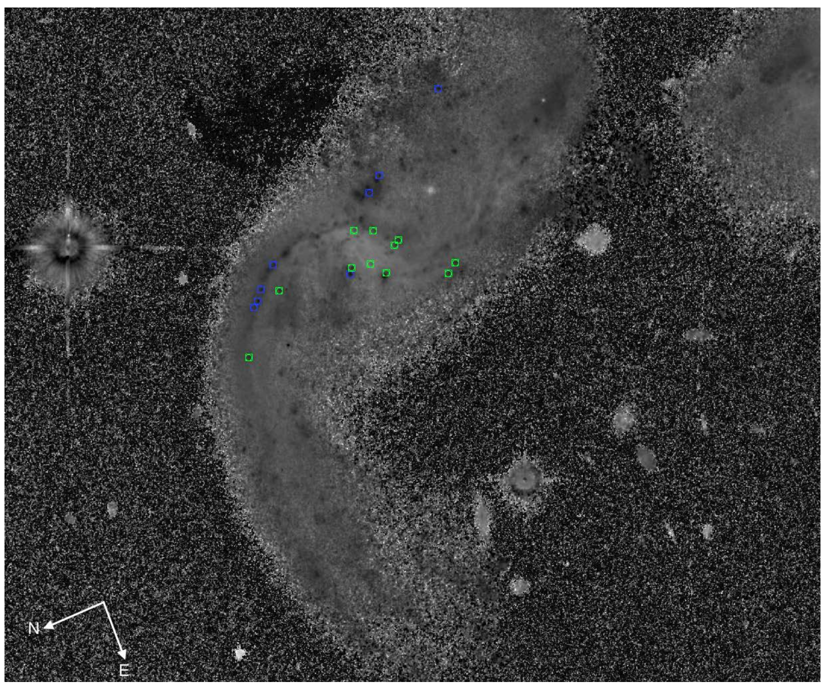

Figure 2.11: Inverted black and white B-I image of Arp 256N taken with HST ACS/WFC F814W and F435W. The bright emission corresponds to redder (i.e. dustier) regions of the galaxy. The blue centroids correspond to clusters found in relatively "dust-free" regions of these galaxies, whereas the green centroids correspond to clusters found in relatively dustier regions of the galaxy.

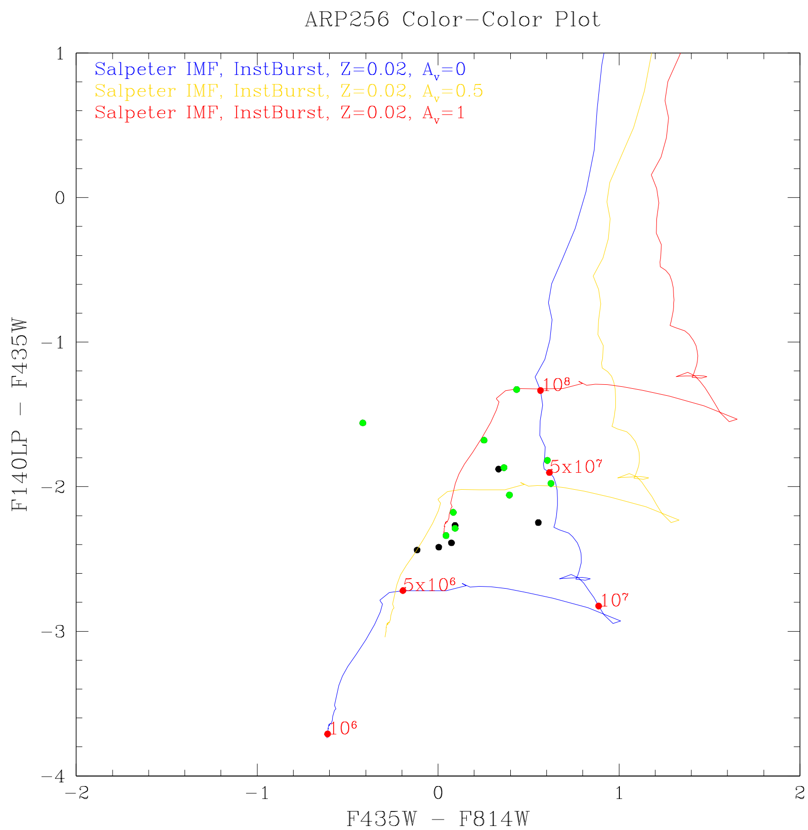

Figure 2.12: Color-Color plot of all star clusters identified in Arp 256N in F814W, F435W, and F140LP plotted against SSP models with various amount of visual extinction. The green points correspond to the clusters found in dustier regions of the galaxy in Figure 2.11.

Table 2.7: Observed Properties of Star Clusters in Arp 256N

ID	RA	Dec	M_B	σ_B	M_I	σ_I	M_{FUV}	σ_{FUV}
1	4.705283874	-10.36593186	-10.52	0.03	-10.40	0.07	-12.96	0.03
2	4.706681456	-10.36309635	-11.05	0.02	-11.05	0.08	-13.47	0.03
3	4.706997794	-10.36259164	-12.33	0.02	-12.88	0.02	-14.58	0.04
4	4.708060796	-10.36212902	-11.79	0.03	-12.41	0.04	-13.77	0.02
5	4.707757416	-10.3616235	-11.16	0.06	-10.74	0.22	-12.72	0.06
6	4.708684462	-10.36263369	-12.69	0.01	-13.05	0.02	-14.56	0.01
7	4.708763384	-10.36246337	-11.99	0.02	-12.38	0.03	-14.05	0.03
8	4.710151015	-10.36378048	-11.10	0.03	-11.14	0.06	-13.44	0.03
9	4.708704027	-10.36100592	-12.08	0.05	-12.17	0.03	-14.37	0.04
10	4.709365918	-10.361838	-12.00	0.04	-12.08	0.13	-14.18	0.03
11	4.708851609	-10.3608711	-13.78	0.01	-13.85	0.02	-16.17	0.01
12	4.710324609	-10.36344198	-11.80	0.02	-12.23	0.02	-13.13	0.06
13	4.707903866	-10.35832277	-13.74	0.01	-14.07	0.02	-15.62	0.01
14	4.708214025	-10.3587839	-11.98	0.02	-12.23	0.04	-13.66	0.02
15	4.708155895	-10.358066	-13.40	0.01	-13.49	0.02	-15.67	0.01
16	4.709517938	-10.35699562	-11.91	0.02	-12.51	0.03	-13.73	0.02

Table 2.8: Derived Properties of Star Clusters in Arp 256N

ID	Log(Age)	σ_{Age}	Log($M/M_{\odot}$)	σ_M	A_V	σ_{A_V}
1	6.54	0.08	4.77	0.22	0.70	0.13
2	6.66	0.19	5.00	0.30	0.60	0.23
3	7.42	0.21	5.84	0.21	0.10	0.11
4	7.32	0.25	5.73	0.25	0.40	0.17
5	6.52	0.01	5.29	0.21	1.20	0.10
6	7.76	0.53	5.68	0.47	0.01	0.44
7	7.63	0.45	5.34	0.36	0.01	0.31
8	6.64	0.11	5.07	0.26	0.70	0.19
9	6.66	0.27	5.47	0.29	0.70	0.22
10	6.44	0.16	5.70	0.28	1.10	0.21
11	6.68	0.26	6.09	0.24	0.60	0.15
12	6.44	0.41	5.94	0.45	1.70	0.42
13	6.72	0.49	6.16	0.42	0.80	0.39
14	6.48	0.07	5.79	0.22	1.40	0.12
15	5.70	0.44	6.52	0.29	1.10	0.23
16	6.76	0.33	5.36	0.30	0.70	0.24

2.7.4 NGC 0695

NGC 0695 is a face-on spiral galaxy with a companion at a projected nuclear separation of $\sim 26''$ (16 kpc) to the northwest. There are multiple spiral arms on the northwestern half of the galaxy, and star clusters are distributed throughout disk. The maximum A_V adopted for this galaxy is 2.8 mags of visual extinction (Kennicutt et al., 2009).

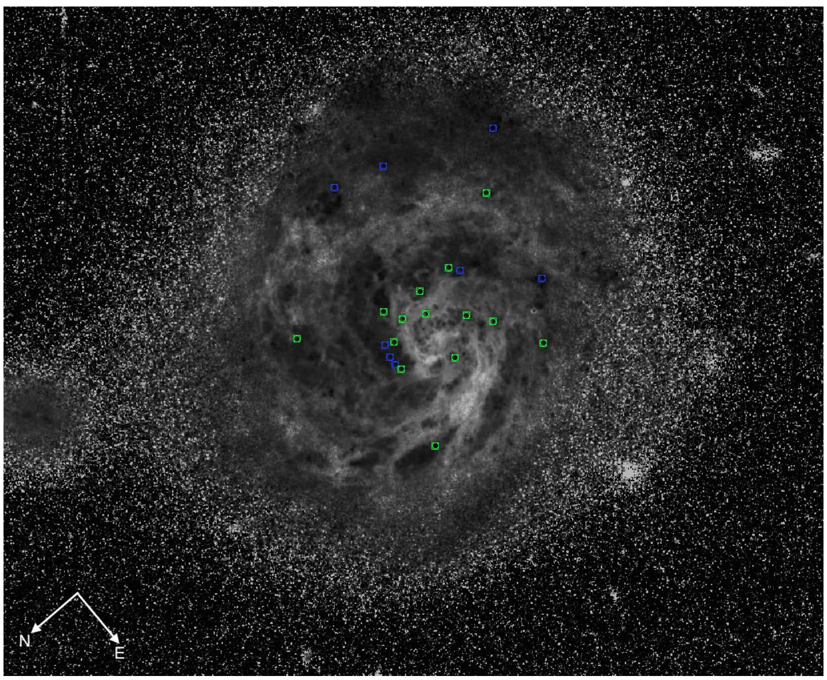

Figure 2.13: Inverted black and white B-I image of NGC 0695 taken with HST ACS/WFC F814W and F435W. The bright emission corresponds to redder (i.e. dustier) regions of the galaxy. The blue centroids correspond to clusters found in relatively "dust-free" regions of these galaxies, whereas the green centroids correspond to clusters found in relatively dustier regions of the galaxy.

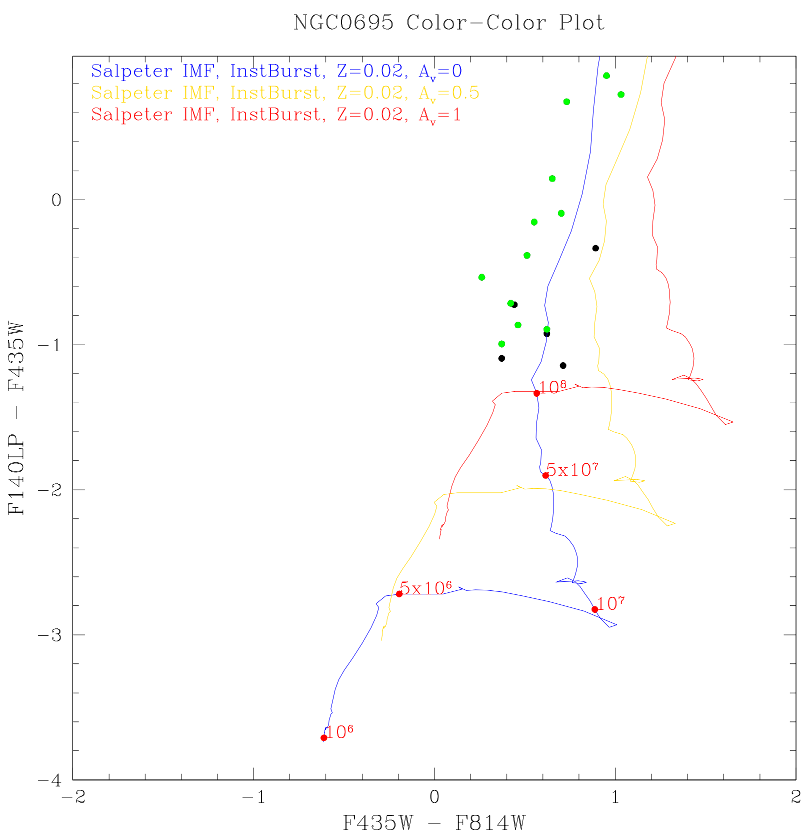

Figure 2.14: Color-Color plot of all star clusters identified in NGC 0695 in F814W, F435W, and F140LP plotted against SSP models with various amount of visual extinction. The green points correspond to the clusters found in dustier regions of the galaxy in Figure 2.13.

Table 2.9: Observed Properties of Star Clusters in NGC 0695

ID	RA	Dec	M_B	σ_B	M_I	σ_I	M_{FUV}	σ_{FUV}
1	27.80620232	22.58288641	-11.35	0.06	-12.24	0.06	-11.68	0.08
2	27.8065178	22.57996324	-11.21	0.02	-11.65	0.03	-11.93	0.06
3	27.80625132	22.58196385	-10.37	0.04	-10.99	0.04	-11.29	0.11
4	27.80849949	22.58172092	-10.96	0.10	-11.58	0.10	-11.85	0.06
5	27.80866289	22.58234757	-13.19	0.02	-13.45	0.04	-13.72	0.02
6	27.808703	22.58307422	-12.36	0.05	-12.82	0.06	-13.22	0.02
7	27.80909168	22.58243561	-12.16	0.02	-12.89	0.06	-11.48	0.10
8	27.80945496	22.58181348	-12.71	0.03	-13.26	0.05	-12.86	0.03
9	27.80898694	22.58283593	-12.19	0.03	-13.14	0.04	-11.33	0.03
10	27.8097772	22.58144334	-13.05	0.01	-13.70	0.01	-12.90	0.02
11	27.80843983	22.58463146	-10.70	0.07	-11.21	0.08	-11.08	0.14
12	27.80929961	22.58314413	-12.17	0.03	-12.87	0.06	-12.26	0.04
13	27.8105601	22.5808227	-10.89	0.02	-11.31	0.03	-11.60	0.05
14	27.80927543	22.58330795	-10.97	0.06	-11.34	0.09	-12.06	0.05
15	27.80952221	22.58331847	-11.14	0.05	-11.85	0.13	-12.28	0.04
16	27.81139357	22.58329741	-11.56	0.02	-11.93	0.04	-12.55	0.03
17	27.80755568	22.58055984	-12.43	0.02	-13.46	0.04	-11.70	0.07

Table 2.10: Derived Properties of Star Clusters in NGC 0695

ID	Log(Age)	σ_{Age}	Log($M/M_{\odot}$)	σ_M	A_V	σ_{A_V}
1	6.70	0.92	6.22	0.76	1.70	0.84
2	6.66	0.82	5.99	0.66	1.40	0.70
3	6.40	0.74	6.05	0.71	1.90	0.76
4	6.70	0.86	5.85	0.63	1.30	0.65
5	6.66	0.40	6.84	0.17	1.50	0.42
6	6.68	0.24	6.40	0.31	1.30	0.25
7	8.56	0.86	7.14	0.17	0.01	0.02
8	8.41	0.01	7.23	0.18	0.01	0.03
9	8.56	0.03	7.26	0.21	0.20	0.10
10	8.46	0.48	7.40	0.17	0.01	0.02
11	8.36	0.52	6.39	0.50	0.01	0.48
12	8.41	0.04	7.07	0.20	0.10	0.10
13	6.66	0.76	5.86	0.64	1.40	0.67
14	6.66	0.40	5.79	0.28	1.20	0.21
15	6.74	0.90	5.83	0.59	1.10	0.61
16	6.66	0.49	6.03	0.18	1.20	0.05
17	8.51	0.04	7.36	0.22	0.30	0.13

2.7.5 UGC 02369

UGC 02369 is a mid-stage merger consisting of a southern face on galaxy (MCG +02-08-029) and an inclined northern galaxy (MCG +02-08-030). The nuclei of the two galaxies are separated by $\sim 21''$ (13 kpc). A spiral arm containing multiple star clusters extends from the nucleus of the southern galaxy towards the northern galaxy. The maximum A_V adopted for this galaxy is 2.3 mags of visual extinction (van Driel et al., 2001).

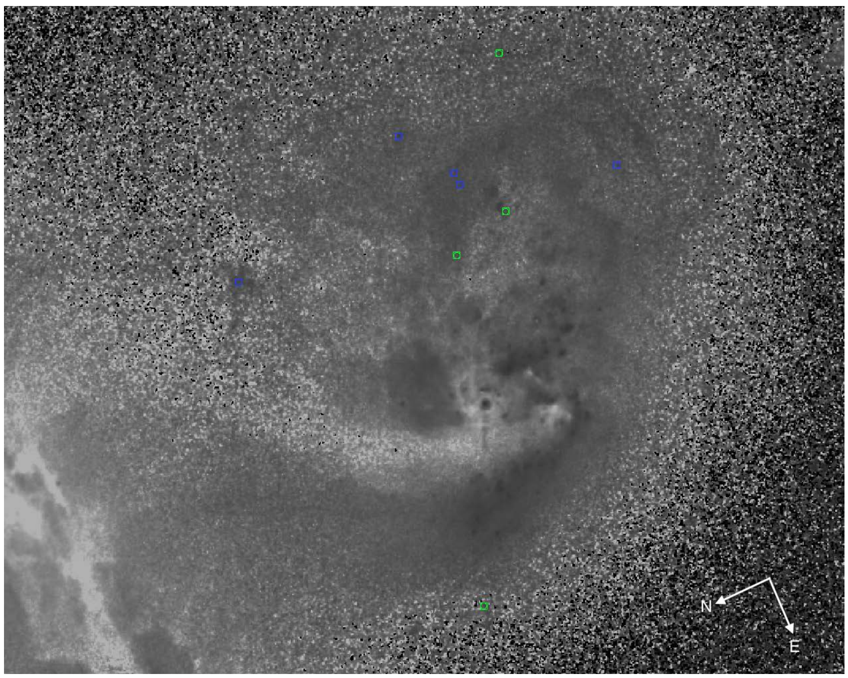

Figure 2.15: Inverted black and white B-I image of UGC 02369 taken with HST ACS/WFC F814W and F435W. The bright emission corresponds to redder (i.e. dustier) regions of the galaxy. The blue centroids correspond to clusters found in relatively "dust-free" regions of these galaxies, whereas the green centroids correspond to clusters found in relatively dustier regions of the galaxy.

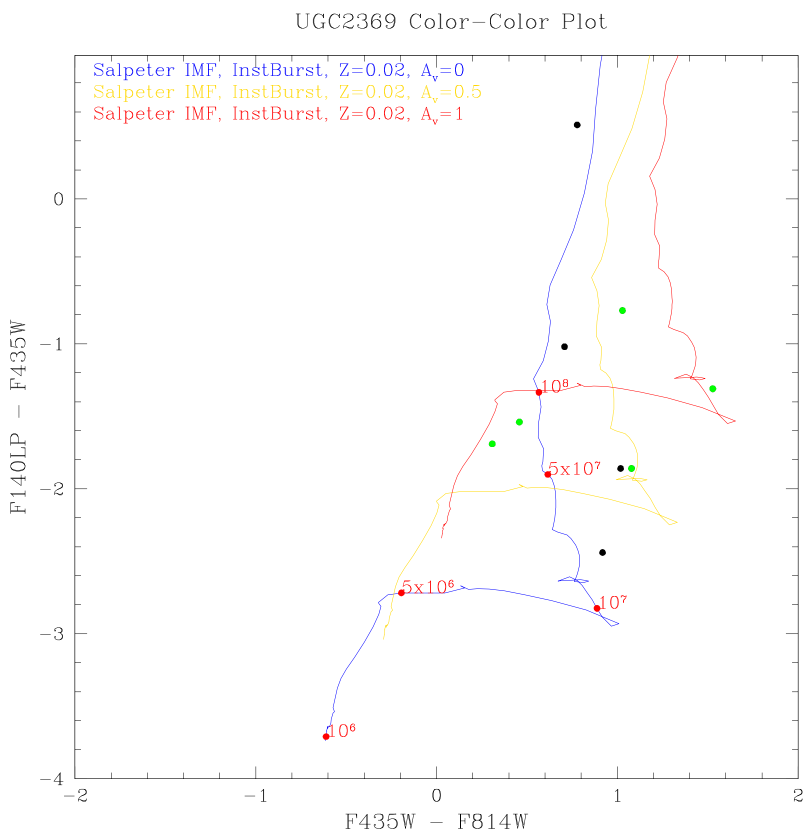

Figure 2.16: Color-Color plot of all star clusters identified in UGC 02369 in F814W, F435W, and F140LP plotted against SSP models with various amount of visual extinction. The green points correspond to the clusters found in dustier regions of the galaxy in Figure 2.15.

Table 2.11: Observed Properties of Star Clusters in UGC 02369

ID	RA	Dec	M_B	σ_B	M_I	σ_I	M_{FUV}	σ_{FUV}
1	43.50963156	14.97660266	-10.85	0.06	-11.31	0.13	-12.39	0.02
2	43.50342276	14.96966218	-9.69	0.10	-10.01	0.15	-11.38	0.05
3	43.5048427	14.97058419	-9.36	0.12	-10.28	0.14	-11.80	0.04
4	43.50519206	14.96870793	-9.54	0.10	-10.56	0.09	-11.40	0.05
5	43.50404048	14.97111855	-12.20	0.01	-12.98	0.01	-11.69	0.04
6	43.50533035	14.97014987	-9.73	0.17	-11.26	0.10	-11.04	0.05
7	43.50518643	14.9734774	-9.84	0.10	-10.55	0.13	-10.86	0.11
8	43.50567241	14.97086958	-9.81	0.11	-10.84	0.10	-10.58	0.11
9	43.50995014	14.97180788	-10.08	0.07	-11.16	0.06	-11.94	0.03

Table 2.12: Derived Properties of Star Clusters in UGC 02369

ID	Log(Age)	σ_{Age}	Log($M/M_{\odot}$)	σ_M	A_V	σ_{A_V}
1	5.10	0.77	5.68	0.52	1.60	0.50
2	6.36	0.58	4.99	0.45	1.40	0.40
3	7.04	0.20	4.47	0.26	0.20	0.15
4	7.63	0.26	4.93	0.26	0.10	0.17
5	6.66	0.03	6.20	0.17	2.20	0.05
6	6.92	0.21	4.98	0.31	1.10	0.19
7	6.72	0.74	4.74	0.59	1.20	0.59
8	7.81	0.55	5.46	0.51	0.70	0.49
9	7.34	0.18	5.22	0.23	0.50	0.12

2.7.6 NGC 1614

NGC 1614 is a late-stage merger with two resolved components in the nucleus separated by $\sim 0.8''$ (300 pc). Beyond the nucleus are two well defined spiral arms, with a significant number of bright clusters scattered throughout this region. The maximum A_V adopted for this galaxy is 4.0 mags of visual extinction (Alonso-Herrero et al., 2001).

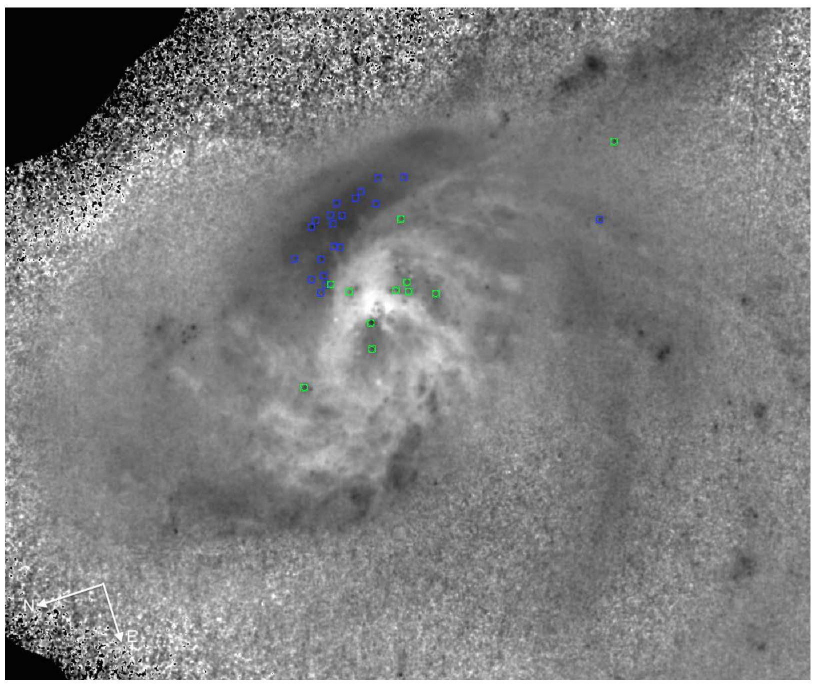

Figure 2.17: Inverted black and white B-I image of NGC 1614 taken with HST ACS/WFC F814W and F435W. The bright emission corresponds to redder (i.e. dustier) regions of the galaxy. The blue centroids correspond to clusters found in relatively "dust-free" regions of these galaxies, whereas the green centroids correspond to clusters found in relatively dustier regions of the galaxy.

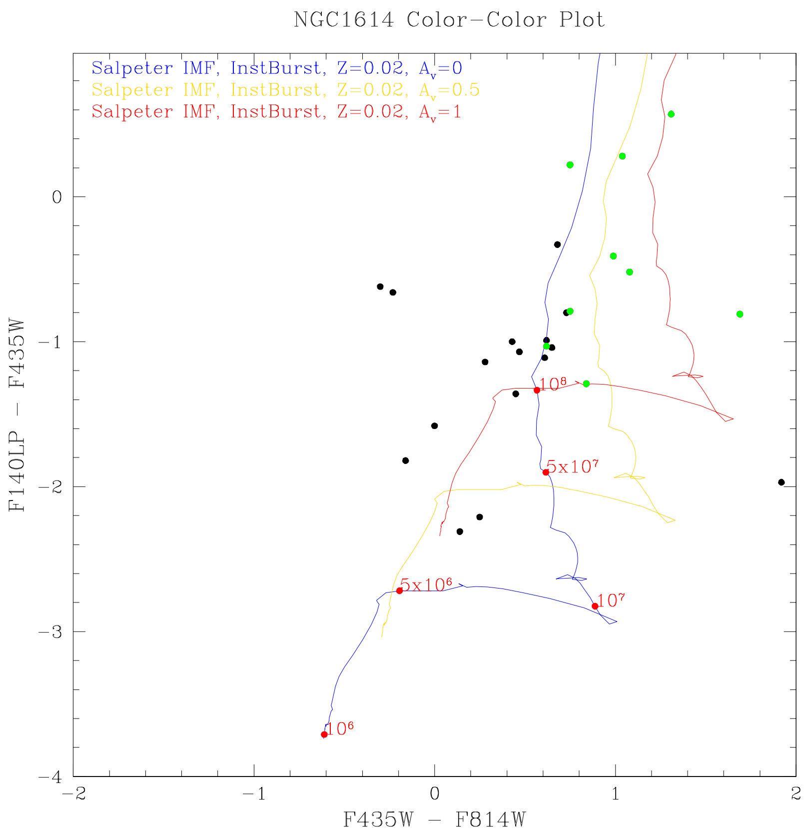

Figure 2.18: Color-Color plot of all star clusters identified in NGC 1614 in F814W, F435W, and F140LP plotted against SSP models with various amount of visual extinction. The green points correspond to the clusters found in dustier regions of the galaxy in Figure 2.17.

Table 2.13: Observed Properties of Star Clusters in NGC 1614

ID	RA	Dec	M_B	σ_B	M_I	σ_I	M_{FUV}	σ_{FUV}
1	68.49833746	-8.5836658	-11.21	0.01	-11.83	0.01	-12.24	0.01
2	68.49787214	-8.579994493	-11.99	0.01	-12.46	0.02	-13.06	0.04
3	68.49775125	-8.5795586	-12.48	0.02	-13.13	0.02	-13.52	0.02
4	68.49797702	-8.579081625	-13.73	0.01	-14.18	0.01	-15.09	0.02
5	68.49796061	-8.578745709	-12.92	0.01	-13.53	0.02	-14.03	0.03
6	68.49813488	-8.578589371	-11.62	0.05	-11.90	0.10	-12.76	0.09
7	68.49855752	-8.57973638	-11.62	0.02	-12.37	0.02	-12.41	0.06
8	68.49957784	-8.583032955	-10.67	0.02	-10.81	0.03	-12.98	0.04
9	68.49815445	-8.578312212	-13.05	0.02	-13.48	0.03	-14.05	0.03
10	68.49829417	-8.578581	-11.86	0.09	-11.86	0.17	-13.44	0.13
11	68.49823898	-8.578206022	-12.72	0.03	-12.49	0.06	-13.38	0.08
12	68.49868598	-8.578484509	-15.33	0.01	-16.06	0.01	-16.13	0.01
13	68.49872601	-8.578589212	-12.07	0.10	-11.77	0.11	-12.69	0.16
14	68.49882795	-8.578206944	-13.22	0.02	-13.47	0.03	-15.43	0.02
15	68.4986906	-8.577771465	-12.76	0.01	-13.38	0.01	-13.75	0.02
16	68.49912105	-8.578165885	-12.53	0.05	-12.37	0.08	-14.35	0.03
17	68.49965474	-8.579516099	-14.21	0.01	-15.25	0.01	-13.93	0.02
18	68.49930324	-8.57824455	-12.07	0.06	-13.76	0.03	-12.88	0.08
19	68.49929236	-8.578158424	-10.73	0.21	-12.65	0.10	-12.70	0.15
20	68.49973941	-8.579291182	-12.81	0.04	-13.80	0.03	-13.22	0.03
21	68.49982001	-8.579497527	-11.54	0.11	-12.38	0.07	-12.83	0.05
22	68.49952214	-8.578509292	-13.29	0.01	-14.60	0.02	-12.72	0.05
23	68.49939493	-8.578038288	-12.50	0.02	-13.18	0.02	-12.83	0.09
24	68.49998928	-8.579944805	-12.74	0.02	-13.82	0.03	-13.26	0.03
25	68.50060521	-8.578602704	-13.65	0.01	-14.40	0.02	-13.43	0.03

Table 2.14: Derived Properties of Star Clusters in NGC 1614

ID	Log(Age)	σ_{Age}	Log($M/M_{\odot}$)	σ_M	A_V	σ_{A_V}
1	6.70	0.22	5.53	0.28	1.50	0.22
2	6.52	0.02	5.89	0.18	1.70	0.06
3	6.66	0.73	6.10	0.66	1.60	0.70
4	6.42	0.48	6.75	0.51	1.70	0.49
5	6.68	0.71	6.22	0.61	1.50	0.63
6	6.52	0.32	5.68	0.39	1.60	0.35
7	6.64	0.84	5.86	0.72	1.80	0.79
8	6.72	0.16	4.77	0.23	0.50	0.15
9	6.52	0.01	6.31	0.17	1.70	0.04
10	6.52	0.19	5.62	0.31	1.30	0.24
11	6.52	0.72	6.18	0.65	1.70	0.69
12	6.64	0.81	7.34	0.76	1.80	0.85
13	6.52	0.91	5.97	0.75	1.80	0.82
14	6.74	0.07	5.78	0.18	0.50	0.06
15	6.36	0.10	6.59	0.22	2.00	0.13
16	6.52	0.01	5.78	0.19	1.10	0.06
17	8.46	0.02	7.40	0.17	0.40	0.04
18	6.82	0.01	5.86	0.20	1.40	0.08
19	7.65	0.77	5.30	0.34	0.01	0.20
20	7.86	0.55	6.73	0.55	0.90	0.55
21	7.59	0.40	5.91	0.42	0.60	0.37
22	6.52	0.66	7.04	0.68	2.90	0.73
23	6.52	0.04	6.35	0.17	2.20	0.57
24	7.72	0.35	6.68	0.31	1.00	0.25
25	8.61	0.02	7.15	0.17	0.10	0.05

2.7.7 2MASX J06094582-2140234

2MASX J06094582-2140234 is a mid-stage merger consisting of two face-on galaxies which appear to overlap and have a projected seperation of $\sim 8.4''$ (6.3 kpc). Prominent rings/arms in each galaxy contain the bulk of the visible star clusters. The maximum A_V adopted for this galaxy is 1.0 mags of visual extinction (Miralles-Caballero et al., 2012).

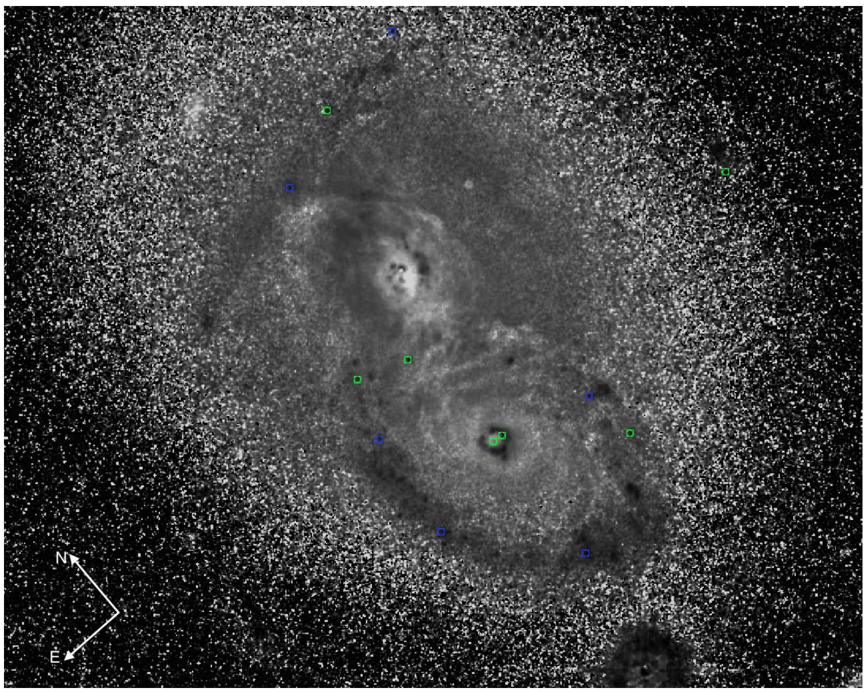

Figure 2.19: Inverted black and white B-I image of 2MASX J06094582-2140234 taken with HST ACS/WFC F814W and F435W. The bright emission corresponds to redder (i.e. dustier) regions of the galaxy. The blue centroids correspond to clusters found in relatively "dust-free" regions of these galaxies, whereas the green centroids correspond to clusters found in relatively dustier regions of the galaxy.

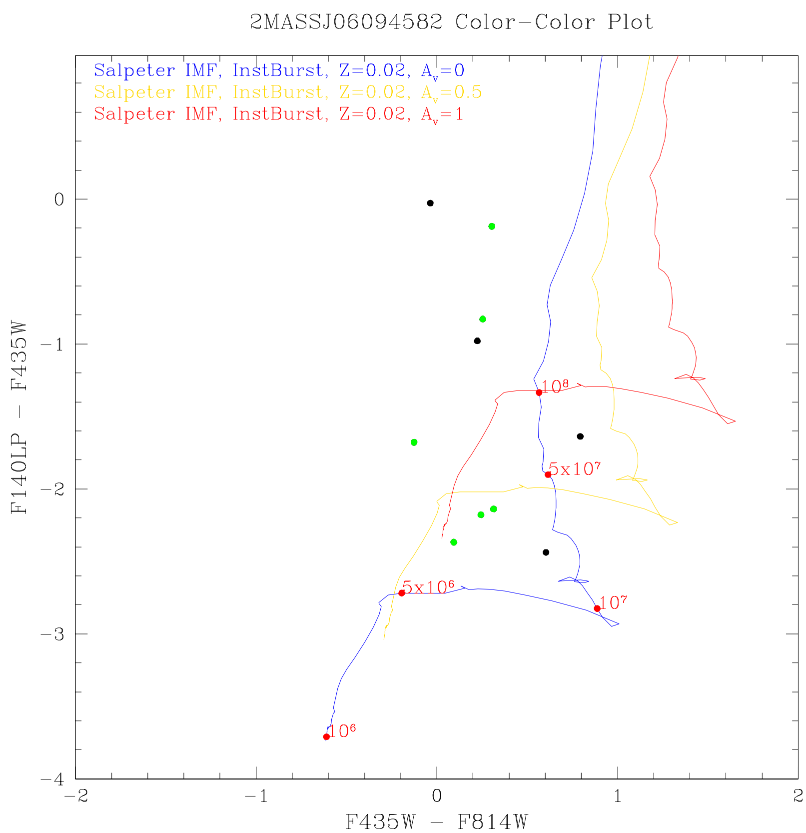

Figure 2.20: Color-Color plot of all star clusters identified in 2MASX J06094582-2140234 in F814W, F435W, and F140LP plotted against SSP models with various amount of visual extinction. The green points correspond to the clusters found in dustier regions of the galaxy in Figure 2.19.

Table 2.15: Observed Properties of Star Clusters in 2MASX J06094582-2140234

ID	RA	Dec	M_B	σ_B	M_I	σ_I	M_{FUV}	σ_{FUV}
1	92.438548	-21.67128502	-10.07	0.09	-10.29	0.14	-11.05	0.04
2	92.43987859	-21.67130163	-10.68	0.06	-10.77	0.10	-13.05	0.01
3	92.43715675	-21.67545341	-11.44	0.02	-11.68	0.04	-13.62	0.02
4	92.4409611	-21.6715528	-11.60	0.03	-12.20	0.05	-14.04	0.05
5	92.4416782	-21.67398257	-12.05	0.03	-11.92	0.12	-13.73	0.02
6	92.44229618	-21.67366993	-10.76	0.07	-11.07	0.15	-12.90	0.01
7	92.44270943	-21.67433539	-10.88	0.06	-10.84	0.18	-10.91	0.03
8	92.44164311	-21.67543932	-14.49	0.03	-14.79	0.09	-14.68	0.05
9	92.44054901	-21.67659996	-10.76	0.05	-11.01	0.10	-11.59	0.04
10	92.44310457	-21.67562528	-11.02	0.07	-11.81	0.07	-12.66	0.01

Table 2.16: Derived Properties of Star Clusters in 2MASX J06094582-2140234

ID	Log(Age)	σ_{Age}	Log($M/M_{\odot}$)	σ_M	A_V	σ_{A_V}
1	6.74	0.09	4.79	0.20	1.00	0.08
2	6.72	0.29	4.78	0.30	0.50	0.24
3	6.74	0.03	5.07	0.19	0.50	0.09
4	6.92	0.05	5.14	0.17	0.20	0.04
5	6.70	0.08	5.55	0.17	0.90	0.05
6	6.74	0.36	4.85	0.35	0.60	0.30
7	7.91	0.03	6.04	0.17	1.00	0.29
8	7.91	0.03	7.48	0.16	1.00	0.20
9	7.16	0.09	5.52	0.18	1.00	0.07
10	7.36	0.31	5.55	0.28	0.60	0.21

2.7.8 2MASX J08370182-4954302

2MASX J08370182-4954302 is a mid-stage merger containing two nuclei separated by $\sim 0.66''$ (0.36 kpc). Surrounding the nuclei are multiple bright star clusters in a spiral ridge just northwest and west of the nuclei. The maximum A_V adopted for this galaxy is 3.7 mags of visual extinction (Rich et al., 2012).

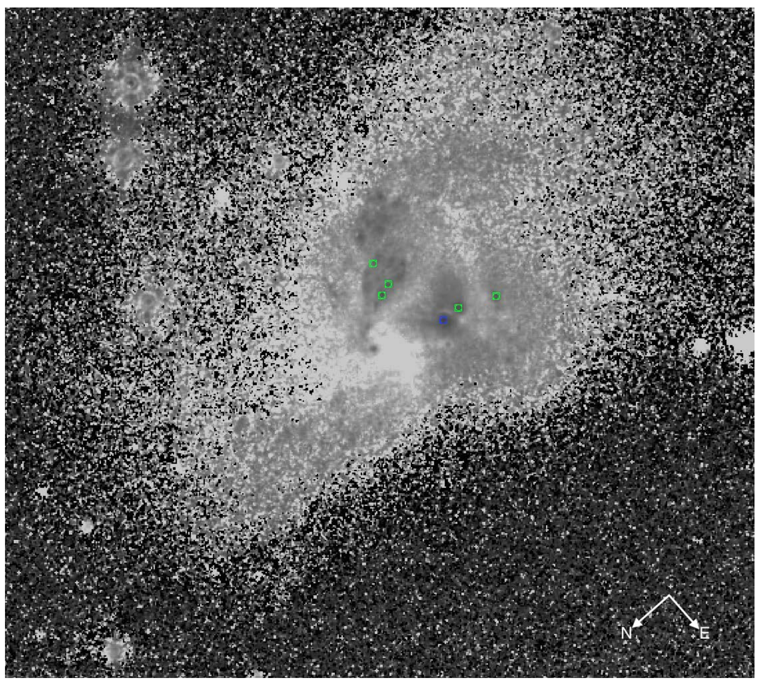

Figure 2.21: Inverted black and white B-I image of 2MASX J08370182-4954302 taken with HST ACS/WFC F814W and F435W. The bright emission corresponds to redder (i.e. dustier) regions of the galaxy. The blue centroids correspond to clusters found in relatively "dust-free" regions of these galaxies, whereas the green centroids correspond to clusters found in relatively dustier regions of the galaxy.

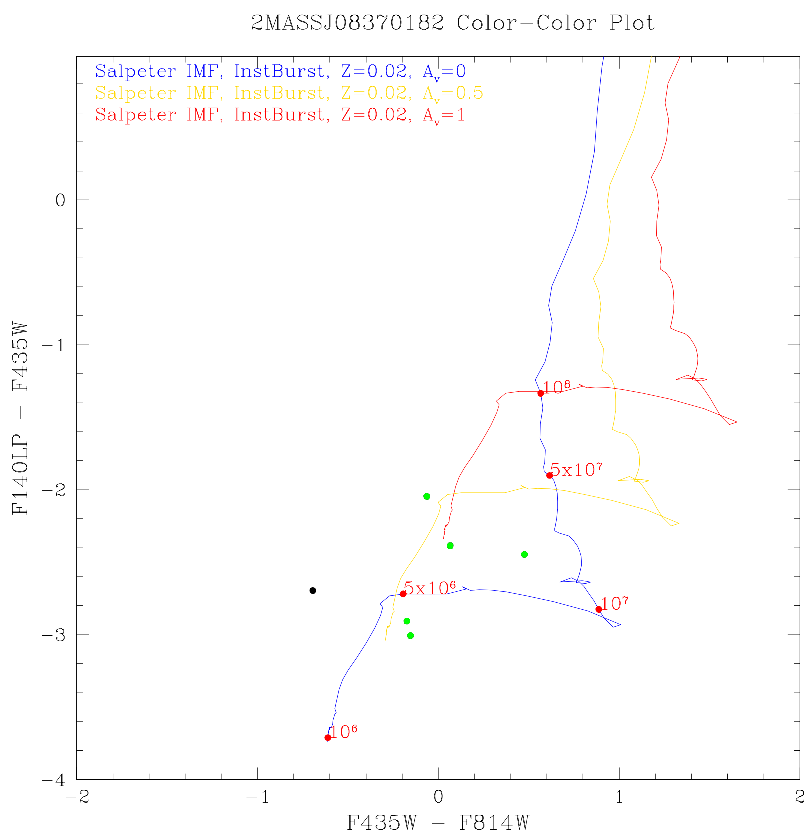

Figure 2.22: Color-Color plot of all star clusters identified in 2MASX J08370182-4954302 in F814W, F435W, and F140LP plotted against SSP models with various amount of visual extinction. The green points correspond to the clusters found in dustier regions of the galaxy in Figure 2.21.

Table 2.17: Observed Properties of Star Clusters in 2MASX J08370182-4954302

ID	RA	Dec	M_B	σ_B	M_I	σ_I	M_{FUV}	σ_{FUV}
1	129.2557186	-49.90846967	-14.83	0.04	-15.31	0.03	-17.28	0.01
2	129.2561197	-49.90840169	-15.24	0.05	-15.31	0.03	-17.63	0.16
3	129.2561534	-49.90828131	-15.85	0.02	-15.68	0.02	-18.76	0.02
4	129.2574869	-49.90904604	-15.42	0.01	-15.36	0.02	-17.47	0.01
5	129.2571648	-49.90869922	-18.38	0.01	-18.23	0.01	-21.39	0.01
6	129.2571314	-49.90851337	-19.79	0.01	-19.10	0.01	-22.49	0.01

Table 2.18: Derived Properties of Star Clusters in 2MASX J08370182-4954302

ID	Log(Age)	σ_{Age}	Log($M/M_{\odot}$)	σ_M	A_V	σ_{A_V}
1	6.86	0.02	6.38	0.18	0.20	0.05
2	5.10	0.64	7.12	0.43	1.00	0.40
3	5.10	0.46	7.15	0.17	0.60	0.02
4	6.66	0.03	6.59	0.16	0.50	0.04
5	5.10	0.41	8.17	0.17	0.60	0.04
6	6.66	0.61	8.07	0.16	0.01	0.24

2.7.9 NGC 2623

Evans et al. (2008) discusses the detailed morphology of this galaxy at length. NGC 2623 is a late-stage merger with dust lanes running along its tidal tails into the nucleus. Several bright clusters are distributed throughout the bulge and in a 'pie-wedge' concentration south of the nucleus. The maximum A_V adopted for this galaxy is 1.9 mags of visual extinction (Privon et al., 2013).

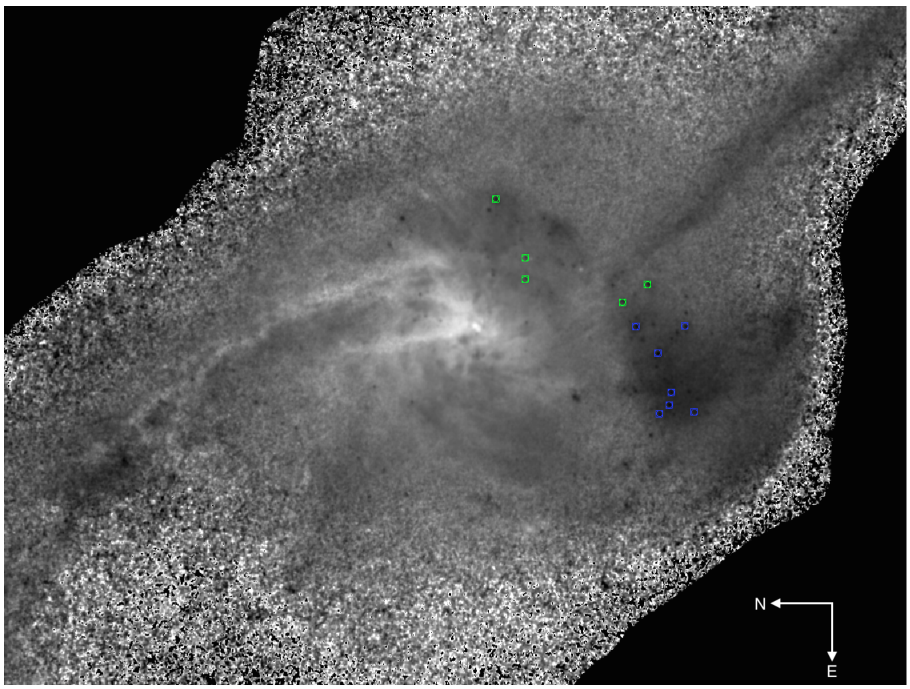

Figure 2.23: Inverted black and white B-I image taken of NGC 2623 with HST ACS/WFC F814W and F435W. The bright emission corresponds to redder (i.e. dustier) regions of the galaxy. The blue centroids correspond to clusters found in relatively "dust-free" regions of these galaxies, whereas the green centroids correspond to clusters found in relatively dustier regions of the galaxy.

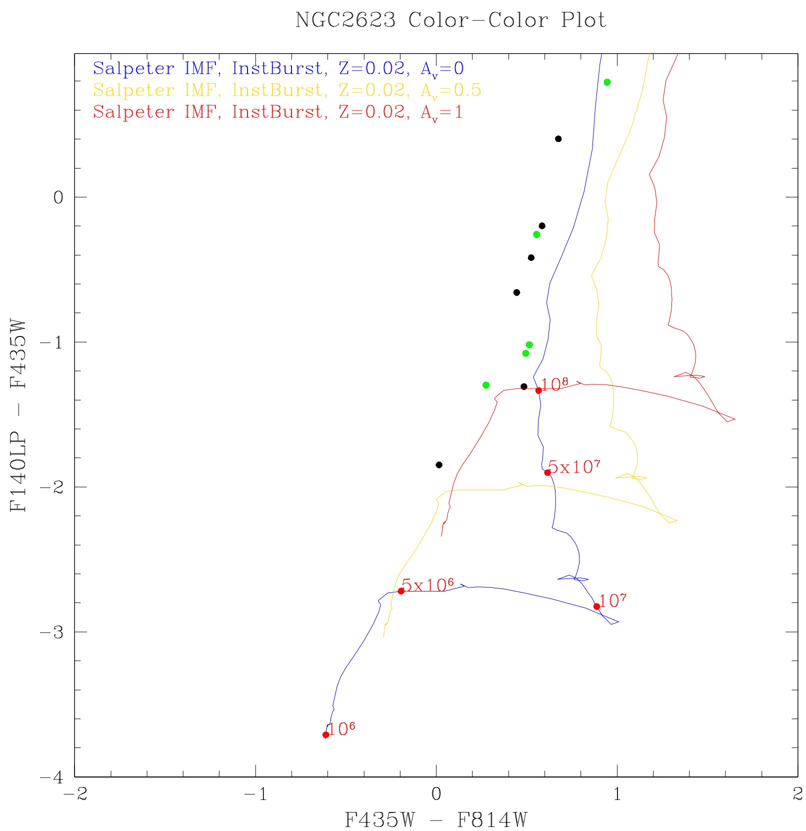

Figure 2.24: Color-Color plot of all star clusters identified in NGC 2623 in F814W, F435W, and F140LP plotted against SSP models with various amount of visual extinction. The green points correspond to the clusters found in dustier regions of the galaxy in Figure 2.23.

Table 2.19: Observed Properties of Star Clusters in NGC 2623

ID	RA	Dec	M_B	σ_B	M_I	σ_I	M_{FUV}	σ_{FUV}
1	129.5980304	25.75459514	-14.04	0.01	-14.98	0.01	-13.25	0.02
2	129.5990031	25.7538954	-11.45	0.02	-11.94	0.05	-12.53	0.04
3	129.5994079	25.75382853	-11.39	0.02	-11.90	0.05	-12.41	0.05
4	129.5990874	25.751723	-11.53	0.01	-12.08	0.01	-11.79	0.05
5	129.5995056	25.75209619	-10.61	0.02	-10.88	0.03	-11.91	0.08
6	129.599766	25.75096143	-11.27	0.01	-11.85	0.01	-11.47	0.03
7	129.5999493	25.75179613	-13.15	0.01	-13.82	0.01	-12.75	0.04
8	129.6003718	25.75134324	-11.08	0.02	-11.09	0.05	-12.93	0.03
9	129.6010618	25.75100371	-11.58	0.01	-12.06	0.02	-12.89	0.03
10	129.6013548	25.75053983	-10.88	0.03	-11.40	0.03	-11.30	0.02
11	129.601522	25.75112441	-11.24	0.02	-11.68	0.02	-11.90	0.08

Table 2.20: Derived Properties of Star Clusters in NGC 2623

ID	Log(Age)	σ_{Age}	Log($M/M_{\odot}$)	σ_M	A_V	σ_{A_V}
1	8.56	0.18	7.33	0.16	0.10	0.02
2	6.54	0.56	5.48	0.50	1.50	0.49
3	6.62	0.47	5.34	0.43	1.30	0.40
4	8.36	0.64	6.16	0.16	0.10	0.03
5	6.66	0.03	4.93	0.19	1.00	0.09
6	6.68	0.72	5.46	0.16	1.50	0.27
7	7.86	0.67	7.25	0.16	1.50	0.29
8	6.66	0.05	4.90	0.21	0.60	0.12
9	6.70	0.57	5.32	0.47	1.00	0.45
10	6.68	0.02	5.30	0.17	1.50	0.03
11	6.66	0.72	5.44	0.60	1.50	0.62

2.7.10 UGC 04881

UGC 04881 is an early-stage merger containing two nuclei separated by $\sim 11''$ (9 kpc). Spiral dust lanes and strings of star clusters surround the NE nucleus. In the SW nucleus a linear distribution of star clusters and a prominent dust lane are seen. The maximum A_V adopted for this galaxy is 1.9 mags of visual extinction (González-Martín et al., 2009).

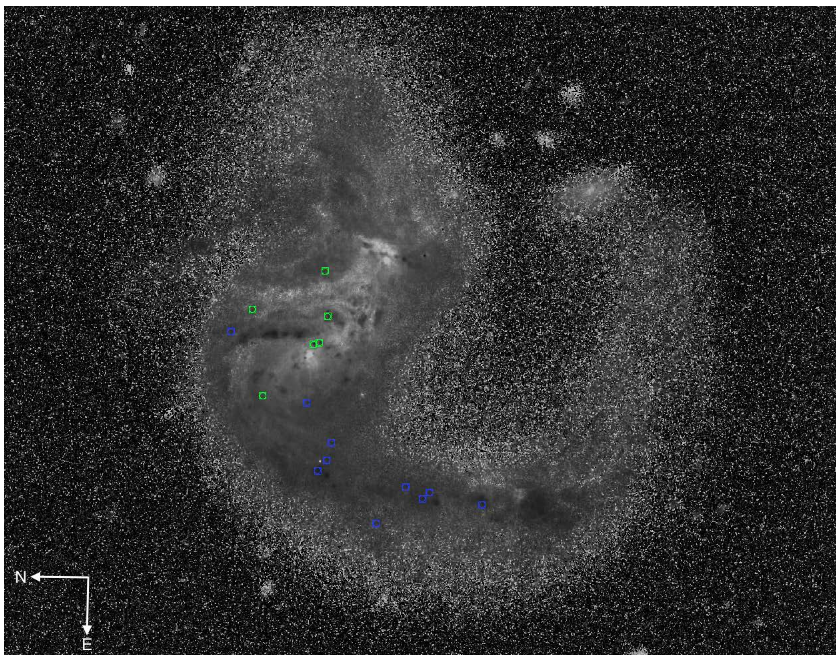

Figure 2.25: Inverted black and white B-I image of UGC 04881 taken with HST ACS/WFC F814W and F435W. The bright emission corresponds to redder (i.e. dustier) regions of the galaxy. The blue centroids correspond to clusters found in relatively "dust-free" regions of these galaxies, whereas the green centroids correspond to clusters found in relatively dustier regions of the galaxy.

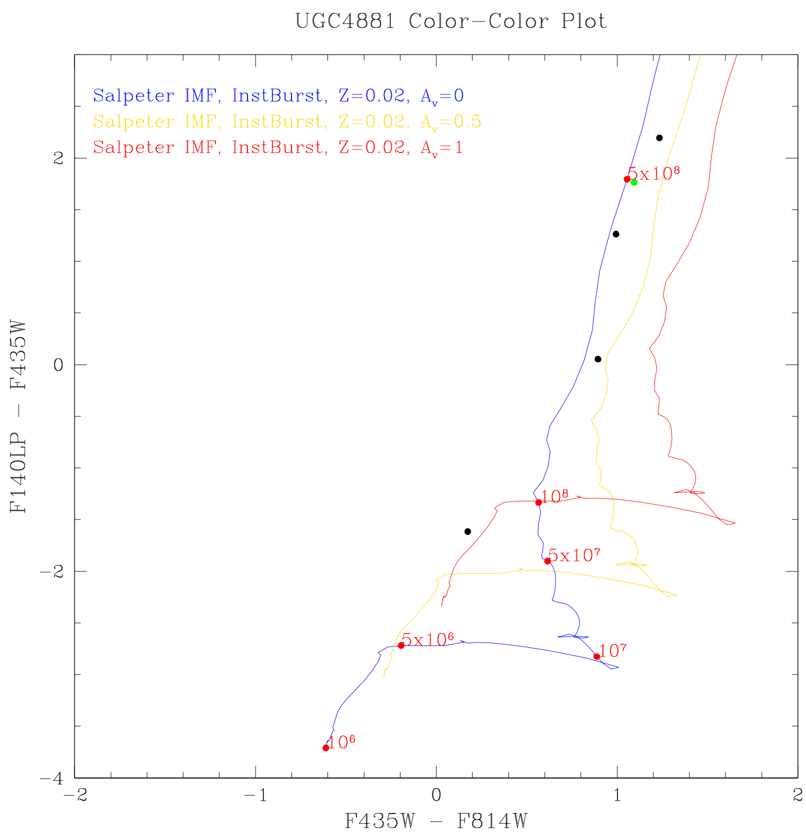

Figure 2.26: Color-Color plot of all star clusters identified in UGC 04881 in F814W, F435W, and F140LP plotted against SSP models with various amount of visual extinction. The green points correspond to the clusters found in dustier regions of the galaxy in Figure 2.25.

Table 2.21: Observed Properties of Star Clusters in UGC 04881

ID	RA	Dec	M_B	σ_B	M_I	σ_I	M_{FUV}	σ_{FUV}
1	138.9806254	44.33224681	-13.41	0.02	-14.51	0.05	-11.65	0.13
2	138.9802968	44.33445408	-12.38	0.02	-13.38	0.01	-11.12	0.14
3	138.9841104	44.33189026	-13.48	0.01	-14.72	0.01	-11.29	0.01
4	138.9857806	44.32941604	-11.38	0.08	-12.28	0.11	-11.33	0.03
5	138.9861709	44.32809268	-10.97	0.13	-11.15	0.20	-12.59	0.16

Table 2.22: Derived Properties of Star Clusters in UGC 04881

ID	Log(Age)	σ_{Age}	Log($M/M_{\odot}$)	σ_M	A_V	σ_{A_V}
1	8.71	0.03	7.17	0.23	0.01	0.16
2	8.06	0.02	7.27	0.19	1.90	0.09
3	8.71	0.10	7.36	0.16	0.30	5.62
4	6.68	0.44	5.71	0.53	1.90	0.52
5	6.66	0.36	4.97	0.42	0.80	0.37

2.7.11 IC 2545

IC 2545 is a late-stage merger being viewed face-on. Dust lanes and strings of star clusters extend from two unresolved nuclei separated by $\sim 0.8''$ (0.54 kpc) in the center of the galaxy. Multiple star clusters are also visible throughout the tidal tails. The maximum A_V adopted for this galaxy is 4.0 mags of visual extinction (van den Broek et al., 1991).

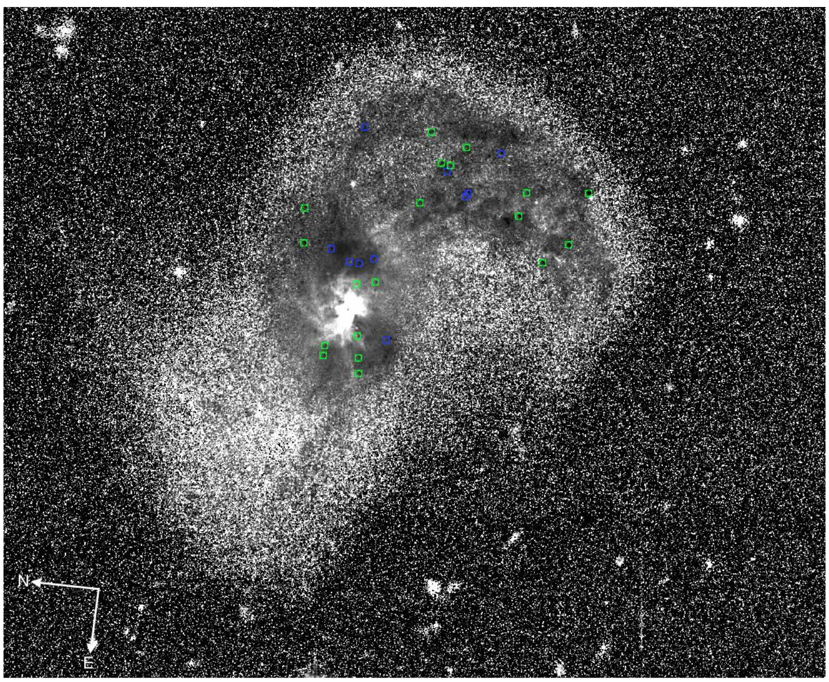

Figure 2.27: Inverted black and white B-I image of IC 2545 taken with HST ACS/WFC F814W and F435W. The bright emission corresponds to redder (i.e. dustier) regions of the galaxy. The blue centroids correspond to clusters found in relatively “dust-free” regions of these galaxies, whereas the green centroids correspond to clusters found in relatively dustier regions of the galaxy.

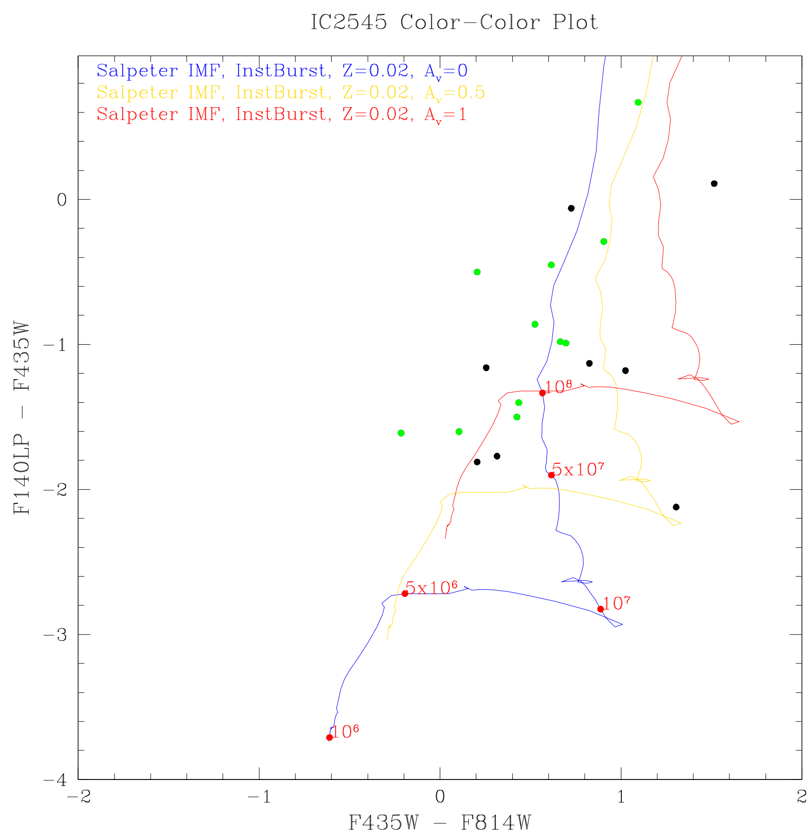

Figure 2.28: Color-Color plot of all star clusters identified in IC 2545 in F814W, F435W, and F140LP plotted against SSP models with various amount of visual extinction. The green points correspond to the clusters found in dustier regions of the galaxy in Figure 2.27.

Table 2.23: Observed Properties of Star Clusters in IC 2545

ID	RA	Dec	M_B	σ_B	M_I	σ_I	M_{FUV}	σ_{FUV}
1	151.5136356	-33.88528106	-10.23	0.08	-11.06	0.08	-11.36	0.11
2	151.5136616	-33.88695096	-10.55	0.07	-10.99	0.08	-11.95	0.11
3	151.5140689	-33.88785616	-10.73	0.07	-11.43	0.06	-11.72	0.13
4	151.5146406	-33.88747231	-9.72	0.13	-10.15	0.15	-11.22	0.26
5	151.5148205	-33.8873956	-10.48	0.09	-10.74	0.13	-11.64	0.17
6	151.515442	-33.88795458	-11.40	0.07	-11.61	0.08	-13.21	0.17
7	151.5153282	-33.88941777	-11.77	0.03	-12.68	0.03	-12.06	0.36
8	151.5152205	-33.89096417	-11.67	0.03	-11.46	0.05	-13.28	0.05
9	151.5155505	-33.88790446	-10.54	0.11	-10.86	0.19	-12.31	0.07
10	151.5161603	-33.88389939	-10.85	0.04	-11.52	0.04	-11.83	0.22
11	151.5172199	-33.88393251	-11.68	0.02	-12.21	0.03	-12.54	0.21
12	151.5168118	-33.8905397	-10.84	0.04	-10.95	0.07	-12.44	0.29
13	151.5177074	-33.88509063	-14.32	0.01	-15.84	0.01	-14.21	0.04
14	151.517576	-33.88570119	-10.70	0.20	-11.73	0.19	-11.88	0.36
15	151.5177403	-33.8853364	-14.65	0.02	-15.38	0.02	-14.71	0.03
16	151.5199867	-33.88613476	-9.91	0.19	-11.22	0.07	-12.03	0.01
17	151.5202629	-33.88460375	-12.84	0.03	-13.94	0.02	-12.17	0.06
18	151.5205798	-33.88546044	-11.59	0.04	-12.21	0.08	-12.04	0.27
19	151.5210485	-33.88549176	-11.29	0.04	-11.50	0.08	-11.79	0.24

Table 2.24: Derived Properties of Star Clusters in IC 2545

ID	Log(Age)	σ_{Age}	Log($M/M_{\odot}$)	σ_M	A_V	σ_{A_V}
1	6.78	0.03	4.88	0.18	1.10	0.29
2	6.34	0.40	5.47	0.18	1.60	0.46
3	8.06	0.54	5.71	0.18	0.20	0.19
4	5.10	0.35	5.23	0.21	1.60	0.26
5	6.66	0.21	4.93	0.19	1.10	0.10
6	6.46	0.33	5.58	0.18	1.20	0.35
7	6.46	0.17	6.31	0.17	2.30	0.51
8	6.66	0.10	5.19	0.17	0.70	0.07
9	6.00	0.31	5.35	0.20	1.40	0.56
10	8.11	0.31	5.73	0.17	0.10	0.55
11	6.64	0.57	5.54	0.17	1.40	0.41
12	6.66	0.11	4.91	0.17	0.80	0.58
13	7.74	0.13	7.60	0.17	1.40	0.41
14	7.63	0.07	5.66	0.27	0.60	0.08
15	6.66	0.59	7.02	0.17	1.90	0.10
16	5.10	0.36	6.58	0.26	4.00	0.06
17	8.41	0.38	6.99	0.17	0.60	0.28
18	8.31	0.26	6.16	0.17	0.10	0.54
19	6.66	0.50	5.46	0.17	1.50	0.22

2.7.12 NGC 3256

NGC 3256 is a late-stage merger containing a large number of star clusters along the inner ($\sim 20''$, or 4 kpc) spiral structure of the nuclear region. The spiral dust lanes extending from the nucleus give this galaxy pockets of high and low extinction. The maximum A_V adopted for this galaxy is 3.3 mags of visual extinction (Rich et al., 2012).

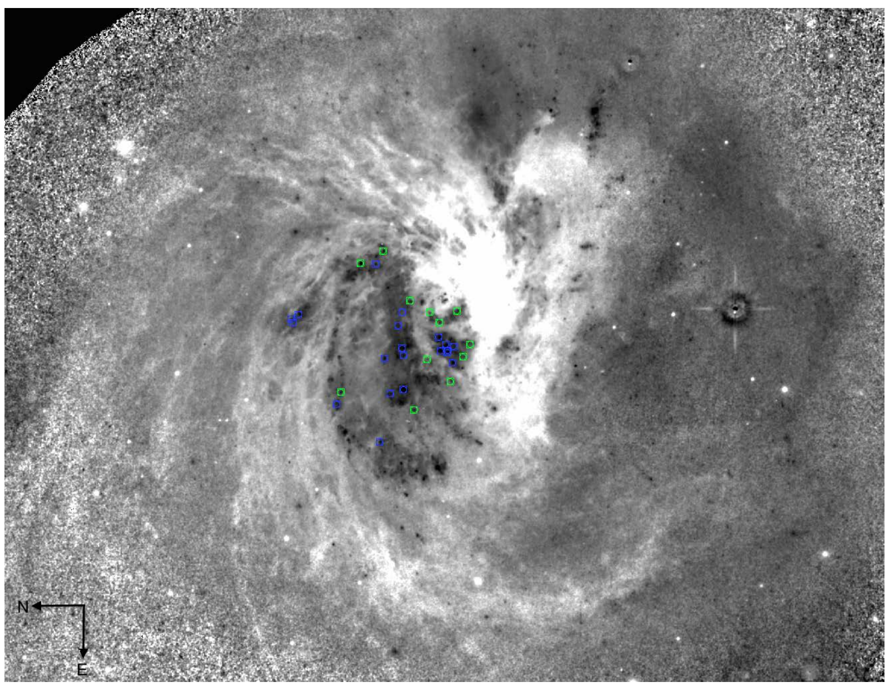

Figure 2.29: Inverted black and white B-I image of NGC 3256 taken with HST ACS/WFC F814W and F435W. The bright emission corresponds to redder (i.e. dustier) regions of the galaxy. The blue centroids correspond to clusters found in relatively "dust-free" regions of these galaxies, whereas the green centroids correspond to clusters found in relatively dustier regions of the galaxy.

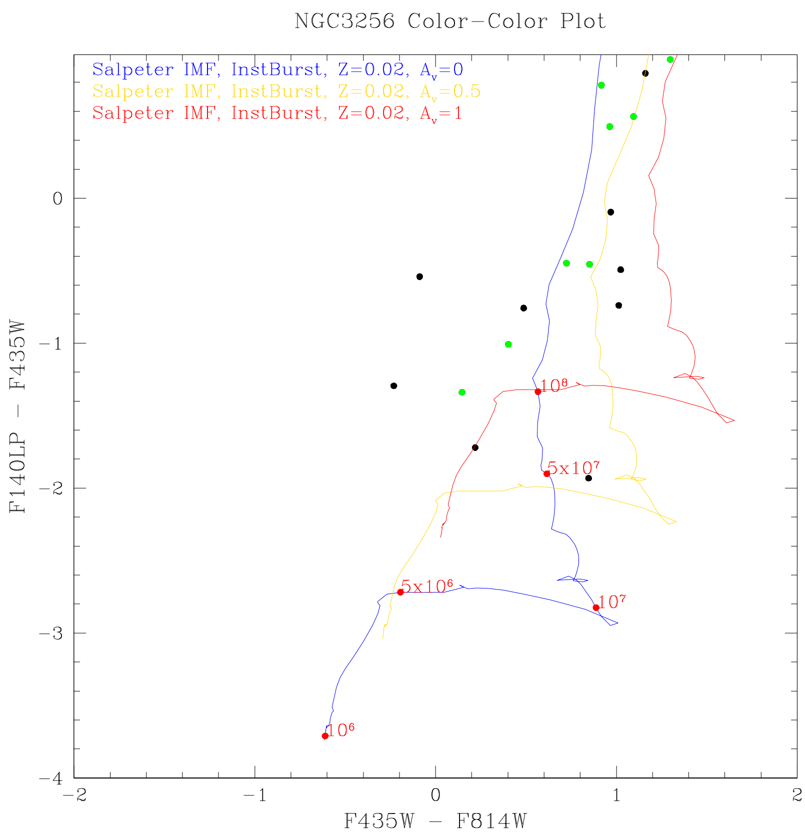

Figure 2.30: Color-Color plot of all star clusters identified in NGC 3256 in F814W, F435W, and F140LP plotted against SSP models with various amount of visual extinction. The green points correspond to the clusters found in dustier regions of the galaxy in Figure 2.29.

Table 2.25: Observed Properties of Star Clusters in NGC 3256

ID	RA	Dec	M_B	σ_B	M_I	σ_I	M_{FUV}	σ_{FUV}
1	156.9608449	-43.9024964	-12.20	0.02	-12.93	0.03	-12.65	0.01
2	156.9612737	-43.90178128	-12.75	0.01	-12.90	0.01	-14.09	0.01
3	156.9630369	-43.90314637	-12.96	0.01	-13.87	0.01	-12.18	0.02
4	156.9636042	-43.9045422	-14.02	0.01	-14.82	0.01	-12.97	0.02
5	156.9634535	-43.90288363	-12.88	0.02	-14.04	0.02	-12.02	0.05
6	156.9635947	-43.90369683	-13.70	0.02	-15.00	0.01	-12.74	0.01
7	156.9633212	-43.89955977	-12.29	0.02	-13.32	0.02	-12.79	0.02
8	156.9634618	-43.89962047	-11.36	0.01	-12.37	0.02	-12.10	0.04
9	156.9640714	-43.90271444	-13.34	0.02	-14.31	0.01	-13.43	0.04
10	156.9646123	-43.90392525	-13.49	0.03	-13.98	0.03	-14.25	0.01
11	156.9652121	-43.90415987	-13.56	0.02	-13.33	0.03	-14.86	0.01
12	156.9653068	-43.90414225	-13.36	0.02	-13.27	0.04	-13.90	0.02
13	156.9655228	-43.9046008	-12.70	0.01	-13.66	0.01	-12.20	0.02
14	156.9654982	-43.90351402	-13.21	0.01	-14.42	0.01	-11.32	0.05
15	156.966498	-43.90415946	-13.52	0.01	-14.61	0.01	-12.95	0.01
16	156.9666609	-43.90272713	-13.74	0.01	-13.96	0.01	-15.46	0.01
17	156.9665347	-43.90083852	-10.75	0.01	-11.16	0.01	-11.76	0.03
18	156.9667894	-43.90232476	-10.09	0.05	-10.93	0.05	-12.02	0.02
19	156.9675522	-43.9029773	-12.70	0.01	-13.55	0.01	-13.15	0.01

Table 2.26: Derived Properties of Star Clusters in NGC 3256

ID	Log(Age)	σ_{Age}	Log($M/M_\odot$)	σ_M	A_V	σ_{A_V}
1	6.68	0.03	5.88	0.18	1.60	0.06
2	6.66	0.12	5.78	0.17	1.00	0.27
3	8.36	0.19	7.10	0.17	0.80	0.07
4	8.41	0.10	7.56	0.17	0.80	0.30
5	8.36	0.03	7.13	0.18	0.90	0.06
6	8.36	0.03	7.51	0.20	1.00	0.11
7	7.86	0.54	6.54	0.42	0.80	0.38
8	7.74	0.02	6.10	0.18	0.80	0.06
9	6.54	0.13	6.61	0.27	2.20	0.20
10	6.66	0.01	6.29	0.17	1.40	0.03
11	6.66	0.47	6.06	0.17	0.90	0.02
12	6.66	0.22	6.24	0.17	1.40	0.03
13	8.31	0.02	6.97	0.17	0.80	0.03
14	8.56	0.03	7.37	0.17	0.80	0.02
15	8.31	0.10	7.30	0.17	0.80	0.08
16	6.52	0.07	6.19	0.26	1.10	0.19
17	6.68	0.01	5.09	0.18	1.20	0.05
18	6.86	0.03	4.80	0.17	0.80	0.37
19	6.44	0.14	6.52	0.25	2.20	0.17

2.7.13 Arp 148

Arp 148 is an early-stage merger and the only example of a ring galaxy in the sample. This $\sim 23''$ (16 kpc) diameter galaxy is comprised of clumps of star clusters along its perimeter, and throughout much of its interior. The maximum A_V adopted for this galaxy is 2.1 mags of visual extinction.

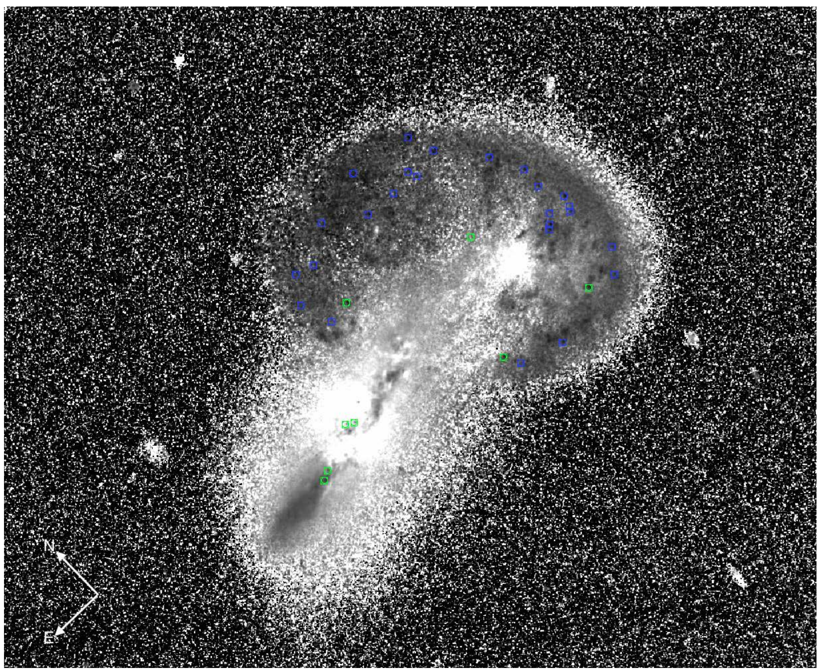

Figure 2.31: Inverted black and white B-I image of Arp 148 taken with HST ACS/WFC F814W and F435W. The bright emission corresponds to redder (i.e. dustier) regions of the galaxy. The blue centroids correspond to clusters found in relatively “dust-free” regions of these galaxies, whereas the green centroids correspond to clusters found in relatively dustier regions of the galaxy.

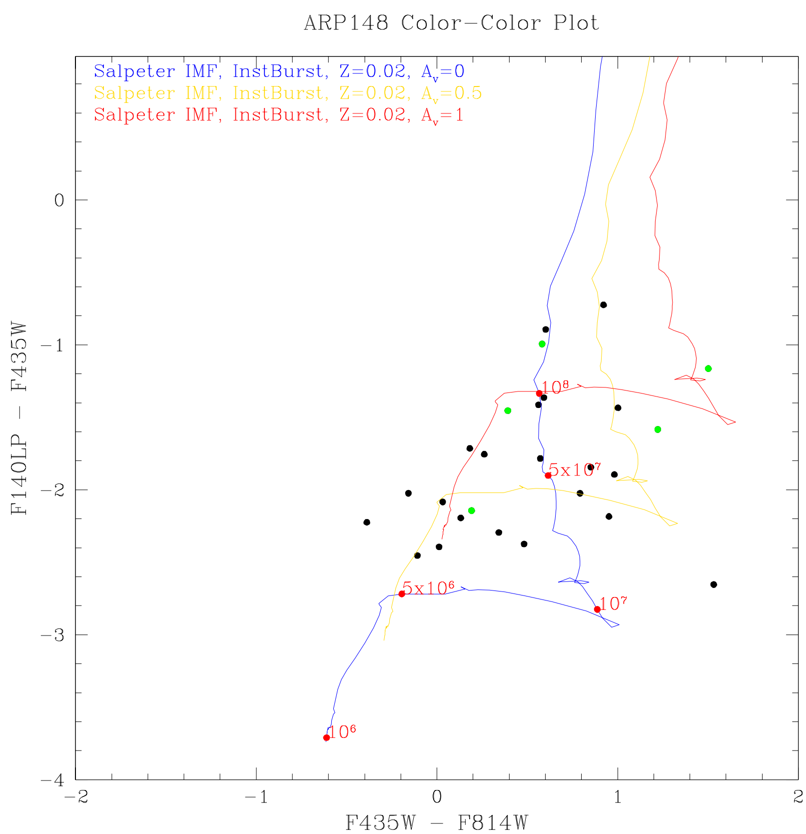

Figure 2.32: Color-Color plot of all star clusters identified in Arp 148 in F814W, F435W, and F140LP plotted against SSP models with various amount of visual extinction. The green points correspond to the clusters found in dustier regions of the galaxy in Figure 2.31.

Table 2.27: Observed Properties of Star Clusters in Arp 148

ID	RA	Dec	M_B	σ_B	M_I	σ_I	M_{FUV}	σ_{FUV}
1	165.968436	40.8519488	-12.21	0.01	-12.34	0.02	-14.41	0.02
2	165.9678663	40.8505602	-11.09	0.05	-11.12	0.10	-13.18	0.07
3	165.9683844	40.85145549	-11.10	0.03	-11.36	0.05	-12.86	0.09
4	165.9691046	40.85164919	-11.30	0.03	-11.90	0.04	-12.20	0.10
5	165.9690976	40.85147869	-11.19	0.03	-12.17	0.03	-13.09	0.09
6	165.967872	40.84958083	-10.44	0.07	-10.45	0.13	-12.84	0.09
7	165.9678992	40.84893317	-9.78	0.14	-11.31	0.08	-12.44	0.14
8	165.9680004	40.84887677	-11.27	0.05	-11.84	0.07	-13.06	0.08
9	165.9682628	40.84916472	-10.83	0.07	-11.39	0.08	-12.25	0.16
10	165.9677623	40.84910158	-11.64	0.03	-11.53	0.07	-14.10	0.03
11	165.9704139	40.85187208	-10.71	0.07	-10.55	0.18	-12.74	0.10
12	165.968608	40.84903015	-11.16	0.06	-11.64	0.09	-13.54	0.05
13	165.967709	40.84993148	-11.37	0.03	-11.55	0.05	-13.09	0.08
14	165.9682107	40.84793431	-10.78	0.11	-11.78	0.09	-12.22	0.16
15	165.9684927	40.8490672	-11.59	0.05	-11.93	0.08	-13.89	0.04
16	165.9687209	40.84766184	-12.23	0.03	-12.82	0.07	-13.60	0.05
17	165.9720438	40.85223589	-10.78	0.04	-11.57	0.04	-12.81	0.10
18	165.969655	40.85013869	-9.45	0.12	-10.67	0.10	-11.04	0.13
19	165.9692811	40.84792405	-13.17	0.02	-13.56	0.04	-14.63	0.02
20	165.9724453	40.852421	-9.47	0.14	-10.32	0.14	-11.32	0.01
21	165.9724057	40.85141491	-11.51	0.02	-11.70	0.04	-13.66	0.07
22	165.9716475	40.84859071	-11.98	0.02	-12.56	0.03	-12.98	0.09
23	165.9715595	40.84827508	-11.99	0.03	-12.91	0.04	-12.72	0.11
24	165.9706662	40.84783769	-10.84	0.04	-10.45	0.16	-13.07	0.08
25	165.9729915	40.85207186	-10.18	0.12	-11.13	0.11	-12.37	0.14
26	165.9748241	40.85035121	-12.83	0.04	-14.33	0.09	-14.00	0.03

Table 2.28: Derived Properties of Star Clusters in Arp 148

ID	Log(Age)	σ_{Age}	$\mathrm{Log}(M/M_{\odot})$	σ_M	A_V	σ_{A_V}
1	5.10	0.67	5.96	0.39	1.10	0.35
2	6.56	0.42	4.91	0.36	0.70	0.32
3	6.70	0.51	4.97	0.34	0.70	0.29
4	6.60	0.56	5.35	0.40	1.40	0.36
5	7.12	0.18	5.44	0.19	0.50	0.10
6	6.36	0.36	5.03	0.34	0.90	0.29
7	5.10	0.01	5.52	0.27	2.10	0.15
8	6.76	0.49	5.02	0.35	0.60	0.30
9	6.74	0.79	4.99	0.55	0.90	0.55
10	6.60	0.57	4.90	0.36	0.30	0.32
11	6.66	0.11	4.70	0.28	0.50	0.20
12	6.86	0.23	4.91	0.20	0.20	0.10
13	6.52	0.18	5.25	0.31	1.10	0.26
14	7.63	0.31	5.58	0.33	0.40	0.26
15	6.76	0.05	4.98	0.18	0.30	0.07
16	6.72	0.70	5.59	0.58	1.00	0.60
17	7.49	0.20	5.42	0.21	0.20	0.13
18	7.34	0.24	5.07	0.27	0.70	0.18
19	6.42	0.22	6.39	0.33	1.50	0.28
20	7.52	0.34	4.97	0.31	0.30	0.22
21	6.72	0.32	4.99	0.35	0.40	0.30
22	6.46	0.46	6.13	0.50	1.80	0.49
23	6.74	0.45	5.72	0.38	1.40	0.34
24	6.66	0.03	4.65	0.21	0.30	0.12
25	7.30	0.23	5.13	0.27	0.30	0.17
26	7.06	0.17	6.35	0.20	1.10	0.11

2.7.14 NGC 3690E

NGC3690 is a mid-stage merger. NGC 3690E contains a multitude of star clusters and dust lanes from the southeast tip of the galaxy to the northwest. The maximum A_V adopted for this galaxy is 3.4 mags of visual extinction (García-Marín et al., 2006).

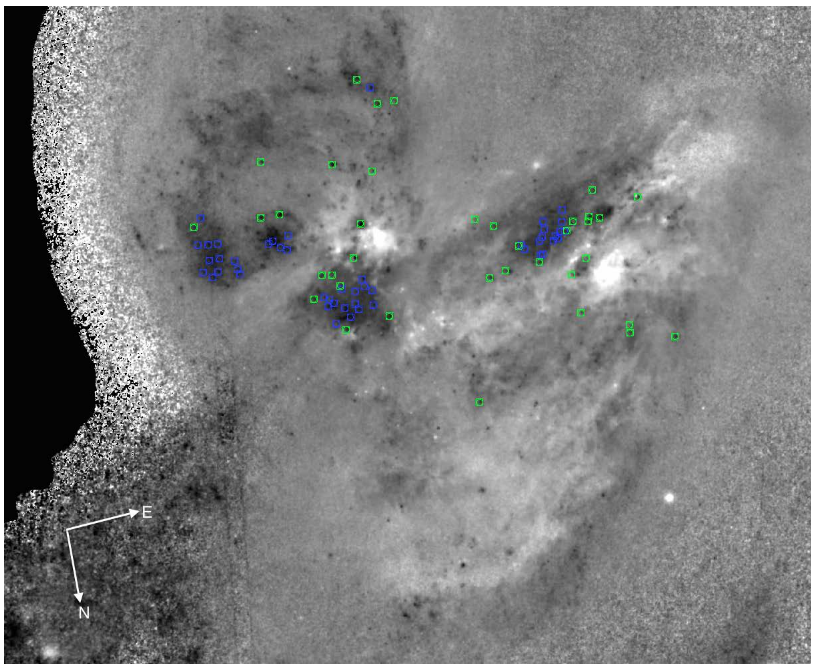

Figure 2.33: Inverted black and white B-I image of NGC 3690E taken with HST ACS/WFC F814W and F435W. The bright emission corresponds to redder (i.e. dustier) regions of the galaxy. The blue centroids correspond to clusters found in relatively "dust-free" regions of these galaxies, whereas the green centroids correspond to clusters found in relatively dustier regions of the galaxy.

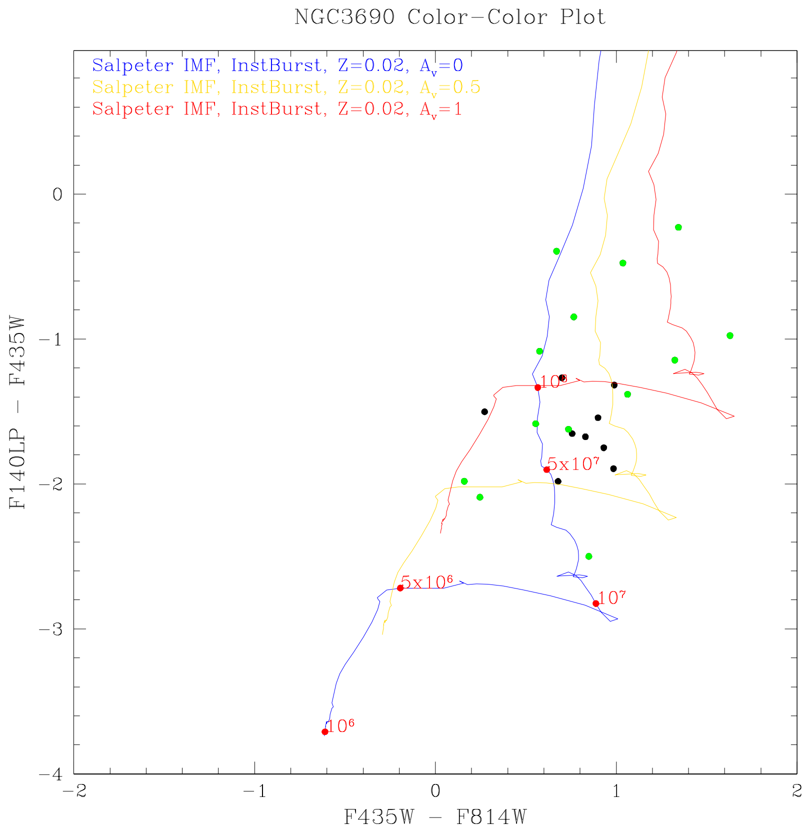

Figure 2.34: Color-Color plot of all star clusters identified in NGC 3690E in F814W, F435W, and F140LP plotted against SSP models with various amount of visual extinction. The green points correspond to the clusters found in dustier regions of the galaxy in Figure 2.33.

Table 2.29: Observed Properties of Star Clusters in NGC 3690E

ID	RA	Dec	M_B	σ_B	M_I	σ_I	M_{FUV}	σ_{FUV}
1	172.1336515	58.56572969	-11.56	0.01	-12.23	0.01	-11.95	0.02
2	172.1424578	58.56116578	-11.76	0.01	-12.83	0.02	-13.14	0.01
3	172.1388005	58.56124188	-10.20	0.05	-11.19	0.04	-11.52	0.05
4	172.1400284	58.56149757	-10.81	0.04	-10.97	0.14	-12.79	0.02
5	172.1345803	58.56118873	-8.96	0.04	-9.81	0.05	-11.46	0.03
6	172.1392395	58.56156972	-12.52	0.02	-14.15	0.01	-13.50	0.02
7	172.1399479	58.56161791	-11.73	0.02	-12.28	0.02	-13.31	0.02
8	172.1386985	58.56153798	-10.07	0.08	-10.97	0.10	-11.61	0.10
9	172.1378106	58.56146996	-10.01	0.04	-11.00	0.04	-11.91	0.04
10	172.1387899	58.56177443	-12.85	0.02	-13.61	0.03	-14.51	0.02
11	172.1385677	58.56177224	-12.15	0.03	-12.98	0.03	-13.82	0.02
12	172.1376673	58.5618607	-11.11	0.03	-11.81	0.03	-12.38	0.04
13	172.138187	58.56197966	-11.39	0.05	-12.33	0.07	-13.14	0.05
14	172.1366287	58.56197706	-10.22	0.18	-12.26	0.06	-11.91	0.06
15	172.1365065	58.56198534	-10.79	0.10	-12.11	0.05	-11.93	0.05
16	172.1367658	58.56209285	-10.89	0.04	-11.16	0.06	-12.39	0.04
17	172.1376122	58.56226713	-10.54	0.10	-11.22	0.08	-12.52	0.05
18	172.1357033	58.56256555	-9.68	0.08	-9.93	0.10	-11.77	0.02
19	172.1349188	58.56268913	-11.06	0.01	-11.80	0.02	-12.68	0.01
20	172.1390305	58.56385382	-11.61	0.02	-12.65	0.02	-12.09	0.02
21	172.1412556	58.56431432	-11.46	0.04	-12.81	0.02	-11.69	0.04
22	172.1412392	58.56451117	-11.52	0.02	-12.28	0.03	-12.36	0.01
23	172.1433592	58.56475551	-11.38	0.01	-11.95	0.01	-12.46	0.01

Table 2.30: Derived Properties of Star Clusters in NGC 3690E

ID	Log(Age)	σ_{Age}	Log($M/M_{\odot}$)	σ_M	A_V	σ_{A_V}
1	8.46	0.01	6.13	0.17	0.01	0.15
2	6.94	0.05	5.66	0.17	1.00	0.35
3	7.00	0.23	5.22	0.24	1.10	0.15
4	6.56	0.43	5.06	0.42	1.00	0.38
5	6.82	0.01	3.99	0.19	0.20	0.06
6	6.82	0.83	5.99	0.18	1.30	0.04
7	7.76	0.31	5.88	0.31	0.20	0.25
8	6.98	0.30	4.99	0.27	0.90	0.19
9	6.84	0.04	4.64	0.19	0.60	0.06
10	7.24	0.15	6.25	0.22	0.70	0.13
11	6.98	0.20	5.77	0.20	0.80	0.10
12	6.74	0.46	5.31	0.41	1.20	0.37
13	6.92	0.12	5.32	0.19	0.70	0.06
14	7.65	0.24	5.21	0.30	0.20	0.15
15	6.84	0.11	5.26	0.22	1.20	0.09
16	6.52	0.30	5.29	0.37	1.40	0.32
17	7.42	0.30	5.23	0.30	0.30	0.21
18	6.72	0.45	4.49	0.42	0.70	0.38
19	7.12	0.20	5.49	0.25	0.80	0.17
20	7.76	0.27	6.26	0.29	1.00	0.22
21	7.57	0.27	6.30	0.29	1.40	0.22
22	8.16	0.84	6.01	0.69	0.20	0.74
23	6.42	0.42	5.91	0.47	1.90	0.44

2.7.15 NGC 3690W

NGC 3690W has the brightest cluster complexes in the merging system located $\sim 6.8''$ (1.6 kpc) from the resolved nucleus. Cluster-rich spiral arms extend north and westward from the nuclear region out to a maximum projected distance of $\sim 58''$ (14 kpc). The maximum A_V adopted for this galaxy is 3.9 mags of visual extinction (García-Marín et al., 2006).

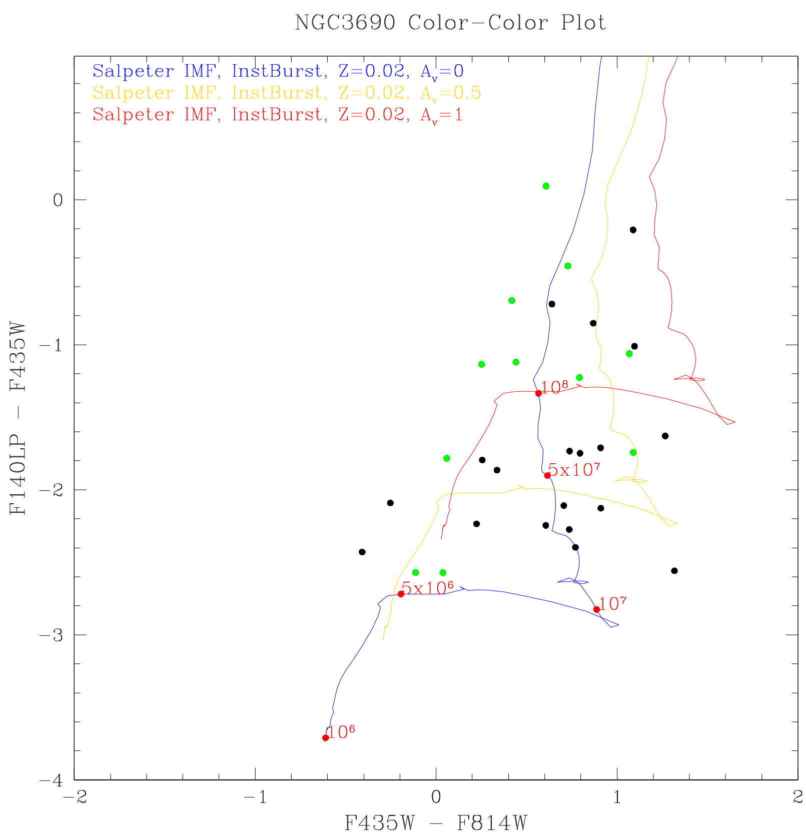

Figure 2.35: Color-Color plot of all star clusters identified in NGC 3690W in F814W, F435W, and F140LP plotted against SSP models with various amount of visual extinction. The green points correspond to the clusters found in dustier regions of the galaxy in Figure 2.33.

Table 2.31: Observed Properties of Star Clusters in NGC 3690W

ID	RA	Dec	M_B	σ_B	M_I	σ_I	M_{FUV}	σ_{FUV}
1	172.1298769	58.55733473	-11.32	0.01	-12.11	0.01	-12.55	0.02
2	172.128158	58.55936534	-10.84	0.01	-10.73	0.02	-13.41	0.01
3	172.1300076	58.5596496	-11.44	0.01	-12.51	0.01	-12.50	0.01
4	172.1253481	58.56042622	-11.36	0.01	-11.42	0.01	-13.14	0.02
5	172.1244337	58.56044047	-10.15	0.03	-10.19	0.04	-12.73	0.02
6	172.1291326	58.56092032	-14.92	0.01	-15.17	0.02	-16.05	0.02
7	172.1248588	58.5610534	-14.22	0.01	-14.83	0.01	-16.47	0.01
8	172.1246296	58.56111739	-11.76	0.03	-12.53	0.01	-14.16	0.02
9	172.1222293	58.56095288	-10.70	0.02	-11.44	0.03	-12.43	0.03
10	172.1251824	58.56124124	-10.38	0.14	-11.70	0.06	-12.94	0.04
11	172.1254777	58.56133083	-10.78	0.04	-11.00	0.06	-13.01	0.03
12	172.1222096	58.56131918	-11.41	0.03	-12.32	0.03	-13.12	0.03
13	172.1230124	58.56163962	-12.19	0.01	-12.99	0.01	-13.94	0.01
14	172.122073	58.5616329	-10.06	0.04	-9.65	0.14	-12.49	0.02
15	172.1231006	58.56176699	-10.62	0.02	-11.36	0.02	-12.90	0.02
16	172.1274401	58.56209845	-11.04	0.07	-12.13	0.05	-12.79	0.03
17	172.126965	58.5620665	-13.05	0.01	-13.66	0.02	-12.96	0.04
18	172.1217838	58.56176205	-11.84	0.01	-12.55	0.01	-13.95	0.01
19	172.128929	58.56247605	-10.89	0.09	-12.16	0.07	-12.52	0.07
20	172.1292452	58.56260576	-12.98	0.01	-14.07	0.01	-13.19	0.02
21	172.1284475	58.56257873	-10.60	0.06	-11.51	0.07	-12.73	0.03
22	172.1269226	58.56262585	-12.87	0.02	-13.74	0.02	-13.72	0.02
23	172.1264357	58.56263441	-13.24	0.02	-13.66	0.03	-13.93	0.02
24	172.1271745	58.56269741	-14.01	0.01	-15.11	0.01	-15.02	0.01
25	172.1292261	58.56297394	-12.57	0.01	-13.21	0.01	-13.29	0.02
26	172.1278642	58.56295651	-12.73	0.03	-12.98	0.04	-14.52	0.02
27	172.1285202	58.56303529	-11.18	0.04	-10.93	0.13	-13.27	0.03
28	172.1299061	58.56329793	-12.44	0.01	-12.88	0.02	-13.56	0.01
29	172.1280723	58.56319834	-12.29	0.05	-12.62	0.05	-14.15	0.02
30	172.1277823	58.56349895	-14.73	0.01	-15.46	0.02	-15.18	0.02

Table 2.32: Derived Properties of Star Clusters in NGC 3690W

ID	Log(Age)	σ_{Age}	Log($M/M_{\odot}$)	σ_M	A_V	σ_{A_V}
1	6.78	0.02	5.27	0.18	1.00	0.05
2	6.42	0.16	5.03	0.19	0.70	0.06
3	7.63	0.34	6.00	0.30	0.70	0.23
4	6.66	0.10	5.07	0.17	0.70	1.12
5	5.10	0.40	5.03	0.18	0.90	0.04
6	6.66	8.74	6.70	0.18	1.10	0.03
7	6.84	0.01	6.26	0.17	0.50	0.30
8	6.88	0.01	5.35	0.17	0.50	0.17
9	6.84	0.01	4.95	0.18	0.70	0.04
10	5.10	0.01	6.71	0.23	3.90	0.02
11	5.10	0.67	5.39	0.29	1.10	0.22
12	6.88	0.04	5.32	0.18	0.70	0.05
13	6.86	0.10	5.59	0.17	0.70	1.12
14	6.52	0.02	4.40	0.19	0.50	0.06
15	6.88	0.01	4.90	0.17	0.50	0.20
16	7.42	0.20	5.65	0.21	0.50	0.09
17	8.31	0.35	6.95	0.35	0.50	0.30
18	6.86	0.01	5.34	0.17	0.50	0.99
19	5.10	0.19	6.92	0.24	3.90	0.12
20	8.01	0.48	6.89	0.41	0.80	0.37
21	6.90	0.10	4.94	0.19	0.50	0.42
22	6.74	0.58	6.02	0.44	1.30	0.41
23	6.66	6.61	6.19	0.18	1.40	0.04
24	7.65	0.29	7.05	0.25	0.70	0.18
25	6.62	0.06	5.92	0.23	1.50	0.14
26	6.38	0.49	6.18	0.36	1.30	0.30
27	6.66	0.08	4.89	0.22	0.50	0.12
28	6.64	0.06	5.73	0.23	1.20	0.15
29	6.72	0.43	5.40	0.35	0.60	0.30
30	6.68	0.03	6.89	0.18	1.60	0.05

2.7.16 NGC 5257E

NGC5257/8 is an early-stage merger system with the E and W nuclei separated by $\sim 80''$ (40 kpc). Star clusters and dust lanes make up the prominent spiral arms seen in the eastern galaxy. The maximum A_V adopted for this galaxy is 2.6 mags of visual extinction (Smith et al., 2014).

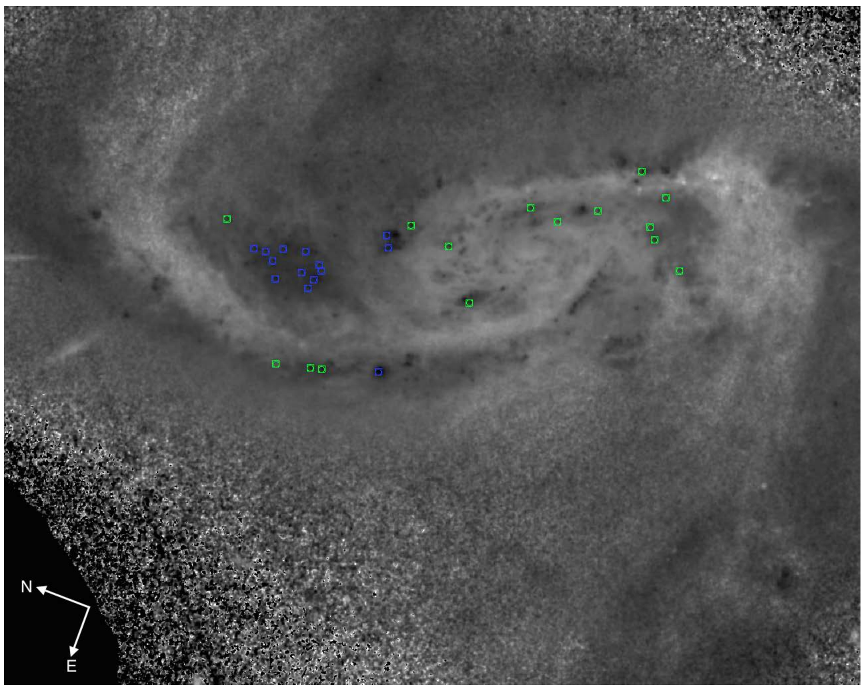

Figure 2.36: Inverted black and white B-I image of NGC 5257E taken with HST ACS/WFC F814W and F435W. The bright emission corresponds to redder (i.e. dustier) regions of the galaxy. The blue centroids correspond to clusters found in relatively "dust-free" regions of these galaxies, whereas the green centroids correspond to clusters found in relatively dustier regions of the galaxy.

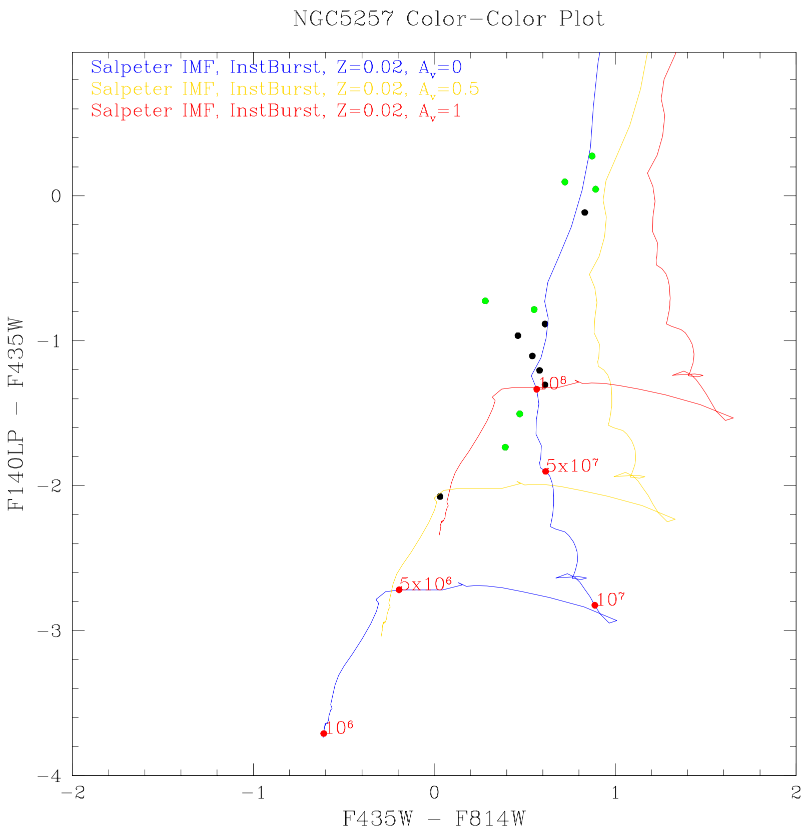

Figure 2.37: Color-Color plot of all star clusters identified in NGC 5257E F814W, F435W, and F140LP plotted against SSP models with various amount of visual extinction. The green points correspond to the clusters found in dustier regions of the galaxy in Figure 2.36.

Table 2.33: Observed Properties of Star Clusters in NGC 5257E

ID	RA	Dec	M_B	σ_B	M_I	σ_I	M_{FUV}	σ_{FUV}
1	204.988389	0.82941763	-15.90	0.01	-16.62	0.02	-15.81	0.01
2	204.9886135	0.828844213	-13.70	0.01	-14.98	0.01	-12.25	0.07
3	204.9893355	0.829802618	-12.13	0.01	-12.41	0.04	-12.86	0.04
4	204.99099	0.832602833	-12.33	0.01	-12.80	0.02	-13.84	0.02
5	204.9913336	0.832908072	-12.27	0.05	-12.88	0.03	-13.58	0.04
6	204.9893535	0.828699614	-12.67	0.02	-13.22	0.03	-13.46	0.02
7	204.9910317	0.83185232	-13.36	0.01	-14.25	0.02	-13.32	0.03
8	204.9915112	0.832786319	-12.80	0.06	-13.26	0.05	-13.77	0.05
9	204.992339	0.834417957	-11.11	0.10	-11.94	0.07	-11.23	0.18
10	204.9921984	0.834047212	-11.78	0.04	-12.36	0.05	-12.99	0.04
11	204.9928594	0.834311205	-13.27	0.01	-13.81	0.01	-14.38	0.01
12	204.9927539	0.833729231	-12.57	0.02	-13.18	0.02	-13.46	0.02
13	204.9917487	0.831103146	-14.21	0.02	-15.08	0.02	-13.94	0.01
14	204.9941781	0.833654938	-13.58	0.01	-15.28	0.01	-12.41	0.06
15	204.9935202	0.831994291	-15.04	0.01	-15.07	0.01	-17.12	0.01
16	204.993914	0.832897563	-12.26	0.04	-12.65	0.05	-14.00	0.01

Table 2.34: Derived Properties of Star Clusters in NGC 5257E

ID	Log(Age)	σ_{Age}	Log($M/M_{\odot}$)	σ_M	A_V	σ_{A_V}
1	8.31	0.01	8.04	0.17	0.40	0.23
2	8.56	0.03	7.46	0.18	0.60	0.07
3	6.66	0.39	5.75	0.17	1.40	0.04
4	6.72	0.67	5.58	0.39	0.90	0.34
5	6.72	0.58	5.61	0.36	1.00	0.30
6	6.66	0.03	5.96	0.19	1.40	0.07
7	8.31	0.49	7.02	0.48	0.40	0.46
8	6.66	0.40	5.96	0.29	1.30	0.22
9	6.66	0.81	5.60	0.66	1.90	0.70
10	6.00	0.44	6.06	0.37	1.80	0.32
11	6.30	0.09	6.68	0.22	1.80	0.13
12	6.52	0.39	6.04	0.31	1.70	0.24
13	8.36	0.02	7.45	0.18	0.50	0.06
14	8.01	0.05	7.66	0.18	1.80	0.04
15	6.56	0.05	6.49	0.21	0.70	0.11
16	6.72	0.43	5.45	0.36	0.70	0.31

2.7.17 NGC 5257W

NGC 5257W contains a prominent group of bright clusters located $\sim 10''$ (5 kpc) south from the nucleus in a $\sim 17''$ (4.2 kpc) long spiral arm. The maximum A_V adopted for this galaxy is 1.8 mags of visual extinction (Smith et al., 2014).

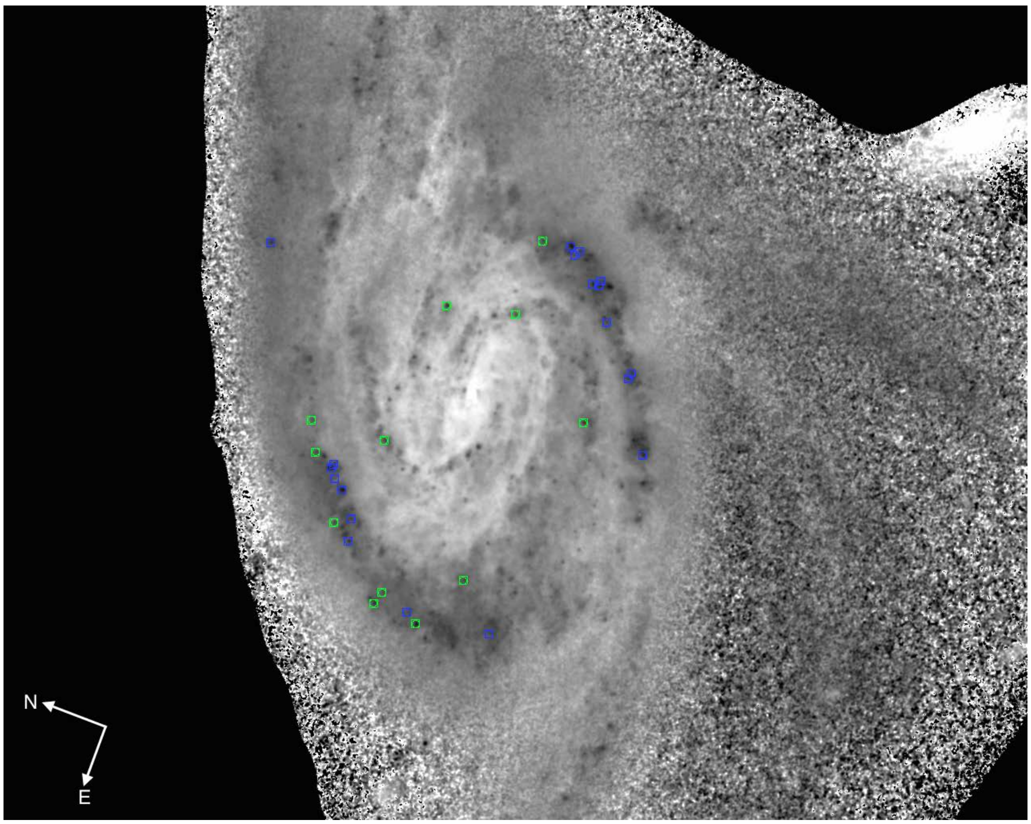

Figure 2.38: Inverted black and white B-I image of NGC 5257W taken with HST ACS/WFC F814W and F435W. The bright emission corresponds to redder (i.e. dustier) regions of the galaxy. The blue centroids correspond to clusters found in relatively "dust-free" regions of these galaxies, whereas the green centroids correspond to clusters found in relatively dustier regions of the galaxy.

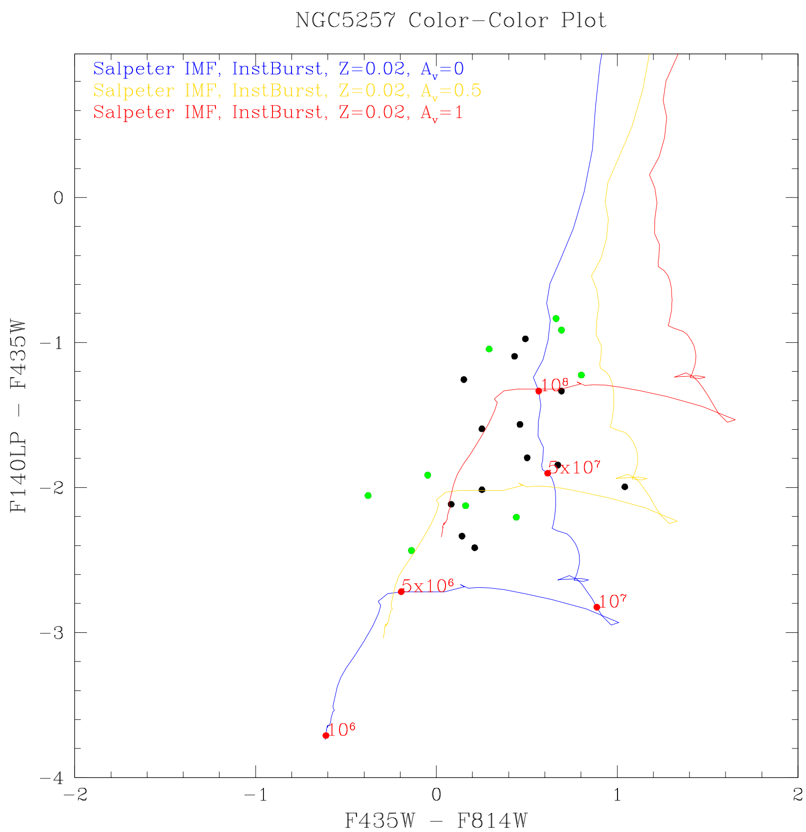

Figure 2.39: Color-Color plot of all star clusters identified in NGC 5257W in F814W, F435W, and F140LP plotted against SSP models with various amount of visual extinction. The green points correspond to the clusters found in dustier regions of the galaxy in Figure 2.38.

Table 2.35: Observed Properties of Star Clusters in NGC 5257W

ID	RA	Dec	M_B	σ_B	M_I	σ_I	M_{FUV}	σ_{FUV}
1	204.9677325	0.839888315	-12.60	0.04	-13.26	0.04	-13.43	0.07
2	204.9676008	0.839405141	-14.32	0.02	-14.40	0.02	-16.43	0.01
3	204.9676117	0.839232784	-13.47	0.04	-13.90	0.05	-14.56	0.02
4	204.9679115	0.838666338	-12.25	0.06	-13.29	0.02	-14.24	0.06
5	204.9680284	0.838781875	-13.85	0.02	-14.10	0.03	-15.44	0.01
6	204.9679985	0.838669059	-13.07	0.06	-13.32	0.06	-15.08	0.04
7	204.969473	0.840889786	-13.17	0.01	-13.46	0.01	-14.21	0.01
8	204.9690871	0.839750205	-12.72	0.05	-13.41	0.07	-13.63	0.02
9	204.96912	0.837489752	-13.63	0.05	-14.12	0.08	-14.60	0.06
10	204.9692242	0.837503427	-15.05	0.02	-15.74	0.02	-16.38	0.01
11	204.970253	0.837864699	-12.01	0.02	-12.17	0.04	-14.13	0.01
12	204.9727531	0.841813782	-11.72	0.06	-11.67	0.09	-13.63	0.04
13	204.9703117	0.836690288	-13.97	0.02	-14.12	0.03	-15.22	0.03
14	204.9728795	0.841450503	-13.65	0.02	-13.86	0.03	-16.06	0.01
15	204.9730222	0.841315721	-12.87	0.04	-13.54	0.03	-14.71	0.02
16	204.9731456	0.841116419	-14.47	0.01	-14.61	0.02	-16.80	0.01
17	204.9735238	0.840747	-12.24	0.06	-12.70	0.07	-13.80	0.08
18	204.9737106	0.840991159	-12.21	0.04	-12.65	0.07	-14.41	0.02
19	204.9738917	0.840626292	-12.65	0.04	-13.15	0.03	-14.44	0.02
20	204.9736297	0.838529841	-13.22	0.03	-14.02	0.02	-14.44	0.02
21	204.974667	0.839754239	-12.11	0.03	-11.73	0.09	-14.16	0.02
22	204.9746698	0.838945129	-12.42	0.02	-12.28	0.05	-14.85	0.01

Table 2.36: Derived Properties of Star Clusters in NGC 5257W

ID	Log(Age)	σ_{Age}	Log($M/M_{\odot}$)	σ_M	A_V	σ_{A_V}
1	6.56	0.64	6.19	0.59	1.80	0.60
2	6.48	0.09	6.57	0.22	1.10	0.13
3	6.48	0.04	6.60	0.20	1.80	0.09
4	6.24	0.02	6.35	0.20	1.80	0.07
5	6.54	0.03	6.42	0.19	1.30	0.07
6	6.72	0.34	5.84	0.32	0.70	0.26
7	6.54	0.01	6.30	0.18	1.60	0.05
8	6.64	0.59	6.25	0.54	1.70	0.53
9	6.54	0.29	6.54	0.35	1.70	0.29
10	6.74	0.32	6.83	0.29	1.10	0.23
11	6.58	0.30	5.50	0.29	0.90	0.22
12	6.54	0.03	5.40	0.21	1.00	0.09
13	6.52	0.01	6.57	0.18	1.50	0.03
14	6.74	0.01	5.90	0.17	0.40	0.02
15	7.30	0.19	6.19	0.21	0.50	0.10
16	6.72	0.01	6.29	0.18	0.50	0.05
17	6.58	0.24	5.81	0.31	1.30	0.24
18	6.76	0.16	5.37	0.19	0.50	0.07
19	6.74	0.17	5.71	0.19	0.80	0.07
20	7.63	0.27	6.60	0.26	0.60	0.19
21	6.52	0.01	5.51	0.18	0.90	0.05
22	6.52	0.05	5.53	0.20	0.70	0.10

2.7.18 NGC 5331S

NGC 5331 is a mid-stage mergering system. NGC 5331S and N have a projected nuclear separation of $\sim 27''$ (19 kpc). Large dust lanes are visible along the near edge of the galaxy, and only a small number of star clusters are visible. The maximum A_V adopted for this galaxy is 3.6 mags of visual extinction (Lutz, 1992).

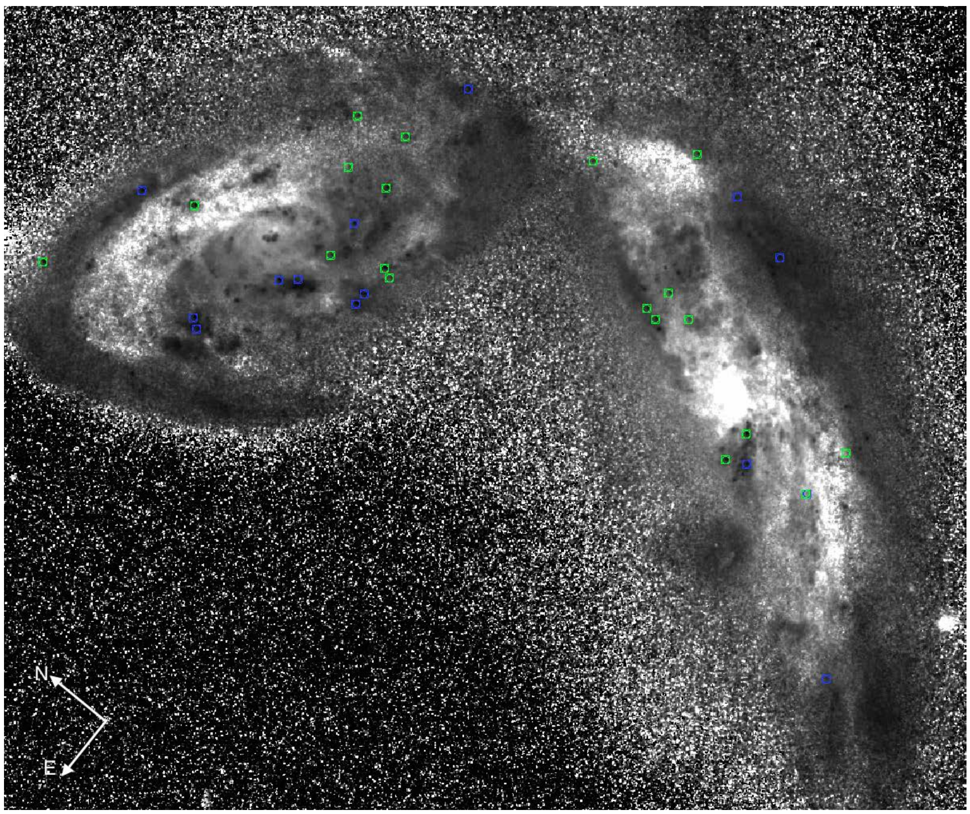

Figure 2.40: Inverted black and white B-I image of NGC 5331S taken with HST ACS/WFC F814W and F435W. The bright emission corresponds to redder (i.e. dustier) regions of the galaxy. The blue centroids correspond to clusters found in relatively "dust-free" regions of these galaxies, whereas the green centroids correspond to clusters found in relatively dustier regions of the galaxy.

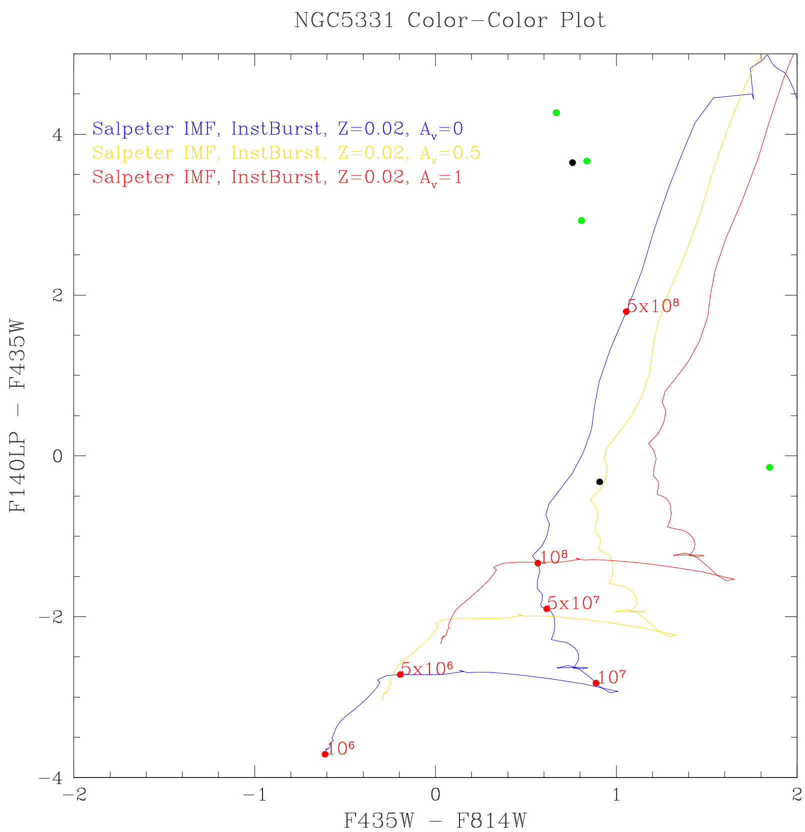

Figure 2.41: Color-Color plot of all star clusters identified in NGC 5331S in F814W, F435W, and F140LP plotted against SSP models with various amount of visual extinction. The green points correspond to the clusters found in dustier regions of the galaxy in Figure 2.40.

Table 2.37: Observed Properties of Star Clusters in NGC 5331S

ID	RA	Dec	M_B	σ_B	M_I	σ_I	M_{FUV}	σ_{FUV}
1	208.0703109	2.098268967	-9.51	0.10	-10.42	0.10	-9.83	0.11
2	208.0667504	2.102795958	-12.63	0.03	-13.47	0.03	-8.96	0.07
3	208.0676478	2.100879121	-15.03	0.01	-15.70	0.01	-10.76	0.27
4	208.0681184	2.100981506	-12.59	0.02	-13.40	0.03	-9.66	0.19
5	208.0672543	2.099466214	-9.90	0.07	-12.06	0.03	-9.13	0.18
6	208.0680338	2.099718103	-9.64	0.10	-11.49	0.10	-9.78	0.26
7	208.068045	2.100690283	-13.34	0.03	-14.10	0.02	-9.69	0.14

Table 2.38: Derived Properties of Star Clusters in NGC 5331S

ID	Log(Age)	σ_{Age}	$\mathrm{Log}(M/M_{\odot})$	σ_M	A_V	σ_{A_V}
1	6.50	0.38	5.53	0.20	2.30	0.37
2	8.76	0.58	8.08	0.17	1.80	0.55
3	8.86	0.44	9.13	0.17	1.80	0.31
4	8.61	0.43	7.93	0.17	1.80	0.28
5	6.80	0.35	5.85	0.19	2.50	0.92
6	6.82	0.51	5.46	0.20	1.90	0.70
7	7.91	0.13	8.70	0.18	3.60	0.05

2.7.19 NGC 5331N

NGC 5331N has a nucleus and two distinct spiral arms, with a small number of star clusters visible throughout the galaxy. The maximum A_V adopted for this galaxy is 1.8 mags of visual extinction (Lutz, 1992).

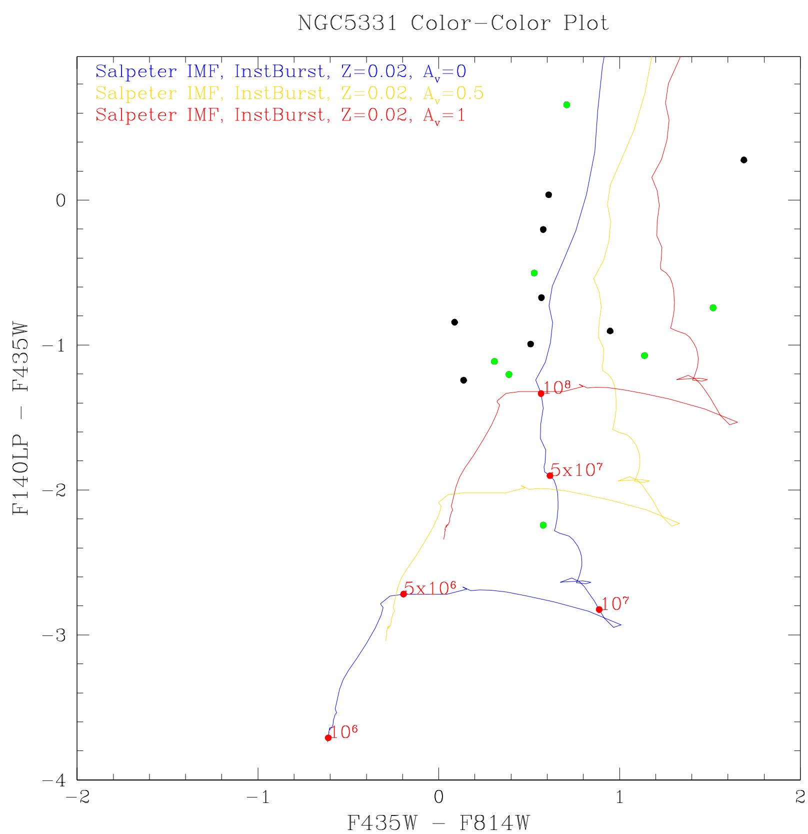

Figure 2.42: Color-Color plot of all star clusters identified in NGC 5331N in F814W, F435W, and F140LP plotted against SSP models with various amount of visual extinction. The green points correspond to the clusters found in dustier regions of the galaxy in Figure 2.40.

Table 2.39: Observed Properties of Star Clusters in NGC 5331N

ID	RA	Dec	M_B	σ_B	M_I	σ_I	M_{FUV}	σ_{FUV}
1	208.0660418	2.10796331	-9.62618	0.07	-10.20	0.10	-11.87	0.10
2	208.0660027	2.107205416	-9.75618	0.07	-10.89	0.07	-10.83	0.07
3	208.0667669	2.107753228	-9.37618	0.09	-10.89	0.08	-10.12	0.11
4	208.068404	2.11027354	-12.4562	0.02	-13.02	0.02	-13.13	0.03
5	208.0682536	2.109496656	-11.5962	0.02	-11.98	0.05	-12.80	0.04
6	208.0667871	2.107126587	-11.0962	0.03	-11.62	0.05	-11.60	0.14
7	208.0674622	2.107317376	-12.2362	0.03	-13.18	0.04	-13.14	0.03
8	208.0684892	2.106770333	-12.9062	0.01	-13.48	0.01	-13.11	0.03
9	208.0678413	2.106630757	-11.5662	0.03	-11.87	0.05	-12.68	0.05
10	208.0683038	2.10672568	-11.4162	0.03	-11.50	0.08	-12.26	0.07
11	208.0686796	2.107921587	-13.8362	0.01	-14.44	0.01	-13.80	0.02
12	208.0666683	2.102976709	-12.5562	0.02	-13.41	0.02	-11.52	0.01
13	208.0698361	2.108671969	-10.3762	0.09	-10.51	0.14	-11.62	0.12
14	208.0685396	2.107683102	-11.6562	0.07	-13.34	0.02	-11.38	0.16
15	208.0699658	2.111094004	-10.4662	0.03	-11.17	0.03	-9.81	0.13
16	208.0697116	2.108783852	-11.8962	0.02	-12.40	0.02	-12.89	0.04

Table 2.40: Derived Properties of Star Clusters in NGC 5331N

ID	Log(Age)	σ_{Age}	Log($M/M_{\odot}$)	σ_M	A_V	σ_{A_V}
1	6.86	0.33	4.64	0.25	0.30	0.15
2	7.54	0.34	5.65	0.30	0.80	0.23
3	7.42	0.24	5.65	0.27	1.20	0.17
4	6.66	0.35	6.23	0.37	1.50	0.32
5	6.66	0.11	5.67	0.27	1.10	0.20
6	8.31	0.01	6.20	0.18	0.01	0.04
7	6.78	0.44	6.09	0.36	1.30	0.30
8	6.66	0.02	6.56	0.18	1.80	0.05
9	6.66	0.04	5.71	0.21	1.20	0.10
10	6.66	0.04	5.70	0.19	1.30	0.07
11	6.68	0.30	6.94	0.17	1.80	0.08
12	8.61	0.15	7.08	0.18	0.10	0.05
13	6.66	0.35	5.13	0.28	1.00	0.19
14	7.65	0.11	6.88	0.22	1.60	0.11
15	8.56	0.02	6.14	0.17	0.01	0.13
16	6.64	0.08	5.86	0.26	1.30	0.18

2.7.20 UGC 09618NED02

Armus et al. (2009) discusses the detailed morphology of this galaxy at length. UGC 09618NED02 is an early-stage merger with the two nuclei separated by $\sim 40''$ (30 kpc). Multiple star clusters are visible along the spiral arms in the face-on galaxy (VV430A). The maximum A_V adopted for this galaxy is 2.4 mags of visual extinction (Leech et al., 1989).

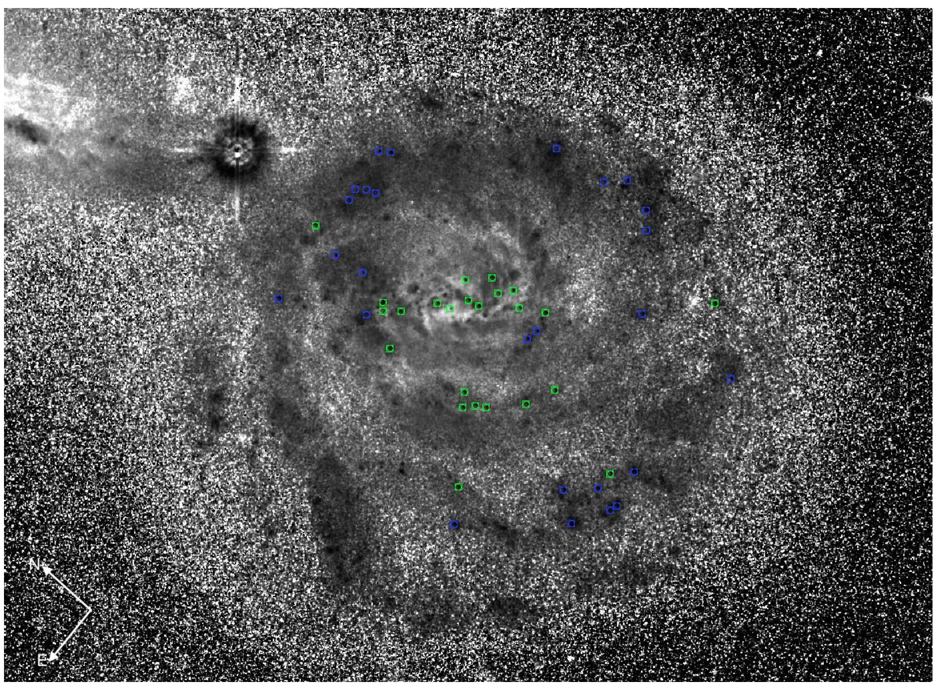

Figure 2.43: Inverted black and white B-I image of UGC 09618NED02 taken with HST ACS/WFC F814W and F435W. The bright emission corresponds to redder (i.e. dustier) regions of the galaxy. The blue centroids correspond to clusters found in relatively "dust-free" regions of these galaxies, whereas the green centroids correspond to clusters found in relatively dustier regions of the galaxy.

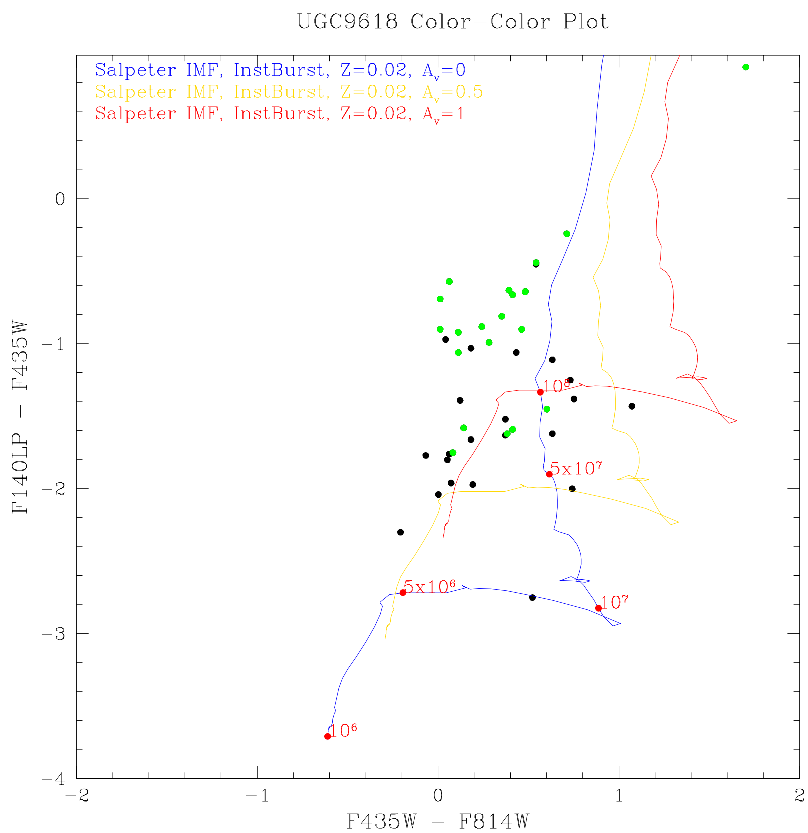

Figure 2.44: Color-Color plot of all star clusters identified in UGC 09618NED02 in F814W, F435W, and F140LP plotted against SSP models with various amount of visual extinction. The green points correspond to the clusters found in dustier regions of the galaxy in Figure 2.43.

Table 2.41: Observed Properties of Star Clusters in UGC 09618NED02

ID	RA	Dec	M_B	σ_B	M_I	σ_I	M_{FUV}	σ_{FUV}
1	224.2502774	24.60907674	-10.22	0.19	-10.97	0.15	-12.23	0.18
2	224.2495249	24.60924743	-11.10	0.03	-11.63	0.04	-13.86	0.18
3	224.2494326	24.60905594	-11.83	0.03	-11.84	0.04	-13.88	0.04
4	224.247693	24.60664702	-11.07	0.08	-12.15	0.05	-12.51	0.14
5	224.2474984	24.6053126	-11.00	0.04	-11.08	0.08	-12.97	0.08
6	224.2477925	24.60476143	-11.71	0.03	-11.78	0.05	-13.48	0.06
7	224.2513684	24.6094958	-12.99	0.02	-13.71	0.02	-13.24	0.07
8	224.2481156	24.6045755	-11.08	0.05	-11.84	0.05	-12.47	0.18
9	224.2516575	24.60893269	-13.11	0.01	-13.66	0.01	-13.57	0.02
10	224.2516642	24.60837604	-11.69	0.07	-12.07	0.08	-13.22	0.07
11	224.2504346	24.60641579	-12.52	0.05	-12.88	0.06	-13.34	0.06
12	224.2504328	24.60598905	-12.40	0.02	-12.52	0.06	-13.33	0.17
13	224.25063	24.60618376	-11.50	0.07	-11.92	0.11	-12.17	0.05
14	224.2519383	24.60779872	-14.50	0.01	-14.62	0.01	-15.57	0.01
15	224.2510431	24.60655958	-13.33	0.04	-13.35	0.13	-14.03	0.03
16	224.2514028	24.6069871	-13.30	0.07	-13.37	0.14	-13.88	0.04
17	224.2510282	24.6063554	-13.65	0.02	-13.90	0.03	-14.54	0.02
18	224.2506515	24.60573423	-11.61	0.05	-11.63	0.08	-12.52	0.14
19	224.2513638	24.60674976	-15.35	0.01	-17.06	0.01	-14.45	0.02
20	224.2518985	24.60745116	-13.16	0.02	-13.71	0.02	-13.61	0.05
21	224.2520755	24.60771662	-11.17	0.14	-11.78	0.13	-12.63	0.12
22	224.2523005	24.60793133	-12.08	0.06	-12.72	0.06	-13.20	0.07
23	224.2504648	24.6053105	-12.88	0.01	-13.37	0.02	-13.53	0.01
24	224.2495097	24.60387414	-11.68	0.03	-12.32	0.05	-13.31	0.14
25	224.2508571	24.60526342	-11.73	0.04	-12.17	0.06	-12.80	0.11
26	224.2510791	24.6053372	-12.61	0.02	-12.80	0.04	-13.65	0.05
27	224.2526081	24.60727308	-12.41	0.04	-12.81	0.04	-13.05	0.08
28	224.2496684	24.60197058	-11.11	0.04	-11.31	0.06	-13.09	0.08
29	224.2516261	24.6044602	-11.22	0.04	-11.31	0.07	-12.98	0.03
30	224.2525706	24.60577791	-11.27	0.03	-11.56	0.06	-12.27	0.17
31	224.2521417	24.60475683	-11.61	0.04	-12.03	0.03	-13.21	0.03
32	224.2525986	24.60531766	-11.85	0.02	-12.32	0.03	-12.76	0.18
33	224.2528334	24.60566186	-11.89	0.03	-12.38	0.03	-12.54	0.15
34	224.2521531	24.60254189	-12.79	0.01	-12.85	0.02	-14.60	0.02
35	224.2524271	24.6028813	-10.56	0.07	-10.95	0.07	-12.19	0.11
36	224.2531559	24.60341951	-11.72	0.03	-11.91	0.04	-13.39	0.06
37	224.2527859	24.60292948	-11.65	0.02	-11.59	0.04	-13.43	0.02
38	224.2541651	24.60499864	-11.06	0.03	-11.21	0.06	-12.65	0.02
39	224.2528804	24.6024864	-12.38	0.02	-12.51	0.03	-13.78	0.04

Table 2.41 continued

Table 2.41: Observed Properties of Star Clusters in UGC 09618NED02 (continued)

ID	RA	Dec	M_B	σ_B	M_I	σ_I	M_{FUV}	σ_{FUV}
40	224.2530173	24.60254644	-11.29	0.06	-11.34	0.07	-12.27	0.18
41	224.2536233	24.60299199	-13.79	0.01	-13.59	0.01	-16.10	0.01
42	224.2548158	24.60471647	-11.68	0.02	-12.06	0.03	-13.32	0.12
43	224.2506179	24.60923582	-12.07	0.03	-12.81	0.04	-13.33	0.06

Table 2.42: Derived Properties of Star Clusters in UGC 09618NED02

ID	Log(Age)	σ_{Age}	Log($M/M_{\odot}$)	σ_M	A_V	σ_{A_V}
1	7.57	0.39	5.17	0.41	0.10	0.32
2	6.88	0.05	4.82	0.16	0.01	0.45
3	6.66	0.09	5.15	0.25	0.50	0.18
4	7.63	0.28	5.70	0.28	0.40	0.21
5	6.64	0.20	4.84	0.34	0.60	0.29
6	6.66	0.03	5.21	0.19	0.70	0.09
7	8.41	0.03	6.73	0.17	0.01	0.05
8	6.76	0.52	5.10	0.38	0.90	0.34
9	6.66	0.02	6.25	0.16	1.60	0.04
10	6.38	0.65	5.87	0.53	1.50	0.52
11	6.66	0.57	5.85	0.49	1.30	0.47
12	6.66	0.53	5.75	0.16	1.20	0.03
13	6.66	0.75	5.55	0.63	1.50	0.66
14	6.66	0.95	6.54	0.16	1.10	0.03
15	6.66	0.57	6.18	0.48	1.30	0.46
16	6.66	0.77	6.22	0.61	1.40	0.63
17	6.66	0.67	6.30	0.16	1.30	0.04
18	6.66	0.16	5.43	0.18	1.20	0.05
19	7.86	0.04	8.29	0.17	1.80	0.05
20	8.36	0.03	6.76	0.16	0.01	0.03
21	6.74	0.75	5.13	0.53	0.90	0.51
22	5.10	0.97	6.34	0.66	1.90	0.70
23	6.66	0.03	6.10	0.16	1.50	0.02
24	6.76	0.47	5.29	0.37	0.80	0.33
25	6.66	0.26	5.48	0.35	1.20	0.31
26	6.66	0.51	5.83	0.17	1.20	0.05
27	6.66	0.75	5.91	0.61	1.50	0.63
28	6.36	0.46	5.45	0.36	1.20	0.31
29	6.66	0.09	5.01	0.24	0.70	0.17
30	6.66	0.43	5.30	0.17	1.20	0.04
31	6.72	0.64	5.24	0.47	0.80	0.45
32	6.66	0.01	5.58	0.16	1.30	0.02
33	6.66	0.03	5.71	0.16	1.50	0.04
34	6.66	0.01	5.64	0.16	0.70	0.03
35	6.00	0.65	5.42	0.50	1.50	0.48
36	6.66	0.25	5.27	0.25	0.80	0.18
37	6.66	0.86	5.19	0.16	0.70	0.04
38	6.66	0.04	5.00	0.20	0.80	0.11
39	6.66	0.07	5.58	0.17	0.90	0.05

Table 2.42 continued

Table 2.42: Derived Properties of Star Clusters in UGC 09618NED02 (continued)

ID	Log(Age)	σ_{Age}	Log($M/M_{\odot}$)	σ_M	A_V	σ_{A_V}
40	6.66	0.35	5.31	0.34	1.20	0.28
41	6.66	0.36	5.83	0.16	0.30	0.06
42	5.10	0.67	5.96	0.38	1.50	0.34
43	6.78	0.55	5.57	0.43	1.00	0.40

2.7.21 IC 4687N

IC 4687 is an early-stage merging system. The two primary galaxies (IC 4686 and IC 4687) have a nuclear separation of $\sim 84''$ (31 kpc). The northern galaxy contains several bright clusters in a nuclear arm stretching north and westward. The maximum A_V adopted for this galaxy is 2.8 mags of visual extinction (Rich et al., 2012).

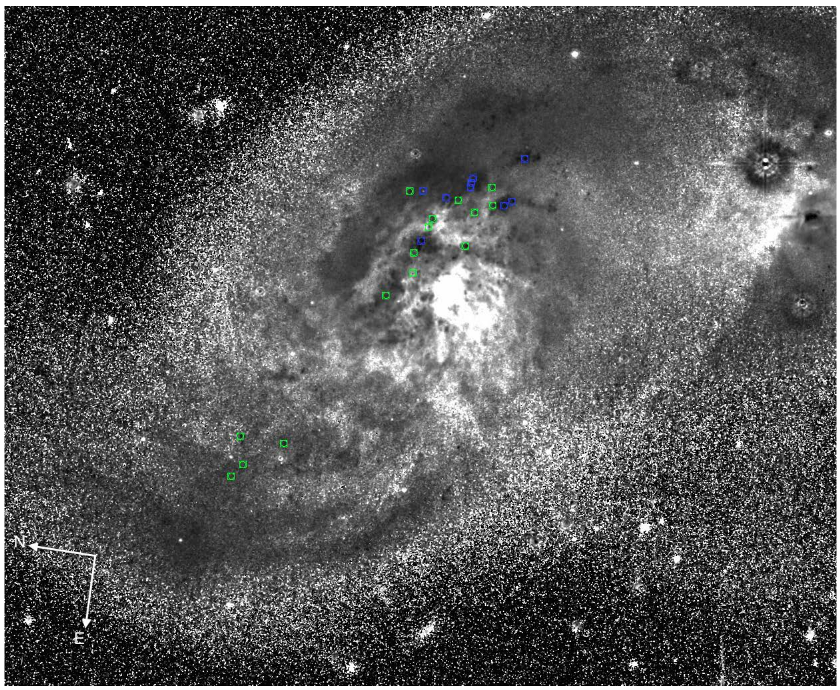

Figure 2.45: Inverted black and white B-I image of IC 4687N taken with HST ACS/WFC F814W and F435W. The bright emission corresponds to redder (i.e. dustier) regions of the galaxy. The blue centroids correspond to clusters found in relatively "dust-free" regions of these galaxies, whereas the green centroids correspond to clusters found in relatively dustier regions of the galaxy.

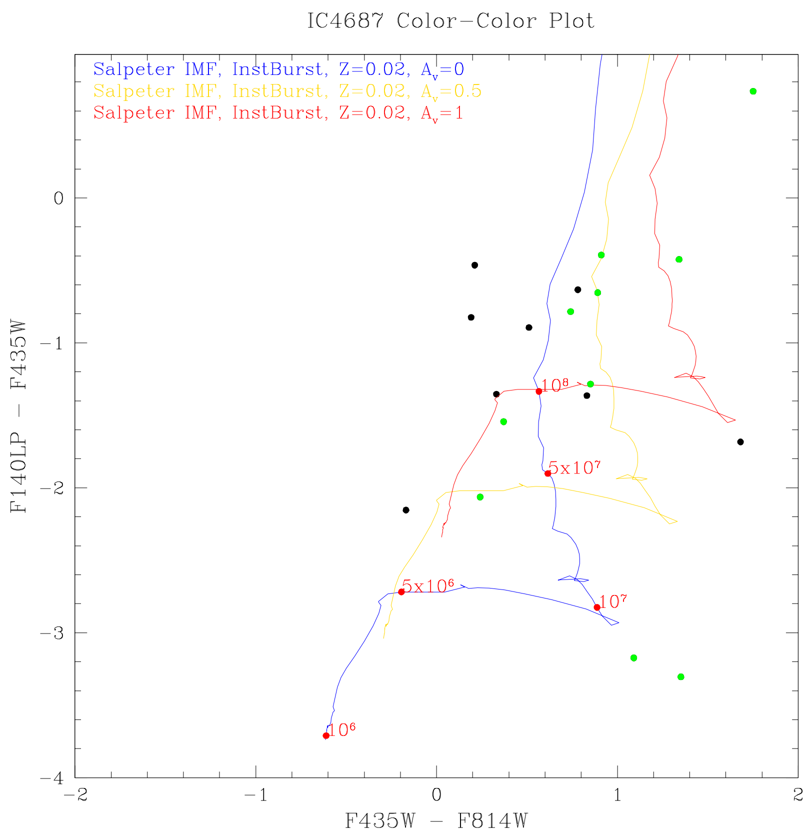

Figure 2.46: Color-Color plot of all star clusters identified in IC 4687N in F814W, F435W, and F140LP plotted against SSP models with various amount of visual extinction. The green points correspond to the clusters found in dustier regions of the galaxy in Figure 2.45.

Table 2.43: Observed Properties of Star Clusters in IC 4687N

ID	RA	Dec	M_B	σ_B	M_I	σ_I	M_{FUV}	σ_{FUV}
1	273.4245591	-57.72132281	-8.50	0.12	-9.60	0.08	-11.68	0.07
2	273.4139193	-57.72470603	-12.61	0.02	-14.37	0.02	-11.88	0.10
3	273.4144883	-57.72459737	-14.21	0.03	-14.55	0.03	-15.57	0.02
4	273.4149949	-57.72446495	-13.59	0.03	-14.94	0.03	-14.02	0.07
5	273.4167849	-57.72402211	-11.55	0.05	-12.45	0.04	-12.21	0.07
6	273.4229748	-57.72139585	-10.56	0.03	-10.94	0.04	-12.11	0.08
7	273.4230317	-57.72231699	-9.93	0.04	-10.18	0.08	-12.00	0.02
8	273.4240561	-57.72152951	-8.93	0.09	-10.29	0.05	-12.24	0.09
9	273.4126981	-57.72621106	-12.88	0.05	-13.10	0.03	-13.35	0.03
10	273.4127251	-57.72525032	-11.08	0.09	-11.83	0.12	-11.87	0.10
11	273.4124913	-57.72636619	-11.88	0.02	-12.08	0.04	-12.71	0.05
12	273.4126885	-57.72499269	-12.73	0.05	-13.52	0.03	-13.37	0.02
13	273.4126222	-57.72421981	-10.61	0.05	-11.47	0.03	-11.90	0.10
14	273.4126044	-57.72447105	-10.59	0.06	-12.28	0.02	-12.28	0.07
15	273.4122004	-57.72543793	-11.09	0.13	-11.61	0.11	-11.99	0.09
16	273.4120619	-57.72591473	-12.36	0.02	-13.28	0.02	-12.76	0.04
17	273.4118376	-57.72547113	-11.04	0.15	-11.88	0.09	-12.41	0.06
18	273.4107751	-57.72651001	-11.29	0.05	-11.13	0.09	-13.45	0.05

Table 2.44: Derived Properties of Star Clusters in IC 4687N

ID	Log(Age)	σ_{Age}	Log($M/M_{\odot}$)	σ_M	A_V	σ_{A_V}
1	6.94	0.01	3.98	0.22	0.01	0.03
2	7.76	0.43	7.13	0.35	1.80	0.30
3	6.66	0.09	6.37	0.27	1.00	0.19
4	7.65	0.37	7.09	0.31	1.10	0.25
5	8.01	0.75	6.16	0.58	0.50	0.59
6	6.36	0.35	5.39	0.37	1.50	0.32
7	6.72	0.45	4.41	0.37	0.50	0.32
8	6.94	0.01	4.15	0.20	0.01	0.01
9	6.66	0.01	6.10	0.18	1.50	0.53
10	6.00	0.85	5.94	0.66	2.10	0.69
11	6.66	0.31	5.60	0.18	1.30	0.05
12	6.70	0.97	6.05	0.70	1.50	0.75
13	7.74	0.38	5.58	0.33	0.40	0.27
14	7.65	0.01	5.36	0.20	0.10	0.08
15	6.68	0.66	5.28	0.62	1.30	0.63
16	8.06	0.86	6.57	0.70	0.60	0.76
17	6.80	0.48	5.20	0.45	1.00	0.39
18	6.66	0.09	4.88	0.24	0.40	0.15

2.7.22 IC 4687S

The southern galaxy contains several bright clusters in the nuclear region as well as a series of dust lanes. Their is little evidence of extended tidal structures which contain star clusters. The maximum A_V adopted for this galaxy is 3.7 mags of visual extinction (Rich et al., 2012).

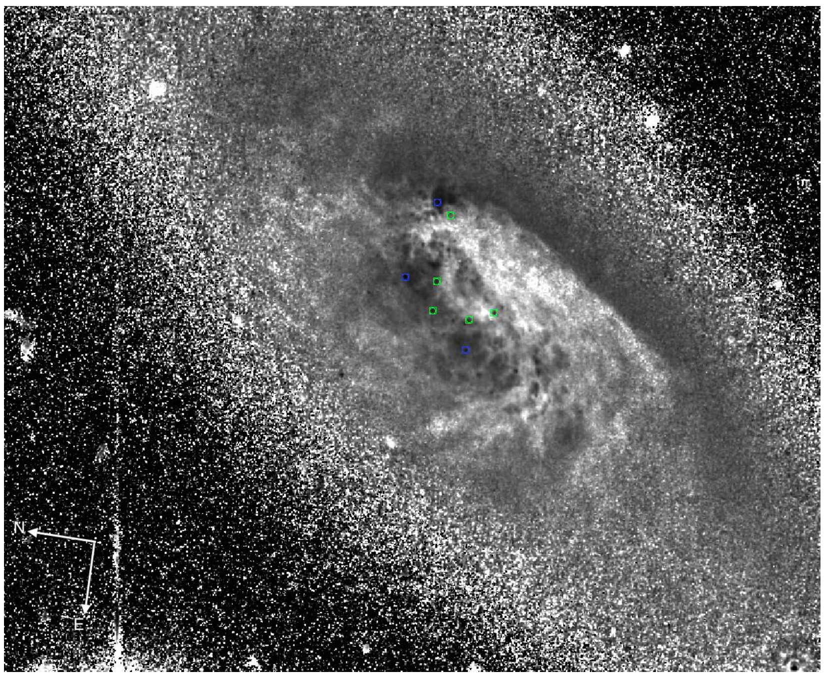

Figure 2.47: Inverted black and white B-I image of IC 4687S taken with HST ACS/WFC F814W and F435W. The bright emission corresponds to redder (i.e. dustier) regions of the galaxy. The blue centroids correspond to clusters found in relatively "dust-free" regions of these galaxies, whereas the green centroids correspond to clusters found in relatively dustier regions of the galaxy.

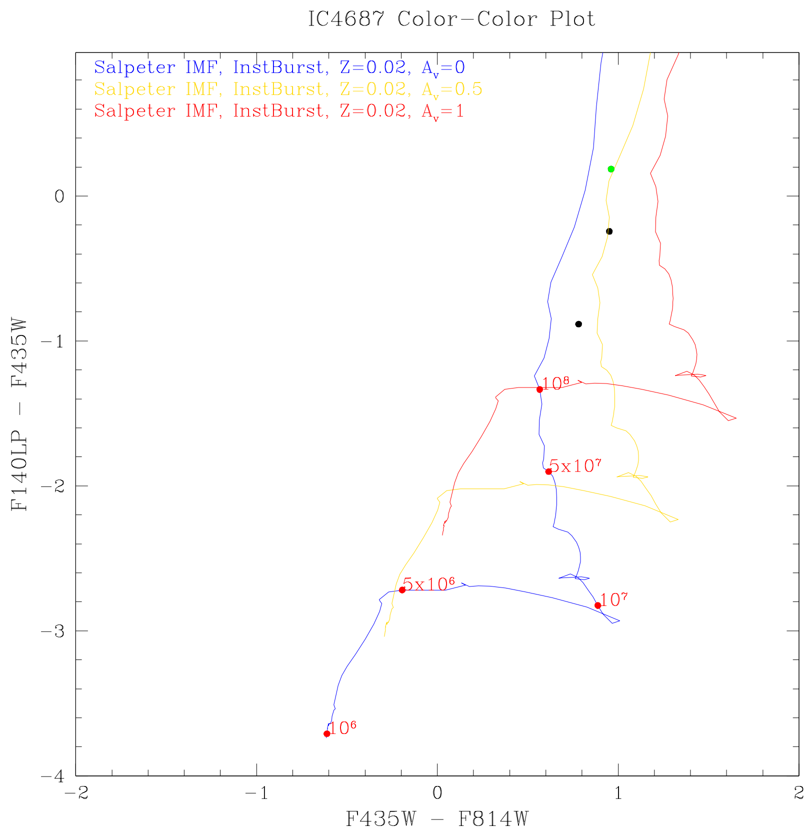

Figure 2.48: Color-Color plot of all star clusters identified in IC 4687S in F814W, F435W, and F140LP plotted against SSP models with various amount of visual extinction. The green points correspond to the clusters found in dustier regions of the galaxy in Figure 2.47.

Table 2.45: Observed Properties of Star Clusters in IC 4687S

ID	RA	Dec	M_B	σ_B	M_I	σ_I	M_{FUV}	σ_{FUV}
1	273.4156651	-57.7476378	-9.47	0.16	-11.63	0.09	-10.47	0.36
2	273.4174919	-57.74709814	-12.71	0.02	-13.50	0.01	-13.60	0.02
3	273.4181417	-57.74844252	-13.11	0.02	-14.08	0.04	-12.93	0.04
4	273.4184439	-57.74809628	-12.50	0.05	-13.27	0.07	-11.14	0.18
5	273.4192425	-57.74811065	-11.58	0.05	-12.54	0.03	-11.83	0.10

Table 2.46: Derived Properties of Star Clusters in IC 4687S

ID	Log(Age)	σ_{Age}	Log($M/M_{\odot}$)	σ_M	A_V	σ_{A_V}
1	6.94	0.11	5.16	0.37	1.50	0.28
2	6.72	0.34	5.94	0.32	1.30	0.26
3	8.41	0.66	6.94	0.66	0.30	0.70
4	8.66	0.03	6.75	0.19	0.01	0.05
5	6.40	0.76	6.19	0.73	2.40	0.79

2.7.23 NGC 6786

NGC 6786 is an early-stage merger consisting of a pair of face-on galaxies with a nuclear separation of $\sim 72''$ (37 kpc). Faint star clusters are seen along the inner spiral structure. The brightest clusters sit at roughly $5''$ (3 kpc) from the southwest nucleus in the large arm/tail extending between the two galaxies. The maximum A_V adopted for this galaxy is 2.0 mags of visual extinction (Martin et al., 1991).

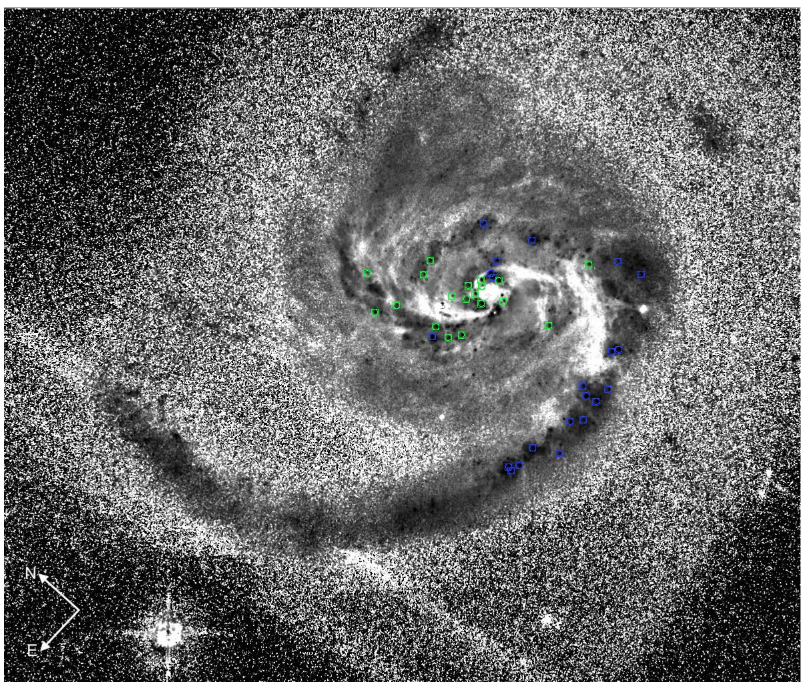

Figure 2.49: Inverted black and white B-I image of NGC 6786 taken with HST ACS/WFC F814W and F435W. The bright emission corresponds to redder (i.e. dustier) regions of the galaxy. The blue centroids correspond to clusters found in relatively "dust-free" regions of these galaxies, whereas the green centroids correspond to clusters found in relatively dustier regions of the galaxy.

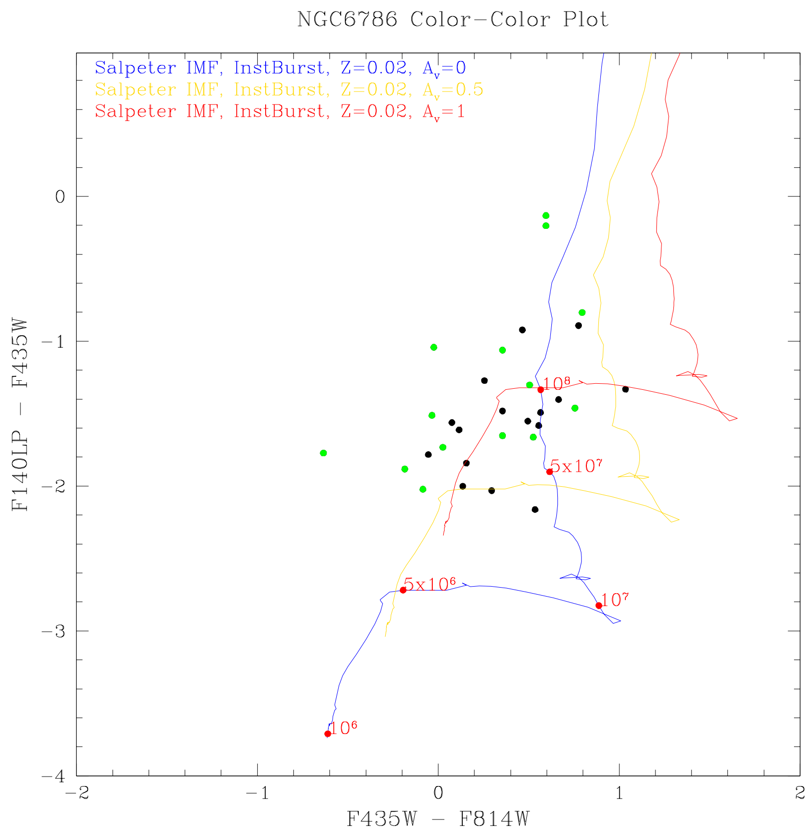

Figure 2.50: Color-Color plot of all star clusters identified in NGC 6786 in F814W, F435W, and F140LP plotted against SSP models with various amount of visual extinction. The green points correspond to the clusters found in dustier regions of the galaxy in Figure 2.49.

Table 2.47: Observed Properties of Star Clusters in NGC 6786

ID	RA	Dec	M_B	σ_B	M_I	σ_I	M_{FUV}	σ_{FUV}
1	287.7197193	73.41100197	-10.99	0.02	-11.66	0.03	-12.39	0.05
2	287.719232	73.40994657	-12.43	0.02	-12.93	0.04	-13.98	0.03
3	287.7238745	73.41165138	-10.79	0.04	-11.30	0.04	-12.09	0.07
4	287.7178111	73.40815357	-9.46	0.06	-10.03	0.06	-10.95	0.22
5	287.7238495	73.41044623	-11.77	0.07	-12.37	0.14	-11.97	0.08
6	287.7234966	73.41051976	-13.43	0.02	-13.41	0.06	-14.47	0.02
7	287.7229265	73.41018561	-15.39	0.01	-15.31	0.01	-17.41	0.01
8	287.7227232	73.41040649	-15.05	0.01	-15.31	0.01	-16.32	0.01
9	287.7229402	73.41032417	-14.37	0.02	-14.51	0.03	-16.37	0.01
10	287.7267694	73.41270096	-9.77	0.18	-11.79	0.04	-10.19	0.11
11	287.7250088	73.41164334	-10.13	0.06	-10.10	0.11	-11.64	0.11
12	287.7242707	73.4107057	-12.76	0.03	-13.56	0.04	-13.56	0.02
13	287.7250077	73.41029358	-14.21	0.03	-13.58	0.10	-15.98	0.01
14	287.7251949	73.41061029	-12.67	0.06	-13.27	0.10	-12.80	0.04
15	287.7254972	73.41090859	-10.45	0.06	-10.27	0.20	-12.33	0.02
16	287.7241289	73.40990629	-12.92	0.02	-14.11	0.05	-11.81	0.09
17	287.7290544	73.4121962	-11.94	0.03	-12.30	0.03	-13.00	0.03
18	287.7242387	73.40883366	-10.24	0.04	-10.27	0.08	-11.97	0.08
19	287.7279844	73.41092482	-11.98	0.02	-12.74	0.03	-13.44	0.02
20	287.7277016	73.41036998	-12.38	0.02	-12.91	0.02	-14.04	0.01
21	287.7287715	73.41090241	-13.47	0.01	-13.63	0.01	-15.31	0.01
22	287.7283128	73.41059111	-11.42	0.03	-11.78	0.04	-13.07	0.03
23	287.7235043	73.40730799	-11.63	0.05	-12.67	0.04	-12.96	0.03
24	287.7270499	73.40763824	-11.77	0.01	-12.55	0.02	-12.66	0.04
25	287.7264275	73.40713593	-10.01	0.07	-10.54	0.10	-12.16	0.07
26	287.7276317	73.40724684	-11.46	0.04	-11.93	0.03	-12.38	0.06
27	287.727598	73.40748488	-12.61	0.01	-12.56	0.02	-14.39	0.01
28	287.7297973	73.40754253	-10.67	0.03	-11.23	0.03	-12.25	0.06
29	287.7327209	73.40798896	-13.58	0.01	-13.70	0.01	-15.19	0.01
30	287.7322458	73.40744712	-9.67	0.04	-9.97	0.07	-11.70	0.20
31	287.7343067	73.40807688	-11.58	0.02	-11.66	0.04	-13.14	0.03
32	287.7349114	73.40817718	-11.63	0.04	-11.99	0.05	-13.11	0.06

Table 2.48: Derived Properties of Star Clusters in NGC 6786

ID	Log(Age)	σ_{Age}	Log($M/M_{\odot}$)	σ_M	A_V	σ_{A_V}
1	6.78	0.49	5.48	0.39	0.90	0.35
2	6.74	0.56	5.97	0.43	0.80	0.40
3	6.22	0.67	5.41	0.50	1.70	0.48
4	6.74	0.55	4.84	0.38	0.90	0.33
5	8.41	0.07	6.64	0.23	0.01	0.13
6	6.66	0.01	6.45	0.17	1.10	0.46
7	6.66	0.34	6.97	0.17	0.50	0.01
8	6.66	0.01	7.10	0.17	1.00	0.11
9	6.44	0.06	6.57	0.21	1.10	0.11
10	7.00	0.17	5.91	0.26	1.70	0.16
11	6.66	0.01	5.03	0.20	0.80	0.07
12	8.01	0.08	6.99	0.22	0.40	0.13
13	6.66	0.04	6.50	0.18	0.50	0.05
14	8.41	0.04	7.00	0.20	0.01	0.07
15	6.66	0.04	5.05	0.23	0.60	0.13
16	8.51	0.05	7.44	0.23	0.50	0.15
17	6.66	0.57	5.86	0.43	1.20	0.40
18	6.66	0.03	5.02	0.21	0.70	0.10
19	7.72	0.44	6.47	0.35	0.30	0.30
20	7.86	0.55	6.55	0.40	0.01	0.36
21	6.48	0.04	6.43	0.22	1.10	0.12
22	5.10	0.04	5.55	0.19	1.50	0.07
23	7.63	0.24	6.37	0.25	0.50	0.16
24	6.72	0.05	5.84	0.18	1.30	0.06
25	6.84	0.35	4.91	0.27	0.40	0.19
26	6.66	0.05	5.67	0.18	1.30	0.02
27	6.66	0.35	5.97	0.18	0.70	0.03
28	6.74	0.57	5.27	0.43	0.80	0.40
29	6.66	0.29	6.41	0.17	0.80	0.04
30	6.72	0.05	4.70	0.20	0.50	0.09
31	6.66	0.58	5.61	0.18	0.80	0.04
32	6.40	0.05	5.67	0.20	1.50	0.08

2.7.24 IRAS 20351+2521

IRAS 20351+2521 is an early-stage merger containing multiple star clusters in the northern region where the spiral arms diffuse into multiple components beyond the inner $\sim 5''$ (4 kpc). The maximum A_V adopted for this galaxy is 4.7 mags of visual extinction, which is lower than the cited value of 9.4 mags, but prevents our model from predicting masses unrealistically high for even the most massive YSCs found in the sample. (Stierwalt et al., 2013).

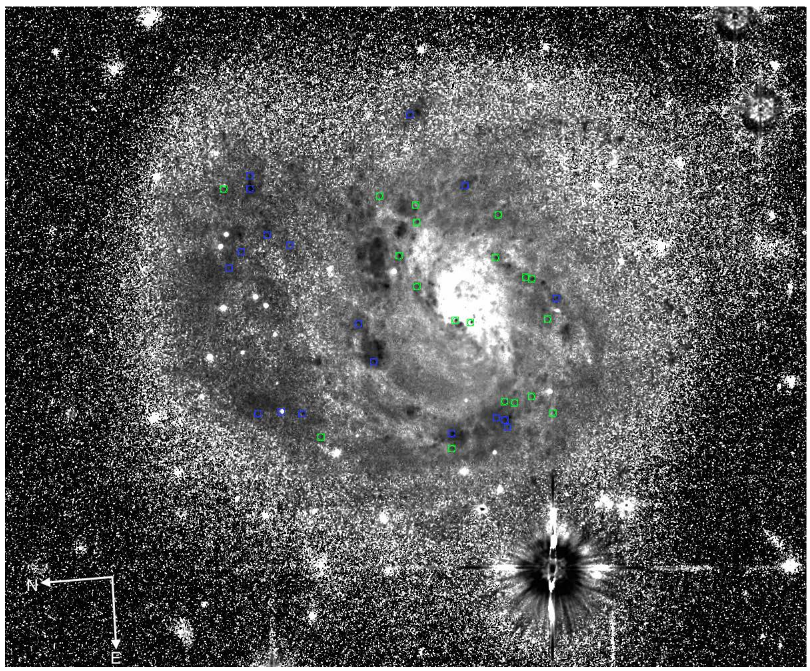

Figure 2.51: Inverted black and white B-I image of IRAS 20351+2521 taken with HST ACS/WFC F814W and F435W. The bright emission corresponds to redder (i.e. dustier) regions of the galaxy. The blue centroids correspond to clusters found in relatively "dust-free" regions of these galaxies, whereas the green centroids correspond to clusters found in relatively dustier regions of the galaxy.

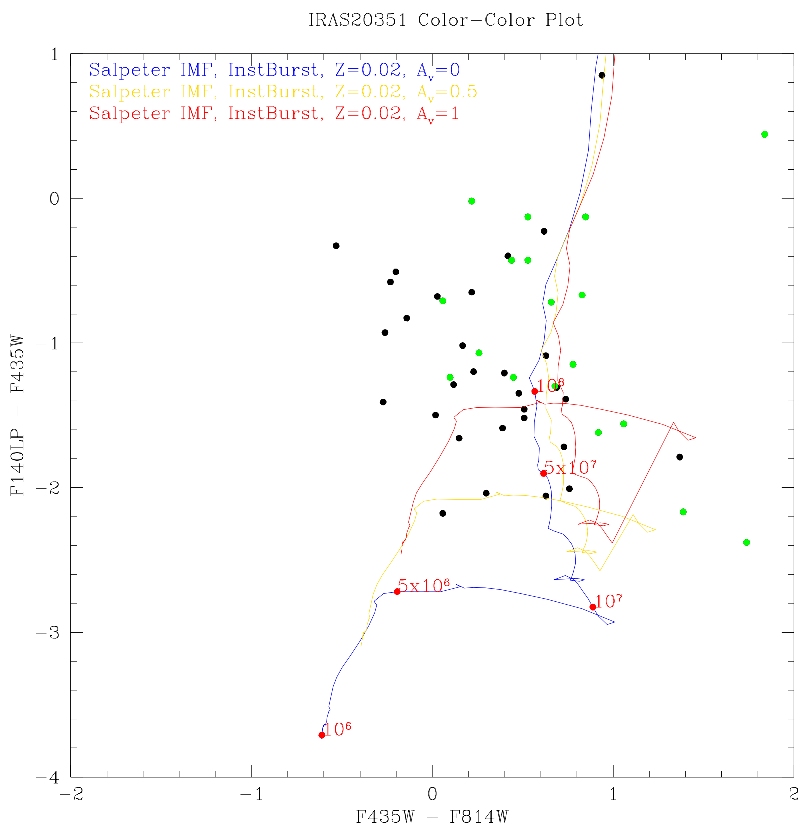

Figure 2.52: Color-Color plot of all star clusters identified in IRAS 20351+2521 in F814W, F435W, and F140LP plotted against SSP models with various amount of visual extinction. The green points correspond to the clusters found in dustier regions of the galaxy in Figure 2.51.

Table 2.49: Observed Properties of Star Clusters in IRAS 20351+2521

ID	RA	Dec	M_B	σ_B	M_I	σ_I	M_{FUV}	σ_{FUV}
1	309.3189111	25.52810092	-11.77	0.04	-11.99	0.06	-12.96	0.25
2	309.3201669	25.53148902	-12.10	0.03	-12.78	0.03	-13.40	0.14
3	309.3204655	25.53148786	-14.20	0.01	-14.34	0.02	-15.85	0.04
4	309.3207482	25.52879944	-11.57	0.05	-12.24	0.05	-12.86	0.05
5	309.3205846	25.52701311	-12.18	0.08	-11.64	0.16	-12.50	0.26
6	309.3209895	25.52805392	-12.80	0.04	-14.63	0.01	-12.35	0.24
7	309.3213802	25.52804452	-12.92	0.03	-13.44	0.03	-13.04	0.17
8	309.3212834	25.52633971	-11.39	0.06	-12.12	0.06	-12.77	0.22
9	309.3215513	25.53117662	-11.92	0.07	-11.68	0.12	-12.49	0.16
10	309.3227499	25.52581676	-12.05	0.06	-12.70	0.07	-12.76	0.16
11	309.3227896	25.52569385	-12.91	0.02	-12.96	0.05	-13.61	0.07
12	309.3232605	25.52520015	-12.72	0.05	-13.34	0.06	-13.80	0.12
13	309.3237357	25.52539922	-11.60	0.05	-12.42	0.03	-12.26	0.22
14	309.3236793	25.52933194	-11.99	0.06	-12.00	0.07	-13.48	0.12
15	309.3256351	25.52614986	-11.60	0.08	-12.04	0.10	-12.83	0.04
16	309.3255973	25.526354	-12.15	0.05	-12.24	0.08	-13.38	0.06
17	309.3256314	25.53101137	-11.60	0.05	-14.92	0.01	-12.71	0.01
18	309.3256579	25.53150391	-11.02	0.08	-11.77	0.06	-13.02	0.21
19	309.3259664	25.52654554	-11.17	0.15	-12.53	0.06	-12.95	0.27
20	309.3261938	25.52631453	-13.23	0.02	-13.84	0.02	-13.45	0.16
21	309.3262881	25.52747562	-13.98	0.02	-14.03	0.02	-16.15	0.01
22	309.3262506	25.53020748	-11.03	0.05	-11.65	0.05	-13.08	0.03

Table 2.50: Derived Properties of Star Clusters in IRAS 20351+2521

ID	Log(Age)	σ_{Age}	Log($M/M_{\odot}$)	σ_M	A_V	σ_{A_V}
1	6.54	0.33	5.69	0.16	1.50	0.02
2	6.74	0.19	5.65	0.16	1.10	0.31
3	6.54	0.32	6.50	0.15	1.20	0.23
4	7.76	0.42	5.92	0.16	0.40	0.20
5	6.52	0.40	6.07	0.18	1.90	0.45
6	6.78	0.05	6.57	0.16	2.30	0.59
7	8.51	0.11	6.72	0.16	0.01	0.53
8	7.70	0.12	5.81	0.17	0.40	0.16
9	6.52	0.23	5.91	0.17	1.80	0.46
10	8.36	0.53	6.26	0.17	0.01	0.19
11	6.52	0.08	6.31	0.16	1.80	0.05
12	6.64	0.37	6.19	0.16	1.60	0.54
13	7.96	0.12	6.13	0.16	0.60	0.08
14	6.52	0.18	5.67	0.17	1.30	0.12
15	6.52	0.29	5.68	0.18	1.60	0.24
16	6.52	0.32	5.84	0.16	1.50	0.24
17	8.11	0.39	6.22	0.16	0.60	0.23
18	6.94	0.52	5.09	0.18	0.50	0.59
19	7.65	0.53	5.53	0.22	0.10	0.36
20	6.52	0.07	6.65	0.16	2.20	0.41
21	6.44	0.19	6.49	0.16	1.10	0.19
22	7.36	0.24	5.39	0.16	0.30	0.58

2.7.25 II ZW 096

Inami et al. (2010) discusses the detailed morphology of this galaxy at length. II Zw 096 is a mid-stage merging system. The western component is a roughly face-on spiral galaxy with star clusters along the spiral arms. The southeast end of the spiral, approximately 11.6″ (8.4 kpc) from the nucleus, contains a distinct cluster-rich region. The maximum A_V adopted for this galaxy is 3.0 mags of visual extinction (Inami et al., 2010).

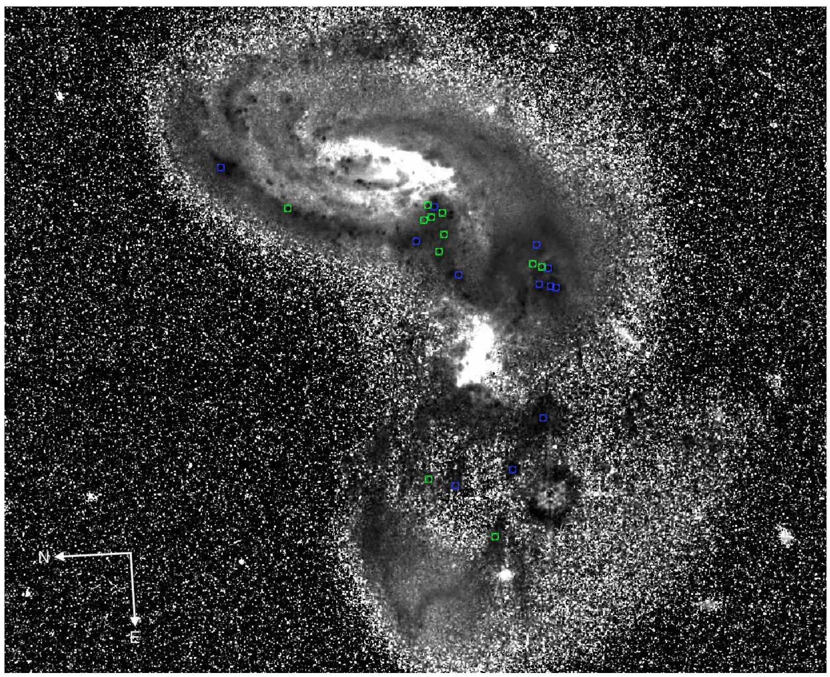

Figure 2.53: Inverted black and white B-I image of II ZW 096 taken with HST ACS/WFC F814W and F435W. The bright emission corresponds to redder (i.e. dustier) regions of the galaxy. The blue centroids correspond to clusters found in relatively "dust-free" regions of these galaxies, whereas the green centroids correspond to clusters found in relatively dustier regions of the galaxy.

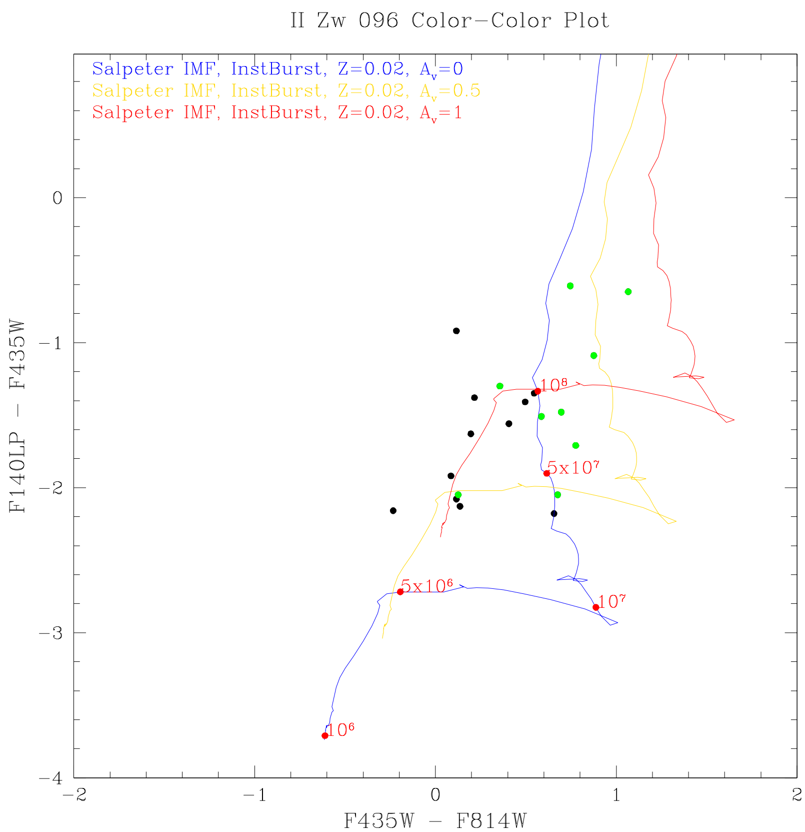

Figure 2.54: Color-Color plot of all star clusters identified in II ZW 096 in F814W, F435W, and F140LP plotted against SSP models with various amount of visual extinction. The green points correspond to the clusters found in dustier regions of the galaxy in Figure 2.53.

Table 2.51: Observed Properties of Star Clusters in II ZW 096

ID	RA	Dec	M_B	σ_B	M_I	σ_I	M_{FUV}	σ_{FUV}
1	314.347937	17.13209914	-14.40	0.02	-14.52	0.01	-16.48	0.01
2	314.3488605	17.12855532	-13.82	0.03	-14.60	0.03	-15.53	0.05
3	314.3490196	17.12831079	-13.91	0.02	-14.50	0.05	-15.42	0.02
4	314.3489006	17.12844657	-14.02	0.05	-14.14	0.07	-14.94	0.12
5	314.3487591	17.13097999	-13.81	0.02	-13.94	0.02	-15.86	0.01
6	314.3491325	17.12863715	-13.77	0.02	-14.84	0.01	-14.42	0.03
7	314.349413	17.12830611	-13.18	0.02	-14.06	0.02	-14.27	0.04
8	314.3494999	17.12879568	-14.29	0.01	-14.38	0.02	-16.21	0.01
9	314.3497151	17.12841414	-16.14	0.01	-16.84	0.01	-17.62	0.01
10	314.3501466	17.12654531	-17.92	0.01	-18.33	0.01	-19.48	0.01
11	314.3501115	17.12664894	-15.51	0.05	-16.26	0.05	-16.12	0.03
12	314.3500502	17.12680274	-13.52	0.11	-13.88	0.19	-14.82	0.07
13	314.3501617	17.12810109	-14.29	0.02	-14.84	0.02	-15.64	0.02
14	314.3504248	17.12671799	-14.41	0.10	-14.91	0.09	-15.82	0.05
15	314.3504765	17.12652561	-16.42	0.01	-16.64	0.02	-17.80	0.02
16	314.350505	17.12642631	-16.31	0.01	-16.51	0.02	-17.94	0.01
17	314.352852	17.12679784	-14.29	0.01	-14.06	0.03	-16.45	0.01
18	314.353755	17.1273767	-13.74	0.01	-13.88	0.02	-15.87	0.01
19	314.3538332	17.12884574	-13.71	0.01	-14.39	0.01	-15.76	0.01
20	314.3539789	17.12839369	-12.26	0.02	-12.92	0.02	-14.44	0.03

Table 2.52: Derived Properties of Star Clusters in II ZW 096

ID	Log(Age)	σ_{Age}	Log($M/M_{\odot}$)	σ_M	A_V	σ_{A_V}
1	6.40	0.08	6.76	0.22	1.20	0.12
2	7.40	0.25	6.64	0.24	0.50	0.16
3	6.74	0.45	6.32	0.39	1.00	0.35
4	6.52	0.53	6.70	0.52	1.70	0.50
5	6.42	0.12	6.52	0.24	1.20	0.16
6	7.63	0.27	7.04	0.26	1.00	0.19
7	7.63	0.26	6.64	0.26	0.70	0.18
8	6.52	0.02	6.49	0.18	1.10	0.06
9	7.65	0.01	7.68	0.17	0.40	0.13
10	5.70	0.62	8.60	0.44	1.60	0.41
11	6.54	0.85	7.45	0.81	2.00	0.93
12	6.54	0.55	6.39	0.53	1.50	0.52
13	6.72	0.61	6.60	0.54	1.20	0.54
14	6.58	0.62	6.73	0.55	1.40	0.55
15	6.54	0.01	7.50	0.17	1.40	0.03
16	6.52	0.01	7.40	0.18	1.30	0.04
17	6.54	0.01	6.33	0.18	0.80	0.05
18	5.70	0.41	6.71	0.27	1.20	0.20
19	6.78	0.07	5.98	0.17	0.50	0.02
20	6.96	0.15	5.57	0.18	0.40	0.06

2.7.26 ESO 148-IG002

ESO 148-IG002 is a late-stage merger with a projected nuclear separation of $\sim 4.7''$ (4.2 kpc). The galaxy has a series of bright clusters which lie along a north-south ridge to the east of the bulge. The maximum A_V adopted for this galaxy is 2.5 mags of visual extinction (Johansson & Bergvall, 1988).

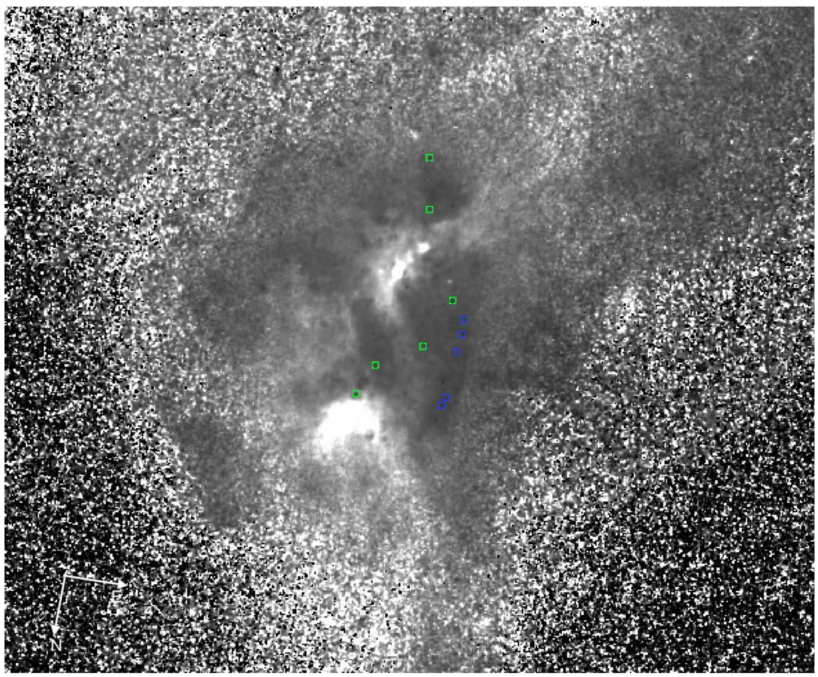

Figure 2.55: Inverted black and white B-I image of ESO 148-IG002 taken with HST ACS/WFC F814W and F435W. The bright emission corresponds to redder (i.e. dustier) regions of the galaxy. The blue centroids correspond to clusters found in relatively "dust-free" regions of these galaxies, whereas the green centroids correspond to clusters found in relatively dustier regions of the galaxy.

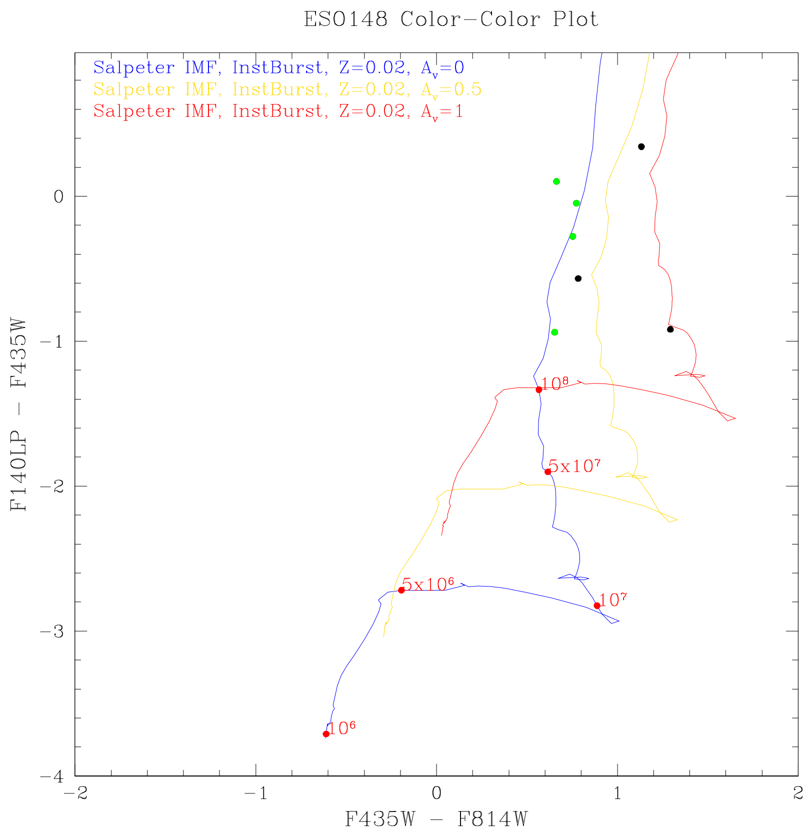

Figure 2.56: Color-Color plot of all star clusters identified in ESO 148-IG002 in F814W, F435W, and F140LP plotted against SSP models with various amount of visual extinction. The green points correspond to the clusters found in dustier regions of the galaxy in Figure 2.55.

Table 2.53: Observed Properties of Star Clusters in ESO 148-IG002

ID	RA	Dec	M_B	σ_B	M_I	σ_I	M_{FUV}	σ_{FUV}
1	348.9465405	-59.05411541	-14.15	0.01	-14.90	0.01	-14.43	0.03
2	348.9468576	-59.0539657	-13.60	0.02	-14.73	0.02	-13.26	0.10
3	348.9462256	-59.05361789	-12.73	0.03	-13.39	0.04	-12.63	0.18
4	348.9469037	-59.05365887	-11.95	0.09	-13.24	0.08	-12.87	0.14
5	348.9454074	-59.05331294	-13.54	0.15	-14.19	0.09	-14.48	0.06
6	348.9468404	-59.05307144	-14.27	0.02	-15.05	0.01	-14.84	0.02
7	348.9456965	-59.05497655	-14.45	0.04	-15.22	0.03	-14.50	0.06

Table 2.54: Derived Properties of Star Clusters in ESO 148-IG002

ID	Log(Age)	σ_{Age}	Log($M/M_{\odot}$)	σ_M	A_V	σ_{A_V}
1	8.46	0.03	7.17	0.16	0.01	0.78
2	8.41	0.40	7.23	0.45	0.60	0.43
3	8.61	0.06	6.73	0.17	0.01	0.02
4	7.65	0.25	6.21	0.24	0.80	0.14
5	8.26	0.79	6.80	0.69	0.01	0.73
6	6.48	0.90	7.13	0.84	2.20	0.97
7	8.56	0.04	7.38	0.17	0.01	0.04

2.7.27 NGC 7674

NGC 7674 an early-stage merger with a face-on spiral galaxy and companions to the northeast and southeast. Star clusters are visible along the prominent spiral arms throughout the galaxy. The maximum A_V adopted for this galaxy is 2.0 mags of visual extinction (Momjian et al., 2003).

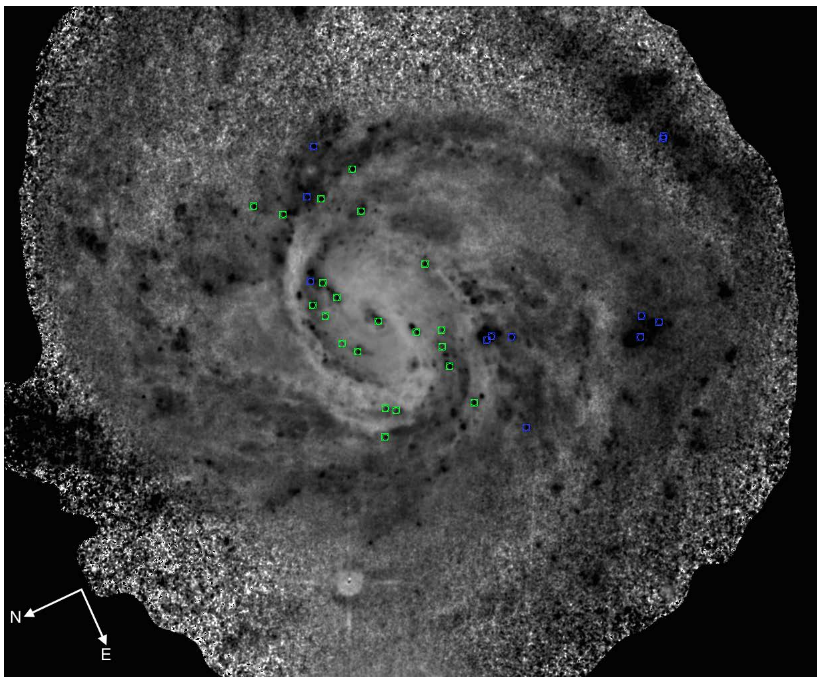

Figure 2.57: Inverted black and white B-I image of NGC 7674 taken with HST ACS/WFC F814W and F435W. The bright emission corresponds to redder (i.e. dustier) regions of the galaxy. The blue centroids correspond to clusters found in relatively "dust-free" regions of these galaxies, whereas the green centroids correspond to clusters found in relatively dustier regions of the galaxy.

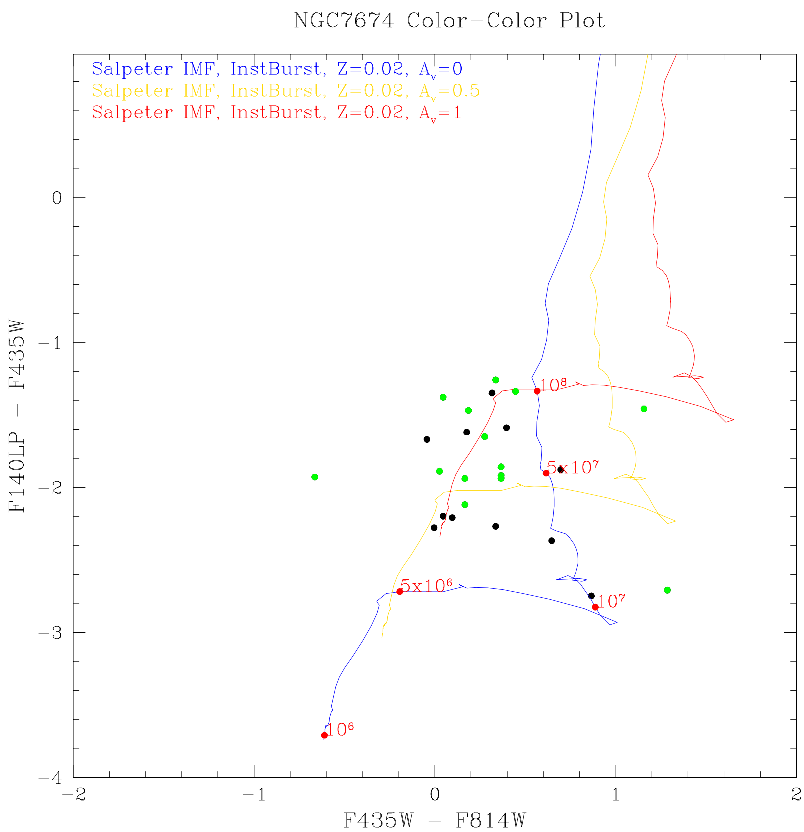

Figure 2.58: Color-Color plot of all star clusters identified in NGC 7674 in F814W, F435W, and F140LP plotted against SSP models with various amount of visual extinction. The green points correspond to the clusters found in dustier regions of the galaxy in Figure 2.57.

Table 2.55: Observed Properties of Star Clusters in NGC 7674

ID	RA	Dec	M_B	σ_B	M_I	σ_I	M_{FUV}	σ_{FUV}
1	351.9831239	8.778349264	-12.20	0.02	-12.57	0.03	-14.06	0.02
2	351.9849596	8.772096618	-11.55	0.02	-11.73	0.04	-13.17	0.05
3	351.9850026	8.772116709	-11.44	0.02	-11.76	0.03	-12.79	0.08
4	351.9832985	8.779441129	-10.77	0.11	-11.11	0.13	-13.04	0.06
5	351.9830552	8.780545473	-10.91	0.03	-11.08	0.05	-12.85	0.04
6	351.9840117	8.778513551	-12.29	0.04	-12.74	0.03	-13.63	0.04
7	351.9849762	8.780046055	-12.87	0.02	-12.92	0.03	-15.07	0.02
8	351.9855017	8.779670342	-12.42	0.04	-12.61	0.09	-13.89	0.06
9	351.9862949	8.779049017	-17.60	0.01	-18.76	0.01	-19.06	0.01
10	351.9882912	8.773938539	-12.62	0.01	-13.32	0.01	-14.50	0.02
11	351.9885463	8.773640234	-11.47	0.03	-12.12	0.05	-13.84	0.03
12	351.9857724	8.780029971	-11.03	0.05	-10.37	0.20	-12.96	0.07
13	351.9869669	8.777906039	-11.45	0.04	-11.50	0.06	-12.83	0.05
14	351.9868119	8.778402264	-13.02	0.01	-13.05	0.03	-14.91	0.01
15	351.9875291	8.777102907	-13.70	0.03	-13.66	0.03	-15.37	0.02
16	351.9886887	8.774122684	-11.76	0.03	-11.76	0.06	-14.04	0.05
17	351.9874886	8.7769875	-11.39	0.19	-12.26	0.16	-14.14	0.04
18	351.9864376	8.77992672	-11.09	0.04	-11.46	0.07	-13.01	0.06
19	351.9873013	8.778022066	-10.96	0.06	-11.33	0.13	-12.90	0.07
20	351.9867238	8.779687958	-12.50	0.03	-12.67	0.04	-14.62	0.01
21	351.9877438	8.778029429	-12.90	0.02	-13.24	0.04	-14.16	0.02
22	351.988047	8.779603842	-10.36	0.13	-11.65	0.09	-13.07	0.03
23	351.9895457	8.777038636	-10.67	0.05	-10.77	0.09	-12.88	0.07
24	351.9886045	8.779833873	-12.05	0.03	-12.33	0.05	-13.70	0.03
25	351.9823723	8.778916581	-11.27	0.03	-11.67	0.04	-12.86	0.07

Table 2.56: Derived Properties of Star Clusters in NGC 7674

ID	Log(Age)	σ_{Age}	Log($M/M_{\odot}$)	σ_M	A_V	σ_{A_V}
1	6.74	0.03	5.48	0.21	0.70	0.11
2	6.52	0.02	5.50	0.19	1.30	0.07
3	6.52	0.03	5.56	0.19	1.50	0.08
4	6.72	0.28	4.87	0.27	0.60	0.17
5	6.52	0.08	5.14	0.22	1.10	0.13
6	6.44	0.10	6.14	0.24	1.70	0.16
7	6.42	0.10	6.09	0.22	1.10	0.14
8	6.52	0.05	5.90	0.20	1.40	0.09
9	6.80	0.03	7.78	0.17	0.90	0.03
10	7.00	0.07	5.97	0.17	0.70	0.04
11	7.00	0.10	5.46	0.17	0.60	1.12
12	6.52	0.01	5.08	0.20	0.90	0.09
13	6.52	0.01	5.51	0.18	1.40	0.04
14	6.52	0.01	5.98	0.17	1.10	0.03
15	6.52	0.01	6.31	0.17	1.20	0.03
16	6.50	0.08	5.39	0.22	0.90	0.13
17	7.00	0.43	5.43	0.27	0.60	0.06
18	6.74	0.18	5.04	0.27	0.70	0.20
19	6.74	0.19	4.98	0.29	0.70	0.22
20	6.58	0.27	5.70	0.27	0.90	0.20
21	6.54	0.01	6.14	0.18	1.50	0.05
22	6.82	0.10	4.76	0.22	0.60	1.12
23	6.68	0.11	4.90	0.24	0.70	0.16
24	6.52	0.28	5.70	0.24	1.30	0.16
25	6.66	0.30	5.41	0.30	1.20	0.23

Chapter 3

A Very Large Array Survey of Luminous Extranuclear Star-forming Regions in Luminous Infrared Galaxies in GOALS

3.1 Introduction

Galaxies with high infrared (IR) luminosities, e.g., luminous infrared galaxies (LIRGs: $10^{11} < L_{\rm IR}[8-1000\mu{\rm m}] < 10^{12}$ $L_\odot$), are rare in the local Universe, yet they are a cosmologically important class of objects that dominate the infrared luminosity density at redshifts $z = 1-2$ (e.g. Murphy et al., 2011a; Magnelli et al., 2011). LIRGs, which are often triggered by the interactions and mergers of gas-rich disk galaxies, have high bolometric luminosities that primarily emanate from nuclear star-formation, as well as active galactic nuclei (AGN) (e.g., Sanders & Mirabel, 1996). In addition to strong nuclear star formation, enhanced star-formation activity has been seen in the outer disks and tidal structures of many interacting galaxies (Schweizer, 1978; Hibbard & van Gorkom, 1996; Smith et al., 2010, 2016).

To fully assess the nature of star formation and AGN activity in LIRGs as a function of merger stage, luminosity, and optical depth, we initiated the Great Observatories All-sky LIRG Survey (GOALS; Armus et al., 2009). The multi-wavelength dataset, which is most complete for LIRGs with $L_{IR} \geq 10^{11.4} L_{\odot}$, contains observations using Chandra (Iwasawa et al., 2011; Torres-Albà et al., 2018), GALEX (Howell et al., 2010), HST (Kim et al., 2013a; Linden et al., 2017), Spitzer (Stierwalt et al., 2013, 2014), Herschel (e.g., Díaz-Santos et al., 2013, 2017; Chu et al., 2017), VLA (e.g. Barcos-Muñoz et al., 2015, 2017) and ALMA (e.g., Xu et al., 2014, 2015; Privon et al., 2017).

These studies have revealed one of the primary challenges in studying LIRGs is that their nuclear regions can be heavily dust-enshrouded, thus necessitating long wavelength observations to unveil their properties (e.g., Condon et al., 1991; Downes & Solomon, 1998; Soifer et al., 2000). Although weak with respect to a galaxies' bolometric luminosity, radio emission is largely optically-thin and unaffected by dust extinction. The emission is primarily powered by stars more massive than $\sim 8M_{\odot}$ which end their lives as core-collapse supernovae, and their remnants are thought to be the primary producers of cosmic ray (CR) electrons that give rise to the diffuse synchrotron emission observed from star-forming galaxies (Condon, 1992). These same massive stars are also responsible for the creation of H II regions that produce radio free-free emission, whose strength is directly proportional to the production rate of ionizing (Lyman continuum) photons.

Ground-observable radio frequencies ($\sim 1 - 100$ GHz) are particularly useful in probing both processes. The nonthermal component typically has a steep spectrum [$S(\nu) \propto \nu^{\alpha_{NT}}$, where $\alpha_{NT} \sim -0.85$], while the thermal (free-free) component is relatively flat ($\alpha_T \sim -0.1$; e.g., Condon, 1992). Accordingly, for globally integrated measurements of star-forming galaxies, lower frequencies (e.g., 1.4 GHz) are generally dominated by nonthermal emission, while the observed fraction of thermal free-free emission increases with frequency, eventually dominating beyond $\sim$ 30 GHz. Thus, by observing galaxies across this frequency range we can separate these two emission components and produce maps of the current star formation activity.

However, a robust decomposition of the radio spectral energy distribution (SED) may be complex. For example: the thermal and nonthermal fractions may vary with galaxy mass (e.g., Hughes et al., 2007; Bell, 2003), the nonthermal spectral index can vary within galaxies (Tabatabaei et al., 2013, 2017), and anomalous microwave emission may add unexpected features to the radio SED in some regions (e.g., Murphy et al., 2011b, 2018b). More relevant to the present study, observations of U/LIRGs over the last decade have revealed that they can have significant variation from system-to-system in their global radio properties (Leroy et al., 2011; Murphy et al., 2013; Barcos-Muñoz et al., 2017).

This was the basis for the GOALS "equatorial" survey, which is a multi-frequency VLA program to image a complete sample of 68 U/LIRGs within the declination range $-20^o < \delta < 20^o$, from $3 - 33$ GHz at resolutions of $10 - 1000$ pc. One of the fundamental goals of this study is to quantify the level of variation we see in the radio SEDs on sub-galactic scales in these galaxies, and determine the validity of applying a two-component power-law model to characterize the star-formation activity of individual regions in LIRGs.

In this paper we examine the radio and near-IR properties of "extranuclear" star-forming regions identified in galaxies in the GOALS equatorial sample. This spatial cut is imposed to control for any contribution to the observed radio continuum emission from a strong central AGN. Thus, we require all regions for which we perform photometric analysis to reside outside the measured mid-infrared (MIR) core of the galaxy, where an AGN would have the largest influence (see Section 3.2 for details). Further, due to the sensitivity of our VLA observations, we are only able to observe the most luminous star-forming regions in the disks of these galaxies. An analysis of the radio continuum properties of nuclear and circumnuclear star-forming regions in LIRGs will be presented in a series of future papers.

The paper is organized as follows: In Section 2 we describe the observations, data reduction, imaging, and sub-sample selection. In Section 3, we describe our ancillary Spitzer data products, and outline our method for identifying individual extranuclear star-forming regions and extracting multi-wavelength photometry. In Section 4, we discuss the radio continuum properties of the sample. In Section 5, we discuss these results in the context of both the far-infrared - radio correlation, as well as the star-formation rate main sequence. In Section 6 we summarize the results.

Throughout this paper, we adopt WMAP Three-Year Cosmology of $H_0 = 73$ km s^{-1} Mpc^{-1}, $\Omega_{\rm matter} = 0.27$, and $\Omega_\Lambda = 0.73$ (Spergel et al., 2007).

3.2 Sample and Data Analysis

Table 3.1: Properties of the 25 GOALS Galaxies in the sub-sample

Name	RA	Dec	D(Mpc)	$\text{Log}(L_{IR}/L_{\odot})$	Core FWHM (kpc)[a]	Inc (°)[b]	PA (°)[b]
MCG-02-01-052	00h18m50.10s	-10d22m42.0s	105.76	11.41	2.28	0.35	55
IC1623	01h07m47.49s	-17d30m25.3s	78.57	11.65	4.60	0.39	123
MCG-03-04-014	01h10m08.96s	-16d51m09.8s	136.17	11.63	4.16	0.85	64
NGC0838	02h09m38.56s	-10d08m49.1s	50.13	11.00	1.65	0.15	84
IC0214	02h14m05.59s	+05d10m23.7s	117.29	11.37	4.79	0.76	139
NGC0877	02h17m59.64s	+14d32m38.6s	50.29	11.04	5.82	0.11	175
UGC02238	02h46m17.49s	+13d05m44.4s	83.37	11.26	3.64	0.52	135
UGC02369	02h54m01.78s	+14d58m14.0s	121.94	11.60	3.52	0.75	30
CGCG465-012	03h54m16.08s	+15d55m43.4s	86.84	11.15	2.61	0.14	89
UGC02982	04h12m22.45s	+05d32m50.6s	67.57	11.13	3.11	0.46	106
UGC03094	04h35m33.83s	+19d10m18.2s	97.06	11.35	4.53	0.39	179
IRAS05442+1732	05h47m11.18s	+17d33m46.7s	74.95	11.25	1.56	0.52	70
IC0563	09h46m20.30s	+03d02m44.0s	87.01	11.19	2.84	0.38	107
NGC3110	10h04m02.11s	-06d28m29.2s	73.48	11.31	2.96	0.32	176
IC2810	11h25m45.05s	+14d40m35.9s	142.89	11.59	3.72	0.39	32
NGC5257	13h39m52.90s	+00d50m24.0s	98.63	11.55	8.98	0.70	96
NGC5258	13h39m57.70s	+00d49m51.0s	98.63	11.55	9.60	0.36	169
NGC5331	13h52m16.20s	+02d06m03.0s	139.1	11.59	5.25	0.35	102
NGC5936	15h30m00.84s	+12d59m21.5s	60.81	11.07	1.33	0.76	60
NGC5990	15h46m16.37s	+02d24m55.7s	58.42	11.06	1.22	0.60	99
CGCG052-037	16h30m56.54s	+04d04m58.4s	104.72	11.38	2.49	0.14	114
IRASF16516-0948	16h54m24.03s	-09d53m20.9s	96.87	11.24	5.40	0.18	110
IRASF17138-1017	17h16m35.60s	-10d20m38.0s	75.84	11.42	3.64	0.59	83
NGC7592	23h18m22.54s	-04d24m58.5s	95.13	11.33	3.76	0.40	90
NGC7679	23h28m46.66s	+03d30m41.1s	67.7	11.05	1.89	0.19	94

[a] 13.2μm core sizes taken from Díaz-Santos et al. (2010).
[b] Inclinations and Position Angles taken from Kim et al. (2013a), Paturel et al. (2003), and Jarrett et al. (2000).

3.2.1 VLA Observations and Data Reduction

The VLA observations were carried out for the full sample during three separate C-configuration cycles in February 2014 (14A-471), February 2016, and March 2016 (16A-204). The maximum baseline of this array configuration is 3.4 km. Three VLA receiver bands were utilized in these observations: the S-band (2-4 GHz), Ku-band (12-18 GHz), and Ka-band (26.5-40 GHz). The 8-bit samplers were used for the S-band observations, delivering 2 GHz of total bandwidth, centered at 3 GHz, by using two 1 GHz baseband pairs, both with right- and left hand circular polarizations. The 3-bit samplers were used in the Ku-band observations, delivering 6 GHz of total bandwidth, centered at 15 GHz, by using three 2 GHz baseband pairs. The 3-bit samplers were also used in the Ka-band observations, delivering 8 GHz of total bandwidth, centered at 33 GHz, by using four 2 GHz baseband pairs. Hereafter, we may refer to the data and/or the images from the S-, Ku-, and Ka-bands as the 3, 15, and 33 GHz data and/or images, respectively.

To reduce and calibrate the VLA data we followed standard calibration and editing procedures, and utilized the VLA calibration pipeline built on the Common Astronomy Software Applications (CASA; McMullin et al., 2007) versions 4.6.0 and 4.7.0. After each pipeline run, we manually inspected the visibilities and calibration tables for evidence of bad antennas, frequency ranges, or time ranges, flagging correspondingly. We also flagged any instances of RFI, for which we removed several significantly affected frequency ranges in the S- and Ku-bands, and very little of the 33 GHz data. After flagging, we re-ran the pipeline, and repeated this process until we could not detect any further signs of poorly-calibrated data. A detailed description of our data reduction procedures can be found in Murphy et al. (2018a).

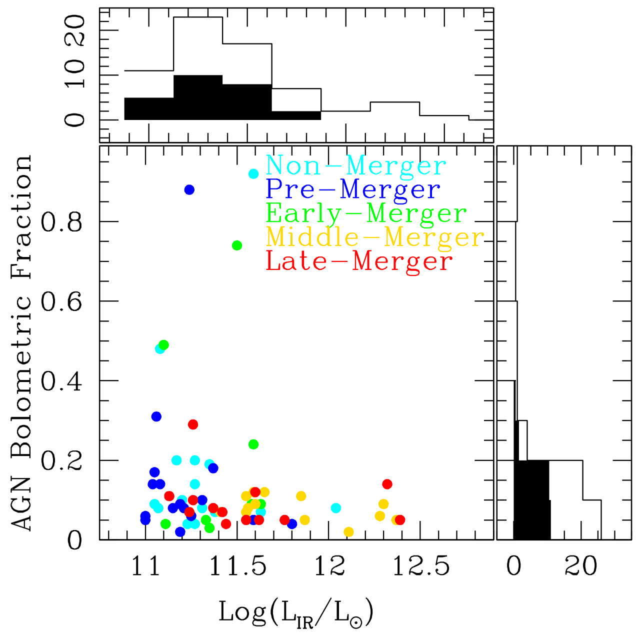

Figure 3.1: The distribution of infrared luminosity and bolometric AGN fraction all galaxies in GOALS within +20 and −20 degrees declination. The AGN fractions are taken from a recent compilation in Díaz-Santos et al. (2017), and the galaxies are color-coded by the observed merger stages taken from Haan et al. (2013) and Stierwalt et al. (2013). The histograms on each side show the full distribution of equatorial GOALS sources, with the black shaded histogram indicating the sub-sample selected for this study. What is clear is nearly all of the galaxies identified in our sub-sample are classified starburst-dominated systems.

3.2.2 Galaxy Selection

The goal of this study is to resolve individual extranuclear regions within LIRGs for which we can perform multi-band photometry, and extract detailed information about their star-formation properties.

We therefore selected from the full sample of 68 equatorial LIRGs the 25 which showed resolved extended structure with the VLA across all three frequency bands (Table 3.1). By targeting galaxies with high L_{IR}, the GOALS sample includes the most extreme starbursts and AGN in the local Universe. Importantly, these galaxies are different from the normal star-forming galaxies studied previously on resolved scales in the local Universe (Alonso-Herrero et al., 2001; Bradley et al., 2006; Liu et al., 2013; Smith et al., 2016). However, in order to properly place our results in the greater context of galaxy evolution, we must also be able to disentangle any contribution of a strong central AGN to the measured luminosities of individual regions.

From our sub-sample of 25 galaxies we see that the majority (22/25) of the extended galaxies in our VLA survey are indeed starburst-dominated, with AGN bolometric fractions under 15% (Díaz-Santos et al., 2017). Figure 3.1 shows that our sub-sample of sources span both the complete range of interaction stages (i.e widely separated disk galaxies to fully merged systems: Haan et al., 2013; Stierwalt et al., 2013), and a luminosity range of $L_{IR} = 10^{11.00-11.65} L_{\odot}$. The final analysis of extranuclear star-forming regions within this sub-sample allows for direct comparison of the luminosity, SFR, radio spectral indices, and overall morphologies of the active star-forming regions in LIRGs and normal spiral galaxies without issues associated with contamination from an AGN or obscuration due to dust.

3.2.3 Interferometric Imaging

Calibrated VLA measurement sets for each source were imaged using the task tclean in CASA version 4.7.0. The mode of tclean was set to multi-frequency synthesis (Conway et al., 1990; Sault & Wieringa, 1994, mfs;). For nearly all sources, we chose to use Briggs weighting with robust=0.5, and set the variable nterms=2, which allows the cleaning procedure to additionally model the spectral index variations on the sky. To help deconvolve extended low-intensity emission, we took advantage of the multiscale clean option (Cornwell, 2008; Rau & Cornwell, 2011) in CASA, searching for structures with scales ~ 1 and 3 times the full width at half-maximum (FWHM) of the synthesized beam. For our S- and Ku-band data we also implemented the widefield uv-plane gridding and the w-projection algorithm with 16 planes to better model the curvature of the low-frequency sky. For those sources where Briggs weighting of robust=0.5 failed to capture any significant emission or structure, we increased this factor in steps of 0.5 towards natural weighting (i.e. robust=2.0) until the source was detected, and the sidelobes were sufficiently suppressed. A summary of the imaging parameters is given in Table 3.2.

Table 3.2: Imaging Parameters

Inputs	Ka-Band	Ku-Band	S-Band
Frequency	33 GHz	15 GHz	3 GHz
Cell[a]	0.12	0.27	0.12
UV-Gridder	Widefield	Widefield	Widefield
Multiscales[b]	0,10,30	0,10,30	0,10,30
Nterms[c]	2	2	2
Robust[d]	1.0 or 0.5	1.0 or 0.5	0.5

[a] The cell size is given in arcseconds/pixel
[b] The scale size is given in pixels, with 0 being a point source.
[c] Number of terms used in Taylor series expansion
[d] The robust weighting scheme was chosen for all images

A primary beam correction was further applied using the CASA task impbcor before analyzing the images. The primary-beam-corrected continuum images at each frequency for two of the targets used in this study are shown in Figure 3.2. Finally, in order to measure flux densities and spectral indices within consistent apertures across all three VLA bands, we convolve the images to a common circularized beam that is closest in size to the image with the lowest resolution for each galaxy. This allows us to make the cleanest comparison of structure across multiple bands, and minimize the effect of using circular apertures to extract photometry. The FWHM of the smoothed beam size for each galaxy is given in Table 3.3, along with the corresponding point-source rms sensitivity of each image.

3.3 Ancillary Data and Region Photometry

3.3.1 Spitzer IRAC Imaging

With the addition of near-IR Spitzer imaging at 3.6, 4.5, 5.8, and 8μm, we can make direct comparisons of the measured 33 GHz SFR, powered by young massive stars, to the total stellar mass (M_*) inferred from the evolved low-mass stellar populations within the same regions. Additionally, we can estimate the total infrared luminosity (L_{IR} [8-1000μm]) per region, and compare these results to the observed low-frequency ($\sim$ 3GHz) radio emission, which has been shown to serve as a reliable proxy of IR emission in local star-forming galaxies via the well-studied IR-radio correlation (Helou et al., 1985; Condon, 1992).

Spitzer IRAC channels (Ch) $1-4$ data were taken as part of GOALS, and details on the associated observation strategies and data reduction steps are available in Mazzarella et al. in prep. IRAC channels $3-4$ (5.8 and 8.0 μm) are primarily sensitive to emission due to polycyclic aromatic hydrocarbons (PAHs; e.g., Leger &

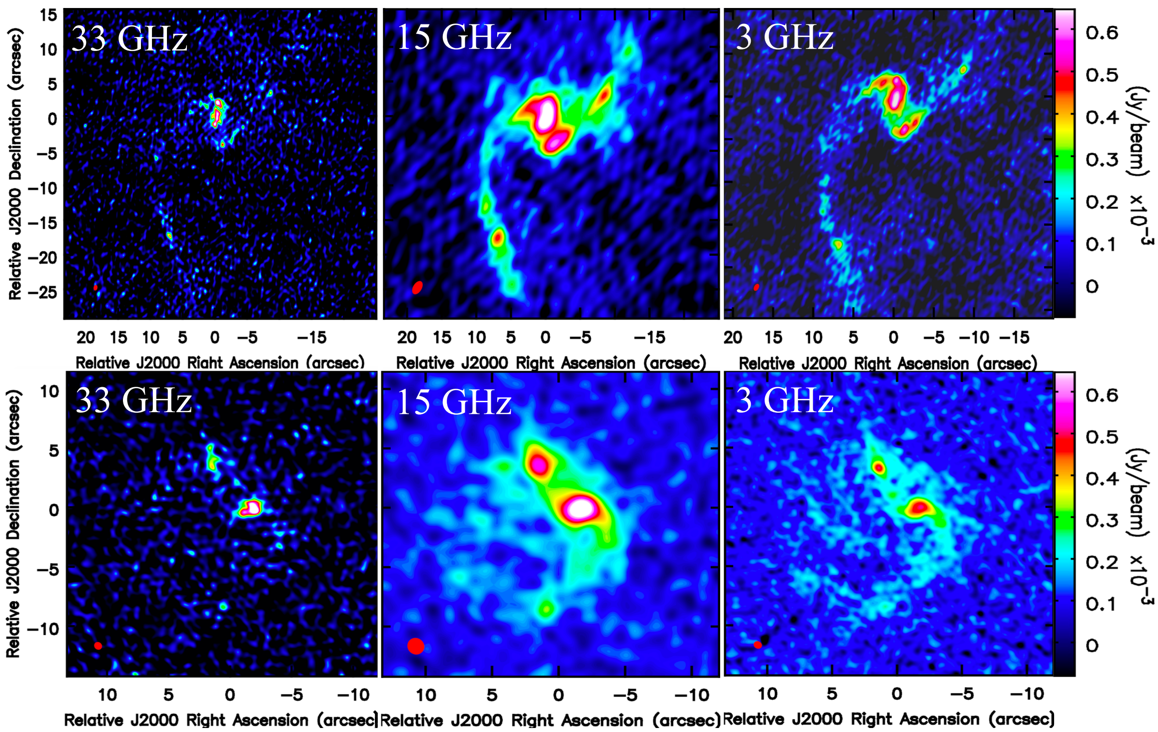

Figure 3.2: Our native-resolution multi-band VLA imaging at 33, 15, and 3 GHz from left to right. The top three panels show CGCG 465-012, and the bottom three panels show NGC 3110. The colormap scaling for each image is given on the right. The solid red ellipse in the bottom corner is the beam size of each image, with angular resolutions of $\sim$ 0.7", 1.4", and 0.7" respectively. These galaxies were chosen as representative cases for the sample, as they live at the median distance of the sub-sample ($\sim$86 Mpc).

Puget, 1984), whereas Spitzer/IRAC NIR channels 1 and 2 (3.6 and 4.5μm) data are treated as free of hot dust emission, except when a powerful AGN is present, and thus primarily sensitive to old stellar emission (e.g., Helou et al., 2004). Lu et al. (2003) used global measurements of nearby star-forming galaxies with ISO, which spanned 3 orders of magnitude in IR-luminosity, to confirm that hot dust does not contribute significantly to the emission below 3 μm. Hunt et al. (2002) further showed that the contribution in Spitzer Ch $1-2$ is on average $3-4\%$, making these bands highly sensitive probes of stellar emission. We therefore utilize the calibration presented in Querejeta et al. (2015) to convert our 3.6 and 4.5μm flux densities to total stellar mass (M_*).

To account for the significant fraction of scattered light in the images due to the structure of the Spitzer point-spread function (PSF), we use the convolution kernels presented in Aniano et al. (2011) to deconvolve the Spitzer PSF from each image, and produce corrected images for each band.

Table 3.3: Source Imaging Characteristics

Name	Program ID	θ_s (arcsec)[a]	σ_{33} (mJy/beam)[b]	σ_{15} (mJy/beam)[b]	σ_3 (mJy/beam)[b]
MCG-02-01-051	14A-471	2.071 x 2.071	3.253	2.193	0.622
IC1623	14A-471	3.018 x 3.018	0.337	0.135	0.833
MCG-03-04-014	14A-471	2.917 x 2.917	0.180	0.064	0.268
NGC0838	14A-471	2.846 x 2.846	0.282	0.096	0.439
IC0214	14A-471	2.171 x 2.171	0.073	0.039	0.139
NGC0877	14A-471	1.851 x 1.851	0.064	0.035	0.060
UGC02238	16A-204/14A-471	1.867 x 1.867	0.061	0.038	0.097
UGC02369	16A-204/14A-471	1.806 x 1.806	0.066	0.046	0.182
CGCG465-012	16A-204/14A-471	1.760 x 1.760	0.042	0.021	0.049
UGC02982	16A-204/14A-471	1.878 x 1.878	0.051	0.025	0.090
UGC03094	14A-471	1.746 x 1.746	0.053	0.027	0.044
IRAS05442+173	14A-471	1.759 x 1.759	0.091	0.065	0.129
IC0563	14A-471	2.086 x 2.086	0.071	0.025	0.055
NGC3110	14A-471	2.431 x 2.431	0.091	0.045	0.146
IC2810	14A-471	2.169 x 2.169	0.065	0.040	0.074
NCG5257	16A-204/14A-471	1.953 x 1.953	0.040	0.025	0.057
NGC5258	16A-204/14A-471	1.953 x 1.953	0.028	0.075	0.101
NCG5331	16A-204/14A-471	1.914 x 1.914	0.045	0.030	0.191
NGC5936	16A-204/14A-471	1.749 x 1.749	0.069	0.039	0.086
NGC5990	16A-204/14A-471	1.860 x 1.860	0.070	0.047	0.060
CGCG052-037	16A-204/14A-471	1.854 x 1.854	1.147	0.031	0.088
IRASF16516-09	16A-204/14A-471	2.334 x 2.334	0.091	0.040	0.262
IRASF17138-10	16A-204/14A-471	2.292 x 2.292	0.127	0.067	0.210
NGC7592	14A-471	2.116 x 2.116	0.141	0.078	0.075
NGC7679	14A-471	1.849 x 1.849	0.060	0.030	0.100

[a] The highest achieved resolution across our three VLA bands
[b] These values represent the PSF rms sensitivities of each image

3.3.2 Extranuclear Region Identification

Extranuclear candidate regions were identified as being discrete knots with a S/N of at least 3 in all three radio bands before a background subtraction of the surrounding diffuse radio emission within the galaxy. The median S/N of the regions selected for photometry is ~10, 37, and 15 for 33 GHz, 15 GHz, and 3 GHz respectively. A full list of regions and their photometric properties are given in additional Tables 3.4 and 3.5. To determine the physical separation for each of the identified candidate regions we compiled the axis-ratio (b/a) and position angle (PA) of all of the host galaxies (see Table 3.1). We adopted a hierarchy whereby values are taken from our HST-GALFIT structural analysis (Kim et al., 2013a) were used first, then values were taken from the latest release of the HYPERLEDA database (Paturel et al., 2003), and finally if necessary we take values from the 2MASS Extended Source Catalog (Jarrett et al., 2000). We then used the equation in Dale et al. (1997) to calculate inclination angle (i) of each galaxy such that,

$$\cos^2(i) = \frac{(b/a)^2 - (b/a)^2_{int}}{1 - (b/a)^2_{int}} \tag{3.1}$$

where a and b are the observed semi-major and semi-minor axes. The intrinsic axial ratio ($(b/a)_{int}$) is 0.2 for morphological types earlier than Sbc, and 0.13 otherwise. These measurements allow us to convert the apparent angular separation of a region to its host galaxy nucleus into a de-projected galactocentric radius (r_G) in units of kpc. We then compared all the measured r_G values of the candidate extranuclear regions to the 13.2μm core sizes (FWHM), as measured from Díaz-Santos et al. (2010) using Spitzer/IRS 2D spectra, which serve as our best probe of the total size of the nuclear regions in these systems. Three galaxies in our sub-sample (IC 1623, NGC 7592, NGC 7679) were not studied in that paper, and therefore we estimate the core-size using the

IRAC 8μm imaging as a proxy. We note that 8μm emission is more extended than the MIR continuum in a significant fraction of LIRGs, making our estimates conservative upper-limits (Díaz-Santos et al., 2011). Of the 50 candidates we manually identified 48 regions in 25 galaxies with r_G values larger than the MIR core radius, and were thus retained in the final sample of extranuclear star-forming regions.

3.3.3 Aperture Photometry

In order to measure beam-matched photometry between the VLA and Spitzer images, we smoothed all VLA, 3.6, and 4.5μm data to a common gaussian beam with a FWHM of 2.5" (the best resolution achievable across all 5 bands). This resulted in a physical resolution of $\sim$ 1 kpc for the median distance to the galaxies in the sample (86 Mpc). In Figure 3.3, the beam-matched images for all three VLA bands as well as the IRAC Ch1 data are shown for the same sources as in Figure 3.2.

We chose an aperture diameter of 4", which is larger than the FWHM of the worst resolution for any galaxy in the sample. To extract consistent photometry for the 8μm data, we applied an empirical aperture correction from Reach et al. (2005) to account for missing flux due to the irregular shape of the IRAC PSF. We verified these empirical corrections gave consistent results when compared with the photometry done on the de-convolved 3.6μm and 4.5μm data alone. For the VLA imaging, the RMS was calculated by scaling the measured uncertainties by the square root of the restoring-beam area to the aperture area to account for the size of the aperture used. Finally, we take the intrinsic VLA flux uncertainty of $\sim$ 3% added in quadrature with our empirically measured noise (Perley & Butler, 2013).

In order to account for the fact that many of these regions are not isolated, but rather, are embedded in larger star-forming disks, we perform a local background subtraction (using an annulus of 1" surrounding the photometric aperture) for each

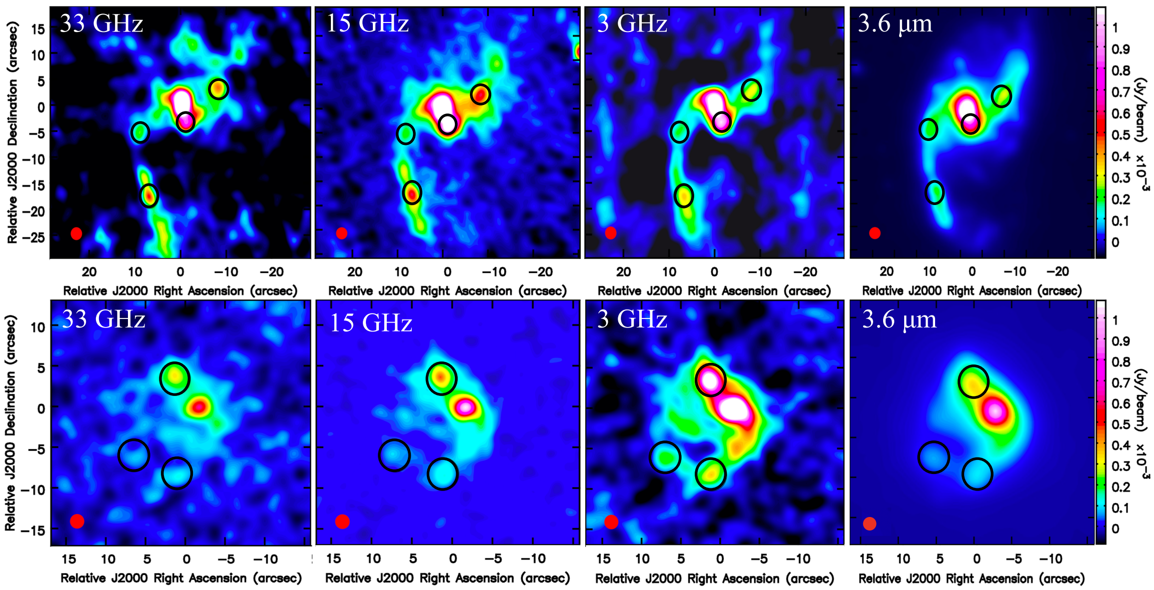

Figure 3.3: Our matched-resolution multi-band VLA imaging at 33, 15, 3 GHz, and 3.6μm IRAC Ch1 from left to right. The top four panels show CGCG 465-012, and the bottom four panels show NGC 3110. The colormap scaling for each image is given on the right. The circularized red beam in the bottom left corner is matched across all 4 images, and is $\sim$ 1.7" and 2.4" for the top and bottom panels respectively. The black circles represent our photometric apertures centered on our confirmed extranuclear star-forming regions. These galaxies were chosen as representative cases for the sample, as they live at the $\sim$ median distance of the sub-sample (86 Mpc).

source in both the VLA and IRAC imaging. This allows us to separate the radio and IR emission directly associated with the young star-forming regions we identify, and is the only way to consistently compare the two wavelength regimes together. The resulting background-subtracted measurements and uncertainties for each region are given in Table 3.5. All further derived quantities and results are based on our background-subtracted photometry.

3.4 Results

With matched-resolution observations at $\sim$ 2.5", which cover three broad windows within the 3 - 33 GHz frequency range, we can measure the spectral slope, the relative contributions of thermal and nonthermal emission, the star-formation rates, and ages of individual star-forming regions within our subsample of equatorial LIRGs.

3.4.1 Radio Spectral Indices

When interpreting the observed radio SEDs of galaxies we adopt a two-component power-law, with the thermal/nonthermal ratio as well as the nonthermal spectral index set as free parameters. For many normal and extreme star-forming galaxies in the local Universe this model adequately describes the dominant physical processes occurring (Condon, 1992; Murphy et al., 2012a). However for U/LIRGs, these models have mainly been applied to globally-integrated measurements, and scarcely studied on sub-galactic scales (Scoville et al., 2017).

To measure the $3-33$ GHz spectral indices we performed a linear least-squares fit to the data with a single power-law representing the combination of thermal and nonthermal emission. Distributions of the full- ($\alpha_{3-33GHz}$) and inter-band ($\alpha_{3-15GHz}$ and $\alpha_{15-33GHz}$) spectral slopes are given in Figure 3.4. The median spectral indices we measure from $3-15$, $15-33$, and $3-33$ GHz are -0.58 ± 0.11, -0.27 ± 0.23, and -0.51 ± 0.13, respectively. This is consistent with the expectation for star-forming regions where the lower frequencies are predominately synchrotron-dominated, and that at higher frequencies the overall radio SED begins to flatten as the contribution of thermal emission increases (Condon, 1992; Leroy et al., 2011; Murphy et al., 2013). Indeed a two-sided Kolmogorov-Smirnoff (KS) test yields a probability of $\leq 10\%$ that $\alpha_{3-15GHz}$ and $\alpha_{15-33GHz}$ are drawn from the same distribution.

By comparison, results from modeling the integrated radio SED's of U/LIRGs, which are dominated by their nuclear emission, show that the radio spectrum of many LIRGs remain steep even at high frequencies (Clemens et al., 2008, 2010; Barcos-Muñoz et al., 2017; Tisanić et al., 2019). Therefore, we conclude that extranuclear

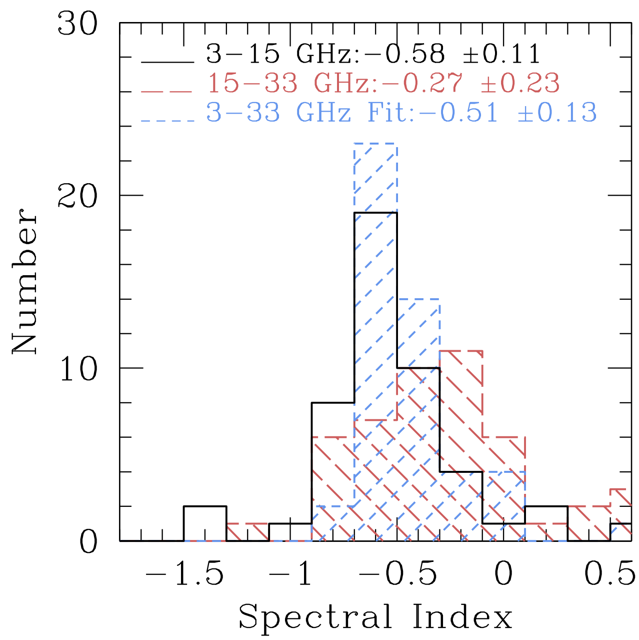

Figure 3.4: The measured spectral index values for all extranuclear regions identified in the GOALS sample. Histograms of the inter- ($3-15$ and $15-33$ GHz) and full-band ($3-33$ GHz) spectral index distributions are shown in blue short-dashed, solid black, and red long-dashed lines respectively. The median values of -0.58 ± 0.11 and -0.27 ± 0.23 for the $3-15$ and $15-33$ GHz spectral index distributions indicates an increasing contribution of thermal free-free emission to the radio SED at increasing frequencies.

star-forming regions in LIRGs have distinctly different radio spectral shapes, and show significantly less system-to-system variation relative to the integrated properties of local U/LIRGs.

This interpretation can be complicated by the fact that low-frequency radio emission traces cosmic rays, which potentially diffuse out of the area covered by our photometric apertures used as they lose energy. Using far-infrared and 22 cm radio emission maps for a sample of 29 nearby spiral galaxies, Murphy et al. (2006b) reported a correlation between the typical CR electron propagation length and the disk-averaged star formation rate, where CR electron propagation is found to decrease with increasing star formation activity (Equation 5). Murphy et al. (2012b) used analogous observations of the LMC and 30 Doradus to derive a CR electron propagation length of $\sim 100 - 140$ pc (corresponding to a $\tau_{cool} \sim 1\text{x}10^5$ yr). These values are consistent with the empirical trend describing spiral galaxies, extrapolated to environments with nearly an order of magnitude higher star-formation rate surface density ($\log(\Sigma_{SFR}) \sim -1$). Using this scaling relation, the measured star formation rate surface densities for the regions in our sample ($-1.5 < \log(\Sigma_{SFR}) < -0.5$: See the following Section), suggest an average CR electron propagation length of $\sim 100 - 200$ pc; this is still several times smaller than the physical scale of our aperture in the closest galaxy in the sample (NGC 0838). Thus we do not expect any missing synchrotron emission on the scales of our photometric apertures due to cosmic ray diffusion.

3.4.2 Thermal Fractions at 33 GHz

As a pilot study, Murphy et al. (2012a) used the Westerbork Synthesis Radio Telescope (WSRT) and Green Bank Telescope (GBT) to construct $1.4 - 33$ GHz SEDs for 50 normal star-forming galaxy nuclei and extranuclear star-forming complexes at a matched resolution of ~ 25". They found evidence that the median thermal fraction at 33 GHz (f_{th}) was $\sim 80 - 90\%$ on physical scales of ≤ 0.5 kpc, with the fraction decreasing to $\sim 60\%$ as the projected size of the photometric aperture increased to ~ 1 kpc. This study served as the basis for the Star Formation in Radio Survey (SFRS: Murphy et al., 2018a), which is a VLA campaign designed to extract the same multi-frequency band photometry as GOALS for 118 galaxy nuclei and extranuclear star-forming regions in a sample of 56 nearby lower-luminosity galaxies at a matched-resolution of ~ 2". By comparing the 33 GHz radio emission to Hα and 24μm observations of 225 discrete star-forming regions, Murphy et al. (2018a) demonstrates that the striking morphological similarities between these tracers on $50 - 100$ pc scales requires the emission from all three to be powered by the same source, namely massive star formation. The complete $3 - 33$ GHz SFRS data and associated analysis will be presented in a forthcoming paper.

In contrast, nonthermal synchrotron has been observed to be the dominant contributor to the global 33 GHz emission (i.e. $f_{th} \leq 50\%$ for $10^{11} < L_{IR} < 10^{12}$) of local U/LIRGs (Barcos-Muñoz et al., 2017). A possible explanation as to why LIRGs may have significantly lower thermal fractions relative to normal star-forming galaxies is that the absorption of a large fraction of ionizing stellar photons by dust grains, densely concentrated in starburst regions, suppresses the production of thermal radio emission relative to what is seen in the more diffuse star-forming regions in normal galaxies. Here we extend this investigation to isolated extranuclear regions in the disks of our LIRG sample.

To calculate the ratio of thermal/nonthermal emission at 33 GHz we use the spectral index, measured in Section 4.1, from $3 - 15$ GHz ($\alpha_{3-15GHz}$) to set the lower-limit on the nonthermal spectral index (α_{NT}) such that $\alpha_{NT} = -0.85$ if $\alpha_{3-15GHz} \geq -0.85$, and $\alpha_{NT} = \alpha_{3-15GHz} - 0.1$ if $\alpha_{3-15GHz} < -0.85$. This latter equation accounts for the fact that the measured 3 - 15 GHz radio spectral slope contains contributions

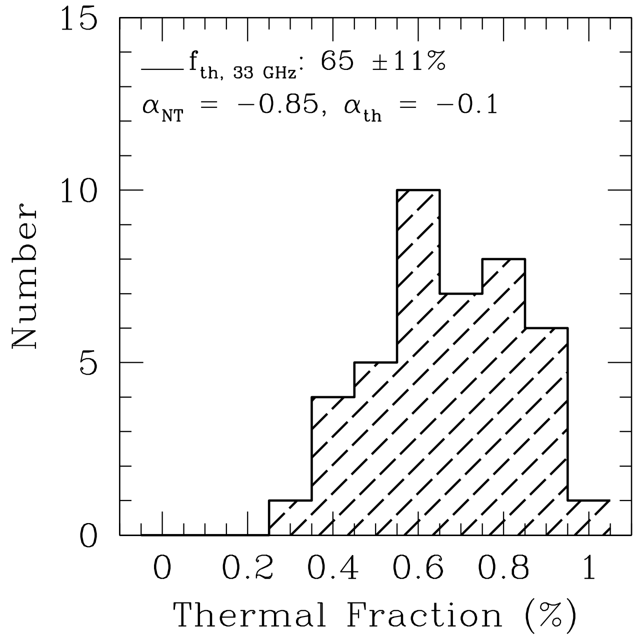

Figure 3.5: The measured 33 GHz thermal fraction values for all extranuclear regions identified in the GOALS sample. The median fraction is $65 \pm 11\%$ for the empirical calibration presented in Equation 2. This value is in good agreement with estimates of the thermal fraction made for star-forming regions in normal star-forming galaxies in the SFRS on the same physical scales (Murphy et al., 2012a, 2018a).

from both non-thermal and thermal free-free emission components, and ultimately represents a lower-limit on the true thermal fraction at 33 GHz. Importantly, only 3/42 regions have $\alpha_{3-15GHz} < -0.85$, and thus we adopt $\alpha_{NT} = -0.85$ for the majority of the regions in our sample. Further, the removal of these three regions does not affect the median of the measured thermal fraction distribution, and are thus not biasing our results in any way. Finally, we assume the same power-law exponent for the thermal emission (~ -0.1), and use the fitted slope from $3 - 33$ GHz to set the overall SED shape. Then, using the prescription in Murphy et al. (2012a), we can calculate the thermal fraction at 33 GHz such that,

$$f_T^{\nu_1} = \frac{\left(\frac{\nu_2}{\nu_1}\right)^{-\alpha} - \left(\frac{\nu_2}{\nu_1}\right)^{-\alpha^{NT}}}{\left(\frac{\nu_2}{\nu_1}\right)^{-0.1} - \left(\frac{\nu_2}{\nu_1}\right)^{-\alpha^{NT}}} \tag{3.2}$$

where ν_1 is the target frequency, α is the observed slope from ν_1 to ν_2, and α^{NT} is the nonthermal spectral index. These values are given in Table 3.4.

In Figure 3.5 we show the resulting thermal fractions of the star-forming regions identified in our sample using the shape of the radio SED as determined in Equation 2. We find that the median thermal fraction is 65% at 33 GHz on $\sim$ kpc-scales in the extranuclear regions of LIRGs. This value is in good agreement with estimates of the thermal fractions for star-forming regions in normal star-forming galaxies on the same physical scales (Murphy et al., 2012a). The results of Figures 3.4 and 3.5 strongly suggest that while extranuclear star-forming regions in LIRGs have a non-negligible contribution from non-thermal synchrotron emission, these regions are much more heavily-dominated by thermal free-free emission relative to the resolved nuclei of local ULIRGs, which in the case of Arp 220 can be as low as $\sim$ 20% on $\sim$ 50 pc scales, and high-redshift star-forming galaxies in the VLA-COSMOS survey (Barcos-Muñoz et al., 2015; Tisanić et al., 2019).

3.4.3 Star Formation Rates

We have shown in the previous two sections that one can use 33 GHz emission to reliably trace the current star formation activity of kpc-sized regions in the disks of both normal and extreme star-forming galaxies in the local Universe. Therefore, we assume that the thermal and nonthermal spectral indices do not vary significantly across the individual extranuclear regions in our sample, and that any differences in the observed SED are due to the relative contribution of each emission mechanism. This allows us to use Equation 10 presented in Murphy et al. (2012a) to convert the measured 33 GHz luminosity (L_{33GHz}) into the current SFR within our apertures, where the assumed thermal and nonthermal power-law indices are -0.1 and -0.85 respectively, and the electron temperature of the gas is 10^4K. In Figure 3.6 we show that the measured range of SFRs for our sample is $\sim 0.05 - 7.5 M_{\odot}\mathrm{yr}^{-1}$, with a clear peak at $\sim 1 M_{\odot}\mathrm{yr}^{-1}$.

Smith et al. (2016) used GALEX near-UV (NUV) and far-UV (FUV) maps, along with Spitzer IRAC (Ch $1-4$), MIPS (24 μm), and archival Hα images to estimate the extinction-corrected SFRs, in 1 kpc apertures, for nearly 700 star-forming regions in 46 interacting and non-interacting galaxy pairs. Importantly, they classify regions in their interacting galaxy sample into "inner-disk", "tidal", and "nuclear" regions, whereas, regions identified in the spiral galaxy sample were classified as either "disk" or "nuclei." They find that the distribution of star-formation rates for both "tidal" and normal galaxy "disk" regions range from $10^{-4} < \mathrm{SFR} < 10^{-1} M_{\odot}$ yr^{-1}. In Figure 3.6, we see that all but one of our regions, as measured in the same ~ 1 kpc apertures, lie beyond the upper-end of this range.

In a new study, Larson et al. (2020) identified over 750 extranuclear star-forming regions in 50 U/LIRGs in GOALS using Paα and Paβ line emission. These regions

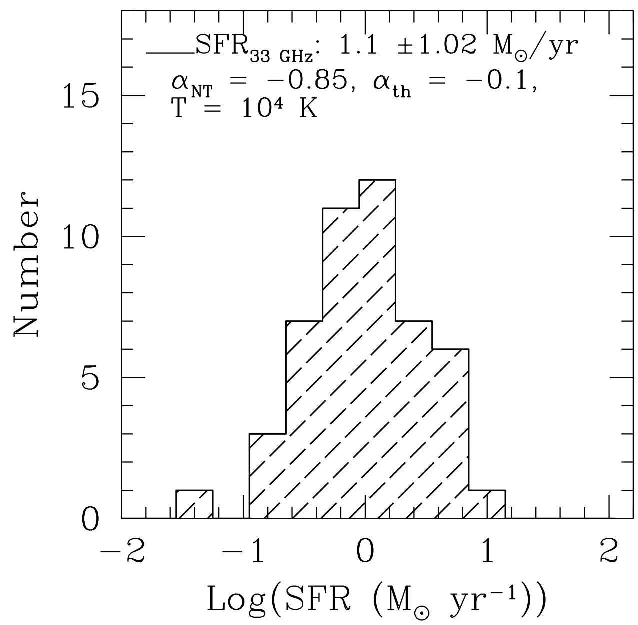

Figure 3.6: The distribution of star-formation rates, as inferred from the measured 33 GHz luminosity (L_{33GHz}), is shown along with the spectral indices assumed for the thermal and nonthermal emission components at 33 GHz. The SFR distribution for our sample shows a clear peak at $\sim 1 M_{\odot}\mathrm{yr}^{-1}$, and lies beyond the upper-end of the range observed for star-forming regions in normal star-forming galaxies in the local Universe (Smith et al., 2016).

range in size from $\sim 50 - 500$ pc with SFRs as low as 0.001 $M_{\odot}\text{yr}^{-1}$ up to 10 $M_{\odot}\text{yr}^{-1}$, consistent with the high SFRs observed for the regions in our sample. These results confirm that a significant population of star-forming regions exist at much lower SFRs in LIRGs, and that the peak observed in our distribution represents the sensitivity of our current radio observations to regions in the outer-disks of these galaxies. Therefore, while we cannot draw conclusions for the entire population of star-forming regions seen in LIRGs, it is clear that the most luminous extranuclear star-forming regions, as identified in the radio, are not seen in large samples of normal *and* interacting galaxies in the local Universe (Smith et al., 2016). This is consistent with numerical simulations which show tidal disturbances can trigger enhancements of the gas turbulence and pressure in the ISM throughout the disks of luminous galaxy mergers, which leads to larger fractions of dense gas, and thus more massive star-forming regions (e.g. Elmegreen, 1993; Hopkins et al., 2008; Struck & Smith, 2012; Kruijssen, 2014). In Section 5 we will examine how the measured SFRs in each region compare to the IR and M_* properties inferred from our near-IR observations.

3.4.4 Model Age Fitting

In this Section we estimate the age of the starburst in each region by examining how thermal and nonthermal affect the measured 3 - 33 GHz radio spectral slope of the starburst as it ages. Since thermal emission is only produced by the shortest-lived (≤ 10 Myr) massive stars, its presence in large amounts relative to synchrotron emission is indicative of very young star formation. This correlation can then be a method of determining approximate ages for the global star formation history of a galaxy.

To quantify these different timescales, we use Starburst 99 (SB99) models with default inputs (solar metallicity and 2-component Kroupa Initial Mass Function), in order to estimate the ionizing photon rate (Q_{H_0} s^{-1}) and supernova rate (N$_{SN}$ yr^{-1}) of a simple stellar population (SSP; Leitherer et al., 1999). To transform these quantities into a theoretical 3 - 33 GHz spectral index as a function of time we use Equations 5 and 8 in Murphy et al. (2012a) respectively, to estimate the total, thermal, and nonthermal luminosity at 3 and 33 GHz (assuming the same values for the thermal and nonthermal spectral index as the previous sections). We stress that this model does not include losses due synchrotron, inverse Compton scattering, or free-free self-absorption. Instead the model is meant to illustrate the effect an aging stellar population has on the radio spectral slope of an isolated HII region. Further, given that the cooling timescale estimated for CR elections in Section 4.1 ($\sim 10^5$ yr) is equal to the time-step used in SB99, we expect synchrotron losses to have a negligible effect on the 3 - 33 GHz radio spectral slope. Rabidoux et al. (2014) used this simple framework to describe the 1.4-33 GHz spectral slope, and thus the average age of the global star-formation activity, in a sample of 27 nearby normal star-forming galaxies. With our sample, we are able to extend this analysis to individual star-forming regions in the disks of luminous starburst galaxies.

To take into account the fact that a single instantaneous starburst may not be representative at the physical scales we are probing ($\sim$1 kpc), we also include SB99 models with a continuous star formation history (SFH) of $SFR = 1 M_{\odot}\mathrm{yr}^{-1}$ using the same metallicity and IMF input as in the instantaneous burst model. One can see that in the continuous SFR model, there are no large jumps in the 3-33 GHz spectral index. Instead, the model transitions smoothly from a very shallow (thermal dominated) spectral slope to an intermediate spectral slope. This model predicts that a spectral index of -0.5 would be expected for a kpc-sized region that has been actively forming stars for $\sim$ 10 Myr. This is consistent with the median spectral index of -0.51 measured for the star-forming regions in our sample.

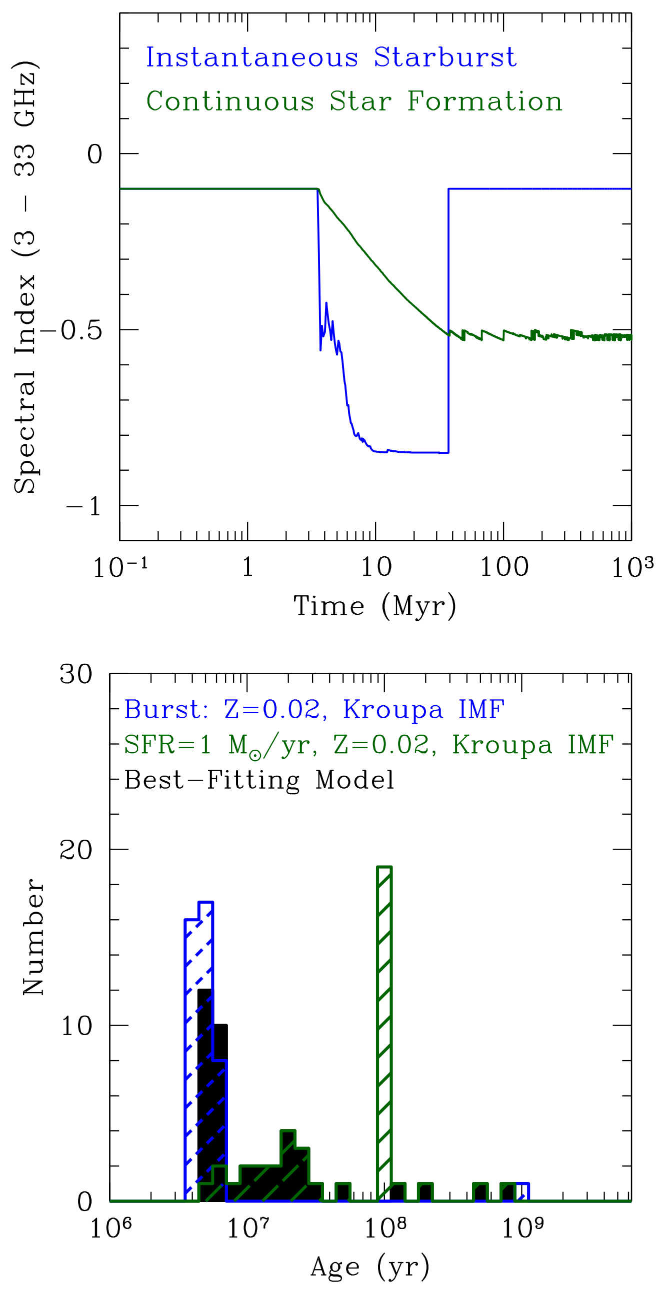

Figure 3.7: Left panel: The two sub-panels show SB99 models of both an instantaneous burst and continuous SFH, using standard Kroupa IMF, and solar metallicities. We perform a χ^2-minimization to the observed $3 - 33$ GHz spectral index of each region. Right panel: The distribution of model ages for both types of SFH (blue and green) and the best-fitting model in each case (black). It is clear that there exists two populations of regions: Those younger than $t \sim 10^7$ yr, which are best-modeled by an instantaneous burst, and those older than $t \sim 10^7$ yr, which are best-modeled by a continuous SFH.

Using both models, we then perform a χ^2 minimization to the observed spectral index for each extranuclear region in the sample. The right panel of Figure 3.7 shows the distribution of fitted-ages considering only the instantaneous burst model in blue, only the continuous model in green, and whichever model better-fits the observed spectral index of each region in black. Overall, the estimated median age of our star-forming regions is ~ 10 Myr, which agrees with the age distributions derived for a large sample of young massive star clusters in a sample of local U/LIRGs in GOALS (Linden et al., 2017). By comparing each model individually, we see that 45% of regions in our sample are best modeled by an instantaneous burst, which indicates that these regions are very young. However, the majority of the star-forming regions are best fit with a continuous SFR model with ages between $10^7 - 10^{7.5}$ yr, and even some regions which are relatively old ($t > 10^8$ yr). Finally, when examining the ages of these regions as a function of merger stage we do not see evidence that the oldest regions are observed exclusively in the latest-stage mergers. This indicates that while the nuclear starburst activity dominates as the merger progresses, prodigious star formation still occurs in the outer-disks of these systems.

3.5 Discussion

For the following analysis, we first create a sub-sample of the 48 star-forming regions, which have $3 - 33$ GHz spectral indices which span a parameter space that can be reliably modeled with one of our two SB99 models ($-1.2 < \alpha_{3-33GHz} < 0.0$). This is to ensure that any differences in the slopes observed are not due to regions that are faint in one of the three radio bands, which could affect both the measured spectral index, and the inferred low-frequency radio luminosity. Particularly, if the region is faint at 33 GHz the assumption that the region is fully sampling the IMF, a key detail which underpins all SFR calibrations, might break down. In total we retain 42/48 regions identified in the initial sample, and in fact the six regions we remove have the lowest S/N ratios across all three bands we identified in the initial candidate selection.

3.5.1 The Infrared – Radio Correlation

The far-infrared – radio correlation (Helou et al., 1985) is an empirical relationship which holds remarkably well for galaxies spanning a wide range in mass and luminosity (Yun et al., 2001). At centimeter wavelengths, the radio continuum is dominated by synchrotron emission, which decays on timescales of ~ 100 Myr for pseudo-continuous star formation in galaxies (Condon, 1992). The infrared (IR) traces the peak of the dust emission, which is a proxy for recent star formation in a starburst galaxy. For a fixed initial mass function (IMF) and star formation history, the production of cosmic rays is roughly equal to the rate of dust-heating from UV photons produced by young stars, such that the IR-radio correlation holds in both normal and extreme star-forming galaxies in the local Universe (Lisenfeld et al., 1996). The physical explanation for the tightness of this correlation has long been debated, given the fact that the methods which produce each emission mechanism have timescales which differ by an order of magnitude.

However, when individual star-forming regions on smaller spatial scales ($\sim$ hundreds of parsecs) are examined in both normal and extreme star-forming galaxies, this correlation can break down, and is sensitive to these various timescales and local SFH, CR propagation, and metallicity of the galaxy (Murphy et al., 2006b). Further, it has been shown with lower-resolution data that ongoing mergers, whose progenitors still share a common envelope, may also exhibit excess radio emission from bridges and tidal tails that is unassociated with the current star-formation activity. This scenario may also explain the seemingly low far-infrared/radio ratios measured for many high-z submillimeter galaxies, a number of which are merger-driven starbursts (Murphy et al., 2013). Here we aim to test whether the infrared – radio correlation will hold on kpc-scales in the extended disks of LIRGs at various stages along the merger sequence, and determine to what level we see evidence for excess non-thermal emission relative to the inferred far-infrared luminosity within individual star-forming regions.

In order to make accurate measurements of infrared luminosity, we require observations at matched resolution to our VLA images, for which MIPS and Herschel data are not sufficient. We therefore used the IRAC Ch4 8μm flux as a proxy for the total-IR ($L_{1-1000\mu m}$) by assuming a fixed IR8 ratio ($L_{TIR}/L_{8\mu m}$). Elbaz et al. (2011) used observations of IRAS selected galaxies, including the full GOALS sample, to determine that the global ratio of total IR luminosity to rest-frame 8μm luminosity follows a distribution centered on IR8 = 4, thus defining an IR main sequence for star-forming galaxies independent of redshift. This study was limited by the fact that the galaxies in their sample were not classified into AGN- and SF-dominated systems. Wu et al. (2010) and Magdis et al. (2013) used the 5MUSES sample of galaxies, which builds on the Elbaz et al. (2011) sample by including spectral diagnostics from Spitzer and Herschel respectively, to isolate galaxies which are dominated by star-formation. Both studies concluded that the IR8 ratio was larger (by up to a factor of 2), than what Elbaz et al. (2011) found for the complete galaxy sample. Following these studies, we used the global $L_{8\mu m}$ and L_{IR} photometry presented in Chu et al. (2017) and Mazzarella et al. in prep to derive a median IR8 ratio of 8.1 ± 2 for the 25 galaxies in our equatorial sub-sample. This is in good agreement with the Wu et al. (2010) and Magdis et al. (2013) calibrations, and consistent with the notion that once AGN-dominated galaxies are removed from the global IR-bright galaxy population the ratio is significantly enhanced in pure starburst-dominated galaxies.

Using the measured $3-15$ GHz radio spectral slope ($\alpha_{3-15GHz}$) we extrapolate the observed 3 GHz flux density of each region to 1.4 GHz and measure the q-ratio (q_{TIR}) defined as the logarithmic ratio of the total infrared to radio flux density for each region. While this measurement differs from the traditional q_{FIR} analysis discussed above, it allows us to make direct comparisons with a recent calibration of the global TIR-radio correlation observed for a large sample of normal star-forming galaxies in the local Universe (Bell, 2003). Overall, we find that the median q_{TIR} derived for kpc-sized regions in our LIRG sample (2.7 ± 0.34) is consistent with the Bell (2003) calibration ($q_{TIR} = 2.64$). While the uncertainty in our IR8 calibration limits the robustness of this result, we do not see strong evidence for regions with a significant excess nonthermal emission associated with tidal bridges and tails. With future ALMA and pre-approved JWST/MIRI programs we will further investigate the physical origin of the infrared – radio correlation by directly measuring the total infrared luminosity, dust, and gas masses of individual star-forming clumps identified in GOALS galaxies.

3.5.2 The Star-Formation Main Sequence

The relationship between the star-formation rate (SFR) and the observed stellar mass (M_*) in galaxies has been extensively investigated over the past decade as means for understanding the evolution of galaxies (e.g., Noeske et al., 2007; Daddi et al., 2007; Elbaz et al., 2011). From these studies it is clear that there are two main modes of star formation that are known to control the growth of galaxies: a relatively steady rate, which defines the star formation rate - stellar mass main sequence (SFMS), and a starburst mode above this sequence. Further, homogeneous collections of the integrated SFMS of galaxies across large ranges in redshift (e.g. Speagle et al., 2014; Kurczynski et al., 2016) show that while the slope remains relatively constant, the fitted zero-point of the relation appears to increase at higher ($z > 1$) redshifts ($SFR \propto M_*^{0.5}$: Speagle et al., 2014), indicating a more significant contribution from starburst galaxies at earlier times.

More recently, several studies (e.g., Wuyts et al., 2013; Cano-Díaz et al., 2016; Maragkoudakis et al., 2017; Medling et al., 2018) have provided evidence that MS-like correlations are also present at sub-galactic scales in a wide variety of galactic environments, by comparing the SFR surface densities (Σ_{SFR}) with stellar-mass surface densities (Σ_{M_*}) for individual sub-galactic regions $\sim$ 1kpc or larger. Thus far observations at high-redshift suggest this correlation has a slope close to unity (Wuyts et al., 2013), whereas at lower redshifts linearity and sub-linearity have been reported (Cano-Díaz et al., 2016; Medling et al., 2018). Here we look to test which of these two modes of star-formation best describes the extranuclear star-forming regions identified in the equatorial GOALS sample, and whether or not a MS-like correlation exists for the most luminous regions in LIRGs.

In Figure 3.8 we compare the star-formation rates and stellar masses of our extranuclear regions with both integrated galaxy properties (left panel) and correlations found for the sub-galactic main sequence (right panel). In the left panel the orange points are globally-integrated measurements from our sub-sample of 25 galaxies taken from U et al. (2012), and in purple are our extranuclear star-forming regions identified with the VLA. The integrated stellar mass measurements from U et al. (2012) used the observed H-band luminosity and a Chabrier IMF, whereas for our SFR calculations and the IRAC-M_* conversion we utilize a Kroupa and Chabrier IMF respectively. However, the differences in the integrated total mass are small compared to our measured uncertainties, and therefore we do not expect to introduce any systematic biases when comparing the two datasets using slightly different IMFs. The light blue points are integrated measurements of galaxies in the SFRS as a reference sample of normal

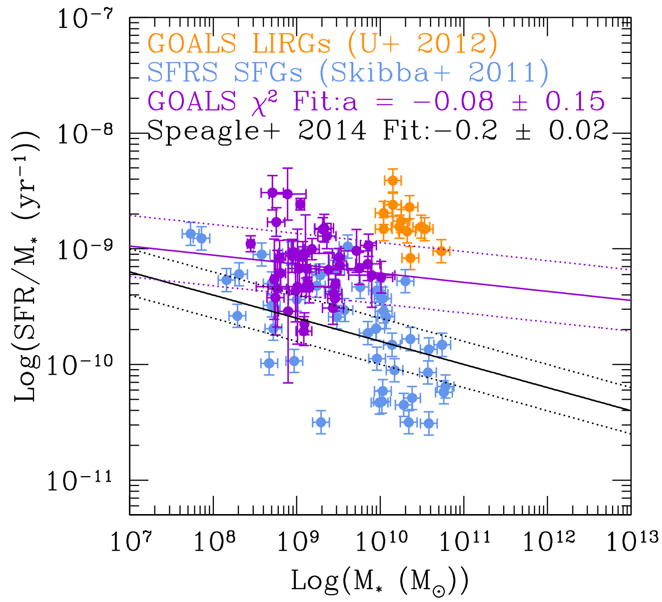

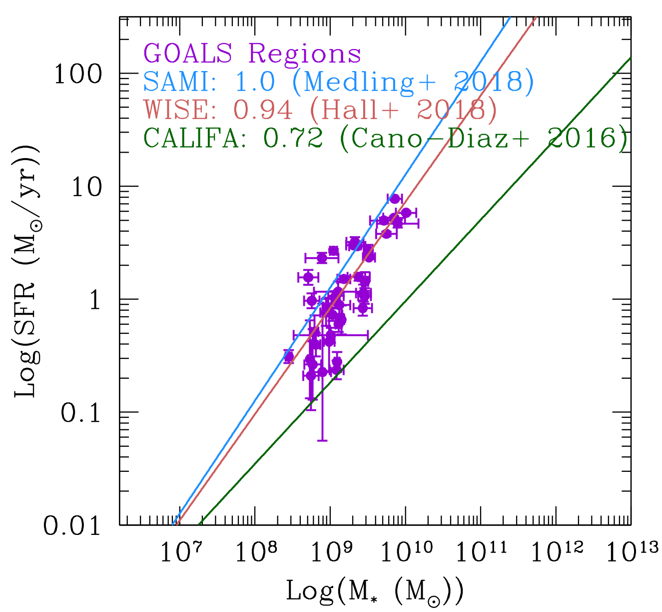

Figure 3.8: Left panel: The sSFR distribution as a function of stellar-mass showing that the global fit from Speagle et al. (2014) is not an appropriate calibration for both the galaxy-integrated (GOALS: orange) and extranuclear star-forming regions in local LIRGs (purple). Further, the specific star formation rate of the extranuclear regions themselves lie at the upper-end of the relation for normal star-forming galaxies in the local Universe (SFRS: blue, Skibba et al., 2011). Right panel: The star-formation main sequence ($SFR - M_*$). In purple we show the results for the extranuclear star-forming regions identified in GOALS. The blue, dark green, and red lines show the resolved galaxy main-sequence, normalized to the GOALS fit presented in the left panel, for the SAMI, CALIFA, and WISE surveys respectively.

star-forming galaxies (Skibba et al., 2011; Murphy et al., 2018a). The solid black line shows the main-sequence as defined by a large homogeneous collection of local spirals taken primarily from SINGS (Speagle et al., 2014). We can see that the galaxies in the SFRS generally follow the local MS calibration, and that the massive extranuclear regions identified in our LIRG sample are consistently above it.

If the integrated measurements of starburst-dominated galaxies were simply the sum of the individual star-forming regions identified within them, then the integrated LIRGs and the extranuclear regions should be well described by a single linear fit. Shown in purple is the fit to only the extranuclear regions, and we can see that the integrated LIRG measurements are systematically offset by ~ 0.2 dex in sSFR. By comparing the median values of sSFR for both the integrated GOALS LIRGs and our individual star-forming regions we find that they make up on average 16.5% of the current star formation activity ($f_{SFR} = SFR_{region}/SFR_{galaxy}$) in their host galaxies. This is consistent with a recent suite of 75 hydrodynamic simulations of major galaxy mergers ($M_{rat} \sim 2.5:1$), which show a median $f_{SFR} \sim 13\%$ in regions from 1 - 10 kpc away from nucleus over a broad range of interaction geometries (Moreno et al., 2015). Further, it is clear that the fit to the local galaxy reference sample is steeper than the relation found for the most luminous GOALS regions identified. Ultimately, this suggests that while the integrated properties of the starburst-dominated LIRGs are driven by the central nuclear starburst, extranuclear regions in LIRGs have elevated sSFRs even relative to normal star-forming galaxies.

In the right panel of Figure 3.8 we show a plot of the star-formation - stellar mass plane for our identified regions with fits to the sub-galactic main sequence overlaid. By normalizing the zero-points of each fit we can test which correlation most accurately represents our star-forming regions, and to what degree the linear or sub-linear relationships found for integrated galaxies hold on kpc-scales in LIRGs. We see clearly

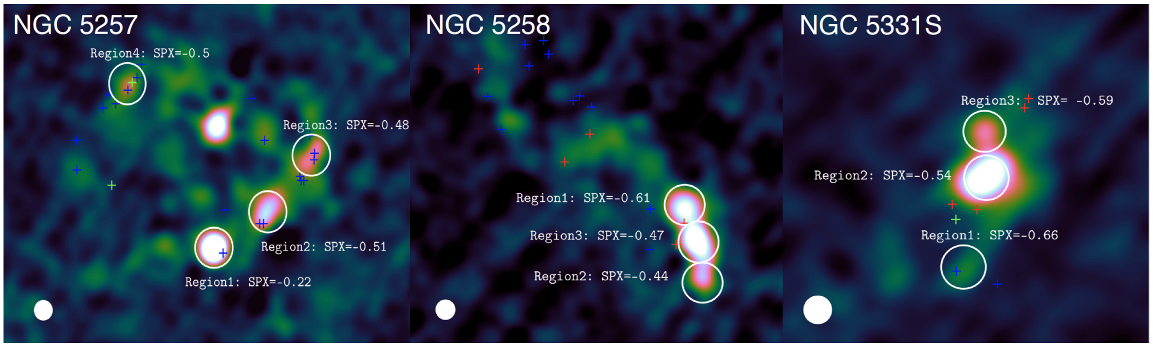

Figure 3.9: The 33 GHz continuum images for NGC 5257 (Left), NGC 5258 (Middle), and NGC 5331S (Right) are shown overlaid with our photometric apertures, the measured $3-33$ GHz radio spectral index, and the locations of super star cluster identified in Linden et al. (2017). The colors of the markers in all panels indicate their age, with $t \leq 10^7$ yr shown in blue, $10^7 < t < 10^8$ yr shown in green, and $t \geq 10^8$ yr shown in red.

that the correlation found for the Calar Alto Legacy Integral Field Area (CALIFA) survey of galaxies is shallower than our distribution of star-forming regions. This discrepancy is likely due to the range of morphological types included in the CALIFA fit, with regions from early-type galaxies systematically flattening the slope of the correlation (Cano-Díaz et al., 2016). Indeed, when the fit is restricted to only late-type galaxies the correlation closely follows the distribution of star-forming regions observed in our VLA sample (Hall et al., 2018; Medling et al., 2018). This confirms that there is a sub-galactic main sequence of star-formation present in LIRGs with both individual star-forming regions and the globally-integrated galaxy measurements, which lie above the locally-calibrated SFRMS.

3.5.3 Spatially Coincident Massive Star Clusters

Radio continuum emission has been used as an effective way to identify ultra-young ($1-3$ Myr) massive star clusters still deeply embedded in their natal birth material (Turner et al., 2000b; Johnson et al., 2001, 2003). Our results from the initial SFRS sample (Murphy et al., 2018a) reveal both purely thermal (and thus very young) sources, as well as sources which have higher nonthermal fractions at 33 GHz. In general, we expect to find that these latter radio sources are associated with regions that contain multiple star clusters visible at optical wavelengths (Evans et al., 2008; Inami et al., 2010; Modica et al., 2012; Mazzarella et al., 2012; Mulia et al., 2015). Four galaxies in our sample, NGC 5257/8 and NGC 5331N/S, have been observed with HST as part of a larger program to search for young, UV-bright, massive star clusters in LIRGs (Linden et al., 2017). In this subsection, we compare the mean spectral index of each region, which tracks the relative fraction of young ($\sim$ 5 Myr) and old ($\geq$ 50 Myr) star-formation to the median cluster age, which tracks the $\sim 1-100$ Myr SFH of the region within our photometric apertures.

At the resolution of our matched-VLA observations, it is unclear if these extranuclear regions are powered primarily by a single massive star cluster, or several lower-mass clusters tightly packed within a group. In Figure 3.9 we show the star clusters identified in these galaxies, color-coded by their modeled ages (i.e., blue $t \leq 10^7$ yr, green $10^7 < t < 10^8$ yr, and red $t \geq 10^8$ yr). In only one case, NGC 5257, do we have significant overlap with regions identified in the radio for which a meaningful comparison of cluster ages, masses, and extinctions to the radio spectral slope can be done. We find that the region in NGC 5257 (left panel), which is the most luminous and shows the flattest $3-33$ GHz spectral index (-0.22), is associated with a single, young ($\sim$ 4 Myr), massive ($M_{cl} \sim 10^7 M_{\odot}$) star cluster, whereas regions with steeper radio spectral indices are coincident with several star clusters whose median age is slightly older ($\sim$ 10 Myr) and mass significantly smaller ($\sim 10^{5.5} M_{\odot}$: Linden et al., 2017).

Overall we do see evidence, albeit in one system, that the luminosity and spectral index of the radio continuum measured at kpc-scale resolution is able to roughly track variations in the median age and mass of the spatially-coincident super star clusters identified in the UV/optical. A more thorough discussion of massive star clusters and their relationship to star-forming regions identified at 33 GHz will be discussed in a forthcoming paper, which will be a comparison of the cluster mass functions, and luminosity distributions of young massive star clusters using HST data available for the SFRS sample of galaxies.

3.6 Summary

We have presented the first results of a high-resolution VLA survey for 25 luminous infrared galaxies (LIRGs) in the Great Observatories All-Sky LIRG Survey (GOALS). Radio emission provides a critical, optically-thin view on the massive star formation activity within deeply embedded HII regions, and it tracks nonthermal emission from relativistic cosmic rays associated with recent supernova in galaxies. We have extracted luminosities, spectral indices, star-formation rate (SFRs), thermal fractions (f_{th}), ages, and stellar masses for a total of 42 individual extranuclear star-forming regions identified as having de-projected galactocentric radii (r_G) which lie outside the 13.2μm core size of the galaxy measured in Díaz-Santos et al. (2010). These "extranuclear'" regions, allow us to cleanly examine the evolution of star-formation activity in LIRGs, free from possible contamination associated with an AGN. Our results indicate that:

(1) The median 3−33 GHz spectral index and thermal fraction at 33 GHz measured for the extranuclear regions identified in our VLA survey is -0.51 ± 0.13 and $65 \pm 11\%$ respectively. These results suggest that on kpc-scales extranuclear star-forming regions in LIRGs have flatter radio spectral slopes, and are much more heavily-dominated by thermal free-free emission relative to the centers of local U/LIRGs. Further, the median $3 - 33$ GHz spectral index observed is consistent with models of continuous star-formation activity over a median lifetime of ~ 10 Myr.

(2) The median derived SFR of the extranuclear regions identified is $\sim 1 M_{\odot}\mathrm{yr}^{-1}$. Despite the sensitivity of our observations to low-mass star-forming regions LIRGs, it is clear that the most luminous extranuclear star-forming clumps identified in our survey are not seen in large samples of normal *or* interacting galaxies in the local Universe (Smith et al., 2016).

(3) The median q_{TIR} derived for our extranuclear star-forming regions (2.71 ± 0.34) is broadly consistent with the IR-radio correlation measured for normal and extreme star-forming galaxies in the local Universe (i.e. $q_{TIR} = 2.64$). This suggests that on kpc-scales in LIRGs we are sampling a representative volume of the ISM over a sufficiently long SFH so as to cause these regions to lie along the correlation.

(4) When we place our regions on the star-formation rate main sequence (SFMS), we find that they are not consistent with their host galaxies' globally-averaged specific star-formation rate (sSFR). This indicates that the nuclear starburst activity predominately drives LIRGs above the SFMS.

With maps of the star-forming regions which energize LIRGs now in possession for the equatorial sample, the next step will be to obtain complementary high-resolution imaging and kinematics of the associated molecular gas, which fuels star formation and AGN activity in these extraordinary galaxies. The combined datasets would serve as a means to measure both the conditions under which star formation is most efficient, and energetic feedback on the ISM at scales that are inaccessible to extreme starbursts being studied at high-redshift.

3.7 Additional Tables

In the following section we present both the derived (thermal fraction, SFR, age, etc.) and observed (IRAC and VLA) properties for 42 extragalactic star-forming regions identified in a sample of 25 galaxies from the Great Observatories All-Sky

LIRG Survey. In Table 3.4, the star formation rates at 33 GHz are calculated using Murphy et al. (2012a), and the Starburst99 model ages for both the continuous and instantaneous starburst are given for region. In Table 3.5, all VLA and Spitzer IRAC photometry is given in mJy.

Table 3.4: Derived Properties of Extranuclear Star-Forming Regions

Region	RA	DEC	SFR[a]	$f_{th,33GHz}$	$L_{IR}{}^{b}$	$L_{1.4GHz}$	$t_{inst}{}^{c}$	t_{cont}	$M_{*}{}^{d}$	sSFR[e]
MCG-02-01-051_e1	00:18:49.81738	-010.21.34.1910	0.88	0.33	36.17	20.50	9.00	6.34	8.96	7.94
IC1623_e1	01:07:46.69656	-017.30.20.5717	1.09	0.56	36.50	21.26	6.68	8.00	9.11	14.15
IC1623_e2	01:07:46.74329	-017.30.27.1956	2.17	0.58	36.81	21.59	6.70	8.00	8.89	13.80
IC1623_e3	01:07:47.07207	-017.30.26.6457	1.47	0.75	36.75	21.41	6.57	8.00	8.71	8.82
MCG-03-04-014_e1	01:10:09.05601	-016.51.12.7120	4.39	0.92	37.32	21.96	6.76	8.00	9.90	7.79
NGC0838_e1	02:09:38.30876	-010.08.49.4349	0.45	0.42	36.52	20.68	6.61	7.10	9.01	1.82
IC0214_e3	02:14:05.02289	+005.10.29.9168	3.01	0.20	36.48	21.68	6.59	8.61	9.33	8.57
IC0214_e2	02:14:05.30829	+005.10.28.6774	2.55	0.48	36.80	21.67	6.70	8.00	9.51	27.93
NGC0877_e2	02:18:00.27225	+014.32.27.0777	0.04	0.31	35.90	20.18	7.57	8.00	8.65	28.68
NGC0877_e1	02:18:00.42413	+014.32.44.6577	0.29	0.37	35.75	20.26	9.00	6.59	8.45	19.40
UGC02369_e1	02:54:01.90424	+014.58.11.5414	4.67	0.40	36.98	22.01	6.76	8.00	9.71	15.99
CGCG465-012_e2	03:54:16.15479	+015.55.35.1392	0.80	0.42	36.24	21.13	6.68	8.00	8.96	7.99
CGCG465-012_e1	03:54:16.18669	+015.55.47.5079	2.82	0.31	36.65	21.70	6.70	8.00	9.31	5.23
CGCG465-012_e3	03:54:16.56956	+015.55.37.3463	0.48	0.40	36.00	20.86	6.64	7.51	8.79	6.32
UGC02982_e5	04:12:22.09337	+005.32.59.1349	0.20	0.83	35.92	20.60	6.75	8.00	8.75	10.08
UGC02982_e2	04:12:22.15321	+005.32.48.3227	0.21	0.31	36.15	20.72	6.77	8.00	8.90	9.50
UGC02982_e3	04:12:22.41490	+005.32.57.9306	0.25	0.96	36.09	20.82	6.79	8.00	8.77	5.55
UGC02982_e4	04:12:23.73820	+005.32.47.1073	0.28	0.70	35.99	20.53	6.61	7.25	8.73	4.42
UGC03094_e1	04:35:33.74264	+019.10.24.0963	1.45	0.84	36.79	20.74	9.00	6.34	9.49	8.16
UGC03094_e3	04:35:33.81702	+019.09.57.8943	1.12	0.48	36.44	20.68	9.00	6.34	9.10	3.50
UGC03094_e2	04:35:33.91205	+019.10.10.0595	1.35	0.76	36.72	21.00	6.56	6.76	9.46	4.36
IRAS05442+173_e1	05:47:10.82732	+017.33.46.2608	0.91	0.31	36.16	20.95	6.56	7.02	8.76	4.08
IC0563_e2	09:46:20.06671	+003.02.43.6972	0.22	0.25	36.15	20.56	6.72	8.00	9.09	22.82
NGC3110_e3	10:04:01.52752	-006.28.26.0344	0.62	0.78	36.39	20.87	6.61	7.22	9.15	8.45
NGC3110_e2	10:04:02.03336	-006.28.33.1477	1.00	0.04	36.73	21.39	6.77	8.00	9.46	6.35
NGC3110_e1	10:04:02.57873	-006.28.46.3525	0.72	0.51	36.27	20.92	6.61	7.18	8.94	4.36
NGC3110_e4	10:04:02.68675	-006.28.35.1127	0.40	0.83	36.22	20.66	6.61	7.18	8.99	6.73
IC2810_e1	11:25:44.92036	+014.40.30.8605	5.07	0.15	36.59	21.28	9.00	6.34	9.42	9.34
NGC5257_e3	13:39:52.19263	+000.50.22.3494	0.68	0.37	36.12	20.97	6.62	7.39	9.03	12.09
NGC5257_e2	13:39:52.58999	+000.50.15.5249	1.01	0.26	36.13	21.21	6.59	8.51	9.08	3.84
NGC5257_e1	13:39:52.94249	+000.50.12.6413	2.52	0.15	36.29	21.28	6.56	6.77	9.04	6.96
NGC5257_e4	13:39:53.54494	+000.50.28.9336	0.56	0.66	36.28	20.92	6.58	7.49	9.11	5.34
NGC5258_e2	13:39:57.09557	+000.49.40.5328	1.42	0.29	36.32	21.26	6.61	7.31	9.18	6.36
NGC5258_e3	13:39:57.12290	+000.49.44.0410	2.77	0.32	36.66	21.58	6.62	7.39	9.36	5.78
NGC5258_e1	13:39:57.23223	+000.49.47.4126	2.20	0.52	36.77	21.62	6.74	8.00	9.52	6.18
NGC5331_e2	13:52:16.03444	+002.06.05.3056	4.93	0.46	37.06	21.98	6.75	8.00	9.85	2.89
NGC5331_e4	13:52:16.20505	+002.06.08.5057	3.56	0.46	36.92	21.80	6.70	8.00	9.75	9.01
NGC5331_e1	13:52:16.30493	+002.05.59.1366	1.06	0.81	36.64	21.24	6.65	8.85	9.44	2.70
NGC5331_e3	13:52:16.32488	+002.06.05.6838	5.47	0.62	37.24	22.10	6.77	8.00	10.01	4.24

Table 3.4 continued

Table 3.4: Derived Properties of Extranuclear Star-Forming Regions (continued)

Region	RA	DEC	SFR[a]	$f_{th,33GHz}$	$L_{IR}{}^{b}$	$L_{1.4GHz}$	$t_{inst}{}^{c}$	t_{cont}	$M_*{}^{d}$	sSFR[e]
NGC5990_e2	15:46:16.07681	+002.25.02.0582	0.26	0.17	36.19	20.55	6.62	7.38	9.09	5.13
NGC5990_e1	15:46:16.52746	+002.24.47.7330	0.63	0.60	36.29	20.81	6.56	7.06	9.13	3.55
IRASF16516-09_e4	16:54:23.40443	-009.53.22.1515	0.83	0.53	36.36	21.03	6.61	7.31	9.12	4.74
IRASF16516-09_e1	16:54:23.80720	-009.53.30.6354	0.94	0.37	36.25	20.89	6.56	6.86	9.07	4.63
IRASF16516-09_e3	16:54:24.67729	-009.53.15.6416	0.31	0.69	36.04	18.65	9.00	6.34	8.77	8.90
IRASF17138-10_e1	17:16:35.79572	-010.20.41.8617	7.27	0.34	37.10	22.05	6.60	8.02	9.86	4.65
NGC7592_e1	23:18:22.18023	-004.25.08.0269	0.37	0.39	35.87	20.54	6.56	6.96	8.81	2.12
NGC7679_e1	23:28:46.50087	+003.30.43.6612	1.48	0.68	36.71	21.37	6.59	8.96	9.38	10.38
NGC7679_e2	23:28:46.89743	+003.30.41.3465	0.78	0.95	36.58	20.91	6.56	7.06	9.43	0.80

[a] Star Formation Rates at 33 GHz Calculated using the prescription in Murphy et al. (2012a)
[b] Derived L_{IR} and $L_{1.4GHz}$ given in log SI units (W/Hz)
[c] Starburst99 model ages for each region given in log(age)
[d] Stellar mass given in units of log $M_{\odot}$
[e] Specific Star Formation Rates given in units of 10^{-10} yr^{-1}

Table 3.5: Observational Properties of Extranuclear Star-Forming Regions

Region	$S_{33GHz}{}^a$	σ_{33GHz}	S_{15GHz}	σ_{15GHz}	S_{3GHz}	σ_{3GHz}	$S_{3.6\mu m}{}^a$	$\sigma_{3.6\mu m}$	$S_{4.5\mu m}$	$\sigma_{4.5\mu m}$	$S_{8.0\mu m}$	$\sigma_{8.0\mu m}$
MCG-02-01-051_e1	0.384	0.084	0.602	0.031	1.546	0.249	0.879	0.257	0.720	0.229	12.240	2.514
IC1623_e1	0.454	0.088	0.489	0.031	1.572	0.253	0.527	0.269	0.383	0.210	5.972	2.223
IC1623_e2	0.426	0.076	0.519	0.021	1.677	0.118	1.034	0.430	0.857	0.342	16.140	4.152
IC1623_e3	0.121	0.077	0.155	0.021	0.443	0.117	0.421	0.111	0.314	0.087	6.157	1.389
MCG-03-04-014_e1	0.073	0.078	0.086	0.021	0.242	0.117	0.287	0.068	0.214	0.054	3.566	1.044
NGC0838_e1	0.061	0.168	0.100	0.042	0.221	0.151	0.506	0.209	0.335	0.141	5.043	0.998
IC0214_e3	0.367	0.146	0.600	0.038	1.353	0.640	0.642	0.747	0.419	0.530	13.790	3.399
IC0214_e2	0.729	0.149	0.752	0.040	2.853	0.663	0.503	0.372	0.440	0.310	28.250	2.560
NGC0877_e2	0.492	0.146	0.183	0.039	1.882	0.659	0.370	0.250	0.371	0.291	24.520	2.220
NGC0877_e1	0.515	0.067	0.397	0.025	0.427	0.077	0.426	0.153	0.302	0.106	5.093	2.000
UGC02369_e1	0.336	0.099	0.087	0.035	0.729	0.160	0.301	0.145	0.186	0.098	6.870	3.510
CGCG465-012_e2	0.207	0.066	0.227	0.026	0.381	0.158	0.432	0.106	0.319	0.081	5.116	0.902
CGCG465-012_e1	0.068	0.064	0.078	0.025	0.002	0.152	0.216	0.098	0.158	0.075	3.128	1.001
CGCG465-012_e3	0.184	0.065	0.306	0.026	0.525	0.157	0.481	0.292	0.352	0.223	6.550	2.523
UGC02982_e5	2.622	0.086	3.248	0.038	8.807	0.236	5.084	2.175	4.530	2.011	59.130	24.14
UGC02982_e2	0.162	0.157	0.096	0.057	0.130	0.900	0.283	0.105	0.208	0.074	3.532	0.947
UGC02982_e3	0.491	0.076	0.493	0.027	2.262	0.198	1.245	1.582	0.755	1.118	30.040	9.995
UGC02982_e4	0.372	0.110	0.628	0.041	0.877	0.286	1.465	1.486	1.141	1.131	35.150	7.380
UGC03094_e1	0.275	0.138	0.297	0.033	0.701	0.171	0.585	0.205	0.453	0.166	9.298	2.172
UGC03094_e3	0.385	0.120	0.699	0.032	2.064	0.172	1.846	0.737	1.377	0.593	26.570	4.901
UGC03094_e2	0.237	0.125	0.316	0.033	0.627	0.174	0.907	0.168	0.673	0.139	12.270	2.050
IRAS05442+173_e1	0.152	0.126	0.126	0.033	0.385	0.174	0.601	0.202	0.428	0.152	8.348	1.782
IC0563_e1	0.537	0.036	0.594	0.022	0.888	0.080	0.481	0.134	0.452	0.157	5.363	2.778
NGC3110_e3	0.214	0.036	0.310	0.022	0.753	0.080	0.456	0.203	0.369	0.166	3.777	1.736
NGC3110_e2	0.146	0.036	0.157	0.022	0.442	0.080	0.359	0.219	0.247	0.168	3.628	1.542
NGC3110_e1	0.120	0.037	0.119	0.023	0.392	0.083	0.452	0.080	0.327	0.059	5.314	0.731
NGC3110_e4	0.470	0.037	0.642	0.021	1.976	0.082	1.220	0.443	0.954	0.355	16.170	4.102
IC2810_e1	0.302	0.039	0.380	0.021	0.858	0.081	0.577	0.240	0.462	0.212	5.760	2.479
NGC5257_e3	0.590	0.039	0.794	0.022	1.784	0.082	0.899	0.405	0.748	0.327	12.690	3.619
NGC5257_e2	0.114	0.038	0.145	0.021	0.405	0.143	0.500	0.199	0.374	0.136	6.111	1.293
NGC5257_e1	0.529	0.036	0.666	0.021	2.276	0.146	1.434	0.862	1.227	0.766	16.050	6.459
NGC5257_e4	0.586	0.036	0.847	0.021	2.977	0.149	2.030	1.178	1.697	1.033	24.070	8.083
NGC5258_e2	0.381	0.034	0.491	0.021	1.504	0.139	1.093	0.610	0.898	0.500	11.730	4.299
NGC5258_e3	0.085	0.193	0.082	0.045	0.175	0.110	0.246	0.076	0.182	0.065	2.191	0.628
NGC5258_e1	0.669	0.105	1.062	0.031	2.308	0.093	1.805	1.110	1.334	0.853	30.120	7.059
NGC5331_e2	0.354	0.106	0.439	0.031	0.809	0.095	1.910	0.979	1.302	0.662	22.540	6.747
NGC5331_e4	0.651	0.076	1.011	0.025	3.143	0.183	1.516	1.023	1.469	0.960	17.190	9.464
NGC5331_e1	0.097	0.096	0.233	0.025	0.519	0.172	0.595	0.296	0.439	0.224	8.395	2.875
NGC5331_e3	0.113	0.101	0.184	0.026	0.652	0.178	0.442	0.205	0.327	0.149	7.221	2.184

Table 3.5 continued

Table 3.5: Observational Properties of Extranuclear Star-Forming Regions (continued)

Region	S_{33GHz}[a]	σ_{33GHz}	S_{15GHz}	σ_{15GHz}	S_{3GHz}	σ_{3GHz}	$S_{3.6\mu m}$[a]	$\sigma_{3.6\mu m}$	$S_{4.5\mu m}$	$\sigma_{4.5\mu m}$	$S_{8.0\mu m}$	$\sigma_{8.0\mu m}$
NGC5990_e2	0.125	0.115	0.134	0.027	0.340	0.178	0.398	0.058	0.287	0.049	5.819	0.789
NGC5990_e1	0.090	0.101	0.139	0.026	0.402	0.175	0.413	0.183	0.299	0.133	4.952	1.444
IRASF16516-09_e4	0.286	0.093	0.322	0.025	0.236	0.206	1.010	0.361	0.749	0.262	15.970	4.950
IRASF16516-09_e1	0.265	0.096	0.311	0.026	0.434	0.211	0.962	0.206	0.718	0.174	13.360	2.582
IRASF16516-09_e3	0.220	0.110	0.324	0.026	0.209	0.208	0.447	0.146	0.364	0.121	6.986	1.627
IRASF17138-10_e1	0.422	0.068	0.413	0.024	0.963	0.102	1.488	0.349	1.080	0.276	16.980	3.557
NGC7592_e1	0.175	0.068	0.215	0.024	0.528	0.102	1.339	0.221	0.955	0.168	13.660	2.446
NGC7679_e1	0.236	0.061	0.183	0.024	0.322	0.092	0.410	0.093	0.332	0.093	5.897	1.529
NGC7679_e2	0.029	0.063	0.142	0.025	0.272	0.094	0.621	0.135	0.471	0.131	8.380	1.737

[a] All VLA and Spitzer IRAC fluxes given in mJy

Chapter 4

The Star Formation in Radio Survey: 3 – 33 GHz Imaging of Nearby Galaxy Nuclei and Extranuclear Star-forming Regions

4.1 Introduction

The radio spectra of star-forming galaxies, typically characterized as a power law ($S_\nu \propto \nu^\alpha$), encode information about the thermal and non-thermal energetic processes which power them. Both thermal (Bremsstrahlung) and non-thermal (synchrotron) emission are associated with massive ($\geq 8M_\odot$) star formation, underlying the basis for the well-known far-infrared (FIR: 42-122μm)-radio correlation (de Jong et al., 1985; Helou et al., 1985; Condon, 1992; Bell, 2003). FIR emission arises from the absorption and re-radiation of UV and optical photons that heat dust grains surrounding massive star-forming regions. The O and B stars in such regions, with lifetimes of ≤ 10 Myr, produce ionizing (Lyman continuum) radiation whose strength is directly proportional to the amount of free-free emission. These same massive stars end their lives as core-collapse supernovae, whose remnants accelerate cosmic ray (CR) electrons/positrons that produce the diffuse non-thermal synchrotron emission observed in star-forming galaxies (Condon, 1992; Koyama et al., 1995; Murphy et al., 2006a; Lacki & Thompson, 2010; Lacki et al., 2010).

However, the connection between the non-thermal synchrotron emission and the current star-formation rate (SFR) of a galaxy is far less direct relative to thermal free-free emission. Variations in the generation and propagation of CRs through the interstellar medium (ISM) can affect the observed low-frequency emission surrounding star-forming regions. Despite the complexity in interpreting this non-thermal emission from galaxies, several empirical (Bell, 2003; Koyama et al., 1995; Murphy et al., 2006a; Heesen et al., 2014; Tabatabaei et al., 2017) and theoretical (Condon, 1992; Murphy et al., 2011b) calibrations for the star-formation rate (SFR) exist in the literature. These studies demonstrate that at frequencies low enough (typically $\sim$ 1 GHz) the emission is dominated by the non-thermal, steep spectrum component ($\alpha^{\rm NT} \sim -0.8$), and at frequencies high enough ($\sim$ 30 GHz) the emission becomes dominated by thermal emission ($\alpha^{\rm T} \sim -0.1$). Hence, radio observations can serve as an excellent, extinction-free, diagnostic for the current SFR within nearby galaxies.

This was the motivation for initiating the Star Formation in Radio Survey (SFRS), which began as a 33 GHz imaging campaign with the Green Bank Telescope (GBT) to study 103 galaxy nuclei and extranuclear star-forming complexes at a matched resolution of 25”. In the initial investigation, Murphy et al. (2012b) used the Westerbork Synthesis Radio Telescope (WSRT) in combination with the GBT to construct

1.7-to-33 GHz radio spectra for 53 galaxy nuclei and extranuclear star-forming regions on ∼kpc scales. They found evidence that the measured thermal fraction at 33 GHz varied significantly for star-forming regions observed at different physical resolution due to the range in galaxy distance. Photometric apertures larger than $\sim$ 1kpc were observed to have thermal fractions as low as $40-50\%$, whereas regions measured with apertures $\leq$1kpc appeared to be heavily dominated by free-free emission, with thermal fractions as high as $\sim 90\%$. However, without high-resolution maps of both free-free and non-thermal emission from individual HII regions within these larger complexes, it is difficult to determine the physical nature of these trends within nearby galaxies.

This study served as the foundation for extending the SFRS into a multi-frequency Karl G. Jansky Very Large Array (VLA) campaign to image hundreds of star-forming regions in 50 galaxies taken from the *Spitzer* Infrared Nearby Galaxies Survey (SINGS: Kennicutt et al., 2003) and the Key Insights on Nearby Galaxies: a Far-Infrared Survey (KINGFISH: Kennicutt et al., 2011). The results from our 33 GHz observations, along with corresponding Hα and *Spitzer*/MIPS 24μm photometry were recently presented in Murphy et al. (2018a), hereafter M18a, and explored the Hα-to-33 GHz and 24μm-to-33 GHz flux density ratios of star-forming regions as a function of galactocentric radius and physical resolution. An outlier of these distributions, NGC 4725 B, was later followed up with higher-frequency observations (Q-band: $\sim$ 44 GHz) in order to confirm this region as the second known source of extragalactic anomalous microwave emission (AME: Murphy et al., 2018b). Building on this analysis, we have also obtained 3 and 15 GHz imaging for the SFRS, allowing us to map the full radio spectrum of each star-forming region at a matched-resolution of $\sim$ 2". In this paper, we focus our presentation on the results associated with the radio spectral indices and corresponding free-free emission fractions for the entire sample.

The paper is organized as follows: In §2 we describe our sample selection, data reduction, and imaging procedure for the 3 - 33 GHz VLA data. In §3 we describe the ancillary data products included in this study as well as the analysis procedures used. Our results are presented in §4, and discussed in §5. Our main conclusions are summarized in §6. In §7 we additionally provide ancillary photometry from the Galaxy Evolution Explorer (GALEX), *Spitzer*, and ground-based Hα observations at a matched resolution of 7" that are not used in the present analysis. Throughout the paper we report the median absolute deviations rather than standard deviations, as this statistic is more resilient against outliers in a data set.

4.2 Sample and Data Analysis

In this section we describe the sample selection, and present the VLA observations along with the data reduction and imaging procedures.

Table 4.1: Galaxy Properties

Galaxy	Type[a]	Dist.[b] (Mpc)	Nuc. Type[c]	D_{25}[a] (arcmin)	i (°)	P.A.[a] (°)
NGC 0337	SBd	19.3	SF	2.9×1.8	52	130
NGC 0628	SAc	7.2	...	10.5×9.5	25	25
NGC 0855	E	9.73	SF	2.6×1.0	70	67[d]
NGC 0925	SABd	9.12	SF	10.5×5.9	57	102
NGC 1097	SBb	14.2	AGN	9.3×6.3	48	130
NGC 1266	SB0	30.6	AGN	1.5×1.0	49	108[d]
NGC 1377	S0	24.6	...	1.8×0.9	61	92
IC 0342	SABcd	3.28	SF(*)	$21.4 \times 20.$	21	153[d]
NGC 1482	SA0	22.6	SF	2.5×1.4	57	103
NGC 2146	Sbab	17.2	SF(*)	6.0×3.4	56	57
NGC 2403	SABcd	3.22	SF(*)	21.9×12.3	57	128
Holmberg II	Im	3.05	...	7.9×6.3	37	16
NGC 2798	SBa	25.8	SF/AGN	2.6×1.0	70	160
NGC 2841	SAb	14.1	AGN	8.1×3.5	66	147
NGC 2976	SAc	3.55	SF	5.9×2.7	64	143
NGC 3049	SBab	19.2	SF	2.2×1.4	51	25
NGC 3077	I0pec	3.83	SF(*)	5.4×4.5	34	45
NGC 3190	SAap	19.3	AGN(*)	4.4×1.5	73	125
NGC 3184	SABcd	11.7	SF	7.4×6.9	21	135
NGC 3198	SBc	14.1	SF	8.5×3.3	68	35
IC 2574	SABm	3.79	SF(*)	13.2×5.4	67	50
NGC 3265	E	19.6	SF	1.3×1.0	39	73
NGC 3351	SBb	9.33	SF	7.4×5.0	48	13
NGC 3521	SABbc	11.2	SF/AGN(*)	11.0×5.1	63	163
NGC 3621	SAd	6.55	AGN	12.3×7.1	55	159
NGC 3627	SABb	9.38	AGN	9.1×4.2	64	173
NGC 3773	SA0	12.4	SF	1.2×1.0	33	165
NGC 3938	SAc	17.9	SF(*)	5.4×4.9	25	29[d]
NGC 4254	SAc	14.4	SF/AGN	5.4×4.7	30	24[d]
NGC 4321	SABbc	14.3	AGN	7.4×6.3	32	30
NGC 4536	SABbc	14.5	SF/AGN	7.6×3.2	66	130
NGC 4559	SABcd	6.98	SF	10.7×4.4	67	150
NGC 4569	SABab	9.86	AGN	9.5×4.4	64	23
NGC 4579	SABb	16.4	AGN	5.9×4.7	37	95
NGC 4594	SAa	9.08	AGN	8.7×3.5	69	90
NGC 4625	SABmp	9.3	SF	2.2×1.9	31	28[d]
NGC 4631	SBd	7.62	SF(*)	15.5×2.7	83	86

Table 4.1 continued

Table 4.1: Galaxy Properties (continued)

Galaxy	Type[a]	Dist.[b] (Mpc)	Nuc. Type[c]	D_{25}[a] (arcmin)	i (°)	P.A.[a] (°)
NGC 4725	SABab	11.9	AGN	10.7 × 7.6	45	35
NGC 4736	SAab	4.66	AGN(*)	11.2 × 9.1	35	105
NGC 4826	SAab	5.27	AGN	10.0 × 5.4	59	115
NGC 5055	SAbc	7.94	AGN	12.6 × 7.2	56	105
NGC 5194	SABbcp	7.62	AGN	11.2 × 6.9	53	163
NGC 5398	SBdm	7.66	⋯	2.8 × 1.7	53	172
NGC 5457	SABcd	6.7	SF(*)	28.8 × 26.	26	29[d]
NGC 5474	SAcd	6.8	SF(*)	4.8 × 4.3	27	98[d]
NGC 5713	SABbcp	21.4	SF	2.8 × 2.5	27	10
NGC 5866	S0	15.3	AGN	4.7 × 1.9	69	128
NGC 6946	SABcd	6.8	SF	11.5 × 9.8	32	53[d]
NGC 7331	SAb	14.5	AGN	10.5 × 3.7	72	171
NGC 7793	SAd	3.91	SF	9.3 × 6.3	48	98

[a] Morphological types, diameters, and position angles were taken from the Third Reference Catalog of Bright Galaxies (RC3: de Vaucouleurs et al., 1991).
[b] Redshift-independent distance taken from the list compiled by Kennicutt et al. (2011), except for the two non-KINGFISH galaxies NGC 5194 (Ciardullo et al., 2002) and NGC 2403 (Freedman et al., 2001).
[c] Nuclear type based on optical spectroscopy: SF = Star-Forming; AGN = Non-thermal emission as given in Table 5 of Moustakas et al. (2010) or (*) Table 4 of Lonsdale Persson & Helou (1987).
[d] Position angle taken from Jarrett et al. (2003).

4.2.1 Sample Selection

The SFRS sample includes targeted observations from 56 nearby galaxies ($d_L < 30$ Mpc) in the SINGS and KINGFISH legacy programs (Table 4.1). All nuclear and extranuclear star-forming regions were chosen to have mid-infrared spectral mappings carried out by the IRS instrument on board *Spitzer*, and *Herschel*/PACS far-infrared spectral mappings, for a combination of the principal atomic ISM cooling lines ([OI] 63μm, [OIII] 88μm, [NII] 122, 205μm, and [CII] 158μm). NGC 5194 and NGC 2403 are exceptions; these galaxies were part of the SINGS sample, but are not formally included in KINGFISH. They were observed with *Herschel* as part of the Very Nearby Galaxy Survey (VNGS; PI: C. Wilson). Similarly, there are additional KINGFISH galaxies that were not part of SINGS, but have existing *Spitzer* data: NGC 5457 (M101), IC 342, NGC 3077, and NGC 2146.

The SINGS and KINGFISH galaxies are fully representative of the integrated properties and ISM conditions found in the local Universe, spanning the full range in morphological types, as well as a factor of 100 in IR luminosity ($L_{\rm IR}$: 8-1000μm), global IR/optical flux ratio, and the star formation rate. Similarly, the spectroscopically targeted star-forming regions included in the SFRS cover the full range of physical conditions found in nearby galaxies, including the extinction-corrected production rate of ionizing photons $Q(H_0)$, metallicity, visual extinction, radiation field intensity, and ionizing stellar temperature.

The full sample over the entire sky consists of 118 star-forming complexes (56 nuclei and 62 extranuclear regions), 112 of which (50 nuclei and 62 extranuclear regions; see Tables 4.2 and 4.3, respectively) are observable with the VLA (i.e., having $\delta > -35°$). The coordinates given in both tables list the pointing center for the VLA observations (see Section 2.2), which correspond to the centers of the *Spitzer* mid-infrared and *Herschel* far-infrared spectral line maps. Morphologies, adopted distances, optically-defined nuclear types, diameters (D_{25}), inclinations (i), and position angles (P.A.) for each source are given in Table 4.1 and described in detail in M18a.

4.2.2 VLA Observations and Data Reduction

The observational set-up and reduction procedure for the Ka-band ($29-37$ GHz) data (11B-032,13A-129) is described in detail in M18a. Observations in the S-band ($2-4$ GHz) were taken during the 2013 VLA B-configuration cycle (13B-215), and utilized the 8-bit sampler. Observations in the Ku-band ($12-18$ GHz) were taken November 2014 in the C-configuration (13B-215) using the 3-bit samplers. Both sets of observations utilized the full available bandwidth of the respective receivers. Given the large range in brightness among our targeted regions, we varied the time spent on-source by estimating the expected $3-15$ GHz flux density using the *Spitzer*/MIPS 24 μm maps. The median integration time for regions in our sample was $\sim$ 10 minutes at both frequencies. The choice of array configurations were made to match the angular resolution (i.e., FWHM of the synthesized beam $\sim$ 2") of the observations at each band. This allows us to probe the same spatial scales across the full $3-33$ GHz frequency range, and ensures that any differences in the measured spectral index of individual star-forming regions is due to physical variation in the region being measured, and not due to resolving out more emission at higher frequencies.

The standard VLA flux density calibrators 3C48, 3C286, and 3C147 were used, and the data reduction procedures presented in M18a are repeated for our present analysis, and briefly described here. To reduce the VLA data, we used the Common Astronomy Software Applications (CASA; McMullin et al., 2007) versions 4.6.0 and 4.7.0, and followed standard calibration and flagging procedures, including the utilization of the VLA calibration pipeline. We further inspected the visibilities and calibration tables for evidence of bad antennas, frequency ranges, and time ranges, flagging correspondingly. We also flagged any instances of radio frequency interference (RFI). Importantly, the fractional bandwidth of our observations lost to RFI flagging is negligible relative to the full bandwidth of the receivers. After flagging, we re-ran the pipeline, and repeated this process until all poorly-calibrated data were removed. For all delay and bandpass tables applied on-the-fly, we used the default nearest-neighbor interpolation. For complex gain and flux density scale tables, we used a linear interpolation.

Table 4.2: Nuclear Source Positions and Imaging Characteristics

			3 GHz			15 GHz		
Galaxy	R.A. (J2000)	Decl. (J2000)	Synthesized Beam	σ (μJy bm^{-1})	σ_{T_b} (mK)	Synthesized Beam	σ (μJy bm^{-1})	σ_{T_b} (mK)
NGC 0337	00 59 50.3	−07 34 44	2.″43 × 1.″74	18.7	597.32	2.″00 × 1.″13	9.1	21.71
NGC 0628	01 36 41.7	+15 46 59	1.″96 × 1.″78	14.0	543.15	1.″55 × 1.″19	9.6	28.14
NGC 0855	02 14 03.7	+27 52 38	1.″80 × 1.″62	13.2	613.61	1.″50 × 1.″25	8.6	24.93
NGC 0925	02 27 17.0	+33 34 43	1.″80 × 1.″59	13.0	611.30	1.″47 × 1.″23	9.1	27.04
NGC 1097	02 46 19.1	−30 16 28	5.″76 × 1.″80	44.9	586.45	3.″81 × 0.″99	16.9	24.11
NGC 1266	03 16 00.8	−02 25 38	2.″20 × 1.″78	14.0	485.33	1.″80 × 1.″17	11.3	28.86
NGC 1377	03 36 38.9	−20 54 06	3.″56 × 1.″71	17.4	385.40	2.″61 × 1.″09	11.6	21.93
IC 0342	03 46 48.5	+68 05 46	2.″23 × 1.″76	41.6	1430.61	1.″72 × 1.″13	11.4	31.44
NGC 1482	03 54 39.5	−20 30 07	3.″25 × 1.″67	16.8	419.18	2.″42 × 1.″33	14.1	23.56
NGC 2146	06 18 37.7	+78 21 25	2.″55 × 1.″55	35.5	1214.57	1.″93 × 0.″94	14.9	44.68
NGC 2403	07 36 50.0	+65 36 04	2.″21 × 1.″53	13.8	551.32	1.″88 × 1.″15	9.8	24.41
Holmberg II	08 19 13.3	+70 43 08	2.″59 × 1.″67	14.9	465.55	1.″97 × 1.″15	9.4	22.41
NGC 2798	09 17 22.8	+41 59 58	2.″13 × 1.″78	14.6	520.66	1.″58 × 1.″38	11.3	27.83
NGC 2841	09 22 02.7	+50 58 36	2.″11 × 1.″62	13.3	526.88	1.″59 × 1.″23	18.1	50.13
NGC 2976	09 47 15.3	+67 55 00	2.″83 × 1.″66	14.4	413.49	2.″02 × 1.″13	9.7	23.08
NGC 3049	09 54 49.6	+09 16 17	2.″14 × 1.″84	14.9	510.77	2.″07 × 1.″13	12.2	27.98
NGC 3077	10 03 19.1	+68 44 02	2.″90 × 1.″67	14.4	402.59	1.″98 × 1.″12	10.2	24.82
NGC 3190	10 18 05.6	+21 49 55	2.″12 × 1.″81	13.5	475.29	1.″61 × 1.″26	8.5	22.63
NGC 3184	10 18 16.7	+41 25 27	2.″42 × 1.″76	14.0	444.09	1.″29 × 1.″18	8.5	30.49
NGC 3198	10 19 54.9	+45 32 59	2.″25 × 1.″66	14.4	521.10	1.″34 × 1.″17	8.5	29.06
IC 2574	10 28 48.4	+68 28 02	2.″96 × 1.″64	14.2	393.53	2.″03 × 1.″14	8.8	20.73
NGC 3265	10 31 06.7	+28 47 48	2.″23 × 1.″78	14.9	505.30	1.″44 × 1.″25	7.8	23.42
NGC 3351	10 43 57.8	+11 42 14	2.″00 × 1.″75	18.4	708.89	1.″95 × 1.″67	15.3	25.34
NGC 3521	11 05 48.9	−00 02 06	3.″07 × 1.″95	19.9	448.93	1.″88 × 1.″19	16.4	39.79
NGC 3621	11 18 16.0	−32 48 42	4.″76 × 1.″53	15.7	291.11	4.″17 × 1.″08	8.5	10.16
NGC 3627	11 20 15.0	+12 59 30	1.″95 × 1.″77	15.7	616.48	2.″36 × 1.″97	14.0	16.23
NGC 3773	11 38 13.0	+12 06 45	1.″95 × 1.″76	13.1	518.26	1.″53 × 1.″14	9.8	30.21
NGC 3938	11 52 49.5	+44 07 14	3.″13 × 1.″73	15.1	376.61	1.″25 × 1.″10	7.9	31.23
NGC 4254	12 18 49.4	+14 24 59	1.″99 × 1.″81	15.3	577.12	1.″53 × 1.″11	9.0	28.58
NGC 4321	12 22 54.9	+15 49 21	1.″89 × 1.″72	15.0	622.65	1.″53 × 1.″17	9.8	29.55
NGC 4536	12 34 27.1	+02 11 17	2.″16 × 1.″86	15.5	524.37	2.″44 × 1.″45	10.2	15.58
NGC 4559	12 35 57.7	+27 57 36	1.″75 × 1.″63	13.6	646.04	1.″32 × 1.″27	9.0	29.13
NGC 4569	12 36 49.8	+13 09 46	2.″01 × 1.″80	15.4	572.68	1.″68 × 1.″18	10.7	29.15
NGC 4579	12 37 43.6	+11 49 02	2.″12 × 1.″85	23.4	807.73	1.″72 × 1.″21	50.9	132.87
NGC 4594	12 39 59.4	−11 37 23	2.″76 × 1.″74	19.7	554.75	2.″01 × 1.″09	13.4	32.88
NGC 4625	12 41 52.4	+41 16 24	1.″73 × 1.″56	13.5	677.51	1.″54 × 1.″17	9.7	29.19
NGC 4631	12 42 05.9	+32 32 22	1.″85 × 1.″76	14.3	597.52	2.″29 × 1.″83	12.9	16.71

Table 4.2 continued

Table 4.2: Nuclear Source Positions and Imaging Characteristics (continued)

Galaxy	R.A. (J2000)	Decl. (J2000)	3 GHz Synthesized Beam	3 GHz σ (μJy bm^{-1})	3 GHz σ_{T_b} (mK)	15 GHz Synthesized Beam	15 GHz σ (μJy bm^{-1})	15 GHz σ_{T_b} (mK)
NGC 4725	12 50 26.6	+25 30 06	1.″85 × 1.″76	13.5	561.64	1.″33 × 1.″26	9.0	29.20
NGC 4736	12 50 53.0	+41 07 14	1.″72 × 1.″55	13.9	706.09	2.″25 × 2.″06	13.4	15.67
NGC 4826	12 56 43.9	+21 41 00	1.″97 × 1.″75	14.3	559.38	1.″46 × 1.″33	10.1	28.20
NGC 5055	13 15 49.2	+42 01 49	1.″76 × 1.″60	12.8	619.07	1.″51 × 1.″17	9.7	29.58
NGC 5194	13 29 52.7	+47 11 43	1.″79 × 1.″57	17.0	820.75	1.″54 × 1.″15	9.3	28.43
NGC 5398	14 01 20.2	−33 04 09	6.″62 × 1.″76	20.6	239.46	3.″98 × 1.″03	8.4	11.09
NGC 5457	14 03 12.6	+54 20 57	1.″82 × 1.″67	13.9	619.05	1.″55 × 1.″10	8.6	27.29
NGC 5474	14 05 01.3	+53 39 44	1.″83 × 1.″71	14.3	616.05	1.″49 × 1.″07	11.9	40.40
NGC 5713	14 40 11.3	−00 17 27	2.″55 × 1.″77	17.6	526.76	2.″35 × 1.″80	15.4	19.67
NGC 5866	15 06 29.5	+55 45 48	1.″92 × 1.″63	13.8	595.03	1.″62 × 1.″20	15.4	42.92
NGC 6946	20 34 52.3	+60 09 14	2.″03 × 1.″64	16.1	655.75	2.″15 × 1.″12	9.5	21.44
NGC 7331	22 37 04.1	+34 24 56	1.″82 × 1.″67	15.1	672.97	1.″51 × 1.″21	10.0	29.80
NGC 7793	23 57 49.2	−32 35 24	4.″77 × 1.″62	14.0	245.06	4.″47 × 1.″08	9.4	10.50

Note — See Murphy et al. (2018a) for the 33 GHz imaging characteristics.

Table 4.3: Extranuclear Source Positions and Imaging Characteristics

Enuc. ID	R.A. (J2000)	Decl. (J2000)	3 GHz Synthesized Beam	3 GHz σ (μJy bm^{-1})	3 GHz σ_{T_b} (mK)	15 GHz Synthesized Beam	15 GHz σ (μJy bm^{-1})	15 GHz σ_{T_b} (mK)
NGC 0628 Enuc. 1	01 36 45.1	+15 47 51	$1''.96 \times 1''.78$	14.0	542.77	$1''.56 \times 1''.21$	9.8	28.16
NGC 0628 Enuc. 2	01 36 37.5	+15 45 12	$1''.96 \times 1''.78$	14.0	544.62	$1''.57 \times 1''.22$	9.6	27.27
NGC 0628 Enuc. 3	01 36 38.8	+15 44 25	$1''.96 \times 1''.78$	14.0	542.12	$1''.57 \times 1''.23$	9.6	26.82
NGC 0628 Enuc. 4	01 36 35.5	+15 50 11	$1''.96 \times 1''.78$	13.8	537.98	$1''.56 \times 1''.20$	8.0	23.07
NGC 1097 Enuc. 1	02 46 23.9	−30 17 51	$5''.76 \times 1''.80$	41.2	537.94	$3''.76 \times 0''.95$	11.8	17.84
NGC 1097 Enuc. 2	02 46 14.4	−30 15 05	$5''.76 \times 1''.80$	38.3	500.07	$3''.80 \times 0''.98$	11.4	16.42
NGC 2403 Enuc. 1	07 36 45.5	+65 37 00	$2''.21 \times 1''.53$	13.7	548.00	$1''.86 \times 1''.16$	9.4	23.61
NGC 2403 Enuc. 2	07 36 52.7	+65 36 46	$2''.21 \times 1''.53$	13.7	547.71	$1''.85 \times 1''.15$	9.5	23.96
NGC 2403 Enuc. 3	07 37 06.9	+65 36 39	$2''.21 \times 1''.53$	13.7	548.41	$1''.84 \times 1''.16$	9.7	24.51
NGC 2403 Enuc. 4	07 37 17.9	+65 33 46	$2''.21 \times 1''.53$	13.7	546.14	$1''.80 \times 1''.15$	9.5	24.86
NGC 2403 Enuc. 5	07 36 19.5	+65 37 04	$2''.21 \times 1''.53$	13.5	541.72	$1''.79 \times 1''.15$	9.5	24.84
NGC 2403 Enuc. 6	07 36 28.5	+65 33 50	$2''.21 \times 1''.53$	13.5	541.23	$1''.77 \times 1''.13$	9.7	26.15
NGC 2976 Enuc. 1	09 47 07.8	+67 55 52	$2''.83 \times 1''.66$	14.5	415.03	$1''.99 \times 1''.13$	9.8	23.62
NGC 2976 Enuc. 2	09 47 24.1	+67 53 57	$2''.83 \times 1''.66$	14.4	412.17	$1''.97 \times 1''.13$	10.0	24.19
NGC 3521 Enuc. 1	11 05 46.3	−00 04 10	$3''.07 \times 1''.95$	19.4	436.89	$1''.92 \times 1''.22$	14.0	32.41
NGC 3521 Enuc. 2	11 05 49.9	−00 03 40	$3''.07 \times 1''.95$	19.8	445.88	$2''.05 \times 1''.11$	11.7	27.66
NGC 3521 Enuc. 3	11 05 47.6	+00 00 33	$3''.07 \times 1''.95$	18.9	425.62	$2''.21 \times 1''.13$	11.6	25.02
NGC 3627 Enuc. 1	11 20 16.2	+12 57 50	$1''.95 \times 1''.77$	15.4	604.26	$1''.50 \times 1''.22$	9.0	26.70
NGC 3627 Enuc. 2	11 20 16.3	+12 58 44	$1''.95 \times 1''.77$	15.7	614.25	$1''.92 \times 1''.41$	15.7	31.48
NGC 3627 Enuc. 3	11 20 16.0	+12 59 52	$1''.95 \times 1''.77$	15.7	616.15	$1''.51 \times 1''.17$	13.4	40.92
NGC 3938 Enuc. 1	11 52 46.4	+44 07 01	$3''.13 \times 1''.73$	15.0	374.91	$1''.27 \times 1''.12$	8.3	31.38
NGC 3938 Enuc. 2	11 53 00.0	+44 07 55	$3''.13 \times 1''.73$	14.8	368.03	$1''.27 \times 1''.12$	8.3	31.40
NGC 4254 Enuc. 1	12 18 49.1	+14 23 59	$1''.99 \times 1''.81$	15.1	567.30	$1''.55 \times 1''.14$	8.5	26.05
NGC 4254 Enuc. 2	12 18 44.6	+14 24 25	$1''.99 \times 1''.81$	15.3	575.22	$1''.51 \times 1''.16$	9.6	29.55
NGC 4321 Enuc. 1	12 22 58.9	+15 49 35	$1''.89 \times 1''.72$	14.9	620.02	$1''.53 \times 1''.18$	9.8	29.30
NGC 4321 Enuc. 2	12 22 49.8	+15 50 29	$1''.89 \times 1''.72$	14.9	618.78	$1''.52 \times 1''.18$	9.9	29.98
NGC 4631 Enuc. 1	12 41 40.8	+32 31 51	$1''.87 \times 1''.75$	14.0	577.02	$1''.66 \times 1''.27$	9.1	23.44
NGC 4631 Enuc. 2	12 42 21.3	+32 33 07	$1''.85 \times 1''.76$	13.9	578.32	$1''.61 \times 1''.28$	9.0	23.48
NGC 4736 Enuc. 1	12 50 56.2	+41 07 20	$1''.72 \times 1''.55$	13.9	705.86	$1''.54 \times 1''.17$	12.9	38.89
NGC 5055 Enuc. 1	13 15 58.0	+42 00 26	$1''.76 \times 1''.60$	13.1	630.58	$1''.50 \times 1''.17$	9.9	30.50
NGC 5194 Enuc. 1	13 29 53.1	+47 12 40	$1''.79 \times 1''.57$	16.8	810.49	$1''.53 \times 1''.14$	9.1	28.20
NGC 5194 Enuc. 2	13 29 44.1	+47 10 21	$1''.74 \times 1''.52$	17.0	863.15	$1''.52 \times 1''.14$	8.9	27.62
NGC 5194 Enuc. 3	13 29 44.6	+47 09 55	$1''.74 \times 1''.52$	16.9	858.25	$1''.52 \times 1''.14$	9.1	28.37
NGC 5194 Enuc. 4	13 29 56.2	+47 14 07	$1''.79 \times 1''.57$	16.0	768.85	$1''.52 \times 1''.14$	9.5	29.61
NGC 5194 Enuc. 5	13 29 59.6	+47 14 01	$1''.79 \times 1''.57$	16.1	773.77	$1''.52 \times 1''.14$	9.7	30.21
NGC 5194 Enuc. 6	13 29 39.5	+47 08 35	$1''.74 \times 1''.52$	15.8	805.61	$1''.51 \times 1''.12$	8.7	27.81
NGC 5194 Enuc. 7	13 30 02.5	+47 09 52	$1''.74 \times 1''.52$	17.8	904.22	$1''.52 \times 1''.11$	9.3	29.80

Table 4.3 continued

Table 4.3: Extranuclear Source Positions and Imaging Characteristics (continued)

Enuc. ID	R.A. (J2000)	Decl. (J2000)	3 GHz Synthesized Beam	3 GHz σ (μJy bm^{-1})	3 GHz σ_{T_b} (mK)	15 GHz Synthesized Beam	15 GHz σ (μJy bm^{-1})	15 GHz σ_{T_b} (mK)
NGC 5194 Enuc. 8	13 30 01.6	+47 12 52	1.″79 × 1.″57	16.7	803.48	1.″58 × 1.″18	9.7	28.04
NGC 5194 Enuc. 9	13 29 59.9	+47 11 12	1.″79 × 1.″57	17.0	819.52	1.″59 × 1.″16	10.7	31.20
NGC 5194 Enuc. 10	13 29 56.7	+47 10 46	1.″74 × 1.″52	18.1	921.23	1.″59 × 1.″16	10.8	31.55
NGC 5194 Enuc. 11	13 29 49.7	+47 13 29	1.″79 × 1.″57	16.3	783.23	1.″57 × 1.″21	12.8	36.27
NGC 5457 Enuc. 1	14 03 10.2	+54 20 58	1.″82 × 1.″67	13.8	615.51	1.″55 × 1.″10	8.4	26.65
NGC 5457 Enuc. 2	14 02 55.0	+54 22 27	1.″81 × 1.″63	14.1	643.39	1.″54 × 1.″09	8.5	27.14
NGC 5457 Enuc. 3	14 03 41.3	+54 19 05	1.″82 × 1.″67	14.1	627.94	4.″68 × 2.″20	25.0	13.13
NGC 5457 Enuc. 4	14 03 53.1	+54 22 06	1.″82 × 1.″73	13.8	590.56	1.″54 × 1.″08	9.5	30.71
NGC 5457 Enuc. 5	14 03 01.1	+54 14 29	1.″81 × 1.″63	13.8	629.72	1.″49 × 1.″07	10.8	36.48
NGC 5457 Enuc. 6	14 02 28.1	+54 16 26	1.″86 × 1.″67	13.7	596.38	1.″53 × 1.″06	11.9	39.68
NGC 5457 Enuc. 7	14 04 29.3	+54 23 46	1.″82 × 1.″73	13.7	589.02	1.″50 × 1.″04	13.0	44.82
NGC 5713 Enuc. 1	14 40 12.1	−00 17 47	2.″55 × 1.″77	17.6	525.60	2.″35 × 1.″80	15.9	20.36
NGC 5713 Enuc. 2	14 40 10.5	−00 17 47	2.″55 × 1.″77	17.6	527.29	2.″35 × 1.″80	15.9	20.36
NGC 6946 Enuc. 1	20 35 16.6	+60 10 57	2.″03 × 1.″64	15.2	616.55	2.″07 × 1.″10	8.3	19.75
NGC 6946 Enuc. 2	20 35 25.1	+60 10 03	2.″03 × 1.″64	15.0	609.01	2.″00 × 1.″09	9.8	24.32
NGC 6946 Enuc. 3	20 34 52.2	+60 12 41	2.″03 × 1.″64	15.0	608.66	2.″09 × 1.″09	8.7	20.65
NGC 6946 Enuc. 4	20 34 19.4	+60 10 09	2.″03 × 1.″64	14.8	603.01	2.″45 × 1.″90	10.1	11.78
NGC 6946 Enuc. 5	20 34 39.0	+60 04 53	2.″06 × 1.″63	15.1	604.38	1.″91 × 1.″11	8.8	22.34
NGC 6946 Enuc. 6	20 35 06.0	+60 11 01	2.″03 × 1.″64	15.7	636.59	1.″95 × 1.″11	8.6	21.28
NGC 6946 Enuc. 7	20 35 11.2	+60 08 60	2.″03 × 1.″64	15.7	636.59	2.″14 × 1.″13	8.8	19.64
NGC 6946 Enuc. 8	20 34 32.2	+60 10 20	2.″05 × 1.″63	15.8	639.98	1.″99 × 1.″11	8.7	21.20
NGC 6946 Enuc. 9	20 35 12.7	+60 08 53	2.″03 × 1.″64	15.7	636.59	2.″14 × 1.″13	8.8	19.64
NGC 7793 Enuc. 1	23 57 48.8	−32 36 59	4.″77 × 1.″62	13.9	243.82	4.″62 × 1.″09	9.6	10.26
NGC 7793 Enuc. 2	23 57 56.1	−32 35 40	4.″77 × 1.″62	14.0	244.33	4.″71 × 1.″11	9.8	10.09
NGC 7793 Enuc. 3	23 57 48.8	−32 34 53	4.″77 × 1.″62	14.0	245.29	4.″47 × 1.″08	8.8	9.84

Note — See Murphy et al. (2018a) for the 33 GHz imaging characteristics.

4.2.3 Interferometric Imaging

Calibrated VLA measurement sets for each source were imaged using the task TCLEAN in CASA version 4.6.0. For some cases, the Ka-band images contain data from observations taken during both the 11B and 13A semesters, but are heavily weighted by the 13A semester observations, as those include significantly more data. The mode of TCLEAN was set to multi-frequency synthesis (MFS; Conway et al., 1990; Sault & Wieringa, 1994). We chose a pixel scale of $0\farcs2$ for all three bands, and adopted Briggs weighting with ROBUST = 0.5 and NTERMS = 2. This allows the cleaning procedure to also model the spectral index variations on the sky. Although this procedure utilizes the large fractional bandwidths of each observation to generate in-band spectral index maps, we do not use them in our analysis given that the signal-to-noise ratio (S/N) of our sources is typically too low for them to be reliable. To help deconvolve extended low-intensity emission, we took advantage of the multiscale CLEAN option (Cornwell, 2008; Rau & Cornwell, 2011) in CASA, searching for structures with scales ∼1 and 3 times the FWHM of the synthesized beam. The choice of our final imaging parameters was the result of extensive experimentation to identify values that yielded the best combination of brightness-temperature sensitivity and reduction of artifacts resulting from strong sidelobes in the naturally weighted beam for these snapshot-like observations.

A primary beam correction was applied using the CASA task IMPBCOR before analyzing the images. The primary-beam-corrected continuum images at $3 - 33$GHz are shown in Figure 4.1. The FWHM of the synthesized beam along with the corresponding point-source and brightness temperature sensitivities for each image are given in Tables 4.2 and 4.3. Finally, in order to accurately compare the flux density measured for each star-forming region across the full $3 - 33$ GHz frequency range, we use the CASA task IMSMOOTH to match all VLA images for each pointing to a common circularized, Gaussian, beam corresponding to the lowest angular resolution among all three frequency bands scaled by a factor of $\sqrt{2}x0\farcs2$ (i.e., the pixel scale). This scaling factor eliminates cases for the convolution kernels used by IMSMOOTH to have length zero in any axis in units of pixels. We additionally crop all images to a common field-of-view (FOV) equal to the FOV of our 33 GHz observations (i.e., a primary beam FWHM of 44").

4.3 Ancillary Data and Photometry

In this section we provide a description of ancillary data used, as well as our procedure for extracting consistent aperture photometry across the full suite of multi-wavelength data available for galaxies in the SFRS.

4.3.1 Ancillary Data

GALEX far-UV (FUV; 1528Å) and near-UV (NUV; 2271Å) data were taken from the GALEX Large Galaxy Atlas (Seibert, 2007). The calibration uncertainty for these data is $\sim 15\%$ in both bands. One galaxy, NGC 1377, does not have existing near- or far-UV imaging.

The Hα data used in this analysis is taken from the compilation presented in Leroy et al. (2012), where details about the data quality and preparation (e.g., correction for [NII] emission) can be found, as well as the SINGS archive. All Hα images were then further corrected for foreground stars. The typical resolution of the seeing-limited Hα images is $\sim 1 - 2$", and the calibration uncertainty among these maps is taken to be $\sim 20\%$. Two galaxies, IC 342 and NGC 2146 do not have Hα imaging from SINGS.

Archival *Spitzer* 8μm and 24μm data were largely taken from the SINGS and Local Volume Legacy (LVL) legacy programs, and have a calibration uncertainty of

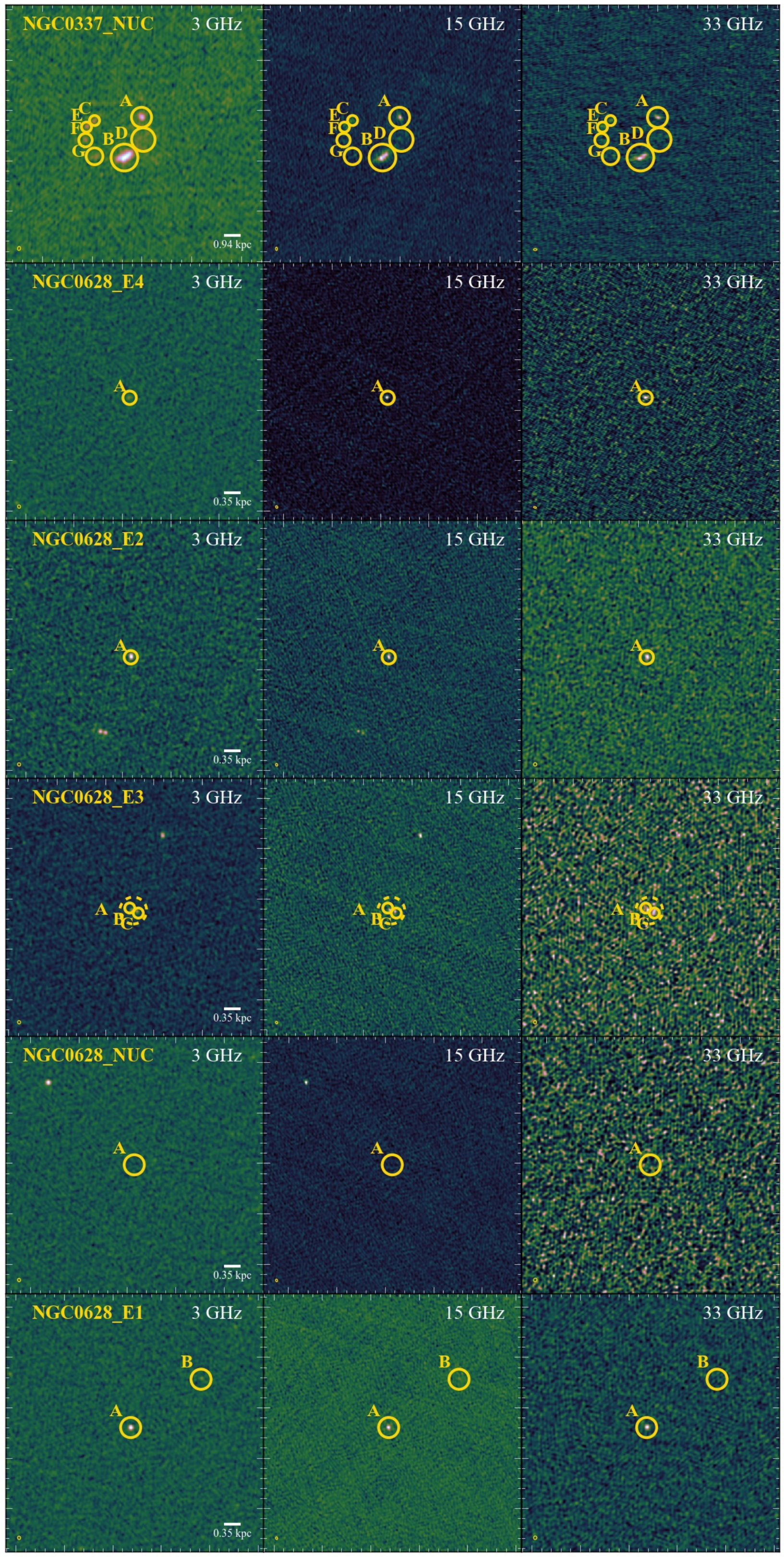

Figure 4.1: 3-panel images for all 56 galaxies in the SFRS showing the combination of our 3 GHz (left), 15 GHz (middle) and 33 GHz (right) observations. The color scale (Green, 2011) is set to one of 4 power-law stretches: [a(p-p$_{min}$)/(p$_{max}$-p$_{min}$)], where p is the pixel value and $a = 1/3$, 0.5, 1.0, and 2.0. A cube-root stretch of $a = 1/3$ was

$\sim 5\%$. Details on the associated observation strategies and data reduction steps can be found in Dale et al. (2007, 2009). Two galaxies, IC 342 and NGC 2146, were not a part of SINGS or LVL; their 24 μm imaging comes from Engelbracht et al. (2008).

Finally, in order to account for the significant differences between the point-spread functions (PSF) of the various telescopes used in this analysis, we implement the convolution kernels presented in Aniano et al. (2011) to convolve the instrumental PSF for each image, and produce a corrected Gaussian beam of 7" at each wavelength.

4.3.2 Region Identification and Aperture Photometry

To identify and characterize potential star-forming regions in the SFRS, we start by searching within an area that is equal to twice the FWHM of the VLA primary beam at 33 GHz ($\sim$ 160"). Any region visually identified in least one radio band is retained for further investigation. The location of all radio-identified sources were compared with the 8 μm maps of each galaxy to determine if the source has a corresponding detection in the mid-IR, and is thus likely associated with a star-forming region. Sources characterized as potential background galaxies have no obvious 8 μm counterpart, and very rarely a 33 GHz counterpart. In total, we visually identified 389 regions for which we perform aperture photometry to determine those that are statistically significant detections. Of the 389 sources visually identified, 377 had a statistically significant detection (i.e., $S/N > 3$) in at least one band, which is given in Table 4.4. For completeness, the remaining 12 sources are still labeled in the panels of Figure 4.1 to demonstrate the full identification process we utilized.

Using the CASA task IMSTAT, we measured and report the $3-33$ GHz flux densities for each region. The size of the apertures were hand-selected to fully encompass the visible extent of the $3-33$ GHz radio flux density of each region, with an additional constraint of having a diameter equal to or larger than the FWHM of the synthesized beam for that pointing. We do not apply aperture corrections to our photometry given that we both convolve all images for a given pointing to common beam and use the same sized aperture at all wavelengths. Photometric uncertainties were conservatively estimated by taking the empirically measured noise from empty regions in each non primary beam corrected image, applying the empirical primary beam correction based on Equation 4 in EVLA Memo 195, and scaling by the ratio of the synthesized beam area to the adopted aperture area. This noise is then added in quadrature with the VLA calibration uncertainty (∼3%; Perley & Butler, 2013). The median size of the apertures used for all 377 sources is 164 ± 6.3pc with a median absolute deviation of 97 pc. The aperture sizes used for each identified region is given in Table 4.4.

We additionally carried out photometry on the full VLA, GALEX, Hα, and *Spitzer*/MIPS 24 μm datasets after matching their resolution (7" FWHM), cropping each image to a common field of view, and re-gridding to a common pixel scale ($0\farcs2$). In total, we identify 180 discrete sources, and critical apertures of 7" were used in all cases. Unlike our native-resolution photometry, we report sources with upper-limits in all radio bands if a statistically significant detection exists in our ancillary GALEX and *Spitzer* imaging. The median size of the apertures used at 7" resolution is 259 ± 7.2 pc with a median absolute deviation of 73 pc. The UV and Hα photometry of each region was corrected for Milky Way extinction using Schlegel et al. (1998) assuming $A_V/E(B-V) = 3.1$ and the modeled extinction curves of Weingartner & Draine (2001) and Draine (2003). The results from our radio photometry are given in Table 4.5. The GALEX, Hα, and *Spitzer*/MIPS 24 μm photometry results, which are presented in Table 4.6, are not used directly in the present analysis, but will be utilized for further studies.

Finally, in order to account for and remove any diffuse emission component that is most likely unassociated with the most recent star formation activity in the disks of these galaxies, we measure a local background value within the vicinity of each star-forming region. The local background was measured by placing an annulus a distance of 1.5 times the synthesized beam FWHM away from the center of the source position in both the full-resolution and smoothed maps. The median surface brightness within this annulus was then multiplied by the effective area of the beam to get an estimate of the local diffuse background emission. These values are given in Table 4.7. Further, we measure the fractional contribution of the background emission for each region, and find that the median value is $4.7 \pm 0.43\%$, $6.6 \pm 0.79\%$, and $3.9 \pm 0.71\%$, with median absolute deviations of 5.3%, 5.4%, and 4.5% for our 3, 15, and 33 GHz observations respectively. Importantly, these values are smaller than the $15 - 40\%$ found for the regions studied at 25" ($\sim$ 1kpc) scales with the GBT (Murphy et al., 2011b).

The regions, listed in Tables 4.4 and 4.5, are named according to the nearest 33 GHz image, with an alphabetical suffix if there are multiple regions corresponding to one image. For example, "NGC 2403 Enuc. 2 B" is the second of three regions within the VLA pointing of extranuclear region 2 in NGC 2403. We distinguish individual sources identified in the 7" smoothed maps by instead using a lowercase letter. For example, "NGC 2403 Enuc. 2 b" is one of two regions in the image of extranuclear region 2 in NGC 2403, and is composed of the sum contribution of "NGC 2403 Enuc. 2 B" and "NGC 2403 Enuc. 2 C" in the full-resolution maps.

Table 4.4: Region Photometry and Derived Parameters

Source ID	R.A. (J2000)	Decl. (J2000)	$S_{3\,\mathrm{GHz}}$ (mJy)	$S_{15\,\mathrm{GHz}}$ (mJy)	$S_{33\,\mathrm{GHz}}$ (mJy)	d_{ap} (pc)	r_{G} (kpc)	α	$f_{\mathrm{T}}^{33\,\mathrm{GHz}}$
Star-Forming Regions									
NGC 0337 D	00 59 49.94	-07 34 47.60	1.19 ± 0.07	0.77 ± 0.04	0.31 ± 0.05	655.	0.921	-0.335 ± 0.042	0.841 ± 0.038
NGC 0337 A	00 59 50.01	-07 34 34.33	0.99 ± 0.06	0.70 ± 0.03	0.28 ± 0.05	561.	0.881	-0.278 ± 0.042	0.888 ± 0.033
NGC 0337 B	00 59 50.69	-07 34 58.26	4.94 ± 0.07	2.66 ± 0.04	1.80 ± 0.07	749.	2.041	-0.399 ± 0.012	0.780 ± 0.012
NGC 0337 C	00 59 51.89	-07 34 36.20	0.30 ± 0.03	0.29 ± 0.02	0.21 ± 0.03	281.	3.735	-0.076 ± 0.060	1.000 ± 0.028
NGC 0337 G	00 59 51.89	-07 34 57.50	0.36 ± 0.05	0.19 ± 0.03	0.17 ± 0.05	468.	3.123	-0.358 ± 0.102	0.820 ± 0.096
NGC 0337 E	00 59 52.22	-07 34 40.10	0.28 ± 0.03	0.27 ± 0.02	0.30 ± 0.03	281.	4.048	0.022 ± 0.059	1.000 ± 0.022
NGC 0337 F	00 59 52.26	-07 34 47.90	0.28 ± 0.04	0.19 ± 0.02	0.22 ± 0.04	374.	3.753	-0.159 ± 0.087	0.968 ± 0.051
NGC 0628 Enuc. 4	01 36 35.69	+15 50 07.22	0.27 ± 0.03	0.26 ± 0.02	0.23 ± 0.03	140.	7.614	-0.043 ± 0.065	1.000 ± 0.029
NGC 0628 Enuc. 2	01 36 37.64	+15 45 07.19	0.51 ± 0.03	0.35 ± 0.02	0.29 ± 0.04	140.	4.468	-0.233 ± 0.044	0.921 ± 0.031
NGC 0628 Enuc. 3 C	01 36 38.63	+15 44 21.40	0.28 ± 0.02	0.21 ± 0.02	0.23 ± 0.04	105.	5.798	-0.149 ± 0.057	0.974 ± 0.033
NGC 0628 Enuc. 3 A†	01 36 38.84	+15 44 22.90	0.51 ± 0.06	0.36 ± 0.04	0.51 ± 0.10	279.	5.724	-0.098 ± 0.080	1.000 ± 0.040
NGC 0628 Enuc. 3 B	01 36 38.99	+15 44 24.40	0.29 ± 0.02	0.20 ± 0.02	0.22 ± 0.04	105.	5.657	-0.195 ± 0.058	0.946 ± 0.037
NGC 0628 Enuc. 1 B	1 36 42.340	+15 48 16.84	< 0.13	0.41 ± 0.04	< 0.66	209.	2.695	⋯	⋯
NGC 0628 Enuc. 1 A	01 36 45.25	+15 47 48.06	0.27 ± 0.04	0.26 ± 0.04	0.26 ± 0.07	209.	2.466	-0.010 ± 0.111	1.000 ± 0.045
NGC 0855 C	02 14 03.56	+27 52 38.30	1.81 ± 0.06	1.06 ± 0.04	0.74 ± 0.07	377.	0.072	-0.346 ± 0.027	0.831 ± 0.025
NGC 0855 A†	02 14 03.80	+27 52 37.85	2.27 ± 0.10	1.55 ± 0.06	0.87 ± 0.11	613.	0.305	-0.279 ± 0.034	0.888 ± 0.026
NGC 0855 B	02 14 04.36	+27 52 36.80	0.37 ± 0.03	0.24 ± 0.02	0.19 ± 0.03	189.	0.910	-0.289 ± 0.062	0.880 ± 0.049
NGC 0925 D	02 27 15.981	+33 33 38.58	0.25 ± 0.02	0.24 ± 0.02	< 0.75	133.	5.510	-0.018 ± 0.082	1.000 ± 0.034
NGC 0925 A	02 27 17.00	+33 34 43.00	0.10 ± 0.03	< 0.06	< 0.09	177.	0.183	⋯	⋯
NGC 0925 B	02 27 20.62	+33 34 29.80	0.22 ± 0.02	0.17 ± 0.02	< 0.21	133.	2.097	-0.174 ± 0.095	0.959 ± 0.057
NGC 1097 Enuc. 2	02 46 14.40	-30 15 04.80	1.32 ± 0.25	< 0.16	0.26 ± 0.08	138.	7.378	-0.684 ± 0.147	0.358 ± 0.301
NGC 1097 D	02 46 18.34	-30 16 31.00	11.86 ± 0.10	2.97 ± 0.04	2.23 ± 0.07	275.	0.813	-0.809 ± 0.009	0.059 ± 0.024
NGC 1097 B	02 46 18.96	-30 16 29.20	7.10 ± 0.10	3.35 ± 0.04	3.03 ± 0.07	275.	0.052	-0.409 ± 0.010	0.769 ± 0.010
NGC 1097 A†	02 46 18.96	-30 16 29.20	104.78 ± 0.35	28.54 ± 0.15	21.13 ± 0.25	964.	0.052	-0.762 ± 0.003	0.183 ± 0.008
NGC 1097 E	02 46 19.08	-30 16 20.20	9.88 ± 0.10	2.96 ± 0.04	1.90 ± 0.07	275.	0.831	-0.733 ± 0.010	0.250 ± 0.022
NGC 1097 C	02 46 19.45	-30 16 33.70	12.16 ± 0.10	3.28 ± 0.04	2.35 ± 0.07	275.	0.514	-0.774 ± 0.008	0.152 ± 0.021
NGC 1097 Enuc. 1	02 46 23.90	-30 17 50.50	< 0.69	< 0.13	0.31 ± 0.05	688.	7.301	⋯	⋯
NGC 1266 C	03 16 00.76	-02 25 36.50	30.00 ± 0.03	8.94 ± 0.02	5.61 ± 0.07	445.	0.390	-0.749 ± 0.001	0.214 ± 0.003
NGC 1266 A†	03 16 00.76	-02 25 39.20	35.62 ± 0.08	6.89 ± 0.04	3.99 ± 0.16	1038.	0.267	-1.015 ± 0.004	0.234 ± 0.008
NGC 1266 B	03 16 00.76	-02 25 42.50	20.53 ± 0.03	4.63 ± 0.02	2.43 ± 0.07	445.	0.964	-0.924 ± 0.003	0.239 ± 0.006
NGC 1377	03 36 39.09	-20 54 06.60	0.20 ± 0.02	0.07 ± 0.02	0.06 ± 0.02	358.	0.344	-0.665 ± 0.141	0.396 ± 0.275
IC 342 B	03 46 47.80	+68 05 46.30	39.31 ± 0.12	18.40 ± 0.03	13.99 ± 0.08	64.	0.065	-0.458 ± 0.002	0.715 ± 0.002
IC 342 A†	03 46 48.45	+68 05 46.30	90.08 ± 0.30	36.82 ± 0.08	27.26 ± 0.20	159.	0.007	-0.539 ± 0.002	0.608 ± 0.003
IC 342 C	03 46 49.14	+68 05 48.40	23.28 ± 0.12	10.38 ± 0.03	8.02 ± 0.08	64.	0.074	-0.482 ± 0.003	0.685 ± 0.004
IC 342 D	03 46 50.918	+68 06 05.89	0.90 ± 0.12	0.13 ± 0.04	< 0.30	64.	0.404	-1.178 ± 0.184	0.227 ± 0.368

Table 4.4 continued

Table 4.4: Region Photometry and Derived Parameters (continued)

Source ID	R.A. (J2000)	Decl. (J2000)	$S_{3\,\mathrm{GHz}}$ (mJy)	$S_{15\,\mathrm{GHz}}$ (mJy)	$S_{33\,\mathrm{GHz}}$ (mJy)	d_{ap} (pc)	r_{G} (kpc)	α	$f_{\mathrm{T}}^{33\,\mathrm{GHz}}$
NGC 1482 C	03 54 38.73	-20 30 07.30	46.27 ± 0.03	12.80 ± 0.02	9.01 ± 0.15	438.	0.272	-0.795 ± 0.001	0.097 ± 0.003
NGC 1482 A†	03 54 38.97	-20 30 08.20	117.13 ± 0.09	24.25 ± 0.06	11.30 ± 0.40	1205.	0.104	-0.978 ± 0.002	0.236 ± 0.004
NGC 1482 B	03 54 39.22	-20 30 08.20	43.02 ± 0.03	12.63 ± 0.02	8.71 ± 0.14	438.	0.516	-0.759 ± 0.001	0.190 ± 0.003
NGC 2146 A	06 18 31.67	+78 21 43.84	6.15 ± 0.14	0.44 ± 0.06	2.29 ± 0.12	417.	3.862	-0.496 ± 0.024	0.667 ± 0.031
NGC 2146 B	06 18 33.90	+78 21 34.94	18.19 ± 0.08	1.15 ± 0.03	5.80 ± 0.06	250.	2.205	-0.542 ± 0.005	0.604 ± 0.007
NGC 2146 C	06 18 35.34	+78 21 30.75	36.86 ± 0.08	1.68 ± 0.03	9.97 ± 0.06	250.	1.322	-0.594 ± 0.002	0.523 ± 0.004
NGC 2146 D	06 18 38.35	+78 21 23.02	248.45 ± 0.22	21.18 ± 0.08	61.74 ± 0.15	667.	0.410	-0.700 ± 0.001	0.324 ± 0.002
NGC 2146 E	06 18 43.83	+78 21 11.70	13.61 ± 0.11	0.58 ± 0.04	3.59 ± 0.09	334.	3.245	-0.619 ± 0.011	0.480 ± 0.019
NGC 2403 Enuc. 5 C	07 36 19.35	+65 37 06.40	0.93 ± 0.03	0.75 ± 0.02	0.74 ± 0.02	62.	3.520	-0.101 ± 0.016	0.999 ± 0.008
NGC 2403 Enuc. 5 A†	07 36 19.84	+65 37 06.70	2.05 ± 0.06	2.09 ± 0.04	1.83 ± 0.05	140.	3.458	-0.038 ± 0.016	1.000 ± 0.007
NGC 2403 Enuc. 5 E	07 36 20.696	+65 38 04.84	0.24 ± 0.03	0.24 ± 0.03	< 0.47	62.	3.428	0.011 ± 0.098	1.000 ± 0.038
NGC 2403 Enuc. 5 B	07 36 22.99	+65 36 49.90	0.17 ± 0.03	0.17 ± 0.02	0.10 ± 0.03	62.	3.150	-0.109 ± 0.104	0.995 ± 0.053
NGC 2403 Enuc. 6 A	07 36 28.69	+65 33 49.95	0.87 ± 0.05	0.87 ± 0.04	0.78 ± 0.03	125.	5.369	-0.048 ± 0.029	1.000 ± 0.013
NGC 2403 Enuc. 6 B	07 36 29.56	+65 34 05.30	0.12 ± 0.03	< 0.06	0.05 ± 0.02	62.	4.933	-0.363 ± 0.165	0.815 ± 0.156
NGC 2403 Enuc. 1 E	07 36 38.042	+65 36 09.31	0.24 ± 0.03	0.29 ± 0.03	< 0.96	62.	1.529	0.110 ± 0.098	1.000 ± 0.030
NGC 2403 Enuc. 1 A	07 36 42.03	+65 36 51.67	0.51 ± 0.03	0.39 ± 0.02	0.25 ± 0.03	62.	1.085	-0.221 ± 0.040	0.929 ± 0.027
NGC 2403 C	07 36 42.562	+65 36 07.23	0.13 ± 0.03	0.14 ± 0.03	< 0.14	62.	0.952	0.038 ± 0.186	1.000 ± 0.067
NGC 2403 Enuc. 1 B	07 36 45.49	+65 37 01.39	1.52 ± 0.06	1.37 ± 0.04	1.14 ± 0.04	125.	1.203	-0.106 ± 0.021	0.997 ± 0.011
NGC 2403 Enuc. 1 C	07 36 45.74	+65 36 39.90	0.47 ± 0.03	0.10 ± 0.02	0.10 ± 0.03	62.	0.753	-0.799 ± 0.093	0.088 ± 0.249
NGC 2403 Enuc. 1 D	07 36 46.71	+65 36 37.50	0.20 ± 0.03	0.13 ± 0.02	0.11 ± 0.03	62.	0.697	-0.257 ± 0.103	0.904 ± 0.075
NGC 2403 Enuc. 2 B	07 36 49.15	+65 36 51.72	0.42 ± 0.04	0.32 ± 0.03	0.28 ± 0.04	94.	1.115	-0.167 ± 0.067	0.963 ± 0.040
NGC 2403 Enuc. 2 D	07 36 52.07	+65 36 48.40	0.64 ± 0.02	0.55 ± 0.02	0.56 ± 0.02	47.	1.258	-0.060 ± 0.018	1.000 ± 0.008
NGC 2403 Enuc. 2 A†	07 36 52.46	+65 36 45.70	2.14 ± 0.06	1.53 ± 0.04	1.48 ± 0.04	125.	1.229	-0.166 ± 0.016	0.964 ± 0.009
NGC 2403 Enuc. 2 C	07 36 52.80	+65 36 45.10	0.60 ± 0.02	0.45 ± 0.02	0.40 ± 0.02	47.	1.247	-0.170 ± 0.021	0.961 ± 0.013
NGC 2403 B	07 36 55.91	+65 35 38.49	0.19 ± 0.03	< 0.08	< 0.13	62.	0.699	...	...
NGC 2403 E	07 36 56.727	+65 35 12.17	0.14 ± 0.03	< 0.10	< 0.58	62.	1.101	...	...
NGC 2403 Enuc. 3 B	07 37 06.66	+65 36 38.40	3.81 ± 0.04	3.15 ± 0.03	2.89 ± 0.04	78.	2.763	-0.116 ± 0.006	0.992 ± 0.003
NGC 2403 Enuc. 4 B	07 37 16.55	+65 33 50.80	< 0.08	0.12 ± 0.02	0.07 ± 0.02	62.	3.305	-0.560 ± 0.358	0.577 ± 0.544
NGC 2403 Enuc. 4 C	07 37 18.14	+65 33 37.90	< 0.08	0.11 ± 0.02	0.08 ± 0.02	62.	3.556	-0.368 ± 0.359	0.810 ± 0.345
NGC 2403 Enuc. 4 A	07 37 18.30	+65 33 49.90	1.00 ± 0.06	0.99 ± 0.04	0.92 ± 0.03	125.	3.446	-0.037 ± 0.028	1.000 ± 0.012
Holmberg II B	08 19 12.69	+70 43 03.80	0.15 ± 0.02	0.14 ± 0.01	0.17 ± 0.02	44.	0.721	0.018 ± 0.078	1.000 ± 0.030
Holmberg II A	08 19 13.09	+70 43 08.90	0.33 ± 0.03	0.31 ± 0.02	0.34 ± 0.03	59.	0.739	-0.003 ± 0.048	1.000 ± 0.019
NGC 2798 B	09 17 22.56	+41 59 51.10	1.76 ± 0.02	0.61 ± 0.02	0.19 ± 0.03	375.	2.580	-0.693 ± 0.022	0.338 ± 0.045
NGC 2798 A	09 17 22.83	+42 00 01.00	11.23 ± 0.06	2.53 ± 0.06	0.93 ± 0.07	1001.	0.217	-0.945 ± 0.013	0.238 ± 0.027
NGC 2841 A	09 22 02.68	+50 58 35.74	0.64 ± 0.04	< 0.18	< 0.08	410.	0.171	...	...
NGC 2976 Enuc. 1 A	09 47 05.09	+67 55 51.70	1.14 ± 0.03	0.76 ± 0.02	0.75 ± 0.05	86.	1.432	-0.219 ± 0.020	0.930 ± 0.014
NGC 2976 Enuc. 1 D	09 47 07.64	+67 55 55.30	2.22 ± 0.02	1.80 ± 0.02	1.56 ± 0.03	69.	1.208	-0.136 ± 0.008	0.981 ± 0.004
NGC 2976 Enuc. 1 C	09 47 07.85	+67 55 48.10	0.48 ± 0.02	0.37 ± 0.01	0.33 ± 0.02	52.	1.111	-0.162 ± 0.027	0.966 ± 0.016

Table 4.4 continued

Table 4.4: Region Photometry and Derived Parameters (continued)

Source ID	R.A. (J2000)	Decl. (J2000)	$S_{3\,\mathrm{GHz}}$ (mJy)	$S_{15\,\mathrm{GHz}}$ (mJy)	$S_{33\,\mathrm{GHz}}$ (mJy)	d_{ap} (pc)	r_{G} (kpc)	α	$f_{\mathrm{T}}^{33\,\mathrm{GHz}}$
NGC 2976 Enuc. 1 B†	09 47 07.85	+67 55 53.98	3.26 ± 0.06	2.49 ± 0.05	2.01 ± 0.08	172.	1.178	-0.182 ± 0.014	0.954 ± 0.008
NGC 2976 B	09 47 13.54	+67 54 54.90	0.17 ± 0.02	0.16 ± 0.02	0.17 ± 0.03	69.	0.432	-0.017 ± 0.090	1.000 ± 0.037
NGC 2976 A	09 47 15.30	+67 55 00.00	< 0.07	0.15 ± 0.02	< 0.10	69.	0.000	…	…
NGC 2976 Enuc. 2 A	09 47 23.94	+67 53 53.40	1.67 ± 0.04	1.46 ± 0.03	1.25 ± 0.06	120.	1.421	-0.098 ± 0.018	1.000 ± 0.009
NGC 2976 Enuc. 2 C	09 47 23.94	+67 54 05.40	0.55 ± 0.04	0.45 ± 0.03	0.40 ± 0.05	103.	1.278	-0.131 ± 0.047	0.984 ± 0.026
NGC 2976 C	09 47 25.079	+67 55 09.45	0.25 ± 0.02	< 0.07	< 0.48	69.	2.002	…	…
NGC 3049 A	09 54 49.56	+09 16 16.05	1.47 ± 0.04	0.53 ± 0.04	0.47 ± 0.04	559.	0.110	-0.546 ± 0.032	0.598 ± 0.048
NGC 3049 B	09 54 50.05	+09 16 25.40	0.32 ± 0.03	0.22 ± 0.02	0.16 ± 0.03	372.	1.033	-0.272 ± 0.070	0.893 ± 0.053
NGC 3049 C	09 54 51.46	+09 16 28.40	0.21 ± 0.02	< 0.06	< 0.10	279.	3.622	…	…
NGC 3077 A	10 03 19.15	+68 43 59.90	11.35 ± 0.06	7.21 ± 0.05	6.19 ± 0.12	186.	0.045	-0.273 ± 0.005	0.892 ± 0.004
NGC 3190 A	10 18 04.31	+21 49 31.79	0.56 ± 0.03	0.61 ± 0.02	1.17 ± 0.04	374.	9.635	0.315 ± 0.024	1.000 ± 0.005
NGC 3184 B	10 18 11.442	+41 24 49.70	0.33 ± 0.04	0.20 ± 0.04	< 1.56	340.	4.382	-0.323 ± 0.153	0.851 ± 0.132
NGC 3184 A	10 18 16.91	+41 25 27.02	0.65 ± 0.04	0.33 ± 0.03	0.30 ± 0.03	340.	0.057	-0.363 ± 0.044	0.815 ± 0.042
NGC 3198 B	10 19 50.990	+45 32 50.16	0.21 ± 0.04	0.14 ± 0.03	< 0.34	410.	5.622	-0.233 ± 0.193	0.921 ± 0.134
NGC 3198 A	10 19 55.02	+45 32 59.24	0.49 ± 0.04	0.28 ± 0.03	0.19 ± 0.05	410.	0.180	-0.354 ± 0.074	0.824 ± 0.068
NGC 3198 C	10 19 57.979	+45 32 28.54	0.17 ± 0.04	0.17 ± 0.03	< 0.39	410.	8.035	0.021 ± 0.201	1.000 ± 0.076
IC 2574 D	10 28 40.72	+68 28 01.39	0.98 ± 0.03	0.31 ± 0.02	0.48 ± 0.08	92.	5.606	-0.596 ± 0.040	0.520 ± 0.066
IC 2574 C	10 28 43.88	+68 28 26.90	0.90 ± 0.04	0.63 ± 0.03	0.77 ± 0.08	129.	6.262	-0.164 ± 0.034	0.965 ± 0.020
IC 2574 A	10 28 48.41	+68 28 03.28	0.60 ± 0.03	0.50 ± 0.02	0.48 ± 0.03	92.	5.247	-0.105 ± 0.031	0.997 ± 0.016
IC 2574 B	10 28 48.78	+68 28 35.90	0.08 ± 0.02	0.11 ± 0.02	< 0.13	73.	6.263	0.157 ± 0.195	1.000 ± 0.053
NGC 3265 A	10 31 06.77	+28 47 48.01	2.76 ± 0.05	0.67 ± 0.03	0.43 ± 0.04	665.	0.090	-0.849 ± 0.024	0.245 ± 0.053
NGC 3351 C	10 43 55.25	+11 41 29.90	2.20 ± 0.04	1.04 ± 0.04	1.21 ± 0.19	181.	2.844	-0.439 ± 0.024	0.737 ± 0.028
NGC 3351 A	10 43 57.67	+11 42 07.19	7.20 ± 0.06	2.75 ± 0.04	1.95 ± 0.05	271.	0.267	-0.572 ± 0.009	0.558 ± 0.013
NGC 3351 B	10 43 57.77	+11 42 18.88	8.84 ± 0.06	3.55 ± 0.04	2.26 ± 0.05	271.	0.271	-0.567 ± 0.007	0.566 ± 0.011
NGC 3521 Enuc. 1	11 05 46.36	-00 04 10.10	0.14 ± 0.04	0.29 ± 0.04	< 0.15	271.	9.918	0.469 ± 0.194	1.000 ± 0.025
NGC 3521 Enuc. 3 A	11 05 47.64	+00 00 32.80	< 0.20	0.31 ± 0.05	< 0.18	489.	9.517	…	…
NGC 3521 Enuc. 2 A	11 05 49.28	-00 03 26.70	0.66 ± 0.04	0.35 ± 0.04	0.28 ± 0.05	271.	4.474	-0.377 ± 0.058	0.802 ± 0.056
NGC 3521 Enuc. 3 C	11 05 49.421	-0 00 29.52	0.99 ± 0.07	< 0.22	< 2.62	489.	6.970	…	…
NGC 3521 Enuc. 2 B	11 05 51.04	-00 03 49.20	0.30 ± 0.04	0.36 ± 0.04	< 0.15	271.	5.824	0.121 ± 0.104	1.000 ± 0.031
NGC 3621 C	11 18 14.878	-32 47 35.40	0.38 ± 0.04	0.32 ± 0.04	< 2.10	191.	2.191	-0.109 ± 0.105	0.995 ± 0.054
NGC 3621 A	11 18 15.21	-32 48 39.60	1.05 ± 0.04	0.27 ± 0.03	< 0.16	191.	0.841	-0.851 ± 0.071	0.245 ± 0.154
NGC 3621 H	11 18 16.465	-32 48 56.84	0.11 ± 0.04	< 0.09	< 0.17	191.	0.574	…	…
NGC 3621 G†	11 18 18.117	-32 49 39.41	2.15 ± 0.07	1.55 ± 0.08	< 2.71	381.	1.967	-0.202 ± 0.040	0.942 ± 0.025
NGC 3621 B	11 18 18.936	-32 47 44.04	0.93 ± 0.05	0.56 ± 0.06	< 2.97	254.	3.029	-0.321 ± 0.074	0.853 ± 0.064
NGC 3621 F	11 18 20.832	-32 48 53.41	0.14 ± 0.04	< 0.12	< 1.22	191.	2.760	…	…
NGC 3621 E	11 18 21.542	-32 49 08.39	0.62 ± 0.04	0.19 ± 0.05	< 4.80	191.	3.143	-0.722 ± 0.162	0.277 ± 0.362
NGC 3627 Enuc. 1 G	11 20 11.500	+12 57 55.42	0.52 ± 0.06	< 0.33	< 2.45	318.	7.592	…	…
NGC 3627 Enuc. 1 F	11 20 12.848	+12 57 56.98	0.24 ± 0.03	< 0.15	< 0.32	182.	5.975	…	…

Table 4.4 continued

Table 4.4: Region Photometry and Derived Parameters (continued)

Source ID	R.A. (J2000)	Decl. (J2000)	$S_{3\,\mathrm{GHz}}$ (mJy)	$S_{15\,\mathrm{GHz}}$ (mJy)	$S_{33\,\mathrm{GHz}}$ (mJy)	d_{ap} (pc)	r_{G} (kpc)	α	$f_{\mathrm{T}}^{33\,\mathrm{GHz}}$
NGC 3627 Enuc. 1 E	11 20 12.989	+12 57 36.49	0.30 ± 0.03	< 0.15	0.40 ± 0.10	182.	6.672	0.124 ± 0.116	1.000 ± 0.034
NGC 3627 B	11 20 13.34	+13 00 21.30	3.99 ± 0.07	2.42 ± 0.10	1.46 ± 0.37	364.	3.072	-0.319 ± 0.028	0.855 ± 0.024
NGC 3627 A	11 20 15.01	+12 59 29.53	1.95 ± 0.05	1.10 ± 0.06	0.69 ± 0.05	273.	0.023	-0.397 ± 0.026	0.781 ± 0.027
NGC 3627 Enuc. 2 D	11 20 16.26	+12 58 44.30	4.11 ± 0.03	2.49 ± 0.04	1.90 ± 0.02	136.	2.534	-0.318 ± 0.005	0.855 ± 0.004
NGC 3627 Enuc. 1 A	11 20 16.33	+12 57 49.39	2.42 ± 0.05	1.44 ± 0.06	1.26 ± 0.05	273.	4.706	-0.282 ± 0.017	0.885 ± 0.013
NGC 3627 Enuc. 2 A†	11 20 16.53	+12 58 44.30	7.18 ± 0.09	4.22 ± 0.12	3.51 ± 0.08	455.	2.781	-0.304 ± 0.010	0.868 ± 0.008
NGC 3627 Enuc. 2 E	11 20 16.71	+12 58 43.40	4.13 ± 0.03	2.10 ± 0.04	1.67 ± 0.02	136.	2.994	-0.385 ± 0.006	0.793 ± 0.006
NGC 3627 Enuc. 2 C	11 20 17.98	+12 59 06.20	0.43 ± 0.03	0.43 ± 0.05	0.24 ± 0.05	182.	4.390	-0.124 ± 0.072	0.987 ± 0.038
NGC 3627 Enuc. 2 B	11 20 18.70	+12 59 24.20	0.77 ± 0.03	0.51 ± 0.06	< 0.38	182.	5.526	-0.259 ± 0.081	0.903 ± 0.060
NGC 3773	11 38 13.02	+12 06 44.10	2.53 ± 0.04	1.34 ± 0.04	1.09 ± 0.05	481.	0.023	-0.372 ± 0.016	0.806 ± 0.016
NGC 3938 B	11 52 46.860	+44 08 07.38	0.28 ± 0.03	< 0.08	< 0.59	434.	5.503	…	…
NGC 3938 Enuc. 2 B	11 52 59.97	+44 08 00.00	0.19 ± 0.02	0.13 ± 0.02	0.18 ± 0.03	347.	11.079	-0.069 ± 0.080	1.000 ± 0.037
NGC 3938 Enuc. 2 A	11 53 00.20	+44 07 48.07	0.34 ± 0.03	0.28 ± 0.02	0.23 ± 0.04	434.	11.048	-0.139 ± 0.061	0.979 ± 0.034
NGC 4254 Enuc. 2 D	12 18 45.82	+14 24 09.80	< 0.09	0.10 ± 0.03	0.17 ± 0.02	279.	5.332	0.670 ± 0.371	1.000 ± 0.029
NGC 4254 Enuc. 2 C	12 18 46.19	+14 24 11.90	< 0.07	< 0.06	0.08 ± 0.02	209.	4.931	…	…
NGC 4254 Enuc. 1 E	12 18 46.77	+14 23 51.00	0.29 ± 0.03	0.11 ± 0.02	< 0.14	279.	5.622	-0.602 ± 0.132	0.509 ± 0.223
NGC 4254 Enuc. 2 E	12 18 47.495	+14 24 41.83	0.14 ± 0.03	< 0.09	< 0.14	279.	2.617	…	…
NGC 4254	12 18 49.54	+14 25 01.40	0.41 ± 0.06	0.52 ± 0.04	0.36 ± 0.05	559.	0.124	-0.008 ± 0.085	1.000 ± 0.034
NGC 4254 Enuc. 1 D	12 18 50.03	+14 24 17.10	0.79 ± 0.04	0.23 ± 0.02	0.35 ± 0.04	349.	3.167	-0.487 ± 0.047	0.678 ± 0.060
NGC 4254 Enuc. 1 B	12 18 50.07	+14 24 06.60	0.21 ± 0.05	0.12 ± 0.03	0.41 ± 0.05	419.	3.924	0.321 ± 0.100	1.000 ± 0.018
NGC 4254 Enuc. 1 C	12 18 50.44	+14 24 22.50	0.21 ± 0.02	< 0.05	0.13 ± 0.03	209.	2.953	-0.204 ± 0.110	0.941 ± 0.071
NGC 4321 Enuc. 2	12 22 49.90	+15 50 28.70	0.17 ± 0.04	< 0.08	0.11 ± 0.03	347.	8.026	-0.176 ± 0.132	0.958 ± 0.080
NGC 4321 C	12 22 54.46	+15 49 21.30	2.57 ± 0.03	1.09 ± 0.02	0.59 ± 0.03	277.	0.500	-0.560 ± 0.014	0.577 ± 0.021
NGC 4321 F	12 22 54.63	+15 49 14.70	0.93 ± 0.02	0.45 ± 0.02	0.31 ± 0.02	208.	0.514	-0.451 ± 0.024	0.723 ± 0.028
NGC 4321 H	12 22 54.92	+15 49 09.90	0.65 ± 0.02	0.31 ± 0.02	0.27 ± 0.02	208.	0.810	-0.401 ± 0.032	0.778 ± 0.033
NGC 4321 A†	12 22 54.92	+15 49 21.00	23.09 ± 0.12	8.99 ± 0.09	5.06 ± 0.11	1040.	0.024	-0.603 ± 0.006	0.508 ± 0.010
NGC 4321 B	12 22 54.94	+15 49 20.40	2.47 ± 0.02	0.79 ± 0.02	0.45 ± 0.02	208.	0.069	-0.707 ± 0.013	0.308 ± 0.028
NGC 4321 G	12 22 54.94	+15 49 29.40	1.77 ± 0.03	0.63 ± 0.02	0.38 ± 0.03	277.	0.605	-0.644 ± 0.022	0.435 ± 0.041
NGC 4321 D	12 22 55.29	+15 49 15.30	3.26 ± 0.03	1.27 ± 0.02	0.83 ± 0.03	277.	0.653	-0.578 ± 0.011	0.549 ± 0.017
NGC 4321 E	12 22 55.38	+15 49 23.40	3.94 ± 0.03	1.39 ± 0.02	0.87 ± 0.03	277.	0.547	-0.641 ± 0.010	0.442 ± 0.018
NGC 4321 Enuc. 1 B	12 22 58.82	+15 48 50.60	0.28 ± 0.02	0.17 ± 0.02	< 0.12	208.	5.246	-0.321 ± 0.094	0.853 ± 0.081
NGC 4536 C	12 34 26.94	+02 11 19.40	33.72 ± 0.03	12.67 ± 0.02	8.01 ± 0.03	281.	0.243	-0.605 ± 0.001	0.504 ± 0.002
NGC 4536 A†	12 34 27.08	+02 11 17.30	88.63 ± 0.10	28.11 ± 0.06	16.57 ± 0.09	844.	0.030	-0.710 ± 0.001	0.303 ± 0.003
NGC 4536 B	12 34 27.34	+02 11 15.50	27.18 ± 0.03	9.90 ± 0.02	6.51 ± 0.03	281.	0.330	-0.617 ± 0.001	0.483 ± 0.002
NGC 4559 E	12 35 55.427	+27 58 01.88	0.15 ± 0.04	0.12 ± 0.04	< 0.15	203.	1.703	-0.106 ± 0.245	0.997 ± 0.125
NGC 4559 C	12 35 56.27	+27 57 40.80	0.20 ± 0.04	0.18 ± 0.03	0.21 ± 0.03	203.	1.294	0.014 ± 0.100	1.000 ± 0.038
NGC 4559 D	12 35 57.59	+27 57 36.90	< 0.12	0.12 ± 0.03	< 0.07	203.	0.090	…	…
NGC 4559 B	12 35 58.36	+27 57 33.90	0.09 ± 0.03	0.16 ± 0.02	0.13 ± 0.02	135.	0.599	0.088 ± 0.123	1.000 ± 0.040

Table 4.4 continued

Table 4.4: Region Photometry and Derived Parameters (continued)

Source ID	R.A. (J2000)	Decl. (J2000)	$S_{3\,\mathrm{GHz}}$ (mJy)	$S_{15\,\mathrm{GHz}}$ (mJy)	$S_{33\,\mathrm{GHz}}$ (mJy)	d_{ap} (pc)	r_{G} (kpc)	α	$f_{\mathrm{T}}^{33\,\mathrm{GHz}}$
NGC 4559 A	12 35 58.45	+27 57 27.90	0.16 ± 0.02	0.10 ± 0.02	0.14 ± 0.01	102.	0.563	-0.051 ± 0.065	1.000 ± 0.029
NGC 4569 A	12 36 49.84	+13 09 46.59	2.89 ± 0.07	1.44 ± 0.07	0.88 ± 0.08	430.	0.051	-0.460 ± 0.026	0.711 ± 0.031
NGC 4579	12 37 43.52	+11 49 05.50	2.04 ± 0.13	2.76 ± 0.22	0.60 ± 0.18	795.	0.103	0.077 ± 0.060	1.000 ± 0.020
NGC 4594	12 39 59.43	-11 37 23.03	0.86 ± 0.09	0.46 ± 0.06	0.83 ± 0.08	440.	0.046	-0.048 ± 0.061	1.000 ± 0.027
NGC 4631 Enuc. 1	12 41 40.47	+32 31 50.00	0.51 ± 0.05	0.66 ± 0.04	0.61 ± 0.04	296.	13.669	0.058 ± 0.050	1.000 ± 0.017
NGC 4625 A	12 41 52.27	+41 16 25.50	< 0.12	0.11 ± 0.03	< 0.06	271.	0.190	···	···
NGC 4631 A	12 42 03.59	+32 32 16.28	7.26 ± 0.03	2.46 ± 0.04	1.51 ± 0.04	148.	3.389	-0.666 ± 0.008	0.393 ± 0.015
NGC 4631 H	12 42 04.17	+32 32 16.60	0.98 ± 0.03	1.31 ± 0.03	0.85 ± 0.04	148.	3.276	0.031 ± 0.019	1.000 ± 0.007
NGC 4631 B	12 42 04.38	+32 32 25.08	5.50 ± 0.04	3.32 ± 0.04	3.07 ± 0.04	185.	1.712	-0.265 ± 0.006	0.898 ± 0.004
NGC 4631 G	12 42 05.07	+32 32 12.40	0.91 ± 0.04	0.73 ± 0.04	0.62 ± 0.04	185.	4.464	-0.155 ± 0.029	0.970 ± 0.017
NGC 4631 Enuc. 2 B	12 42 22.22	+32 32 46.33	1.56 ± 0.07	1.40 ± 0.05	1.39 ± 0.06	369.	6.825	-0.052 ± 0.026	1.000 ± 0.012
NGC 4631 Enuc. 2 C	12 42 23.985	+32 32 08.65	< 0.11	0.22 ± 0.03	< 0.92	185.	12.785	···	···
NGC 4725 C	12 50 24.87	+25 29 22.80	0.22 ± 0.02	0.08 ± 0.02	< 0.12	173.	2.693	-0.597 ± 0.136	0.518 ± 0.226
NGC 4725 A	12 50 26.57	+25 30 02.72	0.07 ± 0.02	0.17 ± 0.01	0.30 ± 0.01	173.	0.034	0.641 ± 0.078	1.000 ± 0.007
NGC 4736 K	12 50 49.204	+41 07 33.20	0.61 ± 0.05	0.78 ± 0.08	< 0.42	136.	1.102	0.154 ± 0.078	1.000 ± 0.021
NGC 4736 J	12 50 49.219	+41 07 23.09	1.01 ± 0.05	0.49 ± 0.08	< 0.36	136.	1.017	-0.447 ± 0.100	0.727 ± 0.116
NGC 4736 I	12 50 49.604	+41 07 09.41	1.27 ± 0.05	0.65 ± 0.07	< 0.29	136.	0.922	-0.416 ± 0.073	0.762 ± 0.079
NGC 4736 G	12 50 49.935	+41 06 41.41	0.27 ± 0.05	< 0.24	< 0.43	136.	1.248	···	···
NGC 4736 L	12 50 50.030	+41 07 50.00	0.56 ± 0.05	< 0.24	< 0.48	136.	1.222	···	···
NGC 4736 H	12 50 50.045	+41 06 53.23	1.28 ± 0.05	1.08 ± 0.07	0.35 ± 0.10	136.	1.002	-0.159 ± 0.045	0.968 ± 0.026
NGC 4736 M	12 50 50.746	+41 07 38.18	0.16 ± 0.05	< 0.21	< 0.25	136.	0.872	···	···
NGC 4736 F	12 50 51.201	+41 06 49.50	1.35 ± 0.05	0.89 ± 0.07	< 0.23	136.	0.846	-0.262 ± 0.053	0.900 ± 0.040
NGC 4736 N	12 50 51.776	+41 07 48.36	0.26 ± 0.05	1.07 ± 0.07	< 0.27	136.	0.991	0.878 ± 0.117	1.000 ± 0.006
NGC 4736 A	12 50 53.050	+41 07 12.50	6.19 ± 0.05	2.13 ± 0.06	1.23 ± 0.05	136.	0.020	-0.668 ± 0.013	0.389 ± 0.025
NGC 4736 O	12 50 53.190	+41 07 46.40	0.17 ± 0.05	0.44 ± 0.07	0.38 ± 0.08	136.	0.914	0.345 ± 0.137	1.000 ± 0.024
NGC 4736 E	12 50 54.070	+41 06 29.06	< 0.14	0.77 ± 0.08	< 0.41	136.	1.200	···	···
NGC 4736 P	12 50 54.541	+41 07 48.36	1.06 ± 0.05	0.30 ± 0.07	0.61 ± 0.10	136.	1.069	-0.316 ± 0.064	0.857 ± 0.054
NGC 4736 D	12 50 54.565	+41 06 36.52	0.59 ± 0.05	1.05 ± 0.08	0.43 ± 0.11	136.	1.029	0.259 ± 0.061	1.000 ± 0.013
NGC 4736 Enuc. 1 D	12 50 55.99	+41 07 26.60	0.16 ± 0.03	0.33 ± 0.05	0.27 ± 0.03	90.	0.869	0.203 ± 0.091	1.000 ± 0.022
NGC 4736 Enuc. 1 A	12 50 56.35	+41 07 17.00	1.55 ± 0.05	1.06 ± 0.08	0.88 ± 0.04	136.	0.860	-0.238 ± 0.022	0.918 ± 0.015
NGC 4736 Enuc. 1 B	12 50 56.65	+41 07 04.40	2.79 ± 0.05	1.59 ± 0.08	1.03 ± 0.05	136.	0.928	-0.399 ± 0.017	0.780 ± 0.018
NGC 4736 Enuc. 1 C	12 50 56.83	+41 06 47.52	1.37 ± 0.05	1.13 ± 0.08	0.64 ± 0.07	136.	1.133	-0.228 ± 0.036	0.924 ± 0.025
NGC 4736 Enuc. 1 E	12 50 56.84	+41 07 23.00	0.09 ± 0.02	< 0.12	0.14 ± 0.02	68.	1.033	0.205 ± 0.126	1.000 ± 0.030
NGC 4826 C	12 56 43.11	+21 40 54.79	0.72 ± 0.02	0.48 ± 0.02	0.22 ± 0.02	77.	0.427	-0.344 ± 0.028	0.833 ± 0.026
NGC 4826 B	12 56 43.11	+21 41 06.79	0.72 ± 0.02	0.53 ± 0.02	0.25 ± 0.02	77.	0.295	-0.295 ± 0.027	0.874 ± 0.021
NGC 4826 A	12 56 43.61	+21 41 00.41	12.21 ± 0.04	4.55 ± 0.04	2.83 ± 0.04	153.	0.034	-0.611 ± 0.005	0.494 ± 0.008
NGC 4826 F†	12 56 43.73	+21 41 00.90	10.97 ± 0.12	9.71 ± 0.12	3.61 ± 0.10	409.	0.049	-0.212 ± 0.009	0.935 ± 0.006
NGC 4826 E	12 56 43.84	+21 41 11.40	0.43 ± 0.02	0.46 ± 0.02	0.14 ± 0.02	77.	0.558	-0.095 ± 0.039	1.000 ± 0.020

Table 4.4 continued

Table 4.4: Region Photometry and Derived Parameters (continued)

Source ID	R.A. (J2000)	Decl. (J2000)	$S_{3\,\mathrm{GHz}}$ (mJy)	$S_{15\,\mathrm{GHz}}$ (mJy)	$S_{33\,\mathrm{GHz}}$ (mJy)	d_{ap} (pc)	r_{G} (kpc)	α	$f_{\mathrm{T}}^{33\,\mathrm{GHz}}$
NGC 4826 D	12 56 44.34	+21 40 55.99	0.57 ± 0.02	0.33 ± 0.02	0.31 ± 0.02	77.	0.250	-0.268 ± 0.029	0.896 ± 0.021
NGC 5055 C	13 15 46.766	+42 02 01.43	0.14 ± 0.03	< 0.07	< 0.11	154.	1.349	···	···
NGC 5055 D	13 15 47.919	+42 01 41.96	0.22 ± 0.03	0.19 ± 0.02	< 0.08	154.	0.722	-0.070 ± 0.104	1.000 ± 0.049
NGC 5055 A	13 15 49.29	+42 01 45.82	1.99 ± 0.04	1.01 ± 0.03	0.33 ± 0.04	231.	0.054	-0.475 ± 0.022	0.693 ± 0.027
NGC 5055 B	13 15 50.20	+42 01 01.90	1.20 ± 0.03	0.29 ± 0.03	< 0.24	154.	2.805	-0.875 ± 0.057	0.243 ± 0.123
NGC 5055 Enuc. 1	13 15 58.32	+42 00 27.10	0.47 ± 0.04	0.43 ± 0.03	0.40 ± 0.03	231.	5.645	-0.060 ± 0.048	1.000 ± 0.022
NGC 5194 Enuc. 6	13 29 39.32	+47 08 38.90	0.68 ± 0.06	0.53 ± 0.03	0.56 ± 0.02	222.	12.377	-0.066 ± 0.038	1.000 ± 0.018
NGC 5194 Enuc. 3 B	13 29 43.77	+47 10 00.65	< 0.19	0.35 ± 0.03	0.13 ± 0.03	222.	7.645	-1.260 ± 0.290	0.224 ± 0.574
NGC 5194 Enuc. 3 A	13 29 45.06	+47 09 58.43	0.81 ± 0.08	0.55 ± 0.04	0.58 ± 0.03	259.	7.051	-0.130 ± 0.045	0.985 ± 0.024
NGC 5194 Enuc. 11 G	13 29 45.117	+47 13 32.37	0.29 ± 0.04	< 0.11	0.30 ± 0.05	148.	5.358	0.017 ± 0.095	1.000 ± 0.036
NGC 5194 Enuc. 11 A	13 29 47.07	+47 13 40.72	0.47 ± 0.04	< 0.10	0.22 ± 0.03	148.	4.942	-0.318 ± 0.063	0.855 ± 0.054
NGC 5194 Enuc. 11 B	13 29 47.52	+47 13 25.14	< 0.13	0.16 ± 0.03	0.18 ± 0.02	148.	4.365	0.203 ± 0.299	1.000 ± 0.073
NGC 5194 Enuc. 11 C	13 29 49.56	+47 13 28.04	< 0.13	0.10 ± 0.03	0.15 ± 0.02	148.	4.057	0.508 ± 0.422	1.000 ± 0.049
NGC 5194 Enuc. 11 D	13 29 49.57	+47 14 00.06	0.85 ± 0.04	0.27 ± 0.03	0.11 ± 0.03	148.	5.220	-0.761 ± 0.068	0.185 ± 0.168
NGC 5194 H	13 29 49.96	+47 11 25.90	2.92 ± 0.09	1.22 ± 0.06	0.29 ± 0.08	296.	1.968	-0.569 ± 0.034	0.563 ± 0.052
NGC 5194 L	13 29 50.26	+47 11 46.90	1.66 ± 0.07	0.66 ± 0.04	0.17 ± 0.05	222.	1.450	-0.614 ± 0.044	0.490 ± 0.076
NGC 5194 M	13 29 50.32	+47 11 37.90	0.68 ± 0.03	0.25 ± 0.02	0.13 ± 0.02	111.	1.520	-0.642 ± 0.051	0.439 ± 0.094
NGC 5194 Enuc. 11 E	13 29 50.48	+47 13 45.15	0.20 ± 0.03	0.23 ± 0.02	0.16 ± 0.02	111.	4.641	-0.118 ± 0.077	0.991 ± 0.041
NGC 5194 A	13 29 50.69	+47 11 55.79	1.41 ± 0.05	0.55 ± 0.03	0.26 ± 0.03	148.	1.185	-0.624 ± 0.032	0.473 ± 0.056
NGC 5194 Enuc. 11 F	13 29 50.92	+47 13 43.64	0.24 ± 0.03	0.14 ± 0.02	0.14 ± 0.02	111.	4.592	-0.251 ± 0.073	0.908 ± 0.053
NGC 5194 K	13 29 51.43	+47 12 00.40	0.86 ± 0.05	0.66 ± 0.03	0.22 ± 0.03	148.	0.876	-0.263 ± 0.039	0.899 ± 0.029
NGC 5194 B	13 29 51.57	+47 12 08.43	1.96 ± 0.05	0.64 ± 0.03	0.38 ± 0.04	148.	1.045	-0.695 ± 0.025	0.335 ± 0.053
NGC 5194 G	13 29 51.79	+47 11 38.50	1.14 ± 0.05	0.48 ± 0.03	0.10 ± 0.03	148.	0.629	-0.580 ± 0.040	0.546 ± 0.063
NGC 5194 J	13 29 52.23	+47 12 03.40	0.59 ± 0.03	0.14 ± 0.02	0.07 ± 0.02	111.	0.777	-0.888 ± 0.079	0.242 ± 0.170
NGC 5194 E	13 29 52.59	+47 11 52.90	12.56 ± 0.09	4.37 ± 0.05	1.69 ± 0.05	296.	0.379	-0.705 ± 0.008	0.313 ± 0.016
NGC 5194 O	13 29 52.61	+47 11 22.90	0.38 ± 0.07	0.47 ± 0.04	< 0.13	222.	0.813	0.131 ± 0.125	1.000 ± 0.036
NGC 5194 I	13 29 52.76	+47 11 42.40	5.37 ± 0.03	1.42 ± 0.02	0.70 ± 0.02	111.	0.037	-0.835 ± 0.008	0.246 ± 0.016
NGC 5194 C†	13 29 52.77	+47 11 40.90	10.73 ± 0.06	2.82 ± 0.03	1.21 ± 0.03	185.	0.082	-0.855 ± 0.007	0.245 ± 0.014
NGC 5194 Enuc. 1 A	13 29 53.22	+47 12 40.00	0.33 ± 0.04	0.10 ± 0.02	0.26 ± 0.03	148.	2.368	-0.102 ± 0.071	0.999 ± 0.036
NGC 5194 Enuc. 4 D	13 29 53.90	+47 14 04.90	< 0.09	< 0.05	0.12 ± 0.02	111.	5.873	···	···
NGC 5194 N	13 29 54.14	+47 11 27.40	1.33 ± 0.07	0.27 ± 0.04	< 0.14	222.	0.919	-0.996 ± 0.098	0.235 ± 0.203
NGC 5194 F	13 29 55.12	+47 11 34.39	0.76 ± 0.06	0.51 ± 0.03	0.31 ± 0.04	185.	1.412	-0.305 ± 0.053	0.867 ± 0.043
NGC 5194 Enuc. 4 C	13 29 55.73	+47 13 48.40	0.16 ± 0.03	0.11 ± 0.02	0.11 ± 0.02	111.	5.770	-0.149 ± 0.099	0.974 ± 0.056
NGC 5194 P	13 29 55.85	+47 11 55.90	0.71 ± 0.05	0.28 ± 0.03	0.16 ± 0.04	148.	2.119	-0.586 ± 0.066	0.536 ± 0.107
NGC 5194 Enuc. 4 E	13 29 56.20	+47 14 08.50	< 0.09	< 0.05	0.05 ± 0.01	111.	6.690	···	···
NGC 5194 Enuc. 10	13 29 56.73	+47 10 45.70	0.71 ± 0.07	0.35 ± 0.04	0.35 ± 0.04	222.	2.829	-0.326 ± 0.063	0.849 ± 0.055
NGC 5194 Enuc. 4 B	13 29 57.62	+47 13 54.82	0.11 ± 0.03	< 0.05	0.07 ± 0.02	111.	6.717	-0.217 ± 0.156	0.932 ± 0.104
NGC 5194 Enuc. 5 B	13 29 58.92	+47 14 09.40	0.27 ± 0.04	0.18 ± 0.03	0.15 ± 0.03	148.	7.776	-0.264 ± 0.100	0.899 ± 0.075

Table 4.4 continued

Table 4.4: Region Photometry and Derived Parameters (continued)

Source ID	R.A. (J2000)	Decl. (J2000)	$S_{3\,\mathrm{GHz}}$ (mJy)	$S_{15\,\mathrm{GHz}}$ (mJy)	$S_{33\,\mathrm{GHz}}$ (mJy)	d_{ap} (pc)	r_{G} (kpc)	α	$f_{\mathrm{T}}^{33\,\mathrm{GHz}}$
NGC 5194 Enuc. 4 F	13 29 59.00	+47 14 09.10	0.21 ± 0.03	0.15 ± 0.02	0.09 ± 0.02	111.	7.798	-0.298 ± 0.095	0.873 ± 0.077
NGC 5194 Enuc. 4 G	13 29 59.59	+47 13 59.50	0.56 ± 0.04	0.29 ± 0.03	0.14 ± 0.03	148.	7.726	-0.456 ± 0.064	0.717 ± 0.076
NGC 5194 Enuc. 5 A	13 29 59.64	+47 13 59.43	0.64 ± 0.05	0.35 ± 0.03	0.38 ± 0.04	185.	7.748	-0.252 ± 0.051	0.908 ± 0.037
NGC 5194 Enuc. 9	13 29 59.84	+47 11 12.60	0.40 ± 0.06	0.36 ± 0.03	0.38 ± 0.04	185.	4.166	-0.021 ± 0.073	1.000 ± 0.030
NGC 5194 Enuc. 8 C	13 30 00.33	+47 13 19.90	0.34 ± 0.04	0.27 ± 0.02	< 0.13	148.	6.815	-0.132 ± 0.097	0.983 ± 0.053
NGC 5194 Enuc. 8 B	13 30 00.69	+47 13 06.93	0.67 ± 0.07	0.64 ± 0.03	0.22 ± 0.05	222.	6.622	-0.128 ± 0.065	0.985 ± 0.035
NGC 5194 Enuc. 7 E	13 30 01.00	+47 09 28.90	< 0.14	0.19 ± 0.02	0.27 ± 0.04	148.	6.204	0.479 ± 0.250	1.000 ± 0.031
NGC 5194 Enuc. 8 A	13 30 01.39	+47 12 51.33	0.55 ± 0.07	0.53 ± 0.03	0.39 ± 0.04	222.	6.591	-0.119 ± 0.065	0.990 ± 0.034
NGC 5194 Enuc. 7 A	13 30 02.28	+47 09 47.77	1.20 ± 0.07	0.40 ± 0.03	0.34 ± 0.05	222.	6.301	-0.612 ± 0.047	0.493 ± 0.081
NGC 5194 Enuc. 7 C	13 30 02.76	+47 09 56.80	0.41 ± 0.05	0.18 ± 0.02	0.17 ± 0.03	148.	6.369	-0.428 ± 0.077	0.748 ± 0.085
NGC 5194 Enuc. 7 B	13 30 03.50	+47 09 41.14	0.32 ± 0.06	0.16 ± 0.03	< 0.13	185.	6.961	-0.420 ± 0.146	0.758 ± 0.159
NGC 5194 Enuc. 7 F	13 30 05.06	+47 10 34.90	5.47 ± 0.05	1.81 ± 0.03	< 0.32	148.	7.231	-0.688 ± 0.010	0.349 ± 0.021
NGC 5194 Enuc. 8 D	13 30 07.391	+47 13 22.05	0.29 ± 0.04	0.20 ± 0.03	< 0.98	148.	10.734	-0.238 ± 0.141	0.918 ± 0.099
NGC 5398	14 01 20.11	-33 04 10.66	2.40 ± 0.06	1.71 ± 0.03	1.68 ± 0.03	334.	1.417	-0.152 ± 0.013	0.972 ± 0.007
NGC 5457 Enuc. 6 A	14 02 28.23	+54 16 26.55	1.05 ± 0.04	0.94 ± 0.04	0.55 ± 0.04	195.	15.711	-0.179 ± 0.028	0.956 ± 0.017
NGC 5457 Enuc. 6 E	14 02 28.34	+54 16 36.20	0.67 ± 0.04	0.45 ± 0.03	0.45 ± 0.03	162.	15.525	-0.183 ± 0.035	0.954 ± 0.022
NGC 5457 Enuc. 6 B	14 02 29.59	+54 16 15.85	2.34 ± 0.05	1.57 ± 0.04	0.76 ± 0.05	227.	15.552	-0.323 ± 0.019	0.851 ± 0.016
NGC 5457 Enuc. 6 C	14 02 30.59	+54 16 09.84	1.01 ± 0.03	0.74 ± 0.03	0.57 ± 0.03	130.	15.416	-0.214 ± 0.022	0.934 ± 0.015
NGC 5457 Enuc. 6 D	14 02 30.64	+54 16 01.20	0.58 ± 0.03	0.37 ± 0.03	0.32 ± 0.04	130.	15.563	-0.260 ± 0.044	0.902 ± 0.032
NGC 5457 Enuc. 6 F	14 02 31.08	+54 15 49.70	0.21 ± 0.02	0.11 ± 0.02	< 0.15	97.	15.678	-0.402 ± 0.137	0.776 ± 0.142
NGC 5457 Enuc. 2 B	14 02 51.05	+54 22 09.50	0.13 ± 0.02	0.12 ± 0.01	< 0.11	97.	7.282	-0.086 ± 0.127	1.000 ± 0.062
NGC 5457 Enuc. 2 C	14 02 59.329	+54 23 23.97	0.16 ± 0.02	0.06 ± 0.02	< 0.78	97.	6.670	-0.631 ± 0.213	0.459 ± 0.384
NGC 5457 Enuc. 5 B	14 03 01.10	+54 14 30.50	1.48 ± 0.03	1.20 ± 0.02	1.13 ± 0.02	130.	13.068	-0.118 ± 0.012	0.991 ± 0.006
NGC 5457 Enuc. 5 A†	14 03 01.17	+54 14 26.90	2.11 ± 0.06	2.16 ± 0.04	1.28 ± 0.05	260.	13.180	-0.114 ± 0.017	0.993 ± 0.009
NGC 5457 Enuc. 5 C	14 03 01.24	+54 14 23.60	0.88 ± 0.03	0.62 ± 0.02	0.68 ± 0.02	130.	13.282	-0.123 ± 0.020	0.988 ± 0.010
NGC 5457 Enuc. 1	14 03 10.17	+54 20 58.10	0.10 ± 0.02	< 0.04	0.08 ± 0.01	97.	0.756	-0.106 ± 0.109	0.997 ± 0.056
NGC 5457	14 03 12.50	+54 20 56.40	0.87 ± 0.05	0.24 ± 0.03	0.37 ± 0.03	195.	0.036	-0.445 ± 0.041	0.729 ± 0.047
NGC 5457 Enuc. 3 E	14 03 34.039	+54 18 36.69	0.23 ± 0.03	0.19 ± 0.05	< 1.61	130.	8.447	-0.121 ± 0.197	0.989 ± 0.105
NGC 5457 Enuc. 3 D	14 03 38.63	+54 18 49.30	0.60 ± 0.03	0.35 ± 0.04	< 0.15	130.	9.430	-0.329 ± 0.072	0.846 ± 0.063
NGC 5457 Enuc. 3 A	14 03 39.85	+54 18 56.58	0.91 ± 0.04	0.87 ± 0.04	0.67 ± 0.05	162.	9.645	-0.093 ± 0.030	1.000 ± 0.015
NGC 5457 Enuc. 3 B	14 03 41.46	+54 19 04.95	11.51 ± 0.07	9.26 ± 0.08	7.34 ± 0.08	292.	9.971	-0.170 ± 0.004	0.962 ± 0.003
NGC 5457 Enuc. 3 C	14 03 42.98	+54 19 24.77	0.97 ± 0.04	0.56 ± 0.06	0.41 ± 0.07	195.	10.132	-0.352 ± 0.052	0.825 ± 0.048
NGC 5457 Enuc. 4 A	14 03 51.86	+54 21 52.80	0.42 ± 0.04	0.25 ± 0.03	0.23 ± 0.03	162.	12.097	-0.271 ± 0.061	0.893 ± 0.047
NGC 5457 Enuc. 4 B	14 03 53.04	+54 21 56.31	0.34 ± 0.04	0.28 ± 0.03	0.26 ± 0.03	162.	12.463	-0.109 ± 0.062	0.996 ± 0.032
NGC 5457 Enuc. 4 C	14 03 53.17	+54 22 06.29	0.83 ± 0.04	0.56 ± 0.03	0.46 ± 0.03	162.	12.530	-0.249 ± 0.029	0.910 ± 0.021
NGC 5457 Enuc. 4 D	14 03 54.01	+54 22 11.21	1.01 ± 0.04	0.58 ± 0.03	0.36 ± 0.03	162.	12.801	-0.385 ± 0.029	0.794 ± 0.029
NGC 5457 Enuc. 7 D†	14 04 29.03	+54 23 48.80	5.95 ± 0.07	4.35 ± 0.07	3.82 ± 0.06	325.	23.774	-0.187 ± 0.008	0.951 ± 0.005
NGC 5457 Enuc. 7 B	14 04 29.24	+54 23 52.98	2.14 ± 0.02	0.75 ± 0.02	0.73 ± 0.02	97.	23.859	-0.496 ± 0.010	0.667 ± 0.013

Table 4.4 continued

Table 4.4: Region Photometry and Derived Parameters (continued)

Source ID	R.A. (J2000)	Decl. (J2000)	$S_{3\,\mathrm{GHz}}$ (mJy)	$S_{15\,\mathrm{GHz}}$ (mJy)	$S_{33\,\mathrm{GHz}}$ (mJy)	d_{ap} (pc)	r_{G} (kpc)	α	$f_{\mathrm{T}}^{33\,\mathrm{GHz}}$
NGC 5713 A	14 40 10.28	-00 17 20.25	1.84 ± 0.03	0.95 ± 0.04	0.60 ± 0.03	415.	2.130	-0.445 ± 0.018	0.730 ± 0.020
NGC 5713 F	14 40 10.34	-00 17 29.10	0.38 ± 0.02	0.32 ± 0.03	0.20 ± 0.02	311.	2.197	-0.212 ± 0.046	0.935 ± 0.030
NGC 5713 B	14 40 10.74	-00 17 19.74	3.75 ± 0.02	1.70 ± 0.03	1.32 ± 0.02	311.	1.329	-0.449 ± 0.006	0.724 ± 0.007
NGC 5713 Enuc. 2	14 40 10.78	-00 17 50.00	1.22 ± 0.05	0.77 ± 0.05	0.28 ± 0.04	623.	3.320	-0.426 ± 0.040	0.751 ± 0.044
NGC 5713 Enuc. 2 A	14 40 10.83	-00 17 36.01	1.93 ± 0.04	1.08 ± 0.05	0.62 ± 0.03	519.	1.999	-0.431 ± 0.020	0.745 ± 0.022
NGC 5713 C	14 40 11.05	-00 17 19.08	5.39 ± 0.02	1.99 ± 0.03	1.48 ± 0.02	311.	0.795	-0.558 ± 0.005	0.579 ± 0.008
NGC 5713 G†	14 40 11.40	-00 17 20.10	11.25 ± 0.12	6.76 ± 0.14	2.16 ± 0.10	1556.	0.174	-0.447 ± 0.012	0.727 ± 0.014
NGC 5713 D	14 40 11.41	-00 17 19.41	7.56 ± 0.02	3.24 ± 0.03	2.39 ± 0.02	311.	0.163	-0.493 ± 0.003	0.671 ± 0.004
NGC 5713 Enuc. 1 A	14 40 12.10	-00 17 47.20	< 0.10	0.19 ± 0.04	< 0.06	415.	3.058	…	…
NGC 5713 E	14 40 12.74	-00 17 18.60	1.38 ± 0.04	0.86 ± 0.05	0.58 ± 0.04	519.	2.158	-0.337 ± 0.026	0.839 ± 0.024
NGC 5866	15 06 29.50	+55 45 47.56	6.88 ± 0.05	4.97 ± 0.03	2.18 ± 0.03	297.	0.071	-0.331 ± 0.005	0.844 ± 0.004
NGC 6946 Enuc. 4 A	20 34 19.08	+60 10 09.81	0.38 ± 0.03	0.34 ± 0.02	0.39 ± 0.02	132.	9.282	0.017 ± 0.037	1.000 ± 0.014
NGC 6946 Enuc. 4 B	20 34 19.20	+60 10 03.69	0.18 ± 0.02	0.21 ± 0.01	0.20 ± 0.01	99.	9.172	0.038 ± 0.056	1.000 ± 0.020
NGC 6946 Enuc. 4 H	20 34 21.880	+60 10 47.83	0.09 ± 0.03	0.12 ± 0.02	0.16 ± 0.04	132.	9.199	0.216 ± 0.172	1.000 ± 0.041
NGC 6946 Enuc. 8 A	20 34 32.29	+60 10 18.61	2.25 ± 0.05	0.73 ± 0.03	0.82 ± 0.05	198.	6.106	-0.550 ± 0.021	0.591 ± 0.031
NGC 6946 Enuc. 5 A	20 34 37.14	+60 05 10.18	< 0.08	< 0.04	0.10 ± 0.02	99.	9.238	…	…
NGC 6946 Enuc. 8 B	20 34 37.489	+60 09 36.47	< 0.11	0.22 ± 0.02	< 0.58	132.	6.106	…	…
NGC 6946 Enuc. 5 B	20 34 39.31	+60 04 52.72	0.33 ± 0.04	0.38 ± 0.02	0.38 ± 0.02	165.	9.695	0.054 ± 0.059	1.000 ± 0.020
NGC 6946 Enuc. 3 A	20 34 49.85	+60 12 40.69	0.10 ± 0.03	0.20 ± 0.02	0.22 ± 0.02	132.	7.743	0.259 ± 0.118	1.000 ± 0.025
NGC 6946 Enuc. 3 B	20 34 51.22	+60 12 42.36	0.12 ± 0.03	0.21 ± 0.02	0.20 ± 0.02	132.	7.727	0.139 ± 0.108	1.000 ± 0.031
NGC 6946 A	20 34 52.18	+60 09 14.60	21.08 ± 0.08	8.50 ± 0.05	4.42 ± 0.15	297.	0.041	-0.570 ± 0.004	0.561 ± 0.007
NGC 6946 Enuc. 3 C	20 34 52.32	+60 12 44.00	0.49 ± 0.05	0.47 ± 0.03	0.43 ± 0.03	198.	7.736	-0.057 ± 0.050	1.000 ± 0.023
NGC 6946 B	20 34 52.90	+60 08 51.80	0.45 ± 0.03	0.39 ± 0.02	0.27 ± 0.06	99.	0.857	-0.101 ± 0.046	1.000 ± 0.023
NGC 6946 C	20 34 53.59	+60 09 18.80	0.74 ± 0.03	0.62 ± 0.02	0.32 ± 0.05	99.	0.356	-0.134 ± 0.028	0.982 ± 0.015
NGC 6946 Enuc. 6 J	20 35 03.14	+60 10 56.40	0.11 ± 0.03	0.07 ± 0.01	0.11 ± 0.03	99.	4.357	-0.099 ± 0.144	1.000 ± 0.072
NGC 6946 Enuc. 6 I	20 35 03.75	+60 10 59.40	0.22 ± 0.03	0.10 ± 0.01	0.10 ± 0.03	99.	4.524	-0.399 ± 0.091	0.780 ± 0.094
NGC 6946 Enuc. 6 H	20 35 04.19	+60 10 54.60	0.19 ± 0.03	0.11 ± 0.01	0.15 ± 0.03	99.	4.457	-0.154 ± 0.087	0.971 ± 0.050
NGC 6946 Enuc. 6 F	20 35 05.20	+60 10 56.40	0.24 ± 0.03	0.06 ± 0.01	0.12 ± 0.02	99.	4.659	-0.406 ± 0.089	0.772 ± 0.094
NGC 6946 Enuc. 6 E	20 35 06.68	+60 11 12.00	< 0.11	0.15 ± 0.02	0.16 ± 0.03	132.	5.295	0.085 ± 0.298	1.000 ± 0.097
NGC 6946 Enuc. 6 B	20 35 07.01	+60 10 45.30	0.34 ± 0.03	0.29 ± 0.01	0.19 ± 0.03	99.	4.709	-0.151 ± 0.052	0.973 ± 0.029
NGC 6946 Enuc. 6 C	20 35 07.81	+60 10 47.10	0.11 ± 0.03	0.06 ± 0.01	< 0.08	99.	4.899	-0.407 ± 0.210	0.772 ± 0.221
NGC 6946 Enuc. 9 E	20 35 09.04	+60 09 22.95	0.13 ± 0.03	0.08 ± 0.02	< 0.12	99.	4.361	-0.277 ± 0.178	0.889 ± 0.137
NGC 6946 Enuc. 9 D	20 35 10.28	+60 09 22.35	0.19 ± 0.04	0.22 ± 0.02	< 0.14	132.	4.689	0.081 ± 0.132	1.000 ± 0.043
NGC 6946 Enuc. 9 A	20 35 11.24	+60 08 57.42	0.86 ± 0.06	0.74 ± 0.03	0.61 ± 0.05	198.	5.111	-0.125 ± 0.039	0.987 ± 0.021
NGC 6946 Enuc. 6 L	20 35 11.31	+60 10 32.99	0.72 ± 0.04	0.24 ± 0.02	0.36 ± 0.10	132.	5.374	-0.585 ± 0.059	0.538 ± 0.095
NGC 6946 Enuc. 9 C	20 35 11.49	+60 09 12.45	0.12 ± 0.03	0.20 ± 0.01	0.11 ± 0.03	99.	5.054	0.101 ± 0.136	1.000 ± 0.042
NGC 6946 Enuc. 9 B	20 35 11.69	+60 09 05.85	0.16 ± 0.03	0.17 ± 0.01	0.13 ± 0.02	99.	5.154	-0.046 ± 0.100	1.000 ± 0.044
NGC 6946 Enuc. 7 A	20 35 12.96	+60 08 50.95	0.19 ± 0.05	0.75 ± 0.02	0.48 ± 0.04	165.	5.630	-0.098 ± 0.089	1.000 ± 0.044

Table 4.4 continued

Table 4.4: Region Photometry and Derived Parameters (continued)

Source ID	R.A. (J2000)	Decl. (J2000)	$S_{3\,\mathrm{GHz}}$ (mJy)	$S_{15\,\mathrm{GHz}}$ (mJy)	$S_{33\,\mathrm{GHz}}$ (mJy)	d_{ap} (pc)	r_{G} (kpc)	α	$f_{\mathrm{T}}^{33\,\mathrm{GHz}}$
NGC 6946 Enuc. 7 B	20 35 14.11	+60 08 51.79	0.13 ± 0.03	0.21 ± 0.01	0.16 ± 0.03	99.	5.918	0.089 ± 0.114	1.000 ± 0.037
NGC 6946 Enuc. 1 A	20 35 16.79	+60 11 00.23	0.69 ± 0.03	0.64 ± 0.02	0.66 ± 0.03	132.	6.989	-0.027 ± 0.027	1.000 ± 0.012
NGC 6946 Enuc. 2 C	20 35 21.36	+60 09 51.93	0.17 ± 0.03	0.17 ± 0.03	< 0.14	132.	7.548	-0.003 ± 0.157	1.000 ± 0.063
NGC 7331 G	22 37 02.38	+34 24 59.90	0.70 ± 0.07	< 0.43	< 0.38	562.	4.675	...	...
NGC 7331 F	22 37 02.52	+34 25 17.90	0.69 ± 0.05	0.43 ± 0.11	< 0.34	422.	3.998	-0.296 ± 0.169	0.874 ± 0.137
NGC 7331 H	22 37 03.11	+34 24 43.40	1.33 ± 0.07	1.18 ± 0.16	< 0.40	633.	3.296	-0.073 ± 0.091	1.000 ± 0.043
NGC 7331 I	22 37 03.83	+34 24 29.30	1.23 ± 0.06	1.47 ± 0.13	< 0.38	492.	2.483	0.112 ± 0.062	1.000 ± 0.019
NGC 7331 A	22 37 04.10	+34 24 56.00	0.16 ± 0.03	0.37 ± 0.07	< 0.16	281.	0.000	0.516 ± 0.175	1.000 ± 0.020
NGC 7331 E	22 37 05.00	+34 25 08.90	0.91 ± 0.07	< 0.48	0.49 ± 0.13	633.	3.053	-0.257 ± 0.118	0.904 ± 0.086
NGC 7331 B	22 37 05.36	+34 24 53.90	0.52 ± 0.05	0.80 ± 0.11	< 0.26	422.	3.445	0.276 ± 0.102	1.000 ± 0.021
NGC 7331 D	22 37 05.77	+34 24 44.90	0.15 ± 0.03	0.45 ± 0.07	< 0.20	281.	4.371	0.673 ± 0.170	1.000 ± 0.013
NGC 7793 Enuc. 1 E	23 57 48.222	-32 36 15.38	0.12 ± 0.02	0.07 ± 0.01	< 0.35	95.	1.430	-0.390 ± 0.188	0.789 ± 0.190
NGC 7793 Enuc. 3	23 57 48.87	-32 34 52.80	0.21 ± 0.02	0.20 ± 0.01	< 0.14	95.	0.992	-0.044 ± 0.083	1.000 ± 0.036
NGC 7793 Enuc. 1 A	23 57 48.89	-32 36 58.60	0.09 ± 0.03	0.07 ± 0.01	< 0.17	114.	2.587	-0.172 ± 0.232	0.961 ± 0.139
NGC 7793 C	23 57 48.94	-32 34 54.60	0.19 ± 0.02	0.17 ± 0.01	0.12 ± 0.04	95.	0.941	-0.096 ± 0.089	1.000 ± 0.045
NGC 7793 A	23 57 49.41	-32 35 26.70	0.23 ± 0.04	0.20 ± 0.02	0.16 ± 0.04	152.	0.097	-0.118 ± 0.109	0.991 ± 0.058
NGC 7793 Enuc. 1 B	23 57 49.68	-32 37 13.00	< 0.09	0.11 ± 0.02	< 0.19	114.	2.962	...	...
NGC 7793 Enuc. 1 C	23 57 51.10	-32 36 49.00	0.18 ± 0.02	0.14 ± 0.01	< 0.21	95.	2.268	-0.153 ± 0.105	0.972 ± 0.060
NGC 7793 Enuc. 2	23 57 56.15	-32 35 40.60	< 0.13	< 0.08	0.14 ± 0.05	171.	1.540	...	...
Likely Background Galaxies									
NGC 0925 C	02 27 15.30	+33 35 28.60	1.37 ± 0.02	0.68 ± 0.02	0.29 ± 0.08	133.	3.375	-0.445 ± 0.020	0.730 ± 0.023
IC 342 E	03 46 45.793	+68 05 29.95	0.79 ± 0.12	0.28 ± 0.04	< 0.29	64.	0.373	-0.637 ± 0.122	0.448 ± 0.223
Holmberg II C	08 19 12.69	+70 43 03.80	0.15 ± 0.02	0.14 ± 0.01	0.17 ± 0.02	44.	2.067	0.018 ± 0.078	1.000 ± 0.030
NGC 2841 B	09 22 00.988	+50 59 05.13	0.11 ± 0.02	< 0.10	< 0.07	205.	2.374	...	...
NGC 2976 Enuc. 1 E	09 47 04.737	+67 56 41.47	0.17 ± 0.02	< 0.07	< 0.39	69.	2.080	...	...
NGC 3077 B	10 03 16.379	+68 43 42.53	0.06 ± 0.02	0.12 ± 0.02	< 0.14	56.	0.456	0.419 ± 0.205	1.000 ± 0.030
NGC 3190 B	10 18 05.64	+21 49 55.91	2.11 ± 0.03	0.67 ± 0.02	0.50 ± 0.03	374.	0.082	-0.664 ± 0.015	0.398 ± 0.030
NGC 3265 B	10 31 11.125	+28 48 07.09	0.36 ± 0.03	0.08 ± 0.02	< 0.52	380.	5.817	-0.965 ± 0.194	0.237 ± 0.406
NGC 3351 D	10 43 55.136	+11 42 05.36	0.32 ± 0.04	0.10 ± 0.03	< 0.21	181.	2.472	-0.738 ± 0.222	0.240 ± 0.516
NGC 3627 Enuc. 1 B	11 20 17.291	+12 56 57.67	0.14 ± 0.03	< 0.16	< 0.44	182.	7.224	...	...
NGC 4569 B	12 36 47.368	+13 10 27.07	0.50 ± 0.03	< 0.12	< 0.46	191.	5.433	...	...
NGC 4625 B	12 41 52.424	+41 17 17.64	0.97 ± 0.03	0.27 ± 0.02	0.34 ± 0.05	180.	2.434	-0.654 ± 0.043	0.417 ± 0.082
NGC 6946 Enuc. 4 F	20 34 23.90	+60 10 42.90	5.79 ± 0.04	1.73 ± 0.03	0.93 ± 0.08	198.	8.611	-0.751 ± 0.012	0.208 ± 0.029
NGC 6946 Enuc. 4 G	20 34 26.24	+60 10 30.59	2.50 ± 0.04	0.88 ± 0.03	0.49 ± 0.10	165.	7.811	-0.652 ± 0.022	0.420 ± 0.042
Likely Associated with Supernovae									

Table 4.4 continued

Table 4.4: Region Photometry and Derived Parameters (continued)

Source ID	R.A. (J2000)	Decl. (J2000)	$S_{3\,\mathrm{GHz}}$ (mJy)	$S_{15\,\mathrm{GHz}}$ (mJy)	$S_{33\,\mathrm{GHz}}$ (mJy)	d_{ap} (pc)	r_{G} (kpc)	α	$f_{\mathrm{T}}^{33\,\mathrm{GHz}}$
NGC 2403 Enuc. 3 D	07 37 17.034	+65 35 57.79	< 0.09	1.73 ± 0.04	< 2.94	62.	3.525	...	...
NGC 4736 B	12 50 52.026	+41 07 15.63	0.16 ± 0.05	< 0.19	< 0.15	136.	0.280	...	...
NGC 4736 C	12 50 52.522	+41 07 01.94	0.16 ± 0.05	< 0.20	< 0.15	136.	0.350	...	...
NGC 5194 D	13 29 55.79	+47 11 45.19	1.22 ± 0.06	0.63 ± 0.03	0.82 ± 0.05	185.	1.909	-0.221 ± 0.030	0.929 ± 0.020
NGC 5194 Enuc. 7 D	13 30 05.12	+47 10 10.90	1.54 ± 0.05	0.17 ± 0.02	< 0.15	148.	7.398	-1.377 ± 0.084	0.221 ± 0.165
NGC 6946 F	20 34 50.927	+60 10 20.35	0.20 ± 0.04	0.11 ± 0.03	< 2.45	132.	2.527	-0.386 ± 0.223	0.792 ± 0.223
NGC 6946 Enuc. 6 D	20 35 08.09	+60 11 13.50	0.28 ± 0.04	0.35 ± 0.02	0.22 ± 0.04	132.	5.557	0.032 ± 0.078	1.000 ± 0.029
NGC 6946 Enuc. 2 B	20 35 25.29	+60 09 58.64	1.23 ± 0.06	1.42 ± 0.04	1.89 ± 0.05	231.	8.572	0.187 ± 0.023	1.000 ± 0.006
NGC 7331 C	22 37 05.60	+34 24 32.90	0.79 ± 0.07	1.85 ± 0.15	0.72 ± 0.15	562.	3.813	0.349 ± 0.065	1.000 ± 0.011
NGC 7793 B	23 57 47.35	-32 35 24.60	0.14 ± 0.02	< 0.04	< 0.11	95.	0.591	...	...
Likely AME Candidates									
NGC 2403 Enuc. 5 D	07 36 20.57	+65 37 08.50	0.64 ± 0.03	0.63 ± 0.02	0.62 ± 0.02	62.	3.362	-0.014 ± 0.022	1.000 ± 0.009
NGC 2403 Enuc. 2 E	07 36 57.88	+65 37 24.39	1.17 ± 0.03	0.96 ± 0.03	1.19 ± 0.08	62.	2.684	-0.075 ± 0.019	1.000 ± 0.009
NGC 2403 Enuc. 3 A	07 37 05.20	+65 36 41.74	0.39 ± 0.03	0.40 ± 0.02	0.52 ± 0.03	62.	2.637	0.108 ± 0.039	1.000 ± 0.012
NGC 2403 Enuc. 3 C	07 37 07.86	+65 36 38.56	2.51 ± 0.03	1.91 ± 0.02	1.89 ± 0.03	62.	2.921	-0.135 ± 0.007	0.982 ± 0.004
NGC 3627 Enuc. 1 D	11 20 13.857	+12 57 09.26	0.41 ± 0.03	0.56 ± 0.05	0.61 ± 0.13	182.	7.171	0.185 ± 0.067	1.000 ± 0.017
NGC 3627 Enuc. 1 C	11 20 14.093	+12 56 59.60	0.45 ± 0.05	0.63 ± 0.08	0.96 ± 0.30	273.	7.467	0.248 ± 0.094	1.000 ± 0.021
NGC 4254 Enuc. 2 A	12 18 46.14	+14 24 19.18	0.12 ± 0.03	0.15 ± 0.03	0.21 ± 0.02	279.	4.669	0.252 ± 0.109	1.000 ± 0.024
NGC 4254 Enuc. 1 A	12 18 49.21	+14 23 57.78	0.34 ± 0.03	0.14 ± 0.02	0.23 ± 0.03	279.	4.437	-0.225 ± 0.059	0.926 ± 0.040
NGC 4631 C	12 42 05.62	+32 32 29.46	1.75 ± 0.03	0.87 ± 0.03	1.25 ± 0.03	148.	1.354	-0.174 ± 0.012	0.959 ± 0.007
NGC 4631 D	12 42 06.24	+32 32 31.70	1.54 ± 0.03	0.53 ± 0.03	0.94 ± 0.03	148.	1.525	-0.248 ± 0.015	0.911 ± 0.011
NGC 4631 E	12 42 07.18	+32 32 33.90	0.94 ± 0.02	0.46 ± 0.03	0.79 ± 0.03	111.	1.740	-0.109 ± 0.016	0.995 ± 0.008
NGC 4631 F	12 42 07.89	+32 32 33.42	6.83 ± 0.04	3.27 ± 0.05	3.98 ± 0.06	222.	1.366	-0.285 ± 0.006	0.882 ± 0.005
NGC 4631 Enuc. 2 A	12 42 21.41	+32 33 06.38	0.60 ± 0.04	0.23 ± 0.02	0.43 ± 0.02	185.	9.993	-0.171 ± 0.034	0.961 ± 0.020
NGC 4725 B	12 50 28.49	+25 30 22.26	0.15 ± 0.02	0.18 ± 0.01	0.35 ± 0.02	173.	1.930	0.414 ± 0.052	1.000 ± 0.008
NGC 5194 Enuc. 2	13 29 44.09	+47 10 22.86	1.33 ± 0.08	0.46 ± 0.03	0.58 ± 0.04	259.	6.852	-0.399 ± 0.035	0.780 ± 0.037
NGC 5194 Enuc. 1 C	13 29 49.39	+47 12 40.90	0.54 ± 0.05	0.46 ± 0.03	0.72 ± 0.05	148.	2.587	0.089 ± 0.045	1.000 ± 0.015
NGC 5194 Enuc. 1 B	13 29 51.98	+47 12 43.90	0.50 ± 0.05	0.48 ± 0.02	0.55 ± 0.03	148.	2.327	0.048 ± 0.043	1.000 ± 0.015
NGC 5194 Enuc. 4 A	13 29 55.50	+47 14 01.50	0.71 ± 0.04	0.29 ± 0.02	0.40 ± 0.02	148.	6.192	-0.253 ± 0.031	0.907 ± 0.023
NGC 5457 Enuc. 2 A	14 02 55.08	+54 22 27.44	0.40 ± 0.04	0.27 ± 0.02	0.37 ± 0.03	162.	6.429	-0.060 ± 0.052	1.000 ± 0.024
NGC 5457 Enuc. 7 A	14 04 28.61	+54 23 52.40	1.07 ± 0.02	0.55 ± 0.02	0.71 ± 0.02	97.	23.668	-0.197 ± 0.013	0.945 ± 0.008
NGC 5457 Enuc. 7 C	14 04 29.45	+54 23 47.11	3.56 ± 0.03	1.80 ± 0.03	1.93 ± 0.02	130.	23.894	-0.285 ± 0.006	0.883 ± 0.005
NGC 6946 Enuc. 4 C	20 34 19.88	+60 10 06.42	1.58 ± 0.03	1.42 ± 0.02	1.56 ± 0.02	132.	9.032	0.001 ± 0.009	1.000 ± 0.004
NGC 6946 Enuc. 4 D	20 34 21.39	+60 10 17.87	0.11 ± 0.03	0.81 ± 0.02	0.69 ± 0.02	132.	8.808	-0.076 ± 0.043	1.000 ± 0.021
NGC 6946 Enuc. 4 E	20 34 22.72	+60 10 34.04	1.35 ± 0.03	1.34 ± 0.02	1.29 ± 0.03	132.	8.741	-0.015 ± 0.013	1.000 ± 0.005
NGC 6946 E	20 34 51.30	+60 09 38.30	0.73 ± 0.05	0.71 ± 0.03	1.27 ± 0.11	165.	0.972	0.121 ± 0.040	1.000 ± 0.012

Table 4.4 continued

Table 4.4: Region Photometry and Derived Parameters (continued)

Source ID	R.A. (J2000)	Decl. (J2000)	$S_{3\,\mathrm{GHz}}$ (mJy)	$S_{15\,\mathrm{GHz}}$ (mJy)	$S_{33\,\mathrm{GHz}}$ (mJy)	d_{ap} (pc)	r_{G} (kpc)	α	$f_{\mathrm{T}}^{33\,\mathrm{GHz}}$
NGC 6946 D	20 34 52.78	+60 09 30.50	0.40 ± 0.04	0.51 ± 0.02	0.54 ± 0.07	132.	0.601	0.132 ± 0.058	1.000 ± 0.017
NGC 6946 Enuc. 6 M	20 35 00.77	+60 11 30.29	0.50 ± 0.04	0.09 ± 0.02	0.45 ± 0.10	132.	5.163	-0.301 ± 0.088	0.870 ± 0.072
NGC 6946 Enuc. 6 G	20 35 06.00	+60 11 00.60	0.79 ± 0.03	0.49 ± 0.01	0.54 ± 0.02	99.	4.894	-0.204 ± 0.021	0.941 ± 0.014
NGC 6946 Enuc. 6 K	20 35 06.20	+60 10 55.50	0.70 ± 0.03	0.38 ± 0.01	0.45 ± 0.02	99.	4.801	-0.246 ± 0.025	0.912 ± 0.018
NGC 6946 Enuc. 6 A†	20 35 06.24	+60 10 58.32	1.84 ± 0.05	1.08 ± 0.03	1.20 ± 0.05	198.	4.876	-0.232 ± 0.019	0.922 ± 0.013
NGC 6946 Enuc. 1 B	20 35 11.25	+60 10 33.89	0.72 ± 0.03	0.36 ± 0.02	0.66 ± 0.08	132.	5.374	-0.287 ± 0.039	0.881 ± 0.031
NGC 6946 Enuc. 2 A	20 35 23.61	+60 09 48.93	0.11 ± 0.03	0.31 ± 0.02	0.36 ± 0.04	132.	8.130	0.379 ± 0.112	1.000 ± 0.018
NGC 7793 Enuc. 1 D	23 57 46.742	-32 36 07.00	0.23 ± 0.02	0.10 ± 0.02	< 0.81	95.	1.393	-0.486 ± 0.122	0.680 ± 0.155

Note — † The aperture used for this region contained multiple smaller individual regions.

Table 4.5: Region Photometry and Derived Parameters at 7″ Angular Resolution

Source ID	R.A. (J2000)	Decl. (J2000)	$S_{3\,\mathrm{GHz}}$ (mJy)	$S_{15\,\mathrm{GHz}}$ (mJy)	$S_{33\,\mathrm{GHz}}$ (mJy)	d_{ap} (pc)	r_{G} (kpc)	α	$f_{\mathrm{T}}^{33\,\mathrm{GHz}}$
Star-Forming Regions									
NGC 0337 a	00 59 50.018	-07 34 33.9	0.53 ± 0.02	0.37 ± 0.01	0.23 ± 0.01	655.	0.945	-0.30 ± 0.03	0.87 ± 0.02
NGC 0337 b	00 59 50.683	-07 34 57.6	1.70 ± 0.05	0.91 ± 0.03	0.61 ± 0.02	655.	1.966	-0.42 ± 0.02	0.76 ± 0.02
NGC 0337 c	00 59 51.995	-07 34 54.9	0.13 ± 0.01	0.12 ± 0.01	0.10 ± 0.02	655.	3.227	-0.10 ± 0.07	1.00 ± 0.03
NGC 0337 d	00 59 52.156	-07 34 38.2	0.25 ± 0.02	0.25 ± 0.01	0.21 ± 0.02	655.	4.061	-0.05 ± 0.04	1.00 ± 0.02
NGC 0628 Enuc. 4	01 36 35.718	+15 50 07.25	0.14 ± 0.01	0.13 ± 0.01	0.12 ± 0.01	244.	7.608	-0.04 ± 0.04	1.00 ± 0.02
NGC 0628 Enuc. 2	01 36 37.645	+15 45 07.2	0.26 ± 0.01	0.15 ± 0.01	0.18 ± 0.01	244.	4.468	-0.22 ± 0.03	0.93 ± 0.02
NGC 0628 Enuc. 3	01 36 38.779	+15 44 23.2	0.27 ± 0.01	0.21 ± 0.01	0.19 ± 0.02	244.	5.720	-0.16 ± 0.03	0.97 ± 0.02
NGC 0628	01 36 41.7	+15 46 59	< 0.03	< 0.02	< 0.04	244.	0.071	···	···
NGC 0628 Enuc. 1	01 36 45.266	+15 47 48.3	0.55 ± 0.02	0.42 ± 0.01	0.29 ± 0.02	244.	2.478	-0.22 ± 0.02	0.93 ± 0.02
NGC 0855	02 14 03.677	+27 52 37.85	0.47 ± 0.02	0.28 ± 0.01	0.22 ± 0.01	330.	0.202	-0.31 ± 0.02	0.86 ± 0.02
NGC 0925	02 27 17	+33 34 43	0.06 ± 0.01	0.04 ± 0.01	< 0.03	310.	0.183	-0.30 ± 0.14	0.87 ± 0.12
NGC 1097 Enuc. 2	02 46 14.4	-30 15 03.992	< 0.19	< 0.04	< 0.06	482.	7.435	···	···
NGC 1097	02 46 18.984	-30 16 28.8	5.57 ± 0.18	2.55 ± 0.08	2.29 ± 0.09	482.	0.020	-0.40 ± 0.02	0.78 ± 0.02
NGC 1097 Enuc. 1 a	02 46 22.557	-30 17 29.9	< 0.21	0.08 ± 0.01	0.08 ± 0.02	482.	5.416	-0.07 ± 0.41	1.00 ± 0.20
NGC 1097 Enuc. 1 b	02 46 22.927	-30 17 48.1	0.33 ± 0.07	< 0.04	0.11 ± 0.02	482.	6.817	-0.48 ± 0.11	0.69 ± 0.14
NGC 1097 Enuc. 1 c	02 46 24.062	-30 17 50.9	< 0.21	< 0.04	0.07 ± 0.02	482.	7.392	···	···
NGC 1266	03 16 00.76	-02 25 37.1	23.46 ± 0.70	6.94 ± 0.21	4.13 ± 0.13	1038.	0.270	-0.73 ± 0.02	0.26 ± 0.04
NGC 1377	03 36 38.9	-20 54 06	< 0.06	< 0.03	< 0.06	835.	0.580	···	···
NGC 1482	03 54 38.966	-20 30 07.8	33.61 ± 1.01	9.61 ± 0.29	6.78 ± 0.21	767.	0.124	-0.69 ± 0.02	0.35 ± 0.04
NGC 2403 Enuc. 6	07 36 28.693	+65 33 49.4	0.34 ± 0.01	0.32 ± 0.01	0.30 ± 0.01	109.	5.380	-0.06 ± 0.02	1.00 ± 0.01
NGC 2403 Enuc. 1 a	07 36 42.061	+65 36 51.898	0.26 ± 0.01	0.20 ± 0.01	0.13 ± 0.01	109.	1.087	-0.22 ± 0.04	0.93 ± 0.02
NGC 2403 Enuc. 1 b	07 36 45.5	+65 37 00.9	0.66 ± 0.02	0.59 ± 0.02	0.55 ± 0.02	109.	1.192	-0.07 ± 0.02	1.00 ± 0.01
NGC 2403 Enuc. 2 a	07 36 49.115	+65 36 51.697	0.35 ± 0.01	0.30 ± 0.01	0.25 ± 0.01	109.	1.113	-0.13 ± 0.03	0.98 ± 0.01
NGC 2403	07 36 50	+65 36 04	< 0.03	< 0.02	< 0.02	109.	0.000	···	···
NGC 2403 Enuc. 2 b	07 36 52.361	+65 36 46.9	0.64 ± 0.02	0.50 ± 0.02	0.49 ± 0.02	109.	1.249	-0.12 ± 0.02	0.99 ± 0.01
NGC 2403 Enuc. 4	07 37 18.19	+65 33 48.1	0.34 ± 0.01	0.33 ± 0.01	0.33 ± 0.01	109.	3.455	-0.01 ± 0.02	1.00 ± 0.01
Holmberg II	08 19 13.058	+70 43 08	0.20 ± 0.01	0.19 ± 0.01	0.21 ± 0.01	104.	0.738	0.01 ± 0.04	1.00 ± 0.01
NGC 2798	09 17 22.854	+42 00 00.4	15.27 ± 0.46	5.71 ± 0.17	2.06 ± 0.06	876.	0.144	-0.80 ± 0.02	0.08 ± 0.05
NGC 2841	09 22 02.668	+50 58 35.7	0.92 ± 0.03	0.89 ± 0.03	0.56 ± 0.02	479.	0.155	-0.18 ± 0.02	0.95 ± 0.01
NGC 2976 Enuc. 1 a	09 47 05.192	+67 55 51.999	0.54 ± 0.02	0.36 ± 0.01	0.35 ± 0.02	120.	1.420	-0.21 ± 0.02	0.94 ± 0.01
NGC 2976 Enuc. 1 b	09 47 07.64	+67 55 54.7	1.23 ± 0.04	1.01 ± 0.03	0.86 ± 0.03	120.	1.201	-0.14 ± 0.02	0.98 ± 0.01
NGC 2976	09 47 13.491	+67 54 53.999	0.11 ± 0.01	0.08 ± 0.01	0.09 ± 0.01	120.	0.462	-0.12 ± 0.07	0.99 ± 0.04
NGC 2976 Enuc. 2 a	09 47 23.834	+67 53 54.9	0.59 ± 0.02	0.51 ± 0.02	0.45 ± 0.02	120.	1.394	-0.11 ± 0.02	0.99 ± 0.01
NGC 2976 Enuc. 2 b	09 47 23.941	+67 54 02.1	0.28 ± 0.01	0.23 ± 0.01	0.21 ± 0.02	120.	1.310	-0.13 ± 0.03	0.98 ± 0.02
NGC 3049	09 54 49.559	+09 16 16.1	1.35 ± 0.04	0.75 ± 0.02	0.55 ± 0.02	652.	0.103	-0.38 ± 0.02	0.80 ± 0.02

Table 4.5 continued

Table 4.5: Region Photometry and Derived Parameters at 7″ Angular Resolution (continued)

Source ID	R.A. (J2000)	Decl. (J2000)	$S_{3\,\mathrm{GHz}}$ (mJy)	$S_{15\,\mathrm{GHz}}$ (mJy)	$S_{33\,\mathrm{GHz}}$ (mJy)	d_{ap} (pc)	r_{G} (kpc)	α	$f_{\mathrm{T}}^{33\,\mathrm{GHz}}$
NGC 3077	10 03 19.15	+68 43 59.90	3.62 ± 0.11	2.31 ± 0.07	1.89 ± 0.06	130.	0.045	-0.27 ± 0.02	0.89 ± 0.01
NGC 3190	10 18 05.643	+21 49 55.9	1.08 ± 0.03	0.50 ± 0.02	0.27 ± 0.01	655.	0.098	-0.55 ± 0.02	0.59 ± 0.03
NGC 3184	10 18 16.94	+41 25 27	0.35 ± 0.01	0.18 ± 0.01	0.14 ± 0.01	397.	0.063	-0.40 ± 0.03	0.78 ± 0.03
NGC 3198	10 19 54.986	+45 32 59.3	0.63 ± 0.02	0.31 ± 0.01	0.12 ± 0.01	479.	0.116	-0.51 ± 0.03	0.65 ± 0.04
IC 2574 a	10 28 43.712	+68 28 26.296	0.29 ± 0.01	0.20 ± 0.01	0.28 ± 0.02	129.	6.253	-0.11 ± 0.03	0.99 ± 0.02
IC 2574 b	10 28 48.4	+68 28 03.5	0.29 ± 0.01	0.23 ± 0.01	0.24 ± 0.01	129.	5.254	-0.10 ± 0.03	1.00 ± 0.01
NGC 3265	10 31 06.768	+28 47 48	1.97 ± 0.06	0.77 ± 0.02	0.44 ± 0.02	665.	0.087	-0.62 ± 0.02	0.48 ± 0.03
NGC 3351 a	10 43 57.677	+11 42 08	2.84 ± 0.09	1.14 ± 0.04	0.78 ± 0.03	317.	0.230	-0.54 ± 0.02	0.60 ± 0.03
NGC 3351 b	10 43 57.8	+11 42 18.5	3.28 ± 0.10	1.37 ± 0.04	0.91 ± 0.03	317.	0.258	-0.54 ± 0.02	0.61 ± 0.03
NGC 3521 Enuc. 1	11 05 46.3	-00 04 08.992	0.05 ± 0.02	0.13 ± 0.02	< 0.07	380.	9.929	0.56 ± 0.21	1.00 ± 0.02
NGC 3521 Enuc. 3	11 05 47.6	+00 00 33.004	< 0.05	0.08 ± 0.01	< 0.05	380.	9.509	...	...
NGC 3521	11 05 48.9	-00 02 06	< 0.06	< 0.10	< 0.05	380.	0.625	...	...
NGC 3521 Enuc. 2 a	11 05 49.34	-00 03 24.2	0.29 ± 0.02	0.13 ± 0.02	0.13 ± 0.03	380.	4.302	-0.39 ± 0.07	0.79 ± 0.07
NGC 3521 Enuc. 2 b	11 05 49.94	-00 03 55.9	< 0.06	< 0.06	0.11 ± 0.03	380.	6.044	...	...
NGC 3621	11 18 16	-32 48 42	0.06 ± 0.02	< 0.04	< 0.07	222.	0.348	...	...
NGC 3627	11 20 15	+12 59 29.4	4.75 ± 0.14	1.73 ± 0.05	1.09 ± 0.04	318.	0.028	-0.62 ± 0.02	0.48 ± 0.03
NGC 3627 Enuc. 1	11 20 16.323	+12 57 49.2	1.33 ± 0.04	1.03 ± 0.03	0.86 ± 0.03	318.	4.712	-0.18 ± 0.02	0.96 ± 0.01
NGC 3627 Enuc. 2	11 20 16.464	+12 58 43.4	4.56 ± 0.14	2.52 ± 0.08	1.97 ± 0.06	318.	2.746	-0.35 ± 0.02	0.82 ± 0.02
NGC 3773	11 38 13.02	+12 06 43.8	0.85 ± 0.03	0.45 ± 0.02	0.39 ± 0.02	421.	0.023	-0.34 ± 0.02	0.84 ± 0.02
NGC 3938 b	11 52 48.191	+44 07 05.9	< 0.03	< 0.02	0.08 ± 0.01	607.	1.407	...	...
NGC 3938 a	11 52 49.5	+44 07 14	< 0.03	< 0.02	< 0.03	607.	0.140	...	...
NGC 3938 Enuc. 2 a	11 53 00.056	+44 08 00	0.09 ± 0.01	0.06 ± 0.01	0.10 ± 0.01	607.	11.158	0.00 ± 0.07	1.00 ± 0.03
NGC 3938 Enuc. 2 b	11 53 00.195	+44 07 48.3	0.15 ± 0.01	0.13 ± 0.01	0.11 ± 0.01	607.	11.049	-0.11 ± 0.05	0.99 ± 0.03
NGC 4254 Enuc. 2 a	12 18 45.777	+14 24 10.4	0.04 ± 0.01	0.05 ± 0.01	0.09 ± 0.01	489.	5.342	0.46 ± 0.12	1.00 ± 0.02
NGC 4254 Enuc. 2 b	12 18 46.128	+14 24 18.8	0.06 ± 0.01	0.07 ± 0.01	0.12 ± 0.01	489.	4.698	0.32 ± 0.08	1.00 ± 0.01
NGC 4254 a	12 18 48.677	+14 24 42.5	0.17 ± 0.01	0.04 ± 0.01	0.07 ± 0.01	489.	1.553	-0.52 ± 0.07	0.64 ± 0.09
NGC 4254 b	12 18 49.668	+14 24 59	0.14 ± 0.01	0.11 ± 0.01	0.11 ± 0.01	489.	0.111	-0.09 ± 0.05	1.00 ± 0.02
NGC 4254 Enuc. 1 b	12 18 50.009	+14 24 06.9	0.07 ± 0.01	0.05 ± 0.01	0.15 ± 0.01	489.	3.886	0.38 ± 0.07	1.00 ± 0.01
NGC 4254 c	12 18 50.102	+14 25 11.6	0.04 ± 0.01	0.09 ± 0.01	0.07 ± 0.01	489.	0.960	0.14 ± 0.13	1.00 ± 0.04
NGC 4254 Enuc. 1 c	12 18 50.194	+14 24 18.6	0.35 ± 0.01	0.12 ± 0.01	0.18 ± 0.01	489.	3.116	-0.41 ± 0.03	0.77 ± 0.03
NGC 4254 d	12 18 51.63	+14 25 08.599	0.30 ± 0.01	0.04 ± 0.01	0.12 ± 0.02	489.	2.344	-0.52 ± 0.05	0.64 ± 0.07
NGC 4254 e	12 18 51.899	+14 24 49.699	0.08 ± 0.01	0.02 ± 0.01	0.13 ± 0.02	489.	2.813	0.17 ± 0.08	1.00 ± 0.02
NGC 4254 f	12 18 51.919	+14 24 40.099	0.04 ± 0.01	< 0.02	0.14 ± 0.02	489.	3.149	0.55 ± 0.14	1.00 ± 0.01
NGC 4321 Enuc. 2 a	12 22 48.844	+15 50 12.8	0.06 ± 0.01	0.05 ± 0.01	0.05 ± 0.01	485.	8.305	-0.10 ± 0.10	1.00 ± 0.05
NGC 4321 Enuc. 2 b	12 22 49.904	+15 50 27.8	0.06 ± 0.01	0.03 ± 0.01	0.05 ± 0.01	485.	7.979	-0.13 ± 0.10	0.98 ± 0.05
NGC 4321 Enuc. 2	12 22 50.652	+15 50 27.2	< 0.03	< 0.02	0.04 ± 0.01	485.	7.285	...	...
NGC 4321 a	12 22 54.651	+15 49 19.8	2.03 ± 0.06	0.81 ± 0.03	0.46 ± 0.02	485.	0.284	-0.61 ± 0.02	0.50 ± 0.03
NGC 4321 b	12 22 55.129	+15 49 20.4	3.01 ± 0.09	1.07 ± 0.03	0.64 ± 0.02	485.	0.270	-0.64 ± 0.02	0.44 ± 0.03

Table 4.5 continued

Table 4.5: Region Photometry and Derived Parameters at 7″ Angular Resolution (continued)

Source ID	R.A. (J2000)	Decl. (J2000)	$S_{3\,\mathrm{GHz}}$ (mJy)	$S_{15\,\mathrm{GHz}}$ (mJy)	$S_{33\,\mathrm{GHz}}$ (mJy)	d_{ap} (pc)	r_{G} (kpc)	α	$f_{\mathrm{T}}^{33\,\mathrm{GHz}}$
NGC 4321 Enuc. 1	12 22 58.9	+15 49 35.003	< 0.03	< 0.02	< 0.02	485.	4.520	...	...
NGC 4536	12 34 27.06	+02 11 18.2	21.45 ± 0.64	7.81 ± 0.23	4.90 ± 0.15	492.	0.126	-0.62 ± 0.02	0.48 ± 0.03
NGC 4559 a	12 35 56.273	+27 57 40.5	0.08 ± 0.01	0.07 ± 0.01	0.08 ± 0.01	237.	1.304	-0.01 ± 0.08	1.00 ± 0.03
NGC 4559 b	12 35 56.455	+27 57 21.3	0.05 ± 0.01	0.07 ± 0.01	0.05 ± 0.01	237.	1.880	0.05 ± 0.12	1.00 ± 0.04
NGC 4559 c	12 35 58.47	+27 57 29.7	0.10 ± 0.01	0.10 ± 0.01	0.11 ± 0.01	237.	0.608	0.02 ± 0.06	1.00 ± 0.02
NGC 4569	12 36 49.8	+13 09 46.6	2.99 ± 0.09	0.92 ± 0.03	0.52 ± 0.02	335.	0.037	-0.73 ± 0.02	0.26 ± 0.04
NGC 4579	12 37 43.518	+11 49 05.6	21.36 ± 0.64	24.39 ± 0.73	30.71 ± 0.92	557.	0.105	0.14 ± 0.02	1.00 ± 0.01
NGC 4594 a	12 39 59.42	-11 37 23	38.94 ± 1.17	45.37 ± 1.36	36.58 ± 1.10	308.	0.052	-0.01 ± 0.02	1.00 ± 0.01
NGC 4631 Enuc. 1	12 41 40.468	+32 31 49.1	0.16 ± 0.01	0.16 ± 0.01	0.14 ± 0.01	259.	13.762	-0.04 ± 0.04	1.00 ± 0.02
NGC 4625	12 41 52.4	+41 16 24	< 0.03	0.04 ± 0.01	0.02 ± 0.01	316.	0.139	-0.91 ± 0.39	0.24 ± 0.82
NGC 4631 a	12 42 03.433	+32 32 17.198	3.50 ± 0.11	1.05 ± 0.03	0.72 ± 0.03	259.	3.189	-0.68 ± 0.02	0.37 ± 0.04
NGC 4631 b	12 42 03.978	+32 32 15.999	1.62 ± 0.05	1.06 ± 0.03	0.58 ± 0.02	259.	3.435	-0.39 ± 0.02	0.79 ± 0.02
NGC 4631 c	12 42 04.31	+32 32 25.299	2.35 ± 0.07	1.36 ± 0.04	1.29 ± 0.04	259.	1.734	-0.26 ± 0.02	0.90 ± 0.01
NGC 4631 d	12 42 05.093	+32 32 10.6	0.36 ± 0.01	0.27 ± 0.01	0.26 ± 0.01	259.	4.988	-0.14 ± 0.03	0.98 ± 0.01
NGC 4631 e	12 42 05.568	+32 32 29.5	0.91 ± 0.03	0.44 ± 0.02	0.61 ± 0.02	259.	1.387	-0.20 ± 0.02	0.94 ± 0.01
NGC 4631 Enuc. 2 b	12 42 21.988	+32 32 45	0.47 ± 0.02	0.33 ± 0.01	0.36 ± 0.01	259.	6.651	-0.14 ± 0.02	0.98 ± 0.01
NGC 4725 a	12 50 26.556	+25 30 03	0.05 ± 0.01	0.10 ± 0.01	0.16 ± 0.01	404.	0.044	0.50 ± 0.07	1.00 ± 0.01
NGC 4736	12 50 53.053	+41 07 12.8	3.83 ± 0.12	1.60 ± 0.05	1.02 ± 0.03	158.	0.014	-0.55 ± 0.02	0.59 ± 0.03
NGC 4736 Enuc. 1 a	12 50 56.412	+41 07 14.3	0.69 ± 0.02	0.45 ± 0.03	0.35 ± 0.02	158.	0.864	-0.29 ± 0.02	0.88 ± 0.02
NGC 4736 Enuc. 1 b	12 50 56.704	+41 07 05	1.08 ± 0.03	0.62 ± 0.03	0.39 ± 0.02	158.	0.939	-0.41 ± 0.02	0.77 ± 0.02
NGC 4736 Enuc. 1 c	12 50 56.784	+41 06 47.6	0.64 ± 0.02	0.46 ± 0.03	0.26 ± 0.02	158.	1.123	-0.31 ± 0.03	0.86 ± 0.03
NGC 4826	12 56 43.556	+21 41 00.6	4.39 ± 0.13	1.62 ± 0.05	1.00 ± 0.03	179.	0.055	-0.62 ± 0.02	0.48 ± 0.03
NGC 5055	13 15 49.308	+42 01 45.1	0.71 ± 0.02	0.35 ± 0.01	0.12 ± 0.01	269.	0.009	-0.55 ± 0.03	0.59 ± 0.04
NGC 5055 Enuc. 1	13 15 58.323	+42 00 27.4	0.18 ± 0.01	0.15 ± 0.01	0.15 ± 0.01	269.	5.630	-0.07 ± 0.04	1.00 ± 0.02
NGC 5194 Enuc. 6 a	13 29 39.324	+47 08 40.7	0.26 ± 0.02	0.20 ± 0.01	0.21 ± 0.01	259.	12.321	-0.09 ± 0.03	1.00 ± 0.01
NGC 5194 Enuc. 3	13 29 45.13	+47 09 57.4	0.33 ± 0.02	0.25 ± 0.01	0.26 ± 0.01	259.	7.048	-0.10 ± 0.03	1.00 ± 0.01
NGC 5194 Enuc. 11 a	13 29 47.138	+47 13 41.298	0.26 ± 0.02	0.06 ± 0.01	0.10 ± 0.01	259.	4.941	-0.42 ± 0.04	0.75 ± 0.05
NGC 5194 Enuc. 11 b	13 29 47.58	+47 13 24.799	< 0.04	0.11 ± 0.01	0.09 ± 0.01	259.	4.340	-0.25 ± 0.17	0.91 ± 0.12
NGC 5194 Enuc. 11 d	13 29 49.582	+47 13 28.7	< 0.04	0.04 ± 0.01	0.07 ± 0.01	259.	4.078	0.74 ± 0.34	1.00 ± 0.02
NGC 5194 Enuc. 11 c	13 29 49.671	+47 14 00.2	0.42 ± 0.02	0.14 ± 0.01	0.06 ± 0.01	259.	5.221	-0.75 ± 0.05	0.22 ± 0.11
NGC 5194c	13 29 50.022	+47 11 31.898	0.76 ± 0.03	0.42 ± 0.02	0.16 ± 0.01	259.	1.804	-0.48 ± 0.03	0.69 ± 0.04
NGC 5194 Enuc. 11 e	13 29 50.642	+47 13 44.9	0.20 ± 0.01	0.18 ± 0.01	0.13 ± 0.01	259.	4.633	-0.18 ± 0.04	0.96 ± 0.02
NGC 5194 b	13 29 51.64	+47 12 06.7	1.09 ± 0.04	0.41 ± 0.02	0.22 ± 0.01	259.	0.977	-0.64 ± 0.02	0.44 ± 0.04
NGC 5194 e	13 29 52.553	+47 11 52.6	3.17 ± 0.10	1.13 ± 0.04	0.46 ± 0.02	259.	0.365	-0.77 ± 0.02	0.17 ± 0.05
NGC 5194 d	13 29 52.729	+47 11 40.6	4.68 ± 0.14	1.24 ± 0.04	0.53 ± 0.02	259.	0.092	-0.89 ± 0.02	0.24 ± 0.04
NGC 5194 Enuc. 1c	13 29 53.129	+47 12 39.4	0.18 ± 0.02	0.06 ± 0.01	0.14 ± 0.01	259.	2.323	-0.13 ± 0.04	0.98 ± 0.02
NGC 5194 Enuc. 4 a	13 29 53.932	+47 14 04.899	< 0.04	< 0.02	0.08 ± 0.01	259.	5.880	...	...
NGC 5194 Enuc. 10 a	13 29 55.346	+47 10 47.199	0.12 ± 0.02	0.07 ± 0.01	0.09 ± 0.01	259.	2.336	-0.16 ± 0.07	0.97 ± 0.04

Table 4.5 continued

Table 4.5: Region Photometry and Derived Parameters at 7″ Angular Resolution (continued)

Source ID	R.A. (J2000)	Decl. (J2000)	$S_{3\,\mathrm{GHz}}$ (mJy)	$S_{15\,\mathrm{GHz}}$ (mJy)	$S_{33\,\mathrm{GHz}}$ (mJy)	d_{ap} (pc)	r_{G} (kpc)	α	$f_{\mathrm{T}}^{33\,\mathrm{GHz}}$
NGC 5194 Enuc. 4c	13 29 55.611	+47 13 50.2	0.16 ± 0.01	0.06 ± 0.01	0.09 ± 0.01	259.	5.798	-0.29 ± 0.05	0.88 ± 0.04
NGC 5194 a	13 29 55.791	+47 11 45.097	0.55 ± 0.02	0.32 ± 0.01	0.35 ± 0.02	259.	1.906	-0.22 ± 0.03	0.93 ± 0.02
NGC 5194 Enuc. 10 b	13 29 56.523	+47 10 46.9	0.25 ± 0.02	0.15 ± 0.01	0.14 ± 0.01	259.	2.723	-0.24 ± 0.04	0.91 ± 0.03
NGC 5194 Enuc. 4 d	13 29 58.733	+47 14 09.398	0.13 ± 0.01	0.08 ± 0.01	0.07 ± 0.01	259.	7.696	-0.28 ± 0.06	0.89 ± 0.05
NGC 5194 Enuc. 5 a	13 29 59.6	+47 13 59.8	0.26 ± 0.02	0.15 ± 0.01	0.17 ± 0.01	259.	7.742	-0.20 ± 0.04	0.94 ± 0.02
NGC 5194 Enuc. 9	13 29 59.782	+47 11 12.3	0.19 ± 0.02	0.17 ± 0.01	0.21 ± 0.01	259.	4.131	0.03 ± 0.04	1.00 ± 0.02
NGC 5194 Enuc. 7 a	13 30 01.029	+47 09 28.599	0.07 ± 0.02	0.11 ± 0.01	0.12 ± 0.02	259.	6.221	0.22 ± 0.11	1.00 ± 0.03
NGC 5194 Enuc. 8	13 30 01.482	+47 12 51.7	0.46 ± 0.02	0.38 ± 0.01	0.29 ± 0.01	259.	6.650	-0.17 ± 0.03	0.96 ± 0.01
NGC 5194 Enuc. 7 b	13 30 02.382	+47 09 48.7	0.45 ± 0.02	0.21 ± 0.01	0.20 ± 0.01	259.	6.329	-0.38 ± 0.03	0.80 ± 0.03
NGC 5194 Enuc. 7 c	13 30 03.471	+47 09 40.3	0.18 ± 0.02	0.07 ± 0.01	0.05 ± 0.01	259.	6.962	-0.55 ± 0.08	0.59 ± 0.11
NGC 5398	14 01 20.105	-33 04 09.2	0.86 ± 0.03	0.62 ± 0.02	0.64 ± 0.02	260.	1.381	-0.13 ± 0.02	0.98 ± 0.01
NGC 5457 Enuc. 6 a	14 02 28.203	+54 16 27.2	0.68 ± 0.02	0.39 ± 0.01	0.40 ± 0.01	227.	15.707	-0.24 ± 0.02	0.91 ± 0.01
NGC 5457 Enuc. 6 b	14 02 29.607	+54 16 15.799	1.02 ± 0.03	0.56 ± 0.02	0.45 ± 0.02	227.	15.550	-0.34 ± 0.02	0.83 ± 0.02
NGC 5457 Enuc. 6 c	14 02 30.566	+54 16 09.798	0.58 ± 0.02	0.42 ± 0.02	0.30 ± 0.02	227.	15.422	-0.25 ± 0.02	0.91 ± 0.02
NGC 5457 Enuc. 5 a	14 03 01.203	+54 14 28.4	0.96 ± 0.03	0.68 ± 0.02	0.72 ± 0.02	227.	13.129	-0.14 ± 0.02	0.98 ± 0.01
NGC 5457 Enuc. 1	14 03 10.2	+54 20 57.8	0.08 ± 0.01	< 0.02	0.05 ± 0.01	227.	0.744	-0.15 ± 0.07	0.97 ± 0.04
NGC 5457	14 03 12.531	+54 20 55.2	0.34 ± 0.01	0.09 ± 0.01	0.15 ± 0.01	227.	0.062	-0.41 ± 0.03	0.77 ± 0.03
NGC 5457 Enuc. 3 a	14 03 38.317	+54 18 51.398	0.30 ± 0.02	0.17 ± 0.02	< 0.10	227.	9.307	-0.36 ± 0.10	0.82 ± 0.09
NGC 5457 Enuc. 3 b	14 03 39.894	+54 18 56.799	0.48 ± 0.02	0.44 ± 0.03	0.35 ± 0.03	227.	9.655	-0.10 ± 0.03	1.00 ± 0.02
NGC 5457 Enuc. 3 c	14 03 41.437	+54 19 04.9	4.27 ± 0.13	3.33 ± 0.10	2.91 ± 0.09	227.	9.964	-0.16 ± 0.02	0.97 ± 0.01
NGC 5457 Enuc. 3 d	14 03 42.912	+54 19 24.699	0.42 ± 0.02	0.24 ± 0.02	0.21 ± 0.03	227.	10.113	-0.31 ± 0.05	0.86 ± 0.04
NGC 5457 Enuc. 4 a	14 03 52.036	+54 21 52.5	0.18 ± 0.01	0.12 ± 0.01	0.10 ± 0.01	227.	12.149	-0.24 ± 0.04	0.91 ± 0.03
NGC 5457 Enuc. 4 b	14 03 52.997	+54 21 57.3	0.20 ± 0.01	0.15 ± 0.01	0.14 ± 0.01	227.	12.453	-0.16 ± 0.04	0.97 ± 0.02
NGC 5457 Enuc. 4 c	14 03 53.203	+54 22 06.3	0.46 ± 0.02	0.26 ± 0.01	0.28 ± 0.01	227.	12.540	-0.22 ± 0.02	0.93 ± 0.01
NGC 5457 Enuc. 4 d	14 03 53.993	+54 22 10.8	0.50 ± 0.02	0.26 ± 0.01	0.25 ± 0.01	227.	12.795	-0.32 ± 0.02	0.86 ± 0.02
NGC 5474	14 05 01.3	+53 39 44	< 0.03	< 0.02	< 0.02	231.	0.070	$\cdots$	$\cdots$
NGC 5713 Enuc. 2 a	14 40 10.8	-00 17 35.5	0.82 ± 0.03	0.48 ± 0.02	0.26 ± 0.01	726.	1.984	-0.44 ± 0.02	0.74 ± 0.03
NGC 5713 Enuc. 2 b	14 40 10.86	-00 17 50.2	0.41 ± 0.02	0.27 ± 0.02	0.09 ± 0.01	726.	3.295	-0.42 ± 0.04	0.75 ± 0.04
NGC 5713	14 40 11.3	-00 17 27	1.42 ± 0.04	0.82 ± 0.03	0.35 ± 0.01	726.	0.795	-0.52 ± 0.02	0.63 ± 0.03
NGC 5713 Enuc. 1	14 40 11.36	-00 17 18.2	5.54 ± 0.17	2.28 ± 0.07	1.44 ± 0.04	726.	0.313	-0.56 ± 0.02	0.57 ± 0.03
NGC 5866	15 06 29.5	+55 45 47.7	5.48 ± 0.17	3.57 ± 0.11	2.01 ± 0.06	519.	0.051	-0.40 ± 0.02	0.78 ± 0.02
NGC 6946 Enuc. 4 c	20 34 22.738	+60 10 34.197	0.68 ± 0.02	0.70 ± 0.02	0.62 ± 0.02	231.	8.739	-0.03 ± 0.02	1.00 ± 0.01
NGC 6946 Enuc. 8	20 34 32.28	+60 10 19.3	1.16 ± 0.04	0.56 ± 0.02	0.58 ± 0.02	231.	6.122	-0.32 ± 0.02	0.85 ± 0.02
NGC 6946 Enuc. 5 a	20 34 37.155	+60 05 10.099	< 0.03	< 0.02	0.07 ± 0.01	231.	9.239	$\cdots$	$\cdots$
NGC 6946 Enuc. 5 b	20 34 39.361	+60 04 52.4	0.14 ± 0.01	0.16 ± 0.01	0.16 ± 0.01	231.	9.704	0.06 ± 0.04	1.00 ± 0.01
NGC 6946 Enuc. 3 a	20 34 49.865	+60 12 40.699	0.04 ± 0.01	0.11 ± 0.01	0.10 ± 0.01	231.	7.742	0.18 ± 0.09	1.00 ± 0.02
NGC 6946 Enuc. 3 b	20 34 52.24	+60 12 43.7	0.19 ± 0.01	0.18 ± 0.01	0.17 ± 0.01	231.	7.729	-0.04 ± 0.03	1.00 ± 0.01
NGC 6946 b	20 34 52.26	+60 09 14.3	19.95 ± 0.60	8.56 ± 0.26	5.55 ± 0.17	231.	0.016	-0.53 ± 0.02	0.62 ± 0.03

Table 4.5 continued

Table 4.5: Region Photometry and Derived Parameters at 7″ Angular Resolution (continued)

Source ID	R.A. (J2000)	Decl. (J2000)	$S_{3\,\mathrm{GHz}}$ (mJy)	$S_{15\,\mathrm{GHz}}$ (mJy)	$S_{33\,\mathrm{GHz}}$ (mJy)	d_{ap} (pc)	r_{G} (kpc)	α	$f_{\mathrm{T}}^{33\,\mathrm{GHz}}$
NGC 6946 Enuc. 6 b	20 35 06.965	+60 10 46.5	0.21 ± 0.01	0.19 ± 0.01	0.12 ± 0.01	231.	4.728	-0.14 ± 0.04	0.98 ± 0.02
NGC 6946 Enuc. 9	20 35 11.086	+60 08 57.45	0.83 ± 0.03	0.73 ± 0.02	0.71 ± 0.02	231.	5.071	-0.07 ± 0.02	1.00 ± 0.01
NGC 6946 Enuc. 7	20 35 12.974	+60 08 50.55	0.26 ± 0.01	0.43 ± 0.01	0.34 ± 0.01	231.	5.637	0.13 ± 0.03	1.00 ± 0.01
NGC 6946 Enuc. 1	20 35 16.801	+60 11 00	0.34 ± 0.01	0.31 ± 0.01	0.34 ± 0.01	231.	6.989	-0.01 ± 0.03	1.00 ± 0.01
NGC 7331	22 37 04.1	+34 24 56	0.05 ± 0.01	0.23 ± 0.03	< 0.07	492.	0.000	0.90 ± 0.18	1.00 ± 0.01
NGC 7793 Enuc. 1	23 57 48.8	-32 36 57.991	0.05 ± 0.01	0.02 ± 0.01	< 0.07	133.	2.574	-0.42 ± 0.25	0.76 ± 0.27
NGC 7793 Enuc. 3	23 57 48.8	-32 34 51.995	0.10 ± 0.01	0.10 ± 0.01	< 0.08	133.	1.016	-0.03 ± 0.09	1.00 ± 0.04
NGC 7793 a	23 57 49.2	-32 35 24	0.06 ± 0.01	0.04 ± 0.01	0.05 ± 0.01	133.	0.174	-0.18 ± 0.14	0.95 ± 0.09
NGC 7793 b	23 57 49.58	-32 35 25.6	0.10 ± 0.01	0.05 ± 0.01	0.07 ± 0.01	133.	0.081	-0.26 ± 0.09	0.90 ± 0.07
NGC 7793 Enuc. 2	23 57 56.1	-32 35 40	< 0.04	< 0.02	< 0.04	133.	1.526	⋯	⋯
Likely Associated with Supernovae									
NGC 6946 Enuc. 6 a	20 35 06.08	+60 10 58.5	0.72 ± 0.02	0.42 ± 0.01	0.48 ± 0.02	231.	4.855	-0.20 ± 0.02	0.94 ± 0.01
Likely AME Candidates									
NGC 2403 Enuc. 5	07 36 19.839	+65 37 05.5	0.64 ± 0.02	0.59 ± 0.02	0.56 ± 0.02	109.	3.464	-0.06 ± 0.02	1.00 ± 0.01
NGC 2403 Enuc. 3	07 37 06.948	+65 36 39	2.01 ± 0.06	1.63 ± 0.05	1.62 ± 0.05	109.	2.811	-0.10 ± 0.02	1.00 ± 0.01
NGC 4254 Enuc. 1 a	12 18 49.203	+14 23 57.9	0.16 ± 0.01	0.07 ± 0.01	0.12 ± 0.01	489.	4.428	-0.18 ± 0.04	0.95 ± 0.03
NGC 4631 f	12 42 06.256	+32 32 31.9	0.79 ± 0.03	0.27 ± 0.01	0.51 ± 0.02	259.	1.566	-0.23 ± 0.02	0.92 ± 0.01
NGC 4631 g	12 42 07.466	+32 32 31.599	1.65 ± 0.05	0.88 ± 0.03	0.97 ± 0.03	259.	0.960	-0.25 ± 0.02	0.91 ± 0.01
NGC 4631 h	12 42 08.059	+32 32 34.899	2.07 ± 0.06	0.97 ± 0.03	1.29 ± 0.04	259.	1.769	-0.24 ± 0.02	0.92 ± 0.01
NGC 4631 Enuc. 2 a	12 42 21.419	+32 33 06.3	0.28 ± 0.01	0.11 ± 0.01	0.18 ± 0.01	259.	9.974	-0.22 ± 0.03	0.93 ± 0.02
NGC 4725 b	12 50 28.484	+25 30 21.899	0.08 ± 0.01	0.11 ± 0.01	0.19 ± 0.01	404.	1.921	0.37 ± 0.06	1.00 ± 0.01
NGC 5194 Enuc. 2	13 29 44.1	+47 10 23.4	0.66 ± 0.02	0.37 ± 0.01	0.39 ± 0.01	259.	6.834	-0.24 ± 0.02	0.92 ± 0.01
NGC 5194 Enuc. 1 a	13 29 49.508	+47 12 40.296	0.29 ± 0.02	0.24 ± 0.01	0.38 ± 0.02	259.	2.534	0.09 ± 0.03	1.00 ± 0.01
NGC 5194 Enuc. 1 b	13 29 52.07	+47 12 43.6	0.28 ± 0.02	0.24 ± 0.01	0.27 ± 0.01	259.	2.322	-0.02 ± 0.03	1.00 ± 0.01
NGC 5194 Enuc. 4 b	13 29 55.493	+47 14 01.6	0.35 ± 0.02	0.13 ± 0.01	0.19 ± 0.01	259.	6.193	-0.28 ± 0.03	0.89 ± 0.02
NGC 5457 Enuc. 2	14 02 55	+54 22 27.5	0.18 ± 0.01	0.11 ± 0.01	0.17 ± 0.01	227.	6.451	-0.05 ± 0.04	1.00 ± 0.02
NGC 5457 Enuc. 7	14 04 29.334	+54 23 47.6	2.15 ± 0.07	1.07 ± 0.03	1.14 ± 0.03	227.	23.861	-0.29 ± 0.02	0.88 ± 0.01
NGC 6946 Enuc. 4 a	20 34 19.842	+60 10 06.6	0.92 ± 0.03	0.75 ± 0.02	0.83 ± 0.03	231.	9.044	-0.06 ± 0.02	1.00 ± 0.01
NGC 6946 Enuc. 4 b	20 34 21.41	+60 10 17.699	0.06 ± 0.01	0.42 ± 0.01	0.34 ± 0.01	231.	8.801	0.13 ± 0.05	1.00 ± 0.01
NGC 6946 a	20 34 51.295	+60 09 39.2	0.35 ± 0.02	0.35 ± 0.01	0.51 ± 0.03	231.	1.004	0.09 ± 0.03	1.00 ± 0.01
NGC 6946 c	20 34 52.742	+60 09 30.5	0.27 ± 0.01	0.34 ± 0.01	0.25 ± 0.03	231.	0.601	0.08 ± 0.04	1.00 ± 0.01
NGC 6946 Enuc. 2 a	20 35 23.572	+60 09 48.899	0.05 ± 0.01	0.16 ± 0.01	0.15 ± 0.01	231.	8.120	0.30 ± 0.08	1.00 ± 0.01
NGC 6946 Enuc. 2 b	20 35 25.381	+60 09 58.8	1.03 ± 0.03	0.76 ± 0.02	0.70 ± 0.02	231.	8.595	-0.17 ± 0.02	0.96 ± 0.01

4.4 Results

Using the 3, 15, and 33 GHz photometry, along with the 8 μm imaging from *Spitzer*, we classify each region as either a star-forming region (SF), a background galaxy candidate (BG), a likely supernova remnant (SNe/R: see Section 5.4), or an anomalous microwave emission candidate (AME: see Section 5.5). In total we have identified 320 star-forming regions, 14 likely background galaxies, 10 likely supernovae/supernova remnants, and 33 AME candidates. Given that we are primarily interested in emission arising from our sample galaxies, the potential background galaxies have been removed from all plots, and are discussed as a separate population of sources in Section 5.3. Regions identified at 7" which include emission from potential AME and SNe/R candidates are correspondingly classified in Table 4.5.

We present results for the spectral index and thermal fraction distributions only including regions identified in the SFRS that have a $S/N \geq 3$ measured in at least two radio bands. This ensures that our fit results are not biased by single detections at one frequency, and allows us to make accurate comparisons with the regions identified in M18a, for which a detection at 33 GHz was required. This requirement removes 4 likely background galaxies, 4 likely supernova remnants, and 34 star-forming regions. These single-band detections are distributed almost uniformly across all three frequency bands: 19, 11, and 12 at 3, 15, and 33 GHz, respectively. Accordingly, in the sample used to study the radio spectral indices and thermal fractions, we have retained 335 (286 SF, 10 BG, 6 SNe/R, and 33 AME) of the 377 sources with a statistically significant detection in at least one band. The median S/N of these 335 sources is 18, 15, and 9 for detections at 3, 15, and 33 GHz, respectively.

We apply the same criteria for sources included in the spectral index and thermal fraction analysis using the 7" smoothed images. This removes 17 star-forming regions.

These single-band detections are also distributed uniformly across all three bands: 7, 4, and 6 at 3, 15, and 33 GHz, respectively. Accordingly, we have retained 163 (142 SF, 0 BG, 1 SNe/R, and 20 AME) of the 180 sources with a statistically significant detection in at least one band. The median S/N of these 163 sources is 24, 23, and 19 for detections at 3, 15, and 33 GHz, respectively.

4.4.1 Spectral Indices

The simplest approach to modeling the radio spectra of galaxies is by adopting a two-component power-law, with the thermal/nonthermal ratio as well as the non-thermal spectral index allowed to vary as free parameters. For many star-forming galaxies in the local Universe, this model adequately describes the dominant physical processes occurring at radio frequencies (Condon, 1992). However, a robust interpretation of the radio spectrum can be complex. For example: the thermal and nonthermal fractions may vary with galaxy mass (e.g. Hughes et al., 2007; Bell, 2003), the nonthermal index can vary within galaxies (Tabatabaei et al., 2017), and AME may add an additional component to the radio spectra at high frequencies in some regions (e.g. Murphy et al., 2010, 2018b).

To measure the $3 - 33$ GHz spectral indices, we performed a linear least-squares fit to the data with a single power-law representing the combination of thermal and nonthermal emission. The distributions of the measured spectral slopes with the 10 likely background galaxies removed are given in the top panel of Figure 4.2 (325 total regions). The median spectral indices we measure from $3-15$, $15-33$, and $3-33$ GHz are -0.25 ± 0.024, -0.20 ± 0.043, and -0.23 ± 0.018, respectively. The median absolute deviation of these distributions is 0.34, 0.61, and 0.27 respectively. Interestingly, we do not see particularly steep spectral indices from $3 - 15$ GHz, indicating that the contribution of non-thermal emission to the radio flux density of individual star-

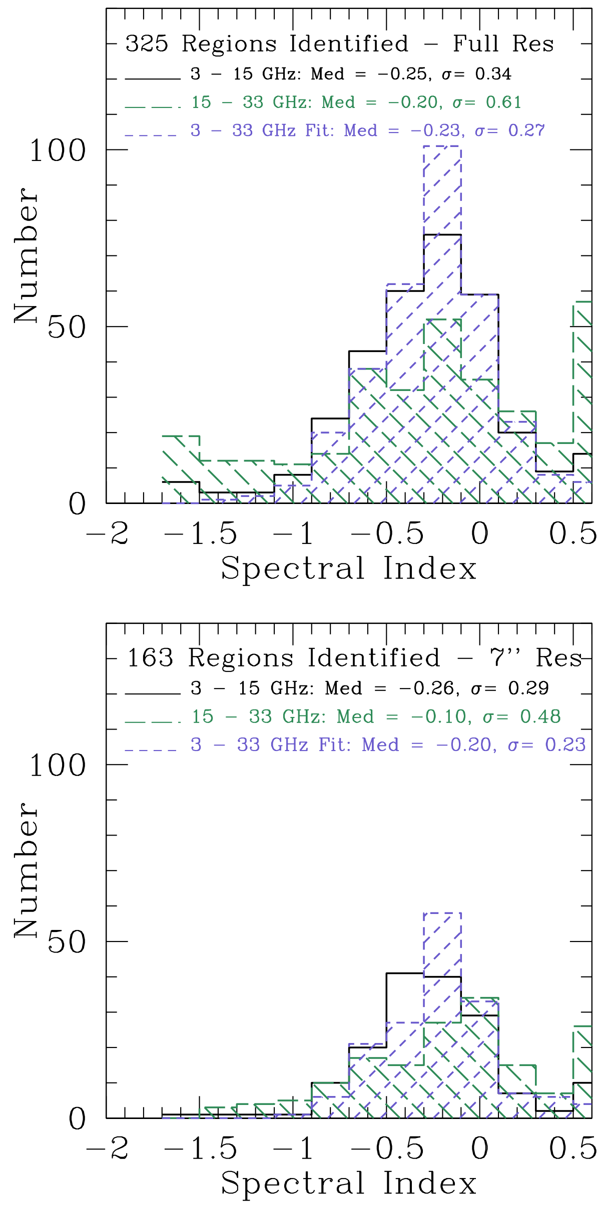

Figure 4.2: Top: The $3-15$ GHz (black), $15-33$ GHz (green), and $3-33$ GHz (purple) radio spectral index distributions for 325 regions identified in the SFRS. The median size of the apertures used is 162 ± 6.5pc. Bottom: The spectral index distributions for 163 7" regions identified in M18a. The median size of the apertures used at 7" resolution is 259 ± 7.2 pc Overall, we find that the $3-33$ GHz distributions measured at $\sim$ 2" and 7" are consistent with one another, implying that free-free emission dominates the radio spectra of star-forming regions on scales up to $\sim$ 500pc. Not included in any of these plots are the likely background galaxy candidates identified.

forming regions is marginal on ~ 100 pc scales in these galaxies. This is consistent with the results presented in Murphy et al. (2012b), where they show that the thermal fraction at 33 GHz increased as function of decreasing linear resolution. Despite the relatively flat spectral slopes from $3 - 15$ GHz, we do see evidence that the spectrum continues to flatten from $15 - 33$ GHz, on average. This is consistent with expectations for star-forming regions, where the radio spectrum is synchrotron-dominated at low frequencies, and flattens at higher frequencies as the contribution of thermal emission increases (Condon et al., 2012; Clemens et al., 2010; Murphy et al., 2013). Finally, we do not see any significant evidence for free-free absorption, which is known to affect the compact central regions of local star-forming and starburst galaxies, and would result in steep spectral indices even at high frequencies (Condon & Yin, 1990; Clemens et al., 2008; Murphy et al., 2013).

In the nearby Universe, the typical radio spectrum of normal star-forming galaxies is well-described by a power-law spectrum with a spectral index of -0.7, and a thermal fraction of $\sim 10\%$ at ~ 1 GHz (Klein et al., 1988; Condon & Yin, 1990), whereas studies of local luminous infrared galaxies (LIRGs) find a flat spectrum around 1 GHz and a steepening spectrum above 10 GHz (Clemens et al., 2008; Leroy et al., 2011; Murphy et al., 2013). New high-resolution observations of a large sample of LIRGs in the Great Observatories All-Sky LIRG Survey (GOALS) have revealed that the steep spectrum seen in highly star-forming galaxies are attributed solely to the nucleus, and that in extranuclear regions the spectral shape is typical of the star-forming regions identified in this study (Linden et al., 2019).

4.4.2 Thermal Fractions

Given the results above, we now calculate the thermal fraction of each region by using the spectral index, measured in Section 4.1, from $3 - 15$ GHz ($\alpha_{3-15\,\mathrm{GHz}}$) to set the lower-limit on the nonthermal spectral index ($\alpha^{\rm NT}$) such that $\alpha^{\rm NT} = -0.83$ if $\alpha_{3-15\,{\rm GHz}} \geq -0.83$, and $\alpha^{\rm NT} = \alpha_{3-15\,{\rm GHz}}$ if $\alpha_{3-15\,GHz} < -0.83$. A constant nonthermal radio spectral index of -0.83 is assumed based on the average non-thermal spectral index found among the 10 star-forming regions studied in NGC 6946 by Murphy et al. (2011b). Furthermore, this value is consistent with the results of Niklas & Beck (1997, i.e., $\alpha^{\rm NT} = -0.83$ with a scatter of $\sigma_{\alpha^{\rm NT}} = 0.13$) for a sample of 74 nearby galaxies. Finally, we adopt a single power-law exponent for the free-free emission (~ -0.1), and use the fit from 3 to 33 GHz to set the overall radio spectral index. Then, using the prescription in Klein et al. (1984), we can calculate the thermal fraction at 33 GHz such that,

$$f_{\rm T}^{\nu_1} = \frac{\left(\frac{\nu_2}{\nu_1}\right)^{-\alpha} - \left(\frac{\nu_2}{\nu_1}\right)^{-\alpha^{\rm NT}}}{\left(\frac{\nu_2}{\nu_1}\right)^{-0.1} - \left(\frac{\nu_2}{\nu_1}\right)^{-\alpha^{\rm NT}}} \tag{4.1}$$

where ν_1 is the target frequency (33 GHz), α is the observed slope from 3 to 33 GHz, and $\alpha^{\rm NT}$ is the nonthermal spectral index. In the top Panel of Figure 4.3 we show the resulting thermal fractions of the star-forming regions in our sample using the empirically measured values from Equation 1. We find that the median value is $92 \pm 0.8\%$ with a median absolute deviation of 11%. This demonstrates that we can reliably use the 33 GHz flux density to infer the total free-free emission, and thus current star formation activity, on the scales of individual HII and star-forming regions. While this result had been suggested by our previous GBT and VLA campaigns (e.g., Murphy et al., 2011b, 2012b, 2018a), this is the first measurement of the 33 GHz thermal fraction based on the shape of the radio spectrum at these frequencies and spatial scales in nearby galaxies.

Further, by restricting our analysis such that we remove all non-SF regions, all apertures containing multiple smaller individual regions, and require $r_{\rm G} \geq 250$pc

(238 regions), we mitigate contamination from any central AGN and can determine broad population statistics for extragalactic HII regions using our cleanest sample of extranuclear star-forming regions. In Figure 4.4 we find that the median thermal fraction is $93 \pm 0.8\%$ with a median absolute deviation of 10%. This value is consistent with the results presented in Figures 4.2, and 4.3, and confirms that supernova remnants, ultra-compact HII regions, and/or AME candidates do not bias our results.

Finally, we measure the thermal fraction at 33 GHz for 163 regions identified at 7" resolution in M18a to be $94 \pm 0.8\%$ with a median absolute deviation of 8%. This result is consistent with the measurements at 2" and confirms that free-free emission dominates the radio spectra of star-forming regions on scales up to ∼500pc. Further, when we apply the same radial cut (i.e., $r_G > 250$pc) and remove all non-SF regions, retaining 111/163 regions, the median thermal fraction at 33 GHz is $97 \pm 0.5\%$ with a median absolute deviation of 4.6%. Thus, it is clear that regardless of the size of the photometric apertures used, isolating extranuclear SF regions in nearby galaxies results in a higher thermal fraction at 33 GHz and a smaller median absolute deviation in the overall distribution.

4.4.3 MCMC Parameter Estimation

From Equation 1 it is clear that reliable estimates for the 33 GHz thermal fraction are sensitive to the value adopted for the nonthermal spectral index ($\alpha^{\rm NT}$). While the median $3 - 15$ GHz spectral index observed for our sample is well below the canonical value (i.e., -0.83), degeneracies may still exist between $\alpha^{\rm NT}$ and $f_{\rm T}$. In this case classical χ^2 fitting methods may underestimate the true uncertainties associated with modeling the radio spectrum as a two-component power-law [i.e., $S(\nu) = A\nu^{\alpha^{\rm NT}} + B\nu^{-0.1}$]. Here, we explore whether the marginalized posterior distributions from a Monte-Carlo Markov Chain (MCMC) analysis better reflect the uncertainties associated with this

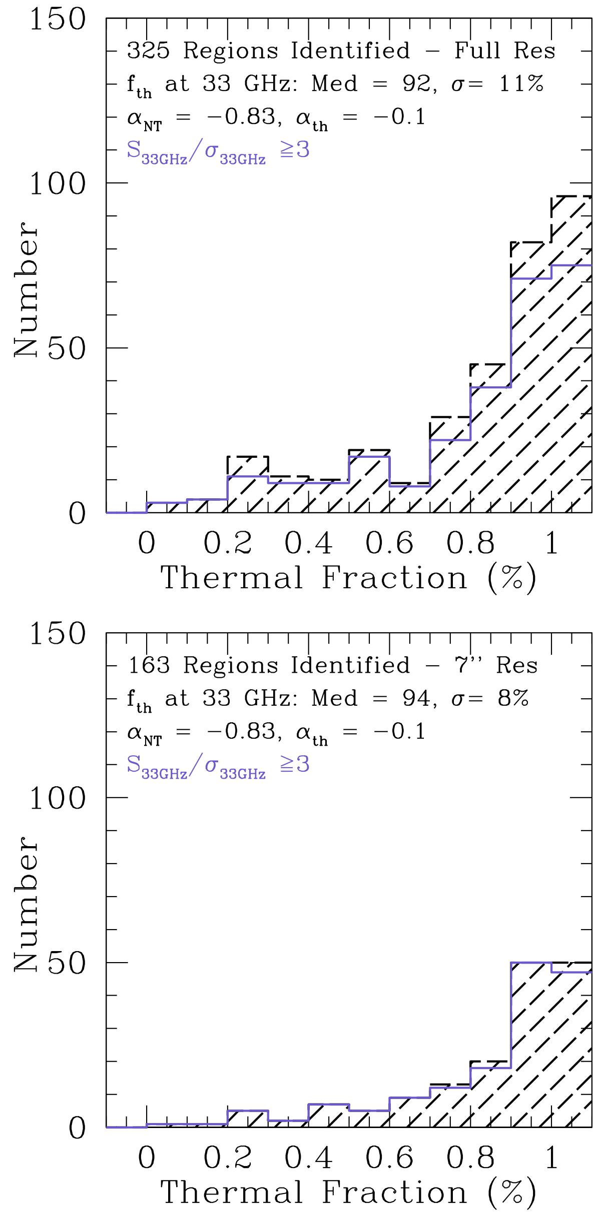

Figure 4.3: Top: The thermal fraction distribution at 33 GHz for 325 star-forming regions in the SFRS (black). In purple we show the distribution for regions with a $S/N \geq 3$ at 33 GHz, demonstrating that the lack of a significant 33 GHz detection does not bias our results. The median size of the apertures used is 162 ± 6.5pc. Bottom: The thermal fraction distribution for 163 7" regions identified in M18a with a $S/N > 3$ in two radio bands. The median size of the apertures used at 7" resolution is 259 ± 7.2 pc. Overall, we find that the median thermal fraction at 33 GHz is $\sim 93\%$, and that this value does not vary significantly from 100 up to ~ 500pc scales in our galaxy sample.

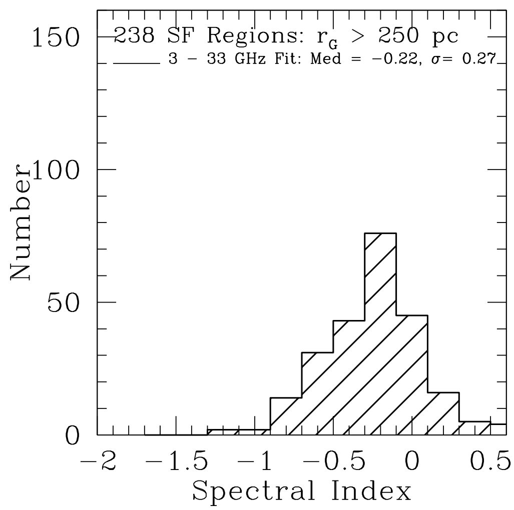

Figure 4.4: The spectral index and thermal fraction distributions for all 238 SF regions with the likely supernova remnants and AME candidates removed, and a requirement of $r_{\mathrm{G}} \geq 250$pc (The same cut adopted in M18a). This represents the cleanest sample of extranuclear star-forming regions for which we can determine broad population statistics for extragalactic HII regions. Ultimately we find that the median spectral index and thermal fraction distributions at 33 GHz are consistent with the results presented in Figures 4.2 and 4.3, confirming that supernova remnants, ultra-compact HII regions, and AME candidates do not bias our results.

decomposition (Hogg et al., 2010).

For this exercise, we use the Python package EMCEE (Foreman-Mackey et al., 2013) to generate posterior probability distributions for each of the fitted parameters (α^{NT}, f_{T}, and A/B) given the typical S/N ratio of our three-band observations. Following Westcott et al. (2018), we parameterize our two-component power-law model at a reference frequency of 1 GHz to avoid dependencies in frequency space. Further, we adopt a gaussian probability distribution function for the nonthermal spectral index whose mean and standard deviation are consistent with the values obtained in Niklas & Beck (1997). Finally, we make a slight modification to Equation 9 presented in

Westcott et al. (2018),

$$P(\theta) \propto H(A,B)e^{\frac{-(\alpha-0.83)^2}{0.13^2}} \tag{4.2}$$

such that H is equal to 1 when the values of A and B are greater than zero. This is done in order to constrain the nonthermal spectral index, thermal fraction, and normalization constants of each component simultaneously. We make 1000 realizations of this model at three different S/N ratios (5, 10, and 50) by randomly selecting a nonthermal spectral index ($-2 < \alpha^{\rm NT} < 0$) and vales of A(B) [$0 < A(B) < 1$], to represent the typical variance in the values observed for our sample.

In Figure 4.5 we plot the relative difference in the input and output thermal fraction as a function of the input nonthermal spectral index. For a fixed S/N per region of 10, and with only three data points, our MCMC modeling can recover the input nonthermal spectral index to within 1σ for $-1.25 < \alpha^{\rm NT} < 0.25$. Importantly, we find that the best-constrained spectra have nonthermal indices very close to the fixed-value adopted for our χ^2-minimization (-0.83). This result demonstrates that adopting fixed values for the $\alpha^{\rm NT}$ does not introduce systematic biases into the derived 33 GHz thermal fractions, over a reasonable set of input conditions for our two-component power-law model. This is an important result for calibrations of the total star-formation rate, which rely on using the observed radio continuum (Murphy et al., 2011b, 2012b).

4.5 Discussion

4.5.1 Trends with Galactocentric Radius

Following the same procedure as M18a, we use the measured position angle (PA) and inclination of each galaxy to convert the angular separation of each star-forming

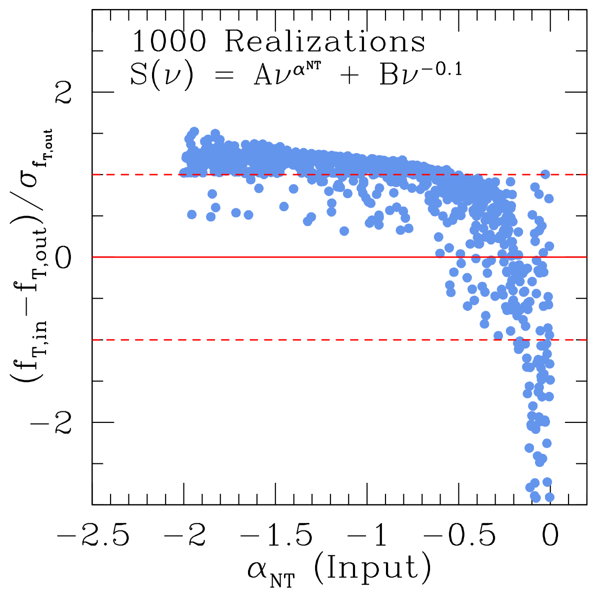

Figure 4.5: The results from our MCMC analysis of 1000 random realizations of 3 - 33 GHz spectra using as a model $S(\nu) = A\nu^{\alpha^{\mathrm{NT}}} + B\nu^{-0.1}$. For these realizations we fix $S/N = 10$ and vary the thermal fraction at 33 GHz by randomly assigning a non-thermal spectral index from 0 to 2, and an A (B) values between 0 and 1. It is clear from this exercise that by fitting our data using an MCMC approach, our ability to recover the true value for the 33 GHz thermal fraction peaks at $\alpha^{\mathrm{NT,in}} \sim -0.8$, which closely resembles the canonical value for the nonthermal spectral index.

region from the nucleus into a de-projected galactocentric radius ($r_{\rm G}$). In M18a we found that the median 33 GHz continuum-to-Hα line flux ratio was statistically larger within $r_{\rm G} < 250$ pc relative to the outer disk regions by a factor of 1.82 ± 0.39, while the ratio of 33 GHz-to-24μm flux densities is lower by a factor of 0.45 ± 0.08. Such a situation may arise if the circumnuclear regions of these galaxies have extended star formation histories in which star formation that has taken place over a longer period of time, resulting in an accumulation of young dust-heating stars in addition to much older bulge stars that boost the 24 μm flux density relative to what is seen in the extranuclear regions. This is largely opposite to what we would expect if there was an additional nonthermal component powering the 33 GHz emission in the central regions of these galaxies, unless the excess dust-heating at 24 μm far exceeds any additional nonthermal emission contribution at 33 GHz.

Therefore, these results suggested that the larger ratio of 33 GHz flux density to Hα line flux found in the central regions of these galaxies may primarily arise from increased extinction. We can now test this picture for 325 discrete regions (background galaxies removed) with detailed radio spectral fitting and thermal fraction estimates, which do not suffer from the effects of variable dust extinction in galaxies. In Figure 4.6 it is clear that the overall dispersion in the measured spectral index and thermal fraction at 33 GHz increases significantly for regions that lie within the 250 pc galactocentric radius cut used in M18a to distinguish extranuclear from nuclear/circumnuclear star-forming regions. In fact, limiting the analysis to sources with $r_{\rm G} < 250$ pc results in a value for the median 33 GHz thermal fraction of $\sim 71 \pm 3.5\%$ with a median absolute deviation of $\sim$18% relative to $\sim 95 \pm 2.2\%$ with a median absolute deviation of $\sim$11% for regions with $r_{\rm G} \geq 250$ pc. Additionally, the scatter of the thermal fraction distribution increases by nearly a factor of 2 within $r_{\rm G} < 250$pc. This confirms that while extinction may play a role in driving the previously seen correlations, excess nonthermal emission is indeed present in many of the circumnuclear star-forming regions observed in the SFRS.

4.5.2 Model Age Fitting

By making use of differences in the timescales associated with thermal (free-free) and synchrotron emission, we can place estimates on the age of star-forming regions by examining how these processes affect the radio spectral indicex from $3-33$ GHz. Since free-free emission is directly associated with ionizing photons that are only produced by the shortest-lived (≤ 10 Myr) massive stars, its presence in large quantities relative to synchrotron emission is indicative of very young star formation.

To better-quantify these different timescales, we use a Starburst 99 (SB99) model of a single instantaneous burst with default inputs (solar metallicity and 2-component Kroupa IMF) run for 1 Gyr (Leitherer et al., 1999). However, in order to take into account the fact that at the median physical scales we are probing, (~ 100 pc), a single, instantaneous starburst may not be representative, we also include SB99 models with a continuous star formation history of SFR $= 1\,M_{\odot}\,\mathrm{yr}^{-1}$ using the same metallicity and IMF input as in the instantaneous burst model (Figure 4.7 - Left Panel). The details of these models, and their application to extranuclear star-forming regions identified in LIRGs is presented in Linden et al. (2019).

For both models we then perform a χ^2 minimization to the observed spectral indices for each star-forming region in the sample. We stress that without including cosmic-ray propagation, which will affect the relative ratio of free-free and nonthermal emission on these scales, this exercise is simply meant to understand how the observed distribution of spectral indices can be represented as a distribution of ages. In the left panel of Figure 4.7 it is clear that our models are insensitive to HII regions with ages $\tau_{Hii} < 3$ Myr and $\tau_{Hii} > 40$ Myr. However, in the intermediate age range we

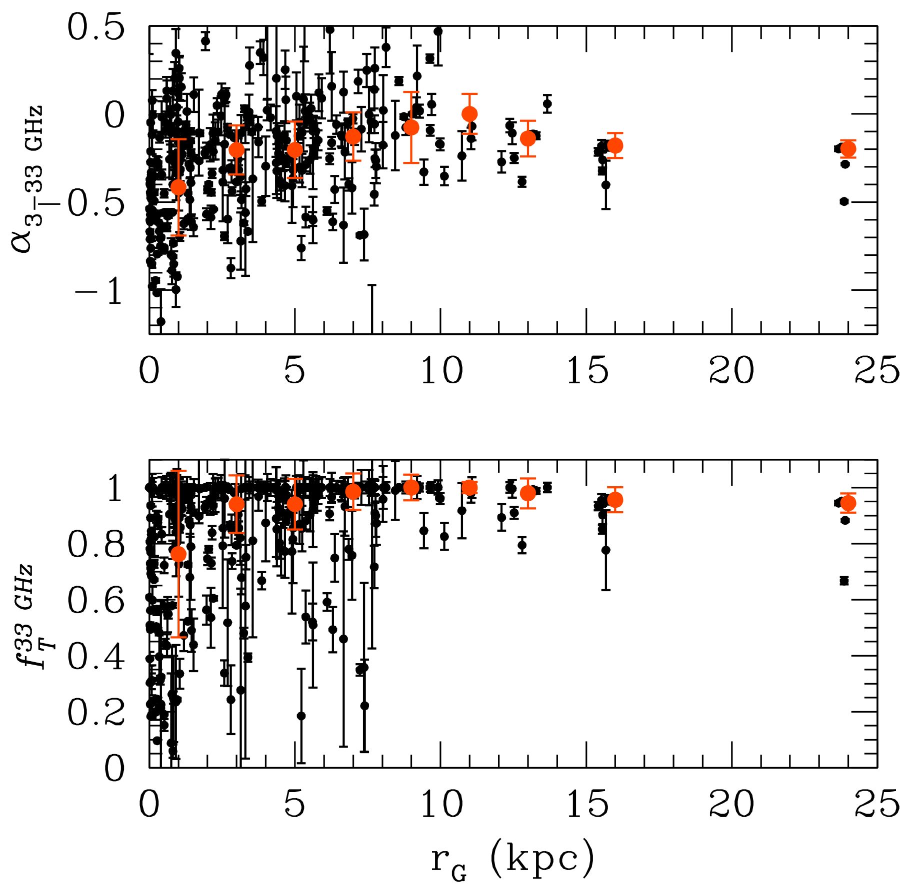

Figure 4.6: The spectral index and 33 GHz thermal fraction distributions plotted against galactocentric radius for all 325 sources identified in Figure 4.2. While we identify regions across the full extent of galaxy disks which are heavily dominated by thermal emission, a clear trend emerges where the scatter in both quantities increases significantly as a function of decreasing galactocentric radius (orange points). In particular, no region with a measured $f_T < 80\%$ is found in any SFRS galaxy beyond a radius of 7 kpc. These trends are reflective of the ongoing star-formation activity occurring in the centers of nearby normal galaxies, and reinforce our ability to successfully capture the SFH of individual HII regions using the $3 - 33$ GHz radio spectral slopes.

find that a typical uncertainty of $4-6\%$ on the observed spectral index corresponds to a $0.1-0.2$ dex uncertainty in age. Therefore while the age of any individual region may be uncertain, the increase in the number of young ($3 < \tau_{Hii} < 10$ Myr) relative to old ($\tau_{Hii} \sim 20-30$ Myr) star-forming regions is robust.

The right panel of Figure 4.7 shows the distribution of fitted ages for the instantaneous burst model in blue and the continuous model in green. Overall, we find that the majority ($\sim$ 70%) of our regions are best-modeled by a continuous burst, with a median age of $\sim$ 10 Myr (grey distribution). Further we find that when all regions are modeled using a continuous SFH, an age-gradient emerges in Figure 4.6. At small r_{G}, the regions with low thermal fractions, which drive the observed scatter, are preferentially older ($\tau_{Hii} \sim 20-30$ Myr). This further supports the notion that the central star-forming regions are, on average, older, and that the associated cosmic ray population in the inner disk of these galaxies is being continuously replenished by ongoing star-formation.

4.5.3 Likely Background Galaxies

For the 10 likely background sources (BG) identified (i.e. sources with no obvious 8 μm counterpart), which have a $S/N \geq 3$ in at least two radio bands, the median $3-33$ GHz spectral index is -0.65 ± 0.04 with a median absolute deviation of 0.3. This value is significantly steeper than the average value measured for the SF regions, and indicates that these sources are primarily dominated by synchrotron emission. This result further suggests that our visual classification scheme involving both radio and near-IR imaging appears to be an effective discriminator for various types of radio sources in surveys of nearby galaxies. Finally, a cross-reference with NED suggests that none of these sources have been previously identified in the literature.

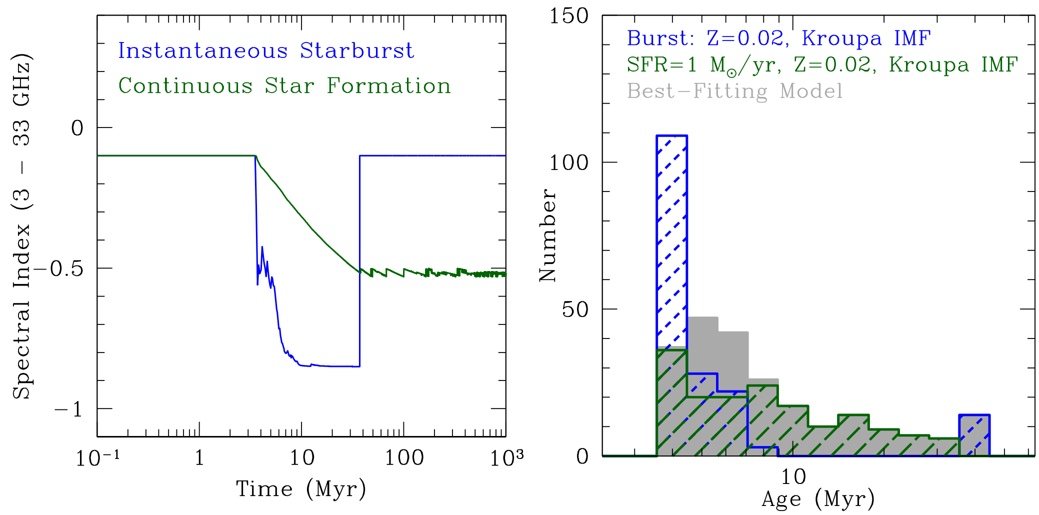

Figure 4.7: Left panel: The evolution of the 3-33 GHz spectral slope in SB99 models of both an instantaneous burst and continuous SFH, using standard Kroupa IMF, and solar metallicities. We perform a χ^2-minimization of these models to the observed $3-33$ GHz spectral index of each region. Right panel: The distribution of model ages for both types of SFH (blue and green) and the best-fitting model in each case (grey). It is clear that there exists two populations of regions: Those younger than $t \sim 10$ Myr, which are best-modeled by an instantaneous burst, and those older than $t \sim 10$ Myr, which are best-modeled by a continuous SFH.

4.5.4 Supernova and Supernova Remnants

In order to identify possible supernova remnants, we cross-correlated our sample of 377 regions against the Open Supernova Catalog (OSC: Guillochon et al., 2017). In total we identify 6 sources as being spatially coincident (within 2") to an identified radio source with a $S/N \geq 3$ in at least two radio bands. The $3-33$ GHz spectral slopes measured are uniformly distributed from -1 to 0.5. This scatter is likely driven by SNe/R at various stages of their evolution, and therefore a large range in the degree of energy loss of the CRs as they propagate through the ISM. For one region identified in NGC 7331, the measured 15 GHz flux density is larger by over an order of magnitude due to a supernova, SN2014C, which was discovered in January of 2014, between the time our 3 and 15 GHz observations of this source were taken (Shivvers et al., 2019).

4.5.5 Anomalous Microwave Emission

Anomalous Microwave Emission (AME) is a known dust-correlated component of Galactic emission that has been detected by cosmic microwave background (CMB) experiments and other radio/microwave instruments at frequencies $10-60$ GHz since the mid-1990s (see Dickinson et al., 2018, and articles within for recent reviews). AME is found to be spatially correlated with far-infrared thermal dust emission, but cannot be explained by synchrotron, or free-free emission mechanisms, and is far in excess of the emission contributed by thermal dust with the power-law opacity consistent with observations at sub-mm wavelengths. The most natural explanation for AME is rotational (electric dipole) emission from ultra-small dust grains (i.e., 'spinning dust': Erickson, 1957; Draine & Lazarian, 1998). The emission forms part of the diffuse Galactic foregrounds that contaminate CMB data, which operate in the frequency range $30-300$ GHz, and hence knowledge of the spatial structure and spectral shape can inform CMB component separation. However, spinning dust emission depends critically on the dust grain size distribution, the type of dust, and the environmental conditions (density, temperature, interstellar radiation field, etc.). Thus, precise measurements of AME can also provide a new window into the ISM, complementing other multiwavelength tracers.

A number of searches for extragalactic AME have been undertaken with WMAP and Planck data (e.g., the Magellanic Clouds and NGC4945: Bot et al., 2010; Peel et al., 2011), all of which were inconclusive. Most recently, we have identified two additional detections of AME in the SFRS sample as having anomalously high 33 GHz-to-24μm flux ratios (NGC 6946 E4 and NGC 4725 B: Murphy et al., 2010, 2018b). NGC 4725 B in particular appears consistent with a highly-embedded ($A_V > 5$ mag) nascent star-forming region, in which young ($\sim$ 3 Myr) massive stars are still en-

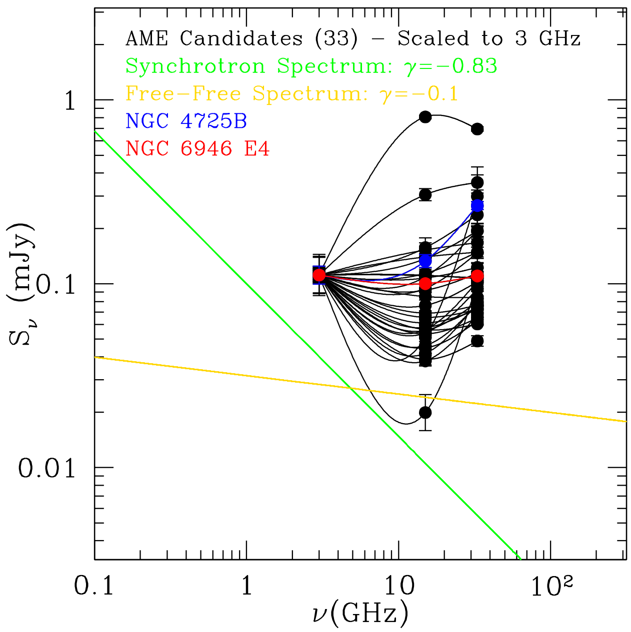

Figure 4.8: The radio spectra of all 33 AME candidates identified in the SFRS as having $3-33$ GHz or $15-33$ GHz spectral indices 3σ greater than $\alpha^{\mathrm{T}}=-0.1$. To demonstrate the diversity of our AME candidate spectra we normalize all flux density measurements to the brightest region detected at 3 GHz. We expect that, similar to NGC 6946 E4 (Red), the regions with decreasing $3-15$ GHz spectral slopes contain a non-negligible amount of synchrotron emission, whereas the regions with very shallow or even rising spectra over this same frequency range (e.g. similiar to NGC 4725 B: Blue) will be dominated by free-free emission.

shrouded by their natal cocoons of gas and dust, lacking enough supernova to produce synchrotron emission.

While it is possible that NGC 4725 B and NGC 6946 E4 represent the most favorable conditions for AME detection, there are likely remaining regions in the SFRS that still harbor AME at a lower level relative to the other emission components (Hensley et al., 2015). Isolating the factors that govern the level of AME in these regions will lend insight into the physical mechanisms powering this emission as well as the nature of its carriers. In particular, we have observed that a common feature among both detections thus far is a shallow or even rising spectra from 3 - 33 GHz, as the contribution from AME increases and eventually dominates beyond $\sim 20\,$GHz. These regions can be identified as having elevated 33 GHz emission relative to the expected extrapolation from lower-frequency radio data using a standard two-component power law.

By measuring the $3-33$ and $15-33\,$GHz spectral indices, we made an initial selection of 58 extragalactic AME candidates as regions that have an 8μm counterpart, a $S/N \geq 3$ in at least 2 radio bands, a de-projected galactocentric radius of $r_{\rm G} > 250$pc, and a measured spectral slope that is $\geq 3\sigma$ above the canonical $\alpha^{\rm T} = -0.1$ value expected for free-free emission. This represents a conservative upper-limit to identify regions by assuming that the non-thermal synchrotron emission is negligible at 33 GHz, and thus does not contribute to the measured slope from $15 - 33\,$GHz. This assumption is well-supported here for our full spectral analysis of over 300 star-forming regions identified in the SFRS, which show that the median thermal fraction measured at 33 GHz on a few ~ 100 pc scales is $\sim 91\%$. We then visually inspected all 58 AME candidates, only retaining 33 regions where the emission was found to be compact, similar to the previously identified extragalactic AME sources. This is done to ensure that any differences in surface brightness sensitivity between our observations would not result in diffuse emission with an artificially flattened spectrum, which is unassociated with an individual source. Our final requirement removes 4 sources (NGC 4254 Enuc. 1 B, NGC 3521 Enuc. 1, NGC 4736 N, and NGC 7331 D), which have very steeply rising 3-15 GHz spectral slopes, but are undetected at 33 GHz, and therefore are not confidently identified as AME candidates.

In Figure 4.8 we plot the $3 - 33\,$GHz spectrum of the 33 AME candidate regions normalized to the highest measured 3 GHz flux density. Viewed in this way we see that many of our AME candidates, similar to NGC 4725 B, have shallow or slightly negative slopes from $3-15\,$GHz, and a much steeper positive slope from $15-33\,$GHz. However, there are some regions which look more similar to NGC 6946 Enuc 4., which have steeper 3−15 GHz slopes and a less significant increase from 15−33 GHz. Importantly, these spectra cannot be explained by a simple combination of synchrotron (green) and free-free (yellow) emission components, suggesting that either an additional emission component peaking at $\gtrsim$ 15 GHz is required (e.g., AME), it is a (very) high-frequency GHz-peaked background galaxy, or the source is variable. A final possibility is that the free-free emission is optically-thick at 33 GHz. However, such 'ultra-compact' HII regions have much higher radio luminosities and SFRs ($\sim 40 - 60$ mJy) then the regions identified here (e.g., Meier et al., 2002).

4.6 Conclusions

We have presented 3, 15, and 33 GHz imaging towards galaxy nuclei and extranuclear star-forming regions in the SFRS, and have identified 335 regions (286 SF, 10 BG, 6 SNe/R, and 33 AME) with $S/N \geq 3$ in at least two radio bands. Through detailed measurements of their radio spectra we have confirmed that:

1. The average local background contribution to the measured 3, 15, and 33 GHz flux densities on $\sim$ 100 pc scales is $\sim 4 - 6\%$. This is significantly smaller than the $15 - 40\%$ found for the sample of regions studied at 25" ($\sim$ 1kpc) scales with the GBT (Murphy et al., 2011b).

2. On $\sim$100 pc scales, the median thermal fraction at 33 GHz of all regions identified as non-background galaxies is $92 \pm 0.8\%$ with a median absolute deviation of 11%. Limiting our analysis to extranuclear ($r_{\rm G} > 250$pc) SF regions, we measure a median thermal fraction of $93 \pm 0.8\%$ with a median absolute deviation of 10%. Further, we find that on 7" scales the median thermal fraction is $94 \pm 0.8\%$, and thus the thermal fraction remains $\geq 90\%$ up to $\sim$ 500 pc scales.

3. We have confirmed through MCMC analysis that we do not introduce systematic biases when interpreting the results of the χ^2-minimization of a two-component power-law model to fit the observed radio spectrum from $3 - 33$ GHz, and that this model can adequately separate the thermal free-free and nonthermal synchrotron emission components over a realistic range of input values.

4. We find a systematic increase in the scatter of the measured spectral indices and thermal fractions as the de-projected galactocentric radius approaches the nucleus. This trend is reflective of the ongoing star-formation activity occurring in centers of these galaxies, and results in a larger contribution of diffuse nonthermal emission.

5. We have identified a sample of 33 sources whose rising $15 - 33$ GHz emission may be due to anomalous microwave emission. Follow-up observations at high (≥ 40 GHz) frequencies will be necessary to confirm these sources as discrete regions of extragalactic AME.

4.7 Additional Figures and Tables

Table 4.6: Ancillary Source Photometry at 7″ Angular Resolution

Source ID	$f_\nu(1528\,\text{Å})$ (μJy)	$f_\nu(2271\,\text{Å})$ (μJy)	$f_{\mathrm{H}\alpha}/10^{-13}$ ($\mathrm{erg\,s^{-1}\,cm^{-2}}$)	$f_\nu(24\,\mu\mathrm{m})$ (mJy)
Star-Forming Regions				
NGC 0337 a	76.38 ± 11.46	163.59 ± 24.54	1.47 ± 0.29	45.73 ± 2.29
NGC 0337 b	104.70 ± 15.71	185.04 ± 27.76	1.83 ± 0.37	81.65 ± 4.08
NGC 0337 c	36.93 ± 5.54	70.52 ± 10.58	0.57 ± 0.11	8.40 ± 0.42
NGC 0337 d	47.19 ± 7.08	87.63 ± 13.15	1.18 ± 0.24	22.25 ± 1.11
NGC 0628 Enuc. 4	67.64 ± 10.15	81.23 ± 12.19	0.53 ± 0.11	9.87 ± 0.50
NGC 0628 Enuc. 2	70.55 ± 10.58	95.46 ± 14.32	0.40 ± 0.08	40.37 ± 2.02
NGC 0628 Enuc. 3	233.35 ± 35.00	282.27 ± 42.34	0.78 ± 0.16	28.94 ± 1.45
NGC 0628	16.96 ± 2.54	41.26 ± 6.19	0.06 ± 0.01	2.41 ± 0.14
NGC 0628 Enuc. 1	94.88 ± 14.23	134.80 ± 20.22	0.73 ± 0.15	75.27 ± 3.76
NGC 0855	146.72 ± 22.01	226.75 ± 34.01	…	18.70 ± 0.94
NGC 0925	182.62 ± 27.39	232.19 ± 34.83	0.34 ± 0.07	2.79 ± 0.15
NGC 1097 Enuc. 2	21.07 ± 3.16	30.92 ± 4.64	…	3.48 ± 0.18
NGC 1097	97.34 ± 14.60	242.71 ± 36.41	…	174.28 ± 8.71
NGC 1097 Enuc. 1 a	20.37 ± 3.06	32.96 ± 4.95	…	10.91 ± 0.55
NGC 1097 Enuc. 1 b	27.26 ± 4.09	42.24 ± 6.34	…	8.85 ± 0.45
NGC 1097 Enuc. 1 c	61.48 ± 9.22	77.38 ± 11.61	…	7.43 ± 0.38
NGC 1266	2.75 ± 0.48	10.77 ± 1.64	…	365.58 ± 18.28
NGC 1377	…	…	…	682.96 ± 34.15
NGC 1482	10.33 ± 1.56	31.06 ± 4.66	…	1279.02 ± 63.95
NGC 2403 Enuc. 6	354.10 ± 53.12	402.03 ± 60.30	1.19 ± 0.24	9.02 ± 0.45
NGC 2403 Enuc. 1 a	48.36 ± 7.25	67.64 ± 10.15	0.14 ± 0.03	3.70 ± 0.18
NGC 2403 Enuc. 1 b	1732.39 ± 259.86	2032.07 ± 304.81	2.70 ± 0.54	84.01 ± 4.20
NGC 2403 Enuc. 2 a	78.83 ± 11.82	101.84 ± 15.28	0.68 ± 0.14	34.77 ± 1.74
NGC 2403	42.11 ± 6.32	78.92 ± 11.84	0.15 ± 0.03	3.38 ± 0.17
NGC 2403 Enuc. 2 b	846.79 ± 127.02	1047.48 ± 157.12	2.32 ± 0.46	58.97 ± 2.95
NGC 2403 Enuc. 4	183.11 ± 27.47	218.95 ± 32.84	0.79 ± 0.16	17.24 ± 0.86
Holmberg II	373.62 ± 56.04	373.64 ± 56.05	1.42 ± 0.28	16.54 ± 0.83
NGC 2798	165.82 ± 24.87	412.77 ± 61.92	4.77 ± 0.95	1084.54 ± 54.23
NGC 2841	145.60 ± 21.84	213.22 ± 31.98	0.25 ± 0.05	12.63 ± 0.63
NGC 2976 Enuc. 1 a	15.95 ± 2.40	24.52 ± 3.68	0.55 ± 0.11	27.12 ± 1.36
NGC 2976 Enuc. 1 b	162.97 ± 24.45	216.89 ± 32.53	3.30 ± 0.66	129.05 ± 6.45
NGC 2976	63.57 ± 9.54	89.68 ± 13.45	0.54 ± 0.11	7.34 ± 0.37
NGC 2976 Enuc. 2 a	130.65 ± 19.60	154.13 ± 23.12	1.91 ± 0.38	53.39 ± 2.67
NGC 2976 Enuc. 2 b	60.44 ± 9.07	74.82 ± 11.23	1.11 ± 0.22	23.00 ± 1.15
NGC 3049	438.18 ± 65.73	736.56 ± 110.48	1.48 ± 0.30	180.25 ± 9.01

Table 4.6 continued

Table 4.6: Ancillary Source Photometry at 7″ Angular Resolution (continued)

Source ID	f_ν(1528 Å) (μJy)	f_ν(2271 Å) (μJy)	$f_{\mathrm{H}\alpha}/10^{-13}$ (erg s^{-1} cm^{-2})	f_ν(24 μm) (mJy)
NGC 3077	...	...	3.35 ± 0.67	... †
NGC 3190	9.88 ± 1.49	57.84 ± 8.68	0.16 ± 0.03	30.72 ± 1.54
NGC 3184	121.52 ± 18.23	243.12 ± 36.48	0.25 ± 0.05	55.49 ± 2.77
NGC 3198	9.78 ± 1.47	29.67 ± 4.45	0.08 ± 0.02	176.88 ± 8.84
IC 2574 a	622.44 ± 93.37	551.40 ± 82.71	1.72 ± 0.34	4.62 ± 0.23
IC 2574 b	114.96 ± 17.24	141.24 ± 21.19	1.70 ± 0.34	19.95 ± 1.00
NGC 3265	164.32 ± 24.65	297.20 ± 44.58	...	141.65 ± 7.08
NGC 3351 a	286.98 ± 43.05	839.02 ± 125.85	2.33 ± 0.47	307.30 ± 15.36
NGC 3351 b	228.22 ± 34.23	655.21 ± 98.28	2.16 ± 0.43	389.75 ± 19.49
NGC 3521 Enuc. 1	14.33 ± 2.15	18.52 ± 2.78	0.12 ± 0.02	6.20 ± 0.31
NGC 3521 Enuc. 3	9.02 ± 1.36	15.39 ± 2.32	0.09 ± 0.02	6.38 ± 0.32
NGC 3521	29.66 ± 4.45	135.30 ± 20.30	0.59 ± 0.12	12.56 ± 0.63
NGC 3521 Enuc. 2 a	12.34 ± 1.86	27.24 ± 4.09	0.27 ± 0.05	18.80 ± 0.94
NGC 3521 Enuc. 2 b	6.25 ± 0.95	12.44 ± 1.87	0.049 ± 0.010	2.59 ± 0.13
NGC 3621	15.55 ± 2.34	48.94 ± 7.34	...	7.92 ± 0.40
NGC 3627	16.12 ± 2.42	100.99 ± 15.15	0.93 ± 0.19	246.46 ± 12.32
NGC 3627 Enuc. 1	5.43 ± 0.83	9.08 ± 1.37	0.38 ± 0.08	170.02 ± 8.50
NGC 3627 Enuc. 2	28.07 ± 4.21	47.67 ± 7.15	0.94 ± 0.19	478.65 ± 23.93
NGC 3773	1163.59 ± 174.54	1035.24 ± 155.29	...	57.96 ± 2.90
NGC 3938 a	45.04 ± 6.76	102.39 ± 15.37	0.06 ± 0.01	5.02 ± 0.25
NGC 3938 Enuc. 2 a	76.37 ± 11.46	80.18 ± 12.04	0.28 ± 0.06	7.65 ± 0.38
NGC 3938 Enuc. 2 b	101.00 ± 15.15	109.29 ± 16.41	0.35 ± 0.07	21.20 ± 1.06
NGC 4254 Enuc. 2 a	82.48 ± 12.37	118.60 ± 17.79	0.34 ± 0.07	13.34 ± 0.67
NGC 4254 Enuc. 2 b	79.65 ± 11.95	122.20 ± 18.33	0.19 ± 0.04	11.10 ± 0.56
NGC 4254 a	43.05 ± 6.46	115.81 ± 17.37	0.45 ± 0.09	32.49 ± 1.62
NGC 4254 Enuc. 1 a	35.31 ± 5.30	53.66 ± 8.05	0.24 ± 0.05	22.07 ± 1.10
NGC 4254 b	41.12 ± 6.17	160.80 ± 24.12	0.61 ± 0.12	53.56 ± 2.68
NGC 4254 Enuc. 1 b	133.40 ± 20.01	208.80 ± 31.32	0.53 ± 0.11	18.13 ± 0.91
NGC 4254 c	38.51 ± 5.78	114.72 ± 17.21	0.40 ± 0.08	25.93 ± 1.30
NGC 4254 Enuc. 1 c	81.14 ± 12.17	145.03 ± 21.76	0.50 ± 0.10	31.93 ± 1.60
NGC 4254 d	48.25 ± 7.24	99.19 ± 14.88	0.24 ± 0.05	14.27 ± 0.71
NGC 4254 e	74.41 ± 11.16	134.91 ± 20.24	0.33 ± 0.07	25.00 ± 1.25
NGC 4254 f	53.17 ± 7.98	101.76 ± 15.26	0.24 ± 0.05	11.40 ± 0.57
NGC 4321 Enuc. 2 a	70.84 ± 10.63	101.18 ± 15.18	0.15 ± 0.03	7.99 ± 0.40
NGC 4321 Enuc. 2 b	78.57 ± 11.79	109.62 ± 16.44	0.15 ± 0.03	6.33 ± 0.32
NGC 4321 Enuc. 2	25.65 ± 3.85	35.61 ± 5.34	0.06 ± 0.01	4.76 ± 0.24
NGC 4321 a	467.33 ± 70.10	1001.88 ± 150.28	0.86 ± 0.17	88.54 ± 4.43
NGC 4321 b	208.14 ± 31.22	535.72 ± 80.36	0.90 ± 0.18	117.01 ± 5.85

Table 4.6 continued

Table 4.6: Ancillary Source Photometry at 7″ Angular Resolution (continued)

Source ID	f_ν(1528 Å) (μJy)	f_ν(2271 Å) (μJy)	$f_{\mathrm{H}\alpha}/10^{-13}$ (erg s^{-1} cm^{-2})	f_ν(24 μm) (mJy)
NGC 4321 Enuc. 1	47.40 ± 7.11	84.43 ± 12.67	0.10 ± 0.02	4.10 ± 0.21
NGC 4536	28.74 ± 4.32	93.49 ± 14.04	1.96 ± 0.39	976.15 ± 48.81
NGC 4559 a	119.11 ± 17.87	167.28 ± 25.09	0.77 ± 0.15	9.99 ± 0.50
NGC 4559 b	199.22 ± 29.88	258.30 ± 38.75	0.61 ± 0.12	5.83 ± 0.29
NGC 4559 c	81.18 ± 12.18	126.24 ± 18.94	0.66 ± 0.13	18.40 ± 0.92
NGC 4569	330.64 ± 49.60	1095.12 ± 164.27	3.27 ± 0.65	312.76 ± 15.64
NGC 4579	89.93 ± 13.49	180.92 ± 27.14	1.94 ± 0.39	96.78 ± 4.84
NGC 4594 a	123.89 ± 18.58	238.40 ± 35.76	0.82 ± 0.16	34.38 ± 1.72
NGC 4625	83.15 ± 12.47	145.11 ± 21.77	0.16 ± 0.03	4.72 ± 0.24
NGC 4631 a	90.42 ± 13.56	105.16 ± 15.77	0.38 ± 0.08	40.73 ± 2.04
NGC 4631 b	99.88 ± 14.98	144.01 ± 21.60	0.48 ± 0.10	85.41 ± 4.27
NGC 4631 c	144.21 ± 21.63	183.56 ± 27.53	0.25 ± 0.05	167.16 ± 8.36
NGC 4631 d	61.78 ± 9.27	92.18 ± 13.83	0.41 ± 0.08	45.26 ± 2.26
NGC 4631 h	50.54 ± 7.58	68.74 ± 10.31	0.30 ± 0.06	268.79 ± 13.44
NGC 4631 Enuc. 2 a	82.13 ± 12.32	106.50 ± 15.98	0.67 ± 0.13	18.86 ± 0.94
NGC 4631 Enuc. 2 b	277.07 ± 41.56	345.20 ± 51.78	1.71 ± 0.34	41.08 ± 2.05
NGC 4725 b	1.91 ± 0.56	5.85 ± 1.00	0.013 ± 0.003	0.30 ± 0.02
NGC 4736	251.70 ± 37.75	926.35 ± 138.95	0.57 ± 0.11	302.54 ± 15.13
NGC 4736 Enuc. 1 a	330.89 ± 49.63	438.76 ± 65.81	0.88 ± 0.18	83.84 ± 4.19
NGC 4736 Enuc. 1 b	208.78 ± 31.32	265.52 ± 39.83	0.81 ± 0.16	88.34 ± 4.42
NGC 4736 Enuc. 1 c	197.88 ± 29.68	257.39 ± 38.61	0.55 ± 0.11	90.39 ± 4.52
NGC 4826	68.74 ± 10.31	227.33 ± 34.10	3.67 ± 0.73	198.25 ± 9.91
NGC 5055	44.22 ± 6.63	169.19 ± 25.38	1.29 ± 0.26	40.56 ± 2.03
NGC 5055 Enuc. 1	79.73 ± 11.96	116.15 ± 17.42	0.68 ± 0.14	22.59 ± 1.13
NGC 5194 Enuc. 6 a	47.29 ± 7.09	57.62 ± 8.64	0.48 ± 0.10	25.76 ± 1.29
NGC 5194 Enuc. 2	276.65 ± 41.50	425.30 ± 63.80	1.48 ± 0.30	98.92 ± 4.95
NGC 5194 Enuc. 3	320.93 ± 48.14	548.20 ± 82.23	0.72 ± 0.14	60.68 ± 3.03
NGC 5194 Enuc. 11 a	150.83 ± 22.62	214.00 ± 32.10	0.46 ± 0.09	13.72 ± 0.69
NGC 5194 Enuc. 11 b	27.82 ± 4.17	44.70 ± 6.70	0.14 ± 0.03	9.92 ± 0.50
NGC 5194 Enuc. 11 d	17.34 ± 2.60	28.96 ± 4.34	0.12 ± 0.02	14.66 ± 0.73
NGC 5194 Enuc. 11 c	10.69 ± 1.60	17.52 ± 2.63	0.09 ± 0.02	2.85 ± 0.14
NGC 5194c	17.54 ± 2.63	46.97 ± 7.05	0.33 ± 0.07	50.31 ± 2.52
NGC 5194 b	97.75 ± 14.66	240.50 ± 36.08	0.65 ± 0.13	36.54 ± 1.83
NGC 5194 Enuc. 1 b	79.39 ± 11.91	179.50 ± 26.93	1.02 ± 0.20	73.51 ± 3.68
NGC 5194 e	135.19 ± 20.28	341.46 ± 51.22	0.72 ± 0.14	30.48 ± 1.52
NGC 5194 d	104.71 ± 15.71	316.95 ± 47.54	1.60 ± 0.32	95.37 ± 4.77
NGC 5194 Enuc. 10 a	15.55 ± 2.33	31.76 ± 4.76	0.19 ± 0.04	19.80 ± 0.99
NGC 5194 Enuc. 4 b	107.63 ± 16.15	171.40 ± 25.71	0.017 ± 0.004	33.66 ± 1.68

Table 4.6 continued

Table 4.6: Ancillary Source Photometry at 7″ Angular Resolution (continued)

Source ID	$f_\nu(1528\,\text{Å})$ (μJy)	$f_\nu(2271\,\text{Å})$ (μJy)	$f_{\mathrm{H}\alpha}/10^{-13}$ ($\mathrm{erg\,s^{-1}\,cm^{-2}}$)	$f_\nu(24\,\mu\mathrm{m})$ (mJy)
NGC 5194 Enuc. 4c	47.73 ± 7.16	75.01 ± 11.25	0.017 ± 0.004	12.98 ± 0.65
NGC 5194 a	239.15 ± 35.87	521.05 ± 78.16	0.63 ± 0.13	104.98 ± 5.25
NGC 5194 Enuc. 10 b	37.37 ± 5.61	70.53 ± 10.58	0.37 ± 0.07	38.48 ± 1.92
NGC 5194 Enuc. 4 d	117.81 ± 17.67	208.64 ± 31.30	0.017 ± 0.004	22.84 ± 1.14
NGC 5194 Enuc. 5 a	244.35 ± 36.65	386.49 ± 57.97	0.017 ± 0.004	32.37 ± 1.62
NGC 5194 Enuc. 9	71.73 ± 10.76	126.37 ± 18.96	0.37 ± 0.07	51.39 ± 2.57
NGC 5194 Enuc. 7 a	63.36 ± 9.50	93.36 ± 14.00	0.42 ± 0.08	9.06 ± 0.45
NGC 5194 Enuc. 8	172.68 ± 25.90	256.71 ± 38.51	0.66 ± 0.13	109.50 ± 5.48
NGC 5194 Enuc. 7 b	142.52 ± 21.38	217.91 ± 32.69	1.10 ± 0.22	50.44 ± 2.52
NGC 5194 Enuc. 7 c	77.98 ± 11.70	110.21 ± 16.53	0.37 ± 0.07	14.50 ± 0.73
NGC 5398	371.57 ± 55.74	454.84 ± 68.23	$\cdots$	94.86 ± 4.74
NGC 5457 Enuc. 6 a	801.24 ± 120.19	854.11 ± 128.12	1.69 ± 0.34	61.86 ± 3.09
NGC 5457 Enuc. 6 b	414.22 ± 62.13	511.89 ± 76.78	1.37 ± 0.27	56.33 ± 2.82
NGC 5457 Enuc. 6 c	240.17 ± 36.03	312.87 ± 46.93	1.22 ± 0.24	63.55 ± 3.18
NGC 5457 Enuc. 5 a	1012.84 ± 151.93	1143.52 ± 171.53	2.53 ± 0.51	74.87 ± 3.74
NGC 5457 Enuc. 1	55.52 ± 8.33	99.52 ± 14.93	0.21 ± 0.04	13.01 ± 0.65
NGC 5457	286.03 ± 42.90	537.52 ± 80.63	0.46 ± 0.09	52.97 ± 2.65
NGC 5457 Enuc. 3 a	94.93 ± 14.24	112.13 ± 16.82	0.49 ± 0.10	15.02 ± 0.75
NGC 5457 Enuc. 3 b	203.99 ± 30.60	238.33 ± 35.75	0.98 ± 0.20	51.61 ± 2.58
NGC 5457 Enuc. 3 c	751.75 ± 112.76	898.85 ± 134.83	4.92 ± 0.98	597.00 ± 29.85
NGC 5457 Enuc. 3 d	36.79 ± 5.52	43.18 ± 6.48	0.30 ± 0.06	38.97 ± 1.95
NGC 5457 Enuc. 4 a	357.24 ± 53.59	375.74 ± 56.36	0.55 ± 0.11	7.03 ± 0.35
NGC 5457 Enuc. 4 b	430.15 ± 64.52	441.69 ± 66.25	0.58 ± 0.12	11.24 ± 0.56
NGC 5457 Enuc. 4 c	422.89 ± 63.43	413.00 ± 61.95	1.16 ± 0.23	39.65 ± 1.98
NGC 5457 Enuc. 4 d	401.84 ± 60.28	432.77 ± 64.92	1.17 ± 0.23	26.85 ± 1.34
NGC 5474	63.65 ± 9.55	97.97 ± 14.70	0.10 ± 0.02	1.23 ± 0.06
NGC 5713 Enuc. 2 a	157.17 ± 23.58	254.86 ± 38.23	0.39 ± 0.08	57.55 ± 2.88
NGC 5713 Enuc. 2 b	36.34 ± 5.45	72.06 ± 10.81	0.06 ± 0.01	32.09 ± 1.60
NGC 5713	91.36 ± 13.70	208.13 ± 31.22	0.06 ± 0.01	54.73 ± 2.74
NGC 5713 Enuc. 1	123.22 ± 18.48	322.24 ± 48.34	0.09 ± 0.02	364.30 ± 18.21
NGC 5866	12.80 ± 1.93	48.21 ± 7.24	$\cdots$	19.91 ± 1.00
NGC 6946 Enuc. 4 b	5.65 ± 0.99	9.19 ± 1.41	$\cdots$	1.06 ± 0.05
NGC 6946 Enuc. 4 c	5.45 ± 0.97	11.02 ± 1.68	$\cdots$	121.25 ± 6.06
NGC 6946 Enuc. 8	6.02 ± 1.04	9.83 ± 1.51	1.34 ± 0.27	78.79 ± 3.94
NGC 6946 Enuc. 5 a	8.29 ± 1.35	11.09 ± 1.69	0.62 ± 0.12	4.21 ± 0.21
NGC 6946 Enuc. 3 a	7.23 ± 1.20	9.65 ± 1.48	1.14 ± 0.23	5.22 ± 0.26
NGC 6946 a	20.27 ± 3.08	37.11 ± 5.58	1.58 ± 0.32	70.92 ± 3.55
NGC 6946 c	6.61 ± 1.12	13.80 ± 2.09	0.97 ± 0.19	43.93 ± 2.20

Table 4.6 continued

Table 4.6: Ancillary Source Photometry at 7″ Angular Resolution (continued)

Source ID	$f_\nu(1528\,\text{Å})$ (μJy)	$f_\nu(2271\,\text{Å})$ (μJy)	$f_{\mathrm{H}\alpha}/10^{-13}$ (erg s^{-1} cm^{-2})	$f_\nu(24\,\mu\text{m})$ (mJy)
NGC 6946 Enuc. 6 a	14.49 ± 2.23	22.62 ± 3.41	2.86 ± 0.57	103.34 ± 5.17
NGC 6946 Enuc. 6 b	8.41 ± 1.36	9.23 ± 1.42	1.02 ± 0.20	42.42 ± 2.12
NGC 6946 Enuc. 7	9.88 ± 1.57	13.28 ± 2.02	1.13 ± 0.23	71.13 ± 3.56
NGC 6946 Enuc. 2 b	134.48 ± 20.18	173.55 ± 26.03	8.20 ± 1.64	67.97 ± 3.40
NGC 7331	8.70 ± 1.31	53.98 ± 8.10	< 0.20	16.82 ± 0.84
NGC 7793 Enuc. 1	384.10 ± 57.61	381.23 ± 57.18	0.64 ± 0.13	5.09 ± 0.25
NGC 7793 Enuc. 3	291.93 ± 43.79	357.16 ± 53.57	0.68 ± 0.14	25.96 ± 1.30
NGC 7793 a	201.40 ± 30.21	286.53 ± 42.98	0.58 ± 0.12	10.60 ± 0.53
NGC 7793 b	313.42 ± 47.01	462.00 ± 69.30	0.69 ± 0.14	15.49 ± 0.77
NGC 7793 Enuc. 2	37.06 ± 5.56	45.85 ± 6.88	0.22 ± 0.04	5.59 ± 0.28
Likely Associated with Supernovae				
NGC 6946 Enuc. 5 b	24.28 ± 3.68	31.79 ± 4.78	2.18 ± 0.44	10.55 ± 0.53
Likely AME Candidates				
NGC 2403 Enuc. 5	1061.51 ± 159.23	1026.40 ± 153.96	2.31 ± 0.46	52.86 ± 2.64
NGC 2403 Enuc. 3	1405.70 ± 210.85	1561.28 ± 234.19	4.83 ± 0.97	284.47 ± 14.22
NGC 3938 b	29.22 ± 4.39	68.29 ± 10.26	0.07 ± 0.01	3.38 ± 0.17
NGC 4631 Enuc. 1	305.75 ± 45.86	392.26 ± 58.84	0.79 ± 0.16	7.55 ± 0.38
NGC 4631 e	106.11 ± 15.92	154.92 ± 23.24	0.45 ± 0.09	92.84 ± 4.64
NGC 4631 f	80.71 ± 12.11	114.54 ± 17.18	0.38 ± 0.08	74.10 ± 3.70
NGC 4631 g	65.91 ± 9.89	88.30 ± 13.25	0.34 ± 0.07	143.47 ± 7.17
NGC 4725 a	39.11 ± 5.89	82.23 ± 12.34	< 0.01	21.29 ± 1.06
NGC 5194 Enuc. 1 a	17.13 ± 2.57	34.57 ± 5.19	0.55 ± 0.11	81.10 ± 4.06
NGC 5194 Enuc. 11 e	14.96 ± 2.24	27.54 ± 4.13	0.25 ± 0.05	23.20 ± 1.16
NGC 5194 Enuc. 1c	40.12 ± 6.02	95.83 ± 14.37	0.68 ± 0.14	32.22 ± 1.61
NGC 5194 Enuc. 4 a	30.59 ± 4.59	41.93 ± 6.29	0.018 ± 0.004	10.45 ± 0.52
NGC 5457 Enuc. 2	237.86 ± 35.68	314.69 ± 47.20	0.68 ± 0.14	24.21 ± 1.21
NGC 5457 Enuc. 7	< 0.26	< 0.46	3.43 ± 0.69	53.60 ± 2.68
NGC 6946 Enuc. 4 a	33.30 ± 5.02	47.68 ± 7.16	$\cdots$	17.07 ± 0.85
NGC 6946 Enuc. 3 b	42.01 ± 6.32	51.32 ± 7.70	2.24 ± 0.45	21.79 ± 1.09
NGC 6946 b	4.34 ± 0.83	11.18 ± 1.71	4.60 ± 0.92	2075.43 ± 103.77
NGC 6946 Enuc. 9	23.67 ± 3.59	36.83 ± 5.53	3.46 ± 0.69	115.07 ± 5.75
NGC 6946 Enuc. 1	29.23 ± 4.41	38.37 ± 5.76	2.83 ± 0.57	46.55 ± 2.33
NGC 6946 Enuc. 2 a	31.82 ± 4.80	41.20 ± 6.19	2.37 ± 0.47	17.27 ± 0.86

Note — † Photometry unreliable and not reported due to saturation by the nucleus in the 24 μm image.

Table 4.7: Local Background Measurements

Source ID	$Back_{3\,GHz}$ (mJy)	$Back_{15\,GHz}$ (mJy)	$Back_{33\,GHz}$ (mJy)	$f_{Back}{}^{3\,GHz}$ (‡)	$f_{Back}{}^{15\,GHz}$ (‡)	$f_{Back}{}^{33\,GHz}$ (‡)
Star-Forming Regions						
NGC 0337 D	0.207	0.099	0.019	0.174	0.130	0.062
NGC 0337 A	0.046	0.070	0.024	0.046	0.100	0.085
NGC 0337 B	0.133	0.059	-0.022	0.027	0.022	0.012
NGC 0337 C	0.026	0.019	0.005	0.087	0.064	0.024
NGC 0337 G	0.030	0.013	-0.005	0.082	0.068	0.032
NGC 0337 E	0.026	0.027	0.010	0.096	0.099	0.034
NGC 0337 F	0.021	0.038	0.023	0.075	0.195	0.104
NGC 0628 Enuc. 4	-0.004	0.013	0.013	0.015	0.049	0.057
NGC 0628 Enuc. 2	0.017	-0.012	0.026	0.033	0.033	0.092
NGC 0628 Enuc. 3 C	0.009	0.010	0.018	0.033	0.050	0.080
NGC 0628 Enuc. 3 A†	-0.007	0.019	-0.012	0.013	0.052	0.024
NGC 0628 Enuc. 3 B	0.023	0.018	0.014	0.080	0.091	0.066
NGC 0628 Enuc. 1 B	⋯	0.063	⋯	⋯	0.156	⋯
NGC 0628 Enuc. 1 A	0.007	0.029	-0.031	0.026	0.114	0.118
NGC 0855 C	0.082	0.071	0.018	0.045	0.067	0.024
NGC 0855 A†	0.057	0.037	-0.042	0.025	0.024	0.049
NGC 0855 B	0.022	0.026	0.022	0.060	0.110	0.120
NGC 0925 D	-0.004	0.005	⋯	0.014	0.022	⋯
NGC 0925 A	0.020	⋯	⋯	0.211	⋯	⋯
NGC 0925 B	-0.001	-0.003	⋯	0.004	0.019	⋯
NGC 1097 Enuc. 2	0.005	⋯	0.000	0.004	⋯	0.002
NGC 1097 D	1.142	0.248	0.223	0.096	0.083	0.100
NGC 1097 B	2.604	0.681	0.481	0.367	0.203	0.159
NGC 1097 A†	5.145	0.574	0.810	0.049	0.020	0.038
NGC 1097 E	1.014	0.248	0.180	0.103	0.084	0.095
NGC 1097 C	1.450	0.285	0.235	0.119	0.087	0.100
NGC 1097 Enuc. 1	⋯	⋯	0.023	⋯	⋯	0.073
NGC 1266 C	0.089	0.039	0.051	0.003	0.004	0.009
NGC 1266 A†	0.079	0.006	0.037	0.002	0.001	0.009
NGC 1266 B	0.121	0.031	0.014	0.006	0.007	0.006
NGC 1377	0.003	-0.005	0.004	0.014	0.073	0.069
IC 342 B	3.176	1.428	1.135	0.081	0.078	0.081
IC 342 A†	2.376	0.743	0.477	0.026	0.020	0.018
IC 342 C	2.542	0.970	0.790	0.109	0.093	0.098
IC 342 D	0.077	0.027	⋯	0.086	0.199	⋯

Table 4.7 continued

Table 4.7: Local Background Measurements (continued)

Source ID	$Back_{3\,GHz}$ (mJy)	$Back_{15\,GHz}$ (mJy)	$Back_{33\,GHz}$ (mJy)	$f_{Back}{}^{3\,GHz}$ (‡)	$f_{Back}{}^{15\,GHz}$ (‡)	$f_{Back}{}^{33\,GHz}$ (‡)
NGC 1482 C	1.810	0.339	0.237	0.039	0.026	0.026
NGC 1482 A†	1.692	0.078	0.255	0.014	0.003	0.023
NGC 1482 B	1.855	0.606	0.270	0.043	0.048	0.031
NGC 2146 A	0.855	0.020	0.101	0.139	0.045	0.044
NGC 2146 B	1.934	0.046	0.377	0.106	0.040	0.065
NGC 2146 C	4.865	0.136	0.971	0.132	0.081	0.097
NGC 2146 D	16.740	-0.052	1.332	0.067	0.002	0.022
NGC 2146 E	2.349	0.122	0.290	0.173	0.210	0.081
NGC 2403 Enuc. 5 C	0.066	0.080	0.049	0.072	0.107	0.066
NGC 2403 Enuc. 5 A†	0.014	0.114	0.045	0.007	0.055	0.025
NGC 2403 Enuc. 5 E	0.004	0.012	···	0.018	0.052	···
NGC 2403 Enuc. 5 B	0.004	0.006	0.006	0.026	0.033	0.059
NGC 2403 Enuc. 6 A	-0.023	0.026	0.008	0.026	0.030	0.011
NGC 2403 Enuc. 6 B	0.015	···	0.000	0.130	···	0.002
NGC 2403 Enuc. 1 E	0.014	0.010	···	0.058	0.035	···
NGC 2403 Enuc. 1 A	-0.001	0.013	-0.001	0.001	0.033	0.003
NGC 2403 C	0.002	0.012	···	0.017	0.091	···
NGC 2403 Enuc. 1 B	0.031	0.066	0.040	0.020	0.048	0.035
NGC 2403 Enuc. 1 C	0.036	0.005	0.003	0.076	0.048	0.035
NGC 2403 Enuc. 1 D	0.022	0.023	0.009	0.108	0.170	0.079
NGC 2403 Enuc. 2 B	-0.008	0.018	-0.002	0.020	0.055	0.009
NGC 2403 Enuc. 2 D	0.039	0.030	0.029	0.061	0.054	0.053
NGC 2403 Enuc. 2 A†	0.024	0.024	0.061	0.011	0.015	0.041
NGC 2403 Enuc. 2 C	0.050	0.025	0.022	0.084	0.055	0.055
NGC 2403 B	0.027	···	···	0.138	···	···
NGC 2403 E	0.013	···	···	0.096	···	···
NGC 2403 Enuc. 3 B	0.177	0.165	0.229	0.046	0.052	0.079
NGC 2403 Enuc. 4 B	···	0.018	0.003	···	0.158	0.039
NGC 2403 Enuc. 4 C	···	0.013	0.008	···	0.122	0.098
NGC 2403 Enuc. 4 A	0.016	0.066	0.034	0.016	0.066	0.037
Holmberg II B	0.006	0.011	0.019	0.041	0.080	0.115
Holmberg II A	0.017	0.016	0.031	0.050	0.050	0.091
NGC 2798 B	0.180	0.041	0.011	0.102	0.067	0.057
NGC 2798 A	0.624	0.184	0.058	0.056	0.073	0.062
NGC 2841 A	-0.003	···	···	0.005	···	···
NGC 2976 Enuc. 1 A	0.043	0.044	0.032	0.038	0.057	0.043
NGC 2976 Enuc. 1 D	0.143	0.101	0.073	0.064	0.056	0.047
NGC 2976 Enuc. 1 C	0.019	0.019	0.019	0.039	0.052	0.059

Table 4.7 continued

Table 4.7: Local Background Measurements (continued)

Source ID	$Back_{3\,GHz}$ (mJy)	$Back_{15\,GHz}$ (mJy)	$Back_{33\,GHz}$ (mJy)	$f_{Back}{}^{3\,GHz}$ (‡)	$f_{Back}{}^{15\,GHz}$ (‡)	$f_{Back}{}^{33\,GHz}$ (‡)
NGC 2976 Enuc. 1 B†	0.106	0.145	0.063	0.032	0.058	0.031
NGC 2976 B	0.014	0.004	-0.001	0.086	0.025	0.005
NGC 2976 A	…	-0.004	…	…	0.027	…
NGC 2976 Enuc. 2 A	0.069	0.068	0.025	0.041	0.046	0.020
NGC 2976 Enuc. 2 C	0.047	0.045	0.015	0.084	0.099	0.038
NGC 2976 C	0.012	…	…	0.048	…	…
NGC 3049 A	0.007	0.021	0.018	0.005	0.039	0.040
NGC 3049 B	0.005	0.014	0.014	0.015	0.066	0.090
NGC 3049 C	0.009	…	…	0.041	…	…
NGC 3077 A	0.523	0.387	0.170	0.046	0.054	0.027
NGC 3190 A	0.024	0.008	0.005	0.043	0.013	0.004
NGC 3184 B	0.013	0.012	…	0.040	0.062	…
NGC 3184 A	0.027	-0.006	-0.004	0.042	0.018	0.012
NGC 3198 B	0.014	0.001	…	0.067	0.005	…
NGC 3198 A	0.020	0.013	-0.023	0.041	0.044	0.120
NGC 3198 C	-0.019	0.015	…	0.112	0.085	…
IC 2574 D	0.032	0.016	0.010	0.033	0.053	0.021
IC 2574 C	0.160	0.112	0.060	0.179	0.178	0.077
IC 2574 A	0.009	0.004	0.011	0.016	0.008	0.023
IC 2574 B	-0.005	0.005	…	0.056	0.049	…
NGC 3265 A	0.145	0.044	0.028	0.053	0.066	0.066
NGC 3351 C	-0.016	-0.022	-0.010	0.007	0.021	0.008
NGC 3351 A	0.497	0.179	0.036	0.069	0.065	0.018
NGC 3351 B	0.409	0.101	0.109	0.046	0.028	0.048
NGC 3521 Enuc. 1	-0.022	0.023	…	0.162	0.080	…
NGC 3521 Enuc. 3 A	…	0.027	…	…	0.085	…
NGC 3521 Enuc. 2 A	0.021	0.016	-0.019	0.032	0.047	0.068
NGC 3521 Enuc. 3 C	0.021	…	…	0.021	…	…
NGC 3521 Enuc. 2 B	0.011	0.012	…	0.037	0.034	…
NGC 3621 C	0.025	0.032	…	0.065	0.099	…
NGC 3621 A	0.060	0.026	…	0.057	0.095	…
NGC 3621 H	0.012	…	…	0.103	…	…
NGC 3621 G†	0.109	0.079	…	0.051	0.051	…
NGC 3621 B	0.035	0.048	…	0.037	0.086	…
NGC 3621 F	0.002	…	…	0.013	…	…
NGC 3621 E	-0.001	-0.010	…	0.002	0.054	…
NGC 3627 Enuc. 1 G	0.037	…	…	0.072	…	…
NGC 3627 Enuc. 1 F	0.015	…	…	0.064	…	…

Table 4.7 continued

Table 4.7: Local Background Measurements (continued)

Source ID	$Back_{3\,GHz}$ (mJy)	$Back_{15\,GHz}$ (mJy)	$Back_{33\,GHz}$ (mJy)	$f_{Back}{}^{3\,GHz}$ (‡)	$f_{Back}{}^{15\,GHz}$ (‡)	$f_{Back}{}^{33\,GHz}$ (‡)
NGC 3627 Enuc. 1 E	-0.002	···	0.003	0.006	···	0.007
NGC 3627 B	0.382	0.392	-0.004	0.096	0.162	0.003
NGC 3627 A	0.008	0.037	0.021	0.004	0.034	0.030
NGC 3627 Enuc. 2 D	0.140	0.073	0.060	0.034	0.029	0.032
NGC 3627 Enuc. 1 A	0.074	0.118	0.035	0.031	0.081	0.028
NGC 3627 Enuc. 2 A†	0.161	0.208	0.029	0.022	0.049	0.008
NGC 3627 Enuc. 2 E	0.197	0.120	0.077	0.048	0.057	0.046
NGC 3627 Enuc. 2 C	-0.008	0.039	0.003	0.019	0.092	0.012
NGC 3627 Enuc. 2 B	0.027	0.059	···	0.035	0.117	···
NGC 3773	0.078	0.049	0.017	0.031	0.036	0.015
NGC 3938 B	0.028	···	···	0.102	···	···
NGC 3938 Enuc. 2 B	0.002	-0.003	0.011	0.009	0.027	0.060
NGC 3938 Enuc. 2 A	-0.007	0.000	-0.003	0.021	0.000	0.013
NGC 4254 Enuc. 2 D	···	0.008	0.019	···	0.081	0.112
NGC 4254 Enuc. 2 C	···	···	0.007	···	···	0.089
NGC 4254 Enuc. 1 E	0.020	0.013	···	0.068	0.114	···
NGC 4254 Enuc. 2 E	-0.003	···	···	0.019	···	···
NGC 4254	0.024	0.095	0.014	0.059	0.185	0.038
NGC 4254 Enuc. 1 D	0.056	0.011	0.014	0.071	0.046	0.040
NGC 4254 Enuc. 1 B	0.033	-0.004	0.023	0.152	0.028	0.056
NGC 4254 Enuc. 1 C	0.002	···	-0.008	0.008	···	0.063
NGC 4321 Enuc. 2	0.014	···	-0.010	0.082	···	0.084
NGC 4321 C	0.424	0.192	0.101	0.165	0.176	0.173
NGC 4321 F	0.215	0.099	0.067	0.231	0.218	0.214
NGC 4321 H	0.115	0.055	0.037	0.176	0.177	0.136
NGC 4321 A†	0.326	0.381	-0.122	0.014	0.042	0.024
NGC 4321 B	0.379	0.153	0.089	0.153	0.193	0.197
NGC 4321 G	0.330	0.115	0.076	0.186	0.184	0.198
NGC 4321 D	0.387	0.173	0.129	0.119	0.135	0.156
NGC 4321 E	0.750	0.277	0.158	0.190	0.199	0.182
NGC 4321 Enuc. 1 B	-0.012	0.008	···	0.043	0.045	···
NGC 4536 C	2.914	0.834	0.455	0.086	0.066	0.057
NGC 4536 A†	1.452	0.485	0.149	0.016	0.017	0.009
NGC 4536 B	2.138	0.635	0.335	0.079	0.064	0.051
NGC 4559 E	-0.017	0.013	···	0.116	0.106	···
NGC 4559 C	-0.013	0.028	0.005	0.065	0.158	0.026
NGC 4559 D	···	0.026	···	···	0.228	···
NGC 4559 B	0.012	0.010	0.002	0.130	0.064	0.018

Table 4.7 continued

Table 4.7: Local Background Measurements (continued)

Source ID	$Back_{3\,GHz}$ (mJy)	$Back_{15\,GHz}$ (mJy)	$Back_{33\,GHz}$ (mJy)	$f_{Back}{}^{3\,GHz}$ (‡)	$f_{Back}{}^{15\,GHz}$ (‡)	$f_{Back}{}^{33\,GHz}$ (‡)
NGC 4559 A	0.002	0.008	0.002	0.014	0.073	0.013
NGC 4569 A	0.253	0.180	0.057	0.088	0.125	0.065
NGC 4579	-0.139	0.254	0.152	0.068	0.092	0.255
NGC 4594	-0.021	0.011	0.021	0.025	0.023	0.026
NGC 4631 Enuc. 1	-0.000	0.064	0.049	0.000	0.097	0.080
NGC 4625 A	…	0.035	…	…	0.323	…
NGC 4631 A	0.044	0.178	0.034	0.006	0.072	0.023
NGC 4631 H	0.128	0.195	0.071	0.130	0.149	0.084
NGC 4631 B	0.456	0.220	0.208	0.083	0.066	0.068
NGC 4631 G	0.043	0.050	0.030	0.047	0.068	0.049
NGC 4631 Enuc. 2 B	0.014	0.042	-0.000	0.009	0.030	0.000
NGC 4631 Enuc. 2 C	…	0.019	…	…	0.088	…
NGC 4725 C	-0.007	0.000	…	0.032	0.006	…
NGC 4725 A	0.003	0.002	0.001	0.038	0.014	0.002
NGC 4736 K	0.004	0.015	…	0.007	0.020	…
NGC 4736 J	0.104	0.001	…	0.103	0.002	…
NGC 4736 I	0.097	0.034	…	0.077	0.052	…
NGC 4736 G	0.044	…	…	0.163	…	…
NGC 4736 L	0.047	…	…	0.084	…	…
NGC 4736 H	0.088	0.080	0.026	0.069	0.074	0.074
NGC 4736 M	-0.016	…	…	0.103	…	…
NGC 4736 F	0.134	0.108	…	0.099	0.121	…
NGC 4736 N	-0.004	0.133	…	0.017	0.124	…
NGC 4736 A	0.193	-0.016	0.021	0.031	0.007	0.017
NGC 4736 O	0.015	0.086	0.024	0.084	0.194	0.062
NGC 4736 E	…	0.141	…	…	0.182	…
NGC 4736 P	0.133	0.036	-0.008	0.126	0.120	0.013
NGC 4736 D	0.015	0.112	0.009	0.025	0.107	0.020
NGC 4736 Enuc. 1 D	0.015	0.015	0.030	0.096	0.044	0.109
NGC 4736 Enuc. 1 A	0.049	0.099	0.093	0.032	0.093	0.106
NGC 4736 Enuc. 1 B	0.148	0.038	0.065	0.053	0.024	0.063
NGC 4736 Enuc. 1 C	-0.002	0.062	0.027	0.001	0.054	0.043
NGC 4736 Enuc. 1 E	0.013	…	0.015	0.148	…	0.110
NGC 4826 C	0.049	0.086	0.033	0.068	0.177	0.152
NGC 4826 B	0.134	0.109	0.039	0.185	0.205	0.155
NGC 4826 A	0.779	0.470	0.174	0.064	0.103	0.062
NGC 4826 F†	0.236	0.899	0.044	0.021	0.093	0.012
NGC 4826 E	0.048	0.087	0.019	0.110	0.189	0.136

Table 4.7 continued

Table 4.7: Local Background Measurements (continued)

Source ID	$\mathrm{Back}_{3\,\mathrm{GHz}}$ (mJy)	$\mathrm{Back}_{15\,\mathrm{GHz}}$ (mJy)	$\mathrm{Back}_{33\,\mathrm{GHz}}$ (mJy)	$\mathrm{f}_{Back}{}^{3\,\mathrm{GHz}}$ (‡)	$\mathrm{f}_{Back}{}^{15\,\mathrm{GHz}}$ (‡)	$\mathrm{f}_{Back}{}^{33\,\mathrm{GHz}}$ (‡)
NGC 4826 D	0.077	0.075	0.030	0.136	0.229	0.096
NGC 5055 C	0.005	...	...	0.033	...	...
NGC 5055 D	0.023	0.040	...	0.106	0.207	...
NGC 5055 A	0.204	0.150	0.066	0.103	0.149	0.197
NGC 5055 B	-0.011	0.002	...	0.010	0.006	...
NGC 5055 Enuc. 1	0.002	0.024	0.020	0.005	0.055	0.050
NGC 5194 Enuc. 6	0.034	0.043	0.044	0.050	0.082	0.078
NGC 5194 Enuc. 3 B	...	0.026	0.022	...	0.074	0.165
NGC 5194 Enuc. 3 A	0.050	0.035	0.040	0.062	0.064	0.069
NGC 5194 Enuc. 11 G	-0.031	...	0.009	0.105	...	0.030
NGC 5194 Enuc. 11 A	0.053	...	0.008	0.114	...	0.036
NGC 5194 Enuc. 11 B	...	0.035	0.010	...	0.220	0.053
NGC 5194 Enuc. 11 C	...	0.004	0.009	...	0.042	0.064
NGC 5194 Enuc. 11 D	0.074	0.029	0.000	0.087	0.109	0.004
NGC 5194 H	0.055	-0.011	-0.017	0.019	0.009	0.060
NGC 5194 L	0.333	0.092	0.031	0.200	0.140	0.179
NGC 5194 M	0.089	0.050	0.012	0.130	0.199	0.090
NGC 5194 Enuc. 11 E	0.018	0.034	0.009	0.086	0.149	0.056
NGC 5194 A	0.240	0.079	0.008	0.170	0.144	0.030
NGC 5194 Enuc. 11 F	0.025	0.015	0.005	0.100	0.101	0.036
NGC 5194 K	0.095	0.108	0.011	0.111	0.165	0.048
NGC 5194 B	0.028	0.018	0.008	0.014	0.029	0.022
NGC 5194 G	0.220	0.095	0.010	0.194	0.198	0.100
NGC 5194 J	0.077	0.036	0.015	0.130	0.261	0.200
NGC 5194 E	0.559	0.306	0.094	0.045	0.070	0.056
NGC 5194 O	0.011	0.111	...	0.028	0.238	...
NGC 5194 I	0.474	0.124	0.039	0.088	0.087	0.055
NGC 5194 C†	0.491	0.203	0.050	0.046	0.072	0.041
NGC 5194 Enuc. 1 A	0.025	0.001	0.007	0.076	0.010	0.027
NGC 5194 Enuc. 4 D	...	...	0.007	...	...	0.057
NGC 5194 N	0.237	0.069	...	0.179	0.258	...
NGC 5194 F	0.024	0.041	0.014	0.032	0.079	0.044
NGC 5194 Enuc. 4 C	0.021	0.004	0.004	0.129	0.036	0.033
NGC 5194 P	0.112	0.014	0.002	0.157	0.048	0.010
NGC 5194 Enuc. 4 E	...	...	0.002	...	...	0.034
NGC 5194 Enuc. 10	0.065	0.041	0.037	0.092	0.117	0.105
NGC 5194 Enuc. 4 B	0.005	...	-0.002	0.046	...	0.026
NGC 5194 Enuc. 5 B	0.021	0.005	0.000	0.079	0.027	0.001

Table 4.7 continued

Table 4.7: Local Background Measurements (continued)

Source ID	$\mathrm{Back}_{3\,\mathrm{GHz}}$ (mJy)	$\mathrm{Back}_{15\,\mathrm{GHz}}$ (mJy)	$\mathrm{Back}_{33\,\mathrm{GHz}}$ (mJy)	$\mathrm{f}_{Back}{}^{3\,\mathrm{GHz}}$ (‡)	$\mathrm{f}_{Back}{}^{15\,\mathrm{GHz}}$ (‡)	$\mathrm{f}_{Back}{}^{33\,\mathrm{GHz}}$ (‡)
NGC 5194 Enuc. 4 F	0.018	0.004	0.000	0.083	0.027	0.003
NGC 5194 Enuc. 4 G	0.029	0.026	-0.000	0.052	0.090	0.004
NGC 5194 Enuc. 5 A	0.024	0.022	0.014	0.038	0.063	0.038
NGC 5194 Enuc. 9	0.002	-0.020	0.010	0.004	0.055	0.026
NGC 5194 Enuc. 8 C	0.005	0.032	⋯	0.014	0.118	⋯
NGC 5194 Enuc. 8 B	0.052	0.048	0.005	0.078	0.075	0.024
NGC 5194 Enuc. 7 E	⋯	0.028	0.002	⋯	0.150	0.008
NGC 5194 Enuc. 8 A	0.070	0.044	-0.012	0.126	0.082	0.030
NGC 5194 Enuc. 7 A	0.103	0.022	0.019	0.086	0.055	0.057
NGC 5194 Enuc. 7 C	0.048	0.009	-0.003	0.117	0.049	0.018
NGC 5194 Enuc. 7 B	0.022	-0.013	⋯	0.067	0.081	⋯
NGC 5194 Enuc. 7 F	0.011	0.052	⋯	0.002	0.029	⋯
NGC 5194 Enuc. 8 D	0.002	-0.018	⋯	0.006	0.092	⋯
NGC 5398	0.000	0.024	0.002	0.000	0.014	0.001
NGC 5457 Enuc. 6 A	0.092	0.099	0.018	0.088	0.106	0.033
NGC 5457 Enuc. 6 E	0.071	0.077	0.024	0.106	0.174	0.052
NGC 5457 Enuc. 6 B	0.183	0.118	0.060	0.078	0.075	0.079
NGC 5457 Enuc. 6 C	0.060	0.066	0.013	0.060	0.090	0.023
NGC 5457 Enuc. 6 D	0.023	0.031	0.005	0.040	0.084	0.016
NGC 5457 Enuc. 6 F	0.009	0.009	⋯	0.042	0.084	⋯
NGC 5457 Enuc. 2 B	0.001	-0.001	⋯	0.007	0.012	⋯
NGC 5457 Enuc. 2 C	-0.007	0.004	⋯	0.046	0.077	⋯
NGC 5457 Enuc. 5 B	0.099	0.118	0.033	0.067	0.099	0.029
NGC 5457 Enuc. 5 A†	0.101	0.115	0.034	0.048	0.053	0.027
NGC 5457 Enuc. 5 C	0.103	0.062	0.045	0.118	0.100	0.065
NGC 5457 Enuc. 1	0.009	⋯	0.005	0.083	⋯	0.058
NGC 5457	0.015	0.021	0.013	0.017	0.086	0.035
NGC 5457 Enuc. 3 E	-0.008	0.003	⋯	0.034	0.016	⋯
NGC 5457 Enuc. 3 D	0.013	0.032	⋯	0.022	0.090	⋯
NGC 5457 Enuc. 3 A	0.029	0.065	0.043	0.032	0.075	0.065
NGC 5457 Enuc. 3 B	0.257	0.299	0.087	0.022	0.032	0.012
NGC 5457 Enuc. 3 C	0.030	0.018	-0.001	0.031	0.033	0.003
NGC 5457 Enuc. 4 A	0.043	0.026	-0.001	0.104	0.101	0.006
NGC 5457 Enuc. 4 B	0.049	0.045	0.010	0.145	0.160	0.038
NGC 5457 Enuc. 4 C	0.081	0.078	0.041	0.098	0.140	0.090
NGC 5457 Enuc. 4 D	0.081	0.047	0.026	0.080	0.081	0.073
NGC 5457 Enuc. 7 D†	0.238	0.130	0.074	0.040	0.030	0.019
NGC 5457 Enuc. 7 B	0.115	0.151	0.081	0.054	0.200	0.111

Table 4.7 continued

Table 4.7: Local Background Measurements (continued)

Source ID	$\mathrm{Back}_{3\,\mathrm{GHz}}$ (mJy)	$\mathrm{Back}_{15\,\mathrm{GHz}}$ (mJy)	$\mathrm{Back}_{33\,\mathrm{GHz}}$ (mJy)	$\mathrm{f}_{Back}{}^{3\,\mathrm{GHz}}$ (‡)	$\mathrm{f}_{Back}{}^{15\,\mathrm{GHz}}$ (‡)	$\mathrm{f}_{Back}{}^{33\,\mathrm{GHz}}$ (‡)
NGC 5713 A	0.095	0.101	0.035	0.052	0.106	0.058
NGC 5713 F	0.035	0.063	0.025	0.094	0.194	0.127
NGC 5713 B	0.234	0.128	0.054	0.062	0.075	0.041
NGC 5713 Enuc. 2	0.100	0.081	-0.013	0.081	0.105	0.046
NGC 5713 Enuc. 2 A	0.185	0.141	0.024	0.096	0.131	0.038
NGC 5713 C	0.420	0.186	0.103	0.078	0.093	0.069
NGC 5713 G†	1.348	1.190	0.271	0.120	0.176	0.126
NGC 5713 D	0.334	0.182	0.096	0.044	0.056	0.040
NGC 5713 Enuc. 1 A	...	0.031	...	...	0.164	...
NGC 5713 E	0.209	0.142	0.016	0.151	0.165	0.028
NGC 5866	0.088	0.105	0.035	0.013	0.021	0.016
NGC 6946 Enuc. 4 A	0.047	0.035	0.045	0.122	0.103	0.116
NGC 6946 Enuc. 4 B	0.004	0.011	0.023	0.020	0.052	0.112
NGC 6946 Enuc. 4 H	-0.002	-0.003	0.000	0.023	0.028	0.002
NGC 6946 Enuc. 8 A	0.223	0.041	0.042	0.099	0.056	0.051
NGC 6946 Enuc. 5 A	...	...	0.007	...	...	0.064
NGC 6946 Enuc. 8 B	...	0.015	...	...	0.067	...
NGC 6946 Enuc. 5 B	0.009	0.027	0.010	0.028	0.071	0.026
NGC 6946 Enuc. 3 A	-0.014	0.014	0.010	0.135	0.069	0.043
NGC 6946 Enuc. 3 B	-0.011	0.029	0.014	0.089	0.143	0.069
NGC 6946 A	0.751	0.529	0.154	0.036	0.062	0.035
NGC 6946 Enuc. 3 C	0.015	0.049	0.028	0.031	0.103	0.065
NGC 6946 B	0.007	0.027	-0.007	0.015	0.069	0.025
NGC 6946 C	0.101	0.060	0.034	0.136	0.096	0.107
NGC 6946 Enuc. 6 J	0.017	0.000	0.014	0.148	0.005	0.138
NGC 6946 Enuc. 6 I	0.025	0.008	0.022	0.113	0.073	0.210
NGC 6946 Enuc. 6 H	0.019	0.004	0.014	0.101	0.034	0.089
NGC 6946 Enuc. 6 F	0.013	0.012	0.015	0.056	0.188	0.127
NGC 6946 Enuc. 6 E	...	0.008	0.008	...	0.050	0.049
NGC 6946 Enuc. 6 B	0.011	0.011	0.001	0.032	0.038	0.007
NGC 6946 Enuc. 6 C	0.006	0.006	...	0.056	0.100	...
NGC 6946 Enuc. 9 E	-0.004	0.006	...	0.031	0.077	...
NGC 6946 Enuc. 9 D	0.031	0.023	...	0.161	0.104	...
NGC 6946 Enuc. 9 A	0.060	0.090	0.033	0.070	0.122	0.053
NGC 6946 Enuc. 6 L	0.051	0.006	0.010	0.072	0.026	0.026
NGC 6946 Enuc. 9 C	-0.007	0.020	0.011	0.057	0.100	0.102
NGC 6946 Enuc. 9 B	0.009	0.024	0.015	0.057	0.143	0.117
NGC 6946 Enuc. 7 A	-0.007	0.045	0.013	0.035	0.060	0.027

Table 4.7 continued

Table 4.7: Local Background Measurements (continued)

Source ID	$Back_{3\,GHz}$ (mJy)	$Back_{15\,GHz}$ (mJy)	$Back_{33\,GHz}$ (mJy)	$f_{Back}{}^{3\,GHz}$ (‡)	$f_{Back}{}^{15\,GHz}$ (‡)	$f_{Back}{}^{33\,GHz}$ (‡)
NGC 6946 Enuc. 7 B	-0.008	0.017	0.009	0.059	0.079	0.057
NGC 6946 Enuc. 1 A	-0.003	0.029	0.031	0.004	0.045	0.047
NGC 6946 Enuc. 2 C	0.003	0.004	...	0.018	0.025	...
NGC 7331 G	0.120	...	...	0.172	...	...
NGC 7331 F	0.073	0.115	...	0.106	0.268	...
NGC 7331 H	0.069	-0.029	...	0.052	0.025	...
NGC 7331 I	0.076	0.143	...	0.062	0.097	...
NGC 7331 A	-0.020	0.045	...	0.123	0.123	...
NGC 7331 E	0.061	...	-0.057	0.067	...	0.117
NGC 7331 B	0.055	0.111	...	0.108	0.138	...
NGC 7331 D	0.014	0.076	...	0.096	0.170	...
NGC 7793 Enuc. 1 E	-0.001	-0.004	...	0.008	0.059	...
NGC 7793 Enuc. 3	-0.006	0.002	...	0.030	0.009	...
NGC 7793 Enuc. 1 A	0.006	0.004	...	0.059	0.051	...
NGC 7793 C	-0.004	0.004	-0.001	0.020	0.025	0.007
NGC 7793 A	-0.008	0.013	-0.003	0.035	0.067	0.016
NGC 7793 Enuc. 1 B	...	0.008	...	...	0.079	...
NGC 7793 Enuc. 1 C	-0.005	0.001	...	0.026	0.005	...
NGC 7793 Enuc. 2	...	...	-0.006	...	...	0.042
Likely Background Galaxies						
NGC 0925 C	-0.001	-0.004	0.003	0.001	0.006	0.011
IC 342 E	0.113	0.039	...	0.143	0.139	...
Holmberg II C	0.006	0.011	0.019	0.041	0.080	0.115
NGC 2841 B	-0.003	...	...	0.026	...	...
NGC 2976 Enuc. 1 E	-0.005	...	...	0.031	...	...
NGC 3077 B	-0.004	0.009	...	0.066	0.078	...
NGC 3190 B	0.089	0.027	0.017	0.042	0.040	0.034
NGC 3265 B	0.001	-0.001	...	0.001	0.017	...
NGC 3351 D	-0.011	0.014	...	0.035	0.139	...
NGC 3627 Enuc. 1 B	-0.000	...	...	0.003	...	...
NGC 4569 B	-0.017	...	...	0.034	...	...
NGC 4625 B	0.001	0.004	0.001	0.001	0.016	0.004
NGC 6946 Enuc. 4 F	0.145	0.105	0.032	0.025	0.061	0.035
NGC 6946 Enuc. 4 G	-0.044	-0.002	0.011	0.018	0.002	0.022
Likely Associated with Supernovae						

Table 4.7 continued

Table 4.7: Local Background Measurements (continued)

Source ID	Back$_{3\,\mathrm{GHz}}$ (mJy)	Back$_{15\,\mathrm{GHz}}$ (mJy)	Back$_{33\,\mathrm{GHz}}$ (mJy)	f$_{Back}$$^{3\,\mathrm{GHz}}$ (‡)	f$_{Back}$$^{15\,\mathrm{GHz}}$ (‡)	f$_{Back}$$^{33\,\mathrm{GHz}}$ (‡)
NGC 2403 Enuc. 3 D	...	-0.038	...	...	0.022	...
NGC 4736 B	-0.016	...	...	0.100	...	...
NGC 4736 C	-0.027	...	...	0.169	...	...
NGC 5194 D	0.034	0.065	0.045	0.028	0.103	0.055
NGC 5194 Enuc. 7 D	0.028	-0.003	...	0.018	0.017	...
NGC 6946 F	0.016	0.012	...	0.079	0.108	...
NGC 6946 Enuc. 6 D	0.004	0.013	-0.003	0.013	0.036	0.015
NGC 6946 Enuc. 2 B	0.006	0.087	0.029	0.005	0.061	0.015
NGC 7331 C	0.040	0.379	0.055	0.051	0.205	0.076
NGC 7793 B	-0.002	...	...	0.013	...	...
Likely AME Candidates						
NGC 2403 Enuc. 5 D	0.045	0.073	0.036	0.071	0.115	0.059
NGC 2403 Enuc. 2 E	0.038	0.057	0.022	0.032	0.059	0.018
NGC 2403 Enuc. 3 A	0.015	0.030	0.033	0.038	0.075	0.063
NGC 2403 Enuc. 3 C	0.112	0.070	0.093	0.045	0.037	0.049
NGC 3627 Enuc. 1 D	0.014	0.048	0.014	0.036	0.086	0.023
NGC 3627 Enuc. 1 C	0.005	0.085	-0.004	0.011	0.134	0.004
NGC 4254 Enuc. 2 A	0.005	0.008	0.011	0.041	0.052	0.049
NGC 4254 Enuc. 1 A	0.013	0.007	0.020	0.037	0.053	0.088
NGC 4631 C	0.115	0.020	0.081	0.066	0.023	0.065
NGC 4631 D	0.065	0.013	0.078	0.042	0.025	0.083
NGC 4631 E	0.075	0.038	0.065	0.080	0.083	0.083
NGC 4631 F	0.418	0.259	0.212	0.061	0.079	0.053
NGC 4631 Enuc. 2 A	0.033	0.006	0.005	0.055	0.027	0.013
NGC 4725 B	-0.003	0.001	0.003	0.024	0.005	0.008
NGC 5194 Enuc. 2	0.019	0.011	0.018	0.015	0.024	0.032
NGC 5194 Enuc. 1 C	0.053	0.030	0.033	0.098	0.064	0.045
NGC 5194 Enuc. 1 B	0.034	0.025	0.023	0.069	0.051	0.043
NGC 5194 Enuc. 4 A	0.040	-0.004	0.018	0.056	0.012	0.044
NGC 5457 Enuc. 2 A	0.020	0.007	0.006	0.050	0.026	0.017
NGC 5457 Enuc. 7 A	0.084	0.071	0.048	0.079	0.127	0.068
NGC 5457 Enuc. 7 C	0.263	0.243	0.162	0.074	0.135	0.084
NGC 6946 Enuc. 4 C	0.026	0.037	0.042	0.017	0.026	0.027
NGC 6946 Enuc. 4 D	-0.001	0.013	0.004	0.011	0.016	0.005
NGC 6946 Enuc. 4 E	0.014	0.035	0.023	0.011	0.026	0.018
NGC 6946 E	0.060	0.062	0.055	0.083	0.086	0.043

Table 4.7 continued

Table 4.7: Local Background Measurements (continued)

Source ID	$\mathrm{Back}_{3\,\mathrm{GHz}}$ (mJy)	$\mathrm{Back}_{15\,\mathrm{GHz}}$ (mJy)	$\mathrm{Back}_{33\,\mathrm{GHz}}$ (mJy)	$\mathrm{f}_{Back}{}^{3\,\mathrm{GHz}}$ (‡)	$\mathrm{f}_{Back}{}^{15\,\mathrm{GHz}}$ (‡)	$\mathrm{f}_{Back}{}^{33\,\mathrm{GHz}}$ (‡)
NGC 6946 D	0.018	0.064	0.005	0.045	0.126	0.010
NGC 6946 Enuc. 6 M	-0.005	-0.012	0.006	0.009	0.133	0.014
NGC 6946 Enuc. 6 G	0.050	0.019	0.044	0.064	0.038	0.080
NGC 6946 Enuc. 6 K	0.063	0.025	0.051	0.090	0.064	0.112
NGC 6946 Enuc. 6 A†	0.080	0.036	0.097	0.043	0.033	0.081
NGC 6946 Enuc. 1 B	0.078	0.006	0.009	0.108	0.016	0.013
NGC 6946 Enuc. 2 A	-0.008	0.028	0.004	0.074	0.092	0.012
NGC 7793 Enuc. 1 D	-0.010	0.001	···	0.044	0.006	···

NOTE — † The aperture used for this star-forming region contained multiple smaller individual regions.
NOTE — ‡ The fractional contribution of the absolute value of the local background measurement to the aperture flux density.

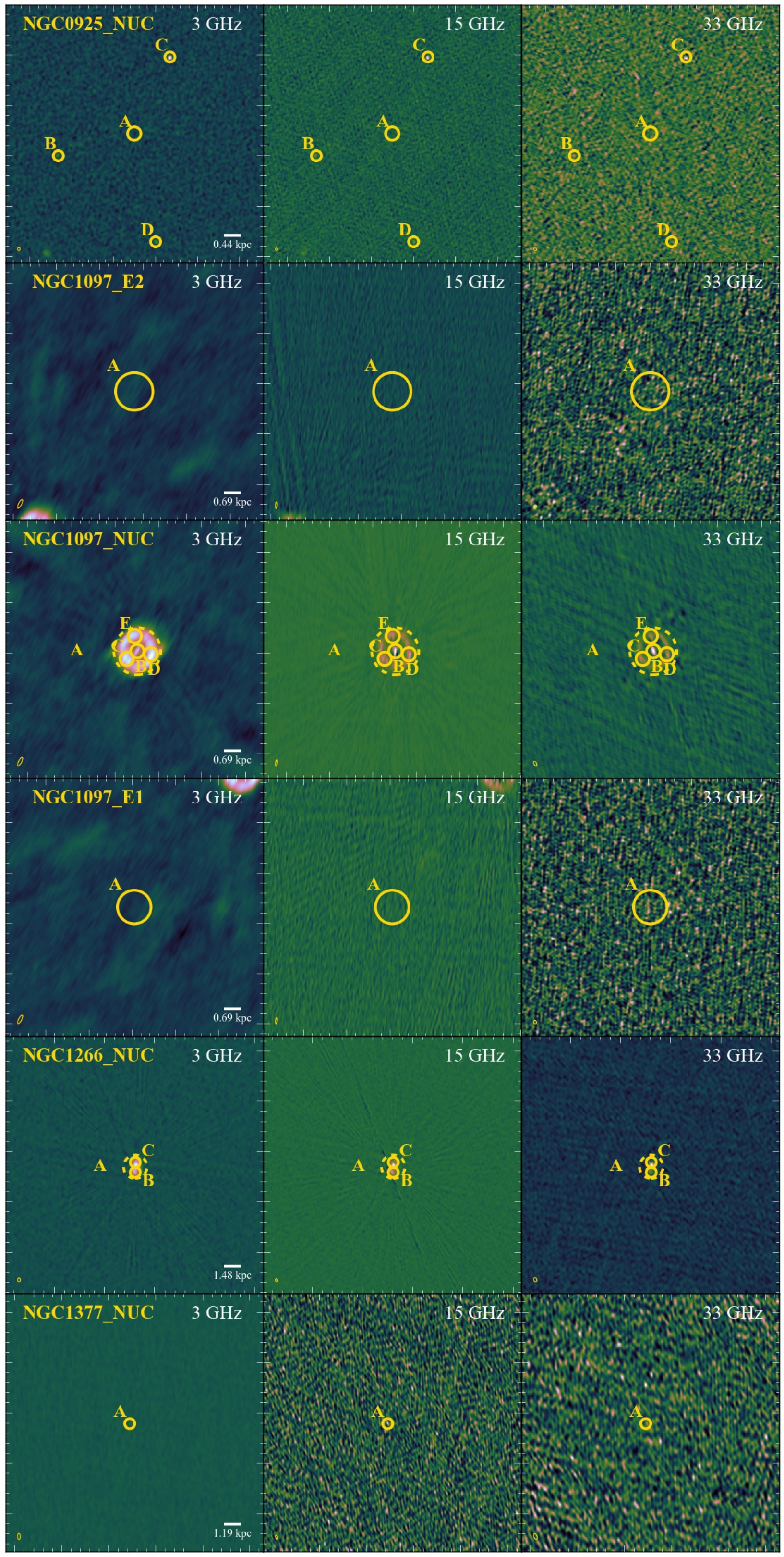

Figure 4.9: See description in Figure 4.1.

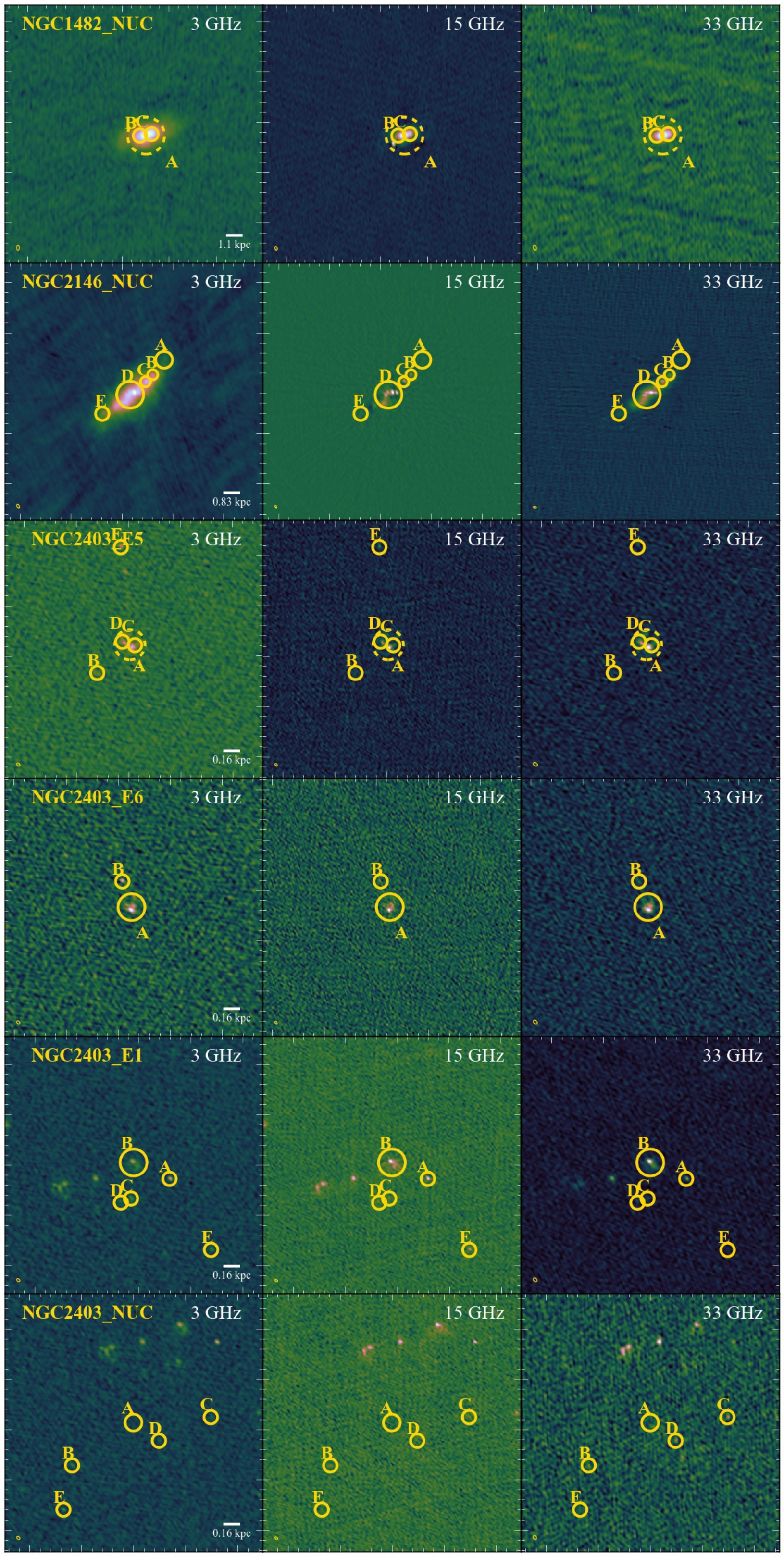

Figure 4.10: See description in Figure 4.1.

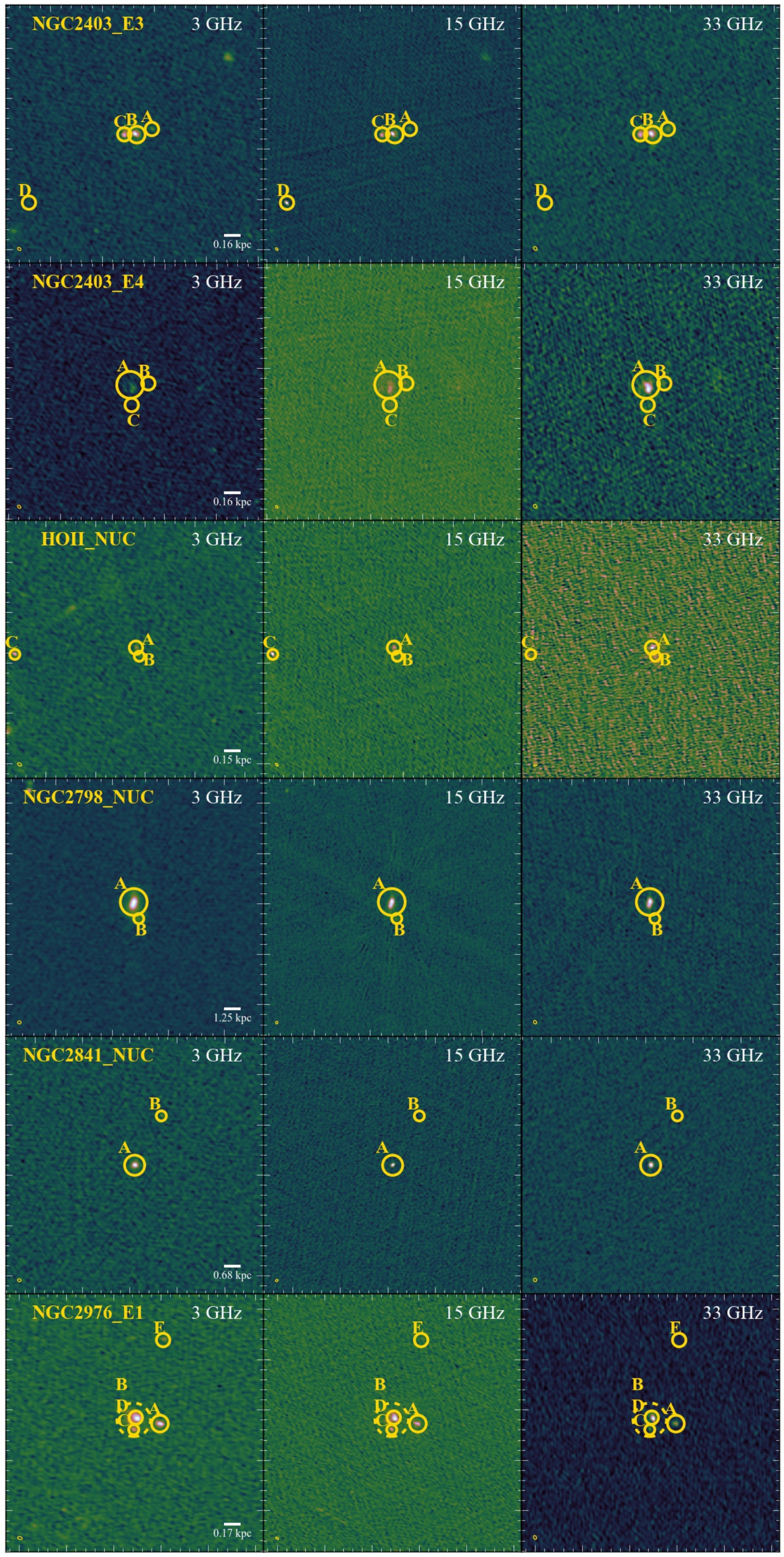

Figure 4.11: See description in Figure 4.1.

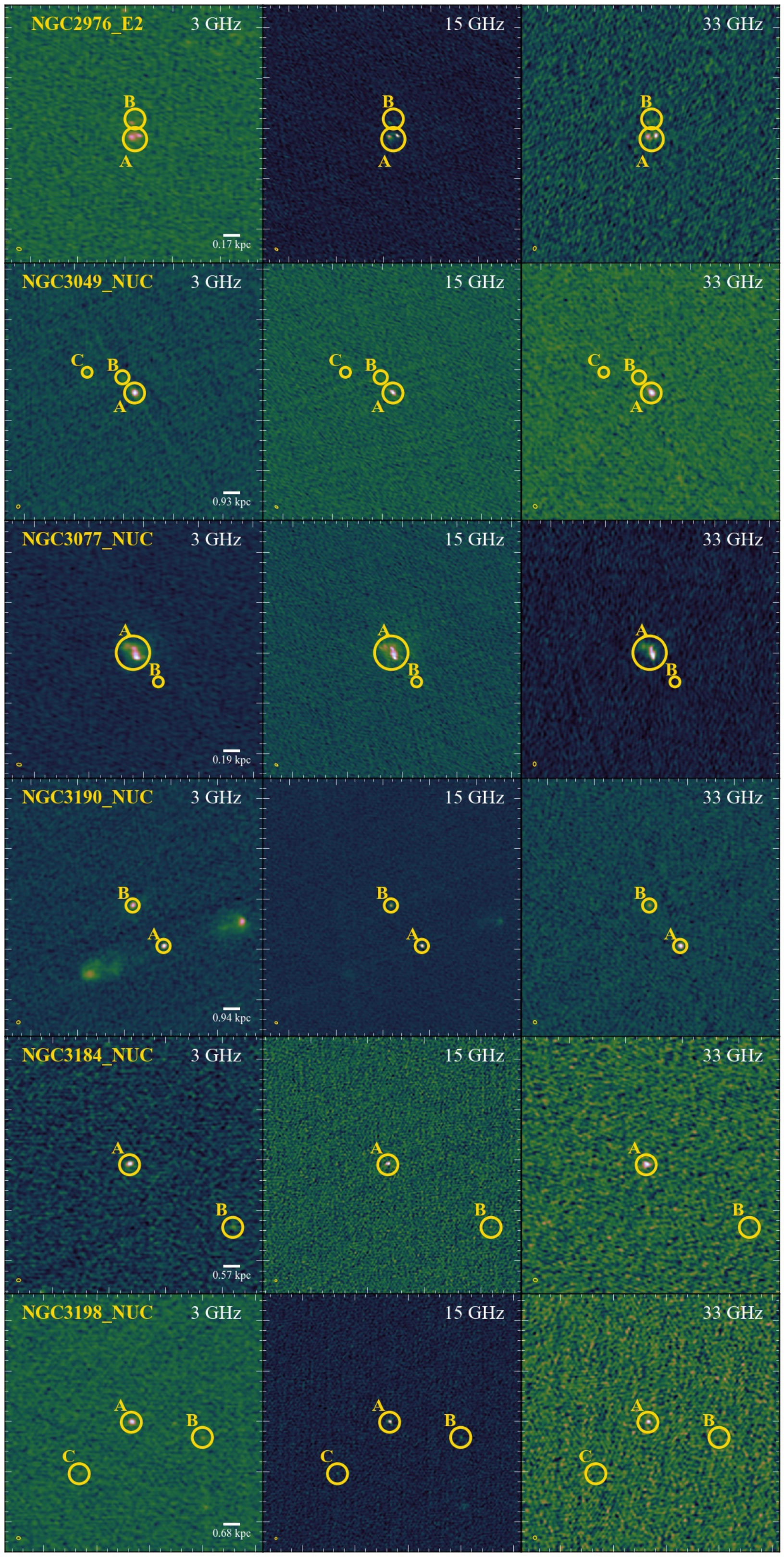

Figure 4.12: See description in Figure 4.1.

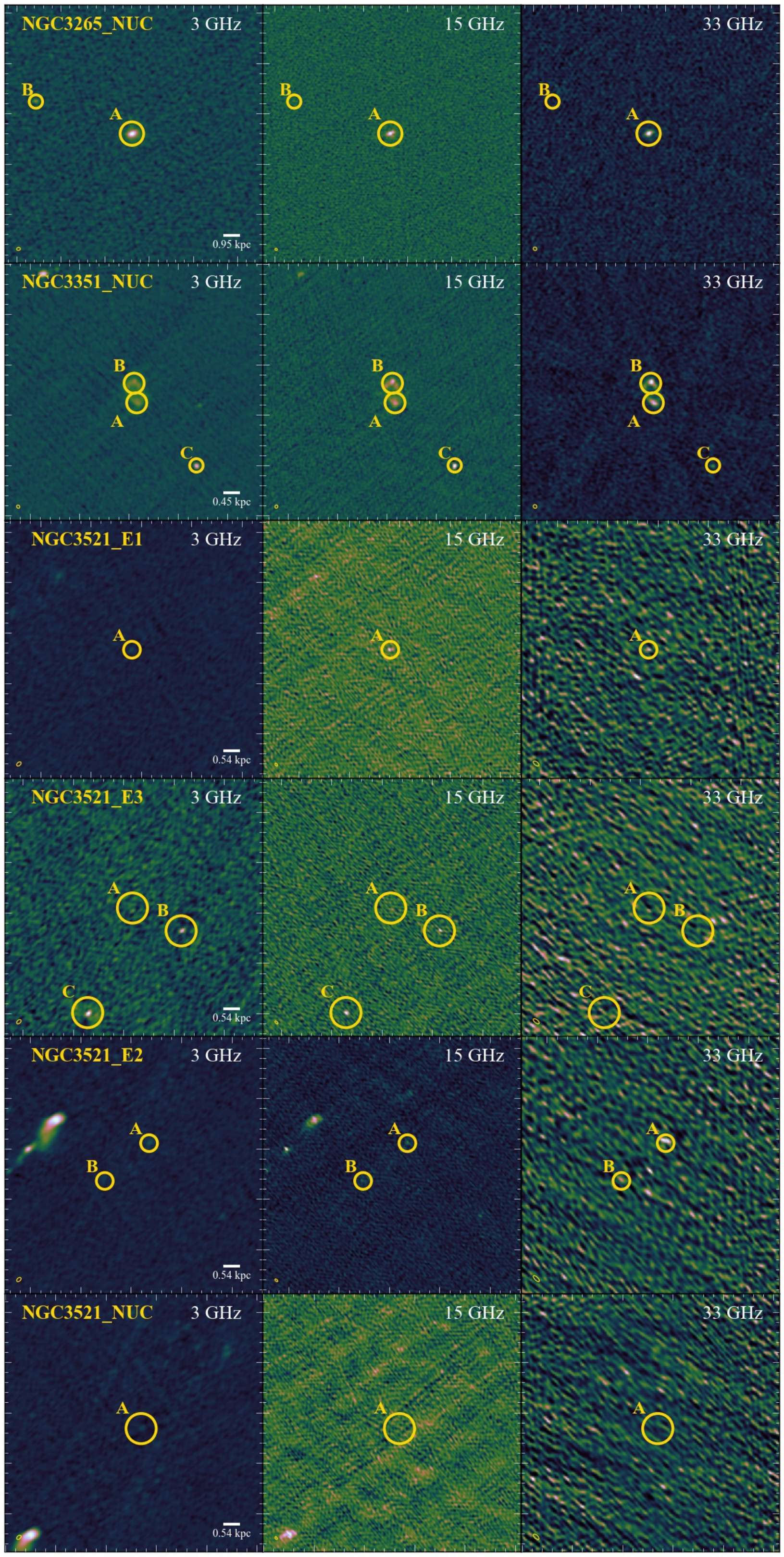

Figure 4.13: See description in Figure 4.1.

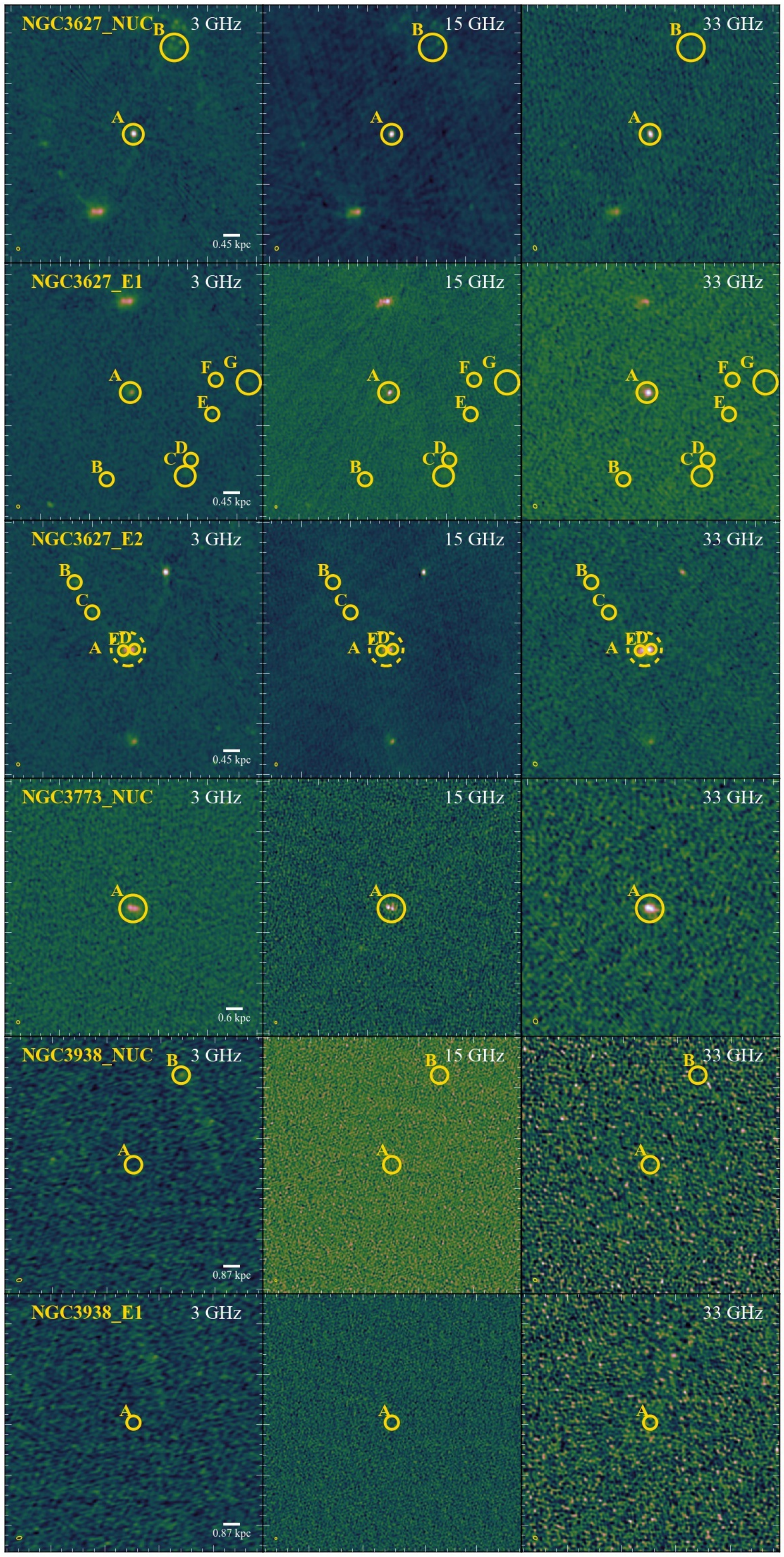

Figure 4.14: See description in Figure 4.1.

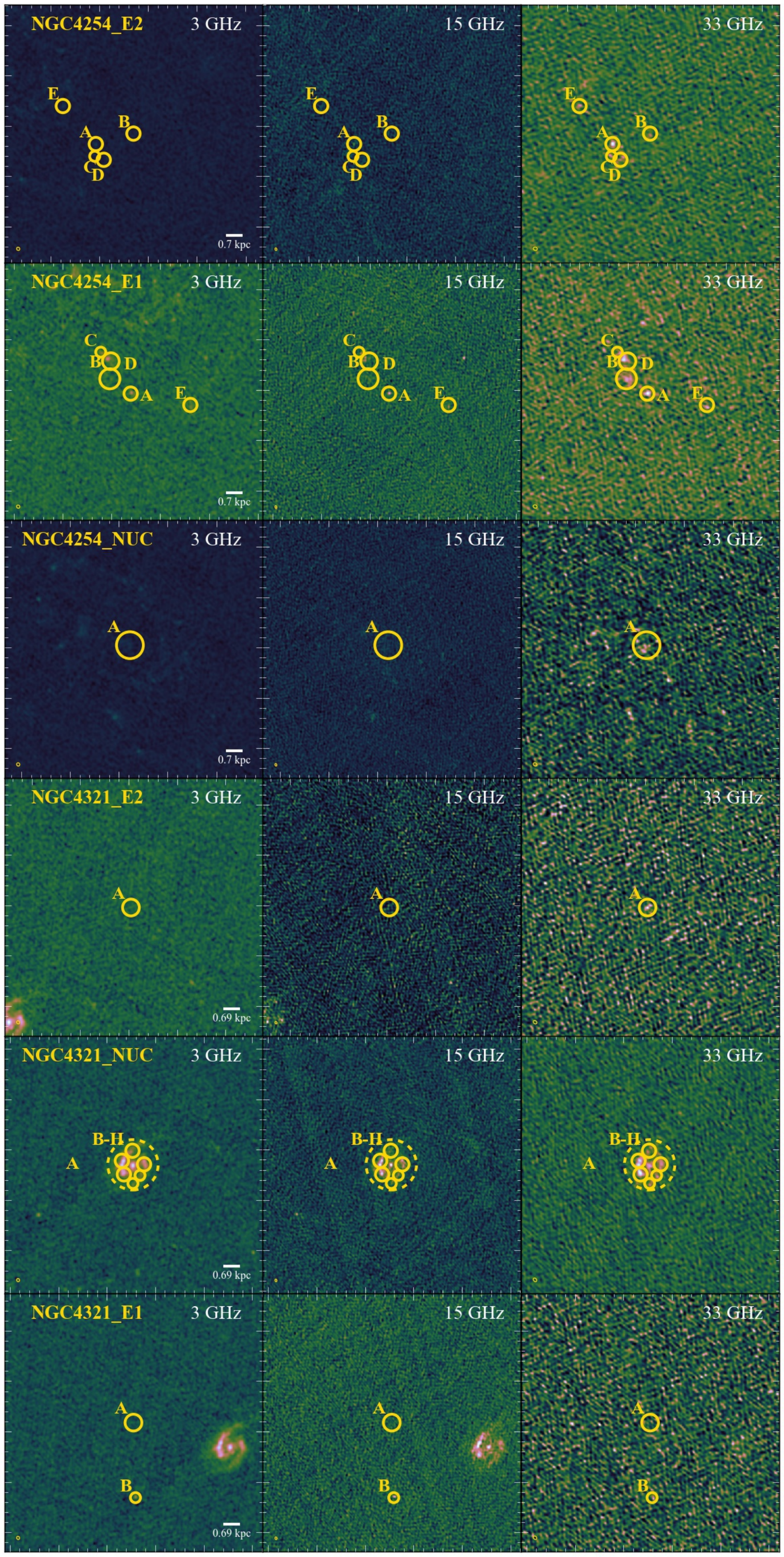

Figure 4.15: See description in Figure 4.1.

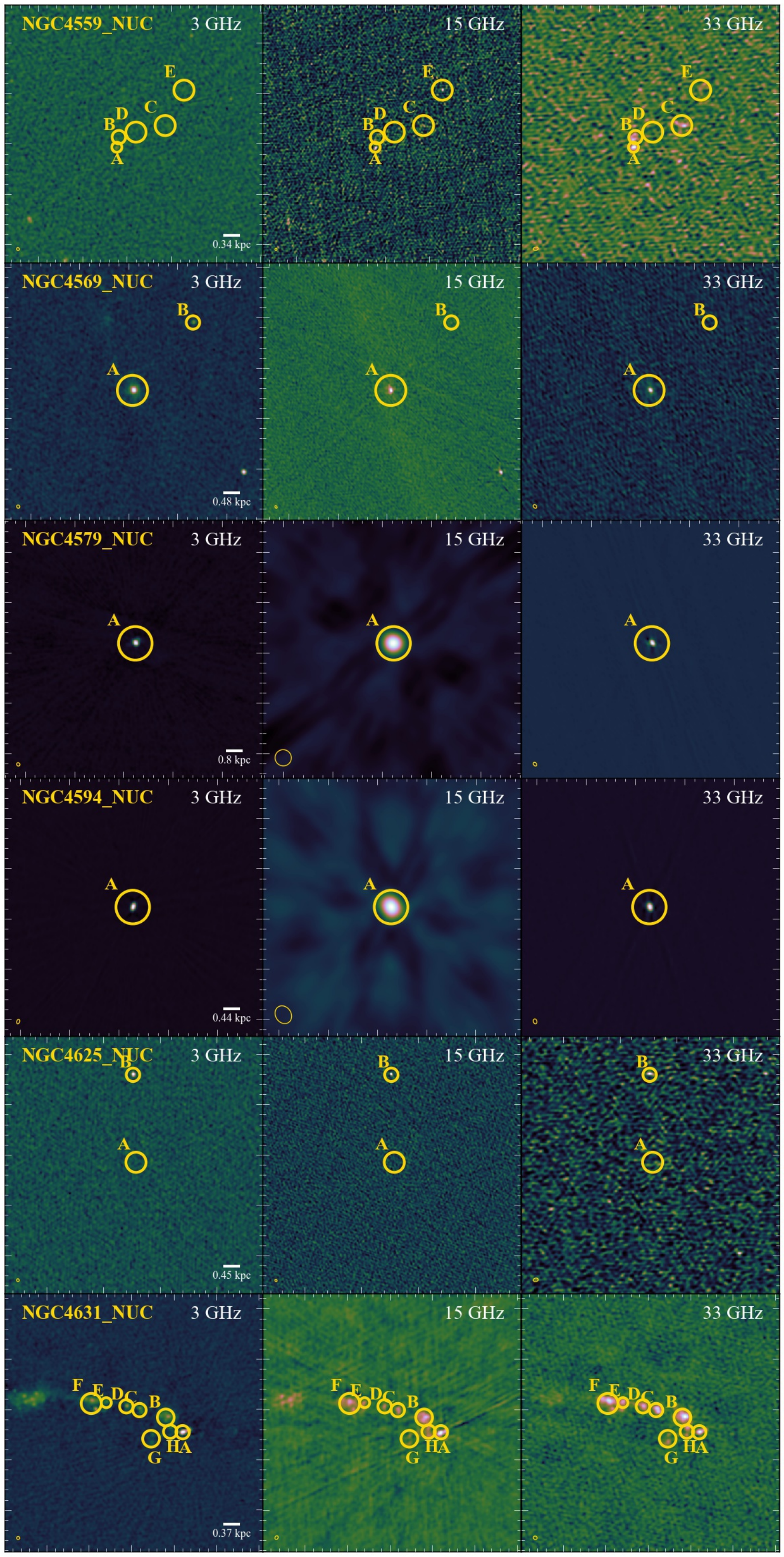

Figure 4.16: See description in Figure 4.1.

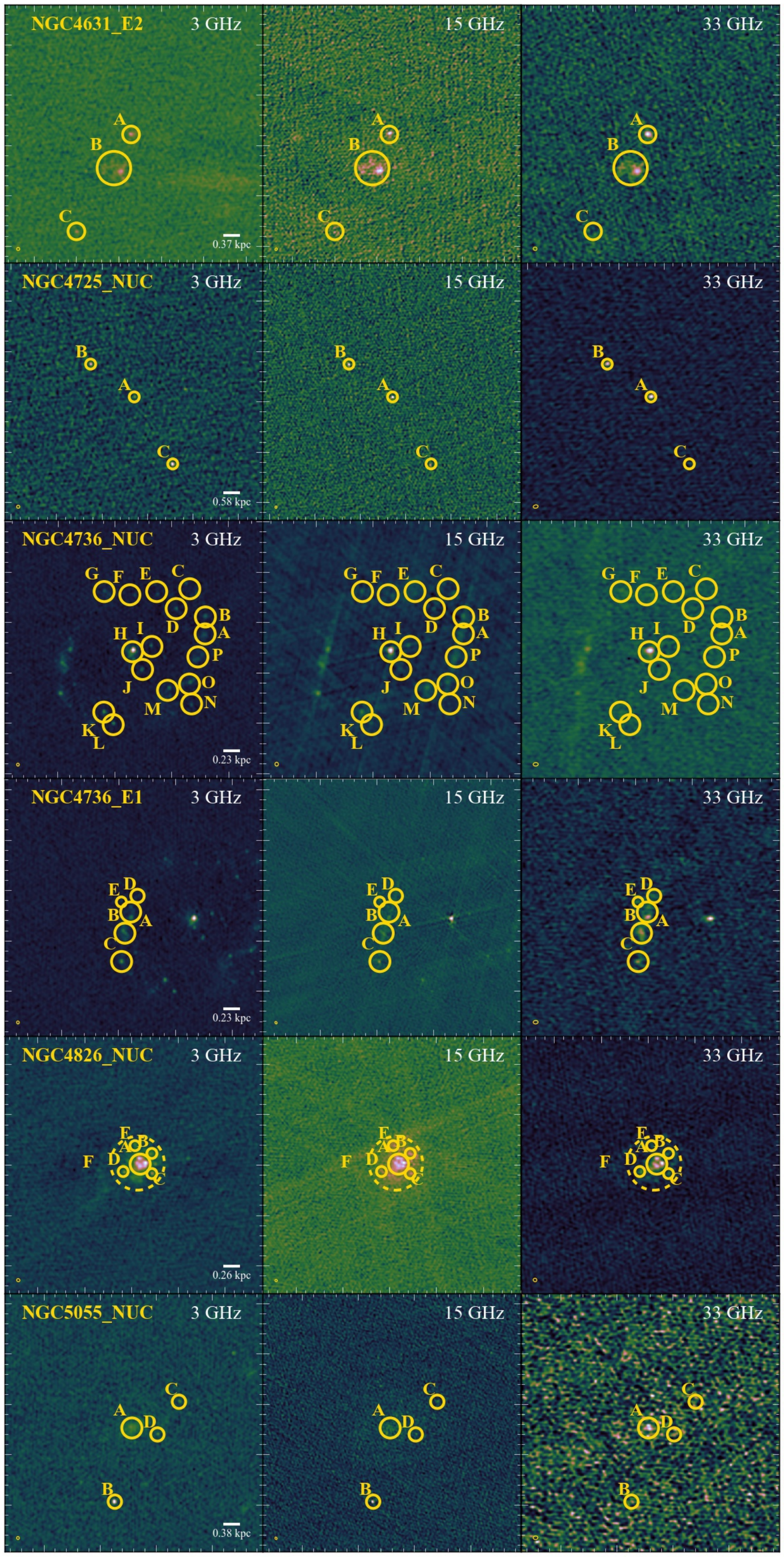

Figure 4.17: See description in Figure 4.1.

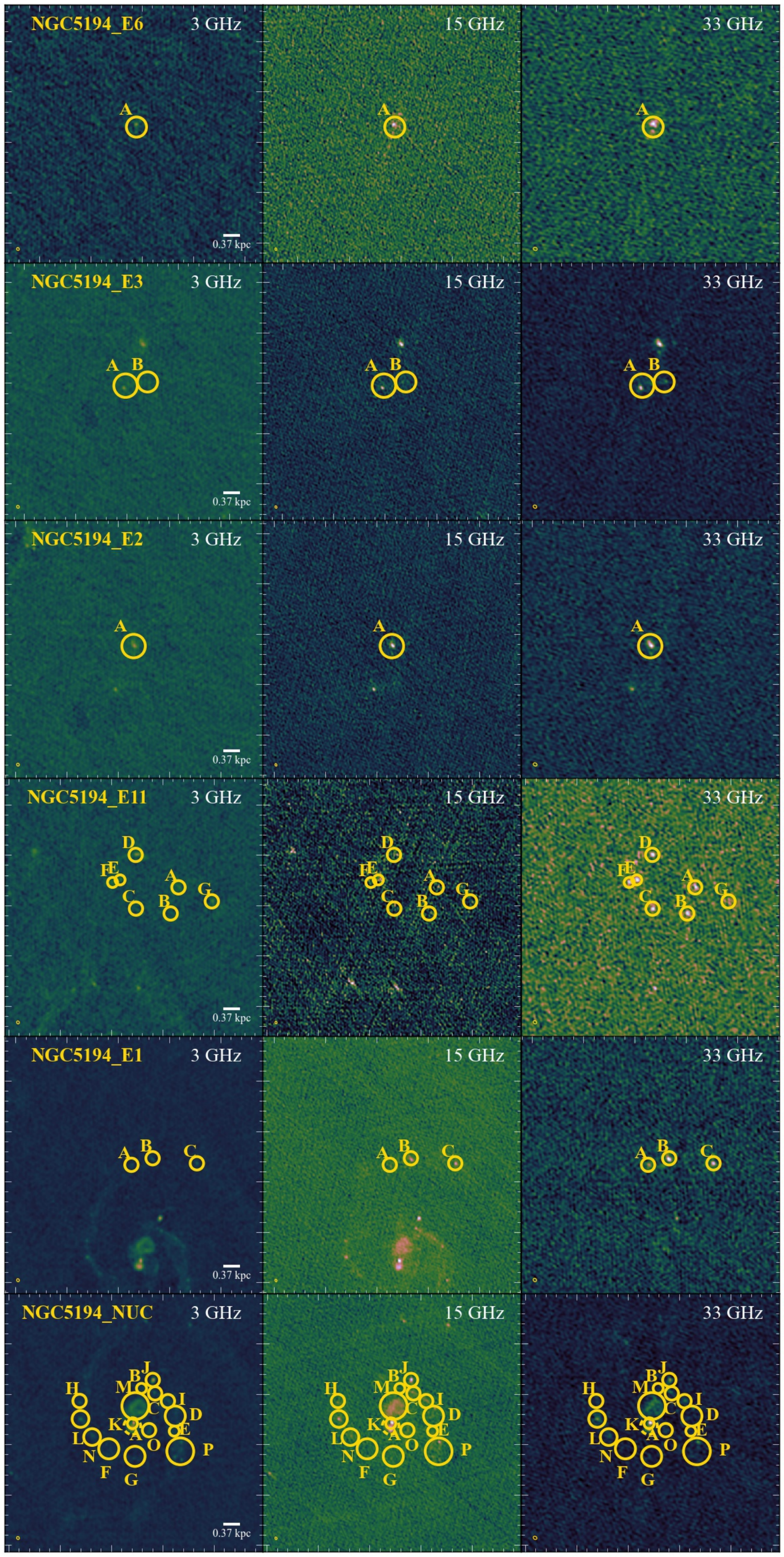

Figure 4.18: See description in Figure 4.1.

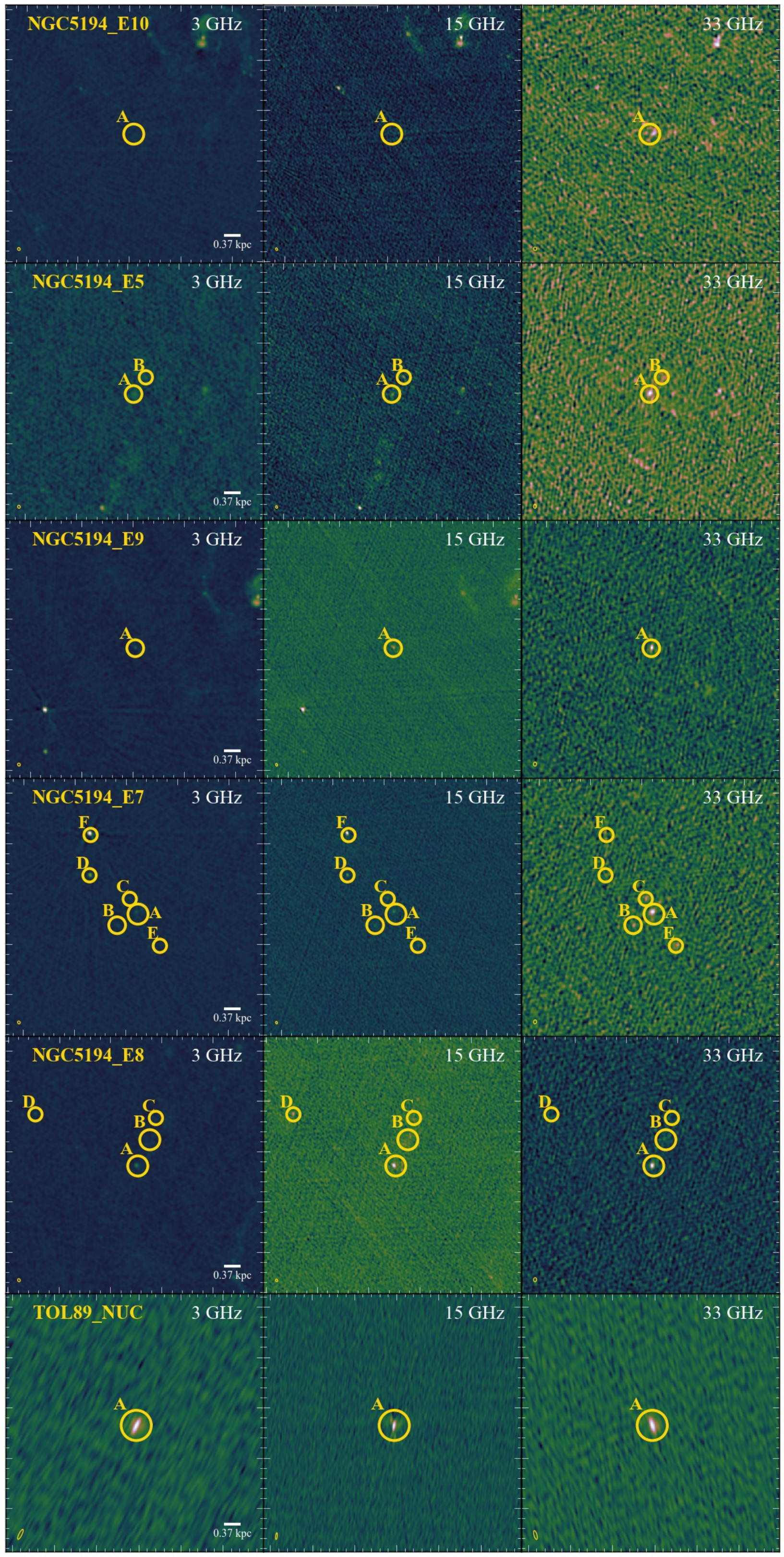

Figure 4.19: See description in Figure 4.1.

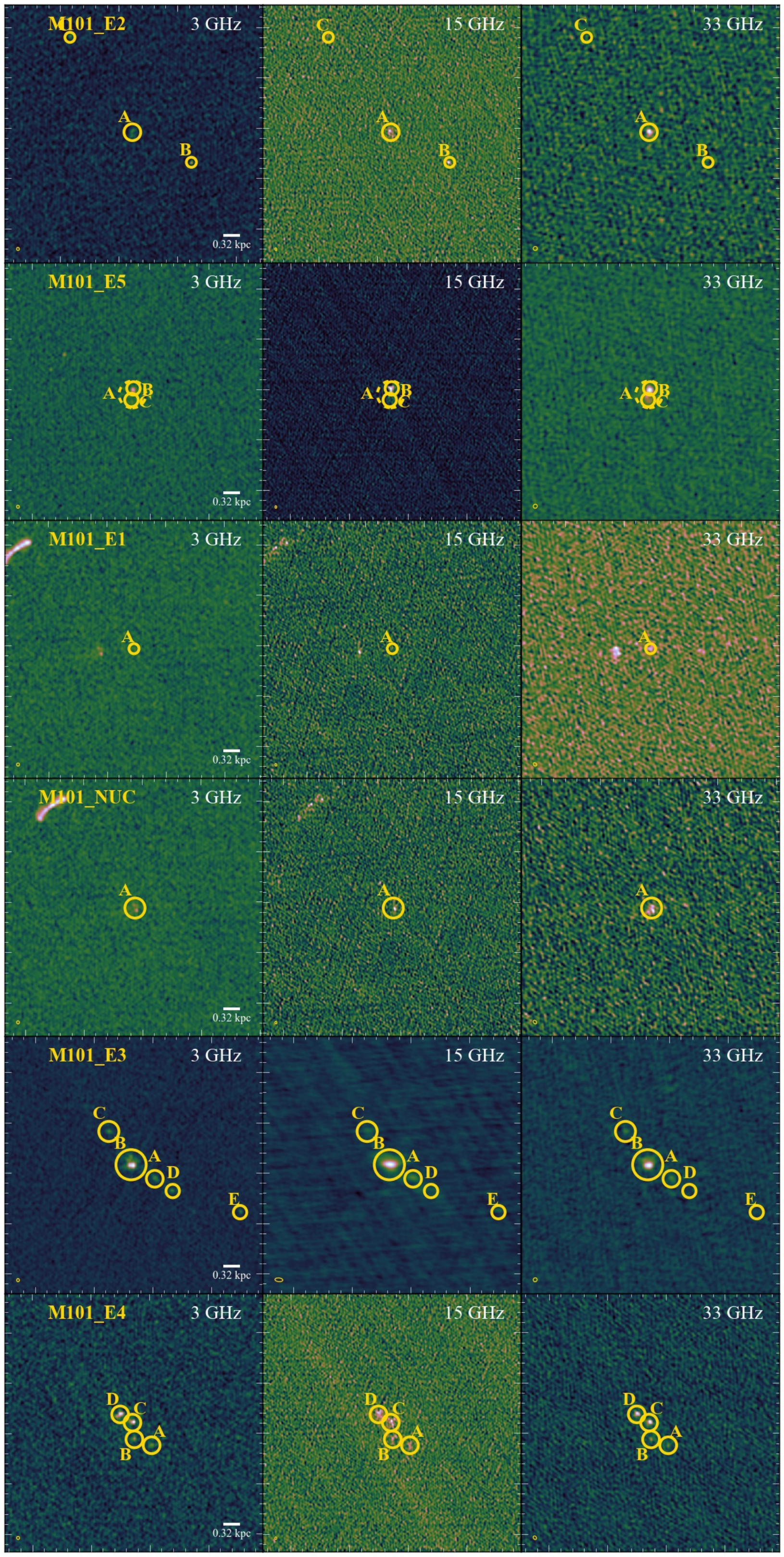

Figure 4.20: See description in Figure 4.1.

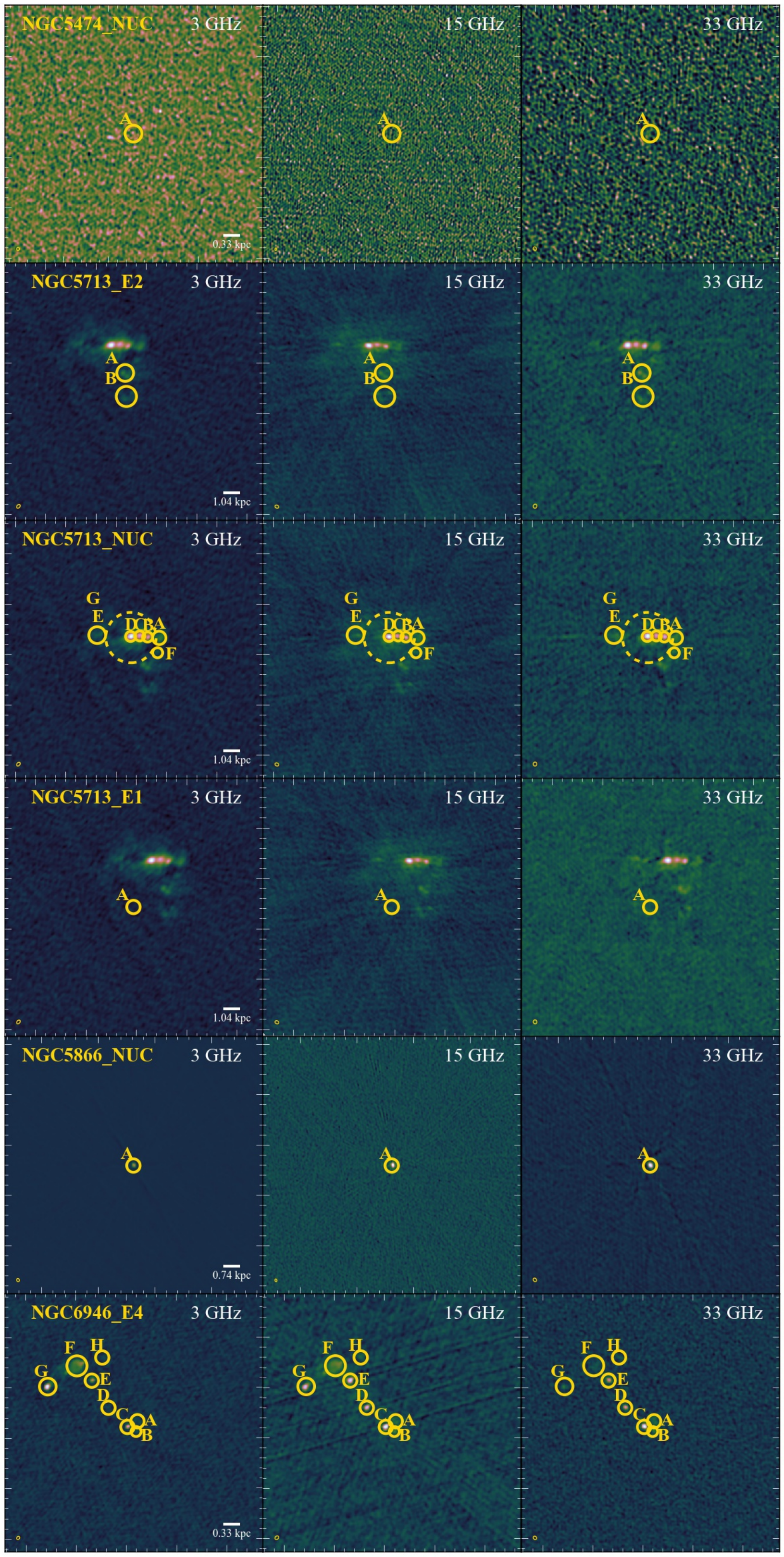

Figure 4.21: See description in Figure 4.1.

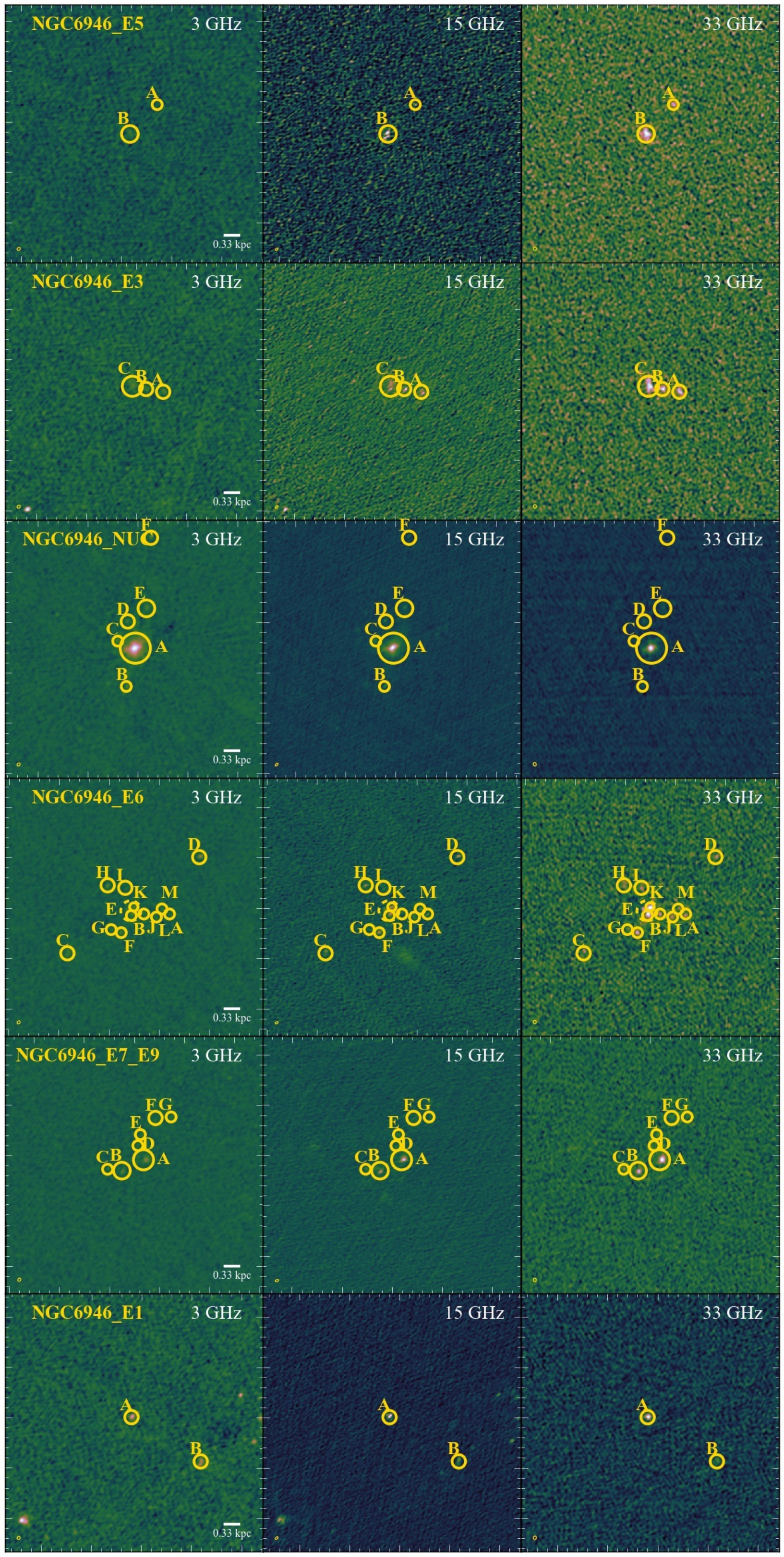

Figure 4.22: See description in Figure 4.1.

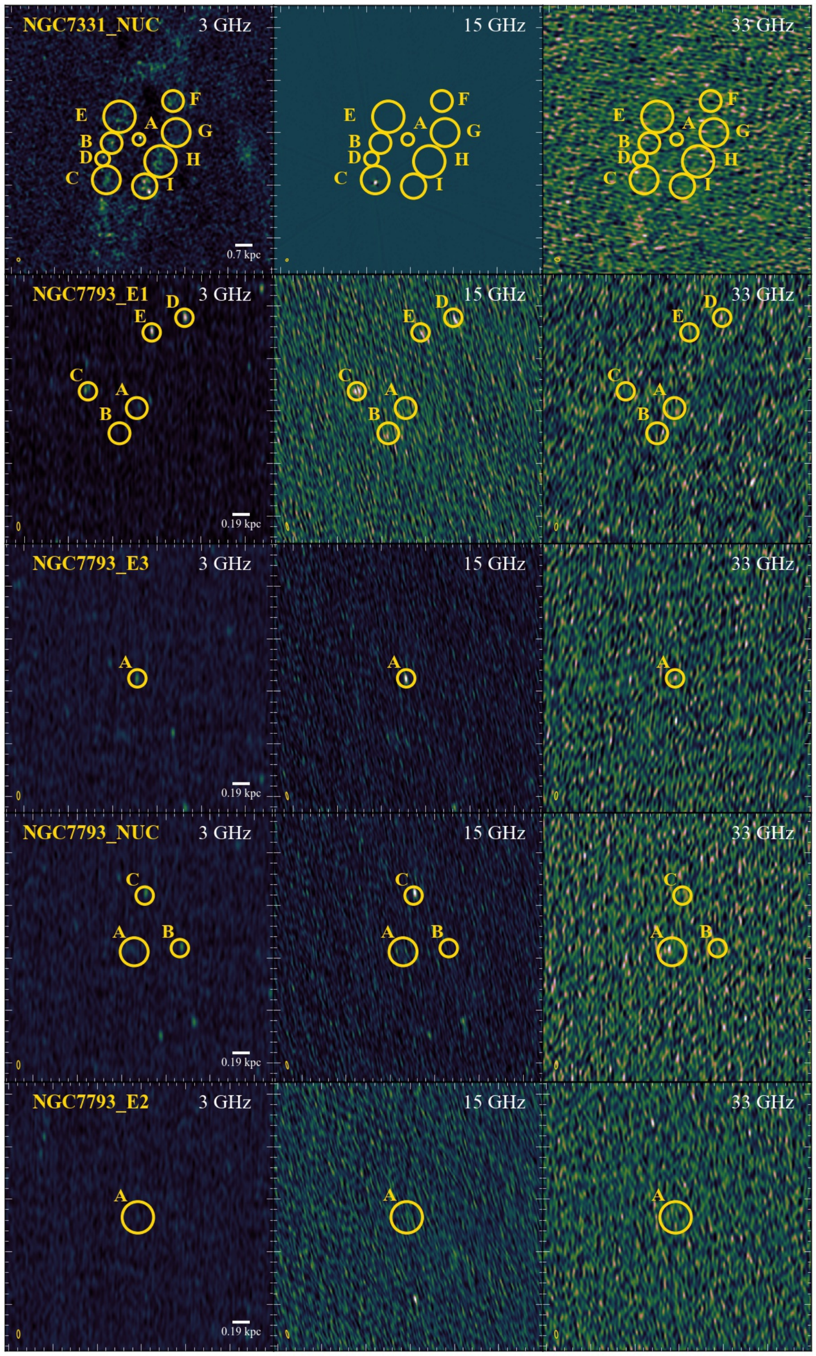

Figure 4.23: See description in Figure 4.1.

Chapter 5

Massive Star Cluster Formation and Destruction in Luminous Infrared Galaxies in GOALS II: A WFC3 Survey of Nearby LIRGs

5.1 Introduction

Star formation activity is observed across a large range of physical scales and interstellar medium (ISM) conditions: from dense, collapsing, pc-sized molecular clouds up to star-forming complexes found over kpc-scales across galactic disks (Kennicutt & Evans, 2012). Connecting star formation over these vastly different scales is essential to understanding how the observed global signatures of galaxy evolution emerge across cosmic time.

Recently, a number of surveys have found that high-redshift star-forming galaxies tend to display turbulent, clumpy disks with extreme star-forming clumps, stellar masses of $\sim 10^{7-8} M_{\odot}$ and sizes of $0.5 - 5$ kpc (Elmegreen et al., 2004, 2009; Daddi et al., 2010; Livermore et al., 2015). These masses are a factor of $\sim$ 100x the typical star-forming clumps observed in quiescent star-forming galaxies in the local Universe. These extreme stellar clumps give rise to super star clusters (SSCs) with masses which can reach $10^{6} M_{\odot}$; i.e., similar to the most massive known globular clusters and 1-2 orders of magnitude more massive than any young cluster found in nearby normal galaxies (Kobulnicky & Johnson, 1999; Whitmore et al., 2014). By contrast, normal star-forming galaxies contain hundreds of smaller mass HII regions (Cook et al., 2016), suggesting a fundamental shift in the way stars form and evolve in galaxies in the early Universe.

However, it is still unclear what the relative importance of both internal and external effects have on altering the universality of the observed properties of star clusters in galaxies. For example, are the characteristics of star cluster formation tightly related to their local environment? High-resolution hydrodynamic simulations of cluster formation show that strong stellar feedback can not only change the efficiency of star formation within giant molecular clouds (GMCs), but also alters the dynamical state of the cluster, and in some cases can disperse the cloud altogether (e.g., Portegies Zwart et al., 2010; Whitmore et al., 2010; Bastian et al., 2012; Fall & Chandar, 2012; Fouesneau et al., 2012; Chandar et al., 2015; Johnson et al., 2017; Li et al., 2017).

When representing the observed cluster initial mass function (CMF) as a Schechter function with a high-mass truncation, observations suggest that the truncation mass varies among different galaxy environments. Analysis of quiescent normal galaxies in the Legacy ExtraGalactic UV Survey (LEGUS) reveals strong evidence of a CMF with a power-law slope of ~ 2 and a characteristic truncation mass (M_c) of $\sim 10^{4-5} M_{\odot}$ (Adamo et al., 2017; Messa et al., 2018), while strongly interacting galaxies are associated with higher values of $M_c \sim 10^{6} M_{\odot}$ (Adamo & Bastian, 2015). Additionally, Bastian et al. (2012), Adamo (2015), and Hollyhead et al. (2016) have found evidence that the CMF varies *within* the disks of several nearby galaxies, showing that the inner-disk SSCs have a truncation mass which is $\sim$ 1.5x larger relative to the distribution of SSCs observed in their outer-disks.

Any turnover or truncation in the CMF may *also* be a reflection of cluster disruption triggered by internal or external mechanisms during the cluster evolutionary process (e.g. Whitmore et al., 2010, 2014). For example, the intrinsic shape and slope of both the cluster luminosity function (CLF) and the CMF as well as the star cluster age distribution have been found to depend directly on the intensity of cluster disruption (Gieles, 2009; Bastian et al., 2012). While Fall et al. (2005) and Whitmore et al. (2007) interpret the age distribution for clusters in the Antennae galaxies as evidence for mass independent disruption (e.g. a relaxation-driven cluster dissolution), Lamers et al. (2005), and Silva-Villa et al. (2014) have suggested that strong tidal forces (e.g., those found galaxy major mergers) and GMCs of high surface density are the dominant physical mechanism which disrupt clusters.

Luminous and Ultra-luminous infrared galaxies (LIRGs: defined as having IR luminosities $L_{IR} > 10^{11} L_{\odot}$; ULIRGs: $L_{IR} > 10^{12} L_{\odot}$) host the most extreme stellar nurseries in the local Universe. The activity in LIRGs is largely interaction triggered, with the progenitors observed to be gas-rich disk galaxies involved in primarily minor interactions (at the low luminosity end) or major merger events. This general framework is supported by theoretical simulations of gas-rich mergers which show the inward flow of star-forming gas via tidal and bar driven dissipation, and the final settling of mergers involving nearly equal mass progenitors into early-type galaxies (Barnes & Hernquist, 1992; Barnes, 2004; Hopkins et al., 2006). As such, LIRGs are the ideal laboratories for testing location-dependent cluster formation and disruption in extreme merger-driven environments; conditions which may be analogous to the star-forming environment of high-redshift galaxies.

To better understand cluster formation and evolution in LIRGs, we previously combined our HST F435W (B) and F814W (I) ACS/WFC data with far-UV ACS/SBC F140LP (FUV) data to age-date ~ 500 clusters in a combined sample of 22 LIRGs (Linden et al., 2017). Overall we find evidence of a steeper decline in the number of clusters per unit time as a function of increasing cluster age ($dN/d\tau \propto \tau^{-0.9}$ for $3 < \tau < 300$ Myr) relative to 'normal' galaxies, which is a further indication that clusters in massive mergers suffer infant mortality at a much more rapid rate than normal star-forming galaxies. A fundamental goal of the present paper is to investigate what role the host galaxy environment, and *localized* ISM conditions within individual LIRGs, play in defining the physical properties and the evolution of SSCs.

The paper is organized as follows: In §2, the sample selection, observations, and data reduction are described. In §3 our method for identifying clusters, and the manner in which the cluster ages and masses are determined is described. In §4 we discuss the completeness limits of our cluster sample. In §5, the age and mass functions are discussed within the context of lower luminosity star-forming galaxies and clusters found in both the inner and outer-disks of our galaxy sample. §6 is a summary of the results.

Throughout this paper, we adopt a WMAP Cosmology of $H_0 = 67.8$ km s^{-1} Mpc^{-1}, $\Omega_{\mathrm{matter}} = 0.308$, and $\Omega_\Lambda = 0.692$ (e.g., see Armus et al., 2009).

5.2 Observations and Data Reduction

Our 2017 study was limited by three issues: *(i)* the small field of view (FOV) of the SBC observations ($30'' \times 30''$: 25 times smaller than the WFC3 FOV) often limited us to clusters in the central regions of the galaxies in our sample; *(ii)* Our completeness-corrected cluster sample contained only the most massive clusters ($M \geq 10^5 M_\odot$)

in each galaxy; and *(iii)* age–extinction degeneracies were present for clusters within particular color ranges. Here, we present HST U- (F336W) band observations of all 10 $L_{\rm IR} > 10^{11.4} L_{\odot}$ LIRGs being observed by *JWST* as part of the ERS program *"A JWST Study of the Starburst-AGN Connection in Merging LIRGs"* and GTO campaigns. These new WFC3/UVIS observations provide vast improvements in sensitivity (~ 10 times) over prior *HST* detectors operating at 0.3μm, and combined with our pre-existing *HST* data (ACS/WFC F435W and F814W data), will provide high-resolution maps of the distribution of star clusters over the entire extent of each LIRG. Further, the F336W filter provides a much improved lever arm for age-dating clusters relative to the F140LP filter, and will allow us to break the reddening–age degeneracy and thus more accurately measure (to within 0.1-0.2 dex in $\log(\tau)$) cluster ages and cluster masses.

Table 5.1: Galaxy Sample Properties

Galaxy	RA	Dec	D_L (Mpc)	σ_{D_L}	MS	Log(LIR)	Log(M_*)	SFR	Log(sSFR)	IR/UV
Arp220	15h34m57.255s	+23d30m11.30s	81.93	5.74	5	12.28	11.06	327.74	-8.55	813.3
IC1623	01h07m47.180s	-17d30m25.30s	84.40	5.93	3	11.71	11.21	94.09	-9.24	11.2
NGC3256	10h27m51.270s	-43d54m13.49s	45.66	3.21	3	11.64	11.06	76.46	-9.17	71.6
NGC6240	16h52m58.871s	+02d24m03.33s	108.67	7.61	4	11.93	11.59	148.44	-9.42	87.1
NGC7469	23h03m15.623s	+08d52m26.39s	66.68	4.68	2	11.65	11.38	80.26	-9.48	20.6

[a] An estimate for the SFR of IRAS 14378-3651 is taken from Strum et al. (2011)
[b] All data for Mrk231 is taken from U et al. (2012)
[c] The data for all remaining sources is taken from Howell et al. (2010)

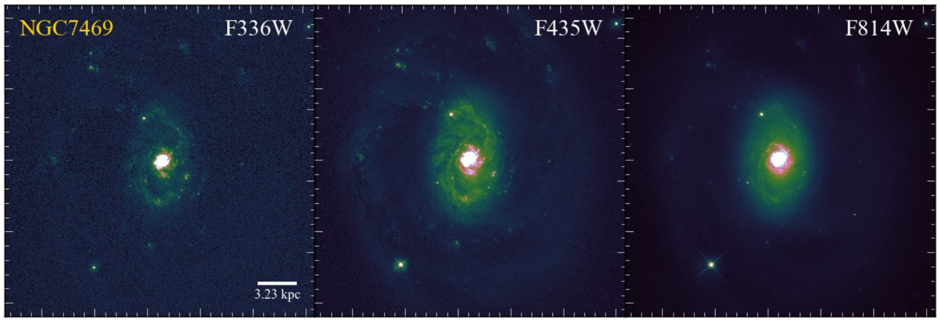

Figure 5.1: A comparison of *HST* WFC3/UVIS F336W image of NGC 7469, relative to archival ACS/WFC F814W and F435W images from Evans et al. in prep. Approximately 200 star clusters are detected at a S/N > 5 in all bands, and a de-convolved FWHM < 2 pixels. These images demonstrate our ability to detect and characterize star clusters throughout the central regions, disks, and extended tidal features of the galaxies in our sample.

The F336W images were obtained from August - November 2018 (PI: A. Evans; PID 15472). Each galaxy was observed with four dithered exposures in ACCUM mode, and when possible, placed at the center of the UVIS2 chip, due to the increased sensitivity at UV wavelengths relative to UVIS1. The approximate integration times for each galaxy is 41 minutes. The data were reduced with the Multidrizzle software provided by STScI to identify and reject cosmic rays and bad pixels, remove geometric distortion, and finally, combine the resulting mosaics with our pre-existing ACS/WFC F435W and F814W observations (see Figures 5.1, 5.12, 5.13, 5.14, and 5.15). The final pixel scale of our WFC3 images is 0.0396”$/pix$. The ACS/WFC and WFC3/UVIS cameras have comparable fields of view (202"x202" and 162"x162" respectively), and cover sufficient area to enable observations of these LIRGs without the need to mosaic.

Finally, to understand the impact of combining results from galaxies which span a factor of ~ 2 in distance, we performed simulations of cluster blending: by progressively smoothing *HST* WFC3 archival imaging of the Antennae Galaxies ($D_{\rm L} = 22$ Mpc: Whitmore et al. (2010), re-identifying star-clusters, and re-computing the luminosity function, we determined that blending begins to hamper our ability to accurately measure cluster properties (age, mass, extinctions), and thus determine the true slope, α, of the underlying cluster mass function, at smoothing lengths of $\geq$ 5 pixels (i.e., $\Delta\alpha > 0.2$). This test demonstrates that clusters can be individually detected and their physical properties can be accurately recovered in galaxies out to a distance of $\sim$ 100 Mpc. Therefore we limit our cluster analysis in this paper to 5/10 systems which have $D_L < 100$Mpc, such that we can be confident our results are not biased towards large, unresolved, complexes of multiple star clusters. The overall properties of these 5 systems are given in Table 5.1.

5.3 Cluster Identification and Model Fitting

Table 5.2: Cluster Detection Statistics and Overall Properties

Galaxy	N_{det}	N_c	M_U Peak	t_c	σ_{t_c}	M_c	σ_{M_c}	A_V	σ_{A_V}
Arp220	108	46	25.29	8.41	0.37	5.78	0.84	0.6	0.59
IC1623	453	180	24.84	6.94	0.56	5.20	0.73	0.5	0.59
NGC3256	1082	549	24.52	8.06	0.89	5.27	1.08	0.7	0.89
NGC6240	141	87	24.96	8.26	0.45	5.72	0.90	0.5	0.74
NGC7469	383	165	24.71	7.61	1.04	4.99	0.84	0.5	0.74

Star clusters in all three bands were selected using the program SExtractor (Bertin & Arnouts, 1996). The identification of clusters and the extraction of photometry is performed after a diffuse background subtraction is applied to each image. This subtraction is described in detail in Linden et al. (2017), and is designed to remove starlight which is unassociated with the compact sources identified in each galaxy. Cluster photometry across all background-subtracted images was then calculated using the IDL package APER (originally modified from DAOPHOT). We used an aperture of radius 3.0 pixels, with an annulus from 4-5 pixels to measure the local background surrounding each cluster. Aperture corrections were calculated based on the flux calibrations of unresolved sources by Sirianni et al. (2005). We additionally applied a correction for foreground Galactic extinction, using the Schlafly & Finkbeiner (2011) dust model combined with the empirical reddening law of Fitzpatrick (1999) available through the NASA Extragalactic Database (NED).

In the process of doing photometry, we also remove sources with a signal-to-noise ratio S/N$<$ 3 and which are not detected in all three filters. In total we extract photometry for 2167 cluster candidates identified in 5 LIRGs. We then used ISHAPE (Larsen, 1999) to measure the 2-D FWHM for all remaining sources by de-convolving the HST instrumental point spread function with a King profile (King, 1966). We find that a cut of 3 pixels FWHM (corresponding to an average cluster size of $R_{eff} \sim 22$ pc) effectively removes extended sources in both the nearest and furthest galaxies in the sample. This value is consistent with the upper-end of sizes observed for open star clusters in the Milky Way, as well as simulations of star cluster formation in dwarf starburst galaxies (Lahén et al., 2020). A total of 1027 confirmed clusters across all 5 LIRGs meet the above criteria, and their bulk properties are given in Table 5.2.

For all confirmed clusters, the measured 3-band fluxes (given for each cluster in Table 5.3) were compared with a library of evolutionary simple stellar population

(SSP) models that were computed using the isochrone synthesis code of Bruzual & Charlot (2003), hereafter referred to as BC03. This code computes the evolution of an instantaneous burst based on a Kroupa IMF and the (e.g., Bertelli et al., 1994) stellar evolution models over an age range of 1 Myr to 10 Gyr. The choice of these models also ensures we can make consistent comparisons with our 2017 results, and that we do not introduce any systematic bias by adopting different SSP model libraries. Further, it has been shown that BC03 models are a better fit to the data relative to the Leitherer et al. (1999) models which have a large red loop for ages $\sim 5-15$Myr, which does not agree with the data (Whitmore & Zhang, 2002). We also choose to adopt a solar metallicity, as suggested for LIRGs by Kewley et al. (2010), and a Calzetti extinction law. The total attenuation of the stellar continuum, $R_V = A(V)/E(B-V)_* = 4.05 \pm 0.8$, is calibrated specifically for starburst galaxies and differs from the typical Milky Way value of $R_V \sim 3.1$ (Calzetti et al., 2000). It has been shown empirically that clusters and HII regions are more heavily attenuated than the underlying stellar continuum, due to the fact that these objects are often found near dusty regions of ongoing star formation (Calzetti et al., 1994).

By adopting a Monte-Carlo approach, we can represent the errors in our model as the full width of the marginalized posterior distribution functions for each derived parameter. In the Appendix we give an example of our model-fitting routine for one cluster in NGC3256, chosen to demonstrate the ability of our model to accurately recover the properties of a young, moderately extincted, $10^4 M_\odot$ cluster (i.e., a prototypical degenerate case for our previous F140LP observations). From Figure 5.16 it is clear that the resulting 1σ errors are within 0.2 dex, and as described above, this is crucial for accurately recovering the true age and mass functions for each system.

Finally, in order to make detailed spatial comparisons of clusters at different radii we adopt a similar methodology to Linden et al. (2019), to compute the de-projected galactocentric radius of each cluster relative to the optical center of each LIRG. We then categorize star clusters in two regimes: those that fall within the mid-infrared (MIR) core of the galaxy (as measured with Spitzer: see Díaz-Santos et al., 2010), and those that fall outside of the MIR core. This is done such that we can compare our results directly the spatial studies of SSCs presented in Hollyhead et al. (2016) and Messa et al. (2018), and test whether or not the merging environment of LIRGs enhances the relative differences in M_c and overall cluster disruption observed for the inner and outer-disks of nearby normal galaxies.

5.4 Mass-Age Diagram and Completeness

Figure 5.2 shows the derived age and corresponding mass of each cluster identified in the sample, and the corresponding values for each cluster are given in Table 5.4. An immediate observation one can make is the lack of lower-mass ($\leq 10^4 M_\odot$) clusters with ages $\geq$ 100Myr. This is primarily due to the fact that clusters dim as they age and eventually become fainter than our UV detection limits. We also note the large number of clusters seen with ages below 10 Myr over the full range of masses. Although the cluster fitting method can create some observed structure in the mass-age diagram, it is unlikely to do so over all masses at young ages. In particular the lack of clusters with ages of $\sim$ 15 Myr is a common feature of model-derived mass-age diagrams of star clusters in galaxies (Gieles et al., 2005; Goddard et al., 2010).

In order to determine the completeness limit of the cluster sample, we used a similar prescription to Linden et al. (2017), and set the limit for each galaxy as the magnitude at which 50% of the clusters are detected at B and I, but are missed at U-band The magnitude distributions for each band are corrected for foreground galactic extinction, and spatially matched to the FOV of ACS/WFC. All 5 LIRGs in the sample span a large range of observed cluster magnitudes ($M_U = -7 \sim -17$

mag, with a median of $M_U = -10$ mag), and have a mean completeness of $M_U \sim -8$ mag. We emphasize that this 50% limit for the sample is not a strong function of the distance to any galaxy. Finally, to minimize the contribution of very luminous clusters in LIRGs with a small number of confirmed SSCs, we calculate a cluster-weighted mean completeness limit for the full sample of 5 LIRGs, and find that the mean shifts only slightly to $M_U = -8.5$. Relative to the cluster sample in Linden et al. (2017) we observe clusters which are an order of magnitude fainter across all age ranges, and thus we are able to probe the cluster mass function over 4 full dex in mass.

By applying this completeness limit to the BC03 model we can define regions of this parameter space (both as a function of cluster ages over a mass range and masses over an age range) where we are observationally complete and thus working with a mass-limited sample of clusters. Mass-limited cluster samples have the advantage over luminosity-limited samples because they recover the underlying shape of the age distribution, and are thus not affected by the distance to each galaxy. Importantly, we also find that the U-band completeness limit is brighter for inner-disk clusters ($M_U = -9.3$) relative to the outer-disk cluster sample. Evaluating differences between the two samples at this more conservative limit will allow for a one-to-one comparison of the resulting SSC distribution functions.

The two cuts were selected to sample distinct regions of the mass and age distribution for which we could maintain completeness. We define Region 1 to be:

$$4.5 < log(M/M_{\odot}) < 8 \tag{5.1}$$

$$6 < log(\tau) < 8.5 \tag{5.2}$$

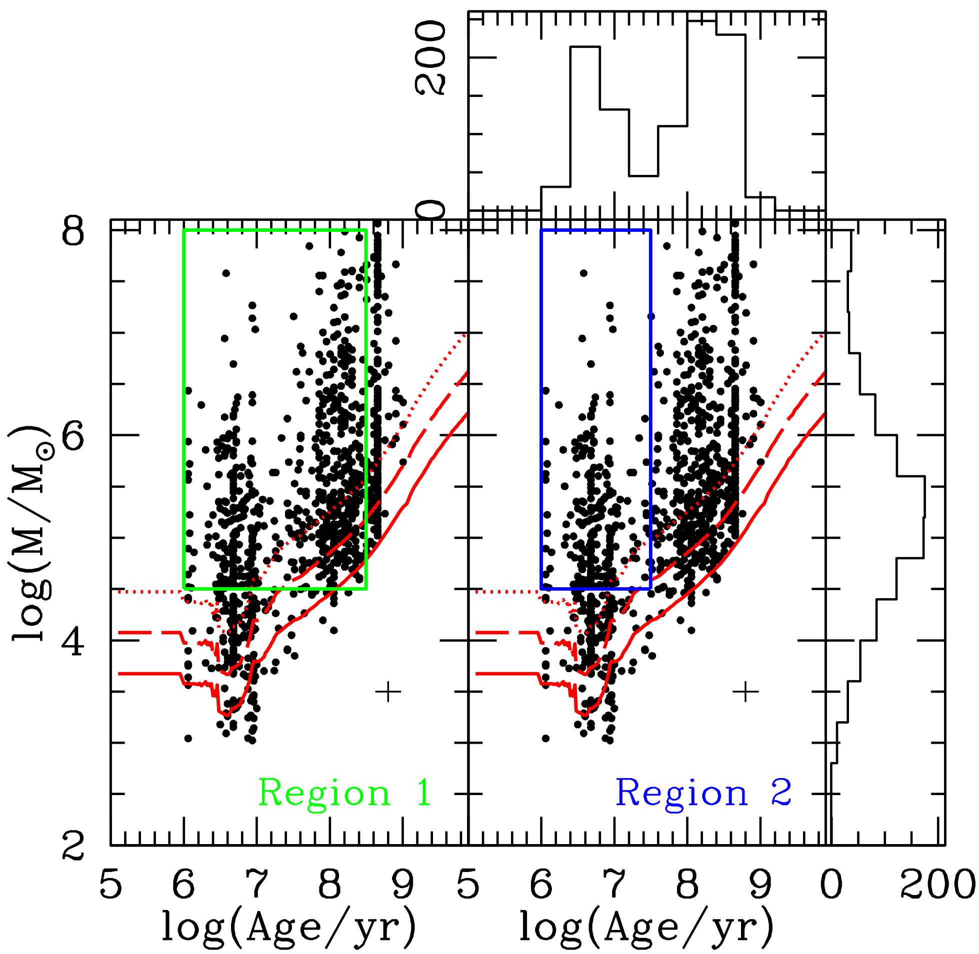

Figure 5.2: The mass, age distribution of all 1027 clusters found in our LIRG sample. The solid, dashed, and dotted red curves represent mass-age tracks produced from the BC03 model with an input of $M_U = -8.5$, $M_U = -9.5$, $M_U = -10.5$ for the 50%, 75%, and 100% completeness limits respectively. The green box in the left panel represent Region 1, and is used for the mass-age cuts applied when analyzing the cluster age distribution. The blue box in the middle panel represents Regions 2, and is used for the mass-ages cut applied when analyzing the cluster mass distribution. The histograms show the distribution of cluster ages and masses for the full sample. The cross on the bottom right of each panel represents the median errors in cluster age and mass bootstrapped from our model.

Region 2 to be:

$$4.5 < log(M/M_{\odot}) < 8 \tag{5.3}$$

$$log(\tau) < 7.5 \tag{5.4}$$

Region 1 is chosen to match, as closely as possible, the age and mass limits from Fall et al. (2005), allowing us to make accurate comparisons to the cluster population of the Antennae Galaxy. Region 2 is chosen to sample the young ($\tau \leq 10^{7.5}$) clusters in our sample within the completeness limit. When analyzing Regions 1 and 2 we exclude the largest mass bin of $log(M/M_{\odot}) = 8.0$. These very high masses are most likely the result of either an imperfect extinction correction or multiple very compact star clusters in close proximity appearing as a single star cluster at the resolution of these images. We note that while clusters of these masses are rare, Bastian et al. (2013) found several clusters in NGC7252 with masses greater than $10^7 M_{\odot}$, including one cluster with a total mass of $\sim 10^8 M_{\odot}$.

5.5 Discussion

After determining ages, masses, and extinctions for the entire cluster sample we directly compare these distributions with those of nearby normal and interacting galaxies. We focus on the interpretation of the derived cluster age distribution and mass functions for both the individual systems and the sample as a whole. Further, we will analyze the inner- and outer-cluster cluster distribution functions for each system. Ultimately, we discuss to what degree the differences observed in our cluster population can be attributed to the extreme star-forming environment unique to LIRGs in the local Universe.

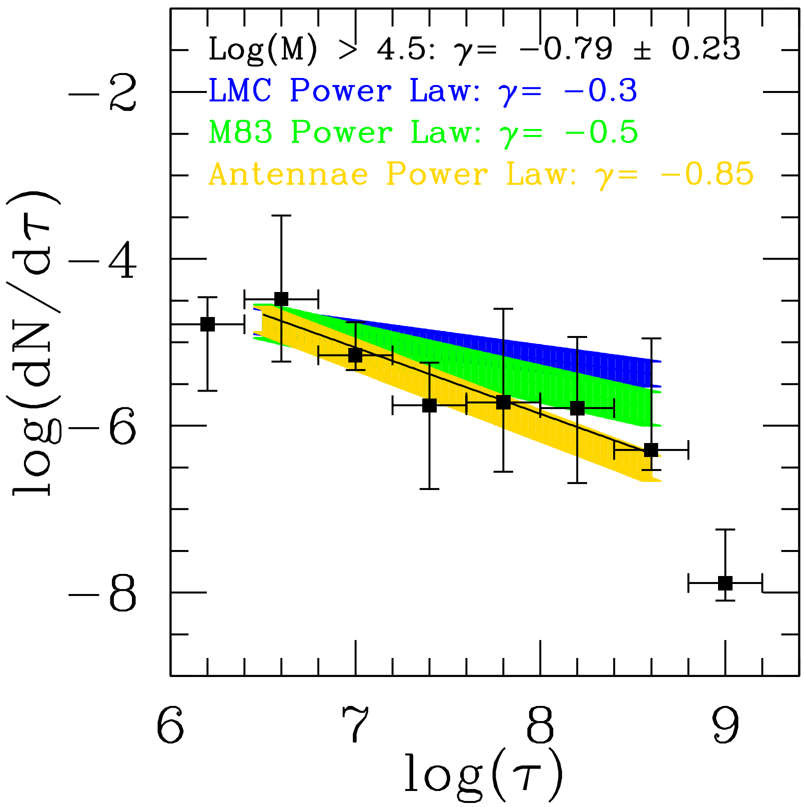

Figure 5.3: The stacked age distribution functions for all 5 galaxies. The black line represent weighted linear least squares fit to the data in Region 1. The blue, green, and yellow age functions of the LMC, M83, and the Antennae respectively, are taken from Adamo & Bastian (2015), and are normalized to the total number of clusters in our sample to best compare the slope for each galaxy.

5.5.1 Age Distribution

We consider the age distribution of clusters in our LIRG sample over Region 1 described in §4. Specifically, we are interested in measuring the power law index γ, where $dN/d\tau = \tau^{\gamma}$. In Figure 5.3 we show the differential number of clusters per time interval, $\log(dN/d\tau)$, versus the median cluster age over that interval, $\log(\tau)$. The plotted data are binned by 0.4 in $\log(\tau)$ so as to fully encapsulate 2σ times the typical model errors of 0.2 in $\log(\tau)$ discussed in §3. For the youngest most massive clusters in the sample a weighted linear least-squares fit to the cluster age distribution results a power-law index of $\gamma = -0.79 \pm 0.23$. While this slope is slightly shallower than both the Antennae age distribution and the results from Linden et al. (2017), we see that the overall slope is steeper than what is measured for several lower mass star-forming galaxies like the LMC.

When examining the age distribution functions for our three most 'cluster-rich' (i.e. $N_c > 100$ SSCs) galaxies, we find that the disruption rates measured for IC 1623, NGC 7469, and NGC 3256 are consistent with the distribution function measured for the full sample (Figures 5.4, 5.5, and 5.6 respectively). Further, we note that all three systems are classified as mid-stage mergers, demonstrating that the similar dynamical states of the ISM within these galaxies sets the overall disruption rate seen.

Finally, by examining the age distribution functions for clusters identified as inner- and outer-disk clusters a striking result emerges. The SSCs classified as inner-disk clusters show a distribution slope of $\gamma = -1.08 \pm 0.17$, whereas SSCs found in the outer-disks have a distribution slope of $\gamma = -0.65 \pm 0.27$ (Figure 5.7). This inner-disk value is consistent with the results from Linden et al. (2017), where the FOV is well-matched to the average MIR core size. This is evidence in favor of location-dependent cluster disruption, where cluster evolution in the central regions of LIRGs are more-strongly influenced by the external tidal field of the ongoing merger. Additionally, since the mass range covered in each spatial sub-sample is identical we conclude that the main physical driver of these differences cannot be internal (e.g. 2-body relaxation) disruption. This effect is seen not only for the full sample, but each of the three 'cluster-rich' LIRGs shown in Figures 5.4, 5.5, and 5.6 respectively.

Importantly, even though the outer-disk disruption rate is shallower than that found for the inner-disk SSCs, it is still significantly steeper than the cluster age distribution functions seen in nearby normal galaxies. Additionally, the magnitude of

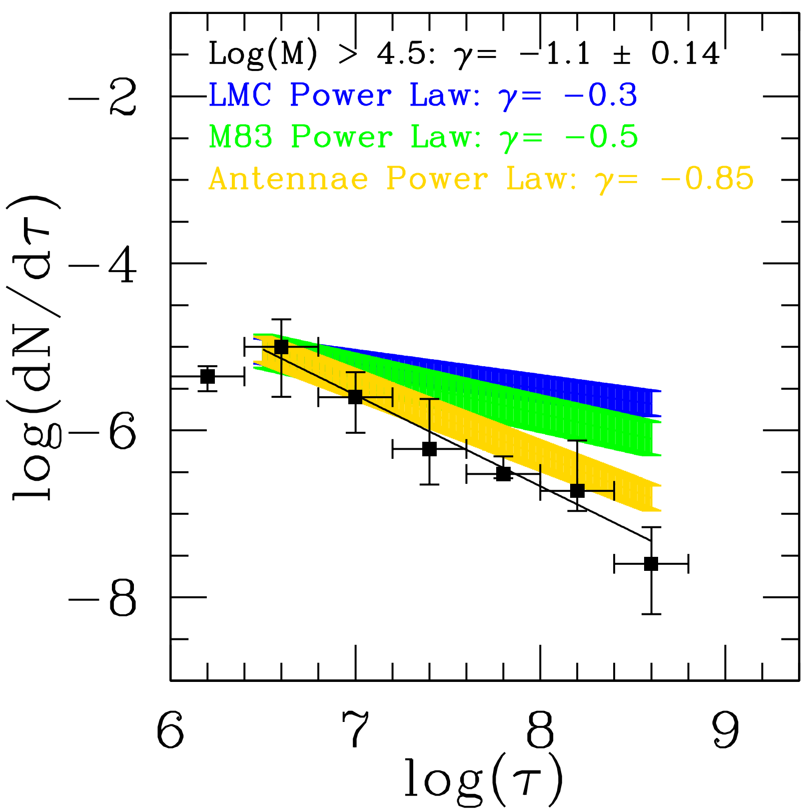

Figure 5.4: The age distribution function for IC1623 which contains 180 confirmed SSCs. We find that the distribution is consistent with the overall slope measured for the full sample.

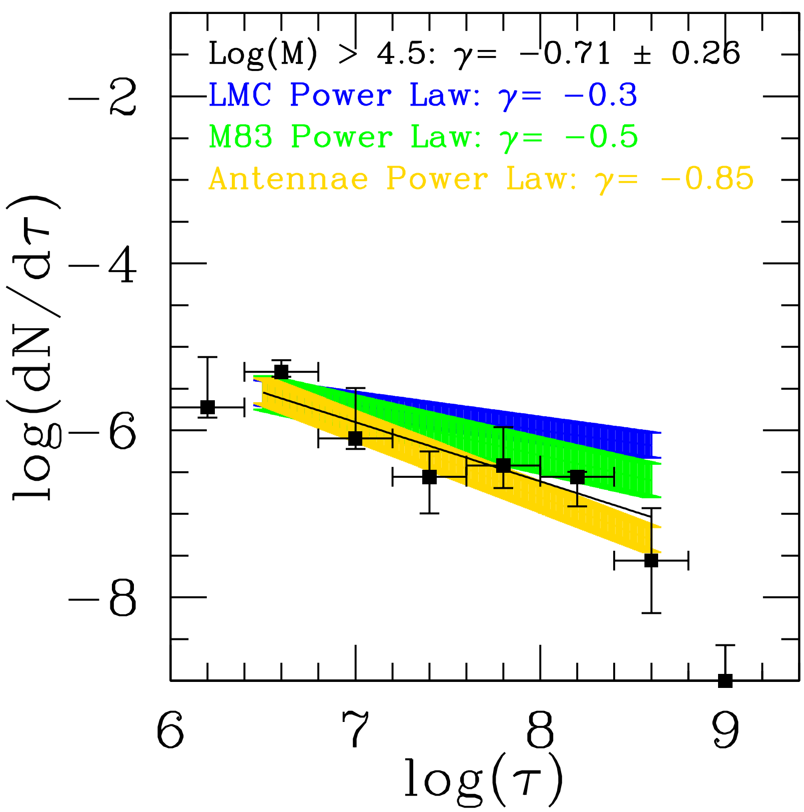

Figure 5.5: The age distribution function for NGC 7469 which contains 165 confirmed SSCs. We find that the distribution is consistent with the overall slope measured for the full sample.

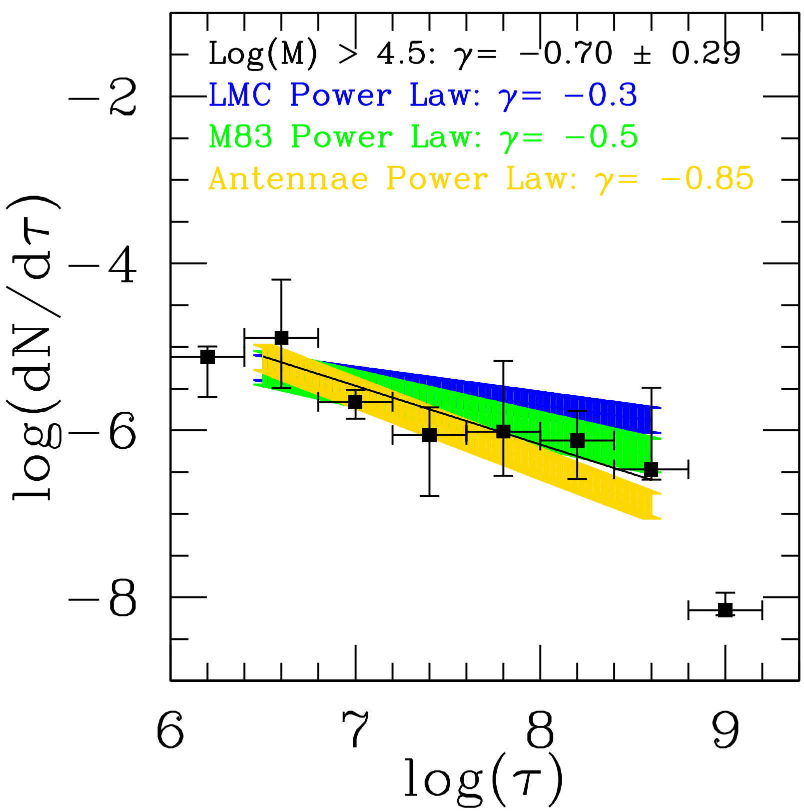

Figure 5.6: The age distribution function for NGC3256 which contains 549 confirmed SSCs. We find that the distribution is consistent with the overall slope measured for the full sample.

the difference seen in γ (~ 0.4 dex) is larger than the differences observed for inner- and outer-disk clusters in nearby normal galaxies. Thus the increases in turbulence and pressure in the ISM are crucial for reaching the extreme values of cluster disruption seen in the nuclear regions in LIRGs, as well as increasing the disruption rates in the extended disks and tidal tails of major galaxy mergers.

Given the above, the most plausible explanation is that clusters are being rapidly destroyed in luminous galaxy mergers at a rate that exceeds the cluster destruction process occurring in nearby normal galaxies at all galactocentric radii. However, the overall magnitude of this disruption is location-dependent: clusters found in the inner-regions of LIRGs show greater disruption rates relative to SSCs identified in their outer-disks.

5.5.2 Mass Function

We consider the mass distribution of clusters in our LIRG sample over Region 2 described in §4. When modeling the CMF we adopt both a simple power-law model and a two component Schechter function of the form $dN/dM = (M/M_c)^{\alpha} e^{(M/M_c)}$, where M_c is the characteristic turnover mass and α is the overall power-law slope. Keeping the binning constant (0.4 in $\log(M)$), and performing a cluster-weighted least-squares fit as a function of mass, we find that clusters with ages $t \leq 10^{7.5}$ yr have $\alpha \sim -1.7 \pm 0.07$ and $M_c = 10^{6.5} M_{\odot}$ (see Figure 5.8). By comparison, α is commonly measured to be -2 for lower luminosity star-forming galaxies with an $M_c \sim 10^{3-4} M_{\odot}$ (Bastian, 2008b; Larsen, 2010; Johnson et al., 2017).

When examining the mass functions for our three most 'cluster-rich' galaxies, we find that the power-law slope and M_c measured for IC 1623, NGC 7469, and NGC 3256 are broadly consistent with the distribution function measured for the full sample (Figures 5.9, 5.10, and 5.11 respectively). Further, we find that the CMF

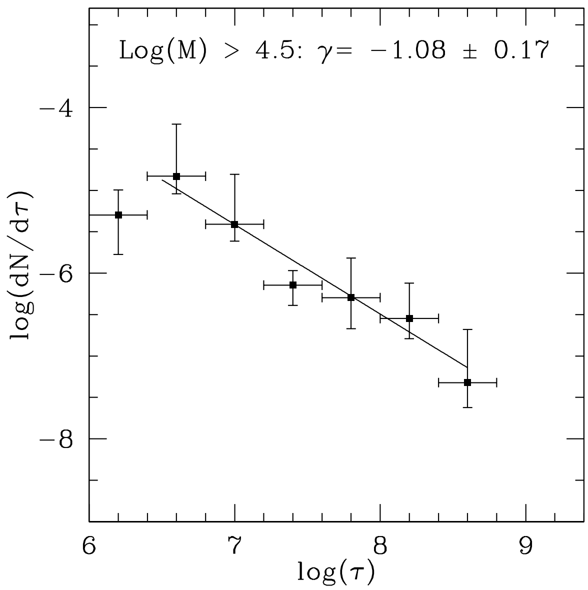

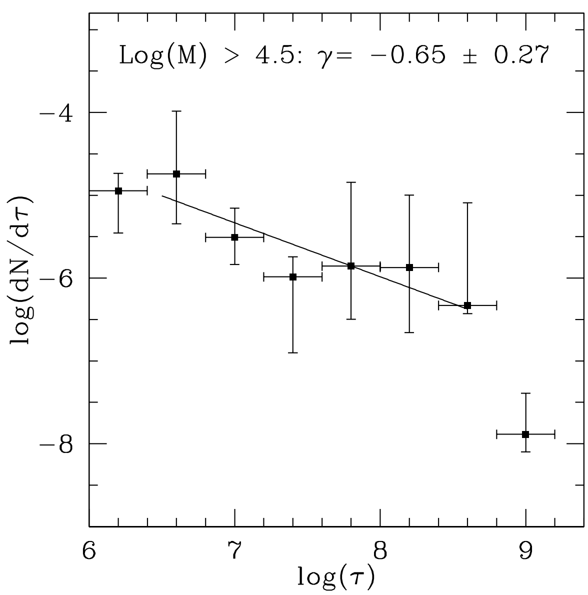

Figure 5.7: The age distribution functions for all 1027 clusters in our sample classified as either inner-disk (top) or outer-disk clusters. We see that the magnitude of the difference γ (~ 0.4 dex) seen between the inner- and outer-disk clusters is larger than what has been found for nearby normal galaxies, and that the disruption rate is higher overall at all galctocentric radii.

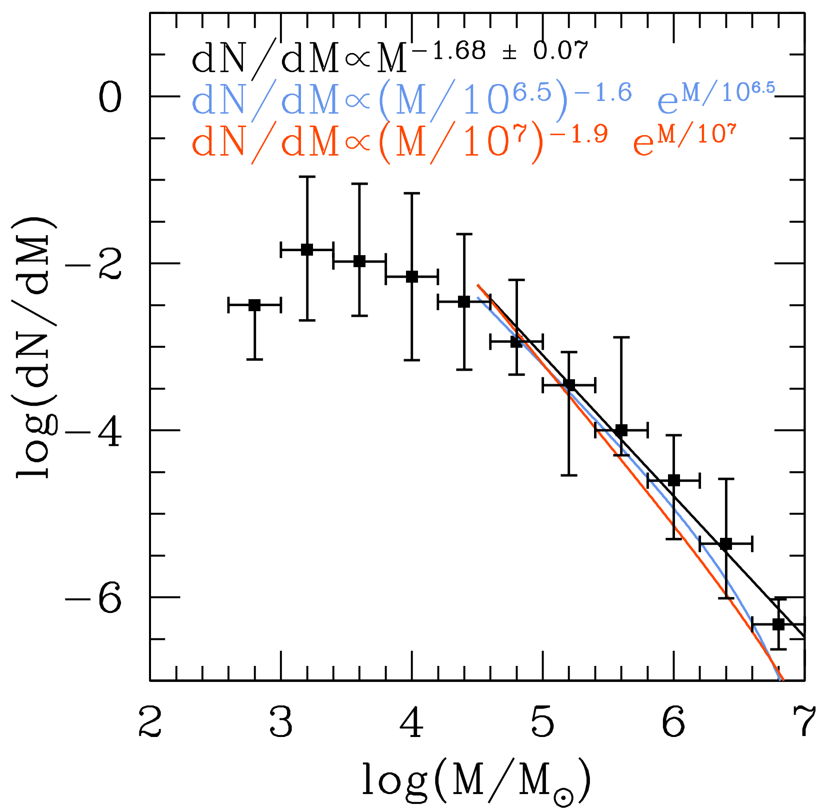

Figure 5.8: The stacked mass distribution function for all 5 galaxies. The black line represents the weighted least squares fits to the data, with analytic Schechter function fits to the empirical distribution overlaid in blue and orange. The values obtained for the M_c are significantly larger than what is observed for lower-luminosity star-forming galaxies in the local Universe.

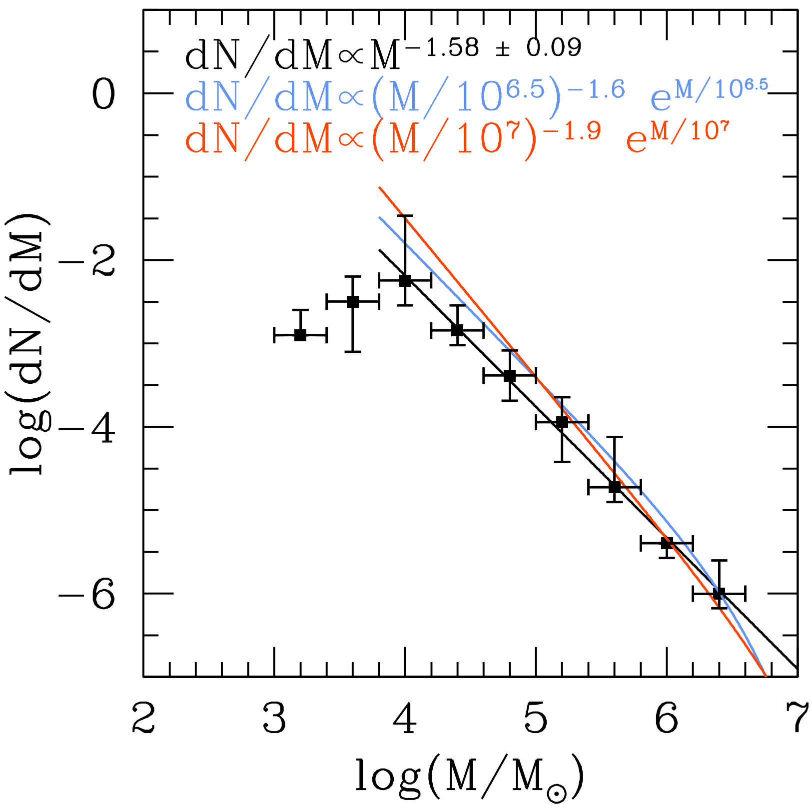

Figure 5.9: The mass distribution function for IC1623. We find that the distribution is consistent with the overall slope and M_c measured for the full sample. These results are consistent with the luminosity function derived from Paβ observations of LIRGs in GOALS (Larson et al., 2020), as well as detailed observations of Arp 299 (Randriamanakoto et al., 2019).

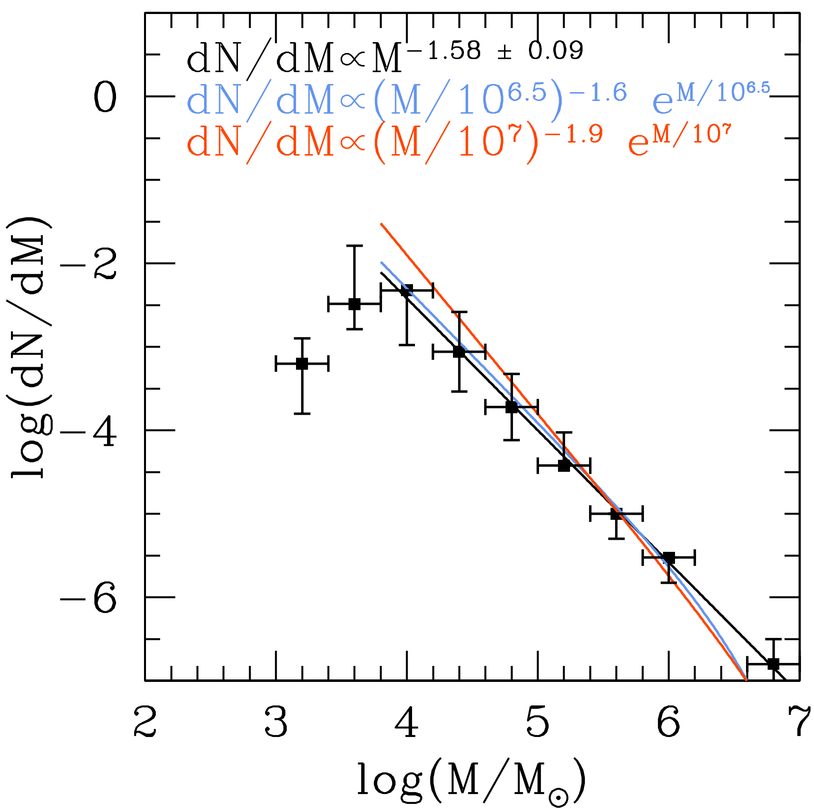

Figure 5.10: The mass distribution function for NGC 7469. We find that the distribution is consistent with the overall slope and M_c measured for the full sample. These results are consistent with the luminosity function derived from Paβ observations of LIRGs in GOALS (Larson et al., 2020), as well as detailed observations of Arp 299 (Randriamanakoto et al., 2019).

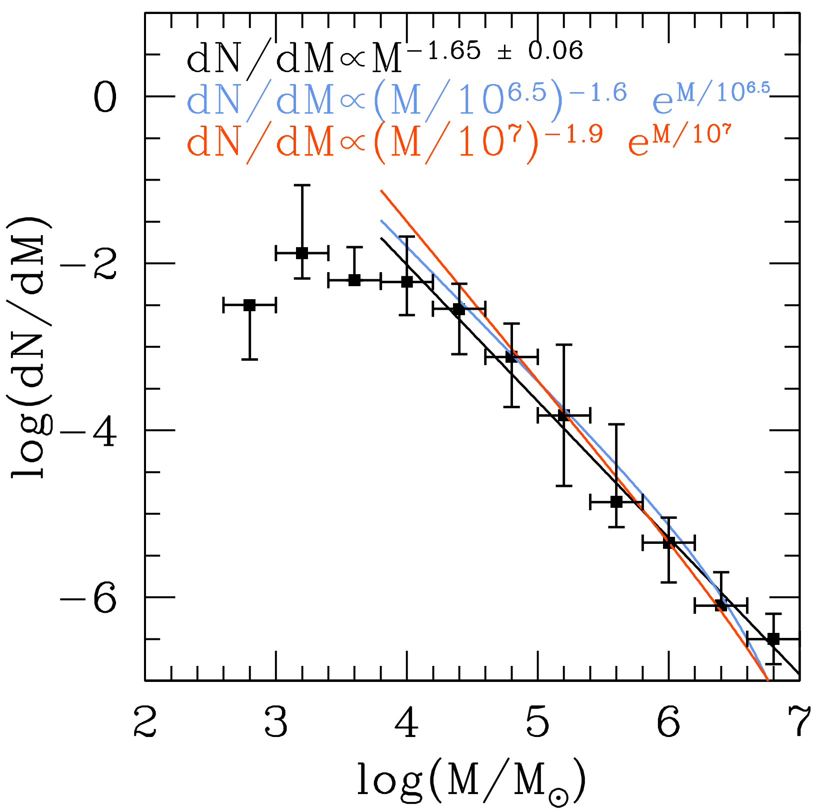

Figure 5.11: The mass distribution function for NGC3256. We find that the distribution is consistent with the overall slope and M_c measured for the full sample. These results are consistent with the luminosity function derived from Paβ observations of LIRGs in GOALS (Larson et al., 2020), as well as detailed observations of Arp 299 (Randriamanakoto et al., 2019).

does not vary significantly for clusters classified as inner- and outer-disk clusters, when adopting a common completeness limit of $M_U = -9.3$ between the two subsamples. This is consistent with detailed results for another well-studied LIRG, Arp 299, which show differences in the derived M_c of $\leq$ a factor of 2 between the two galaxy nuclei and the extended disk (Randriamanakoto et al., 2019). Therefore, the cluster disruption in these galaxies appears to be mostly mass-independent (i.e., we find that $\gamma \sim -0.7$ from $M_\odot = 10^4 - 10^7$), consistent with the results from Whitmore et al. (2010).

Although we find that the derived CMF is slightly shallower than the value in Linden et al. (2017), our value is consistent with the luminosity functions derived from Paβ observations of LIRGs in GOALS (Larson et al., 2020). Further, recent hydrodynamical simulations of cluster formation in nearby starburst galaxies reveal that the underlying CMF is steeper when the observed M_c increases. Thus, due to the limited sensitivity of the observations in Linden et al. (2017), we expect to observe a shallower CMF for these new observations which span a much larger range in cluster mass, and which detect clusters at $M \sim 10^4 M_\odot$ (Maji et al., 2017; Lahén et al., 2020).

Further, by limiting our analysis of the CMF to clusters with $t < 10^{7.5}$yr, spatial differences in the observed cluster disruption will not be strongly reflected in the underlying CMF. It is only by examining older clusters, which can not be done effectively for inner-disk clusters due to completeness, that the differences in the disruption rate would result in significant changes to the observed CMF (Kruijssen et al., 2012).

Given the above, it appears that the differences in the slope observed for young clusters in our LIRG sample relative to normal star-forming galaxies is caused primarily by a much higher disruption rate, which makes the overall CMF shallower. However we emphasize that this disruption does not appear to be mass-dependent, but rather is strongly coupled to the local ISM environment, such that clusters in the inner- and outer-disk form with the same general properties, but evolve much differently over time.

5.6 Summary

Hubble Space Telescope WFC3/UVIS (F336W) and ACS/WFC optical (F435W and F814W) observations of a sample of 10 LIRGs in the GOALS sample were obtained. These observations have been utilized to derive the ages and masses of the star clusters contained within the 5 most nearby systems in order to examine the cluster properties in extreme starburst environments relative to those in nearby, lower luminosity star-forming galaxies. The following conclusions are reached:

(1) We have detected 1027 clusters throughout the disks of these 5 LIRGs. These clusters have $S/N \geq 3$ in all three filters and de-convolved FWHMs as measured by ISHAPE of ≤ 3 pixels, corresponding to a median physical size of $\sim$22pc.

(2) The derived cluster age distribution implies a disruption rate of $dN/d\tau = \tau^{-0.7+/-0.2}$ for cluster masses $\geq 10^{4.5} M_{\odot}$. This is consistent with the general framework that ongoing mergers destroy clusters at a much higher rate due to the high external pressure induced from a strong tidal field. The measured γ is steeper than what has been observed in lower-luminosity star-forming galaxies in the local Universe.

(3) The derived cluster masses imply a CMF for our sample galaxies of $dN/dM = M^{-1.6+/-0.1}$, with an $M_c \sim 10^{6.5}$. Together with the fact that we do not see a significant change in the age distribution slope as a function of mass, we interpret our mass function slope as evidence against mass-dependent cluster disruption down to $M \geq 10^{4.5} M_{\odot}$.

(4) Differences in the slope of the observed cluster age distributions between inner- and outer-disk clusters provides some of the clearest evidence to date of location-dependent cluster evolution. Not only does this effect appear to be ubiquitous in

LIRGs, but the magnitude of this affect is amplified even relative to strong gradients of cluster disruption observed in normal star-forming galaxies in the local Universe.

5.7 Additional Figures and Tables

Table 5.3: Observational Properties of Individual Star Clusters

ID	R.A.	Decl.	f_{336}	$\sigma_{f_{336}}$	f_{435}	$\sigma_{f_{435}}$	f_{814}	$\sigma_{f_{814}}$
Arp 220								
1	233.74666905	23.48058170	1.075E-18	3.203E-20	9.253E-18	1.506E-20	5.168E-17	7.533E-20
2	233.72954905	23.47581741	1.697E-17	9.117E-20	2.644E-17	1.953E-20	1.255E-17	2.068E-20
3	233.74843760	23.48274548	2.944E-19	2.420E-20	8.171E-19	9.830E-21	7.722E-19	4.422E-21
4	233.75164401	23.48438602	4.567E-18	5.312E-20	8.369E-18	1.328E-20	3.465E-18	7.760E-21
5	233.76469429	23.49254708	3.297E-19	2.675E-20	2.083E-18	1.102E-20	6.016E-18	9.323E-21
6	233.72821835	23.48265615	5.766E-19	3.298E-20	6.279E-19	1.437E-20	4.247E-19	9.874E-21
7	233.73230262	23.48457584	5.755E-19	2.967E-20	4.693E-19	1.175E-20	1.211E-18	7.633E-21
8	233.73185992	23.48615206	2.393E-19	2.958E-20	4.498E-19	1.322E-20	2.180E-19	7.017E-21
9	233.72501290	23.48691445	2.611E-19	3.092E-20	2.137E-18	1.274E-20	6.633E-18	1.295E-20
10	233.72839999	23.48868241	2.254E-19	3.553E-20	1.186E-19	1.238E-20	1.247E-19	6.176E-21
11	233.73231080	23.49079122	6.964E-19	3.483E-20	2.870E-19	1.725E-20	4.972E-20	7.296E-21
12	233.75803382	23.50158592	1.075E-18	3.496E-20	1.088E-18	1.565E-20	6.393E-19	8.781E-21
13	233.74391918	23.49905783	2.922E-19	2.995E-20	1.052E-18	1.410E-20	4.472E-19	7.512E-21
14	233.74684317	23.50064463	3.789E-19	3.288E-20	1.275E-18	1.565E-20	5.078E-19	7.132E-21
15	233.74843808	23.50266525	1.334E-17	8.666E-20	2.296E-17	2.192E-20	9.757E-18	1.861E-20
16	233.73915751	23.50074409	2.658E-19	3.698E-20	3.854E-19	2.944E-20	1.022E-19	1.429E-20
17	233.73723734	23.50060951	3.768E-19	4.241E-20	2.799E-19	2.576E-20	1.909E-19	1.486E-20
18	233.73927170	23.50207210	2.302E-19	4.168E-20	9.969E-19	7.184E-20	7.815E-19	5.176E-20
19	233.74440108	23.50393092	7.650E-19	3.744E-20	2.888E-18	2.197E-20	1.117E-18	1.105E-20
20	233.71486086	23.49613826	2.231E-19	4.288E-20	3.707E-19	2.059E-20	1.344E-19	1.126E-20
21	233.74486807	23.50467514	6.282E-19	3.554E-20	1.457E-18	2.079E-20	4.334E-19	9.539E-21
22	233.74023130	23.50352484	2.144E-18	5.879E-20	2.098E-18	5.488E-20	3.679E-19	5.733E-20
23	233.73899471	23.50421279	3.497E-19	4.227E-20	9.742E-19	4.366E-20	6.219E-19	3.625E-20
24	233.73652731	23.50352957	5.017E-19	3.946E-20	1.053E-18	3.343E-20	4.890E-19	1.215E-20
25	233.75923556	23.51003412	2.005E-18	3.924E-20	2.322E-18	1.672E-20	2.911E-18	2.615E-20
26	233.73690711	23.50405544	5.512E-19	4.206E-20	1.230E-18	3.472E-20	3.585E-19	1.582E-20
27	233.75544911	23.50925410	2.262E-19	3.310E-20	2.886E-19	1.335E-20	1.014E-19	4.624E-21
28	233.73689378	23.50444370	2.166E-18	5.457E-20	4.659E-18	3.783E-20	2.166E-18	1.520E-20
29	233.74041087	23.50651057	4.000E-19	3.536E-20	1.303E-18	1.757E-20	4.949E-19	7.995E-21
30	233.74117528	23.50700297	4.086E-19	3.658E-20	1.228E-18	1.670E-20	6.329E-19	9.523E-21
31	233.73779793	23.50730509	3.582E-18	5.240E-20	6.187E-18	2.381E-20	2.099E-18	9.205E-21
32	233.73724699	23.50687723	2.229E-19	2.828E-20	2.698E-19	1.594E-20	8.228E-20	6.741E-21
33	233.73677185	23.50697629	7.068E-19	3.711E-20	1.285E-18	1.856E-20	3.920E-19	8.279E-21
34	233.73977452	23.50795556	4.435E-19	3.560E-20	1.273E-18	1.692E-20	5.154E-19	7.126E-21
35	233.74090543	23.50824739	2.340E-19	3.558E-20	5.473E-19	1.923E-20	1.880E-19	7.785E-21
36	233.73959535	23.51000195	2.035E-18	4.027E-20	3.707E-18	1.990E-20	1.169E-18	8.221E-21
37	233.73975800	23.51020709	8.615E-19	3.580E-20	1.430E-18	1.852E-20	4.318E-19	5.670E-21
38	233.73909140	23.51001044	6.218E-19	3.550E-20	1.280E-18	1.359E-20	3.546E-19	6.219E-21
39	233.74326893	23.51143905	3.913E-19	3.768E-20	1.406E-18	1.349E-20	1.262E-18	5.684E-21
40	233.72747609	23.50737438	2.971E-19	3.595E-20	4.304E-19	1.719E-20	3.374E-19	1.722E-20
41	233.74159646	23.51241000	2.906E-19	3.112E-20	8.493E-19	1.238E-20	7.953E-19	5.692E-21
42	233.71264167	23.51070808	2.901E-18	4.785E-20	2.288E-19	2.043E-20	6.346E-20	1.600E-20
43	233.71578654	23.51292516	2.437E-19	2.843E-20	2.163E-19	1.007E-20	8.592E-20	4.633E-21
44	233.71278254	23.51029146	1.812E-19	2.797E-20	2.071E-19	1.028E-20	1.065E-19	4.618E-21
45	233.72331540	23.51772209	6.416E-17	1.929E-19	1.095E-16	4.981E-20	5.620E-17	9.385E-20
46	233.72969311	23.51835216	2.103E-19	2.699E-20	5.403E-19	1.041E-20	3.713E-19	5.174E-21
IC 1623								
1	16.95633044	-17.51200123	5.614E-19	3.419E-20	4.714E-19	1.147E-20	2.434E-19	4.812E-21

Table 5.3 continued

Table 5.3: Observational Properties of Individual Star Clusters (continued)

ID	R.A.	Decl.	f_{336}	$\sigma_{f_{336}}$	f_{435}	$\sigma_{f_{435}}$	f_{814}	$\sigma_{f_{814}}$
2	16.95253257	-17.50621356	3.652E-19	3.165E-20	3.606E-19	2.837E-20	1.280E-19	1.146E-20
3	16.95205630	-17.50641360	2.858E-19	3.545E-20	8.337E-19	2.646E-20	3.052E-19	8.422E-21
4	16.95048863	-17.50346183	5.593E-19	3.925E-20	6.141E-19	3.124E-20	2.139E-19	1.323E-20
5	16.95104913	-17.50486336	6.584E-19	4.938E-20	5.483E-19	3.920E-20	2.823E-19	1.366E-20
6	16.95068209	-17.50340830	7.313E-19	3.798E-20	8.730E-20	1.849E-20	2.045E-19	8.422E-21
7	16.95086391	-17.50551010	1.012E-17	7.723E-20	1.487E-17	8.861E-20	5.280E-18	2.979E-20
8	16.95118741	-17.50487325	2.285E-19	3.419E-20	3.027E-19	3.442E-20	8.163E-20	8.563E-21
9	16.95101639	-17.50470637	2.489E-19	4.178E-20	2.396E-19	3.060E-20	8.014E-20	1.352E-20
10	16.95095311	-17.50527787	4.783E-19	6.457E-20	7.788E-19	5.960E-20	8.238E-20	1.974E-20
11	16.95093328	-17.50508371	8.623E-19	8.483E-20	9.167E-19	7.140E-20	1.464E-19	1.939E-20
12	16.95171234	-17.50695885	5.036E-19	4.685E-20	8.215E-19	1.976E-20	2.715E-19	9.342E-21
13	16.95065637	-17.50614370	1.559E-19	4.685E-20	6.186E-19	4.494E-20	3.058E-19	1.592E-20
14	16.95043989	-17.50552899	4.086E-19	6.331E-20	7.018E-19	5.674E-20	2.627E-19	2.024E-20
15	16.95113776	-17.50660988	2.466E-19	4.052E-20	4.016E-19	2.677E-20	8.438E-20	1.472E-20
16	16.95105745	-17.50694837	2.268E-18	3.672E-20	1.832E-18	2.964E-20	6.313E-19	1.267E-20
17	16.95068447	-17.50576596	2.957E-19	5.064E-20	5.256E-19	5.960E-20	1.926E-19	2.123E-20
18	16.95108197	-17.50676510	3.091E-19	3.545E-20	1.406E-19	2.614E-20	4.829E-20	1.210E-20
19	16.95033162	-17.50556879	2.469E-19	6.331E-20	2.157E-19	4.303E-20	1.231E-19	2.173E-20
20	16.95038334	-17.50589927	4.212E-19	6.837E-20	5.789E-19	7.522E-20	7.940E-20	2.222E-20
21	16.95013922	-17.50592391	7.629E-19	4.938E-20	1.127E-18	7.363E-20	4.206E-19	2.597E-20
22	16.95031758	-17.50600715	2.770E-19	5.064E-20	1.222E-18	6.120E-20	2.691E-19	2.286E-20
23	16.95067378	-17.50689977	2.364E-19	4.052E-20	4.129E-19	2.996E-20	9.346E-20	1.132E-20
24	16.95022909	-17.50592562	2.543E-19	5.824E-20	8.618E-19	9.116E-20	1.002E-19	2.534E-20
25	16.95019588	-17.50910260	1.508E-17	6.331E-20	1.123E-17	5.068E-20	2.546E-18	1.430E-20
26	16.95039123	-17.50908629	2.451E-19	6.204E-20	5.280E-19	5.132E-20	1.090E-19	1.316E-20
27	16.95016335	-17.50889778	6.688E-19	5.444E-20	5.892E-19	2.741E-20	1.119E-19	6.157E-21
28	16.94965175	-17.50783823	4.912E-19	5.191E-20	3.199E-19	2.741E-20	1.284E-19	8.917E-21
29	16.94834474	-17.50542353	8.319E-19	4.305E-20	1.190E-18	3.251E-20	4.160E-19	1.840E-20
30	16.94844561	-17.50609887	1.985E-18	4.052E-20	1.343E-18	3.984E-20	9.092E-19	1.561E-19
31	16.94848474	-17.50653432	6.584E-19	5.824E-20	1.645E-18	2.187E-19	3.058E-18	3.574E-19
32	16.94810215	-17.50520785	1.024E-18	4.811E-20	7.403E-19	3.283E-20	1.624E-19	1.684E-20
33	16.94938903	-17.50790363	4.818E-19	5.191E-20	4.288E-19	1.626E-20	9.346E-20	1.047E-20
34	16.94982933	-17.50865188	2.750E-19	4.938E-20	2.056E-19	1.466E-20	3.871E-20	5.803E-21
35	16.94831767	-17.50556353	1.355E-19	3.798E-20	1.791E-19	1.912E-20	7.803E-20	1.366E-20
36	16.94788979	-17.50704320	1.168E-18	4.811E-20	1.015E-18	3.283E-20	1.537E-17	3.627E-19
37	16.94796530	-17.50619881	1.668E-18	4.178E-20	1.496E-18	3.379E-20	1.938E-19	2.668E-20
38	16.94775249	-17.50748391	3.430E-19	4.811E-20	1.550E-18	1.163E-19	4.650E-18	2.149E-19
39	16.94738526	-17.50544901	1.406E-18	4.558E-20	1.112E-18	2.550E-20	2.673E-19	1.175E-20
40	16.94667828	-17.50453376	2.115E-18	6.710E-20	2.077E-18	3.155E-20	4.955E-19	1.069E-20
41	16.94797596	-17.50705069	1.459E-18	4.938E-20	1.357E-18	3.187E-20	5.565E-19	1.192E-19
42	16.94656704	-17.50467706	7.353E-18	1.102E-19	5.705E-18	9.435E-20	1.526E-18	2.491E-20
43	16.94779151	-17.50712866	3.740E-19	4.052E-20	1.809E-19	3.283E-20	2.236E-18	1.640E-19
44	16.94699694	-17.50741455	5.955E-17	3.621E-19	7.349E-17	3.643E-19	3.069E-17	5.154E-19
45	16.94771317	-17.50825017	4.330E-19	5.064E-20	7.262E-19	8.861E-20	2.341E-19	4.317E-20
46	16.94701401	-17.50545129	5.191E-19	4.178E-20	5.575E-19	1.976E-20	1.742E-19	5.591E-21
47	16.94901299	-17.51114634	1.245E-18	5.951E-20	1.500E-18	4.303E-20	5.903E-19	1.720E-20
48	16.94672266	-17.50715451	8.130E-18	8.103E-20	6.203E-18	1.023E-19	1.230E-18	4.628E-20
49	16.94665211	-17.50644229	5.542E-17	2.747E-19	3.976E-17	1.377E-19	6.007E-18	4.331E-20
50	16.94487361	-17.50520980	3.702E-18	1.026E-19	2.520E-18	1.259E-19	8.779E-19	2.817E-20
51	16.94848420	-17.50990232	5.244E-19	3.165E-20	6.777E-19	1.530E-20	1.375E-19	6.086E-21
52	16.94568878	-17.50346874	5.416E-19	4.178E-20	5.811E-19	2.327E-20	7.295E-20	8.634E-21
53	16.94865535	-17.51069539	1.065E-18	3.798E-20	7.724E-19	1.849E-20	1.144E-19	6.794E-21
54	16.94788019	-17.50887849	3.806E-19	3.798E-20	4.573E-19	3.092E-20	1.097E-19	1.231E-20

Table 5.3 continued

Table 5.3: Observational Properties of Individual Star Clusters (continued)

ID	R.A.	Decl.	f_{336}	$\sigma_{f_{336}}$	f_{435}	$\sigma_{f_{435}}$	f_{814}	$\sigma_{f_{814}}$
55	16.94611424	-17.50504089	4.939E-19	3.292E-20	3.714E-19	2.359E-20	9.591E-20	7.077E-21
56	16.94586076	-17.50474111	5.900E-19	4.811E-20	8.430E-19	4.239E-20	9.269E-20	1.564E-20
57	16.94673324	-17.50756951	2.719E-19	5.064E-20	3.341E-18	1.023E-19	9.805E-18	8.896E-20
58	16.94653624	-17.50664128	8.849E-18	8.230E-20	6.999E-18	5.514E-20	2.211E-18	1.571E-20
59	16.94571606	-17.50502864	7.081E-19	4.558E-20	5.508E-19	3.347E-20	1.415E-19	9.766E-21
60	16.94642201	-17.50653938	2.996E-19	5.698E-20	2.171E-19	5.674E-20	1.814E-19	1.805E-20
61	16.94609444	-17.50684683	8.832E-18	2.013E-19	6.992E-18	1.345E-19	1.910E-18	8.393E-20
62	16.94851864	-17.51175005	2.115E-18	5.571E-20	2.703E-18	3.665E-20	8.524E-19	1.394E-20
63	16.94695343	-17.50788322	3.539E-19	4.938E-20	5.924E-19	5.960E-20	5.300E-19	2.470E-20
64	16.94596527	-17.50528918	1.185E-19	3.545E-20	1.453E-19	2.231E-20	7.376E-20	7.926E-21
65	16.94554006	-17.50516756	2.837E-19	4.052E-20	4.432E-19	3.793E-20	3.106E-19	1.387E-20
66	16.94814280	-17.51088046	3.971E-18	4.305E-20	2.830E-18	1.976E-20	6.709E-19	6.794E-21
67	16.94649315	-17.50688953	3.125E-19	4.558E-20	2.771E-19	3.283E-20	5.849E-20	1.543E-20
68	16.94806248	-17.51104933	1.568E-18	4.178E-20	1.334E-18	1.562E-20	2.743E-19	6.723E-21
69	16.94668298	-17.50813649	2.660E-19	3.925E-20	2.486E-19	5.355E-20	2.307E-19	1.840E-20
70	16.94523450	-17.50543945	1.401E-18	6.331E-20	1.166E-18	6.853E-20	3.766E-19	2.944E-20
71	16.94596982	-17.50675972	2.210E-17	2.937E-19	1.821E-17	4.660E-19	4.816E-18	1.062E-19
72	16.94790166	-17.51054506	5.814E-19	4.052E-20	5.222E-19	1.721E-20	9.635E-20	4.954E-21
73	16.94653027	-17.50801146	7.771E-19	4.052E-20	8.430E-19	6.693E-20	6.929E-19	3.446E-20
74	16.94664310	-17.50798344	6.768E-19	5.571E-20	5.448E-19	6.725E-20	2.425E-19	2.824E-20
75	16.94469242	-17.50462346	1.390E-18	4.431E-20	1.517E-18	2.486E-20	4.087E-19	1.189E-20
76	16.94632061	-17.50847149	1.099E-18	4.938E-20	8.779E-19	6.120E-20	4.807E-19	3.227E-20
77	16.94706286	-17.50918149	4.761E-19	3.419E-20	5.957E-19	3.410E-20	1.609E-19	1.019E-20
78	16.94539804	-17.50612096	7.764E-18	2.912E-19	9.688E-18	2.754E-19	4.065E-18	7.402E-20
79	16.94443423	-17.50612894	2.576E-17	1.318E-18	2.870E-17	1.180E-18	9.338E-18	3.961E-19
80	16.94493662	-17.50543667	3.532E-18	8.230E-20	8.738E-18	7.554E-20	3.126E-18	2.611E-20
81	16.94562496	-17.50631558	2.283E-17	5.710E-19	1.596E-17	1.428E-19	2.007E-18	4.756E-20
82	16.94603294	-17.50733177	2.783E-18	1.519E-19	1.792E-18	2.193E-19	9.887E-19	8.407E-20
83	16.94605884	-17.50779829	6.517E-19	1.481E-19	8.682E-19	1.600E-19	4.641E-19	4.841E-20
84	16.94580845	-17.50693241	3.297E-18	2.393E-19	2.452E-18	3.716E-19	1.081E-18	6.766E-20
85	16.94536056	-17.50639931	3.157E-18	1.823E-19	2.205E-18	2.961E-19	6.012E-19	6.008E-20
86	16.94551416	-17.50640928	2.170E-17	3.583E-19	1.848E-17	2.531E-19	3.403E-18	7.112E-20
87	16.94593957	-17.50724312	8.373E-18	2.697E-19	8.706E-18	3.254E-19	2.269E-18	1.367E-19
88	16.94613973	-17.50834675	2.428E-17	3.216E-19	1.612E-17	2.059E-19	4.372E-18	9.122E-20
89	16.94512230	-17.50650886	3.719E-17	3.153E-19	2.405E-17	3.952E-19	5.084E-18	1.150E-19
90	16.94585570	-17.50726300	6.888E-18	2.811E-19	5.784E-18	2.566E-19	1.705E-18	1.734E-19
91	16.94489295	-17.50604674	5.718E-18	1.545E-19	4.842E-18	1.823E-19	1.430E-18	5.718E-20
92	16.94502255	-17.50560673	3.927E-18	9.749E-20	3.086E-18	7.490E-20	4.507E-19	3.319E-20
93	16.94783152	-17.51213470	3.726E-19	4.558E-20	6.096E-19	3.060E-20	1.278E-19	1.189E-20
94	16.94442520	-17.50456042	2.529E-19	4.685E-20	3.106E-19	3.857E-20	1.947E-19	9.837E-21
95	16.94475320	-17.50638446	1.830E-17	6.128E-19	2.071E-17	4.580E-19	3.095E-18	9.702E-20
96	16.94755000	-17.51192017	7.239E-19	3.798E-20	9.066E-19	1.689E-20	2.851E-19	6.582E-21
97	16.94474936	-17.50674853	1.844E-18	2.064E-19	3.738E-18	3.264E-19	1.258E-18	9.858E-20
98	16.94441549	-17.50493532	2.670E-18	7.217E-20	1.773E-18	1.007E-19	3.453E-19	2.095E-20
99	16.94568228	-17.50871399	1.223E-17	3.013E-19	1.100E-17	3.264E-19	3.521E-18	6.461E-20
100	16.94619290	-17.50867259	2.765E-19	4.938E-20	3.947E-19	7.586E-20	1.527E-19	2.413E-20
101	16.94484887	-17.50645786	4.101E-17	6.229E-19	2.624E-17	6.231E-19	4.833E-18	1.282E-19
102	16.94347100	-17.50539574	1.013E-18	5.064E-20	4.645E-19	6.630E-20	5.585E-19	1.826E-20
103	16.94458030	-17.50604284	6.043E-18	4.330E-19	5.493E-18	1.075E-18	2.894E-18	3.104E-19
104	16.94523547	-17.50724339	2.519E-17	9.661E-19	1.702E-17	8.338E-19	5.217E-18	2.498E-19
105	16.94471028	-17.50654275	3.685E-17	2.811E-19	2.246E-17	2.473E-19	5.742E-18	1.142E-19
106	16.94484441	-17.50731209	1.345E-17	3.267E-19	1.240E-17	3.605E-19	2.234E-18	1.194E-19
107	16.94529652	-17.50696060	3.309E-18	2.304E-19	1.120E-18	2.802E-19	8.975E-19	1.022E-19

Table 5.3 continued

Table 5.3: Observational Properties of Individual Star Clusters (continued)

ID	R.A.	Decl.	f_{336}	$\sigma_{f_{336}}$	f_{435}	$\sigma_{f_{435}}$	f_{814}	$\sigma_{f_{814}}$
108	16.94604740	-17.50861820	3.398E-19	5.698E-20	1.002E-18	7.809E-20	1.244E-19	3.220E-20
109	16.94450188	-17.50589294	8.063E-18	4.685E-19	7.465E-18	1.162E-18	2.523E-18	3.947E-19
110	16.94507437	-17.50730590	8.404E-18	4.343E-19	4.367E-18	5.900E-19	1.528E-18	2.024E-19
111	16.94446724	-17.50660169	8.972E-18	3.621E-19	9.959E-18	5.976E-19	3.889E-18	1.928E-19
112	16.94677407	-17.51086637	1.185E-18	4.558E-20	9.142E-19	1.785E-20	2.058E-19	6.086E-21
113	16.94392911	-17.50487175	3.916E-18	9.116E-20	2.483E-18	1.090E-19	8.292E-19	1.727E-20
114	16.94429147	-17.50601627	8.939E-18	5.837E-19	7.136E-18	7.962E-19	2.282E-18	2.262E-19
115	16.94419815	-17.50725981	1.393E-17	3.355E-19	1.702E-17	3.978E-19	9.715E-18	1.396E-19
116	16.94476738	-17.50773736	1.505E-16	3.417E-18	7.604E-17	1.862E-18	3.457E-17	6.248E-19
117	16.94601069	-17.50961177	3.568E-19	6.204E-20	6.777E-19	2.486E-20	2.311E-19	1.054E-20
118	16.94503203	-17.50725411	5.031E-18	2.988E-19	2.431E-18	5.396E-19	1.315E-18	1.008E-19
119	16.94387100	-17.50533456	1.510E-18	1.228E-19	2.447E-18	1.348E-19	5.042E-19	4.451E-20
120	16.94532616	-17.50827867	1.911E-18	6.457E-20	1.203E-18	6.598E-20	2.290E-19	1.946E-20
121	16.94368746	-17.50579165	9.326E-18	4.520E-19	8.698E-18	5.157E-19	2.830E-18	1.663E-19
122	16.94462324	-17.50689982	2.660E-17	3.963E-19	2.513E-17	5.211E-19	8.223E-18	1.568E-19
123	16.94473716	-17.50751418	8.443E-18	5.178E-19	2.820E-18	5.932E-19	3.019E-18	2.132E-19
124	16.94300966	-17.50628011	3.306E-19	5.951E-20	9.996E-19	5.291E-20	5.042E-19	2.718E-20
125	16.94469923	-17.50742410	1.018E-17	3.773E-19	6.796E-18	4.545E-19	2.703E-18	2.117E-19
126	16.94524097	-17.50838478	1.060E-18	5.571E-20	1.942E-18	5.323E-20	6.758E-19	2.548E-20
127	16.94507848	-17.50908089	1.525E-18	6.331E-20	1.704E-18	9.403E-20	2.789E-19	2.725E-20
128	16.94455091	-17.50689931	2.366E-17	4.609E-19	2.405E-17	5.842E-19	7.999E-18	2.179E-19
129	16.94369925	-17.50482191	2.550E-19	5.064E-20	3.350E-19	5.642E-20	6.204E-20	1.500E-20
130	16.94348525	-17.50476631	5.008E-19	6.331E-20	4.376E-19	4.048E-20	1.408E-19	1.139E-20
131	16.94370207	-17.50503064	1.318E-18	4.811E-20	1.078E-18	3.889E-20	3.540E-19	1.345E-20
132	16.94391632	-17.50614127	6.316E-17	1.714E-18	6.101E-17	3.138E-18	1.099E-17	9.703E-19
133	16.94448205	-17.50686745	6.004E-18	4.558E-19	9.355E-18	4.692E-19	4.360E-18	2.138E-19
134	16.94325276	-17.50482699	2.734E-19	5.064E-20	7.090E-19	4.526E-20	4.087E-19	1.734E-20
135	16.94405903	-17.50663429	3.778E-18	2.051E-19	6.980E-18	8.912E-19	3.643E-18	2.613E-19
136	16.94599924	-17.51073000	2.623E-18	4.431E-20	1.804E-18	2.295E-20	3.690E-19	7.289E-21
137	16.94362613	-17.50523415	6.099E-19	6.457E-20	7.064E-19	5.355E-20	1.541E-19	2.548E-20
138	16.94357871	-17.50468637	4.158E-19	4.685E-20	4.133E-19	3.379E-20	7.984E-20	1.663E-20
139	16.94488240	-17.50893981	2.107E-17	1.621E-19	2.118E-17	1.756E-19	5.448E-18	3.793E-20
140	16.94626154	-17.51119157	3.838E-19	4.305E-20	3.950E-19	1.785E-20	5.865E-20	7.077E-21
141	16.94588817	-17.51089841	4.717E-18	8.230E-20	3.325E-18	3.283E-20	6.302E-19	8.917E-21
142	16.94514853	-17.51013722	1.929E-18	8.483E-20	1.858E-18	3.857E-20	7.781E-19	2.003E-20
143	16.94477565	-17.50931635	1.055E-18	5.318E-20	1.436E-19	2.008E-20	3.135E-19	1.083E-20
144	16.94539874	-17.50988429	6.762E-19	4.305E-20	9.269E-19	1.785E-20	2.632E-19	7.643E-21
145	16.94380233	-17.50700346	1.041E-17	8.230E-20	9.485E-18	1.144E-19	4.348E-18	3.722E-20
146	16.94321757	-17.50686744	4.890E-19	5.191E-20	1.409E-18	7.682E-20	5.870E-19	2.335E-20
147	16.94365095	-17.50666039	2.496E-18	1.076E-19	2.567E-18	1.399E-19	7.019E-19	7.933E-20
148	16.94568136	-17.51085915	3.236E-18	6.204E-20	2.888E-18	4.590E-20	5.694E-19	1.352E-20
149	16.94414639	-17.50765777	1.492E-18	1.215E-19	5.418E-19	1.479E-19	3.680E-19	7.332E-20
150	16.94473685	-17.50901090	1.446E-18	6.457E-20	1.137E-18	7.490E-20	2.705E-19	3.814E-20
151	16.94504825	-17.50948933	2.277E-19	4.431E-20	1.737E-19	1.976E-20	2.488E-20	6.794E-21
152	16.94483832	-17.50999876	2.801E-19	4.305E-20	3.164E-19	1.881E-20	9.269E-20	1.125E-20
153	16.94469176	-17.50967262	8.647E-19	4.305E-20	6.771E-19	2.518E-20	1.576E-19	9.908E-21
154	16.94290549	-17.50704751	1.387E-16	6.900E-19	9.218E-17	4.137E-19	1.325E-17	8.124E-20
155	16.94370572	-17.50832507	2.607E-18	7.470E-20	2.586E-18	1.294E-19	7.452E-19	4.848E-20
156	16.94409766	-17.50911108	6.712E-19	4.811E-20	6.342E-19	3.697E-20	2.418E-19	1.677E-20
157	16.94403590	-17.50843953	2.103E-18	7.344E-20	1.395E-18	7.968E-20	2.402E-19	2.392E-20
158	16.94288694	-17.50804084	3.088E-16	8.901E-19	2.143E-16	6.534E-19	3.372E-17	1.321E-19
159	16.94356748	-17.50773847	1.532E-18	1.190E-19	1.379E-18	1.367E-19	2.431E-19	6.766E-20
160	16.94363860	-17.50867677	5.312E-19	6.710E-20	8.088E-19	7.905E-20	3.700E-19	2.470E-20

Table 5.3 continued

Table 5.3: Observational Properties of Individual Star Clusters (continued)

ID	R.A.	Decl.	f_{336}	$\sigma_{f_{336}}$	f_{435}	$\sigma_{f_{435}}$	f_{814}	$\sigma_{f_{814}}$
161	16.94330935	-17.50804303	2.325E-17	6.077E-19	1.867E-17	5.498E-19	3.301E-18	1.411E-19
162	16.94350924	-17.50824502	1.202E-17	5.204E-19	1.166E-17	2.116E-19	5.029E-19	8.853E-20
163	16.94348745	-17.50818249	9.874E-18	5.963E-19	1.058E-17	8.584E-19	5.679E-19	1.404E-19
164	16.94262805	-17.50666804	2.406E-19	3.925E-20	7.710E-19	2.614E-20	2.926E-19	1.012E-20
165	16.94307059	-17.50789003	4.063E-17	9.217E-19	3.517E-17	1.010E-18	5.892E-18	2.656E-19
166	16.94350724	-17.50958650	1.997E-18	4.431E-20	1.440E-18	3.060E-20	4.360E-19	1.274E-20
167	16.94321868	-17.50811481	4.334E-18	3.013E-19	4.561E-18	3.583E-19	4.914E-19	8.216E-20
168	16.94362562	-17.50921760	3.931E-19	5.191E-20	3.998E-19	4.399E-20	8.893E-20	1.982E-20
169	16.94224459	-17.50657923	7.608E-19	4.052E-20	9.626E-19	2.741E-20	2.663E-19	8.988E-21
170	16.94257322	-17.50789783	2.834E-18	1.013E-19	2.246E-18	1.692E-19	7.090E-19	5.294E-20
171	16.94349206	-17.50922670	2.692E-19	5.318E-20	4.167E-19	5.450E-20	2.098E-19	2.413E-20
172	16.94285362	-17.50916149	1.592E-18	6.204E-20	1.971E-18	6.502E-20	8.707E-19	2.696E-20
173	16.94182555	-17.50669495	3.364E-19	3.672E-20	5.514E-19	2.040E-20	1.200E-19	7.289E-21
174	16.94214490	-17.50796068	2.330E-19	5.191E-20	2.841E-19	6.120E-20	1.807E-19	1.812E-20
175	16.94231194	-17.50846233	2.453E-19	5.064E-20	2.367E-19	4.654E-20	6.538E-20	1.592E-20
176	16.94181275	-17.50791589	1.911E-19	4.052E-20	2.705E-19	2.422E-20	7.269E-20	1.090E-20
177	16.94179844	-17.50821217	3.740E-19	4.178E-20	6.221E-19	3.920E-20	1.606E-19	1.359E-20
178	16.93764322	-17.50227181	6.213E-19	3.419E-20	5.299E-19	2.486E-20	1.231E-19	6.794E-21
179	16.93774879	-17.50216195	2.390E-19	3.039E-20	2.380E-19	1.275E-20	4.964E-20	7.006E-21
180	16.93912642	-17.50743955	2.178E-18	3.419E-20	1.789E-18	1.402E-20	9.582E-19	1.154E-20
NGC 3256								
1	156.93884766	-43.92097221	6.340E-18	3.039E-20	1.161E-17	1.330E-20	5.056E-18	9.351E-21
2	156.93744620	-43.91740127	8.743E-17	2.178E-19	3.952E-16	1.070E-19	2.690E-16	6.922E-19
3	156.95745764	-43.92664192	3.559E-18	2.912E-20	2.466E-17	1.430E-20	6.604E-17	5.693E-20
4	156.95374348	-43.92440077	1.022E-17	3.292E-20	3.651E-17	3.128E-20	3.609E-17	5.215E-20
5	156.96045449	-43.92614191	5.167E-17	4.811E-20	8.114E-17	7.435E-20	3.731E-17	4.452E-20
6	156.95752259	-43.92269244	2.469E-18	3.039E-20	1.823E-17	1.301E-20	5.468E-17	1.356E-19
7	156.97554076	-43.92994067	2.036E-16	1.380E-19	3.809E-16	1.919E-19	1.147E-16	2.306E-19
8	156.97618084	-43.93021153	2.636E-18	3.419E-20	5.537E-18	1.310E-20	3.460E-18	6.551E-21
9	156.95100673	-43.91893797	1.165E-18	3.292E-20	8.450E-18	1.325E-20	3.896E-17	5.273E-20
10	156.94127425	-43.91313687	2.757E-17	4.305E-20	9.325E-17	3.313E-20	6.238E-17	1.096E-19
11	156.94714675	-43.91639882	3.242E-19	2.532E-20	4.146E-18	1.025E-20	2.345E-17	3.609E-20
12	156.96913345	-43.92619552	4.243E-19	2.785E-20	3.678E-19	1.404E-20	8.500E-20	5.315E-21
13	156.93423236	-43.91048447	9.956E-18	2.785E-20	3.967E-17	2.043E-20	4.159E-17	6.968E-20
14	156.97895383	-43.92953007	1.302E-17	4.558E-20	5.640E-17	2.452E-20	6.878E-17	8.281E-20
15	156.97219268	-43.92697195	8.832E-18	3.672E-20	4.700E-19	1.970E-20	1.592E-19	7.455E-21
16	156.93841101	-43.91122321	1.840E-17	3.292E-20	3.532E-17	2.638E-20	2.116E-17	3.010E-20
17	156.95308589	-43.91751934	4.263E-18	2.912E-20	9.604E-18	1.373E-20	6.814E-18	1.336E-20
18	156.96117790	-43.91918148	5.955E-17	5.064E-20	1.934E-16	1.427E-19	5.010E-17	1.757E-19
19	156.93484278	-43.90815336	5.960E-19	2.785E-20	5.456E-18	1.168E-20	3.078E-17	4.418E-20
20	156.93340912	-43.90679055	4.513E-17	9.369E-20	1.214E-16	7.009E-20	6.903E-17	1.131E-19
21	156.95490521	-43.91610704	1.927E-17	3.165E-20	3.595E-17	1.920E-20	1.954E-17	2.679E-20
22	156.96762055	-43.92110589	7.608E-18	3.165E-20	5.346E-17	3.576E-20	5.795E-17	1.640E-19
23	156.94317504	-43.91056299	8.482E-18	2.912E-20	2.952E-17	2.196E-20	3.193E-17	3.953E-20
24	156.94763684	-43.91159584	4.492E-19	3.039E-20	1.220E-18	1.050E-20	1.889E-18	5.591E-21
25	156.94766341	-43.90845900	1.411E-16	9.496E-20	3.370E-16	2.778E-19	2.620E-16	4.809E-19
26	156.93636547	-43.90514154	5.235E-19	3.292E-20	1.459E-18	1.160E-20	4.506E-19	4.215E-21
27	156.94689970	-43.90798821	3.201E-18	3.925E-20	2.014E-17	1.508E-20	7.208E-17	9.675E-20
28	156.93122742	-43.90240066	3.655E-19	3.292E-20	3.960E-19	1.436E-20	1.680E-19	5.842E-21
29	156.95342552	-43.91155529	3.474E-19	3.798E-20	1.137E-18	1.259E-20	4.264E-19	6.225E-21
30	156.96178853	-43.91510158	5.793E-19	2.659E-20	8.552E-19	1.595E-20	4.308E-19	7.568E-21

Table 5.3 continued

Table 5.3: Observational Properties of Individual Star Clusters (continued)

ID	R.A.	Decl.	f_{336}	$\sigma_{f_{336}}$	f_{435}	$\sigma_{f_{435}}$	f_{814}	$\sigma_{f_{814}}$
31	156.93353557	-43.90218017	4.212E-19	2.406E-20	3.611E-19	1.189E-20	4.331E-19	1.307E-20
32	156.94614817	-43.90720160	2.042E-18	3.039E-20	1.124E-17	1.455E-20	1.621E-17	2.227E-20
33	156.97392461	-43.91926581	1.864E-18	3.165E-20	4.239E-18	1.476E-20	3.717E-18	6.004E-21
34	156.93357450	-43.90197365	5.210E-19	2.912E-20	5.702E-19	1.381E-20	2.185E-19	8.524E-21
35	156.96037462	-43.91301866	4.427E-19	3.039E-20	9.308E-19	1.791E-20	3.170E-19	8.457E-21
36	156.95436576	-43.91004567	1.713E-16	1.304E-19	3.905E-16	1.616E-19	2.161E-16	2.823E-19
37	156.97167758	-43.91755250	7.449E-19	2.659E-20	3.949E-19	1.875E-20	1.526E-19	2.668E-20
38	156.95792447	-43.91159703	4.302E-19	3.165E-20	8.003E-19	1.930E-20	2.649E-19	9.889E-21
39	156.95946585	-43.91197679	3.565E-19	2.912E-20	6.357E-19	2.252E-20	2.499E-19	1.073E-20
40	156.95965488	-43.91190180	2.283E-18	3.672E-20	2.667E-18	1.752E-20	7.710E-19	9.610E-21
41	156.95494342	-43.90949121	5.917E-19	3.292E-20	8.615E-19	1.880E-20	2.644E-19	1.188E-20
42	156.96493240	-43.91253843	1.246E-15	8.762E-19	2.334E-16	1.004E-18	4.080E-16	1.898E-18
43	156.95701200	-43.91048419	6.422E-19	3.545E-20	4.078E-19	1.761E-20	7.896E-20	8.349E-21
44	156.95533966	-43.90937999	5.327E-19	3.798E-20	6.632E-19	2.321E-20	2.273E-19	1.353E-20
45	156.95906397	-43.91098668	4.831E-19	3.292E-20	8.775E-19	1.777E-20	2.920E-19	7.889E-21
46	156.95549131	-43.90919028	1.064E-18	3.925E-20	1.145E-18	2.740E-20	1.667E-19	1.053E-20
47	156.95411551	-43.90861452	2.640E-19	3.039E-20	9.640E-19	2.254E-20	2.977E-19	9.270E-21
48	156.95916078	-43.91077381	4.120E-19	3.292E-20	2.597E-19	1.406E-20	4.388E-20	8.919E-21
49	156.95671687	-43.90971900	5.928E-19	2.532E-20	4.318E-19	1.408E-20	1.521E-19	6.728E-21
50	156.95381773	-43.90800067	9.291E-19	2.785E-20	1.963E-18	2.008E-20	6.284E-19	9.174E-21
51	156.95582353	-43.90921061	3.207E-19	3.925E-20	3.618E-19	3.238E-20	1.111E-19	1.328E-20
52	156.95603538	-43.90895053	1.183E-18	6.077E-20	1.372E-18	5.578E-20	3.036E-19	2.420E-20
53	156.95653521	-43.90924048	6.596E-19	3.545E-20	1.473E-18	1.845E-20	5.529E-19	9.304E-21
54	156.96031942	-43.91070331	1.634E-18	3.545E-20	1.589E-18	1.541E-20	5.061E-19	9.816E-21
55	156.95606245	-43.90909246	8.055E-19	5.064E-20	1.144E-18	4.255E-20	3.580E-19	2.080E-20
56	156.95944952	-43.91042975	1.043E-18	2.912E-20	1.692E-18	1.840E-20	6.604E-19	1.033E-20
57	156.94829267	-43.90258662	7.750E-16	7.647E-19	9.411E-16	6.068E-19	4.494E-16	1.351E-18
58	156.95685186	-43.90891193	4.597E-18	8.483E-20	2.927E-18	7.396E-20	9.537E-19	3.257E-20
59	156.95334755	-43.90708981	1.083E-18	3.798E-20	3.023E-18	2.191E-20	1.021E-18	1.215E-20
60	156.95444771	-43.90785442	1.087E-18	3.672E-20	7.886E-19	2.624E-20	2.339E-19	1.153E-20
61	156.95333896	-43.90684600	1.832E-18	3.798E-20	1.450E-18	2.873E-20	4.136E-19	1.213E-20
62	156.95705639	-43.90891457	2.590E-18	7.723E-20	2.152E-18	6.312E-20	8.148E-19	1.476E-20
63	156.95739104	-43.90902907	2.478E-19	4.305E-20	2.619E-19	2.259E-20	1.229E-19	9.747E-21
64	156.95734618	-43.90912698	5.158E-19	4.178E-20	4.262E-19	1.511E-20	1.058E-19	7.516E-21
65	156.95338349	-43.90723131	5.235E-19	4.178E-20	6.230E-19	2.734E-20	2.011E-19	1.463E-20
66	156.95610520	-43.90852118	4.735E-19	3.545E-20	2.067E-19	1.841E-20	5.344E-20	7.871E-21
67	156.95456390	-43.90784788	5.578E-19	3.165E-20	7.366E-19	2.286E-20	1.411E-19	1.440E-20
68	156.95363989	-43.90719227	5.491E-19	3.292E-20	3.588E-19	1.698E-20	1.179E-19	9.003E-21
69	156.95913639	-43.90951848	8.388E-19	4.431E-20	7.559E-19	2.925E-20	1.843E-19	1.189E-20
70	156.95689966	-43.90868849	6.843E-19	4.052E-20	4.656E-19	3.550E-20	6.354E-20	1.003E-20
71	156.98253530	-43.91904570	2.568E-18	2.659E-20	1.404E-17	1.745E-20	1.826E-17	2.694E-20
72	156.96922651	-43.91367951	6.038E-19	3.419E-20	2.005E-18	1.850E-20	6.255E-19	1.381E-20
73	156.95562870	-43.90770258	3.062E-18	5.444E-20	1.965E-18	3.254E-20	3.547E-19	1.602E-20
74	156.95533310	-43.90778386	7.728E-19	3.165E-20	6.218E-19	2.281E-20	6.192E-20	9.785E-21
75	156.95737323	-43.90857024	8.647E-19	4.431E-20	3.401E-19	2.409E-20	1.734E-19	1.471E-20
76	156.95816204	-43.90864059	3.266E-19	3.419E-20	3.201E-19	1.383E-20	5.052E-20	1.034E-20
77	156.95788389	-43.90855930	6.334E-19	3.672E-20	1.881E-19	1.714E-20	3.721E-20	6.777E-21
78	156.95611596	-43.90756984	1.048E-17	6.204E-20	5.755E-18	5.057E-20	9.226E-19	2.685E-20
79	156.95964400	-43.90649378	7.313E-19	6.204E-20	6.913E-19	8.704E-20	2.341E-19	5.771E-20
80	156.95529594	-43.90720634	3.743E-19	3.672E-20	2.798E-19	3.170E-20	8.666E-20	1.377E-20
81	156.95540365	-43.90710586	2.550E-19	4.178E-20	2.788E-19	3.567E-20	3.910E-19	1.469E-20
82	156.95470121	-43.90642398	5.254E-19	3.292E-20	1.621E-18	3.266E-20	6.007E-19	1.707E-20
83	156.97128877	-43.91376125	6.750E-19	3.419E-20	1.463E-18	2.024E-20	5.075E-19	8.537E-21

Table 5.3 continued

Table 5.3: Observational Properties of Individual Star Clusters (continued)

ID	R.A.	Decl.	f_{336}	$\sigma_{f_{336}}$	f_{435}	$\sigma_{f_{435}}$	f_{814}	$\sigma_{f_{814}}$
84	156.97554351	-43.91454571	3.938E-19	3.419E-20	3.145E-18	1.321E-20	1.126E-17	1.386E-20
85	156.95409299	-43.90642573	3.057E-19	3.798E-20	1.566E-18	2.889E-20	5.112E-19	1.834E-20
86	156.95533669	-43.90662628	6.645E-18	4.938E-20	1.678E-17	4.845E-20	5.601E-18	2.422E-20
87	156.95333530	-43.90544671	6.793E-18	4.558E-20	1.645E-17	3.879E-20	5.246E-18	1.880E-20
88	156.97153545	-43.91370638	7.945E-19	3.419E-20	1.709E-18	1.951E-20	5.136E-19	8.046E-21
89	156.95592200	-43.90702145	7.857E-19	4.431E-20	1.634E-18	3.186E-20	5.280E-19	1.419E-20
90	156.95495577	-43.90659717	7.807E-19	4.178E-20	2.453E-18	2.365E-20	7.228E-19	1.142E-20
91	156.95318761	-43.90572830	3.754E-19	3.292E-20	1.067E-18	1.871E-20	2.904E-19	1.119E-20
92	156.95480545	-43.90656599	4.721E-19	3.545E-20	9.438E-19	3.066E-20	2.376E-19	1.258E-20
93	156.95683378	-43.90717887	1.857E-18	5.064E-20	1.427E-18	6.126E-20	7.590E-19	3.936E-20
94	156.96613161	-43.91110881	1.637E-18	3.419E-20	2.249E-18	1.705E-20	6.550E-19	9.564E-21
95	156.95566285	-43.90672476	1.310E-18	4.178E-20	3.224E-18	3.576E-20	9.083E-19	1.918E-20
96	156.95402896	-43.90566505	2.347E-18	3.545E-20	6.121E-18	3.365E-20	1.978E-18	1.928E-20
97	156.95590568	-43.90688373	7.219E-19	4.685E-20	7.306E-19	2.761E-20	1.884E-19	1.085E-20
98	156.97698659	-43.91578322	4.831E-19	2.659E-20	1.379E-18	1.324E-20	4.248E-19	5.562E-21
99	156.95563421	-43.90657308	5.676E-19	4.178E-20	1.636E-18	3.890E-20	4.955E-19	1.339E-20
100	156.95621895	-43.90662705	1.474E-18	5.064E-20	2.508E-18	4.462E-20	6.871E-19	2.666E-20
101	156.96062426	-43.90789397	3.389E-19	2.785E-20	8.552E-19	3.173E-20	8.674E-19	2.772E-20
102	156.95604294	-43.90592346	7.483E-19	4.178E-20	1.267E-18	5.078E-20	6.629E-19	2.610E-20
103	156.95613270	-43.90656936	1.500E-18	4.178E-20	4.158E-18	3.323E-20	1.291E-18	2.034E-20
104	156.97455145	-43.91364903	1.123E-18	3.039E-20	2.626E-18	2.927E-20	7.926E-19	1.245E-20
105	156.95573870	-43.90638089	6.004E-19	3.545E-20	1.578E-18	3.775E-20	6.672E-19	1.624E-20
106	156.96000946	-43.90752771	6.932E-18	3.798E-20	3.361E-17	1.240E-19	3.482E-17	1.526E-19
107	156.95650861	-43.90541893	5.416E-17	2.114E-19	8.235E-17	2.884E-19	3.576E-17	1.228E-19
108	156.95604489	-43.90548918	1.780E-17	1.215E-19	2.489E-17	2.232E-19	7.309E-18	1.347E-19
109	156.95532007	-43.90629013	2.732E-19	3.672E-20	1.992E-19	2.494E-20	8.666E-20	1.189E-20
110	156.94111097	-43.89878772	6.657E-17	5.318E-20	1.721E-16	7.672E-20	1.070E-16	1.592E-19
111	156.95481472	-43.90599679	5.988E-19	4.178E-20	1.114E-18	5.505E-20	4.312E-19	2.152E-20
112	156.95679527	-43.90680587	3.236E-19	4.811E-20	4.976E-19	3.578E-20	1.370E-19	2.148E-20
113	156.95709281	-43.90649168	8.576E-19	6.204E-20	8.085E-19	4.814E-20	4.233E-19	2.538E-20
114	156.95716996	-43.90564136	2.304E-18	5.444E-20	3.723E-18	1.114E-19	1.265E-18	5.166E-20
115	156.94653083	-43.90175339	8.342E-18	3.292E-20	1.322E-17	1.701E-20	5.570E-18	8.774E-21
116	156.96489556	-43.90978952	3.465E-19	3.165E-20	1.263E-18	1.914E-20	3.613E-19	7.653E-21
117	156.95563927	-43.90594618	1.497E-18	3.925E-20	2.729E-18	6.208E-20	7.451E-19	1.910E-20
118	156.95975695	-43.90612789	5.960E-19	4.558E-20	1.434E-18	1.131E-19	3.089E-18	1.064E-19
119	156.95509228	-43.90573560	2.564E-19	3.419E-20	5.814E-19	2.867E-20	1.543E-19	1.471E-20
120	156.95463111	-43.90520576	4.614E-19	3.798E-20	8.062E-19	2.104E-20	2.756E-19	1.180E-20
121	156.95514593	-43.90532161	8.419E-19	3.165E-20	1.974E-18	2.698E-20	6.715E-19	1.224E-20
122	156.96628972	-43.91019294	3.859E-19	2.912E-20	1.238E-18	1.676E-20	4.633E-19	8.764E-21
123	156.96188541	-43.90829672	1.621E-18	1.304E-19	2.040E-18	1.692E-19	8.852E-19	4.001E-20
124	156.95829771	-43.90547061	1.743E-17	1.102E-19	3.771E-17	1.610E-19	1.425E-17	8.747E-20
125	156.95778312	-43.90546413	1.325E-18	4.685E-20	3.122E-18	6.970E-20	2.217E-18	5.902E-20
126	156.96304865	-43.90820349	3.339E-19	3.419E-20	1.026E-18	3.269E-20	1.080E-18	2.247E-20
127	156.95837244	-43.90635866	4.695E-19	4.811E-20	1.287E-18	1.502E-19	1.799E-18	9.561E-20
128	156.95969239	-43.90628711	5.537E-19	4.685E-20	2.206E-18	6.547E-20	1.420E-18	6.973E-20
129	156.95977215	-43.90664624	2.057E-18	7.090E-20	7.252E-18	1.012E-19	6.544E-18	8.175E-20
130	156.96088589	-43.90711937	3.373E-19	3.798E-20	4.350E-19	2.884E-20	3.860E-19	2.186E-20
131	156.95599927	-43.90536722	2.933E-18	7.344E-20	4.056E-18	1.348E-19	1.053E-18	5.443E-20
132	156.95847822	-43.90574484	1.505E-18	7.217E-20	1.878E-18	1.753E-19	2.807E-18	6.175E-20
133	156.95622177	-43.90533009	2.249E-18	8.736E-20	2.355E-18	1.101E-19	6.678E-19	5.735E-20
134	156.95659686	-43.90520740	1.808E-18	8.863E-20	4.410E-18	1.398E-19	1.729E-18	7.222E-20
135	156.96033033	-43.90620386	1.700E-17	1.051E-19	2.388E-17	1.957E-19	1.056E-17	1.366E-19
136	156.96318047	-43.90776302	7.003E-19	3.292E-20	8.326E-19	2.125E-20	4.654E-19	1.061E-20

Table 5.3 continued

Table 5.3: Observational Properties of Individual Star Clusters (continued)

ID	R.A.	Decl.	f_{336}	$\sigma_{f_{336}}$	f_{435}	$\sigma_{f_{435}}$	f_{814}	$\sigma_{f_{814}}$
137	156.96022960	-43.90666541	9.640E-19	7.597E-20	1.391E-18	7.477E-20	3.673E-19	2.557E-20
138	156.95769584	-43.90567902	7.353E-19	5.191E-20	1.598E-18	8.458E-20	2.891E-19	4.203E-20
139	156.95861107	-43.90598720	4.439E-18	7.470E-20	5.210E-18	1.800E-19	2.934E-18	1.030E-19
140	156.95650684	-43.90456139	1.478E-18	4.178E-20	4.521E-18	7.377E-20	3.098E-18	3.256E-20
141	156.97872391	-43.91425663	3.628E-19	3.165E-20	9.029E-19	1.441E-20	3.202E-19	5.339E-21
142	156.95810310	-43.90563250	5.013E-18	8.610E-20	5.734E-18	1.521E-19	3.560E-18	1.505E-19
143	156.96442828	-43.90829078	5.041E-19	3.798E-20	8.033E-19	1.725E-20	2.649E-19	1.038E-20
144	156.96066193	-43.90663202	9.122E-19	6.204E-20	9.499E-19	1.021E-19	5.710E-19	4.061E-20
145	156.97594030	-43.91312425	5.317E-19	3.925E-20	1.365E-18	1.477E-20	5.757E-19	7.730E-21
146	156.96732301	-43.90944293	3.555E-19	3.419E-20	9.438E-19	1.492E-20	2.536E-19	7.458E-21
147	156.95659284	-43.90475126	1.225E-18	5.571E-20	3.207E-18	8.685E-20	2.918E-18	3.294E-20
148	156.96056235	-43.90603901	3.635E-18	9.749E-20	4.278E-18	2.159E-19	4.009E-18	1.095E-19
149	156.96332659	-43.90635665	1.143E-17	9.876E-20	1.305E-17	1.626E-19	2.830E-18	2.367E-19
150	156.95663076	-43.90488669	6.675E-19	4.431E-20	1.234E-18	7.621E-20	3.437E-19	2.611E-20
151	156.96473789	-43.90839751	4.208E-19	4.052E-20	1.048E-19	2.152E-20	8.876E-20	9.388E-21
152	156.96251534	-43.90708731	3.500E-19	3.292E-20	9.403E-19	3.250E-20	7.646E-19	3.220E-20
153	156.96613387	-43.90843470	9.266E-19	4.431E-20	1.091E-18	2.337E-20	3.759E-19	8.397E-21
154	156.95646473	-43.90475092	5.771E-19	5.064E-20	4.067E-19	8.656E-20	1.880E-19	3.222E-20
155	156.95666237	-43.90483942	4.756E-19	5.318E-20	1.311E-18	6.027E-20	6.124E-19	3.269E-20
156	156.95494389	-43.90359056	3.615E-19	2.659E-20	2.505E-18	1.742E-20	2.129E-18	8.730E-21
157	156.96233647	-43.90660297	7.836E-19	4.305E-20	1.913E-18	7.934E-20	7.562E-19	5.670E-20
158	156.96533630	-43.90816737	3.905E-18	4.811E-20	4.116E-18	4.250E-20	1.626E-18	1.541E-20
159	156.96516420	-43.90829846	1.897E-18	4.305E-20	1.284E-18	3.102E-20	2.774E-19	2.047E-20
160	156.95731750	-43.90478988	1.692E-18	4.305E-20	5.552E-18	3.088E-20	5.720E-18	1.788E-20
161	156.95971631	-43.90578098	1.133E-17	2.785E-19	1.909E-17	6.482E-19	8.958E-18	2.693E-19
162	156.96166663	-43.90665227	1.210E-18	4.938E-20	1.508E-18	6.313E-20	8.876E-19	3.134E-20
163	156.96514902	-43.90817530	6.201E-19	3.419E-20	6.392E-19	3.859E-20	5.870E-20	1.548E-20
164	156.96253053	-43.90687197	1.166E-18	3.292E-20	2.827E-18	2.649E-20	3.353E-18	2.437E-20
165	156.96080477	-43.90626776	2.115E-18	8.230E-20	2.587E-18	1.668E-19	9.450E-19	7.117E-20
166	156.96495726	-43.90796308	5.846E-19	4.178E-20	1.018E-18	1.957E-20	4.932E-19	1.469E-20
167	156.95994527	-43.90548344	5.381E-18	4.178E-20	1.913E-17	8.736E-20	2.006E-17	1.330E-19
168	156.96823950	-43.90933360	1.210E-18	3.292E-20	2.858E-18	1.752E-20	9.338E-19	8.803E-21
169	156.97851443	-43.91371174	9.756E-19	4.052E-20	2.455E-18	1.687E-20	7.431E-19	6.267E-21
170	156.95486892	-43.90332340	1.649E-18	3.292E-20	6.138E-18	2.902E-20	2.624E-18	1.917E-20
171	156.96069771	-43.90529659	6.387E-18	7.850E-20	1.144E-17	1.507E-19	7.926E-18	1.417E-19
172	156.94241138	-43.89688033	9.910E-18	3.672E-20	6.657E-17	4.189E-20	9.932E-17	2.393E-19
173	156.96073777	-43.90548231	3.852E-18	6.710E-20	1.070E-17	1.471E-19	1.917E-17	2.503E-19
174	156.96548169	-43.90775509	9.438E-19	3.798E-20	1.362E-18	2.213E-20	7.590E-19	1.663E-20
175	156.96589261	-43.90808275	5.803E-19	4.052E-20	6.357E-19	2.656E-20	2.298E-19	1.612E-20
176	156.98032180	-43.91376883	5.215E-17	5.064E-20	1.245E-16	7.740E-20	8.066E-17	8.562E-20
177	156.96095669	-43.90607984	2.917E-18	7.723E-20	3.278E-18	1.222E-19	9.643E-19	6.414E-20
178	156.96186919	-43.90655109	2.874E-19	3.672E-20	8.258E-19	4.463E-20	1.496E-19	4.034E-20
179	156.96219728	-43.90664461	5.809E-19	4.178E-20	1.076E-18	4.305E-20	6.389E-19	4.810E-20
180	156.96834012	-43.90916765	1.117E-18	3.419E-20	2.892E-18	1.552E-20	1.006E-18	9.704E-21
181	156.96552534	-43.90798698	5.819E-19	4.938E-20	6.316E-19	4.634E-20	1.181E-19	3.040E-20
182	156.97246038	-43.91093024	3.723E-19	4.178E-20	4.827E-19	1.289E-20	1.684E-19	6.179E-21
183	156.96572756	-43.90797276	2.742E-19	4.558E-20	9.873E-19	4.261E-20	3.403E-19	2.165E-20
184	156.96263285	-43.90615869	4.139E-19	4.178E-20	2.607E-18	8.268E-20	5.570E-18	8.521E-20
185	156.95239216	-43.90205293	1.009E-18	3.039E-20	2.845E-18	1.529E-20	9.877E-19	7.610E-21
186	156.96481413	-43.90740548	4.778E-19	2.785E-20	1.084E-18	2.024E-20	3.673E-19	1.268E-20
187	156.95825090	-43.90421708	3.562E-19	4.811E-20	1.683E-18	4.735E-20	1.456E-18	2.685E-20
188	156.96718448	-43.90762301	1.761E-17	6.077E-20	2.005E-17	3.520E-20	7.403E-18	3.317E-20
189	156.96391973	-43.90690119	1.381E-18	4.938E-20	1.471E-18	4.224E-20	4.557E-19	2.404E-20

Table 5.3 continued

Table 5.3: Observational Properties of Individual Star Clusters (continued)

ID	R.A.	Decl.	f_{336}	$\sigma_{f_{336}}$	f_{435}	$\sigma_{f_{435}}$	f_{814}	$\sigma_{f_{814}}$
190	156.96722379	-43.90838804	2.821E-19	3.925E-20	8.735E-19	1.939E-20	3.161E-19	1.553E-20
191	156.96631762	-43.90761804	2.767E-18	4.052E-20	4.656E-18	2.187E-20	2.275E-18	1.469E-20
192	156.96336363	-43.90599341	4.567E-18	4.178E-20	7.587E-18	1.202E-19	8.453E-18	1.831E-19
193	156.96574162	-43.90763400	7.601E-19	4.178E-20	7.615E-19	2.374E-20	8.532E-20	1.246E-20
194	156.96678720	-43.90761856	1.402E-18	3.545E-20	3.555E-18	2.580E-20	1.133E-18	1.535E-20
195	156.96421109	-43.90674773	6.725E-19	4.431E-20	9.693E-19	6.558E-20	2.449E-19	5.222E-20
196	156.97777690	-43.91265048	6.926E-19	4.052E-20	1.675E-19	1.261E-20	6.442E-20	6.002E-21
197	156.97177762	-43.90955621	2.462E-18	3.672E-20	4.037E-18	2.287E-20	1.298E-18	9.180E-21
198	156.96426889	-43.90622973	2.103E-18	4.178E-20	2.444E-18	4.008E-20	1.651E-18	4.278E-20
199	156.96166953	-43.90424508	3.601E-19	6.584E-20	1.417E-18	1.175E-19	1.563E-18	1.380E-19
200	156.96093562	-43.90429566	1.681E-18	1.013E-19	6.529E-18	1.750E-19	2.037E-17	2.646E-19
201	156.95556058	-43.90237819	1.258E-18	4.431E-20	2.827E-18	2.258E-20	1.283E-18	1.143E-20
202	156.96567603	-43.90538134	2.901E-18	1.089E-19	8.129E-18	3.101E-19	1.123E-17	2.247E-19
203	156.93973313	-43.89563522	9.552E-19	3.165E-20	1.336E-18	1.022E-20	5.731E-19	6.892E-21
204	156.98380012	-43.91447669	7.821E-19	3.545E-20	1.897E-18	1.460E-20	5.358E-19	5.444E-21
205	156.94559856	-43.89807779	1.268E-18	3.292E-20	3.439E-18	1.345E-20	2.627E-18	6.187E-21
206	156.95844415	-43.90338923	2.941E-19	3.798E-20	5.671E-19	2.451E-20	3.534E-19	1.696E-20
207	156.94311370	-43.89655744	7.100E-18	4.305E-20	1.034E-17	1.284E-20	5.339E-18	8.390E-21
208	156.97971198	-43.91260618	3.582E-19	2.912E-20	5.078E-19	1.245E-20	2.250E-19	5.831E-21
209	156.96400761	-43.90578556	1.413E-18	4.558E-20	5.624E-18	9.368E-20	4.569E-18	2.045E-19
210	156.96508663	-43.90605436	9.386E-19	5.571E-20	1.410E-18	5.319E-20	7.012E-19	3.929E-20
211	156.96130256	-43.90452501	7.081E-18	1.165E-19	1.025E-17	3.290E-19	6.221E-18	3.200E-19
212	156.97057019	-43.90844777	5.977E-19	3.545E-20	1.486E-18	1.911E-20	4.637E-19	8.745E-21
213	156.98414354	-43.91409917	2.016E-18	3.292E-20	4.505E-18	1.820E-20	1.400E-18	8.318E-21
214	156.97085579	-43.90851480	5.396E-19	3.798E-20	8.489E-19	1.795E-20	4.272E-19	7.528E-21
215	156.96212839	-43.90442809	7.166E-18	7.344E-20	1.654E-17	8.230E-20	1.122E-17	2.468E-19
216	156.96031923	-43.90354069	4.484E-18	5.571E-20	8.914E-18	1.896E-19	8.967E-18	1.958E-19
217	156.96585801	-43.90593403	9.181E-18	8.610E-20	9.828E-18	1.717E-19	3.965E-18	1.227E-19
218	156.96055992	-43.90365843	2.038E-18	1.127E-19	6.737E-18	2.222E-19	4.171E-18	1.533E-19
219	156.95874062	-43.90298759	3.996E-19	3.419E-20	2.460E-18	3.377E-20	6.284E-18	4.324E-20
220	156.96417502	-43.90494260	6.663E-19	5.191E-20	2.750E-18	1.223E-19	8.763E-18	4.144E-19
221	156.96236355	-43.90377154	1.235E-18	4.052E-20	4.278E-18	7.563E-20	3.147E-18	1.401E-19
222	156.96009188	-43.90332168	1.950E-18	4.431E-20	2.850E-18	8.721E-20	1.989E-18	5.939E-20
223	156.96072554	-43.90172113	1.456E-18	8.230E-20	2.908E-18	1.040E-19	1.721E-18	5.144E-20
224	156.95987796	-43.90189958	1.125E-18	4.685E-20	2.803E-18	6.908E-20	4.076E-18	4.123E-20
225	156.95971117	-43.90267911	1.300E-18	3.672E-20	3.665E-18	5.401E-20	2.431E-18	3.196E-20
226	156.96430898	-43.90487839	2.347E-18	4.431E-20	6.212E-18	1.134E-19	6.255E-18	5.286E-19
227	156.96001143	-43.90256080	1.793E-18	6.584E-20	2.861E-18	8.557E-20	9.235E-19	3.285E-20
228	156.95210071	-43.89999988	2.170E-19	3.545E-20	2.160E-19	1.349E-20	8.407E-20	6.494E-21
229	156.96597320	-43.90430135	2.752E-17	4.317E-19	3.449E-17	4.436E-19	1.450E-17	1.664E-19
230	156.96555602	-43.90554950	2.694E-18	9.496E-20	2.694E-18	1.465E-19	1.156E-18	4.451E-20
231	156.96578141	-43.90563102	1.901E-18	9.623E-20	1.359E-18	1.466E-19	3.683E-19	6.620E-20
232	156.96627000	-43.90587978	4.572E-19	3.419E-20	1.020E-18	2.400E-20	4.557E-19	2.615E-20
233	156.95921647	-43.90272858	6.990E-19	4.052E-20	2.212E-18	6.481E-20	1.645E-18	2.795E-20
234	156.96407104	-43.90423553	1.248E-16	7.483E-19	1.328E-16	1.239E-18	5.089E-17	7.254E-19
235	156.96616853	-43.90567220	9.317E-19	4.305E-20	1.633E-18	4.331E-20	7.867E-19	6.625E-20
236	156.96435927	-43.90447681	1.146E-17	3.457E-19	1.643E-17	6.536E-19	3.673E-18	3.605E-19
237	156.96610384	-43.90556757	1.568E-18	5.318E-20	1.536E-18	4.610E-20	5.353E-19	3.507E-20
238	156.96019859	-43.90249667	7.272E-19	5.064E-20	4.747E-18	1.204E-19	1.170E-17	6.742E-20
239	156.96282351	-43.90401105	3.789E-19	6.331E-20	3.006E-18	1.597E-19	4.016E-18	3.099E-19
240	156.96445532	-43.90417049	1.363E-17	5.533E-19	1.970E-17	8.526E-19	7.977E-18	3.680E-19
241	156.96234509	-43.90306759	1.748E-18	1.266E-19	4.726E-18	3.355E-19	5.122E-18	3.270E-19
242	156.96422703	-43.90455556	3.392E-18	3.938E-19	6.768E-18	6.071E-19	1.496E-18	3.335E-19

Table 5.3 continued

Table 5.3: Observational Properties of Individual Star Clusters (continued)

ID	R.A.	Decl.	f_{336}	$\sigma_{f_{336}}$	f_{435}	$\sigma_{f_{435}}$	f_{814}	$\sigma_{f_{814}}$
243	156.96217600	-43.90371116	7.518E-19	4.178E-20	9.464E-19	5.935E-20	1.165E-18	1.446E-19
244	156.96479245	-43.90457208	4.903E-18	1.152E-19	8.865E-18	3.031E-19	6.752E-18	3.852E-19
245	156.96108547	-43.90293833	1.787E-18	5.318E-20	3.145E-18	1.229E-19	1.274E-18	1.483E-19
246	156.96488623	-43.90447166	7.153E-18	2.583E-19	7.441E-18	3.377E-19	6.068E-18	4.081E-19
247	156.98478588	-43.91285302	1.303E-18	3.672E-20	3.122E-18	1.605E-20	9.511E-19	6.790E-21
248	156.96686999	-43.90499547	4.990E-19	3.292E-20	1.124E-18	4.505E-20	9.555E-19	8.794E-20
249	156.96432774	-43.90413175	1.501E-17	1.403E-18	1.678E-17	1.596E-18	8.391E-18	6.346E-19
250	156.96549585	-43.90453634	2.871E-17	4.317E-19	3.545E-17	6.543E-19	1.684E-17	3.205E-19
251	156.96004762	-43.90197868	5.517E-19	3.925E-20	1.883E-18	4.363E-20	2.551E-18	4.577E-20
252	156.96695180	-43.90385693	6.247E-17	2.773E-19	8.583E-17	5.657E-19	3.976E-17	2.830E-19
253	156.95819826	-43.90058033	1.059E-16	1.304E-19	2.390E-16	1.291E-19	1.009E-16	1.560E-19
254	156.96130855	-43.90220626	3.471E-17	3.469E-19	2.433E-17	5.688E-19	8.223E-18	2.663E-19
255	156.96397375	-43.90349896	3.481E-17	5.305E-19	7.400E-17	8.538E-19	5.565E-17	1.176E-18
256	156.96644587	-43.90423656	2.241E-17	1.735E-19	1.680E-17	3.033E-19	5.319E-18	1.700E-19
257	156.96507520	-43.90362793	9.720E-17	1.314E-18	8.848E-17	1.687E-18	1.964E-17	5.753E-19
258	156.96540958	-43.90381893	3.761E-17	8.496E-19	3.682E-17	1.363E-18	9.415E-18	3.270E-19
259	156.96678791	-43.90472006	1.579E-18	3.545E-20	2.607E-18	5.724E-20	1.817E-18	8.629E-20
260	156.96405464	-43.90339802	9.232E-17	7.521E-19	1.068E-16	1.273E-18	5.908E-17	1.091E-18
261	156.96564666	-43.90364229	7.552E-16	1.840E-18	6.945E-16	2.927E-18	1.545E-16	7.016E-19
262	156.98891348	-43.91375524	6.173E-18	3.292E-20	1.103E-17	1.550E-20	6.430E-18	1.010E-20
263	156.97416262	-43.90739181	2.834E-19	3.419E-20	1.106E-18	1.641E-20	3.738E-19	8.222E-21
264	156.96320214	-43.90270946	2.559E-17	3.532E-19	2.533E-17	6.376E-19	1.001E-17	2.530E-19
265	156.96234450	-43.90269442	5.092E-18	2.710E-19	5.650E-18	5.202E-19	1.969E-18	3.213E-19
266	156.96448914	-43.90367949	3.702E-17	7.407E-19	4.644E-17	1.347E-18	1.350E-17	5.367E-19
267	156.96349759	-43.90284674	3.330E-17	1.874E-19	5.537E-17	4.054E-19	2.100E-17	2.427E-19
268	156.95322084	-43.89860811	9.956E-19	3.545E-20	3.562E-18	1.669E-20	1.337E-18	6.727E-21
269	156.95899072	-43.90105795	3.841E-19	3.545E-20	1.862E-18	2.071E-20	5.710E-19	9.617E-21
270	156.96371734	-43.90311558	1.015E-17	1.887E-19	1.077E-17	6.290E-19	6.209E-18	2.525E-19
271	156.96619292	-43.90397505	7.785E-17	5.925E-19	5.792E-17	7.697E-19	1.116E-17	2.068E-19
272	156.96377967	-43.90288761	7.266E-18	1.937E-19	9.377E-18	2.649E-19	2.143E-18	1.767E-19
273	156.96531855	-43.90335342	5.624E-18	2.634E-19	2.487E-18	4.801E-19	6.360E-18	2.482E-19
274	156.96449479	-43.90301462	4.294E-18	9.243E-20	7.944E-18	3.254E-19	3.965E-18	1.428E-19
275	156.96566795	-43.90385926	1.331E-16	1.448E-18	8.497E-17	1.164E-18	1.520E-17	4.708E-19
276	156.96522753	-43.90372035	1.485E-17	1.099E-18	1.637E-17	8.683E-19	1.284E-18	3.377E-19
277	156.96250725	-43.90229709	3.723E-18	1.456E-19	5.205E-18	3.576E-19	1.407E-18	2.165E-19
278	156.96213417	-43.90190815	8.584E-18	1.494E-19	2.790E-17	2.559E-19	2.048E-17	1.394E-19
279	156.96422561	-43.90299628	5.476E-18	1.102E-19	7.615E-18	2.927E-19	4.536E-18	1.593E-19
280	156.96312080	-43.90198826	1.344E-18	1.089E-19	1.340E-18	2.554E-19	2.634E-18	1.097E-19
281	156.96576630	-43.90384331	9.473E-17	1.435E-18	6.724E-17	9.865E-19	1.312E-17	4.096E-19
282	156.96230920	-43.90218451	4.374E-18	1.114E-19	3.490E-18	2.364E-19	1.485E-18	1.481E-19
283	156.96389893	-43.90258481	3.077E-17	5.178E-19	4.805E-17	6.821E-19	2.454E-17	3.352E-19
284	156.96392069	-43.90275696	9.892E-18	5.356E-19	8.687E-18	4.965E-19	2.666E-18	2.611E-19
285	156.96158246	-43.90184476	1.170E-17	3.001E-19	1.777E-17	3.190E-19	1.052E-17	2.232E-19
286	156.96340072	-43.90260747	7.087E-18	2.469E-19	8.905E-18	3.198E-19	3.381E-18	1.722E-19
287	156.96442567	-43.90283659	6.774E-18	4.305E-19	1.197E-17	6.085E-19	7.838E-18	2.606E-19
288	156.96181123	-43.90192991	1.440E-17	2.634E-19	8.775E-18	2.973E-19	2.205E-18	9.171E-20
289	156.95940972	-43.90087343	5.172E-19	3.419E-20	1.738E-18	2.520E-20	7.064E-19	1.150E-20
290	156.96853251	-43.90479479	8.703E-19	3.545E-20	1.321E-18	3.323E-20	4.312E-19	2.281E-20
291	156.96306461	-43.90230699	2.533E-18	1.849E-19	1.840E-18	3.867E-19	8.291E-19	1.162E-19
292	156.96701145	-43.90370970	6.393E-18	1.279E-19	5.573E-18	3.503E-19	8.036E-19	1.106E-19
293	156.95994626	-43.90048362	7.435E-19	3.545E-20	2.861E-18	4.400E-20	1.940E-18	2.509E-20
294	156.96531909	-43.90277529	1.555E-17	4.355E-19	1.643E-17	6.749E-19	3.235E-18	1.737E-19
295	156.96453715	-43.90241111	5.153E-17	4.178E-19	6.762E-17	6.538E-19	2.859E-17	3.326E-19

Table 5.3 continued

Table 5.3: Observational Properties of Individual Star Clusters (continued)

ID	R.A.	Decl.	f_{336}	$\sigma_{f_{336}}$	f_{435}	$\sigma_{f_{435}}$	f_{814}	$\sigma_{f_{814}}$
296	156.96595248	-43.90321280	5.332E-17	3.862E-19	6.632E-17	6.571E-19	3.144E-17	2.784E-19
297	156.96284223	-43.90222700	3.685E-17	2.368E-19	2.050E-17	4.633E-19	4.005E-18	1.411E-19
298	156.96376381	-43.90240866	8.631E-18	3.267E-19	8.174E-18	3.530E-19	2.608E-18	1.566E-19
299	156.96273090	-43.90167849	1.721E-18	8.989E-20	3.355E-18	1.673E-19	1.108E-18	7.596E-20
300	156.96393747	-43.90242741	1.535E-17	4.799E-19	1.800E-17	6.384E-19	6.466E-18	2.310E-19
301	156.98675372	-43.91239945	3.628E-19	3.545E-20	8.190E-19	1.382E-20	2.481E-19	4.865E-21
302	156.96173013	-43.90148065	6.381E-17	1.557E-19	4.546E-17	2.153E-19	7.926E-18	1.276E-19
303	156.96331880	-43.90222849	6.984E-18	1.785E-19	7.120E-18	2.633E-19	1.742E-18	1.245E-19
304	156.97682181	-43.90815965	4.576E-19	3.039E-20	6.493E-19	1.916E-20	1.544E-19	8.299E-21
305	156.96679613	-43.90353347	3.468E-18	4.976E-19	6.293E-18	3.746E-19	1.760E-18	2.089E-19
306	156.96489771	-43.90280364	1.840E-17	4.571E-19	1.083E-17	5.511E-19	5.930E-18	2.767E-19
307	156.96407668	-43.90258996	5.097E-18	4.773E-19	9.063E-18	5.514E-19	1.924E-18	4.371E-19
308	156.96684490	-43.90372481	2.750E-18	1.127E-19	2.362E-18	4.009E-19	2.598E-18	2.461E-19
309	156.96207495	-43.90170772	1.607E-17	2.330E-19	7.306E-18	2.237E-19	7.295E-19	1.778E-19
310	156.96599462	-43.90296381	9.164E-18	3.368E-19	1.621E-17	5.986E-19	7.555E-18	2.212E-19
311	156.96215142	-43.90122533	3.272E-18	3.849E-19	6.043E-18	4.151E-19	1.235E-18	1.955E-19
312	156.96164385	-43.90077627	9.386E-18	1.355E-19	1.154E-17	1.622E-19	7.077E-18	8.064E-20
313	156.95880779	-43.89976766	2.330E-18	2.785E-20	7.199E-18	1.830E-20	3.072E-18	1.859E-20
314	156.96061426	-43.90055715	1.542E-18	4.178E-20	4.044E-18	2.973E-20	1.590E-18	2.134E-20
315	156.96749448	-43.90236265	1.808E-17	2.861E-19	3.952E-17	3.385E-19	7.604E-18	1.942E-19
316	156.96595453	-43.90276580	1.302E-17	3.469E-19	9.586E-18	5.478E-19	3.807E-18	1.827E-19
317	156.96512783	-43.90262660	1.377E-17	8.876E-19	1.694E-17	1.445E-18	6.012E-18	3.460E-19
318	156.96466092	-43.90259956	9.516E-18	3.419E-19	1.060E-17	7.860E-19	2.301E-18	2.644E-19
319	156.96351252	-43.90207736	3.702E-18	8.610E-20	4.917E-18	1.261E-19	1.158E-18	5.485E-20
320	156.97741908	-43.90703766	9.578E-17	5.824E-20	2.172E-16	6.074E-20	1.129E-16	2.011E-19
321	156.96147605	-43.90101612	2.990E-18	8.103E-20	4.480E-18	9.551E-20	3.132E-18	7.096E-20
322	156.96542272	-43.90248501	1.857E-16	8.825E-19	2.428E-16	1.578E-18	7.583E-17	4.186E-19
323	156.96201284	-43.90149225	3.225E-18	1.874E-19	1.488E-18	2.299E-19	8.626E-19	8.411E-20
324	156.96805912	-43.90375056	3.439E-18	1.355E-19	2.597E-18	9.575E-20	7.410E-19	3.583E-20
325	156.96697003	-43.90317673	7.538E-18	4.140E-19	9.855E-18	4.420E-19	3.078E-18	2.566E-19
326	156.96533450	-43.90265855	3.297E-17	7.407E-19	1.753E-17	1.452E-18	2.028E-18	3.262E-19
327	156.97029175	-43.90446179	8.381E-19	3.292E-20	4.791E-18	2.208E-20	1.632E-17	1.897E-20
328	156.96189546	-43.90131202	4.048E-18	1.988E-19	2.554E-18	2.302E-19	6.690E-19	1.099E-19
329	156.96576821	-43.90192675	3.953E-17	1.975E-19	3.303E-17	2.001E-19	9.643E-18	7.430E-20
330	156.96528121	-43.90225444	5.115E-18	1.355E-19	2.580E-18	2.039E-19	1.944E-18	8.198E-20
331	156.95664863	-43.89862688	1.020E-18	3.925E-20	1.018E-18	1.912E-20	2.784E-19	6.987E-21
332	156.98005756	-43.90844601	7.828E-19	2.659E-20	8.281E-18	1.322E-20	2.396E-17	3.065E-20
333	156.96364180	-43.90140899	8.197E-18	1.000E-19	8.403E-18	1.593E-19	3.052E-18	9.840E-20
334	156.96880668	-43.90386683	5.337E-19	5.824E-20	1.546E-18	5.725E-20	3.550E-19	3.203E-20
335	156.96569993	-43.90249962	4.247E-17	3.494E-19	4.476E-17	2.601E-19	1.240E-17	1.127E-19
336	156.96489947	-43.90240449	3.443E-18	1.912E-19	3.952E-18	3.895E-19	1.024E-18	1.567E-19
337	156.96670952	-43.90314635	2.890E-17	7.318E-19	1.619E-17	7.367E-19	3.943E-18	3.272E-19
338	156.96914974	-43.90428909	2.821E-18	4.811E-20	1.779E-18	3.874E-20	3.295E-19	1.624E-20
339	156.96846253	-43.90386561	6.517E-19	5.951E-20	3.361E-19	4.335E-20	1.203E-19	2.716E-20
340	156.96136278	-43.90053560	3.449E-19	3.925E-20	1.008E-18	4.198E-20	2.011E-18	5.309E-20
341	156.95799335	-43.89862843	1.059E-18	4.431E-20	3.757E-18	2.061E-20	1.685E-18	9.895E-21
342	156.95748990	-43.89881871	3.186E-19	4.305E-20	1.248E-18	2.081E-20	7.116E-19	1.207E-20
343	156.96783904	-43.90338259	1.630E-18	6.837E-20	1.957E-18	8.292E-20	1.408E-18	4.415E-20
344	156.96230741	-43.90103826	5.347E-18	1.570E-19	3.468E-18	1.494E-19	1.617E-18	9.744E-20
345	156.96381721	-43.90164495	2.315E-18	8.610E-20	3.743E-18	1.118E-19	9.363E-19	6.862E-20
346	156.96355711	-43.90117044	9.569E-18	8.989E-20	1.607E-17	1.404E-19	8.021E-18	9.164E-20
347	156.96551798	-43.90255613	1.553E-17	4.963E-19	3.920E-17	1.012E-18	1.272E-17	3.823E-19
348	156.96901945	-43.90383178	2.829E-18	6.204E-20	2.266E-18	7.832E-20	7.731E-19	2.603E-20

Table 5.3 continued

Table 5.3: Observational Properties of Individual Star Clusters (continued)

ID	R.A.	Decl.	f_{336}	$\sigma_{f_{336}}$	f_{435}	$\sigma_{f_{435}}$	f_{814}	$\sigma_{f_{814}}$
349	156.96459047	-43.90219388	2.044E-18	1.177E-19	3.236E-18	1.486E-19	8.231E-19	9.042E-20
350	156.96018954	-43.89961625	8.365E-18	3.798E-20	1.374E-17	3.883E-20	4.515E-18	2.351E-20
351	156.96189836	-43.90080985	2.113E-18	7.344E-20	2.626E-18	9.457E-20	9.941E-19	6.869E-20
352	156.96332771	-43.90144937	1.063E-18	6.584E-20	1.913E-18	1.570E-19	7.824E-19	7.823E-20
353	156.96870795	-43.90300391	8.404E-18	6.964E-20	7.915E-18	7.943E-20	3.759E-18	4.991E-20
354	156.96590609	-43.90241021	8.160E-18	1.861E-19	4.953E-18	2.006E-19	2.238E-18	1.016E-19
355	156.96889997	-43.90376095	6.850E-19	6.077E-20	8.357E-19	7.535E-20	1.671E-19	3.208E-20
356	156.96605501	-43.90222459	3.870E-18	8.736E-20	4.546E-18	1.187E-19	1.153E-18	4.591E-20
357	156.96832247	-43.90358297	1.259E-18	1.177E-19	2.174E-18	1.748E-19	4.392E-19	6.942E-20
358	156.96837743	-43.90273936	1.035E-17	9.116E-20	1.277E-17	1.669E-19	6.141E-18	6.779E-20
359	156.96793553	-43.90316486	5.809E-19	7.850E-20	5.760E-19	5.699E-20	5.024E-19	4.293E-20
360	156.96454585	-43.90165058	1.016E-18	5.824E-20	1.439E-18	6.793E-20	7.116E-19	3.241E-20
361	156.96931738	-43.90377758	9.783E-19	4.305E-20	9.542E-19	3.353E-20	3.441E-19	2.115E-20
362	156.96386617	-43.90142113	3.062E-18	1.013E-19	3.905E-18	1.329E-19	1.538E-18	4.878E-20
363	156.96295342	-43.90089309	4.150E-18	1.203E-19	2.406E-18	1.820E-19	6.733E-19	5.906E-20
364	156.96583775	-43.90228367	2.540E-18	2.127E-19	6.310E-18	2.082E-19	1.315E-18	5.987E-20
365	156.96212646	-43.90039630	1.267E-18	4.305E-20	2.136E-18	7.124E-20	1.332E-18	4.312E-20
366	156.96303197	-43.90097243	2.909E-18	7.850E-20	3.452E-18	1.084E-19	5.865E-19	5.625E-20
367	156.96384860	-43.90106105	1.320E-18	6.584E-20	1.600E-18	7.482E-20	1.042E-18	5.606E-20
368	156.96963623	-43.90347211	2.526E-19	3.292E-20	5.527E-19	3.296E-20	2.413E-19	2.258E-20
369	156.96712825	-43.90243080	1.569E-16	7.103E-19	1.100E-16	7.777E-19	2.088E-17	3.207E-19
370	156.98723872	-43.91035225	9.810E-17	1.228E-19	2.790E-16	8.407E-20	1.268E-16	2.395E-19
371	156.96801103	-43.90267107	3.927E-17	1.747E-19	3.799E-17	2.228E-19	1.382E-17	1.010E-19
372	156.96993709	-43.90376518	2.505E-19	3.419E-20	2.086E-19	1.945E-20	1.060E-19	1.334E-20
373	156.96510416	-43.90150582	4.314E-19	4.938E-20	6.469E-19	7.466E-20	4.013E-19	3.576E-20
374	156.96624833	-43.90216116	6.920E-19	6.584E-20	1.435E-18	6.539E-20	5.642E-19	2.960E-20
375	156.96449718	-43.90130908	1.830E-18	6.204E-20	2.272E-18	1.016E-19	7.955E-19	3.147E-20
376	156.97048785	-43.90322368	3.449E-16	1.329E-18	2.692E-16	7.861E-19	5.339E-17	5.330E-19
377	156.96648330	-43.90212243	4.086E-18	7.344E-20	4.342E-18	8.982E-20	1.342E-18	3.324E-20
378	156.96635143	-43.90192720	2.219E-18	6.837E-20	3.186E-18	6.364E-20	1.573E-18	3.374E-20
379	156.94183480	-43.88989975	3.949E-16	4.242E-19	4.939E-16	3.963E-19	2.079E-16	5.592E-19
380	156.96348486	-43.90067738	2.266E-18	1.304E-19	2.345E-18	1.048E-19	6.678E-19	4.299E-20
381	156.97088629	-43.90386338	3.971E-19	3.925E-20	3.519E-19	1.984E-20	7.774E-20	1.050E-20
382	156.96902423	-43.90300987	1.511E-18	4.685E-20	1.871E-18	5.767E-20	8.453E-19	3.686E-20
383	156.96374433	-43.90080314	8.243E-18	1.659E-19	1.047E-17	2.220E-19	4.869E-18	1.091E-19
384	156.96287693	-43.90064436	3.373E-19	4.938E-20	2.933E-19	5.579E-20	9.546E-20	2.507E-20
385	156.96620122	-43.90188059	1.343E-18	6.584E-20	1.014E-18	7.476E-20	4.068E-19	3.446E-20
386	156.96464558	-43.90080483	3.782E-19	3.798E-20	1.325E-18	5.751E-20	9.041E-19	3.549E-20
387	156.96853770	-43.90248963	7.693E-19	4.811E-20	5.977E-19	5.993E-20	1.597E-18	2.385E-20
388	156.96691958	-43.90206385	5.254E-18	7.344E-20	3.785E-18	1.020E-19	9.769E-19	5.170E-20
389	156.96839412	-43.90256879	1.448E-18	6.331E-20	1.706E-18	6.689E-20	1.177E-18	5.129E-20
390	156.96397666	-43.90083518	1.432E-18	6.331E-20	1.440E-18	6.970E-20	3.752E-19	7.177E-20
391	156.96661657	-43.90166698	1.217E-18	5.571E-20	1.770E-18	4.284E-20	5.816E-19	2.938E-20
392	156.96804670	-43.90217280	1.223E-18	5.318E-20	1.320E-18	7.226E-20	7.356E-19	3.617E-20
393	156.96334066	-43.90044924	7.750E-19	4.052E-20	6.299E-19	3.785E-20	1.942E-19	2.265E-20
394	156.96914783	-43.90281574	9.792E-19	5.318E-20	1.612E-18	6.663E-20	4.552E-19	3.814E-20
395	156.96992341	-43.90328590	9.837E-19	5.444E-20	1.751E-18	5.351E-20	7.860E-19	3.283E-20
396	156.96553303	-43.90057481	8.906E-18	7.090E-20	9.828E-18	8.979E-20	2.926E-18	4.295E-20
397	156.96291118	-43.90026035	4.726E-19	4.178E-20	4.480E-19	5.706E-20	1.989E-19	3.373E-20
398	156.96376415	-43.90026893	1.388E-18	4.305E-20	9.937E-19	5.788E-20	2.445E-19	3.163E-20
399	156.96931175	-43.90282649	4.827E-19	5.191E-20	8.497E-19	1.344E-19	1.926E-19	4.791E-20
400	156.97387364	-43.90462602	2.645E-18	3.165E-20	6.212E-18	1.670E-20	4.225E-18	9.175E-21
401	156.96762102	-43.90213882	3.134E-18	1.203E-19	1.648E-18	1.672E-19	6.610E-19	8.204E-20

Table 5.3 continued

Table 5.3: Observational Properties of Individual Star Clusters (continued)

ID	R.A.	Decl.	f_{336}	$\sigma_{f_{336}}$	f_{435}	$\sigma_{f_{435}}$	f_{814}	$\sigma_{f_{814}}$
402	156.98902876	-43.91086935	9.828E-18	3.165E-20	1.922E-17	1.883E-20	1.128E-17	1.527E-20
403	156.96887850	-43.90248865	4.208E-18	5.951E-20	3.802E-18	3.702E-20	7.025E-19	5.961E-20
404	156.96336805	-43.89969989	3.516E-18	8.736E-20	4.278E-18	1.016E-19	1.068E-18	6.228E-20
405	156.96700486	-43.90163934	8.003E-19	4.178E-20	9.551E-19	3.973E-20	2.511E-19	2.515E-20
406	156.96334712	-43.90012988	3.154E-19	4.685E-20	3.099E-19	4.398E-20	2.822E-19	2.829E-20
407	156.96988870	-43.90272229	2.631E-18	4.811E-20	2.471E-18	6.386E-20	7.506E-19	3.254E-20
408	156.96809905	-43.90201005	1.120E-18	4.811E-20	2.478E-18	5.814E-20	1.078E-18	3.789E-20
409	156.96572837	-43.90112720	6.190E-19	3.798E-20	3.813E-19	4.982E-20	7.817E-20	1.959E-20
410	156.96624533	-43.90063742	3.706E-18	8.230E-20	3.096E-18	8.690E-20	1.456E-18	3.536E-20
411	156.96464277	-43.90053127	3.572E-18	1.228E-19	2.531E-18	2.058E-19	7.702E-19	7.688E-20
412	156.96540875	-43.90096707	1.600E-18	5.571E-20	1.639E-18	5.910E-20	3.485E-19	3.696E-20
413	156.96305232	-43.89951927	2.796E-18	4.178E-20	3.339E-18	5.111E-20	2.032E-18	3.327E-20
414	156.96769305	-43.90170495	4.451E-19	4.305E-20	8.450E-19	3.788E-20	6.758E-19	2.581E-20
415	156.96361024	-43.89950945	6.311E-17	3.115E-19	7.573E-17	5.614E-19	2.442E-17	2.482E-19
416	156.96585747	-43.90087696	5.153E-19	3.545E-20	2.819E-19	4.054E-20	3.954E-19	1.770E-20
417	156.96848955	-43.90214338	6.387E-19	4.178E-20	5.162E-19	5.533E-20	1.836E-19	2.382E-20
418	156.96419839	-43.90027781	3.709E-19	3.798E-20	3.355E-19	5.705E-20	1.853E-19	3.962E-20
419	156.97029770	-43.90272906	3.685E-19	5.191E-20	1.000E-18	7.390E-20	1.596E-19	2.817E-20
420	156.96849977	-43.90161302	9.308E-18	5.444E-20	1.006E-17	3.881E-20	4.860E-18	2.149E-20
421	156.96343512	-43.89932107	2.543E-18	4.305E-20	5.003E-18	1.426E-19	5.353E-18	5.123E-20
422	156.96749737	-43.90158558	4.127E-19	4.052E-20	3.477E-19	4.446E-20	1.326E-19	1.749E-20
423	156.96896366	-43.90181708	1.418E-18	5.951E-20	1.281E-18	8.531E-20	4.641E-19	6.720E-20
424	156.96589122	-43.90063040	1.020E-18	5.444E-20	9.446E-19	7.536E-20	3.683E-19	2.962E-20
425	156.97009299	-43.90238211	1.186E-18	7.597E-20	2.027E-18	1.071E-19	3.286E-19	4.572E-20
426	156.96853228	-43.90132563	3.117E-19	6.077E-20	7.643E-19	7.610E-20	3.019E-19	3.348E-20
427	156.96927180	-43.90197844	1.148E-18	6.331E-20	1.598E-18	8.034E-20	9.075E-19	4.137E-20
428	156.96807452	-43.90161414	9.071E-19	4.178E-20	1.150E-18	6.132E-20	5.892E-19	2.473E-20
429	156.96992824	-43.90243305	2.031E-18	6.331E-20	2.785E-18	9.167E-20	1.265E-19	3.334E-20
430	156.96969521	-43.90203525	9.308E-19	7.344E-20	1.185E-18	8.168E-20	5.024E-19	5.477E-20
431	156.97527538	-43.90410365	2.451E-18	3.165E-20	1.952E-17	1.902E-20	4.719E-17	6.924E-20
432	156.95963026	-43.89795914	3.091E-19	4.052E-20	6.805E-19	1.812E-20	4.148E-19	8.986E-21
433	156.97069481	-43.90270926	1.504E-18	7.977E-20	8.373E-19	1.285E-19	3.132E-19	7.645E-20
434	156.96940968	-43.90199752	4.459E-18	9.116E-20	3.177E-18	1.041E-19	9.841E-19	4.759E-20
435	156.96921501	-43.90158245	1.642E-17	1.684E-19	1.579E-17	1.008E-19	5.314E-18	4.903E-20
436	156.96782396	-43.90113016	1.193E-18	4.811E-20	2.146E-18	6.028E-20	9.441E-19	3.409E-20
437	156.96512165	-43.89991726	3.079E-19	3.419E-20	7.566E-19	3.307E-20	2.920E-19	4.150E-20
438	156.96655672	-43.90086261	8.190E-19	3.925E-20	1.212E-18	4.900E-20	3.707E-19	2.072E-20
439	156.96881721	-43.90148975	1.179E-18	5.951E-20	1.497E-18	4.416E-20	4.523E-19	2.897E-20
440	156.96424103	-43.89976767	4.374E-19	5.318E-20	9.631E-19	5.818E-20	4.697E-19	2.595E-20
441	156.96954320	-43.90227084	4.792E-19	4.685E-20	2.540E-19	5.152E-20	1.958E-19	2.901E-20
442	156.96579179	-43.90061788	1.039E-18	5.698E-20	8.458E-19	8.935E-20	2.028E-19	4.941E-20
443	156.96670719	-43.90082234	1.160E-18	3.798E-20	1.169E-18	5.206E-20	4.776E-19	2.775E-20
444	156.96955203	-43.90203514	1.131E-18	8.230E-20	1.100E-18	8.181E-20	3.639E-19	4.161E-20
445	156.96486850	-43.89989693	1.373E-18	4.811E-20	2.765E-18	6.247E-20	1.849E-18	2.994E-20
446	156.96818214	-43.90136777	4.814E-19	4.558E-20	1.249E-18	5.764E-20	7.064E-19	2.774E-20
447	156.96604099	-43.90068425	3.810E-19	5.064E-20	4.467E-19	6.901E-20	1.914E-19	4.310E-20
448	156.97090594	-43.90277637	6.481E-18	1.481E-19	4.962E-18	1.000E-19	1.355E-18	3.148E-20
449	156.96434699	-43.89900479	3.859E-18	6.331E-20	4.216E-18	9.951E-20	3.857E-18	4.045E-20
450	156.96357643	-43.89913911	1.264E-18	4.938E-20	1.384E-18	8.117E-20	4.114E-19	3.465E-20
451	156.97046581	-43.90182401	8.175E-19	5.444E-20	8.003E-19	6.150E-20	3.422E-19	2.250E-20
452	156.96609547	-43.90060657	1.880E-18	5.191E-20	9.499E-19	7.078E-20	3.918E-19	2.936E-20
453	156.96546958	-43.90013362	7.650E-19	4.052E-20	1.278E-18	5.054E-20	5.985E-19	4.680E-20
454	156.96723457	-43.90100402	2.636E-19	4.052E-20	8.018E-19	4.631E-20	1.492E-19	1.919E-20

Table 5.3 continued

Table 5.3: Observational Properties of Individual Star Clusters (continued)

ID	R.A.	Decl.	f_{336}	$\sigma_{f_{336}}$	f_{435}	$\sigma_{f_{435}}$	f_{814}	$\sigma_{f_{814}}$
455	156.96811589	-43.90129612	7.414E-19	4.811E-20	1.612E-18	7.203E-20	6.107E-19	3.584E-20
456	156.96440956	-43.89969443	3.713E-19	4.305E-20	9.394E-19	5.262E-20	8.088E-19	3.006E-20
457	156.96392250	-43.89932169	9.901E-18	1.064E-19	1.242E-17	1.065E-19	4.987E-18	1.071E-19
458	156.95602797	-43.89474299	2.827E-17	4.305E-20	4.108E-17	2.226E-20	1.008E-16	2.263E-19
459	156.97051630	-43.90228229	1.871E-18	1.000E-19	1.194E-18	1.684E-19	8.133E-19	5.649E-20
460	156.97046521	-43.90212053	7.693E-18	8.736E-20	6.241E-18	7.957E-20	2.354E-18	3.509E-20
461	156.96699346	-43.90053533	7.865E-18	7.344E-20	6.167E-18	5.439E-20	1.483E-18	2.369E-20
462	156.96958357	-43.90188192	5.734E-19	5.571E-20	4.262E-19	5.621E-20	1.196E-19	3.129E-20
463	156.96747223	-43.90039767	1.162E-17	1.418E-19	1.179E-17	1.928E-19	4.928E-18	8.794E-20
464	156.96887054	-43.90078757	6.762E-18	8.736E-20	6.357E-18	1.031E-19	2.236E-18	7.267E-20
465	156.96748834	-43.90089298	4.306E-19	3.672E-20	4.177E-19	4.157E-20	2.071E-19	1.840E-20
466	156.99362656	-43.91154892	2.944E-17	6.077E-20	5.026E-17	1.903E-20	2.064E-17	2.945E-20
467	156.96339261	-43.89915171	3.884E-19	4.178E-20	6.167E-19	6.227E-20	2.472E-19	2.091E-20
468	156.96627912	-43.90029366	1.518E-18	6.457E-20	1.337E-18	6.817E-20	1.716E-19	4.594E-20
469	156.96826016	-43.90102678	5.054E-18	4.811E-20	4.752E-18	7.336E-20	1.915E-18	2.816E-20
470	156.96710647	-43.90017448	5.120E-18	6.457E-20	7.629E-18	7.930E-20	3.649E-18	3.739E-20
471	156.97196529	-43.90188082	1.260E-17	4.431E-20	2.675E-17	3.401E-20	1.705E-17	2.874E-20
472	156.96821513	-43.90087233	6.094E-19	5.444E-20	8.296E-19	4.224E-20	3.748E-19	2.439E-20
473	156.96866650	-43.90055488	5.708E-17	2.760E-19	3.455E-17	2.922E-19	7.738E-18	9.702E-20
474	156.97116602	-43.90202827	4.661E-19	3.798E-20	4.366E-19	4.027E-20	5.601E-19	1.166E-20
475	156.97150677	-43.90221864	4.652E-18	4.938E-20	3.726E-18	2.634E-20	7.397E-19	1.304E-20
476	156.96701645	-43.90039944	1.052E-18	6.964E-20	1.162E-18	4.149E-20	1.336E-19	3.561E-20
477	156.97686197	-43.90427391	8.849E-19	3.292E-20	3.125E-18	1.577E-20	1.235E-18	8.985E-21
478	156.96785276	-43.90055541	2.858E-19	5.318E-20	4.661E-19	6.229E-20	3.793E-19	3.746E-20
479	156.95946595	-43.89701723	3.595E-19	4.052E-20	4.708E-19	1.642E-20	1.731E-19	8.444E-21
480	156.97047261	-43.90162402	1.322E-17	6.077E-20	1.201E-17	4.237E-20	3.755E-18	2.297E-20
481	156.96781364	-43.90021480	1.080E-18	7.344E-20	8.947E-19	1.408E-19	7.295E-19	4.633E-20
482	156.97022060	-43.90154100	1.630E-18	6.584E-20	1.909E-18	7.214E-20	7.222E-19	3.018E-20
483	156.97029604	-43.90147214	2.840E-18	4.431E-20	2.722E-18	3.755E-20	8.795E-19	2.478E-20
484	156.96801313	-43.90046705	1.496E-18	5.064E-20	1.450E-18	7.427E-20	3.860E-19	5.676E-20
485	156.96848262	-43.90042917	6.614E-18	2.241E-19	4.648E-18	1.536E-19	1.726E-18	7.560E-20
486	156.96929139	-43.90101675	2.585E-18	6.584E-20	1.327E-18	8.120E-20	3.316E-19	4.495E-20
487	156.96812472	-43.90051853	5.857E-19	5.824E-20	7.232E-19	1.015E-19	3.238E-19	4.155E-20
488	156.97339070	-43.90255927	7.901E-19	3.292E-20	8.489E-19	3.233E-20	2.799E-19	2.003E-20
489	156.97322084	-43.90242946	3.513E-18	3.925E-20	3.227E-18	2.656E-20	9.058E-19	1.014E-20
490	156.96929779	-43.90085459	5.491E-19	6.077E-20	7.054E-19	5.471E-20	3.447E-19	2.947E-20
491	156.97062911	-43.90154360	2.944E-19	5.064E-20	2.489E-19	4.248E-20	5.859E-20	1.497E-20
492	156.97035757	-43.90129821	2.455E-19	3.419E-20	4.120E-19	3.013E-20	2.385E-19	1.834E-20
493	156.96455609	-43.89899276	3.225E-19	4.305E-20	8.996E-19	3.936E-20	3.643E-19	2.010E-20
494	156.96949069	-43.90061829	3.778E-18	4.685E-20	3.074E-18	4.180E-20	8.738E-19	2.877E-20
495	156.96741871	-43.90013266	5.814E-19	4.305E-20	6.951E-19	4.106E-20	1.319E-19	1.675E-20
496	156.96864136	-43.90044577	2.757E-18	1.203E-19	2.767E-18	1.138E-19	9.914E-19	5.662E-20
497	156.97285043	-43.90199144	1.594E-18	3.292E-20	4.314E-18	2.609E-20	1.507E-18	1.267E-20
498	156.96031742	-43.89640270	3.468E-19	3.292E-20	1.633E-18	1.733E-20	4.171E-18	1.007E-20
499	156.95469049	-43.89421775	6.287E-19	3.545E-20	1.624E-18	1.479E-20	5.344E-19	5.767E-21
500	156.96092957	-43.89693393	5.201E-19	3.545E-20	1.637E-18	1.950E-20	6.672E-19	1.186E-20
501	156.96163131	-43.89729861	3.523E-19	3.545E-20	8.296E-20	1.803E-20	7.438E-20	8.923E-21
502	156.96931180	-43.90050443	6.990E-19	3.672E-20	5.008E-19	2.667E-20	1.072E-19	2.187E-20
503	156.96371593	-43.89750349	4.071E-19	3.925E-20	1.254E-18	2.076E-20	4.020E-19	9.029E-21
504	156.96701370	-43.89845763	6.393E-19	3.419E-20	1.501E-18	3.346E-20	6.796E-19	1.814E-20
505	156.96674967	-43.89841730	9.155E-19	3.672E-20	1.833E-18	3.272E-20	8.658E-19	1.963E-20
506	156.96408230	-43.89607554	2.960E-19	3.292E-20	1.352E-18	1.651E-20	7.142E-19	7.878E-21
507	156.97155840	-43.89897163	2.965E-17	4.052E-20	4.962E-17	2.327E-20	2.343E-17	2.370E-20

Table 5.3 continued

Table 5.3: Observational Properties of Individual Star Clusters (continued)

ID	R.A.	Decl.	f_{336}	$\sigma_{f_{336}}$	f_{435}	$\sigma_{f_{435}}$	f_{814}	$\sigma_{f_{814}}$
508	156.98917296	-43.90634238	2.166E-17	4.305E-20	3.750E-17	1.838E-20	1.734E-17	2.438E-20
509	156.97327428	-43.89990345	1.109E-18	3.419E-20	1.140E-18	1.612E-20	1.935E-19	9.406E-21
510	156.97796328	-43.90144616	3.015E-18	2.912E-20	7.496E-18	2.467E-20	2.746E-18	1.024E-20
511	156.96299289	-43.89525749	2.855E-19	2.532E-20	5.426E-19	1.424E-20	2.232E-19	7.711E-21
512	156.96555586	-43.89569185	1.713E-18	3.039E-20	1.008E-17	2.298E-20	2.169E-17	3.239E-20
513	156.96792713	-43.89680019	2.602E-19	3.165E-20	2.360E-19	2.289E-20	5.585E-20	9.307E-21
514	156.95800469	-43.89175885	2.144E-17	3.925E-20	3.743E-17	2.628E-20	1.987E-17	2.850E-20
515	156.96932886	-43.89592692	1.469E-18	3.798E-20	3.949E-18	3.182E-20	1.487E-18	2.120E-20
516	156.96665651	-43.89442613	8.373E-19	4.305E-20	1.930E-18	1.738E-20	2.219E-18	8.379E-21
517	156.98035517	-43.89904304	2.803E-19	2.912E-20	5.110E-19	1.203E-20	1.702E-19	5.344E-21
518	156.95638244	-43.88811673	1.259E-17	4.178E-20	3.057E-17	1.976E-20	2.167E-17	3.106E-20
519	156.95573319	-43.88771989	2.001E-17	3.672E-20	7.186E-17	4.588E-20	6.859E-17	7.858E-20
520	156.98691938	-43.89969763	5.411E-17	5.444E-20	1.655E-16	8.387E-20	8.730E-17	1.746E-19
521	156.98081187	-43.89755219	1.460E-18	2.785E-20	1.284E-17	3.027E-20	7.018E-17	1.566E-19
522	156.98099552	-43.89722382	1.705E-16	8.356E-20	7.326E-16	3.576E-19	4.838E-16	2.601E-18
523	156.96665709	-43.89163681	1.280E-18	3.039E-20	3.493E-18	1.683E-20	2.553E-18	7.224E-21
524	156.95679011	-43.88720663	1.443E-18	2.912E-20	6.010E-18	1.169E-20	6.865E-18	8.564E-21
525	156.98283248	-43.89724447	2.111E-17	3.545E-20	6.608E-17	3.584E-20	5.637E-17	8.051E-20
526	156.96225457	-43.88963410	4.033E-19	2.659E-20	7.232E-19	1.227E-20	3.687E-19	6.315E-21
527	156.99356711	-43.90150271	1.892E-17	3.672E-20	7.857E-17	2.987E-20	7.681E-17	1.141E-19
528	156.98024285	-43.89324242	4.366E-17	4.052E-20	1.893E-16	1.444E-19	1.183E-16	2.555E-19
529	156.96672789	-43.88881672	1.630E-19	3.165E-20	3.555E-19	1.324E-20	6.255E-20	5.244E-21
530	156.96694280	-43.88839385	6.241E-18	3.292E-20	3.269E-17	2.619E-20	1.502E-19	2.790E-20
531	156.98170050	-43.89432434	8.980E-18	3.292E-20	2.935E-17	2.142E-20	2.891E-17	3.781E-20
532	156.96669914	-43.88778218	3.978E-19	3.798E-20	1.104E-18	1.532E-20	1.210E-19	5.502E-21
533	156.98611250	-43.89466877	7.989E-18	3.925E-20	1.735E-17	1.829E-20	1.183E-17	1.871E-20
534	156.97911499	-43.89078392	2.264E-18	3.039E-20	8.442E-18	1.462E-20	9.108E-18	9.925E-21
535	156.94823582	-43.87732679	9.300E-18	4.685E-20	7.749E-17	5.042E-20	1.393E-16	2.472E-19
536	156.98459178	-43.89363179	4.239E-19	3.039E-20	3.536E-19	1.176E-20	1.361E-19	5.864E-21
537	156.94897854	-43.87702456	2.952E-16	1.380E-19	5.619E-16	2.463E-19	2.928E-16	6.406E-19
538	156.96824727	-43.88576750	4.622E-17	4.178E-20	1.144E-16	4.707E-20	8.014E-17	8.947E-20
539	156.97961782	-43.88997718	8.906E-17	6.710E-20	2.604E-16	1.005E-19	1.473E-16	2.806E-19
540	156.98102107	-43.89074402	1.772E-17	3.545E-20	6.669E-17	2.898E-20	6.568E-17	6.746E-20
541	156.99812300	-43.89662207	3.094E-18	3.039E-20	2.174E-17	1.675E-20	6.466E-17	1.158E-19
542	156.97328104	-43.88639462	4.770E-19	2.912E-20	1.286E-18	1.158E-20	4.477E-19	6.228E-21
543	156.97582917	-43.88763393	4.220E-19	2.532E-20	2.858E-19	1.349E-20	6.833E-20	5.577E-21
544	156.98400667	-43.89044102	1.251E-18	2.659E-20	4.177E-18	1.482E-20	4.323E-18	7.216E-21
545	156.98113142	-43.88656155	1.923E-18	3.292E-20	2.008E-19	1.305E-20	9.805E-20	4.739E-21
546	156.95614751	-43.87602045	4.423E-17	8.103E-20	1.230E-16	9.651E-20	6.617E-17	1.233E-19
547	156.97311560	-43.88392803	2.717E-17	5.191E-20	1.068E-16	4.202E-20	8.547E-17	1.008E-19
548	156.96503241	-43.87997958	2.464E-17	3.925E-20	8.311E-17	4.102E-20	7.569E-17	1.071E-19
549	157.00231613	-43.89812959	2.512E-18	4.431E-20	1.439E-19	1.023E-20	1.169E-19	4.438E-21
NGC 6240								
1	253.24515130	2.38534182	5.361E-19	2.532E-20	3.896E-19	1.483E-20	7.497E-20	7.313E-21
2	253.24047615	2.38519567	3.417E-19	2.912E-20	4.308E-19	1.406E-20	1.151E-19	5.622E-21
3	253.23333549	2.38556914	4.112E-19	2.912E-20	2.923E-19	1.196E-20	3.240E-19	8.009E-21
4	253.23564869	2.38686154	4.366E-19	2.912E-20	4.194E-19	1.359E-20	1.435E-19	5.066E-21
5	253.25668925	2.39042609	4.546E-18	3.165E-20	1.020E-17	1.482E-20	9.022E-18	1.276E-20
6	253.23559710	2.38910411	2.063E-17	3.798E-20	7.084E-17	5.583E-20	6.399E-17	1.148E-19
7	253.24812327	2.39208147	9.308E-18	3.165E-20	1.980E-17	1.813E-20	1.387E-17	1.953E-20
8	253.25816558	2.39357130	7.800E-19	3.165E-20	7.507E-18	1.352E-20	2.180E-17	3.475E-20

Table 5.3 continued

Table 5.3: Observational Properties of Individual Star Clusters (continued)

ID	R.A.	Decl.	f_{336}	$\sigma_{f_{336}}$	f_{435}	$\sigma_{f_{435}}$	f_{814}	$\sigma_{f_{814}}$
9	253.25082071	2.39236890	6.004E-19	2.659E-20	1.002E-18	1.223E-20	5.106E-19	4.946E-21
10	253.23670312	2.39162345	6.523E-18	3.419E-20	1.538E-17	1.327E-20	1.123E-17	1.630E-20
11	253.25728151	2.39666685	1.108E-16	9.116E-20	1.944E-16	7.902E-20	9.650E-17	1.748E-19
12	253.25470713	2.39694100	8.458E-17	6.964E-20	1.541E-16	1.022E-19	7.313E-17	1.599E-19
13	253.24901586	2.39492336	4.310E-19	3.292E-20	1.023E-18	2.583E-20	2.925E-19	9.617E-21
14	253.24234150	2.39393143	3.062E-19	3.798E-20	4.883E-19	1.310E-20	1.649E-19	6.406E-21
15	253.24963781	2.39575050	3.621E-19	3.039E-20	6.508E-19	1.270E-20	3.169E-19	5.983E-21
16	253.25492129	2.39713235	3.754E-19	3.672E-20	4.702E-19	2.468E-20	2.022E-19	9.969E-21
17	253.24314783	2.39565316	7.497E-19	3.292E-20	1.481E-18	2.098E-20	4.366E-19	1.148E-20
18	253.24251968	2.39542343	3.392E-19	2.785E-20	4.400E-19	1.687E-20	1.603E-19	1.312E-20
19	253.25243654	2.39729142	1.096E-18	3.419E-20	2.562E-18	1.253E-20	1.917E-18	7.007E-21
20	253.24436899	2.39631137	6.346E-19	3.292E-20	1.308E-18	1.786E-20	5.703E-19	1.343E-20
21	253.24307536	2.39640000	3.924E-19	3.039E-20	4.194E-19	2.369E-20	1.945E-19	1.898E-20
22	253.24322707	2.39637935	3.402E-19	3.292E-20	5.570E-19	2.378E-20	1.714E-19	2.282E-20
23	253.24312432	2.39696325	1.281E-18	4.431E-20	1.448E-18	4.481E-20	4.709E-19	2.338E-20
24	253.24299719	2.39670392	2.811E-19	3.292E-20	5.710E-19	2.548E-20	2.791E-19	2.040E-20
25	253.24329986	2.39691354	8.130E-19	3.798E-20	1.267E-18	4.059E-20	3.459E-19	1.782E-20
26	253.24262471	2.39688156	5.196E-19	4.305E-20	3.922E-19	3.001E-20	3.459E-19	2.417E-20
27	253.24174335	2.39680610	6.236E-19	3.798E-20	1.024E-18	3.186E-20	3.727E-19	1.188E-20
28	253.24336226	2.39712508	2.154E-18	3.925E-20	2.106E-18	3.577E-20	5.512E-19	2.121E-20
29	253.24337638	2.39720791	4.354E-19	4.052E-20	4.276E-19	3.292E-20	1.813E-19	2.919E-20
30	253.24757706	2.39799195	4.863E-19	3.672E-20	1.528E-18	2.064E-20	5.158E-19	1.026E-20
31	253.24813805	2.39833217	4.881E-19	3.419E-20	1.411E-18	2.632E-20	5.173E-19	1.567E-20
32	253.24689718	2.39788548	2.903E-19	4.052E-20	8.231E-19	2.021E-20	2.107E-19	1.058E-20
33	253.24237446	2.39731928	2.587E-19	5.698E-20	6.672E-19	7.729E-20	1.051E-19	2.998E-20
34	253.24259246	2.39761712	2.667E-18	7.217E-20	2.155E-18	6.503E-20	3.128E-19	3.434E-20
35	253.24227234	2.39755709	3.236E-18	4.558E-20	3.170E-18	3.618E-20	1.181E-18	2.268E-20
36	253.24257913	2.39773317	1.084E-18	5.444E-20	1.335E-18	6.930E-20	5.216E-19	2.616E-20
37	253.24317086	2.39811056	1.197E-18	5.064E-20	1.456E-18	3.582E-20	5.901E-19	2.539E-20
38	253.24907644	2.39892912	2.401E-19	3.798E-20	1.264E-19	1.965E-20	1.224E-19	8.221E-21
39	253.24250252	2.39843340	1.271E-18	4.558E-20	2.490E-18	4.819E-20	9.893E-19	2.227E-20
40	253.24159369	2.39813236	3.845E-19	3.419E-20	2.883E-19	2.211E-20	9.535E-20	1.013E-20
41	253.24271851	2.39828728	6.282E-19	5.191E-20	9.017E-19	6.371E-20	2.675E-19	4.288E-20
42	253.24658172	2.39953176	3.204E-19	4.052E-20	8.014E-19	3.231E-20	3.645E-19	1.431E-20
43	253.24266953	2.39823284	3.761E-19	5.444E-20	7.654E-19	3.709E-20	2.209E-19	2.983E-20
44	253.24153726	2.39824639	1.936E-19	3.672E-20	5.246E-19	2.172E-20	1.751E-19	9.459E-21
45	253.24267030	2.39864638	4.158E-19	3.925E-20	9.512E-19	3.602E-20	4.181E-19	1.594E-20
46	253.24527332	2.39986197	6.004E-19	3.419E-20	1.958E-18	6.605E-20	6.536E-19	9.775E-20
47	253.24764612	2.39993632	4.863E-19	3.798E-20	9.942E-19	1.663E-20	3.315E-19	9.178E-21
48	253.24248767	2.39928171	3.186E-19	3.165E-20	4.272E-19	2.553E-20	1.078E-19	1.268E-20
49	253.24562505	2.40138001	7.003E-18	4.052E-20	2.294E-17	9.963E-20	5.401E-17	1.846E-18
50	253.24230052	2.40008215	4.708E-19	3.419E-20	7.302E-19	1.667E-20	2.113E-19	7.914E-21
51	253.24781458	2.40103551	1.695E-19	2.785E-20	1.745E-19	2.191E-20	7.253E-20	1.167E-20
52	253.24240365	2.40004637	4.290E-19	3.292E-20	3.409E-19	2.440E-20	4.881E-20	9.695E-21
53	253.24651268	2.40157141	2.685E-19	3.039E-20	5.653E-19	5.146E-20	5.337E-19	3.872E-20
54	253.24198229	2.40029909	2.107E-19	3.672E-20	2.789E-19	1.644E-20	9.614E-20	7.980E-21
55	253.24161732	2.40070025	1.030E-18	4.431E-20	1.687E-18	1.697E-20	5.211E-19	7.668E-21
56	253.24539029	2.40194555	5.671E-19	3.925E-20	1.224E-18	6.470E-20	1.253E-18	1.868E-19
57	253.24533188	2.40145244	4.398E-19	3.545E-20	1.611E-18	5.414E-20	2.142E-18	3.110E-19
58	253.24132512	2.40104050	3.462E-19	3.292E-20	4.842E-19	1.276E-20	1.674E-19	5.935E-21
59	253.24309240	2.40147076	3.343E-19	4.052E-20	5.742E-19	2.354E-20	2.399E-19	1.109E-20
60	253.24688458	2.40208826	3.942E-19	3.419E-20	1.252E-18	3.114E-20	6.645E-19	1.572E-20
61	253.24418894	2.40237315	3.085E-19	4.052E-20	6.449E-19	2.505E-20	1.772E-19	1.781E-20

Table 5.3 continued

Table 5.3: Observational Properties of Individual Star Clusters (continued)

ID	R.A.	Decl.	f_{336}	$\sigma_{f_{336}}$	f_{435}	$\sigma_{f_{435}}$	f_{814}	$\sigma_{f_{814}}$
62	253.24944382	2.40381842	1.219E-18	3.039E-20	8.292E-18	1.989E-20	4.113E-17	5.541E-20
63	253.24532189	2.40345725	4.224E-19	3.292E-20	1.232E-18	3.322E-20	9.465E-19	4.674E-20
64	253.24618614	2.40355361	2.845E-19	3.039E-20	7.933E-19	2.286E-20	2.349E-19	1.326E-20
65	253.24579298	2.40372720	2.340E-18	3.545E-20	1.797E-18	4.366E-20	1.515E-19	3.345E-20
66	253.24584533	2.40406226	4.743E-18	3.292E-20	9.680E-18	5.224E-20	3.192E-18	2.441E-20
67	253.24726875	2.40405837	3.279E-19	3.419E-20	8.667E-19	1.801E-20	3.891E-19	1.104E-20
68	253.24214302	2.40366567	3.834E-19	2.785E-20	3.350E-19	1.747E-20	6.965E-20	6.659E-21
69	253.24297200	2.40423948	2.803E-19	3.165E-20	4.767E-19	1.798E-20	1.645E-19	7.725E-21
70	253.24767954	2.40616166	7.009E-17	8.863E-20	9.381E-17	4.815E-20	6.162E-17	9.767E-20
71	253.24633860	2.40526817	2.142E-19	3.545E-20	6.784E-19	2.711E-20	5.793E-19	1.279E-20
72	253.24691685	2.40587743	1.716E-19	3.672E-20	3.932E-19	3.646E-20	5.018E-20	1.207E-20
73	253.24731503	2.40635434	8.767E-19	3.419E-20	2.161E-18	4.722E-20	7.094E-19	1.679E-20
74	253.24773395	2.40717036	2.377E-19	3.419E-20	4.241E-19	2.297E-20	1.252E-19	1.077E-20
75	253.24506137	2.40652895	2.834E-19	3.419E-20	2.664E-19	1.414E-20	3.462E-20	6.785E-21
76	253.24549787	2.40688002	2.202E-19	3.925E-20	4.332E-19	2.345E-20	4.722E-20	1.143E-20
77	253.24215445	2.40756337	2.345E-18	3.039E-20	1.097E-17	1.836E-20	1.835E-17	2.376E-20
78	253.25007399	2.40912610	3.490E-19	3.292E-20	3.704E-19	1.752E-20	1.574E-19	6.748E-21
79	253.24792139	2.40923885	5.537E-19	3.039E-20	7.912E-19	1.887E-20	2.845E-19	7.948E-21
80	253.24896894	2.41431070	7.421E-17	6.204E-20	1.246E-16	9.937E-20	6.920E-17	9.984E-20
81	253.23769922	2.41262272	2.531E-19	2.532E-20	1.472E-18	1.279E-20	3.181E-18	5.952E-21
82	253.23343459	2.41236471	5.172E-19	3.545E-20	5.816E-19	1.397E-20	5.988E-19	8.398E-21
83	253.23527375	2.41266781	1.202E-18	2.659E-20	3.914E-18	1.369E-20	4.216E-18	7.660E-21
84	253.24402929	2.41529519	3.848E-19	2.659E-20	3.972E-18	1.496E-20	3.679E-17	5.100E-20
85	253.25304715	2.41962069	2.092E-17	4.178E-20	5.580E-17	4.754E-20	4.580E-17	6.248E-20
86	253.24731039	2.42039366	4.787E-19	3.419E-20	2.978E-19	1.364E-20	1.167E-19	5.322E-21
87	253.23219293	2.41474032	3.757E-19	2.912E-20	3.050E-19	1.235E-20	7.081E-20	5.339E-21
NGC 7469 - Center								
1	345.81639435	8.87467401	4.622E-19	3.925E-20	1.534E-18	3.334E-20	6.530E-19	3.334E-20
2	345.81512694	8.87171669	1.210E-17	3.444E-19	9.244E-18	3.676E-19	1.737E-18	8.244E-20
3	345.81589433	8.87320648	6.105E-18	1.747E-19	8.804E-18	2.303E-19	2.725E-18	1.016E-19
4	345.81526622	8.87184595	1.899E-18	8.230E-20	1.479E-18	1.523E-19	2.341E-19	4.774E-20
5	345.81580281	8.87360089	5.676E-18	9.876E-20	3.759E-18	2.784E-19	4.859E-18	1.930E-19
6	345.81555728	8.87481639	4.800E-19	5.191E-20	1.740E-18	7.539E-20	1.003E-18	6.202E-20
7	345.81562581	8.87384424	5.078E-17	8.559E-19	8.540E-17	1.864E-18	3.399E-17	1.831E-18
8	345.81449665	8.87292069	6.282E-18	1.026E-19	6.250E-18	1.990E-19	1.465E-18	6.956E-20
9	345.81529776	8.87481599	2.773E-18	6.331E-20	4.076E-18	9.873E-20	1.767E-18	1.132E-19
10	345.81542053	8.87422320	2.040E-16	3.805E-18	2.400E-16	1.992E-18	8.004E-17	3.376E-18
11	345.81529029	8.87412003	3.503E-17	1.257E-18	1.074E-17	2.078E-18	1.610E-17	1.469E-18
12	345.81521742	8.87360080	8.243E-17	5.235E-18	6.929E-17	6.165E-18	1.988E-17	3.562E-18
13	345.81501397	8.87341535	2.174E-16	2.318E-18	1.978E-16	1.514E-18	5.906E-17	6.567E-19
14	345.81540620	8.87380879	8.404E-17	1.621E-18	9.338E-17	1.683E-18	1.396E-17	2.111E-18
15	345.81425826	8.87261055	7.629E-19	4.685E-20	1.046E-18	3.760E-20	1.552E-19	2.173E-20
16	345.81465936	8.87387687	1.706E-16	3.707E-18	1.561E-16	4.522E-18	5.719E-17	2.389E-18
17	345.81403150	8.87253350	7.538E-19	5.951E-20	8.485E-19	4.466E-20	1.293E-19	2.721E-20
18	345.81497817	8.87429340	2.533E-17	1.031E-18	4.919E-17	1.169E-19	2.952E-17	9.362E-20
19	345.81323222	8.87290411	6.139E-19	4.178E-20	7.012E-19	3.925E-20	1.913E-19	1.649E-20
NGC 7469 - Extended Galaxy and Companion								
1	345.82127974	8.86185301	5.041E-19	3.039E-20	3.135E-19	1.453E-20	8.849E-20	4.697E-21
2	345.82458059	8.87213263	4.863E-19	3.419E-20	1.093E-18	1.439E-20	9.703E-19	6.672E-21
3	345.82136277	8.87153169	2.702E-19	3.419E-20	3.547E-19	1.394E-20	1.050E-19	6.305E-21

Table 5.3 continued

Table 5.3: Observational Properties of Individual Star Clusters (continued)

ID	R.A.	Decl.	f_{336}	$\sigma_{f_{336}}$	f_{435}	$\sigma_{f_{435}}$	f_{814}	$\sigma_{f_{814}}$
4	345.82071313	8.87128493	1.902E-18	5.951E-20	2.155E-18	4.000E-20	3.040E-19	1.094E-20
5	345.81985348	8.87039921	5.172E-19	3.292E-20	6.834E-19	1.459E-20	1.895E-19	6.091E-21
6	345.81899980	8.86894326	9.947E-19	3.798E-20	9.042E-19	2.080E-20	2.590E-19	8.051E-21
7	345.81605889	8.86463471	4.480E-19	3.292E-20	1.166E-18	1.288E-20	8.561E-19	6.026E-21
8	345.82263255	8.87599218	4.534E-19	3.039E-20	6.884E-19	1.764E-20	1.497E-19	6.743E-21
9	345.82059002	8.87341911	2.968E-19	3.798E-20	7.255E-19	2.469E-20	3.085E-19	1.041E-20
10	345.83094757	8.89157504	6.270E-19	2.659E-20	7.084E-19	1.172E-20	3.040E-19	5.050E-21
11	345.81791879	8.87292105	3.420E-19	5.444E-20	2.894E-19	5.069E-20	2.944E-19	1.797E-20
12	345.81834083	8.87272819	2.424E-19	3.798E-20	4.175E-19	4.475E-20	1.466E-19	2.411E-20
13	345.81746896	8.87188429	1.332E-18	3.419E-20	1.196E-18	3.433E-20	3.716E-19	1.901E-20
14	345.81797084	8.87195213	3.848E-19	3.672E-20	6.130E-19	3.345E-20	1.314E-19	1.336E-20
15	345.81790192	8.87213663	1.873E-18	4.558E-20	1.306E-18	4.861E-20	3.689E-19	1.423E-20
16	345.81782421	8.87240132	3.117E-18	6.457E-20	3.053E-18	6.749E-20	9.938E-19	2.754E-20
17	345.81658439	8.87143448	4.338E-18	4.052E-20	3.780E-18	4.032E-20	8.168E-19	1.676E-20
18	345.81763209	8.87244769	4.661E-18	1.241E-19	3.794E-18	1.109E-19	6.933E-19	3.033E-20
19	345.81784046	8.87216780	4.112E-19	4.431E-20	4.179E-19	6.267E-20	1.139E-19	2.054E-20
20	345.81748732	8.87257458	3.361E-18	5.824E-20	2.495E-18	8.546E-20	7.101E-19	2.845E-20
21	345.81799200	8.87315871	9.937E-19	4.305E-20	1.254E-18	4.733E-20	4.216E-19	1.820E-20
22	345.81824251	8.87343495	4.097E-19	3.039E-20	3.815E-19	2.042E-20	1.289E-19	1.133E-20
23	345.81756258	8.87256198	2.655E-18	8.863E-20	2.348E-18	6.678E-20	4.922E-19	2.453E-20
24	345.81616187	8.87066640	4.101E-19	3.925E-20	5.108E-19	2.093E-20	1.552E-19	9.490E-21
25	345.81561668	8.87036233	5.900E-18	4.431E-20	4.582E-18	3.464E-20	1.005E-18	1.103E-20
26	345.82151171	8.87919991	4.196E-19	3.672E-20	6.085E-19	1.102E-20	3.237E-19	5.808E-21
27	345.81663248	8.87192775	1.732E-18	5.444E-20	2.118E-18	6.014E-20	5.259E-19	1.829E-20
28	345.81605291	8.87153156	7.700E-18	8.863E-20	7.486E-18	7.051E-20	1.733E-18	3.270E-20
29	345.81624452	8.87115586	2.834E-19	3.925E-20	3.286E-19	1.356E-20	5.751E-20	1.134E-20
30	345.81591648	8.87123671	3.532E-19	3.292E-20	6.827E-19	2.086E-20	2.819E-19	1.210E-20
31	345.81779786	8.87478598	4.572E-17	5.318E-20	7.424E-17	3.661E-20	3.080E-17	4.995E-20
32	345.81389542	8.86802732	6.351E-19	3.039E-20	5.344E-19	1.391E-20	1.500E-19	5.272E-21
33	345.81818930	8.87480198	5.196E-19	3.165E-20	4.133E-19	1.934E-20	9.975E-20	9.653E-21
34	345.81542489	8.87146317	5.187E-19	3.039E-20	1.219E-18	2.467E-20	2.925E-19	1.275E-20
35	345.81720549	8.87439761	8.873E-19	4.685E-20	8.918E-19	3.199E-20	2.003E-19	2.868E-20
36	345.81451573	8.87059950	1.003E-18	4.685E-20	1.464E-18	1.828E-20	4.696E-19	7.981E-21
37	345.82032124	8.87946683	1.312E-18	3.925E-20	1.490E-18	1.815E-20	2.665E-19	6.450E-21
38	345.81490060	8.87177466	1.032E-17	1.228E-19	1.103E-17	7.562E-20	2.861E-18	2.729E-20
39	345.82804443	8.89174830	1.941E-19	4.431E-20	2.577E-19	2.332E-20	1.470E-19	1.192E-20
40	345.81668866	8.87471520	3.595E-19	4.685E-20	5.319E-19	3.336E-20	2.487E-19	1.908E-20
41	345.82788424	8.89236374	1.710E-18	4.431E-20	2.183E-18	5.719E-20	1.023E-18	3.994E-20
42	345.81663315	8.87543820	3.993E-19	5.571E-20	1.294E-18	6.093E-20	1.452E-19	2.678E-20
43	345.81637017	8.87579040	6.190E-19	4.938E-20	1.355E-18	1.991E-20	5.912E-19	1.238E-20
44	345.82868823	8.89516136	3.204E-18	3.039E-20	1.801E-17	1.498E-20	2.850E-17	3.939E-20
45	345.81627362	8.87529555	5.167E-18	4.431E-20	2.400E-19	3.379E-20	9.139E-20	1.525E-20
46	345.81966350	8.88067717	2.264E-19	4.558E-20	1.949E-19	1.958E-20	6.122E-20	7.330E-21
47	345.81337578	8.87122047	4.455E-19	4.052E-20	6.354E-19	1.680E-20	1.754E-19	9.736E-21
48	345.81922002	8.88045533	5.993E-19	6.964E-20	7.654E-19	7.100E-20	2.336E-19	1.682E-20
49	345.82691552	8.89270419	3.591E-19	3.672E-20	8.346E-19	4.823E-20	7.637E-19	4.151E-20
50	345.81606196	8.87570077	3.608E-19	4.685E-20	2.454E-19	2.981E-20	6.230E-20	1.832E-20
51	345.81397845	8.87239419	8.544E-19	4.305E-20	1.590E-19	2.664E-20	6.869E-20	1.461E-20
52	345.81358337	8.87258522	9.810E-19	4.938E-20	1.057E-18	2.572E-20	4.015E-19	1.539E-20
53	345.81217509	8.87017694	4.484E-19	3.798E-20	4.946E-19	1.287E-20	9.911E-20	7.861E-21
54	345.81841431	8.88036093	2.619E-19	3.925E-20	4.388E-19	2.302E-20	1.085E-19	7.296E-21
55	345.81277269	8.87260910	1.079E-18	3.672E-20	1.367E-18	4.168E-20	4.298E-19	1.648E-20
56	345.81304149	8.87281417	4.067E-19	3.165E-20	3.055E-19	2.408E-20	1.825E-19	1.182E-20

Table 5.3 continued

Table 5.3: Observational Properties of Individual Star Clusters (continued)

ID	R.A.	Decl.	f_{336}	$\sigma_{f_{336}}$	f_{435}	$\sigma_{f_{435}}$	f_{814}	$\sigma_{f_{814}}$
57	345.82583966	8.89319707	4.259E-19	4.305E-20	9.142E-19	6.743E-20	5.708E-19	5.304E-20
58	345.82606528	8.89338389	5.322E-19	6.710E-20	7.590E-19	1.314E-19	4.926E-19	7.394E-20
59	345.81267568	8.87281898	3.706E-19	4.052E-20	2.445E-19	2.017E-20	8.972E-20	1.073E-20
60	345.82589987	8.89334665	1.182E-18	7.090E-20	1.426E-18	7.854E-20	5.401E-19	8.012E-20
61	345.82576380	8.89367168	1.062E-17	6.837E-20	8.739E-18	1.419E-19	2.796E-18	1.224E-19
62	345.81254270	8.87410346	4.196E-18	6.964E-20	7.555E-18	1.017E-19	3.249E-18	4.553E-20
63	345.81266940	8.87387270	9.438E-19	5.571E-20	1.786E-18	5.815E-20	4.854E-19	2.506E-20
64	345.81297757	8.87441692	2.824E-19	3.419E-20	4.453E-19	3.901E-20	1.840E-19	2.225E-20
65	345.81686209	8.88046063	3.160E-19	3.419E-20	4.883E-19	2.807E-20	1.660E-19	9.379E-21
66	345.81664870	8.88037867	7.306E-19	4.685E-20	1.695E-18	3.490E-20	4.326E-19	1.404E-20
67	345.82498232	8.89379140	3.516E-18	4.811E-20	4.833E-18	6.976E-20	2.616E-18	8.852E-20
68	345.81212646	8.87393880	5.841E-19	4.305E-20	1.450E-18	1.856E-20	4.692E-19	9.893E-21
69	345.82013939	8.88602752	5.115E-19	3.798E-20	4.511E-19	1.298E-20	9.676E-20	4.984E-21
70	345.82532167	8.89392735	5.724E-19	3.798E-20	1.989E-18	5.944E-20	3.024E-19	4.336E-20
71	345.81262593	8.87469727	1.471E-18	4.178E-20	1.537E-18	3.744E-20	5.064E-19	2.204E-20
72	345.81239187	8.87469379	2.858E-19	3.925E-20	3.444E-19	3.087E-20	8.931E-20	1.314E-20
73	345.81262875	8.87527968	9.326E-19	3.798E-20	1.073E-18	7.026E-20	2.123E-19	2.907E-20
74	345.81211465	8.87535733	1.048E-18	3.419E-20	1.696E-18	2.386E-20	5.708E-19	1.385E-20
75	345.81265306	8.87559530	5.819E-19	5.318E-20	6.290E-19	3.677E-20	2.595E-19	1.646E-20
76	345.81222525	8.87482786	3.709E-19	3.925E-20	4.960E-19	2.436E-20	1.313E-19	1.356E-20
77	345.82479232	8.89522774	1.315E-18	3.419E-20	1.848E-18	2.565E-20	8.640E-19	1.313E-20
78	345.82386790	8.89364815	2.052E-19	4.052E-20	7.675E-19	3.623E-20	8.153E-19	8.712E-20
79	345.81204080	8.87568083	4.310E-19	3.925E-20	5.705E-19	3.948E-20	2.029E-19	1.179E-20
80	345.81212343	8.87574249	1.146E-18	5.444E-20	1.105E-18	3.460E-20	3.662E-19	1.249E-20
81	345.82407346	8.89450861	7.915E-18	5.951E-20	8.852E-18	3.509E-20	3.771E-18	3.004E-20
82	345.81371017	8.87843456	1.134E-18	6.204E-20	1.696E-18	4.305E-20	4.415E-19	1.473E-20
83	345.81187374	8.87571663	4.212E-19	4.052E-20	4.445E-19	4.551E-20	3.792E-19	1.882E-20
84	345.81207108	8.87611163	5.337E-19	3.925E-20	1.335E-18	3.549E-20	4.657E-19	1.881E-20
85	345.81331884	8.87855391	1.349E-18	4.685E-20	1.566E-18	2.069E-20	5.820E-19	1.181E-20
86	345.81310214	8.87758368	1.261E-18	4.685E-20	1.096E-18	3.564E-20	1.769E-19	1.142E-20
87	345.81220739	8.87609897	2.524E-19	4.558E-20	2.400E-19	5.527E-20	1.007E-19	1.900E-20
88	345.82443880	8.89518904	2.814E-19	3.292E-20	4.591E-19	3.573E-20	2.631E-19	1.291E-20
89	345.81384776	8.87893102	2.614E-19	2.912E-20	3.170E-19	1.449E-20	7.094E-20	8.540E-21
90	345.81331973	8.87833037	1.242E-18	4.178E-20	1.103E-18	2.195E-20	1.531E-19	7.931E-21
91	345.81275406	8.87762213	9.038E-19	4.178E-20	8.787E-19	3.877E-20	2.955E-19	1.036E-20
92	345.81200599	8.87646099	5.682E-19	4.178E-20	9.185E-19	3.853E-20	2.569E-19	1.565E-20
93	345.81188495	8.87647528	5.087E-19	3.672E-20	5.285E-19	2.574E-20	1.628E-19	1.037E-20
94	345.82328688	8.89400694	1.132E-18	4.558E-20	1.975E-18	6.121E-20	2.402E-18	1.049E-19
95	345.81391936	8.87956957	2.505E-19	3.672E-20	3.850E-19	1.375E-20	8.011E-20	5.737E-21
96	345.82311887	8.89408455	1.790E-18	5.698E-20	1.900E-18	8.603E-20	5.847E-19	5.601E-20
97	345.82353986	8.89483045	2.971E-19	3.672E-20	4.816E-19	2.775E-20	8.553E-19	2.876E-20
98	345.82351866	8.89577736	3.775E-19	3.292E-20	1.207E-18	1.991E-20	4.679E-19	1.136E-20
99	345.81451040	8.88162578	1.897E-19	4.052E-20	2.896E-19	2.666E-20	8.825E-20	9.986E-21
100	345.81486023	8.88206402	3.880E-19	3.039E-20	1.590E-19	1.691E-20	7.029E-20	5.473E-21
101	345.82246419	8.89495527	1.230E-18	4.305E-20	2.676E-18	5.676E-20	2.209E-18	8.319E-20
102	345.81440054	8.88161058	3.764E-19	3.798E-20	2.846E-19	1.761E-20	8.858E-20	6.990E-21
103	345.82143958	8.89341357	8.160E-19	3.672E-20	6.872E-19	2.004E-20	2.302E-19	1.082E-20
104	345.81352710	8.88167826	2.675E-19	3.292E-20	4.591E-19	1.312E-20	1.517E-19	5.822E-21
105	345.81141857	8.87880605	6.032E-19	4.305E-20	8.627E-19	2.147E-20	1.965E-19	9.533E-21
106	345.82111830	8.89379307	9.578E-19	3.419E-20	1.079E-18	2.089E-20	2.692E-19	1.035E-20
107	345.81164886	8.87954013	4.708E-19	3.798E-20	5.151E-19	1.782E-20	9.721E-20	6.802E-21
108	345.81117971	8.87887204	6.351E-19	3.798E-20	6.948E-19	1.861E-20	1.890E-19	7.758E-21
109	345.82189055	8.89570739	8.115E-18	7.343E-20	9.841E-18	1.412E-19	5.192E-18	9.447E-20

Table 5.3 continued

Table 5.3: Observational Properties of Individual Star Clusters (continued)

ID	R.A.	Decl.	f_{336}	$\sigma_{f_{336}}$	f_{435}	$\sigma_{f_{435}}$	f_{814}	$\sigma_{f_{814}}$
110	345.82101349	8.89388683	4.903E-19	3.419E-20	5.319E-19	1.925E-20	1.271E-19	9.814E-21
111	345.81173093	8.87992485	5.210E-19	4.305E-20	4.847E-19	1.428E-20	9.874E-20	7.924E-21
112	345.82182092	8.89566349	3.582E-18	5.318E-20	5.222E-18	9.427E-20	2.811E-18	7.402E-20
113	345.82192679	8.89586901	5.922E-19	7.723E-20	4.276E-19	1.006E-19	3.192E-19	3.918E-20
114	345.81228068	8.88153816	2.775E-18	7.597E-20	1.811E-18	7.902E-20	3.178E-19	2.049E-20
115	345.82154644	8.89576605	8.743E-19	5.951E-20	1.962E-18	1.212E-19	6.844E-19	5.526E-20
116	345.81172247	8.88049312	3.852E-19	3.292E-20	5.473E-19	1.313E-20	1.637E-19	4.613E-21
117	345.81204213	8.88134741	8.615E-19	5.318E-20	9.017E-19	4.149E-20	2.413E-19	1.540E-20
118	345.81475305	8.88522858	3.942E-19	3.672E-20	3.593E-19	1.782E-20	8.760E-20	6.603E-21
119	345.82171686	8.89619604	3.177E-18	6.204E-20	1.951E-18	7.122E-20	5.761E-19	6.042E-20
120	345.82152673	8.89617838	5.004E-18	4.685E-20	3.752E-18	6.514E-20	1.152E-18	4.113E-20
121	345.81200931	8.88190571	2.954E-19	3.925E-20	2.681E-19	1.418E-20	1.542E-19	1.100E-20
122	345.82156418	8.89625251	7.179E-19	5.571E-20	5.990E-19	5.488E-20	4.132E-19	3.429E-20
123	345.82027037	8.89446942	1.343E-18	3.672E-20	1.194E-18	2.614E-20	2.552E-19	9.748E-21
124	345.81742292	8.89112015	7.414E-17	6.457E-20	3.454E-17	2.665E-20	1.134E-17	2.204E-20
125	345.81137008	8.88229775	7.133E-18	1.266E-19	6.063E-18	5.952E-20	1.072E-18	3.435E-20
126	345.81183950	8.88247159	7.524E-19	3.798E-20	9.278E-19	1.673E-20	2.513E-19	6.574E-21
127	345.81093239	8.88177534	1.409E-18	3.925E-20	1.210E-18	2.407E-20	2.277E-19	8.374E-21
128	345.80736417	8.87701731	1.471E-18	3.798E-20	1.330E-18	3.852E-20	5.782E-19	1.208E-20
129	345.80731325	8.87663674	4.019E-19	3.419E-20	5.261E-19	2.670E-20	2.046E-19	8.818E-21
130	345.80975043	8.88025052	1.374E-18	3.419E-20	9.364E-19	1.389E-20	1.188E-19	5.198E-21
131	345.80749197	8.87711233	8.584E-19	4.558E-20	5.075E-19	2.484E-20	5.661E-20	1.394E-20
132	345.80733030	8.87690597	3.343E-19	4.178E-20	2.886E-19	2.839E-20	6.429E-20	1.174E-20
133	345.80706838	8.87684858	3.251E-19	3.798E-20	4.785E-19	2.080E-20	2.332E-19	7.725E-21
134	345.80710899	8.87750647	2.982E-19	3.798E-20	2.948E-19	2.284E-20	1.485E-19	8.296E-21
135	345.81843717	8.89512076	4.274E-19	3.292E-20	3.485E-19	1.616E-20	3.108E-20	7.213E-21
136	345.80781459	8.87917751	2.419E-19	3.292E-20	2.120E-19	1.150E-20	6.411E-20	4.716E-21
137	345.81087078	8.88417250	5.650E-19	2.912E-20	5.827E-19	2.046E-20	1.241E-19	6.484E-21
138	345.81783654	8.89589327	7.580E-19	3.419E-20	5.774E-19	1.718E-20	1.645E-19	5.989E-21
139	345.80976998	8.88420889	2.235E-19	2.532E-20	1.884E-18	1.276E-20	3.831E-18	6.747E-21
140	345.80486403	8.87793776	8.342E-19	3.545E-20	7.472E-19	1.321E-20	1.702E-19	4.704E-21
141	345.81682879	8.89709615	1.606E-18	3.419E-20	9.503E-19	1.962E-20	1.579E-19	7.201E-21
142	345.81613516	8.89750027	2.858E-18	3.798E-20	1.884E-18	2.103E-20	2.901E-19	8.428E-21
143	345.81623084	8.89751488	5.857E-19	3.672E-20	5.103E-19	2.295E-20	1.320E-19	6.900E-21
144	345.81579688	8.89783028	3.536E-19	3.039E-20	4.667E-19	1.778E-20	1.055E-19	6.155E-21
145	345.81143349	8.89265260	4.551E-19	2.785E-20	5.019E-19	1.291E-20	2.755E-19	5.067E-21
146	345.81424789	8.89966892	7.374E-19	2.912E-20	4.233E-19	1.167E-20	8.688E-20	4.755E-21

Table 5.4: Derived Properties of Individual Star Clusters

ID	R.A.	Decl.	t_c	σ_{t_c}	M_c	σ_{M_c}	A_V	σ_{A_V}
Arp 220								
1	233.74666905	23.48058170	8.657	0.111	8.905	0.045	4.5	0.20
2	233.72954905	23.47581741	8.057	0.117	7.100	0.054	0.9	0.16
3	233.74843760	23.48274548	8.957	0.311	6.359	0.061	0.8	0.53
4	233.75164401	23.48438602	8.307	0.108	6.617	0.042	0.6	0.23
5	233.76469429	23.49254708	8.657	0.125	7.714	0.045	3.4	0.22
6	233.72821835	23.48265615	7.440	0.633	5.219	0.378	1.2	1.04
7	233.73230262	23.48457584	6.940	0.013	5.457	0.060	2.6	0.10
8	233.73185992	23.48615206	8.307	0.229	5.457	0.068	0.8	0.30
9	233.72501290	23.48691445	8.657	0.100	7.807	0.042	3.6	0.20
10	233.72839999	23.48868241	6.940	0.180	4.216	0.344	1.4	0.37
11	233.73231080	23.49079122	6.060	0.156	3.897	0.142	0.3	0.20
12	233.75803382	23.50158592	7.420	0.625	5.337	0.374	1	1.03
13	233.74391918	23.49905783	8.657	0.082	5.866	0.042	0.4	0.18
14	233.74684317	23.50064463	8.657	0.079	5.896	0.042	0.3	0.17
15	233.74843808	23.50266525	8.256	0.109	7.028	0.049	0.6	0.16
16	233.73915751	23.50074409	8.256	0.267	4.935	0.176	0	0.24
17	233.73723734	23.50060951	6.960	0.410	4.336	0.360	0.9	0.97
18	233.73927170	23.50207210	8.657	0.143	6.323	0.059	1.3	0.27
19	233.74440108	23.50393092	8.657	0.066	6.338	0.026	0.6	0.14
20	233.71486086	23.49613826	8.256	0.228	5.126	0.112	0.4	0.25
21	233.74486807	23.50467514	8.507	0.065	5.663	0.052	0	0.21
22	233.74023130	23.50352484	6.680	0.046	4.680	0.102	0.9	0.20
23	233.73899471	23.50421279	8.607	0.195	6.094	0.060	0.9	0.33
24	233.73652731	23.50352957	8.407	0.187	5.787	0.064	0.6	0.32
25	233.75923556	23.51003412	6.920	0.185	5.740	0.205	2.1	0.13
26	233.73690711	23.50405544	8.457	0.060	5.547	0.039	0	0.16
27	233.75544911	23.50925410	8.006	0.724	4.846	0.314	0.4	0.77
28	233.73689378	23.50444370	8.457	0.171	6.428	0.035	0.5	0.31
29	233.74041087	23.50651057	8.657	0.075	5.900	0.030	0.3	0.16
30	233.74117528	23.50700297	8.657	0.114	6.067	0.047	0.6	0.21
31	233.73779793	23.50730509	8.407	0.082	6.262	0.034	0	0.17
32	233.73724699	23.50687723	8.006	0.701	4.713	0.308	0.2	0.78
33	233.73677185	23.50697629	8.407	0.060	5.556	0.034	0	0.13
34	233.73977452	23.50795556	8.657	0.088	5.913	0.043	0.3	0.17
35	233.74090543	23.50824739	8.557	0.108	5.325	0.057	0	0.16

Table 5.4 continued

Table 5.4: Derived Properties of Individual Star Clusters (continued)

ID	R.A.	Decl.	t_c	σ_{t_c}	M_c	σ_{M_c}	A_V	σ_{A_V}
36	233.73959535	23.51000195	8.407	0.064	6.021	0.026	0	0.15
37	233.73975800	23.51020709	8.357	0.066	5.576	0.037	0	0.11
38	233.73909140	23.51001044	8.407	0.046	5.521	0.031	0	0.13
39	233.74326893	23.51143905	8.607	0.138	6.546	0.046	1.5	0.24
40	233.72747609	23.50737438	7.677	0.632	5.411	0.290	1.6	0.97
41	233.74159646	23.51241000	8.907	0.270	6.367	0.065	0.9	0.45
42	233.71264167	23.51070808	6.060	0.129	3.751	0.049	0	0.22
43	233.71578654	23.51292516	6.440	0.649	4.545	0.371	2.4	1.03
44	233.71278254	23.51029146	7.628	0.660	4.700	0.333	0.9	1.00
45	233.72331540	23.51772209	8.157	0.105	7.783	0.047	0.9	0.16
46	233.72969311	23.51835216	8.857	0.268	5.909	0.066	0.5	0.45
IC 1623								
1	16.95633044	-17.51200123	7.260	0.511	4.805	0.405	0.7	1.02
2	16.95253257	-17.50621356	7.653	0.648	4.742	0.324	0.3	1.02
3	16.95205630	-17.50641360	8.657	0.073	5.724	0.044	0.1	0.08
4	16.95048863	-17.50346183	6.680	0.588	4.675	0.256	1.7	0.78
5	16.95104913	-17.50486336	7.260	0.546	4.871	0.415	0.7	1.04
6	16.95068209	-17.50340830	6.940	0.012	4.348	0.062	0.9	0.15
7	16.95086391	-17.50551010	8.157	0.105	6.697	0.045	0.3	0.16
8	16.95118741	-17.50487325	8.107	0.716	4.805	0.331	0	0.85
9	16.95101639	-17.50470637	7.653	0.657	4.513	0.378	0.2	1.02
10	16.95095311	-17.50527787	6.680	0.045	4.223	0.133	0.9	0.26
11	16.95093328	-17.50508371	6.680	0.057	4.333	0.118	0.8	0.25
12	16.95171234	-17.50695885	8.307	0.108	5.498	0.047	0.2	0.14
13	16.95065637	-17.50614370	8.657	0.154	5.809	0.056	0.5	0.28
14	16.95043989	-17.50552899	8.307	0.226	5.532	0.099	0.4	0.30
15	16.95113776	-17.50660988	8.256	0.156	5.020	0.114	0	0.02
16	16.95105745	-17.50694837	6.080	0.628	5.720	0.375	2.2	1.03
17	16.95068447	-17.50576596	8.357	0.391	5.387	0.176	0.3	0.43
18	16.95108197	-17.50676510	6.960	0.321	3.710	0.368	0	0.67
19	16.95033162	-17.50556879	7.240	0.640	4.491	0.421	0.8	1.10
20	16.95038334	-17.50589927	6.680	0.188	4.119	0.397	0.9	0.66
21	16.95013922	-17.50592391	8.157	0.157	5.629	0.067	0.4	0.21
22	16.95031758	-17.50600715	8.607	0.062	5.704	0.051	0	0.32
23	16.95067378	-17.50689977	8.256	0.141	5.020	0.097	0	0.00
24	16.95022909	-17.50592562	8.307	0.121	5.202	0.092	0	0.02

Table 5.4 continued

Table 5.4: Derived Properties of Individual Star Clusters (continued)

ID	R.A.	Decl.	t_c	σ_{t_c}	M_c	σ_{M_c}	A_V	σ_{A_V}
25	16.95019588	-17.50910260	6.820	0.321	5.352	0.406	0.3	0.62
26	16.95039123	-17.50908629	8.256	0.202	5.083	0.134	0	0.05
27	16.95016335	-17.50889778	6.680	0.067	4.184	0.086	0.8	0.24
28	16.94965175	-17.50783823	6.980	0.491	4.112	0.419	0.2	1.03
29	16.94834474	-17.50542353	8.157	0.107	5.601	0.047	0.3	0.16
30	16.94844561	-17.50609887	6.940	0.040	4.918	0.148	0.6	0.25
31	16.94848474	-17.50653432	7.907	0.643	7.002	0.304	3.1	0.77
32	16.94810215	-17.50520785	6.520	0.320	4.502	0.412	1.3	0.64
33	16.94938903	-17.50790363	6.660	0.152	4.157	0.300	1	0.50
34	16.94982933	-17.50865188	6.560	0.282	3.733	0.384	0.9	0.51
35	16.94831767	-17.50556353	7.957	0.776	4.850	0.384	0.7	1.05
36	16.94788979	-17.50704320	6.940	0.007	7.141	0.003	5	0.04
37	16.94796530	-17.50619881	6.680	0.042	4.409	0.086	0.5	0.18
38	16.94775249	-17.50748391	8.307	0.352	7.597	0.081	3.8	0.54
39	16.94738526	-17.50544901	6.760	0.302	4.358	0.405	0.5	0.62
40	16.94667828	-17.50453376	6.680	0.057	4.887	0.076	1.1	0.19
41	16.94797596	-17.50705069	6.480	0.657	5.352	0.390	2.4	1.08
42	16.94656704	-17.50467706	6.480	0.339	5.617	0.406	1.7	0.65
43	16.94779151	-17.50712866	6.940	0.019	6.319	0.129	4.7	0.20
44	16.94699694	-17.50741455	7.857	0.616	7.401	0.256	0.7	0.76
45	16.94771317	-17.50825017	8.357	0.580	5.427	0.220	0.1	0.55
46	16.94701401	-17.50545129	7.857	0.609	5.028	0.260	0.2	0.77
47	16.94901299	-17.51114634	7.857	0.618	5.660	0.259	0.6	0.76
48	16.94672266	-17.50715451	6.560	0.239	5.264	0.376	1	0.59
49	16.94665211	-17.50644229	6.720	0.105	5.684	0.156	0.1	0.37
50	16.94487361	-17.50520980	7.020	0.206	4.913	0.219	0	0.15
51	16.94848420	-17.50990232	6.680	0.608	4.381	0.300	1.2	0.09
52	16.94568878	-17.50346874	6.680	0.038	3.972	0.079	0.5	0.17
53	16.94865535	-17.51069539	6.640	0.082	4.076	0.126	0.4	0.30
54	16.94788019	-17.50887849	8.057	0.676	4.956	0.337	0	0.66
55	16.94611424	-17.50504089	6.460	0.336	4.473	0.401	1.7	0.65
56	16.94586076	-17.50474111	6.680	0.033	4.234	0.077	0.8	0.16
57	16.94673324	-17.50756951	8.657	0.083	8.103	0.040	3.7	0.18
58	16.94653624	-17.50664128	7.440	0.631	5.737	0.369	0	1.01
59	16.94571606	-17.50502864	6.840	0.330	4.122	0.405	0.4	0.65
60	16.94642201	-17.50653938	6.940	0.579	4.400	0.498	1.1	1.07
61	16.94609444	-17.50684683	6.840	0.346	5.279	0.406	0.5	0.69
62	16.94851864	-17.51175005	8.057	0.125	5.846	0.061	0.2	0.16

Table 5.4 continued

Table 5.4: Derived Properties of Individual Star Clusters (continued)

ID	R.A.	Decl.	t_c	σ_{t_c}	M_c	σ_{M_c}	A_V	σ_{A_V}
63	16.94695343	-17.50788322	7.807	0.668	5.878	0.318	1.9	1.01
64	16.94596527	-17.50528918	7.720	0.711	4.755	0.488	1	1.06
65	16.94554006	-17.50516756	7.857	0.672	5.594	0.310	1.5	0.95
66	16.94814280	-17.51088046	6.320	0.322	5.502	0.396	1.6	0.56
67	16.94649315	-17.50688953	6.680	0.320	3.917	0.433	0.9	0.78
68	16.94806248	-17.51104933	6.660	0.079	4.601	0.105	0.9	0.29
69	16.94668298	-17.50813649	6.980	0.590	4.674	0.429	1.5	1.06
70	16.94523450	-17.50543945	7.477	0.655	5.039	0.369	0.1	1.02
71	16.94596982	-17.50675972	6.800	0.311	5.688	0.401	0.6	0.66
72	16.94790166	-17.51054506	6.680	0.055	4.081	0.064	0.7	0.18
73	16.94653027	-17.50801146	7.180	0.582	5.358	0.408	1.5	1.03
74	16.94664310	-17.50798344	7.300	0.593	4.798	0.397	0.5	1.04
75	16.94469242	-17.50462346	7.907	0.629	5.380	0.267	0	0.68
76	16.94632061	-17.50847149	6.920	0.217	4.741	0.253	0.8	0.31
77	16.94706286	-17.50918149	8.057	0.168	5.078	0.111	0	0.08
78	16.94539804	-17.50612096	7.857	0.624	6.520	0.258	0.7	0.77
79	16.94443423	-17.50612894	7.857	0.622	6.787	0.254	0.3	0.77
80	16.94493662	-17.50543667	8.657	0.067	6.698	0.047	0	0.06
81	16.94562496	-17.50631558	6.600	0.056	5.240	0.063	0.2	0.16
82	16.94603294	-17.50733177	6.960	0.171	5.044	0.236	0.5	0.17
83	16.94605884	-17.50779829	6.680	0.710	5.183	0.585	2.4	1.07
84	16.94580845	-17.50693241	7.000	0.572	5.093	0.410	0.4	1.03
85	16.94536056	-17.50639931	6.880	0.351	4.713	0.404	0.2	0.71
86	16.94551416	-17.50640928	6.680	0.060	5.634	0.069	0.7	0.20
87	16.94593957	-17.50724312	7.857	0.575	6.109	0.252	0	0.65
88	16.94613973	-17.50834675	6.900	0.361	5.521	0.404	0	0.65
89	16.94512230	-17.50650886	6.060	0.197	6.434	0.191	1.4	0.11
90	16.94585570	-17.50726300	6.820	0.650	5.269	0.385	0.7	1.00
91	16.94489295	-17.50604674	7.568	0.655	5.662	0.375	0	0.97
92	16.94502255	-17.50560673	6.680	0.055	4.648	0.077	0.3	0.19
93	16.94783152	-17.51213470	8.057	0.114	5.044	0.075	0	0.21
94	16.94442520	-17.50456042	7.628	0.661	5.124	0.365	1.2	1.03
95	16.94475320	-17.50638446	6.680	0.035	5.603	0.047	0.7	0.12
96	16.94755000	-17.51192017	8.006	0.167	5.330	0.087	0.2	0.17
97	16.94474936	-17.50674853	8.457	0.138	6.155	0.064	0	0.19
98	16.94441549	-17.50493532	6.340	0.223	5.131	0.258	1.3	0.20
99	16.94568228	-17.50871399	6.540	0.637	5.972	0.345	1.9	1.02
100	16.94619290	-17.50867259	8.057	0.784	5.208	0.385	0.6	1.09

Table 5.4 continued

Table 5.4: Derived Properties of Individual Star Clusters (continued)

ID	R.A.	Decl.	t_c	σ_{t_c}	M_c	σ_{M_c}	A_V	σ_{A_V}
101	16.94484887	-17.50645786	6.240	0.201	6.295	0.199	1.2	0.11
102	16.94347100	-17.50539574	6.940	0.015	4.848	0.065	1	0.10
103	16.94458030	-17.50604284	7.340	0.625	5.973	0.385	0.8	1.04
104	16.94523547	-17.50724339	6.900	0.514	5.606	0.432	0.1	0.85
105	16.94471028	-17.50654275	6.880	0.193	5.634	0.164	0	0.12
106	16.94484441	-17.50731209	6.680	0.047	5.445	0.061	0.7	0.15
107	16.94529652	-17.50696060	6.940	0.030	4.805	0.125	0.1	0.15
108	16.94604740	-17.50861820	8.307	0.068	5.334	0.062	0	0.04
109	16.94450188	-17.50589294	7.602	0.645	5.971	0.362	0.2	1.04
110	16.94507437	-17.50730590	6.920	0.408	5.096	0.389	0	0.81
111	16.94446724	-17.50660169	6.600	0.576	5.967	0.247	2	0.79
112	16.94677407	-17.51086637	6.760	0.299	4.220	0.402	0.4	0.62
113	16.94392911	-17.50487175	6.920	0.189	4.785	0.232	0	0.07
114	16.94429147	-17.50601627	6.860	0.616	5.380	0.386	0.6	1.01
115	16.94419815	-17.50725981	7.628	0.572	6.802	0.258	1.1	0.94
116	16.94476738	-17.50773736	6.940	0.014	6.392	0.043	0	0.01
117	16.94601069	-17.50961177	8.457	0.135	5.423	0.058	0	0.14
118	16.94503203	-17.50725411	6.940	0.193	5.011	0.272	0.1	0.27
119	16.94387100	-17.50533456	8.256	0.106	5.781	0.078	0	0.20
120	16.94532616	-17.50827867	6.320	0.196	4.930	0.186	1.2	0.15
121	16.94368746	-17.50579165	6.560	0.619	5.824	0.313	1.8	1.01
122	16.94462324	-17.50689982	7.602	0.581	6.492	0.277	0.2	0.98
123	16.94473716	-17.50751418	6.940	0.016	5.447	0.068	0.5	0.13
124	16.94300966	-17.50628011	8.657	0.152	6.029	0.061	0.5	0.27
125	16.94469923	-17.50742410	6.980	0.180	5.437	0.214	0.2	0.15
126	16.94524097	-17.50838478	8.407	0.083	5.890	0.033	0.1	0.16
127	16.94507848	-17.50908089	6.680	0.039	4.635	0.072	0.9	0.15
128	16.94455091	-17.50689931	7.720	0.568	6.619	0.241	0.3	0.78
129	16.94369925	-17.50482191	6.680	0.640	4.064	0.443	1.2	0.88
130	16.94348525	-17.50476631	7.519	0.656	4.690	0.359	0.2	1.02
131	16.94370207	-17.50503064	6.400	0.650	5.221	0.364	2.1	1.02
132	16.94391632	-17.50614127	6.680	0.045	6.179	0.072	0.8	0.16
133	16.94448205	-17.50686745	8.057	0.151	6.736	0.072	0.9	0.17
134	16.94325276	-17.50482699	8.757	0.242	5.950	0.065	0.4	0.40
135	16.94405903	-17.50663429	8.256	0.832	6.760	0.218	0.9	0.95
136	16.94599924	-17.51073000	6.840	0.305	4.437	0.367	0	0.48
137	16.94362613	-17.50523415	7.907	0.620	5.028	0.348	0	0.70
138	16.94357871	-17.50468637	6.680	0.144	4.123	0.349	1	0.56

Table 5.4 continued

Table 5.4: Derived Properties of Individual Star Clusters (continued)

ID	R.A.	Decl.	t_c	σ_{t_c}	M_c	σ_{M_c}	A_V	σ_{A_V}
139	16.94488240	-17.50893981	6.680	0.557	5.996	0.247	1.3	0.60
140	16.94626154	-17.51119157	6.680	0.045	3.888	0.092	0.6	0.20
141	16.94588817	-17.51089841	6.760	0.303	4.630	0.401	0.1	0.59
142	16.94514853	-17.51013722	7.519	0.667	5.528	0.364	0.6	1.03
143	16.94477565	-17.50931635	6.940	0.012	4.667	0.068	1.4	0.15
144	16.94539874	-17.50988429	8.157	0.095	5.331	0.051	0	0.03
145	16.94380233	-17.50700346	7.420	0.627	6.162	0.374	0.6	1.03
146	16.94321757	-17.50686744	8.657	0.101	6.054	0.045	0.3	0.18
147	16.94365095	-17.50666039	7.857	0.573	5.586	0.273	0	0.75
148	16.94568136	-17.51085915	6.680	0.056	4.878	0.061	0.8	0.18
149	16.94414639	-17.50765777	6.940	0.414	4.395	0.310	0	0.70
150	16.94473685	-17.50901090	6.540	0.314	4.731	0.425	1.4	0.69
151	16.94504825	-17.50948933	6.680	0.263	3.403	0.388	0.3	0.49
152	16.94483832	-17.50999876	7.957	0.658	4.788	0.330	0.1	0.83
153	16.94469176	-17.50967262	6.800	0.299	4.154	0.411	0.4	0.63
154	16.94290549	-17.50704751	6.560	0.218	6.177	0.306	0.5	0.35
155	16.94370572	-17.50832507	6.640	0.568	5.162	0.246	1.5	0.75
156	16.94409766	-17.50911108	6.800	0.662	4.541	0.347	1.2	1.03
157	16.94403590	-17.50843953	6.500	0.231	4.625	0.320	1	0.33
158	16.94288694	-17.50804084	6.740	0.223	6.371	0.320	0	0.41
159	16.94356748	-17.50773847	6.680	0.228	4.549	0.403	0.8	0.64
160	16.94363860	-17.50867677	8.057	0.770	5.669	0.309	0.9	0.87
161	16.94330935	-17.50804303	6.640	0.075	5.609	0.097	0.7	0.26
162	16.94350924	-17.50824502	6.600	0.036	4.861	0.039	0	0.72
163	16.94348745	-17.50818249	6.680	0.041	4.875	0.069	0	0.05
164	16.94262805	-17.50666804	8.657	0.081	5.698	0.049	0.1	0.12
165	16.94307059	-17.50789003	6.680	0.050	5.851	0.057	0.6	0.16
166	16.94350724	-17.50958650	7.140	0.521	4.777	0.383	0	0.89
167	16.94321868	-17.50811481	6.680	0.047	4.780	0.114	0.4	0.21
168	16.94362562	-17.50921760	6.680	0.602	4.161	0.397	1.1	0.87
169	16.94224459	-17.50657923	8.107	0.087	5.318	0.052	0	0.04
170	16.94257322	-17.50789783	7.440	0.618	5.243	0.383	0	1.01
171	16.94349206	-17.50922670	8.057	0.812	5.442	0.349	1	1.05
172	16.94285362	-17.50916149	6.680	0.597	5.383	0.248	2.1	0.76
173	16.94182555	-17.50669495	8.057	0.101	4.990	0.067	0	0.32
174	16.94214490	-17.50796068	6.540	0.675	4.948	0.614	3	1.07
175	16.94231194	-17.50846233	7.757	0.650	4.478	0.509	0	0.96
176	16.94181275	-17.50791589	8.157	0.757	4.790	0.358	0	0.78

Table 5.4 continued

Table 5.4: Derived Properties of Individual Star Clusters (continued)

ID	R.A.	Decl.	t_c	σ_{t_c}	M_c	σ_{M_c}	A_V	σ_{A_V}
177	16.94179844	-17.50821217	8.307	0.100	5.252	0.073	0	0.01
178	16.93764322	-17.50227181	6.580	0.142	4.286	0.240	1.2	0.52
179	16.93774879	-17.50216195	6.680	0.086	3.893	0.201	1	0.39
180	16.93912642	-17.50743955	7.020	0.203	5.123	0.213	0.7	0.18
NGC 3256								
1	156.93884766	-43.92097221	8.256	0.109	6.191	0.048	0.7	0.21
2	156.93744620	-43.91740127	8.657	0.069	8.320	0.045	1.4	0.15
3	156.95745764	-43.92664192	8.657	0.089	8.173	0.031	3.4	0.17
4	156.95374348	-43.92440077	8.657	0.131	7.478	0.048	1.6	0.23
5	156.96045449	-43.92614191	8.107	0.110	6.985	0.051	0.8	0.16
6	156.95752259	-43.92269244	8.657	0.088	8.139	0.045	3.6	0.17
7	156.97554076	-43.92994067	8.407	0.058	7.441	0.036	0	0.05
8	156.97618084	-43.93021153	8.307	0.359	6.173	0.060	1.2	0.60
9	156.95100673	-43.91893797	8.707	0.135	8.101	0.049	4	0.23
10	156.94127425	-43.91313687	8.657	0.098	7.606	0.027	1.1	0.19
11	156.94714675	-43.91639882	8.657	0.076	8.062	0.043	4.8	0.16
12	156.96913345	-43.92619552	6.720	0.129	3.339	0.213	0.8	0.49
13	156.93423236	-43.91048447	8.657	0.107	7.598	0.028	1.8	0.20
14	156.97895383	-43.92953007	8.657	0.104	7.851	0.047	2	0.20
15	156.97219268	-43.92697195	6.920	0.130	3.410	0.209	0	0.17
16	156.93841101	-43.91122321	8.157	0.114	6.854	0.053	1.2	0.17
17	156.95308589	-43.91751934	8.256	0.375	6.517	0.058	1.5	0.64
18	156.96117790	-43.91918148	8.607	0.047	7.221	0.027	0	0.06
19	156.93484278	-43.90815336	8.657	0.098	8.131	0.046	4.6	0.19
20	156.93340912	-43.90679055	8.657	0.144	7.549	0.048	0.7	0.24
21	156.95490521	-43.91610704	8.207	0.111	6.802	0.046	1	0.16
22	156.96762055	-43.92110589	8.657	0.063	7.898	0.045	2.4	0.14
23	156.94317504	-43.91056299	8.657	0.164	7.449	0.050	1.7	0.27
24	156.94763684	-43.91159584	8.157	0.131	6.165	0.059	2.7	0.17
25	156.94766341	-43.90845900	9.006	0.363	8.195	0.058	0.3	0.63
26	156.93636547	-43.90514154	8.607	0.054	5.166	0.044	0	0.02
27	156.94689970	-43.90798821	8.657	0.144	8.281	0.048	3.7	0.24
28	156.93122742	-43.90240066	7.653	0.610	4.264	0.285	0.6	0.97
29	156.95342552	-43.91155529	8.657	0.076	5.222	0.041	0.2	0.15
30	156.96178853	-43.91510158	7.957	0.679	5.005	0.267	1	0.76
31	156.93353557	-43.90218017	6.940	0.017	4.248	0.072	1.7	0.10

Table 5.4 continued

Table 5.4: Derived Properties of Individual Star Clusters (continued)

ID	R.A.	Decl.	t_c	σ_{t_c}	M_c	σ_{M_c}	A_V	σ_{A_V}
32	156.94614817	-43.90720160	8.657	0.082	7.364	0.025	2.5	0.17
33	156.97392461	-43.91926581	8.157	0.146	6.239	0.049	1.8	0.24
34	156.93357450	-43.90197365	7.757	0.571	4.450	0.234	0.5	0.77
35	156.96037462	-43.91301866	8.507	0.088	4.925	0.045	0	0.02
36	156.95436576	-43.91004567	8.407	0.252	7.927	0.070	0.9	0.44
37	156.97167758	-43.91755250	6.960	0.385	3.456	0.151	0	0.37
38	156.95792447	-43.91159703	8.407	0.080	4.782	0.039	0	0.11
39	156.95946585	-43.91197679	8.307	0.131	4.867	0.045	0.5	0.23
40	156.95965488	-43.91190180	7.957	0.666	5.037	0.262	0.1	0.72
41	156.95494342	-43.90949121	8.207	0.095	4.720	0.047	0.1	0.10
42	156.96493240	-43.91253843	6.940	0.013	7.266	0.079	2	0.13
43	156.95701200	-43.91048419	6.380	0.200	3.726	0.214	1.2	0.18
44	156.95533966	-43.90937999	8.006	0.687	4.582	0.279	0.3	0.77
45	156.95906397	-43.91098668	8.407	0.080	4.825	0.035	0	0.12
46	156.95549131	-43.90919028	6.680	0.036	3.684	0.057	0.7	0.13
47	156.95411551	-43.90861452	8.657	0.055	5.020	0.043	0	0.04
48	156.95916078	-43.91077381	6.500	0.223	3.178	0.317	0.9	0.35
49	156.95671687	-43.90971900	7.260	0.533	3.785	0.403	0.1	1.01
50	156.95381773	-43.90800067	8.507	0.067	5.237	0.051	0	0.03
51	156.95582353	-43.90921061	7.907	0.644	4.195	0.317	0.2	0.91
52	156.95603538	-43.90895053	7.907	0.633	4.638	0.306	0	0.48
53	156.95653521	-43.90924048	8.657	0.086	5.278	0.049	0	0.08
54	156.96031942	-43.91070331	6.580	0.566	4.350	0.245	1.7	0.82
55	156.95606245	-43.90909246	8.207	0.106	4.849	0.052	0.1	0.13
56	156.95944952	-43.91042975	8.207	0.108	5.217	0.046	0.5	0.16
57	156.94829267	-43.90258662	7.720	0.571	7.844	0.242	0.9	0.76
58	156.95685186	-43.90891193	6.920	0.455	4.182	0.411	0	0.71
59	156.95334755	-43.90708981	8.657	0.060	5.583	0.027	0.1	0.08
60	156.95444771	-43.90785442	6.880	0.501	3.646	0.369	0.3	0.94
61	156.95333896	-43.90684600	6.480	0.476	4.404	0.391	1.8	0.92
62	156.95705639	-43.90891457	7.100	0.620	4.373	0.376	0.3	1.03
63	156.95739104	-43.90902907	6.540	0.660	3.988	0.361	2.5	1.03
64	156.95734618	-43.90912698	6.740	0.290	3.365	0.390	0.7	0.62
65	156.95338349	-43.90723131	7.957	0.676	4.464	0.282	0.2	0.78
66	156.95610520	-43.90852118	6.060	0.167	3.563	0.198	1	0.29
67	156.95456390	-43.90784788	8.057	0.089	4.463	0.065	0	0.42
68	156.95363989	-43.90719227	6.920	0.517	3.268	0.404	0	0.84
69	156.95913639	-43.90951848	6.640	0.102	3.808	0.171	1.2	0.39

Table 5.4 continued

Table 5.4: Derived Properties of Individual Star Clusters (continued)

ID	R.A.	Decl.	t_c	σ_{t_c}	M_c	σ_{M_c}	A_V	σ_{A_V}
70	156.95689966	-43.90868849	6.580	0.239	3.092	0.352	0.3	0.44
71	156.98253530	-43.91904570	8.657	0.079	7.399	0.026	2.4	0.16
72	156.96922651	-43.91367951	8.657	0.059	5.363	0.025	0.1	0.11
73	156.95562870	-43.90770258	6.460	0.204	4.218	0.212	1.1	0.12
74	156.95533310	-43.90778386	6.680	0.040	3.153	0.075	0.1	0.13
75	156.95737323	-43.90857024	6.960	0.014	3.467	0.053	0	0.14
76	156.95816204	-43.90864059	6.680	0.054	3.188	0.138	0.7	0.28
77	156.95788389	-43.90855930	6.060	0.144	3.043	0.079	0	0.01
78	156.95611596	-43.90756984	6.060	0.172	4.894	0.120	0.9	0.09
79	156.95964400	-43.90649378	6.740	0.646	3.833	0.380	1.2	1.04
80	156.95529594	-43.90720634	6.880	0.565	3.244	0.392	0.4	0.96
81	156.95540365	-43.90710586	6.960	0.553	4.357	0.445	2.1	1.08
82	156.95470121	-43.90642398	8.657	0.072	5.406	0.026	0.3	0.15
83	156.97128877	-43.91376125	8.557	0.078	5.172	0.051	0	0.00
84	156.97554351	-43.91454571	8.657	0.100	7.498	0.042	3.8	0.20
85	156.95409299	-43.90642573	8.657	0.064	5.330	0.039	0.3	0.15
86	156.95533669	-43.90662628	8.657	0.059	6.297	0.032	0	0.01
87	156.95333530	-43.90544671	8.607	0.058	6.241	0.031	0	0.08
88	156.97153545	-43.91370638	8.457	0.056	5.115	0.027	0	0.06
89	156.95592200	-43.90702145	8.457	0.070	5.114	0.047	0	0.00
90	156.95495577	-43.90659717	8.657	0.049	5.403	0.028	0	0.04
91	156.95318761	-43.90572830	8.557	0.065	4.962	0.050	0	0.31
92	156.95480545	-43.90656599	8.357	0.046	4.763	0.022	0	0.06
93	156.95683378	-43.90717887	6.920	0.170	4.237	0.204	0.7	0.11
94	156.96613161	-43.91110881	8.157	0.089	5.048	0.046	0	0.05
95	156.95566285	-43.90672476	8.507	0.060	5.407	0.031	0	0.28
96	156.95402896	-43.90566505	8.657	0.057	5.848	0.030	0	0.00
97	156.95590568	-43.90688373	6.680	0.563	3.864	0.249	1.3	0.63
98	156.97698659	-43.91578322	8.657	0.054	5.179	0.026	0	0.01
99	156.95563421	-43.90657308	8.607	0.053	5.213	0.048	0	0.04
100	156.95621895	-43.90662705	8.307	0.047	5.186	0.041	0	0.02
101	156.96062426	-43.90789397	8.207	0.397	5.687	0.070	2	0.61
102	156.95604294	-43.90592346	8.107	0.112	5.278	0.050	1	0.16
103	156.95613270	-43.90656936	8.657	0.054	5.663	0.026	0	0.00
104	156.97455145	-43.91364903	8.557	0.062	5.392	0.051	0	0.18
105	156.95573870	-43.90638089	8.657	0.100	5.440	0.030	0.3	0.18
106	156.96000946	-43.90752771	8.657	0.079	7.581	0.025	2	0.16
107	156.95650861	-43.90541893	8.057	0.111	6.957	0.052	0.8	0.16

Table 5.4 continued

Table 5.4: Derived Properties of Individual Star Clusters (continued)

ID	R.A.	Decl.	t_c	σ_{t_c}	M_c	σ_{M_c}	A_V	σ_{A_V}
108	156.95604489	-43.90548918	8.207	0.090	6.134	0.047	0	0.05
109	156.95532007	-43.90629013	7.000	0.579	3.335	0.416	0.4	1.06
110	156.94111097	-43.89878772	8.507	0.197	7.663	0.054	0.9	0.32
111	156.95481472	-43.90599679	8.357	0.120	5.091	0.045	0.4	0.24
112	156.95679527	-43.90680587	8.256	0.193	4.465	0.123	0	0.17
113	156.95709281	-43.90649168	7.120	0.615	4.292	0.388	0.9	1.04
114	156.95716996	-43.90564136	8.256	0.093	5.495	0.043	0.3	0.15
115	156.94653083	-43.90175339	8.157	0.107	6.127	0.045	0.6	0.16
116	156.96489556	-43.90978952	8.657	0.050	5.110	0.041	0	0.02
117	156.95563927	-43.90594618	8.357	0.048	5.246	0.025	0	0.01
118	156.95975695	-43.90612789	6.600	0.555	5.875	0.262	4.8	0.73
119	156.95509228	-43.90573560	8.407	0.080	4.610	0.052	0	0.00
120	156.95463111	-43.90520576	8.357	0.097	4.849	0.042	0.2	0.16
121	156.95514593	-43.90532161	8.607	0.063	5.336	0.052	0	0.01
122	156.96628972	-43.91019294	8.657	0.073	5.291	0.027	0.3	0.16
123	156.96188541	-43.90829672	7.907	0.629	5.211	0.282	0.7	0.83
124	156.95829771	-43.90547061	8.557	0.091	6.642	0.053	0.1	0.09
125	156.95778312	-43.90546413	9.006	0.342	6.105	0.059	0.2	0.60
126	156.96304865	-43.90820349	8.907	0.271	5.969	0.060	1.1	0.46
127	156.95837244	-43.90635866	8.207	0.922	6.127	0.263	2.5	1.00
128	156.95969239	-43.90628711	8.657	0.086	5.963	0.043	1.1	0.18
129	156.95977215	-43.90664624	8.657	0.121	6.719	0.029	1.5	0.21
130	156.96088589	-43.90711937	7.477	0.654	4.762	0.372	1.7	1.04
131	156.95599927	-43.90536722	8.107	0.064	5.249	0.038	0	0.03
132	156.95847822	-43.90574484	7.020	0.494	5.301	0.409	2.3	1.01
133	156.95622177	-43.90533009	7.907	0.593	4.913	0.263	0	0.76
134	156.95659686	-43.90520740	8.657	0.085	5.793	0.048	0.1	0.12
135	156.96033033	-43.90620386	7.957	0.680	6.347	0.260	0.8	0.74
136	156.96318047	-43.90776302	6.560	0.587	4.593	0.275	2.7	0.99
137	156.96022960	-43.90666541	8.157	0.105	4.822	0.061	0	0.02
138	156.95769584	-43.90567902	8.357	0.046	4.968	0.043	0	0.08
139	156.95861107	-43.90598720	6.780	0.610	5.098	0.303	1.9	1.01
140	156.95650684	-43.90456139	8.657	0.126	6.266	0.048	1	0.22
141	156.97872391	-43.91425663	8.657	0.075	5.047	0.048	0	0.04
142	156.95810310	-43.90563250	6.820	0.667	5.213	0.358	1.9	1.03
143	156.96442828	-43.90829078	8.256	0.103	4.782	0.045	0.2	0.14
144	156.96066193	-43.90663202	6.080	0.637	5.224	0.382	3.1	1.04
145	156.97594030	-43.91312425	8.657	0.101	5.338	0.047	0.2	0.18

Table 5.4 continued

Table 5.4: Derived Properties of Individual Star Clusters (continued)

ID	R.A.	Decl.	t_c	σ_{t_c}	M_c	σ_{M_c}	A_V	σ_{A_V}
146	156.96732301	-43.90944293	8.457	0.075	4.821	0.057	0	0.18
147	156.95659284	-43.90475126	9.006	0.348	6.320	0.057	0.6	0.61
148	156.96056235	-43.90603901	7.080	0.589	5.373	0.399	1.7	1.04
149	156.96332659	-43.90635665	6.680	0.608	5.027	0.304	1.2	0.51
150	156.95663076	-43.90488669	8.357	0.064	4.905	0.046	0	0.05
151	156.96473789	-43.90839751	6.940	0.018	3.116	0.110	0.1	0.18
152	156.96251534	-43.90708731	8.407	0.282	5.616	0.061	1.5	0.48
153	156.96613387	-43.90843470	7.857	0.646	4.742	0.263	0.4	0.78
154	156.95646473	-43.90475092	6.980	0.580	3.649	0.403	0.4	1.04
155	156.95666237	-43.90483942	8.657	0.126	5.422	0.062	0.4	0.23
156	156.95494389	-43.90359056	8.657	0.063	6.368	0.041	2	0.14
157	156.96233647	-43.90660297	8.657	0.093	5.433	0.053	0.1	0.14
158	156.96533630	-43.90816737	7.677	0.567	5.249	0.254	0.5	0.88
159	156.96516420	-43.90829846	6.440	0.223	4.225	0.264	1.4	0.21
160	156.95731750	-43.90478988	8.807	0.190	6.682	0.051	1.3	0.31
161	156.95971631	-43.90578098	8.157	0.108	6.386	0.043	0.8	0.16
162	156.96166663	-43.90665227	6.560	0.569	4.898	0.258	2.8	0.92
163	156.96514902	-43.90817530	6.680	0.040	3.324	0.107	0.5	0.20
164	156.96253053	-43.90687197	8.107	0.111	6.290	0.050	2.3	0.17
165	156.96080477	-43.90626776	7.957	0.658	5.190	0.272	0.4	0.80
166	156.96495726	-43.90796308	8.207	0.128	5.155	0.047	0.8	0.17
167	156.95994527	-43.90548344	8.657	0.144	7.253	0.036	1.7	0.24
168	156.96823950	-43.90933360	8.607	0.061	5.489	0.033	0	0.06
169	156.97851443	-43.91371174	8.607	0.054	5.400	0.031	0	0.14
170	156.95486892	-43.90332340	8.657	0.068	6.150	0.025	0.7	0.15
171	156.96069771	-43.90529659	8.057	0.139	6.466	0.064	1.5	0.16
172	156.94241138	-43.89688033	8.657	0.070	8.195	0.045	2.7	0.15
173	156.96073777	-43.90548231	8.057	0.126	7.245	0.063	3.1	0.16
174	156.96548169	-43.90775509	7.907	0.639	5.236	0.265	1.1	0.77
175	156.96589261	-43.90808275	7.807	0.578	4.479	0.250	0.4	0.78
176	156.98032180	-43.91376883	8.407	0.292	7.538	0.057	1.1	0.51
177	156.96095669	-43.90607984	7.907	0.650	5.099	0.270	0.1	0.77
178	156.96186919	-43.90655109	8.607	0.079	4.932	0.075	0	0.04
179	156.96219728	-43.90664461	8.157	0.138	5.342	0.066	1.2	0.21
180	156.96834012	-43.90916765	8.657	0.063	5.536	0.046	0	0.06
181	156.96552534	-43.90798698	6.680	0.559	3.672	0.353	1.1	0.68
182	156.97246038	-43.91093024	8.006	0.719	4.486	0.298	0.4	0.75
183	156.96572756	-43.90797276	8.657	0.067	5.071	0.061	0	0.08

Table 5.4 continued

Table 5.4: Derived Properties of Individual Star Clusters (continued)

ID	R.A.	Decl.	t_c	σ_{t_c}	M_c	σ_{M_c}	A_V	σ_{A_V}
184	156.96263285	-43.90615869	8.657	0.105	7.013	0.044	3	0.20
185	156.95239216	-43.90205293	8.657	0.066	5.559	0.047	0.1	0.10
186	156.96481413	-43.90740548	8.607	0.071	5.081	0.051	0	0.03
187	156.95825090	-43.90421708	8.657	0.101	6.066	0.041	1.5	0.20
188	156.96718448	-43.90762301	6.680	0.593	5.567	0.248	1.8	0.76
189	156.96391973	-43.90690119	7.857	0.600	4.779	0.248	0.2	0.76
190	156.96722379	-43.90838804	8.657	0.071	5.070	0.043	0.1	0.08
191	156.96631762	-43.90761804	8.157	0.105	5.779	0.046	0.8	0.16
192	156.96336363	-43.90599341	6.720	0.568	5.940	0.257	3.3	0.90
193	156.96574162	-43.90763400	6.680	0.037	3.416	0.079	0.5	0.16
194	156.96678720	-43.90761856	8.607	0.052	5.568	0.049	0	0.04
195	156.96421109	-43.90674773	8.207	0.128	4.715	0.094	0	0.15
196	156.97777690	-43.91265048	6.960	0.407	3.144	0.121	0	0.24
197	156.97177762	-43.90955621	8.307	0.079	5.515	0.042	0.2	0.12
198	156.96426889	-43.90622973	6.480	0.667	5.347	0.358	3.2	1.03
199	156.96166953	-43.90424508	8.657	0.215	6.167	0.080	1.8	0.38
200	156.96093562	-43.90429566	8.107	0.120	7.457	0.052	3.9	0.17
201	156.95556058	-43.90237819	8.507	0.147	5.623	0.051	0.4	0.24
202	156.96567603	-43.90538134	8.207	0.142	6.921	0.063	2.5	0.22
203	156.93973313	-43.89563522	8.006	0.679	5.087	0.256	0.7	0.70
204	156.98380012	-43.91447669	8.507	0.061	5.179	0.051	0	0.25
205	156.94559856	-43.89807779	8.457	0.240	6.121	0.056	1.3	0.40
206	156.95844415	-43.90338923	8.207	0.365	5.105	0.104	1.2	0.45
207	156.94311370	-43.89655744	7.957	0.667	6.093	0.270	1	0.78
208	156.97971198	-43.91260618	7.957	0.699	4.674	0.285	0.8	0.75
209	156.96400761	-43.90578556	8.657	0.087	6.572	0.026	1.5	0.17
210	156.96508663	-43.90605436	8.006	0.686	5.214	0.249	0.9	0.70
211	156.96130256	-43.90452501	7.857	0.613	6.183	0.254	1.3	0.77
212	156.97057019	-43.90844777	8.607	0.058	5.191	0.034	0	0.10
213	156.98414354	-43.91409917	8.507	0.066	5.585	0.052	0	0.11
214	156.97085579	-43.90851480	8.057	0.169	5.079	0.083	1	0.17
215	156.96212839	-43.90442809	8.307	0.342	6.738	0.056	1.4	0.60
216	156.96031923	-43.90354069	7.957	0.673	6.586	0.267	2.1	0.77
217	156.96585801	-43.90593403	6.580	0.566	5.347	0.244	2.1	0.85
218	156.96055992	-43.90365843	8.657	0.098	6.412	0.033	1	0.19
219	156.95874062	-43.90298759	8.657	0.120	7.103	0.044	3.2	0.22
220	156.96417502	-43.90494260	8.207	0.226	7.153	0.063	3.9	0.34
221	156.96236355	-43.90377154	8.657	0.102	6.324	0.047	1.2	0.19

Table 5.4 continued

Table 5.4: Derived Properties of Individual Star Clusters (continued)

ID	R.A.	Decl.	t_c	σ_{t_c}	M_c	σ_{M_c}	A_V	σ_{A_V}
222	156.96009188	-43.90332168	7.757	0.574	5.655	0.244	1.5	0.76
223	156.96072554	-43.90172113	8.207	0.142	5.804	0.059	1.2	0.25
224	156.95987796	-43.90189958	8.006	0.141	6.421	0.066	2.7	0.16
225	156.95971117	-43.90267911	8.657	0.156	6.136	0.051	0.9	0.26
226	156.96430898	-43.90487839	8.307	0.370	6.626	0.068	2	0.65
227	156.96001143	-43.90256080	8.256	0.084	5.329	0.044	0.2	0.13
228	156.95210071	-43.89999988	6.780	0.661	3.410	0.344	1.3	1.01
229	156.96597320	-43.90430135	7.857	0.627	6.401	0.261	0.7	0.77
230	156.96555602	-43.90554950	7.568	0.659	5.045	0.357	0.6	1.02
231	156.96578141	-43.90563102	6.880	0.371	3.825	0.412	0.2	0.82
232	156.96627000	-43.90587978	8.757	0.152	5.234	0.067	0	0.25
233	156.95921647	-43.90272858	8.607	0.131	6.009	0.049	1.2	0.23
234	156.96407104	-43.90423553	6.720	0.567	6.310	0.245	1.6	0.79
235	156.96616853	-43.90567220	8.207	0.116	5.359	0.059	0.8	0.21
236	156.96435927	-43.90447681	8.107	0.069	5.843	0.062	0	0.08
237	156.96610384	-43.90556757	7.628	0.577	4.679	0.265	0.3	0.97
238	156.96019859	-43.90249667	8.657	0.098	7.372	0.045	3.2	0.19
239	156.96282351	-43.90401105	8.657	0.086	6.740	0.049	2.4	0.20
240	156.96445532	-43.90417049	8.057	0.121	6.287	0.061	0.7	0.16
241	156.96234509	-43.90306759	8.307	0.382	6.561	0.067	2.1	0.63
242	156.96422703	-43.90455556	8.357	0.108	5.624	0.090	0	0.10
243	156.96217600	-43.90371116	6.900	0.566	4.855	0.393	2.4	1.03
244	156.96479245	-43.90457208	8.006	0.673	6.369	0.229	1.6	0.67
245	156.96108547	-43.90293833	8.307	0.110	5.566	0.084	0.5	0.27
246	156.96488623	-43.90447166	7.220	0.524	5.636	0.394	1.4	1.01
247	156.98478588	-43.91285302	8.557	0.059	5.465	0.052	0	0.18
248	156.96686999	-43.90499547	8.207	0.391	5.655	0.076	1.7	0.64
249	156.96432774	-43.90413175	6.560	0.656	5.799	0.340	2.5	1.03
250	156.96549585	-43.90453634	6.620	0.574	6.012	0.242	2.3	0.76
251	156.96004762	-43.90197868	8.907	0.274	6.436	0.057	1.5	0.47
252	156.96695180	-43.90385693	7.957	0.662	6.913	0.274	0.8	0.78
253	156.95819826	-43.90058033	8.707	0.116	7.550	0.050	0	0.18
254	156.96130855	-43.90220626	7.040	0.514	5.233	0.403	0	0.92
255	156.96397375	-43.90349896	8.207	0.155	7.374	0.061	1.5	0.26
256	156.96644587	-43.90423656	7.100	0.587	5.116	0.383	0	0.95
257	156.96507520	-43.90362793	6.680	0.064	5.801	0.080	1	0.22
258	156.96540958	-43.90381893	6.680	0.520	5.522	0.230	1.2	0.62
259	156.96678791	-43.90472006	7.907	0.663	5.715	0.265	1.5	0.78

Table 5.4 continued

Table 5.4: Derived Properties of Individual Star Clusters (continued)

ID	R.A.	Decl.	t_c	σ_{t_c}	M_c	σ_{M_c}	A_V	σ_{A_V}
260	156.96405464	-43.90339802	7.602	0.621	6.866	0.320	1	1.01
261	156.96564666	-43.90364229	6.680	0.061	6.694	0.077	1	0.20
262	156.98891348	-43.91375524	8.107	0.107	6.318	0.047	1.2	0.16
263	156.97416262	-43.90739181	8.657	0.064	5.175	0.028	0.2	0.13
264	156.96320214	-43.90270946	6.760	0.633	5.455	0.333	1.3	1.01
265	156.96234450	-43.90269442	6.680	0.617	4.964	0.304	1.7	0.98
266	156.96448914	-43.90367949	8.057	0.106	6.355	0.060	0.1	0.09
267	156.96349759	-43.90284674	8.256	0.105	6.725	0.045	0.4	0.16
268	156.95322084	-43.89860811	8.657	0.067	5.808	0.026	0.5	0.15
269	156.95899072	-43.90105795	8.657	0.062	5.378	0.023	0.3	0.14
270	156.96371734	-43.90311558	6.460	0.658	5.932	0.369	3	1.03
271	156.96619292	-43.90397505	6.740	0.262	5.291	0.390	0.3	0.60
272	156.96377967	-43.90288761	8.057	0.065	5.583	0.059	0	0.14
273	156.96531855	-43.90335342	6.940	0.014	5.420	0.040	1.8	0.09
274	156.96449479	-43.90301462	8.207	0.110	6.089	0.043	0.9	0.17
275	156.96566795	-43.90385926	6.460	0.202	5.854	0.207	1.1	0.12
276	156.96522753	-43.90372035	6.680	0.037	4.677	0.102	0.4	0.19
277	156.96250725	-43.90229709	8.157	0.122	5.403	0.083	0	0.14
278	156.96213417	-43.90190815	8.657	0.116	7.148	0.045	1.2	0.21
279	156.96422561	-43.90299628	7.807	0.584	5.965	0.245	1.2	0.76
280	156.96312080	-43.90198826	6.960	0.422	5.254	0.353	2.4	0.98
281	156.96576630	-43.90384331	6.800	0.308	5.330	0.401	0.1	0.60
282	156.96230920	-43.90218451	6.900	0.568	4.550	0.394	0.7	1.03
283	156.96389893	-43.90258481	8.006	0.143	6.791	0.065	1	0.16
284	156.96392069	-43.90275696	7.556	0.649	5.285	0.361	0.1	1.02
285	156.96158246	-43.90184476	7.957	0.656	6.434	0.268	1.2	0.78
286	156.96340072	-43.90260747	7.957	0.660	5.774	0.266	0.5	0.78
287	156.96442567	-43.90283659	8.057	0.157	6.434	0.079	1.4	0.17
288	156.96181123	-43.90192991	6.880	0.188	4.553	0.148	0	0.12
289	156.95940972	-43.90087343	8.657	0.075	5.487	0.044	0.4	0.16
290	156.96853251	-43.90479479	8.207	0.097	4.955	0.046	0.2	0.14
291	156.96306461	-43.90230699	7.000	0.588	4.308	0.399	0.4	1.04
292	156.96701145	-43.90370970	6.680	0.053	4.316	0.105	0.5	0.22
293	156.95994626	-43.90048362	8.657	0.082	6.118	0.046	1.2	0.16
294	156.96531909	-43.90277529	6.680	0.041	5.028	0.052	1	0.13
295	156.96453715	-43.90241111	7.907	0.657	6.721	0.266	0.7	0.78
296	156.96595248	-43.90321280	6.700	0.575	6.251	0.248	2.1	0.76
297	156.96284223	-43.90222700	6.060	0.164	5.564	0.101	1.1	0.09

Table 5.4 continued

Table 5.4: Derived Properties of Individual Star Clusters (continued)

ID	R.A.	Decl.	t_c	σ_{t_c}	M_c	σ_{M_c}	A_V	σ_{A_V}
298	156.96376381	-43.90240866	6.560	0.573	5.121	0.267	1.8	0.95
299	156.96273090	-43.90167849	8.457	0.073	5.440	0.037	0	0.09
300	156.96393747	-43.90242741	7.907	0.629	6.001	0.261	0.4	0.77
301	156.98675372	-43.91239945	8.457	0.079	4.800	0.046	0	0.04
302	156.96173013	-43.90148065	6.560	0.259	5.357	0.377	0.8	0.55
303	156.96331880	-43.90222849	6.680	0.549	4.797	0.248	1.2	0.64
304	156.97682181	-43.90815965	8.057	0.055	4.410	0.045	0	0.14
305	156.96679613	-43.90353347	8.357	0.102	5.629	0.074	0	0.08
306	156.96489771	-43.90280364	6.940	0.015	5.068	0.061	0.4	0.10
307	156.96407668	-43.90258996	8.307	0.081	5.739	0.071	0	0.05
308	156.96684490	-43.90372481	6.940	0.453	4.968	0.372	1.5	0.97
309	156.96207495	-43.90170772	6.060	0.163	4.521	0.116	0	0.09
310	156.96599462	-43.90296381	8.207	0.109	6.350	0.046	0.8	0.16
311	156.96215142	-43.90122533	8.307	0.088	5.544	0.066	0	0.03
312	156.96164385	-43.90077627	7.602	0.597	5.998	0.285	1.2	1.00
313	156.95880779	-43.89976766	8.657	0.081	6.163	0.026	0.5	0.17
314	156.96061426	-43.90055715	8.657	0.084	5.790	0.045	0.2	0.15
315	156.96749448	-43.90236265	8.307	0.035	6.278	0.023	0	1.32
316	156.96595453	-43.90276580	7.240	0.475	5.164	0.383	0.2	0.99
317	156.96512783	-43.90262660	7.957	0.674	6.000	0.284	0.4	0.82
318	156.96466092	-43.90259956	6.680	0.565	4.934	0.288	1.2	0.66
319	156.96351252	-43.90207736	8.057	0.050	5.293	0.034	0	0.31
320	156.97741908	-43.90703766	8.457	0.219	7.616	0.056	0.7	0.38
321	156.96147605	-43.90101612	7.807	0.588	5.885	0.240	1.5	0.76
322	156.96542272	-43.90248501	8.107	0.110	7.108	0.055	0.1	0.14
323	156.96201284	-43.90149225	6.940	0.034	4.137	0.102	0.1	0.13
324	156.96805912	-43.90375056	6.080	0.378	5.044	0.368	1.9	0.76
325	156.96697003	-43.90317673	8.107	0.120	5.714	0.073	0.1	0.18
326	156.96533450	-43.90265855	6.460	0.191	4.805	0.202	0.4	0.20
327	156.97029175	-43.90446179	8.507	0.190	7.518	0.051	3.7	0.30
328	156.96189546	-43.90131202	6.880	0.239	4.020	0.338	0	0.44
329	156.96576821	-43.90192675	6.820	0.657	5.355	0.380	0.7	0.96
330	156.96528121	-43.90225444	6.940	0.014	4.620	0.059	0.6	0.10
331	156.95664863	-43.89862688	6.680	0.568	4.017	0.251	1.3	0.68
332	156.98005756	-43.90844601	8.657	0.066	7.901	0.026	4	0.15
333	156.96364180	-43.90140899	6.720	0.566	5.063	0.255	1.5	0.84
334	156.96880668	-43.90386683	8.457	0.084	5.024	0.062	0	0.22
335	156.96569993	-43.90249962	7.907	0.605	6.189	0.263	0	0.71

Table 5.4 continued

Table 5.4: Derived Properties of Individual Star Clusters (continued)

ID	R.A.	Decl.	t_c	σ_{t_c}	M_c	σ_{M_c}	A_V	σ_{A_V}
336	156.96489947	-43.90240449	7.957	0.627	5.152	0.313	0	0.82
337	156.96670952	-43.90314635	6.060	0.164	5.624	0.121	1.4	0.14
338	156.96914974	-43.90428909	6.100	0.194	4.512	0.172	1.2	0.10
339	156.96846253	-43.90386561	6.960	0.424	3.396	0.359	0	0.76
340	156.96136278	-43.90053560	8.006	0.314	6.233	0.198	3.2	0.25
341	156.95799335	-43.89862843	8.657	0.071	5.954	0.026	0.7	0.15
342	156.95748990	-43.89881871	8.657	0.100	5.583	0.043	0.8	0.20
343	156.96783904	-43.90338259	6.500	0.667	5.286	0.362	3.3	1.03
344	156.96230741	-43.90103826	6.960	0.034	4.535	0.082	0.3	0.11
345	156.96381721	-43.90164495	8.256	0.058	5.319	0.047	0	0.13
346	156.96355711	-43.90117044	8.157	0.106	6.366	0.048	0.9	0.16
347	156.96551798	-43.90255613	8.607	0.056	6.614	0.049	0	0.02
348	156.96901945	-43.90383178	7.420	0.625	4.614	0.377	0.1	1.03
349	156.96459047	-43.90219388	8.256	0.070	5.266	0.063	0	0.02
350	156.96018954	-43.89961625	8.307	0.083	6.050	0.032	0.2	0.14
351	156.96189836	-43.90080985	7.907	0.656	5.209	0.264	0.5	0.79
352	156.96332771	-43.90144937	8.256	0.159	5.354	0.075	0.6	0.32
353	156.96870795	-43.90300391	6.300	0.639	5.857	0.366	2.7	1.03
354	156.96590609	-43.90241021	6.940	0.023	4.605	0.062	0.2	0.10
355	156.96889997	-43.90376095	8.057	0.635	4.538	0.361	0	0.71
356	156.96605501	-43.90222459	8.057	0.663	5.288	0.293	0	0.51
357	156.96832247	-43.90358297	8.256	0.115	5.057	0.084	0	0.01
358	156.96837743	-43.90273936	6.660	0.573	5.629	0.236	2.3	0.76
359	156.96793553	-43.90316486	7.000	0.565	4.359	0.427	1.5	1.07
360	156.96454585	-43.90165058	7.957	0.665	5.188	0.273	0.9	0.77
361	156.96931738	-43.90377758	6.740	0.597	4.023	0.283	1.3	1.00
362	156.96386617	-43.90142113	7.907	0.659	5.431	0.269	0.6	0.78
363	156.96295342	-43.90089309	6.900	0.207	4.059	0.220	0	0.19
364	156.96583775	-43.90228367	8.307	0.037	5.495	0.014	0	0.24
365	156.96212646	-43.90039630	8.006	0.168	5.595	0.083	1.3	0.17
366	156.96303197	-43.90097243	6.680	0.036	4.317	0.062	1	0.15
367	156.96384860	-43.90106105	7.556	0.650	5.166	0.354	1.3	1.02
368	156.96963623	-43.90347211	8.507	0.179	4.867	0.090	0.3	0.30
369	156.96712825	-43.90243080	6.520	0.306	5.896	0.399	1.1	0.58
370	156.98723872	-43.91035225	8.657	0.097	7.730	0.045	0.4	0.19
371	156.96801103	-43.90267107	6.780	0.614	5.602	0.310	1.2	1.01
372	156.96993709	-43.90376518	7.240	0.591	3.703	0.409	0.6	1.07
373	156.96510416	-43.90150582	7.907	0.688	5.015	0.319	1.3	1.02

Table 5.4 continued

Table 5.4: Derived Properties of Individual Star Clusters (continued)

ID	R.A.	Decl.	t_c	σ_{t_c}	M_c	σ_{M_c}	A_V	σ_{A_V}
374	156.96624833	-43.90216116	8.557	0.133	5.233	0.051	0.1	0.21
375	156.96449718	-43.90130908	7.957	0.671	5.125	0.273	0.4	0.78
376	156.97048785	-43.90322368	6.720	0.185	6.057	0.318	0.5	0.56
377	156.96648330	-43.90212243	7.857	0.598	5.249	0.245	0.2	0.76
378	156.96635143	-43.90192720	7.957	0.669	5.531	0.268	0.9	0.77
379	156.94183480	-43.88989975	7.857	0.625	7.557	0.257	0.7	0.77
380	156.96348486	-43.90067738	6.680	0.587	4.427	0.256	1.4	0.75
381	156.97088629	-43.90386338	6.600	0.185	3.381	0.345	1.1	0.56
382	156.96902423	-43.90300987	7.807	0.589	5.148	0.245	0.8	0.76
383	156.96374433	-43.90080314	6.680	0.601	5.488	0.255	2.2	0.76
384	156.96287693	-43.90064436	7.519	0.635	3.849	0.419	0.2	1.00
385	156.96620122	-43.90188059	7.260	0.547	4.263	0.401	0.3	1.02
386	156.96464558	-43.90080483	8.657	0.115	5.767	0.044	1.1	0.22
387	156.96853770	-43.90248963	6.940	0.015	4.985	0.065	2.5	0.11
388	156.96691958	-43.90206385	6.340	0.321	5.004	0.372	1.7	0.54
389	156.96839412	-43.90256879	7.505	0.667	5.225	0.363	1.4	1.03
390	156.96397666	-43.90083518	6.680	0.564	4.164	0.293	1.3	0.75
391	156.96661657	-43.90166698	8.157	0.102	5.046	0.047	0.2	0.15
392	156.96804670	-43.90217280	6.480	0.666	4.924	0.364	2.9	1.03
393	156.96334066	-43.90044924	7.477	0.626	4.050	0.380	0	1.00
394	156.96914783	-43.90281574	8.307	0.064	5.005	0.049	0	0.04
395	156.96992341	-43.90328590	8.256	0.113	5.378	0.049	0.7	0.18
396	156.96553303	-43.90057481	7.907	0.638	5.581	0.266	0.1	0.77
397	156.96291118	-43.90026035	7.477	0.645	4.211	0.375	0.6	1.06
398	156.96376415	-43.90026893	6.860	0.332	3.647	0.414	0.2	0.66
399	156.96931175	-43.90282649	8.307	0.793	4.691	0.348	0	0.91
400	156.97387364	-43.90462602	8.357	0.328	6.299	0.059	1.3	0.58
401	156.96762102	-43.90213882	6.960	0.049	4.097	0.197	0	0.01
402	156.98902876	-43.91086935	8.207	0.120	6.580	0.051	1.1	0.18
403	156.96887850	-43.90248865	6.680	0.051	4.319	0.085	0.8	0.19
404	156.96336805	-43.89969989	8.057	0.113	5.257	0.082	0	0.10
405	156.96700486	-43.90163934	8.057	0.656	4.617	0.223	0	0.53
406	156.96334712	-43.90012988	6.920	0.580	4.032	0.423	1.6	1.07
407	156.96988870	-43.90272229	6.720	0.565	4.379	0.252	1.2	0.88
408	156.96809905	-43.90201005	8.557	0.132	5.569	0.051	0.3	0.22
409	156.96572837	-43.90112720	6.300	0.232	3.779	0.364	1.2	0.46
410	156.96624533	-43.90063742	7.320	0.549	4.944	0.404	0.6	1.03
411	156.96464277	-43.90053127	6.900	0.510	4.147	0.397	0.2	0.93

Table 5.4 continued

Table 5.4: Derived Properties of Individual Star Clusters (continued)

ID	R.A.	Decl.	t_c	σ_{t_c}	M_c	σ_{M_c}	A_V	σ_{A_V}
412	156.96540875	-43.90096707	6.680	0.049	4.097	0.090	1.1	0.21
413	156.96305232	-43.89951927	6.760	0.634	4.933	0.334	2	1.02
414	156.96769305	-43.90170495	8.006	0.720	5.397	0.280	1.7	0.68
415	156.96361024	-43.89950945	8.006	0.670	6.591	0.269	0.2	0.77
416	156.96585747	-43.90087696	6.940	0.017	4.127	0.063	1.4	0.11
417	156.96848955	-43.90214338	7.100	0.618	3.700	0.387	0.2	1.03
418	156.96419839	-43.90027781	7.300	0.623	4.117	0.401	0.9	1.08
419	156.97029770	-43.90272906	8.357	0.065	4.717	0.041	0	0.04
420	156.96849977	-43.90161302	7.591	0.633	5.730	0.335	0.8	1.01
421	156.96343512	-43.89932107	7.907	0.653	6.356	0.269	2.2	0.78
422	156.96749737	-43.90158558	7.420	0.633	3.902	0.383	0.3	1.04
423	156.96896366	-43.90181708	6.500	0.658	4.537	0.372	2.2	1.05
424	156.96589122	-43.90063040	6.500	0.659	4.457	0.360	2.3	1.04
425	156.97009299	-43.90238211	8.256	0.097	5.018	0.071	0	0.39
426	156.96853228	-43.90132563	8.657	0.186	5.039	0.103	0.1	0.32
427	156.96927180	-43.90197844	6.680	0.605	4.826	0.250	2.5	0.76
428	156.96807452	-43.90161414	7.757	0.574	5.006	0.243	1	0.76
429	156.96992824	-43.90243305	6.680	0.028	3.738	0.082	0.3	0.15
430	156.96969521	-43.90203525	7.907	0.648	4.970	0.281	0.7	0.83
431	156.97527538	-43.90410365	8.657	0.074	8.074	0.025	3.5	0.15
432	156.95963026	-43.89795914	8.357	0.323	5.239	0.078	1.1	0.51
433	156.97069481	-43.90270926	6.960	0.427	3.789	0.366	0	0.79
434	156.96940968	-43.90199752	6.900	0.558	4.247	0.398	0.2	0.87
435	156.96921501	-43.90158245	6.740	0.577	5.188	0.275	1.2	0.97
436	156.96782396	-43.90113016	8.256	0.108	5.462	0.048	0.7	0.19
437	156.96512165	-43.89991726	8.657	0.120	5.038	0.096	0.1	0.19
438	156.96655672	-43.90086261	8.207	0.089	4.866	0.045	0.1	0.09
439	156.96881721	-43.90148975	8.057	0.116	4.914	0.065	0.2	0.14
440	156.96424103	-43.89976767	8.507	0.219	5.211	0.067	0.5	0.36
441	156.96954320	-43.90227084	6.940	0.194	3.615	0.323	0.6	0.39
442	156.96579179	-43.90061788	6.560	0.350	3.884	0.430	1.3	0.84
443	156.96670719	-43.90082234	6.540	0.629	4.532	0.334	2.3	1.02
444	156.96955203	-43.90203514	7.677	0.636	4.523	0.317	0.2	1.02
445	156.96486850	-43.89989693	8.207	0.136	5.845	0.060	1.3	0.21
446	156.96818214	-43.90136777	8.607	0.184	5.520	0.052	0.7	0.31
447	156.96604099	-43.90068425	7.757	0.683	4.442	0.371	0.7	1.08
448	156.97090594	-43.90277637	6.440	0.348	5.014	0.396	1.8	0.66
449	156.96434699	-43.89900479	7.040	0.513	5.290	0.401	1.6	1.02

Table 5.4 continued

Table 5.4: Derived Properties of Individual Star Clusters (continued)

ID	R.A.	Decl.	t_c	σ_{t_c}	M_c	σ_{M_c}	A_V	σ_{A_V}
450	156.96357643	-43.89913911	7.907	0.625	4.729	0.265	0.1	0.78
451	156.97046581	-43.90182401	6.820	0.661	4.049	0.356	1.3	1.03
452	156.96609547	-43.90060657	6.960	0.021	3.860	0.044	0	0.14
453	156.96546958	-43.90013362	8.157	0.114	5.214	0.057	0.8	0.20
454	156.96723457	-43.90100402	8.357	0.070	4.642	0.041	0	0.08
455	156.96811589	-43.90129612	8.557	0.097	5.274	0.052	0.1	0.11
456	156.96440956	-43.89969443	9.006	0.349	5.737	0.070	0.5	0.56
457	156.96392250	-43.89932169	7.907	0.643	5.938	0.262	0.6	0.77
458	156.95602797	-43.89474299	6.980	0.156	7.032	0.164	3.1	0.10
459	156.97051630	-43.90228229	6.940	0.155	4.286	0.210	0.7	0.14
460	156.97046521	-43.90212053	6.880	0.605	4.748	0.384	0.7	1.03
461	156.96699346	-43.90053533	6.540	0.309	4.797	0.409	1.4	0.62
462	156.96958357	-43.90188192	6.360	0.489	4.096	0.420	1.8	0.89
463	156.96747223	-43.90039767	6.780	0.632	5.200	0.336	1.4	1.01
464	156.96887054	-43.90078757	7.580	0.633	5.266	0.336	0.3	1.01
465	156.96748834	-43.90089298	6.120	0.642	4.698	0.377	2.8	1.04
466	156.99362656	-43.91154892	8.207	0.109	6.736	0.045	0.6	0.17
467	156.96339261	-43.89915171	8.207	0.768	4.785	0.214	0.5	0.73
468	156.96627912	-43.90029366	6.680	0.050	3.755	0.125	0.6	0.24
469	156.96826016	-43.90102678	6.520	0.667	5.154	0.357	2.3	1.02
470	156.96710647	-43.90017448	8.006	0.178	5.943	0.099	0.9	0.18
471	156.97196529	-43.90188082	8.256	0.370	6.864	0.066	1.3	0.62
472	156.96821513	-43.90087233	7.907	0.675	4.862	0.286	0.8	0.78
473	156.96866650	-43.90055488	6.060	0.176	5.938	0.131	1.4	0.09
474	156.97116602	-43.90202827	6.940	0.155	4.381	0.210	1.8	0.14
475	156.97150677	-43.90221864	6.720	0.124	4.195	0.195	0.5	0.49
476	156.96701645	-43.90039944	6.680	0.039	3.761	0.106	0.8	0.20
477	156.97686197	-43.90427391	8.657	0.068	5.762	0.047	0.5	0.15
478	156.96785276	-43.90055541	6.680	0.726	4.596	0.358	3.1	1.05
479	156.95946595	-43.89701723	8.006	0.715	4.526	0.304	0.5	0.76
480	156.97047261	-43.90162402	7.602	0.608	5.454	0.306	0.1	1.00
481	156.96781364	-43.90021480	6.960	0.506	4.410	0.423	1.2	1.02
482	156.97022060	-43.90154100	7.857	0.609	5.046	0.256	0.5	0.76
483	156.97029604	-43.90147214	6.580	0.569	4.588	0.253	1.7	0.91
484	156.96801313	-43.90046705	6.640	0.551	4.188	0.288	1.4	0.74
485	156.96848262	-43.90042917	7.020	0.205	4.559	0.211	0.1	0.20
486	156.96929139	-43.90101675	6.060	0.163	4.394	0.161	1.1	0.22
487	156.96812472	-43.90051853	6.680	0.683	4.278	0.336	2.1	1.05

Table 5.4 continued

Table 5.4: Derived Properties of Individual Star Clusters (continued)

ID	R.A.	Decl.	t_c	σ_{t_c}	M_c	σ_{M_c}	A_V	σ_{A_V}
488	156.97339070	-43.90255927	6.680	0.586	4.093	0.254	1.6	0.77
489	156.97322084	-43.90242946	6.580	0.544	4.555	0.270	1.5	0.79
490	156.96929779	-43.90085459	7.807	0.622	4.777	0.296	0.9	0.93
491	156.97062911	-43.90154360	6.580	0.471	3.289	0.438	1.2	0.84
492	156.97035757	-43.90129821	8.057	0.785	4.869	0.313	1.2	0.83
493	156.96455609	-43.89899276	8.657	0.100	5.151	0.060	0.2	0.16
494	156.96949069	-43.90061829	7.505	0.571	4.760	0.395	0	0.96
495	156.96741871	-43.90013266	6.680	0.580	3.691	0.314	1.1	0.60
496	156.96864136	-43.90044577	6.560	0.569	4.752	0.263	2	0.92
497	156.97285043	-43.90199144	8.657	0.065	5.748	0.027	0.1	0.08
498	156.96031742	-43.89640270	8.907	0.255	6.920	0.057	2.6	0.42
499	156.95469049	-43.89421775	8.657	0.059	5.278	0.032	0	0.00
500	156.96092957	-43.89693393	8.657	0.081	5.471	0.025	0.4	0.17
501	156.96163131	-43.89729861	6.940	0.020	3.023	0.156	0.1	0.20
502	156.96931180	-43.90050443	6.480	0.312	3.733	0.447	1.4	0.68
503	156.96371593	-43.89750349	8.657	0.058	5.152	0.042	0	0.02
504	156.96701370	-43.89845763	8.557	0.135	5.395	0.050	0.4	0.22
505	156.96674967	-43.89841730	8.357	0.133	5.464	0.050	0.7	0.29
506	156.96408230	-43.89607554	8.657	0.075	5.622	0.040	0.9	0.17
507	156.97155840	-43.89897163	8.157	0.107	6.803	0.047	0.8	0.16
508	156.98917296	-43.90634238	8.207	0.110	6.670	0.048	0.7	0.16
509	156.97327428	-43.89990345	6.680	0.039	3.758	0.055	0.8	0.13
510	156.97796328	-43.90144616	8.657	0.070	6.010	0.035	0.1	0.08
511	156.96299289	-43.89525749	8.357	0.149	4.830	0.050	0.5	0.26
512	156.96555586	-43.89569185	8.657	0.097	7.596	0.047	3	0.18
513	156.96792713	-43.89680019	6.600	0.422	3.258	0.387	1.2	0.83
514	156.95800469	-43.89175885	8.157	0.105	6.783	0.047	1	0.16
515	156.96932886	-43.89592692	8.657	0.077	5.769	0.026	0.2	0.13
516	156.96665651	-43.89442613	8.057	0.120	6.143	0.062	2.4	0.16
517	156.98035517	-43.89904304	8.407	0.096	4.592	0.042	0	0.12
518	156.95638244	-43.88811673	8.357	0.316	7.038	0.056	1.4	0.56
519	156.95573319	-43.88771989	8.657	0.123	7.766	0.033	1.6	0.22
520	156.98691938	-43.89969763	8.657	0.097	7.652	0.046	0.7	0.18
521	156.98081187	-43.89755219	8.657	0.103	8.460	0.046	4.5	0.19
522	156.98099552	-43.89722382	8.657	0.071	8.547	0.046	1.3	0.15
523	156.96665709	-43.89163681	8.807	0.213	6.183	0.053	0.7	0.35
524	156.95679011	-43.88720663	8.657	0.106	6.830	0.046	1.9	0.20
525	156.98283248	-43.89724447	8.657	0.161	7.597	0.052	1.3	0.27

Table 5.4 continued

Table 5.4: Derived Properties of Individual Star Clusters (continued)

ID	R.A.	Decl.	t_c	σ_{t_c}	M_c	σ_{M_c}	A_V	σ_{A_V}
526	156.96225457	-43.88963410	8.207	0.123	5.056	0.046	0.9	0.16
527	156.99356711	-43.90150271	8.657	0.093	7.831	0.046	1.7	0.18
528	156.98024285	-43.89324242	8.657	0.069	7.948	0.026	1.3	0.15
529	156.96672789	-43.88881672	8.057	0.112	4.096	0.068	0	0.77
530	156.96694280	-43.88839385	6.120	0.153	4.092	0.061	0	0.58
531	156.98170050	-43.89432434	8.757	0.177	7.350	0.051	1.3	0.28
532	156.96669914	-43.88778218	8.057	0.052	4.362	0.044	0	9.52
533	156.98611250	-43.89466877	8.256	0.385	6.728	0.065	1.4	0.65
534	156.97911499	-43.89078392	8.607	0.130	6.894	0.047	1.8	0.22
535	156.94823582	-43.87732679	8.657	0.065	8.476	0.025	3.2	0.15
536	156.98459178	-43.89363179	7.420	0.620	3.911	0.380	0.3	1.04
537	156.94897854	-43.87702456	8.207	0.112	7.987	0.045	1	0.18
538	156.96824727	-43.88576750	8.907	0.292	7.667	0.056	0.4	0.51
539	156.97961782	-43.88997718	8.657	0.112	7.867	0.048	0.7	0.21
540	156.98102107	-43.89074402	8.607	0.113	7.730	0.047	1.7	0.21
541	156.99812300	-43.89662207	8.657	0.093	8.223	0.028	3.6	0.18
542	156.97328104	-43.88639462	8.657	0.063	5.226	0.031	0.1	0.07
543	156.97582917	-43.88763393	6.880	0.223	3.045	0.268	0	0.22
544	156.98400667	-43.89044102	8.557	0.178	6.505	0.052	1.7	0.29
545	156.98113142	-43.88656155	6.960	0.014	3.239	0.045	0	0.18
546	156.95614751	-43.87602045	8.657	0.120	7.495	0.047	0.6	0.21
547	156.97311560	-43.88392803	8.657	0.088	7.805	0.033	1.4	0.17
548	156.96503241	-43.87997958	8.607	0.139	7.740	0.049	1.5	0.23
549	157.00231613	-43.89812959	6.940	0.015	3.447	0.075	0.8	0.15
NGC 6240								
1	253.24515130	2.38534182	6.540	0.290	4.286	0.404	1.1	0.62
2	253.24047615	2.38519567	8.057	0.145	5.112	0.098	0	0.02
3	253.23333549	2.38556914	6.940	0.015	4.912	0.068	1.5	0.11
4	253.23564869	2.38686154	6.560	0.606	4.732	0.290	1.9	0.99
5	253.25668925	2.39042609	8.157	0.130	7.470	0.053	1.8	0.20
6	253.23559710	2.38910411	8.657	0.130	8.559	0.048	1.5	0.22
7	253.24812327	2.39208147	8.207	0.398	7.591	0.054	1.4	0.65
8	253.25816558	2.39357130	8.657	0.070	8.680	0.025	3.9	0.15
9	253.25082071	2.39236890	8.157	0.108	6.011	0.050	0.9	0.16
10	253.23670312	2.39162345	8.307	0.352	7.606	0.057	1.5	0.61
11	253.25728151	2.39666685	8.157	0.108	8.288	0.046	0.9	0.16

Table 5.4 continued

Table 5.4: Derived Properties of Individual Star Clusters (continued)

ID	R.A.	Decl.	t_c	σ_{t_c}	M_c	σ_{M_c}	A_V	σ_{A_V}
12	253.25470713	2.39694100	8.256	0.110	8.219	0.049	0.8	0.17
13	253.24901586	2.39492336	8.457	0.069	5.722	0.048	0	0.12
14	253.24234150	2.39393143	8.307	0.140	5.452	0.066	0.2	0.17
15	253.24963781	2.39575050	8.207	0.144	5.805	0.058	0.8	0.20
16	253.25492129	2.39713235	7.857	0.628	5.386	0.272	0.7	0.78
17	253.24314783	2.39565316	8.407	0.049	5.865	0.023	0	0.02
18	253.24251968	2.39542343	8.006	0.700	5.298	0.275	0.4	0.78
19	253.25243654	2.39729142	8.307	0.365	6.833	0.071	1.5	0.63
20	253.24436899	2.39631137	8.407	0.142	6.094	0.051	0.5	0.27
21	253.24307536	2.39640000	6.780	0.648	4.697	0.331	1.6	1.03
22	253.24322707	2.39637935	8.357	0.106	5.436	0.077	0	0.15
23	253.24312432	2.39696325	7.857	0.633	5.663	0.262	0.3	0.77
24	253.24299719	2.39670392	8.407	0.233	5.795	0.083	0.6	0.37
25	253.24329986	2.39691354	8.256	0.065	5.708	0.043	0	0.07
26	253.24262471	2.39688156	6.940	0.066	4.875	0.154	1.2	0.15
27	253.24174335	2.39680610	8.256	0.108	5.834	0.046	0.4	0.17
28	253.24336226	2.39712508	6.600	0.551	5.151	0.245	1.4	0.61
29	253.24337638	2.39720791	6.820	0.658	4.622	0.363	1.3	1.06
30	253.24757706	2.39799195	8.657	0.063	6.126	0.043	0.1	0.10
31	253.24813805	2.39833217	8.657	0.073	6.158	0.026	0.2	0.13
32	253.24689718	2.39788548	8.407	0.060	5.566	0.032	0	0.09
33	253.24237446	2.39731928	8.307	0.159	5.360	0.122	0	0.11
34	253.24259246	2.39761712	6.680	0.053	4.715	0.092	0.4	0.20
35	253.24227234	2.39755709	7.591	0.610	5.866	0.301	0.4	1.00
36	253.24257913	2.39773317	7.857	0.638	5.780	0.263	0.6	0.77
37	253.24317086	2.39811056	7.857	0.615	5.825	0.253	0.6	0.76
38	253.24907644	2.39892912	6.940	0.268	4.395	0.437	1.1	0.77
39	253.24250252	2.39843340	8.457	0.117	6.273	0.036	0.2	0.25
40	253.24159369	2.39813236	7.160	0.592	4.324	0.390	0.1	1.01
41	253.24271851	2.39828728	8.207	0.168	5.535	0.109	0	0.23
42	253.24658172	2.39953176	8.657	0.145	6.014	0.063	0.3	0.23
43	253.24266953	2.39823284	8.407	0.111	5.598	0.085	0	0.08
44	253.24153726	2.39824639	8.557	0.099	5.563	0.052	0	0.01
45	253.24267030	2.39864638	8.657	0.144	6.045	0.065	0.2	0.23
46	253.24527332	2.39986197	8.657	0.075	6.436	0.081	0.5	0.19
47	253.24764612	2.39993632	8.457	0.088	5.754	0.046	0	0.05
48	253.24248767	2.39928171	8.107	0.169	5.129	0.115	0	0.07
49	253.24562505	2.40138001	8.107	0.107	8.604	0.048	3.4	0.16

Table 5.4 continued

Table 5.4: Derived Properties of Individual Star Clusters (continued)

ID	R.A.	Decl.	t_c	σ_{t_c}	M_c	σ_{M_c}	A_V	σ_{A_V}
50	253.24230052	2.40008215	8.307	0.082	5.518	0.054	0	0.02
51	253.24781458	2.40103551	6.560	0.658	4.507	0.371	2.2	1.05
52	253.24240365	2.40004637	6.680	0.134	3.918	0.282	0.4	0.47
53	253.24651268	2.40157141	8.057	0.798	6.259	0.304	2	0.90
54	253.24198229	2.40029909	8.057	0.752	5.133	0.322	0.4	0.80
55	253.24161732	2.40070025	8.357	0.073	5.918	0.039	0	0.08
56	253.24539029	2.40194555	8.057	0.239	6.642	0.150	2.1	0.41
57	253.24533188	2.40145244	8.807	0.216	7.194	0.105	1.7	0.39
58	253.24132512	2.40104050	8.107	0.165	5.353	0.083	0.3	0.17
59	253.24309240	2.40147076	8.256	0.183	5.687	0.064	0.6	0.24
60	253.24688458	2.40208826	8.657	0.106	6.382	0.034	0.7	0.20
61	253.24418894	2.40237315	8.407	0.079	5.512	0.054	0	0.03
62	253.24944382	2.40381842	8.807	0.192	9.007	0.052	3.9	0.30
63	253.24532189	2.40345725	8.757	0.191	6.616	0.052	0.9	0.31
64	253.24618614	2.40355361	8.557	0.065	5.708	0.052	0	0.13
65	253.24579298	2.40372720	6.680	0.041	4.413	0.070	0	0.07
66	253.24584533	2.40406226	8.457	0.071	6.737	0.046	0	0.02
67	253.24726875	2.40405837	8.657	0.123	6.042	0.050	0.3	0.21
68	253.24214302	2.40366567	6.640	0.089	4.191	0.151	1	0.37
69	253.24297200	2.40423948	8.307	0.123	5.484	0.048	0.3	0.18
70	253.24767954	2.40616166	6.580	0.566	7.580	0.250	2.9	0.82
71	253.24633860	2.40526817	8.657	0.223	6.454	0.063	1.3	0.37
72	253.24691685	2.40587743	8.256	0.241	5.082	0.179	0	0.01
73	253.24731503	2.40635434	8.607	0.057	6.207	0.050	0	0.02
74	253.24773395	2.40717036	8.357	0.100	5.309	0.066	0	0.08
75	253.24506137	2.40652895	6.680	0.053	3.797	0.133	0.4	0.26
76	253.24549787	2.40688002	8.057	0.773	5.034	0.477	0	0.08
77	253.24215445	2.40756337	8.657	0.122	8.250	0.047	2.5	0.21
78	253.25007399	2.40912610	7.628	0.631	5.062	0.306	0.6	0.99
79	253.24792139	2.40923885	8.107	0.112	5.613	0.050	0.4	0.16
80	253.24896894	2.41431070	8.057	0.115	8.189	0.048	1.2	0.16
81	253.23769922	2.41262272	8.657	0.122	7.578	0.043	2.9	0.22
82	253.23343459	2.41236471	7.260	0.506	5.636	0.409	1.8	1.03
83	253.23527375	2.41266781	8.507	0.214	7.324	0.056	1.8	0.35
84	253.24402929	2.41529519	8.807	0.071	9.217	0.046	5	0.09
85	253.25304715	2.41962069	8.407	0.289	8.238	0.056	1.5	0.51
86	253.24731039	2.42039366	6.940	0.149	4.115	0.186	0	0.09
87	253.23219293	2.41474032	6.740	0.275	4.013	0.391	0.6	0.60

Table 5.4 continued

Table 5.4: Derived Properties of Individual Star Clusters (continued)

ID	R.A.	Decl.	t_c	σ_{t_c}	M_c	σ_{M_c}	A_V	σ_{A_V}
NGC 7469 - Center								
1	345.81639435	8.87467401	8.657	0.085	5.940	0.042	0.4	0.18
2	345.81512694	8.87171669	6.720	0.181	5.030	0.312	0.4	0.56
3	345.81589433	8.87320648	8.207	0.095	6.220	0.046	0.1	0.11
4	345.81526622	8.87184595	6.680	0.251	4.204	0.395	0.4	0.57
5	345.81580281	8.87360089	6.940	0.014	5.722	0.060	1.5	0.10
6	345.81555728	8.87481639	8.657	0.101	6.262	0.047	0.9	0.20
7	345.81562581	8.87384424	8.256	0.108	7.453	0.051	0.5	0.17
8	345.81449665	8.87292069	6.680	0.052	5.179	0.069	1.1	0.17
9	345.81529776	8.87481599	8.057	0.133	6.146	0.069	0.8	0.18
10	345.81542053	8.87422320	7.907	0.654	7.556	0.267	0.3	0.77
11	345.81529029	8.87412003	6.940	0.014	5.942	0.114	0.6	0.17
12	345.81521742	8.87360080	7.544	0.609	6.619	0.391	0	0.97
13	345.81501397	8.87341535	6.560	0.574	6.944	0.282	1.7	0.97
14	345.81540620	8.87380879	6.680	0.038	6.199	0.087	0.9	0.17
15	345.81425826	8.87261055	8.057	0.689	5.085	0.390	0	0.26
16	345.81465936	8.87387687	7.505	0.665	7.159	0.359	0.4	1.03
17	345.81403150	8.87253350	6.680	0.044	4.229	0.123	1	0.23
18	345.81497817	8.87429340	8.157	0.117	7.484	0.047	1.2	0.17
19	345.81323222	8.87290411	7.957	0.660	4.895	0.293	0	0.72
NGC 7469 - Extended Galaxy and Companion								
1	345.82127974	8.86185301	6.900	0.400	3.641	0.441	0	0.83
2	345.82458059	8.87213263	8.157	0.171	6.144	0.068	1.8	0.25
3	345.82136277	8.87153169	8.107	0.251	4.753	0.169	0.1	0.16
4	345.82071313	8.87128493	6.680	0.034	4.428	0.044	0.7	0.12
5	345.81985348	8.87039921	8.107	0.087	4.982	0.043	0	0.03
6	345.81899980	8.86894326	7.628	0.553	4.780	0.277	0	0.89
7	345.81605889	8.86463471	8.907	0.266	6.210	0.057	0.5	0.45
8	345.82263255	8.87599218	8.057	0.035	4.897	0.034	0	0.38
9	345.82059002	8.87341911	8.657	0.129	5.561	0.048	0.2	0.20
10	345.83094757	8.89157504	7.720	0.568	5.112	0.245	0.7	0.78
11	345.81791879	8.87292105	6.960	0.543	4.578	0.453	1.5	1.07
12	345.81834083	8.87272819	8.357	0.355	5.057	0.182	0.2	0.43
13	345.81746896	8.87188429	7.591	0.622	4.933	0.328	0.1	1.01
14	345.81797084	8.87195213	8.256	0.110	5.012	0.078	0	0.13

Table 5.4 continued

Table 5.4: Derived Properties of Individual Star Clusters (continued)

ID	R.A.	Decl.	t_c	σ_{t_c}	M_c	σ_{M_c}	A_V	σ_{A_V}
15	345.81790192	8.87213663	6.880	0.378	4.305	0.379	0.2	0.71
16	345.81782421	8.87240132	7.677	0.566	5.452	0.245	0.2	0.83
17	345.81658439	8.87143448	6.660	0.077	4.922	0.102	1	0.28
18	345.81763209	8.87244769	6.600	0.076	4.745	0.100	0.8	0.27
19	345.81784046	8.87216780	7.857	0.645	4.618	0.363	0	0.99
20	345.81748732	8.87257458	6.880	0.377	4.625	0.362	0.3	0.74
21	345.81799200	8.87315871	8.006	0.670	5.343	0.233	0.3	0.63
22	345.81824251	8.87343495	7.602	0.644	4.497	0.332	0.2	1.02
23	345.81756258	8.87256198	6.680	0.066	4.662	0.086	0.9	0.22
24	345.81616187	8.87066640	8.057	0.702	4.936	0.283	0.2	0.70
25	345.81561668	8.87036233	6.740	0.281	4.783	0.396	0.5	0.62
26	345.82151171	8.87919991	7.907	0.667	5.367	0.283	1.1	0.77
27	345.81663248	8.87192775	8.057	0.109	5.436	0.080	0	0.15
28	345.81605291	8.87153156	6.680	0.054	5.259	0.067	1.1	0.18
29	345.81624452	8.87115586	6.680	0.058	3.837	0.160	1	0.33
30	345.81591648	8.87123671	8.357	0.154	5.418	0.051	0.5	0.26
31	345.81779786	8.87478598	8.157	0.108	7.359	0.048	0.6	0.15
32	345.81389542	8.86802732	6.800	0.641	4.026	0.387	0.7	0.93
33	345.81818930	8.87480198	6.760	0.303	3.745	0.415	0.5	0.65
34	345.81542489	8.87146317	8.407	0.041	5.360	0.024	0	0.09
35	345.81720549	8.87439761	6.680	0.526	4.384	0.274	1.2	0.65
36	345.81451573	8.87059950	8.157	0.098	5.448	0.052	0.2	0.14
37	345.82032124	8.87946683	6.680	0.037	4.399	0.046	0.9	0.12
38	345.81490060	8.87177466	7.857	0.603	6.023	0.266	0	0.63
39	345.82804443	8.89174830	6.640	0.701	4.542	0.352	2.6	1.02
40	345.81668866	8.87471520	8.057	0.740	5.312	0.305	0.9	0.80
41	345.82788424	8.89236374	6.680	0.603	5.295	0.249	2.2	0.76
42	345.81663315	8.87543820	8.307	0.040	5.262	0.022	0	0.41
43	345.81637017	8.87579040	8.507	0.148	5.745	0.050	0.3	0.24
44	345.82868823	8.89516136	8.657	0.085	8.114	0.046	2.6	0.17
45	345.81627362	8.87529555	6.060	0.138	3.767	0.075	0	0.04
46	345.81966350	8.88067717	6.820	0.661	3.668	0.372	0.8	0.99
47	345.81337578	8.87122047	8.157	0.111	4.978	0.059	0	0.00
48	345.81922002	8.88045533	8.057	0.719	5.111	0.306	0.2	0.82
49	345.82691552	8.89270419	8.157	0.409	6.071	0.084	1.9	0.58
50	345.81606196	8.87570077	6.880	0.360	3.523	0.432	0.1	0.78
51	345.81397845	8.87239419	6.060	0.133	3.639	0.053	0	0.13
52	345.81358337	8.87258522	7.720	0.568	5.183	0.238	0.5	0.78

Table 5.4 continued

Table 5.4: Derived Properties of Individual Star Clusters (continued)

ID	R.A.	Decl.	t_c	σ_{t_c}	M_c	σ_{M_c}	A_V	σ_{A_V}
53	345.81217509	8.87017694	6.680	0.044	4.006	0.069	1	0.17
54	345.81841431	8.88036093	8.256	0.120	4.874	0.073	0	0.09
55	345.81277269	8.87260910	8.057	0.136	5.368	0.068	0.2	0.16
56	345.81304149	8.87281417	6.940	0.183	4.125	0.237	0.7	0.19
57	345.82583966	8.89319707	8.307	0.350	5.875	0.093	1.2	0.58
58	345.82606528	8.89338389	6.700	0.694	5.054	0.357	2.6	1.07
59	345.81267568	8.87281898	7.000	0.546	3.764	0.411	0.1	1.01
60	345.82589987	8.89334665	7.907	0.641	5.437	0.269	0.5	0.84
61	345.82576380	8.89367168	6.480	0.659	5.776	0.361	2	1.02
62	345.81254270	8.87410346	8.307	0.108	6.488	0.041	0.6	0.19
63	345.81266940	8.87387270	8.357	0.045	5.546	0.035	0	0.01
64	345.81297757	8.87441692	8.157	0.751	5.141	0.217	0.6	0.67
65	345.81686209	8.88046063	8.207	0.146	5.018	0.067	0.2	0.18
66	345.81664870	8.88037867	8.407	0.042	5.520	0.022	0	0.08
67	345.82498232	8.89379140	7.857	0.611	6.244	0.255	1.1	0.76
68	345.81212646	8.87393880	8.607	0.063	5.679	0.051	0	0.06
69	345.82013939	8.88602752	6.660	0.084	3.997	0.126	1	0.32
70	345.82532167	8.89392735	8.607	0.051	5.692	0.056	0	0.50
71	345.81262593	8.87469727	6.640	0.573	4.858	0.239	1.7	0.76
72	345.81239187	8.87469379	8.057	0.674	4.658	0.345	0	0.81
73	345.81262875	8.87527968	6.680	0.586	4.418	0.317	1.2	0.63
74	345.81211465	8.87535733	8.307	0.090	5.635	0.034	0.2	0.14
75	345.81265306	8.87559530	6.720	0.620	4.528	0.291	1.7	0.98
76	345.81222525	8.87482786	8.107	0.149	4.842	0.097	0	0.06
77	345.82479232	8.89522774	7.957	0.670	5.732	0.269	0.8	0.77
78	345.82386790	8.89364815	8.657	0.212	6.349	0.092	1.7	0.38
79	345.81204080	8.87568083	8.006	0.720	5.050	0.291	0.4	0.79
80	345.81212343	8.87574249	7.653	0.571	4.994	0.264	0.2	0.94
81	345.82407346	8.89450861	6.580	0.567	5.838	0.244	2.2	0.80
82	345.81371017	8.87843456	8.256	0.084	5.474	0.046	0	0.13
83	345.81187374	8.87571663	7.260	0.579	5.007	0.414	1.5	1.05
84	345.81207108	8.87611163	8.657	0.069	5.700	0.047	0	0.03
85	345.81331884	8.87855391	7.857	0.608	5.447	0.252	0.5	0.76
86	345.81310214	8.87758368	6.680	0.048	4.159	0.063	0.6	0.16
87	345.81220739	8.87609897	7.505	0.649	4.452	0.903	0.6	1.07
88	345.82443880	8.89518904	8.006	0.745	5.361	0.308	1.2	0.82
89	345.81384776	8.87893102	8.057	0.690	4.613	0.369	0	0.58
90	345.81331973	8.87833037	6.680	0.041	4.040	0.053	0.4	0.14

Table 5.4 continued

Table 5.4: Derived Properties of Individual Star Clusters (continued)

ID	R.A.	Decl.	t_c	σ_{t_c}	M_c	σ_{M_c}	A_V	σ_{A_V}
91	345.81275406	8.87762213	6.560	0.570	4.691	0.262	1.9	0.93
92	345.81200599	8.87646099	8.307	0.069	5.252	0.057	0	0.01
93	345.81188495	8.87647528	6.680	0.581	4.325	0.254	1.5	0.77
94	345.82328688	8.89400694	7.677	0.567	6.337	0.247	2.3	0.86
95	345.81391936	8.87956957	8.057	0.698	4.658	0.360	0	0.20
96	345.82311887	8.89408455	7.807	0.592	5.335	0.262	0.2	0.77
97	345.82353986	8.89483045	6.880	0.626	5.399	0.394	3.2	1.06
98	345.82351866	8.89577736	8.657	0.078	5.780	0.027	0.3	0.16
99	345.81451040	8.88162578	8.256	0.785	4.775	0.311	0.1	0.75
100	345.81486023	8.88206402	6.960	0.027	3.604	0.054	0	0.08
101	345.82246419	8.89495527	8.157	0.131	6.480	0.055	1.7	0.20
102	345.81440054	8.88161058	6.880	0.609	3.739	0.380	0.4	0.99
103	345.82143958	8.89341357	6.840	0.661	4.249	0.365	0.8	1.03
104	345.81352710	8.88167826	8.357	0.114	5.046	0.055	0.1	0.14
105	345.81141857	8.87880605	8.057	0.042	5.012	0.036	0	0.31
106	345.82111830	8.89379307	7.907	0.630	5.034	0.276	0	0.56
107	345.81164886	8.87954013	6.680	0.042	3.968	0.064	0.9	0.16
108	345.81117971	8.87887204	7.907	0.633	4.861	0.275	0	0.69
109	345.82189055	8.89570739	6.720	0.566	5.927	0.249	2.1	0.82
110	345.82101349	8.89388683	6.680	0.580	4.151	0.286	1.2	0.61
111	345.81173093	8.87992485	6.680	0.062	3.970	0.097	0.9	0.23
112	345.82182092	8.89566349	7.907	0.657	6.302	0.266	1.1	0.78
113	345.82192679	8.89586901	6.940	0.558	4.408	0.430	0.9	1.06
114	345.81228068	8.88153816	6.500	0.214	4.560	0.241	1	0.17
115	345.82154644	8.89576605	8.607	0.094	5.834	0.057	0	0.08
116	345.81172247	8.88049312	8.207	0.114	4.966	0.064	0	0.07
117	345.81204213	8.88134741	7.857	0.593	4.945	0.267	0	0.69
118	345.81475305	8.88522858	6.660	0.151	4.003	0.295	1.2	0.54
119	345.82171686	8.89619604	6.900	0.407	4.442	0.405	0	0.80
120	345.82152673	8.89617838	6.880	0.573	4.858	0.373	0.4	0.93
121	345.81200931	8.88190571	7.200	0.588	4.396	0.409	0.9	1.07
122	345.82156418	8.89625251	6.980	0.464	4.616	0.387	1	1.00
123	345.82027037	8.89446942	6.680	0.067	4.371	0.083	0.9	0.22
124	345.81742292	8.89112015	6.920	0.015	5.775	0.031	0	0.42
125	345.81137008	8.88229775	6.680	0.056	4.916	0.061	0.6	0.18
126	345.81183950	8.88247159	8.057	0.093	5.090	0.061	0	0.01
127	345.81093239	8.88177534	6.680	0.060	4.270	0.070	0.7	0.19
128	345.80736417	8.87701731	7.440	0.637	5.092	0.373	0.5	1.03

Table 5.4 continued

Table 5.4: Derived Properties of Individual Star Clusters (continued)

ID	R.A.	Decl.	t_c	σ_{t_c}	M_c	σ_{M_c}	A_V	σ_{A_V}
129	345.80731325	8.87663674	8.006	0.690	5.074	0.289	0.5	0.77
130	345.80975043	8.88025052	6.600	0.069	3.832	0.108	0.2	0.25
131	345.80749197	8.87711233	6.560	0.211	3.531	0.293	0.1	0.27
132	345.80733030	8.87690597	6.600	0.302	3.786	0.406	1.1	0.72
133	345.80706838	8.87684858	8.006	0.714	5.232	0.303	0.9	0.77
134	345.80710899	8.87750647	6.400	0.647	4.833	0.377	2.8	1.04
135	345.81843717	8.89512076	6.680	0.043	3.342	0.082	0	0.13
136	345.80781459	8.87917751	6.540	0.667	4.025	0.347	1.8	0.98
137	345.81087078	8.88417250	6.680	0.044	4.129	0.057	1.1	0.14
138	345.81783654	8.89589327	6.140	0.377	4.858	0.374	1.9	0.77
139	345.80976998	8.88420889	8.657	0.080	7.368	0.039	3.1	0.17
140	345.80486403	8.87793776	6.660	0.075	4.268	0.094	1.1	0.26
141	345.81682879	8.89709615	6.060	0.183	4.641	0.146	1	0.10
142	345.81613516	8.89750027	6.540	0.224	4.406	0.299	0.7	0.30
143	345.81623084	8.89751488	6.740	0.224	3.977	0.346	0.8	0.63
144	345.81579688	8.89783028	8.057	0.672	4.756	0.293	0	0.17
145	345.81143349	8.89265260	7.556	0.663	5.002	0.354	1	1.02
146	345.81424789	8.89966892	6.060	0.167	4.416	0.115	1.2	0.10

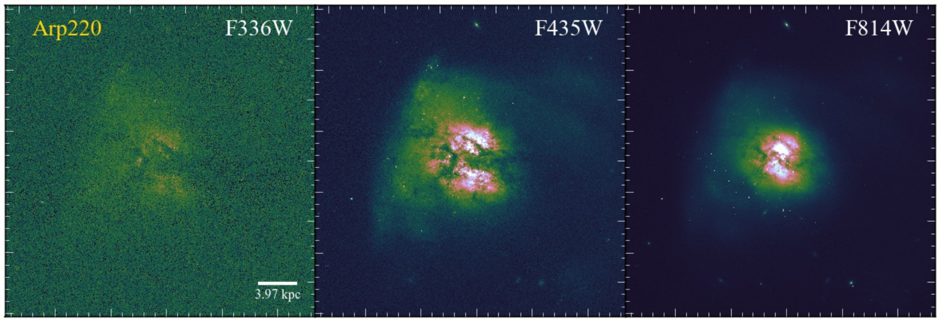

Figure 5.12: Same as Figure 5.1

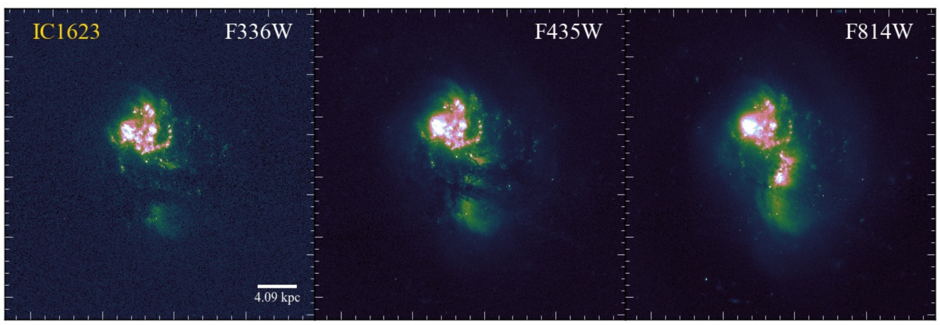

Figure 5.13: Same as Figure 5.1

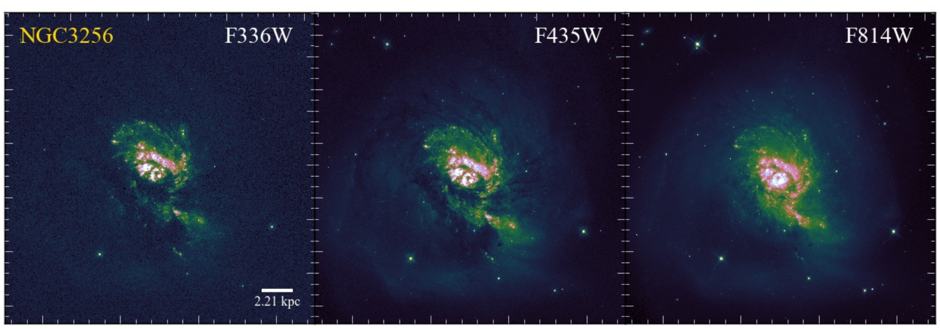

Figure 5.14: Same as Figure 5.1

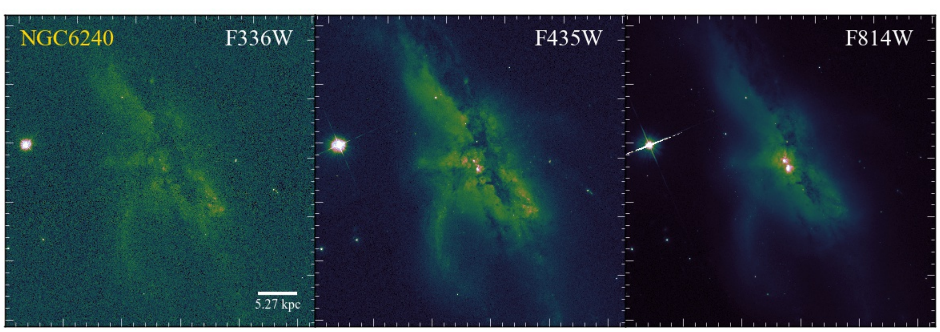

Figure 5.15: Same as Figure 5.1

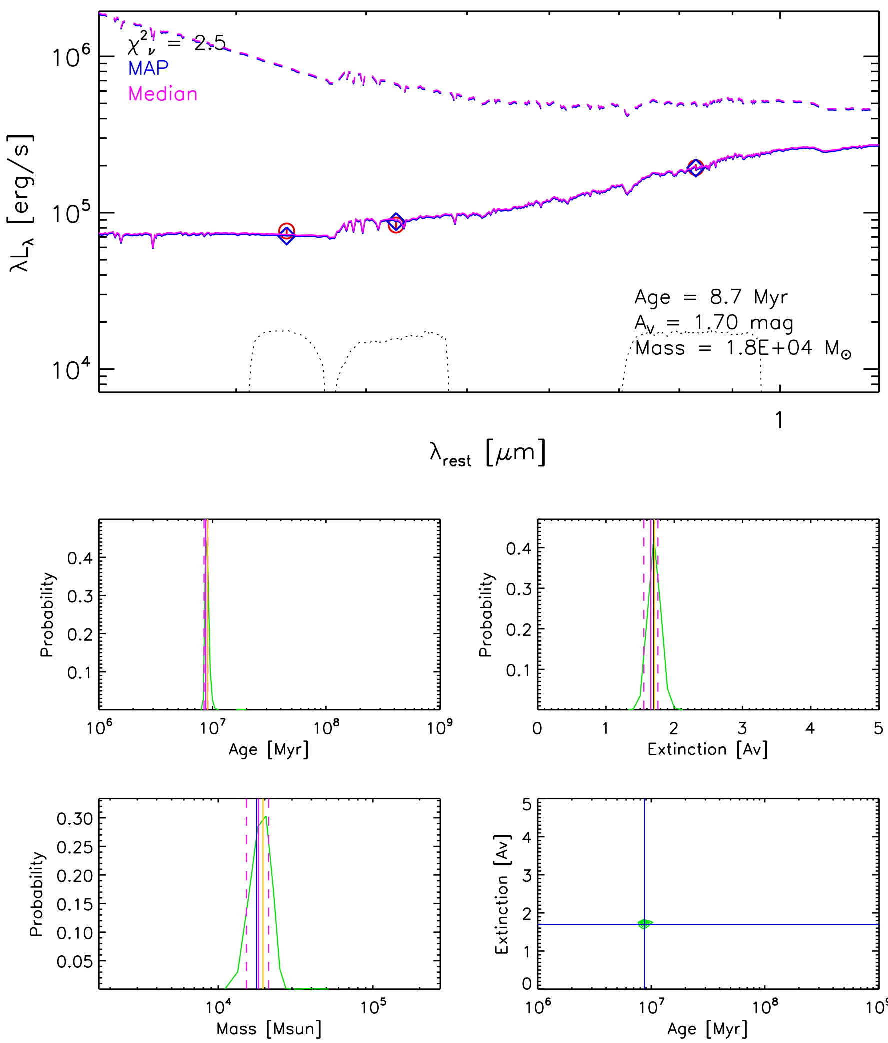

Figure 5.16: Example SED and resulting model fit for a cluster with an age of 8.7 Myr (blue) with an extinction of $A_V = 1.7$ mags. The dashed lines correspond to the unextincted SEDs for each model. In the example SEDs provided, this combination of filters can be used to uniquely solve for cluster age relative to the F140LP observations used in our previous study. Finally, in the lower Panels the resulting 1σ errors for the age, mass, and extinction are shown as dashed pink lines superimposed over the marginalized posterior distribution for each parameter (green curves).

Chapter 6

Conclusion

A fundamental goal in extragalactic astrophysics is to provide a robust observational foundation for understanding the causal physics behind star formation in galaxies. However, a purely theoretical understanding of the complex phase transitions of the ISM, and the recycling of material into stars and back as galaxies evolve, has yet to be fully developed. To build a complete theory of the role of star and cluster formation in galaxy evolution requires accurate measurements of the current (i.e., few Myr) star formation rate and available gas content within galaxies over a range of physical scales ($\sim 10 - 1000$pc) and star-forming environments. This thesis presented a study of star formation in a sample of luminous infrared galaxies (LIRGs) and normal star-forming galaxies in the local ($z < 0.1$) Universe. The study made use of Hubble Space Telescope (HST), Spitzer Space Telescope and Jansky Very Large Array (VLA) data. The analysis of these data sets has allowed us to make fundamental conclusions about the nature and (in the case of star clusters) fate of star formation in a broad range of star-forming environments.

In Chapter 2 we present the results of a HST ACS/HRC FUV, ACS/WFC optical study into the cluster populations of a sample of 22 LIRGs in the Great Observatories

All-Sky LIRG Survey (GOALS). Through integrated broadband photometry we have derived ages and masses for a total of 484 star clusters contained within the central (30"x30") of these systems, allowing us to examine the properties of star clusters found in the extreme environments of LIRGs relative to lower luminosity star-forming galaxies in the local Universe. We find that by adopting a Bruzual & Charlot simple stellar population (SSP) model, the age distribution of clusters declines as $dN/d\tau = \tau^{-0.9+/-0.3}$, consistent with the age distribution derived for the Antennae Galaxies, and interpreted as evidence for rapid cluster disruption occurring in the strong tidal fields of merging galaxies. The large number of $10^6 M_\odot$ young clusters identified in the sample also suggests that LIRGs are capable of producing more high-mass clusters than what is observed to date in any lower luminosity star-forming galaxy in the local Universe.

In Chapter 3 we presented the first results of a high-resolution 3, 15, and 33 GHz VLA imaging survey of LIRGs in GOALS. From the full sample of 68 galaxies, we have selected 25 LIRGs that show resolved extended emission at sufficient sensitivity to image individual regions of star-formation activity beyond the nucleus. We have made extinction-free measurements of the luminosities and spectral indices for a total of 48 individual star-forming regions identified as having de-projected galactocentric radii (r_G) that lie outside the 13.2μm core of the galaxy. The median $3-33$ GHz spectral index and 33 GHz thermal fraction measured for these "extranuclear" regions is -0.51 ± 0.13 and $65 \pm 11\%$ respectively. These values are consistent with measurements made on matched spatial scales in normal star-forming galaxies, and suggests that these regions are more heavily-dominated by thermal free-free emission relative to the centers of local ULIRGs. Further, we find that the median star-formation rate derived for these regions is $\sim 1 M_\odot$ yr^{-1}, and when we place them on the sub-galactic star-forming main sequence of galaxies (SFMS), we find they are offset from their host galaxies' globally-averaged specific star-formation rates (sSFRs). We conclude that while nuclear starburst activity drives LIRGs above the SFMS, extranuclear star-formation still proceeds in a more extreme fashion relative to what is seen in local spiral galaxies.

In Chapter 4, we presented 3, 15, and 33 GHz VLA imaging towards galaxy nuclei and extranuclear star-forming regions in normal star-forming galaxies as part of the Star Formation in Radio Survey (SFRS). With $3-33$ GHz radio spectra, we measured the spectral indices and corresponding thermal free-free emission fractions for a sample of 335 discrete regions having significant detections in at least two radio bands. We find that the median thermal fraction at 33 GHz is $92 \pm 0.8\%$ with a median absolute deviation of 11%. Limiting the sample to 238 sources that are confidently identified as star-forming regions, and not affected by potential AGN contamination (i.e., excluding star-forming regions with $r_{\rm G} \leq 250$ pc), results in a median thermal fraction of $93 \pm 0.8\%$ with a median absolute deviation of 10%. Together, these results confirm that free-free emission dominates the radio spectra of star-forming regions on size scales up to ∼500 pc in normal star-forming galaxies. We additionally find a factor of ∼1.6 increase in the scatter of the measured spectral index and thermal fraction distributions as a function of decreasing galactocentric radius. This trend is likely reflective of the continuous star-formation activity occurring in the galaxy centers, resulting a larger contribution of diffuse nonthermal emission relative to star-forming regions in the disk.

Finally, in Chapter 5 we presented the results of a HST WFC3 NUV and ACS/WFC optical study into the cluster populations of a sample of 5 LIRGs in GOALS. The filter selection and the depth of the WFC3 NUV images provide an improved age estimate and wider field of view, respectively, over our prior (Chapter 2) study. Through integrated broadband photometry we have derived ages and masses for a total of

1027 star clusters contained throughout the disks of these systems. Differences in the slope of the observed cluster age distribution between inner- ($dN/d\tau = \tau^{-1.1+/-0.2}$) and outer-disk ($dN/d\tau = \tau^{-0.6+/-0.3}$) clusters provides some of the clearest evidence to date of location-dependent cluster evolution in LIRGs. Thus, not only does rapid cluster disruption appear to be ubiquitous in LIRGs at all galactocentric radii, the magnitude of the differences between inner- and outer-disk cluster disruption are amplified relative to observations of nearby normal star-forming galaxies. Given this, it appears that the differences in the observed cluster distribution function (CMF) observed for SSCs in our LIRG samples relative to normal star-forming galaxies is caused primarily by a rapid cluster disruption, which flattens the observed CMF relative to an underlying initial cluster mass function.

References

Adamo, A. 2015, arXiv e-prints, arXiv:1511.05567

Adamo, A., & Bastian, N. 2015, arXiv e-prints, arXiv:1511.08212

Adamo, A., Ryon, J. E., Messa, M., et al. 2017, The Astrophysical Journal, 841, 131

Alonso-Herrero, A., Engelbracht, C. W., Rieke, M. J., Rieke, G. H., & Quillen, A. C. 2001, The Astrophysical Journal, 546, 952

Anders, P., Bissantz, N., Boysen, L., de Grijs, R., & Fritze-v. Alvensleben, U. 2007, Monthly Notices of the Royal Astronomical Society, 377, 91

Aniano, G., Draine, B. T., Gordon, K. D., & Sandstrom, K. 2011, Publications of the Astronomical Society of the Pacific, 123, 1218

Armus, L., Mazzarella, J. M., Evans, A. S., et al. 2009, Publications of the Astronomical Society of the Pacific, 121, 559

Axford, W. I., Leer, E., & Skadron, G. 1977, in International Cosmic Ray Conference, Vol. 11, International Cosmic Ray Conference, 132

Baade, W., & Minkowski, R. 1954, The Astrophysical Journal, 119, 215

Barcos-Muñoz, L., Leroy, A. K., Evans, A. S., et al. 2015, The Astrophysical Journal, 799, 10

—. 2017, The Astrophysical Journal, 843, 117

Barnes, J. E. 2004, Monthly Notices of the Royal Astronomical Society, 350, 798

Barnes, J. E., & Hernquist, L. 1992, Annual Review of Astronomy and Astrophysics, 30, 705

Bastian, N. 2008a, Astronomical Society of the Pacific Conference Series, Vol. 390, Dynamical Masses of Young Star Clusters: Constraints on the Stellar IMF and Star Formation Efficiency, ed. J. H. Knapen, T. J. Mahoney, & A. Vazdekis, 47

—. 2008b, Monthly Notices of the Royal Astronomical Society, 390, 759

Bastian, N. 2016, in EAS Publications Series, Vol. 80-81, EAS Publications Series, 5–37

Bastian, N., Emsellem, E., Kissler-Patig, M., & Maraston, C. 2006, Astronomy and Astrophysics, 445, 471

Bastian, N., & Lardo, C. 2018, Annual Review of Astronomy and Astrophysics, 56, 83

Bastian, N., Schweizer, F., Goudfrooij, P., Larsen, S. S., & Kissler-Patig, M. 2013, Monthly Notices of the Royal Astronomical Society, 431, 1252

Bastian, N., & Silva-Villa, E. 2013, Monthly Notices of the Royal Astronomical Society, 431, L122

Bastian, N., Adamo, A., Gieles, M., et al. 2012, Monthly Notices of the Royal Astronomical Society, 419, 2606

Bell, A. R. 1978a, Monthly Notices of the Royal Astronomical Society, 182, 147

—. 1978b, Monthly Notices of the Royal Astronomical Society, 182, 443

Bell, E. F. 2003, The Astrophysical Journal, 586, 794

Bertelli, G., Bressan, A., Chiosi, C., Fagotto, F., & Nasi, E. 1994, Astronomy and Astrophysics Supplement Series, 106, 275

Bertin, E., & Arnouts, S. 1996, Astronomy and Astrophysics Supplement Series, 117, 393

Bik, A., Östlin, G., Hayes, M., et al. 2015, Astronomy and Astrophysics, 576, L13

Bik, A., Östlin, G., Menacho, V., et al. 2018, Astronomy and Astrophysics, 619, A131

Blandford, R. D., & Ostriker, J. P. 1978, The Astrophysical Journal Letters, 221, L29

Bolton, J. G., Stanley, G. J., & Slee, O. B. 1949, Nature, 164, 101

Bot, C., Ysard, N., Paradis, D., et al. 2010, Astronomy and Astrophysics, 523, A20

Bouwens, R. J., Illingworth, G. D., Oesch, P. A., et al. 2015, The Astrophysical Journal, 811, 140

Bradley, T. R., Knapen, J. H., Beckman, J. E., & Folkes, S. L. 2006, Astronomy and Astrophysics, 459, L13

Bruzual, G., & Charlot, S. 2003, Monthly Notices of the Royal Astronomical Society, 344, 1000

Calzetti, D., Armus, L., Bohlin, R. C., et al. 2000, The Astrophysical Journal, 533, 682

Calzetti, D., Kinney, A. L., & Storchi-Bergmann, T. 1994, The Astrophysical Journal, 429, 582

Calzetti, D., Meurer, G. R., Bohlin, R. C., et al. 1997, The Astronomical Journal, 114, 1834

Cameron, E., Carollo, C. M., Oesch, P., et al. 2010, Monthly Notices of the Royal Astronomical Society, 409, 346

Cano-Díaz, M., Sánchez, S. F., Zibetti, S., et al. 2016, The Astrophysical Journal Letters, 821, L26

Cassata, P., Cimatti, A., Franceschini, A., et al. 2005, Monthly Notices of the Royal Astronomical Society, 357, 903

Chandar, R., Fall, S. M., & Whitmore, B. C. 2010, The Astrophysical Journal, 711, 1263

—. 2015, The Astrophysical Journal, 810, 1

Chien, L. 2010, Astronomical Society of the Pacific Conference Series, Vol. 423, Star Formation History in Merging Galaxies, ed. B. Smith, J. Higdon, S. Higdon, & N. Bastian, 197

Chien, L.-H., Barnes, J. E., Kewley, L. J., & Chambers, K. C. 2007, The Astrophysical Journal Letters, 660, L105

Chu, J. K., Sanders, D. B., Larson, K. L., et al. 2017, The Astrophysical Journal Supplement Series, 229, 25

Ciardullo, R., Feldmeier, J. J., Jacoby, G. H., et al. 2002, The Astrophysical Journal, 577, 31

Clemens, M. S., Scaife, A., Vega, O., & Bressan, A. 2010, Monthly Notices of the Royal Astronomical Society, 405, 887

Clemens, M. S., Vega, O., Bressan, A., et al. 2008, Astronomy and Astrophysics, 477, 95

Condon, J. J. 1992, Annual Review of Astronomy and Astrophysics, 30, 575

Condon, J. J., Huang, Z.-P., Yin, Q. F., & Thuan, T. X. 1991, The Astrophysical Journal, 378, 65

Condon, J. J., & Yin, Q. F. 1990, The Astrophysical Journal, 357, 97

Condon, J. J., Cotton, W. D., Fomalont, E. B., et al. 2012, The Astrophysical Journal, 758, 23

Conway, J. E., Cornwell, T. J., & Wilkinson, P. N. 1990, Monthly Notices of the Royal Astronomical Society, 246, 490

Cook, D. O., Dale, D. A., Lee, J. C., et al. 2016, Monthly Notices of the Royal Astronomical Society, 462, 3766

Cornwell, T. J. 2008, IEEE Journal of Selected Topics in Signal Processing, 2, 793

Daddi, E., Dickinson, M., Morrison, G., et al. 2007, The Astrophysical Journal, 670, 156

Daddi, E., Elbaz, D., Walter, F., et al. 2010, The Astrophysical Journal Letters, 714, L118

Dale, D. A., Giovanelli, R., Haynes, M. P., et al. 1997, The Astronomical Journal, 114, 455

Dale, D. A., Gil de Paz, A., Gordon, K. D., et al. 2007, The Astrophysical Journal, 655, 863

Dale, D. A., Cohen, S. A., Johnson, L. C., et al. 2009, The Astrophysical Journal, 703, 517

Dale, J. E., Ercolano, B., & Bonnell, I. A. 2015, Monthly Notices of the Royal Astronomical Society, 451, 987

Dametto, N. Z., Riffel, R., Pastoriza, M. G., et al. 2014, Monthly Notices of the Royal Astronomical Society, 443, 1754

de Grijs, R., Anders, P., Bastian, N., et al. 2003, Monthly Notices of the Royal Astronomical Society, 343, 1285

de Jong, T., Klein, U., Wielebinski, R., & Wunderlich, E. 1985, Astronomy and Astrophysics, 147, L6

de Vaucouleurs, G., de Vaucouleurs, A., Corwin, Herold G., J., et al. 1991

Díaz-Santos, T., Charmandaris, V., Armus, L., et al. 2010, The Astrophysical Journal, 723, 993

Díaz-Santos, T., Charmandaris, V., Armus, L., et al. 2011, The Astrophysical Journal, 741, 32

Díaz-Santos, T., Armus, L., Charmandaris, V., et al. 2013, The Astrophysical Journal, 774, 68

—. 2017, The Astrophysical Journal, 846, 32

Dickinson, C., Ali-Haïmoud, Y., Barr, A., et al. 2018, , 80, 1

Downes, D., & Solomon, P. M. 1998, The Astrophysical Journal, 507, 615

Draine, B. T. 2003, Annual Review of Astronomy and Astrophysics, 41, 241

Draine, B. T., & Lazarian, A. 1998, The Astrophysical Journal, 508, 157

Driver, S. P., Fernández-Soto, A., Couch, W. J., et al. 1998, The Astrophysical Journal Letters, 496, L93

Driver, S. P., Windhorst, R. A., Ostrander, E. J., et al. 1995, The Astrophysical Journal Letters, 449, L23

Elbaz, D., Dickinson, M., Hwang, H. S., et al. 2011, Astronomy and Astrophysics, 533, A119

Elmegreen, B. G. 1993, The Astrophysical Journal Letters, 419, L29

Elmegreen, B. G., Elmegreen, D. M., & Hirst, A. C. 2004, The Astrophysical Journal, 612, 191

Elmegreen, D. M., Elmegreen, B. G., Marcus, M. T., et al. 2009, The Astrophysical Journal, 701, 306

Elmegreen, D. M., Elmegreen, B. G., Rubin, D. S., & Schaffer, M. A. 2005, The Astrophysical Journal, 631, 85

Engelbracht, C. W., Rieke, G. H., Gordon, K. D., et al. 2008, The Astrophysical Journal, 678, 804

Erickson, W. C. 1957, The Astrophysical Journal, 126, 480

Evans, A. S., Vavilkin, T., Pizagno, J., et al. 2008, The Astrophysical Journal Letters, 675, L69

Fall, S. M., & Chandar, R. 2012, The Astrophysical Journal, 752, 96

Fall, S. M., Chandar, R., & Whitmore, B. C. 2005, The Astrophysical Journal Letters, 631, L133

—. 2009, The Astrophysical Journal, 704, 453

Fitzpatrick, E. L. 1999, Publications of the Astronomical Society of the Pacific, 111, 63

Foreman-Mackey, D., Hogg, D. W., Lang, D., & Goodman, J. 2013, Publications of the Astronomical Society of the Pacific, 125, 306

Fouesneau, M., Lançon, A., Chandar, R., & Whitmore, B. C. 2012, The Astrophysical Journal, 750, 60

Freedman, W. L., Madore, B. F., Gibson, B. K., et al. 2001, The Astrophysical Journal, 553, 47

García-Marín, M., Colina, L., Arribas, S., Alonso-Herrero, A., & Mediavilla, E. 2006, The Astrophysical Journal, 650, 850

Gieles, M. 2009, , 324, 299

Gieles, M., Bastian, N., Lamers, H. J. G. L. M., & Mout, J. N. 2005, Astronomy and Astrophysics, 441, 949

Glazebrook, K., Ellis, R., Santiago, B., & Griffiths, R. 1995, Monthly Notices of the Royal Astronomical Society, 275, L19

Gnedin, O. Y., & Ostriker, J. P. 1997, The Astrophysical Journal, 474, 223

Goddard, Q. E., Bastian, N., & Kennicutt, R. C. 2010, Monthly Notices of the Royal Astronomical Society, 405, 857

González Delgado, R. M., Cerviño, M., Martins, L. P., Leitherer, C., & Hauschildt, P. H. 2005, Monthly Notices of the Royal Astronomical Society, 357, 945

González-Martín, O., Masegosa, J., Márquez, I., & Guainazzi, M. 2009, The Astrophysical Journal, 704, 1570

Gratton, R. G., Villanova, S., Lucatello, S., et al. 2012, Astronomy and Astrophysics, 544, A12

Green, D. A. 2011, Bulletin of the Astronomical Society of India, 39, 289

Guillochon, J., Parrent, J., Kelley, L. Z., & Margutti, R. 2017, The Astrophysical Journal, 835, 64

Haan, S., Armus, L., Surace, J. A., et al. 2013, Monthly Notices of the Royal Astronomical Society, 434, 1264

Hall, C., Courteau, S., Jarrett, T., et al. 2018, The Astrophysical Journal, 865, 154

Hanbury Brown, R., & Hazard, C. 1952, Nature, 170, 364

Harris, D. E. 1962, The Astrophysical Journal, 135, 661

Harris, J., & Zaritsky, D. 2009, The Astronomical Journal, 138, 1243

Heesen, V., Brinks, E., Leroy, A. K., et al. 2014, The Astronomical Journal, 147, 103

Helou, G., Soifer, B. T., & Rowan-Robinson, M. 1985, The Astrophysical Journal Letters, 298, L7

Helou, G., Roussel, H., Appleton, P., et al. 2004, The Astrophysical Journal Supplement Series, 154, 253

Hensley, B., Murphy, E., & Staguhn, J. 2015, Monthly Notices of the Royal Astronomical Society, 449, 809

Herenz, E. C., Hayes, M., Papaderos, P., et al. 2017, Astronomy and Astrophysics, 606, L11

Hibbard, J. E., & van Gorkom, J. H. 1996, The Astronomical Journal, 111, 655

Hogg, D. W., Bovy, J., & Lang, D. 2010, arXiv e-prints, arXiv:1008.4686

Hollyhead, K., Adamo, A., Bastian, N., Gieles, M., & Ryon, J. E. 2016, Monthly Notices of the Royal Astronomical Society, 460, 2087

Homeier, N., Gallagher, J. S., I., & Pasquali, A. 2002, Astronomy and Astrophysics, 391, 857

Hopkins, P. F., Cox, T. J., Hernquist, L., et al. 2013, Monthly Notices of the Royal Astronomical Society, 430, 1901

Hopkins, P. F., Hernquist, L., Cox, T. J., et al. 2006, The Astrophysical Journal Supplement Series, 163, 1

Hopkins, P. F., Hernquist, L., Cox, T. J., & Kereš, D. 2008, The Astrophysical Journal Supplement Series, 175, 356

Howard, C. S., Pudritz, R. E., Harris, W. E., & Klessen, R. S. 2018, Monthly Notices of the Royal Astronomical Society, 475, 3121

Howell, J. H., Armus, L., Mazzarella, J. M., et al. 2010, The Astrophysical Journal, 715, 572

Hughes, A., Staveley-Smith, L., Kim, S., Wolleben, M., & Filipović, M. 2007, Monthly Notices of the Royal Astronomical Society, 382, 543

Humphreys, R. M., & Davidson, K. 1979, The Astrophysical Journal, 232, 409

Hunt, L. K., Giovanardi, C., & Helou, G. 2002, Astronomy and Astrophysics, 394, 873

Hunter, D. A., Elmegreen, B. G., Dupuy, T. J., & Mortonson, M. 2003, The Astronomical Journal, 126, 1836

Im, M., Griffiths, R. E., Naim, A., et al. 1999, The Astrophysical Journal, 510, 82

Inami, H., Armus, L., Surace, J. A., et al. 2010, The Astronomical Journal, 140, 63

Iwasawa, K., Sanders, D. B., Teng, S. H., et al. 2011, Astronomy and Astrophysics, 529, A106

Jarrett, T. H., Chester, T., Cutri, R., et al. 2000, The Astronomical Journal, 119, 2498

Jarrett, T. H., Chester, T., Cutri, R., Schneider, S. E., & Huchra, J. P. 2003, The Astronomical Journal, 125, 525

Johansson, L., & Bergvall, N. 1988, Astronomy and Astrophysics, 192, 81

Johnson, K. E. 2004, Astronomical Society of the Pacific Conference Series, Vol. 322, Extragalactic Ultracompact HII Regions: Probing the Birth Environments of Super Star Clusters, ed. H. J. G. L. M. Lamers, L. J. Smith, & A. Nota, 339

Johnson, K. E., Indebetouw, R., & Pisano, D. J. 2003, The Astronomical Journal, 126, 101

Johnson, K. E., & Kobulnicky, H. A. 2003, The Astrophysical Journal, 597, 923

Johnson, K. E., Kobulnicky, H. A., Massey, P., & Conti, P. S. 2001, The Astrophysical Journal, 559, 864

Johnson, L. C., Seth, A. C., Dalcanton, J. J., et al. 2016, The Astrophysical Journal, 827, 33

—. 2017, The Astrophysical Journal, 839, 78

Karl, S. J., Fall, S. M., & Naab, T. 2011, The Astrophysical Journal, 734, 11

Kennicutt, R. C., & Evans, N. J. 2012, Annual Review of Astronomy and Astrophysics, 50, 531

Kennicutt, R. C., Hao, C., Calzetti, D., et al. 2009, The Astrophysical Journal, 703, 1672

Kennicutt, R. C., Calzetti, D., Aniano, G., et al. 2011, Publications of the Astronomical Society of the Pacific, 123, 1347

Kennicutt, Jr., R. C., Armus, L., Bendo, G., et al. 2003, Publications of the Astronomical Society of the Pacific, 115, 928

Kewley, L. J., Rupke, D., Zahid, H. J., Geller, M. J., & Barton, E. J. 2010, The Astrophysical Journal Letters, 721, L48

Kim, D.-C., Evans, A. S., Vavilkin, T., et al. 2013a, The Astrophysical Journal, 768, 102

Kim, J.-h., Krumholz, M. R., Wise, J. H., et al. 2013b, The Astrophysical Journal, 775, 109

King, I. R. 1966, The Astronomical Journal, 71, 64

Klein, U., Wielebinski, R., & Beck, R. 1984, Astronomy and Astrophysics, 135, 213

Klein, U., Wielebinski, R., & Morsi, H. W. 1988, Astronomy and Astrophysics, 190, 41

Ko, H. C., & Kraus, J. D. 1955, Nature, 176, 221

Kobulnicky, H. A., & Johnson, K. E. 1999, The Astrophysical Journal, 527, 154

Koyama, K., Petre, R., Gotthelf, E. V., et al. 1995, Nature, 378, 255

Kruijssen, J. M. D. 2012, Monthly Notices of the Royal Astronomical Society, 426, 3008

Kruijssen, J. M. D. 2014, in The Labyrinth of Star Formation, Vol. 36, 437

—. 2015, Monthly Notices of the Royal Astronomical Society, 454, 1658

Kruijssen, J. M. D., Pelupessy, F. I., Lamers, H. J. G. L. M., et al. 2012, Monthly Notices of the Royal Astronomical Society, 421, 1927

Krymskii, G. F. 1977, Akademiia Nauk SSSR Doklady, 234, 1306

Kurczynski, P., Gawiser, E., Acquaviva, V., et al. 2016, The Astrophysical Journal Letters, 820, L1

Lacki, B. C., & Thompson, T. A. 2010, The Astrophysical Journal, 717, 196

Lacki, B. C., Thompson, T. A., & Quataert, E. 2010, The Astrophysical Journal, 717, 1

Lada, C. J., & Lada, E. A. 2003, Annual Review of Astronomy and Astrophysics, 41, 57

Lahén, N., Naab, T., Johansson, P. H., et al. 2020, The Astrophysical Journal, 891, 2

Lamers, H. J. G. L. M., Gieles, M., & Portegies Zwart, S. F. 2005, Astronomy and Astrophysics, 429, 173

Larsen, S. S. 1999, Astronomy and Astrophysics Supplement Series, 139, 393

—. 2009, Astronomy and Astrophysics, 494, 539

—. 2010, Philosophical Transactions of the Royal Society of London Series A, 368, 867

Larsen, S. S., & Richtler, T. 2000, Astronomy and Astrophysics, 354, 836

—. 2006, Astronomy and Astrophysics, 459, 103

Larson, K. L., Díaz-Santos, T., Armus, L., et al. 2020, The Astrophysical Journal, 888, 92

Leech, K. J., Penston, M. V., Terlevich, R., et al. 1989, Monthly Notices of the Royal Astronomical Society, 240, 349

Leger, A., & Puget, J. L. 1984, Astronomy and Astrophysics, 500, 279

Leitherer, C., Schaerer, D., Goldader, J. D., et al. 1999, The Astrophysical Journal Supplement Series, 123, 3

Lerche, I. 1980, Astronomy and Astrophysics, 85, 141

Leroy, A. K., Evans, A. S., Momjian, E., et al. 2011, The Astrophysical Journal Letters, 739, L25

Leroy, A. K., Bigiel, F., de Blok, W. J. G., et al. 2012, The Astronomical Journal, 144, 3

Li, H., Gnedin, O. Y., Gnedin, N. Y., et al. 2017, The Astrophysical Journal, 834, 69

Linden, S. T., Evans, A. S., Rich, J., et al. 2017, The Astrophysical Journal, 843, 91

Linden, S. T., Song, Y., Evans, A. S., et al. 2019, The Astrophysical Journal, 881, 70

Lisenfeld, U., Voelk, H. J., & Xu, C. 1996, Astronomy and Astrophysics, 314, 745

Liu, G., Calzetti, D., Kennicutt, Robert C., J., et al. 2013, The Astrophysical Journal, 772, 27

Livermore, R. C., Jones, T. A., Richard, J., et al. 2015, Monthly Notices of the Royal Astronomical Society, 450, 1812

Lonsdale Persson, C. J., & Helou, G. 1987, The Astrophysical Journal, 314, 513

Lotz, J. M., Primack, J., & Madau, P. 2004, The Astronomical Journal, 128, 163

Lu, N., Helou, G., Werner, M. W., et al. 2003, The Astrophysical Journal, 588, 199

Lutz, D. 1992, Astronomy and Astrophysics, 259, 462

Ma, J., Caucal, P., Noterdaeme, P., et al. 2015, Monthly Notices of the Royal Astronomical Society, 454, 1751

Magdis, G. E., Rigopoulou, D., Helou, G., et al. 2013, Astronomy and Astrophysics, 558, A136

Magnelli, B., Elbaz, D., Chary, R. R., et al. 2011, Astronomy and Astrophysics, 528, A35+

Magnelli, B., Popesso, P., Berta, S., et al. 2013, Astronomy and Astrophysics, 553, A132

Maíz Apellániz, J., Úbeda, L., Walborn, N. R., & Nelan, E. P. 2005, arXiv e-prints, astro

Maji, M., Zhu, Q., Li, Y., et al. 2017, The Astrophysical Journal, 844, 108

Maoz, D., Barth, A. J., Ho, L. C., Sternberg, A., & Filippenko, A. V. 2001, The Astronomical Journal, 121, 3048

Maragkoudakis, A., Zezas, A., Ashby, M. L. N., & Willner, S. P. 2017, Monthly Notices of the Royal Astronomical Society, 466, 1192

Maraston, C., Bastian, N., Saglia, R. P., et al. 2004, Astronomy and Astrophysics, 416, 467

Martin, J. M., Bottinelli, L., Dennefeld, M., & Gouguenheim, L. 1991, Astronomy and Astrophysics, 245, 393

Mazzarella, J. M., Iwasawa, K., Vavilkin, T., et al. 2012, The Astronomical Journal, 144, 125

McMullin, J. P., Waters, B., Schiebel, D., Young, W., & Golap, K. 2007, in Astronomical Society of the Pacific Conference Series, Vol. 376, Astronomical Data Analysis Software and Systems XVI, ed. R. A. Shaw, F. Hill, & D. J. Bell, 127

Medling, A. M., Cortese, L., Croom, S. M., et al. 2018, Monthly Notices of the Royal Astronomical Society, 475, 5194

Meier, D. S., Turner, J. L., & Beck, S. C. 2002, The Astronomical Journal, 124, 877

Messa, M., Adamo, A., Calzetti, D., et al. 2018, Monthly Notices of the Royal Astronomical Society, 477, 1683

Meurer, G. R., Heckman, T. M., Leitherer, C., et al. 1995, The Astronomical Journal, 110, 2665

Miller, B. W., Whitmore, B. C., Schweizer, F., & Fall, S. M. 1997, The Astronomical Journal, 114, 2381

Miralles-Caballero, D., Colina, L., & Arribas, S. 2012, Astronomy and Astrophysics, 538, A61

Modica, F., Vavilkin, T., Evans, A. S., et al. 2012, The Astronomical Journal, 143, 16

Momjian, E., Romney, J. D., Carilli, C. L., & Troland, T. H. 2003, The Astrophysical Journal, 597, 809

Moreno, J., Torrey, P., Ellison, S. L., et al. 2015, Monthly Notices of the Royal Astronomical Society, 448, 1107

Moustakas, J., Kennicutt, Jr., R. C., Tremonti, C. A., et al. 2010, The Astrophysical Journal Supplement Series, 190, 233

Mulia, A. J., Chandar, R., & Whitmore, B. C. 2015, The Astrophysical Journal, 805, 99

Murphy, E. J., Chary, R.-R., Dickinson, M., et al. 2011a, The Astrophysical Journal, 732, 126

Murphy, E. J., Dong, D., Momjian, E., et al. 2018a, The Astrophysical Journal Supplement Series, 234, 24

Murphy, E. J., Linden, S. T., Dong, D., et al. 2018b, The Astrophysical Journal, 862, 20

Murphy, E. J., Porter, T. A., Moskalenko, I. V., Helou, G., & Strong, A. W. 2012a, The Astrophysical Journal, 750, 126

Murphy, E. J., Stierwalt, S., Armus, L., Condon, J. J., & Evans, A. S. 2013, The Astrophysical Journal, 768, 2

Murphy, E. J., Braun, R., Helou, G., et al. 2006a, The Astrophysical Journal, 638, 157

Murphy, E. J., Helou, G., Braun, R., et al. 2006b, The Astrophysical Journal Letters, 651, L111

Murphy, E. J., Helou, G., Condon, J. J., et al. 2010, The Astrophysical Journal Letters, 709, L108

Murphy, E. J., Condon, J. J., Schinnerer, E., et al. 2011b, The Astrophysical Journal, 737, 67

Murphy, E. J., Bremseth, J., Mason, B. S., et al. 2012b, The Astrophysical Journal, 761, 97

Niklas, S., & Beck, R. 1997, Astronomy and Astrophysics, 320, 54

Noeske, K. G., Weiner, B. J., Faber, S. M., et al. 2007, The Astrophysical Journal Letters, 660, L43

Oey, M. S., Herrera, C. N., Silich, S., et al. 2017, The Astrophysical Journal Letters, 849, L1

Overzier, R. A., Heckman, T. M., Schiminovich, D., et al. 2010, The Astrophysical Journal, 710, 979

Pasquali, A., de Grijs, R., & Gallagher, J. S. 2003, Monthly Notices of the Royal Astronomical Society, 345, 161

Paturel, G., Petit, C., Prugniel, P., et al. 2003, Astronomy and Astrophysics, 412, 45

Peel, M. W., Dickinson, C., Davies, R. D., Clements, D. L., & Beswick, R. J. 2011, Monthly Notices of the Royal Astronomical Society, 416, L99

Perley, R. A., & Butler, B. J. 2013, The Astrophysical Journal Supplement Series, 204, 19

Portegies Zwart, S. F., McMillan, S. L. W., & Gieles, M. 2010, Annual Review of Astronomy and Astrophysics, 48, 431

Privon, G. C., Barnes, J. E., Evans, A. S., et al. 2013, The Astrophysical Journal, 771, 120

Privon, G. C., Aalto, S., Falstad, N., et al. 2017, The Astrophysical Journal, 835, 213

Querejeta, M., Meidt, S. E., Schinnerer, E., et al. 2015, The Astrophysical Journal Supplement Series, 219, 5

Rabidoux, K., Pisano, D. J., Kepley, A. A., Johnson, K. E., & Balser, D. S. 2014, The Astrophysical Journal, 780, 19

Randriamanakoto, Z., Väisänen, P., Ryder, S. D., & Ranaivomanana, P. 2019, Monthly Notices of the Royal Astronomical Society, 482, 2530

Rau, U., & Cornwell, T. J. 2011, Astronomy and Astrophysics, 532, A71

Reach, W. T., Megeath, S. T., Cohen, M., et al. 2005, Publications of the Astronomical Society of the Pacific, 117, 978

Reines, A. E., Johnson, K. E., & Hunt, L. K. 2008, The Astronomical Journal, 136, 1415

Relaño, M., Lisenfeld, U., Pérez-González, P. G., Vílchez, J. M., & Battaner, E. 2007, The Astrophysical Journal Letters, 667, L141

Rich, J. A., Torrey, P., Kewley, L. J., Dopita, M. A., & Rupke, D. S. N. 2012, The Astrophysical Journal, 753, 5

Rupke, D. S. N., Veilleux, S., & Baker, A. J. 2008, The Astrophysical Journal, 674, 172

Salpeter, E. E. 1955, The Astrophysical Journal, 121, 161

Sanders, D. B., Mazzarella, J. M., Kim, D.-C., Surace, J. A., & Soifer, B. T. 2003, The Astronomical Journal, 126, 1607

Sanders, D. B., & Mirabel, I. F. 1996, Annual Review of Astronomy and Astrophysics, 34, 749

Sault, R. J., & Wieringa, M. H. 1994, Astronomy and Astrophysics Supplement Series, 108, 585

Schlafly, E. F., & Finkbeiner, D. P. 2011, The Astrophysical Journal, 737, 103

Schlegel, D. J., Finkbeiner, D. P., & Davis, M. 1998, The Astrophysical Journal, 500, 525

Schweizer, F. 1978, The Astrophysical Journal, 220, 98

Schweizer, F. 2000, in Astronomy, physics and chemistry of $H^{+}{}_{3}$, Vol. 358, 2063

Schweizer, F., Miller, B. W., Whitmore, B. C., & Fall, S. M. 1996, The Astronomical Journal, 112, 1839

Schweizer, F., & Seitzer, P. 1998, The Astronomical Journal, 116, 2206

Scoville, N., Murchikova, L., Walter, F., et al. 2017, The Astrophysical Journal, 836, 66

Seibert, M. 2007, The Galex Large Galaxy Atlas (glga), GALEX Proposal, ,

Shivvers, I., Filippenko, A. V., Silverman, J. M., et al. 2019, Monthly Notices of the Royal Astronomical Society, 482, 1545

Shklovskii, I. S. 1953, , 30, 15

Silva-Villa, E., Adamo, A., Bastian, N., Fouesneau, M., & Zackrisson, E. 2014, Monthly Notices of the Royal Astronomical Society, 440, L116

Sirianni, M., Jee, M. J., Benítez, N., et al. 2005, Publications of the Astronomical Society of the Pacific, 117, 1049

Skibba, R. A., Engelbracht, C. W., Dale, D., et al. 2011, The Astrophysical Journal, 738, 89

Smith, B. J., Giroux, M. L., Struck, C., & Hancock, M. 2010, The Astronomical Journal, 139, 1212

Smith, B. J., Soria, R., Struck, C., et al. 2014, The Astronomical Journal, 147, 60

Smith, B. J., Zaragoza-Cardiel, J., Struck, C., Olmsted, S., & Jones, K. 2016, The Astronomical Journal, 151, 63

Soifer, B. T., Neugebauer, G., Matthews, K., et al. 2000, The Astronomical Journal, 119, 509

Speagle, J. S., Steinhardt, C. L., Capak, P. L., & Silverman, J. D. 2014, The Astrophysical Journal Supplement Series, 214, 15

Spergel, D. N., Bean, R., Doré, O., et al. 2007, The Astrophysical Journal Supplement Series, 170, 377

Stierwalt, S., Armus, L., Surace, J. A., et al. 2013, arXiv:1302.4477, arXiv:1302.4477

Stierwalt, S., Armus, L., Charmandaris, V., et al. 2014, The Astrophysical Journal, 790, 124

Struck, C., & Smith, B. J. 2012, Monthly Notices of the Royal Astronomical Society, 422, 2444

Tabatabaei, F. S., Schinnerer, E., Murphy, E. J., et al. 2013, Astronomy and Astrophysics, 552, A19

Tabatabaei, F. S., Schinnerer, E., Krause, M., et al. 2017, The Astrophysical Journal, 836, 185

Tisanić, K., Smolčić, V., Delhaize, J., et al. 2019, Astronomy and Astrophysics, 621, A139

Torres-Albà, N., Iwasawa, K., Díaz-Santos, T., et al. 2018, Astronomy and Astrophysics, 620, A140

Turner, J. L., Beck, S. C., & Ho, P. T. P. 2000a, The Astrophysical Journal Letters, 532, L109

—. 2000b, The Astrophysical Journal Letters, 532, L109

U, V., Sanders, D. B., Mazzarella, J. M., et al. 2012, The Astrophysical Journal Supplement Series, 203, 9

van den Bergh, S., Abraham, R. G., Ellis, R. S., et al. 1996, The Astronomical Journal, 112, 359

van den Broek, A. C., van Driel, W., de Jong, T., et al. 1991, Astronomy and Astrophysics Supplement Series, 91, 61

van Driel, W., Gao, Y., & Monnier-Ragaigne, D. 2001, Astronomy and Astrophysics, 368, 64

Vavilkin, T. 2011, PhD thesis, Department of Physics & Astronomy, Stony Brook University, Stony Brook, NY 11794-3800, USA

Weingartner, J. C., & Draine, B. T. 2001, The Astrophysical Journal, 548, 296

Westcott, J., Brinks, E., Hindson, L., Beswick, R., & Heesen, V. 2018, Monthly Notices of the Royal Astronomical Society, 475, 5116

Whitmore, B. C., Chandar, R., Bowers, A. S., et al. 2014, The Astronomical Journal, 147, 78

Whitmore, B. C., Chandar, R., & Fall, S. M. 2007, The Astronomical Journal, 133, 1067

Whitmore, B. C., Miller, B. W., Schweizer, F., & Fall, S. M. 1997, The Astronomical Journal, 114, 1797

Whitmore, B. C., & Schweizer, F. 1995, The Astronomical Journal, 109, 960

Whitmore, B. C., & Zhang, Q. 2002, The Astronomical Journal, 124, 1418

Whitmore, B. C., Zhang, Q., Leitherer, C., et al. 1999, The Astronomical Journal, 118, 1551

Whitmore, B. C., Chandar, R., Schweizer, F., et al. 2010, The Astronomical Journal, 140, 75

Wilson, C. D., Harris, W. E., Longden, R., & Scoville, N. Z. 2006, The Astrophysical Journal, 641, 763

Wu, Y., Helou, G., Armus, L., et al. 2010, The Astrophysical Journal, 723, 895

Wuyts, S., Förster Schreiber, N. M., Nelson, E. J., et al. 2013, The Astrophysical Journal, 779, 135

Xu, C. K., Cao, C., Lu, N., et al. 2014, The Astrophysical Journal, 787, 48

—. 2015, The Astrophysical Journal, 799, 11

Yun, M. S., Reddy, N. A., & Condon, J. J. 2001, The Astrophysical Journal, 554, 803

Zepf, S. E., Ashman, K. M., English, J., Freeman, K. C., & Sharples, R. M. 1999, The Astronomical Journal, 118, 752

Zhang, Q., & Fall, S. M. 1999, The Astrophysical Journal Letters, 527, L81